Multivalent Redox-Active Molecular Assemblies

PHILIP ANTHONY HOPE

Durham University
Department of Chemistry

Multivalent Redox-Active Molecular Assemblies

Philip Anthony Hope

A Thesis Submitted for the Degree of Doctor of Philosophy

August 2021

Dedicated to my Friends and Family

Table of Contents

Abstract

Although supramolecular strategies can be successful in mediating the assembly of π-surfaces, these assemblies rely solely on typically weak, non-covalent interactions. A macromolecular approach (Chapter 1) provides an opportunity for even greater control as covalent scaffolds can reinforce and/or direct the assembly of π-surfaces whilst also taking advantage of non-covalent interactions that drive self-assembly. Mediating π-assembly *via* macromolecular scaffolds can provide access to, i) robust materials owing to the macromolecular sizes, ii) molecules that have high fidelity, iii) materials that have hierarchical ordering (i.e., multiple levels of assembly) and iv) materials that have advanced functioning. The arrangement of functional aromatic units in three-dimensional (3D) space is relatively unexplored, whereas one-dimensional (1D) assembly of said units has been a target for supramolecular chemists over the last 30 years. This thesis will discuss these two macromolecular strategies towards guiding π-aromatic units: firstly, using a fullerene hexakis-adduct scaffold (Chapters 2 and 3) that pre-organises and positions the pendant aromatic units in 3D space, and secondly, using a polypeptide (Chapter 5) that capitalises on β-sheet forming peptide sequences and an artificial β-turn to organise embedded functional units into 1D assemblies. In both strategies, the macromolecular scaffolds facilitate a structure of order that organises photo- and/or redox-active units that can be investigated for their fundamental optoelectronic properties as well as potential applications (Chapter 4) such as in photovoltaics, photocatalysis and semiconductor devices. The macromolecular strategy in controlling π-assembly is still in its nascency, however, this thesis demonstrates the untapped potential bestowed upon multivalent, redox-active macromolecular materials.

Declaration

The scientific work described in this Thesis was carried out in the Chemistry Department at Durham University between May 2017 and August 2021. Unless otherwise stated, it is the work of the author and has not been submitted in whole or in support of an application for another degree or qualification at this or any other University or institute of learning.

Signed: P. Hope

Date: 11th August 2021

Conferences Attended and Presentations Given

1. International Symposium on Suprabiomolecular Systems, (online). 2021| **Attended.**
2. RSC Organic Division Online Symposium (UK, online). 2020 | **Oral Presentation.**
3. The Soft Matter Showcase (UK, online). 2020 | **Poster Presentation.**
4. RSC Macrocyclic and Supramolecular Chemistry Meeting, Canterbury (UK). 2019 | **Poster Presentation.**
5. Early Stage Career Researcher Meeting: RSC Macrocyclic and Supramolecular Chemistry Meeting, Lincoln (UK). 2019 | **Poster Presentation.**
6. International Symposium on Suprabiomolecular Systems 2019, Barcelona (Spain). 2019 | **Poster Presentation.**
7. NEPIC Technology Showcase Event 2019 Oral presentation, Middlesbrough (UK). 2019 | **Oral Presentation.**
8. Functional Organic Materials Symposium, Durham (UK). 2019 | **Attended.**
9. Durham University Chemistry Postgraduate Gala, Durham (UK). 2019 | **Oral Presentation.**
10. SUPR@LYON, Lyon (France). 2018 | **Poster Presentation.**
11. Soft Matter Showcase, Edinburgh (UK). 2018 | **Poster Presentation.**
12. MULTI-APP Marie Curie Network Symposium, Padova (Italy). 2018 | **Poster Presentation.**
13. Chemical Nanoscience Chem, Newcastle (UK). 2018 | **Poster Presentation.**
14. Durham University Chemistry Postgraduate Gala, Durham (UK). 2018 | **Poster Presentation.**

15. Early Stage Career Researcher Meeting: RSC Macrocyclic and Supramolecular Chemistry Meeting. Southampton (UK). 2017 | **Poster Presentation.**

16. European Symposium on Organic Reactivity, Durham (UK). 2017 | **Poster Presentation.**

17. International Symposium on Macrocyclic and Supramolecular Chemistry, Cambridge (United Kingdom). 2017 | **Poster Presentation.**

Awards, Grants and Scholarships

1. **St Mary's College, Principal's Grant —** Funding of £100 to attend an international chemistry conference (online). February 2021.

2. **The Soft Matter Showcase 2020 — Poster Prize** | **'**Multivalent Fullerene Adducts for Functional Materials', poster prize (£100) for best overall poster presentation. July 2020.

3. **Royal Society of Chemistry Travel Bursary (Intercontinental)** | Grant of £400 to disseminate research at an international chemistry conference. Dec 2019.

4. **Royal Society of Chemistry Travel Bursary (Continental)** | Grant of £280 to disseminate research at supramolecular chemistry conference, Supr@Lyon. Dec 2018.

5. **Chemical Nanoscience Symposium — Poster Prize** | 'Macromolecular Assembly of π-Embedded Synthetic Polypeptides', poster prize winner (£150) for best overall poster presentation. Mar 2018.

Acknowledgements

Don't worry about a thing, 'cause every little thing gonna be all right

Alyssa-Jennifer Avestro. I will be forever grateful for the opportunities you have provided me over the last five years. I had absolutely no idea how much I would learn, and how many skills I would develop, at the beginning of my PhD and it is down to your perseverance that I have become a better chemist, writer and mentor. Whatever lies ahead of me, I am grateful for the foundations that were made in the Avestro Group. Thank you, Alyssa, for the guidance, memories and friends that I've made along the way as a member of the group.

Paul McGonigal. Thank you for all your support during the last five years and for always making things run as smoothly as possible. I have really enjoyed being a part of the McGonigal Group and I have learned so much under your guidance. Thank you, Paul.

Durham University and Funding Agencies. I am grateful to Durham University for providing me endless resources and to the EPSRC and RSC for funding my research over the past five years.

Collaborators. Krishnamurthy Munusamy, Marc Etherington, David Palacios-Gomez, Victor Chechik, Mark Wilson, Chris Groves. Thank you all for the numerous meetings, whether it has been for experiment planning or data interrogation a lot of insights have been made that without your help would not have advanced the research. I look forward to seeing our published work in the not too distant future.

Academic Staff. Matt Kitching and James Walton for pints and science talk.

Technical Staff. Thank you to the following members of staff responsible for their technical support: Juan A Aguilar Malavia for running 2D NMR measurements. David Parker and Peter Stokes for proving high-resolution accurate mass support. Dmitry Yufit for X-ray crystallography. Aileen Congreve for UV-Vis, PL and FTIR measurement help. Chunyong Li for fsTA measurements.

Key Players. I would never have reached the end of the PhD if it hadn't been for Andrew Turley, Kasid Khan and Aisha Bismillah. Throughout the last few years you have all been instrumental in getting me to the finish line, which has finally arrived! The memories we have made are genuinely fantastic and I look forward to making many more, in whichever corner of the globe we happen to be in at the time. Thank you to the lads in Sunderland for keeping me sane during the toughest times as well—work hard, play hard.

Friends of CG233. A massive shout out to everyone in the office (past and present) for maintaining a great atmosphere in and out of the lab that keeps everyone sane. Without this, no one would get to the end of the day, never mind the PhD! There are too many people to list, but if I've gone for a pint with you, count yourself as instrumental to this Thesis.

Friends of York. It has been a pleasure to work with all of you and I have enjoyed our discussions throughout the last couple of years. Thank you for helping to get me over the finish line. A special thank you to Pavan and Suresh, the two best postdocs of all time.

My family. Thank you for putting up with me these last five years. I know it has been annoying and difficult having me finish late and sacrificing plans last minute because of my work. There really is nothing I can do to return the support you have given me during my PhD and I dedicate my Thesis to all of you (including you two, Bosun and Daisy). Time to put away the camping table in the front room. Cheers!

Abbreviations

Ac	Acetyl
AFM	Atomic force micrscopy
ASAP	Atmospheric solids analysis probe
BM	Burstein–Moss
BODIPY	Dipyrrometheneboron difluoride
Bu	Butyl
CD	Circular Dichorism
COSY	^{1}H-^{1}H Correlation Spectroscopy
CT	Charge Transfer
CV	Cyclic Voltammetry
DFT	Density functional theory
DAN	1,5-Dialkoxynaphthalene
DBU	1,8-Diazabicyclo[5.4.0]undec-7-ene
DCC	N,N'-Dicyclohexylcarbodiimide
DCU	dicyclohexylurea
DIPEA	N,N-Diisopropylethylamine
DLS	Dynamic light scattering
DMB	dimethoxybenzyl
DMF	Dimethylformamide
DMSO	Dimethyl sulfoxide
DNA	Deoxyribonucleic acid
DRS	Diffuse reflectance spectroscopy
EDC•HCl	1-(3-Dimethylaminopropyl)-3-ethylcarbodiimide hydrochloride
ENDOR	Electron nuclear double resonance
EPR	Electron paramagnetic resonance
ESI-MS	Electrospray Ionisation Mass Spectrometry
Et	Ethyl
EtOH	Ethanol
EtOAc	Ethyl acetate
eV	Electron volt
FA	Fullerene-acceptor
FRET	Förster resonance energy transfer
FTIR	Fourier-transform infrared spectroscopy
GPC	Gel Permeation Chromatography
HATU	1-[Bis(dimethylamino)methylene]-1H-1,2,3-triazolo[4,5-b]pyridinium 3-oxide hexafluorophosphate
HFIP	Hexafluoroisopropanol
HMBC	Heteronuclear Multiple Bond Correlation
HOBt	Hydroxybenzotriazole
HOMO	Highest Occupied Molecular Orbital
HSQC	Heteronuclear Single Quantum Coherence
LUMO	Lowest Unoccupied Molecular Orbital

MALDI-TOF	Matrix-assisted laser desorption ionization time-of-flight
MeOH	Methanol
Me	Methyl
MCH	Methylcyclohexane
MD	Molecular Dynamics
MIM	Mechanically Interlocked Molecule
Mn	Number average molecular weight
Mw	Weight average molecular weight
NDI	Naphthalene diimide
NFA	Non-fullerene acceptor
NIR	Near-infrared
NOESY	Nuclear Overhauser Effect Spectroscopy
o-DCB	1,2-Dichlorobenzene
OED	Organic electronic device
OTTLE	Optically Transparent Thin Layer Electrochemical
PCBM	Phenyl-C61-butyric acid methyl ester
PDI	Perylene diimide
PSC	Perovskite solar cell
PXRD	Powder X-ray diffraction
PYSCHE	Pure Shift Yielded by Chirp Excitation
RESP	Restrained electrostatic potential atomic partial
RNA	Ribonucleic acid
SCLC	Space-charge-limited current
SEM	Scanning electron microscopy
SOMO	Singly occupied molecular orbital
STM	Scanning tunneling microscopy
TBAF	Tetrabutylammonium fluoride
TBF	Tetrabenzofluorene
TBTA	Tris(benzyltriazolylmethyl)amine
TEM	Transmission electron microscopy
TFA	Trifluoroacetic acid
THF	Tetrahydrofuran
TLC	Thin-layer chromatography
TMS	Trimethylsilyl
UV–Vis	Ultraviolet–visible
VT	Variable-temperature
XRD	X-ray diffraction

Note: conventional abbreviations for units, physical quantities and stereochemical terms are not included here.

Chapter 1| Macromolecular Strategies for π-Assembly in Organic Molecules

Synopsis

Aromatic π-assemblies can be observed, monitored and exploited for emergent applications in organic photo- and redox-active materials. It is still a challenge to guide π-interactions in functional aromatic assemblies that have desirable orbital overlap as the orientation of interacting π-surfaces is largely dictated by electrostatic interactions. Supramolecular materials are a popular approach towards guiding π-assembly, however, limitations such as their sensitivity to pH, moisture, temperature, stress and propensity to aggregate into electrostatically favourable orientations hamper their use in a device setting. π-Assembly using macromolecular scaffolds can help to overcome some of these issues by providing access to: i) more robust materials, ii) more reliable assembly processes, iii) materials that have hierarchical ordering, and iv) materials that have advanced functioning. This introductory chapter will first cover the fundamentals of aromatic assembly using rylene diimides as a canonical π-motif, before describing two macromolecular strategies for guiding π-assembly. The recent trends in fullerene hexakis-adduct chemistry to achieve three-dimensional (3D) aromatic assembly are explored. Following this, the ever popular peptide–π conjugate strategies and the less explored polymer π-assembling systems that hope to achieve hierarchical one-dimensional (1D) aromatic assemblies are summarised.

1.1 Aromatic π-Assembly

In supramolecular and organic materials chemistry, the assembly of π-surfaces—whether by intramolecular interactions or intermolecular multicomponent ensembles—can lead to emergent optical, electronic and electrochemical properties that are not present in the lone monomer. For example, favourable overlap of π-orbitals lowers the overall energetics of a π-assembled system to enable lowered barriers for charge transport in materials.[1,2] Fundamental developments in π-mediated assembly strategies (especially within the solid state) can pave the way to novel materials that can serve applications in organic electronics, including semiconductors[3], solar cells[4], light-emitting devices[5], batteries[6], etc. In order to enable these long-term goals, fundamental research to understand (and ideally control) π-assembly at the molecular level remains paramount. This introduction surveys different approaches that researchers have taken over the decades to characterise and achieve aromatic assembly. Arguably the most popular approach to directing π-assembly is through supramolecular systems, i.e., from multicomponent assembly. However, supramolecular materials have inherent limitations such as their sensitivity to neighbouring environments (i.e., pH, moisture, temperature, stress, etc.) and preference to aggregate into non-desirable nanoscale orderings. Mediating π-assembly *via* macromolecular architectures can help to overcome some of these issues by providing access to: i) more robust materials owing to the high molecular weight building blocks, ii) more reliable assembly processes and iii) materials that have hierarchical ordering (i.e., multiple levels of assembly). Moreover, macromolecular π-assembly is a relatively unexplored approach towards guiding the assembly of π-surfaces. In this introduction, π-assembly mediated by macromolecular architectures is given preference and we draw examples from biological systems to inspire the design of synthetic materials.

Aromatic assembly is ubiquitous in nature, and is common in stabilising the structures of enzymatic proteins, ribonucleic acid (RNA) and deoxyribonucleic acid (DNA). In the case of proteins, aromatic interactions are important in forming 2°, 3° and 4° structures that in turn arise owing to the order of amino acids in the 1° polypeptide sequence (Figure 1.1a). The utility of peptide sequences to organise aromatic interactions is featured in this thesis (Chapter 5) and will be covered in Section 1.5.1. Of all the biomolecules, DNA is a particularly good example of how aromatic interactions can influence structure at the hierarchical level. The biological macromolecule exemplifies a cooperative balance of hydrogen bonding, i.e., owing to complimentary Watson-Crick base pairing rules, and aromatic π-assembly interactions.[7] The intermolecular π-interactions are especially important in the geometry of DNA, wherein the stacking of π-surfaces is dictated by favourable electronic distributions across proximal

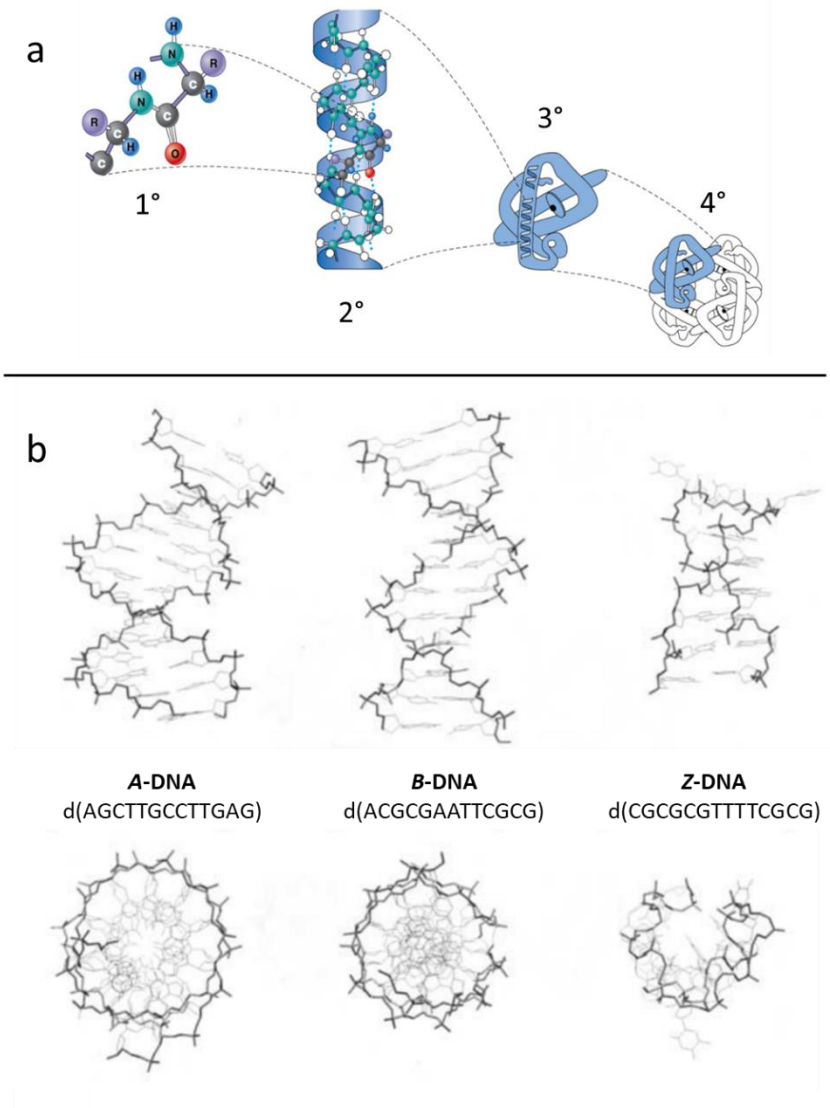

Figure 1.1. a) Structural hierarchical ordering of proteins: 1° structure of amino acids, 2° Structure generating localised pleated sheets and helical motifs, 3° structure of the folded, globular protein, and 4° structure of a multicomponent protein complex. b) *A*-, *B*-and *Z*-DNA, as seen from the side (top) and looking down the axis (bottom) of the double stranded helix.

aromatic units. Ultimately, the π-assembly is responsible for the helicity observed in double stranded DNA. Indeed, the three families of DNA helices, *A*-DNA, *B*-DNA and *Z*-DNA all have different conformations (Figure 1.1b). Driven almost solely by the stacking of the individual nucleotide bases, i.e, the sequence of π-stacked base pairs, the resulting helical pitches of *A*-DNA, *B*-DNA and *Z*-DNA are 28°, 34° and 45° respectively.[8]

It is still a challenge to design synthetic systems that can form hierarchical structures which are reminiscent of DNA. Synthetic chemists have capitalised on π-interactions in various systems that allow for fundamental supramolecular investigations as well as materials that have bespoke properties and applications. For instance, polymers are a popular approach toward enforcing aromatic interactions for functional materials; **P3HT**[9] (Figure 1.2a) is an electron rich polymer that can facilitate charge transfer in binary donor–acceptor mixtures. Similarly, dendrimers are

also polymeric molecules that have been decorated with aromatic molecules (e.g., pyrene[10], Figure 1.2b) to explore π-assembly and function in three-dimensional (3D) space. Arguably one of the most popular strategies to control and manipulate π-interactions is through supramolecular assemblies[11] (Figure 1.2c) of small molecules. Here, noncovalent interactions such as hydrogen bonding and electrostatic interactions can be used to drive assembly of aromatic molecules into favourable orientations for bespoke applications. In contrast, covalent or mechanical bond enforcement of π-interactions is also an approach that has been successful in controlling the order of aromatic molecules. Serving as a key example, mechanically interlocked molecules (MIMs) capitalise on the threading of a macrocycle over a stoppered chain (i.e., a rotaxane) or another macrocycle (i.e., a catenane[12], Figure 1.2d) and in turn aromatic assemblies are enforced. Ultimately, many strategies exist to dictate and exploit π-assembly for not only fundamental π-interaction investigations, but also for access to functional organic materials.

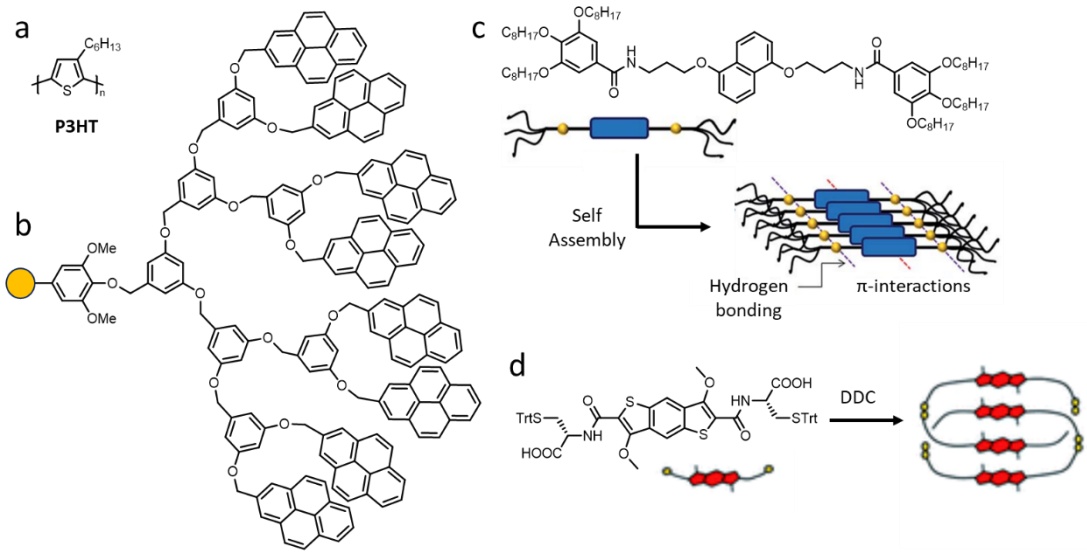

Figure 1.2. Different strategies to aromatic assembly: a) optoelectronic polymers, e.g., **P3HT**, b) dendrimers, e.g., light-harvesting pyrene dendrimers, c) supramolecular assemblies, e.g., self-assembly *via* hydrogen bonding and aliphatic interactions and d) covalent enforcement, e.g., a [2]-catenane MIM.

This Thesis details relatively unexplored strategies (i.e., macromolecular approaches) towards guiding π-assemblies, initially to study fundamental π-interactions with future aims of device implementation in various applications. The differing optical, electronic and electrochemical properties of π-aromatic molecules and their assemblies are exemplified in the various functions they show promise. Such applications include their use in diodes, transistors, semiconductors, photovoltaic cells as well as artificial photosynthetic devices where charge transport and conductivity properties are fundamentally important. In comparison to traditional metal-based materials, organic-based electronics can offer more tuneable alternatives that are both low cost and from a sustainable source. Yet, despite the breadth of knowledge–and understanding of functional aromatic compounds and the forces that dictate their properties in

OEDs–there are few examples that bare commercial application. For instance, organic based solar cells (OSCs) offer attractive features such as low weight, semitransparency, flexibility, low-temperature processing, low materials consumption and the tunability of the optoelectronic properties, however, these features can be more difficult to instil into traditional metal based electronics.[13] Moreover, the commercial applications of OEDs are plagued with issues such as short device lifetimes, molecular and material stability (i.e., O_2, H_2O, heat, irradiation, stress), fabrication on a large scale and the use of toxic solvents that are needed for their processing.[14,15] π-Assembly in macromolecular systems may allow for some of the limitations to be overcome by providing access to materials with high integrity. There is still a great need to develop new strategies that allow for complete control of the aggregation of functional photo- and redox-active molecules for tailored properties and high performing functional organic materials.

1.2 π-Assembly of Redox-Active Aromatics

One of the fundamental challenges that continues to persist in the generation of aromatic assembled materials is the difficulty in controlling the orientation and alignment of interacting aromatic molecules. As aromatic molecules possess quadrupole moments[16] with regions of high and low electron density, the molecules will try to adopt the most favourable electrostatic configurations upon interacting (Figure 1.3).[17] For example, benzene has a charge distribution

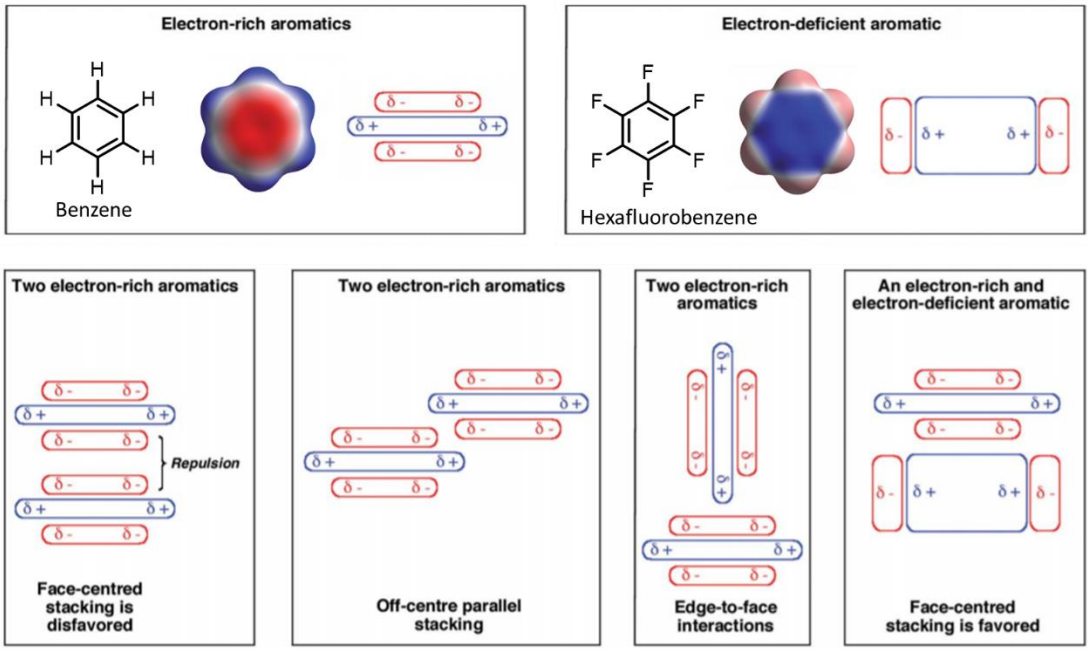

Figure 1.3. Illustration of the electrostatics (B3LYP/ 6-31G*) involved in the orientations of typical aromatic interactions that are dictated by quadrupole moments. Benzene and hexafluorobenzene are used to describe the assembly for electron-rich and electron-deficient aromatic rings, respectively.

(c.f., intrinsic quadrupole moment Q_{zz} = –8.5 B[18]) which favours edge-to-face interactions when interacting with like molecules (i.e., upon homo-assembly). In contrast, the electron withdrawing fluorine atoms of hexafluorobenzene causes an inversion in the charge distribution (c.f., intrinsic quadrupole moment Q_{zz} = +9.5 B[18]) in comparison to benzene. Here, homo-assembly of electron deficient molecules favours off-centre parallel stacking of molecules. These effects can be further demonstrated with common redox-active molecules, such as perylene and perylene diimide (PDI). Like benzene, perylene (Figure 1.4a) has electron density concentrated on the *p*-orbitals central to the periphery of its carbon framework; perpendicular to the aromatic ring, electron density is much less. The introduction of two imides in PDI[19] (Figure 1.4b), and therefore the inclusion of four carbonyls to perylene, changes the electron-rich core into a positive electrostatic region. Both perylene and PDI have large quadrupole moments parallel and perpendicular to their molecular axes, respectively, and therefore self-assembly processes are typically dominated by edge-to-face and off-centre parallel π-interactions.[20]

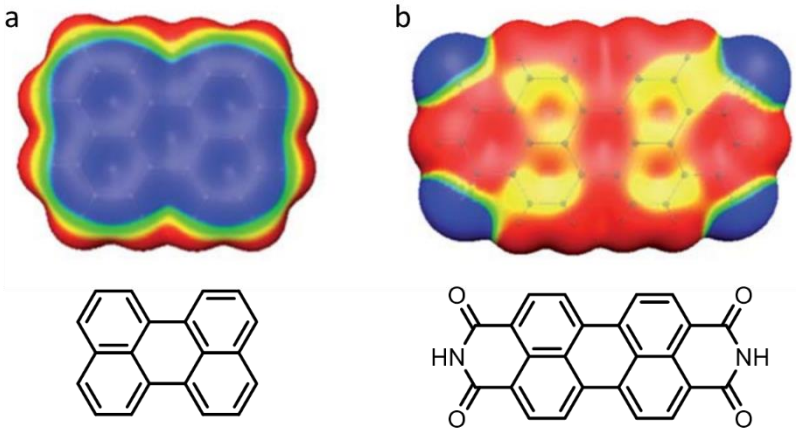

Figure 1.4. Representative electrostatic potential V_s of a) perylene and b) perylenediimide[19]. Colours illustrate electron-rich (blue) and electron-poor (red) areas.

As demonstrated by perylene and PDI, the inclusion of two electron withdrawing imide groups to the aromatic core greatly affects the energies of the highest occupied molecular orbitals (HOMO or E_{HOMO}) as well as the lowest unoccupied molecular orbitals (LUMO or E_{LUMO}). The difference in energy between the two molecular orbitals is the bandgap, which compared to metal semiconductor materials is relatively large. Electron rich molecules, such as pyrene, pentacene and polythiophenes, can facilitate charge-transport serving as *p*-type semiconductor materials.[21] Here, electrons situated in the HOMO are high in energy and can be easily oxidised to generate charge carriers. Conversely, electron deficient molecules such as PDI have low-lying HOMOs and LUMOs, which can facilitate *n*-type semiconductor properties, i.e., these molecules are readily reduced to form charge carriers.[22,23] For both *p*- and *n*-type molecules, the intermolecular aggregation and π-orbital coupling is of paramount importance

in order to obtain efficient charge delocalisation in the bulk material. Controlling the distance and orientation of interacting π-surfaces is therefore not only of fundamental interest to supramolecular chemistry, but also in designing organic materials for charge transport and conductivity applications.

Whereas the characterisation of individual molecules is important for rationalising the bulk material properties, the performance level (e.g., for charge transport) is often highly sensitive to the intermolecular ordering of π-systems. For assembling π-surfaces, there are four different classes of packing motifs: i) herringbone packing (face-to-edge, Figure 1.5a) with poor π–π orbital overlap, ii) herringbone packing or slipped π-stacking (Figure 1.5b) with π–π orbital overlap between adjacent molecules, iii) lamellar packing (Figure 1.5c) with 1D π-stacking, and iv) lamellar packing (Figure 1.5d) with two-dimensional π-stacking.[24] Arguably, the latter two forms where π-orbital overlap is maximised is considered the most efficient packing of molecules for applications such as charge transport, i.e., *via* the shortest route through the material. Molecular design and engineering has focused on obtaining materials that inherently have 2D lamellar packing, yet, it is a challenge to direct π-assembly into these most desired assemblies.

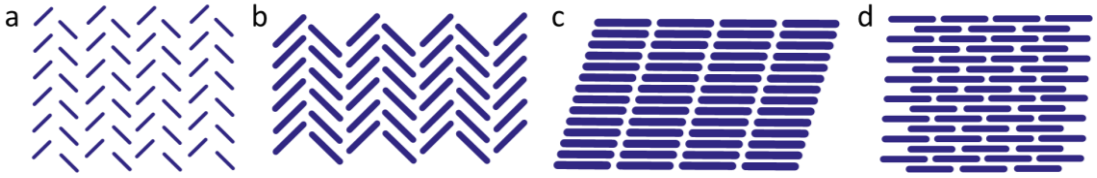

Figure 1.5. Molecular packing motifs of planar aromatics. a) herringbone packing (face-to-edge) with no significant π-π overlap, b) herringbone packing with π-π overlap, c) 1D lamellar packing and d) 2D lamellar packing.

Whereas homo-assembly of aromatic molecules can result in varied packing arrangements, hetro-assembly between electron rich and electron deficient aromatic molecules can lead to more predictable assemblies. Here, a Lewis acid–Lewis base type interaction exists with the partial transfer of electron density from the donor to the acceptor—this is known a charge transfer (CT) interaction.[25] The properties of these aromatic CT assemblies are heavily dependent on the efficiency and directionality of the π-orbital interactions between stacks which are typically face-centred (Figure 1.3). Here, hetro-assembly is useful in driving the co-assembly of donor and acceptor units into arrays where π-interactions are aligned, however, for homo-assembly it is still a challenge to enforce face-centred π-interactions.

1.3 Rylene Diimide Assembly

One of the staple redox-active aromatic units that is used to probe the effectiveness of π-assembly strategies is naphthalene diimide (NDI, Figure 1.6). NDI is the smallest member of the rylene diimide family and possesses important properties for OEDs, i.e., high electron affinity, good charge carrier mobility, thermal and oxidative stability. NDIs are attractive molecules because they can be readily synthesised from the corresponding dianhydride with amino functionalised molecules. Indeed, multiple strategies exist for both symmetric and asymmetric functionalisation. Furthermore, core substitution[26] chemistry is also possible which can significantly change the optoelectronic properties of the NDI unit. The straightforward synthesis and optoelectronic properties has poised NDI as an attractive unit for modelling systems that direct favourable π-assembly in pursuit of functional organic materials. As such, NDI has been used in Chapters 2 and 5 to probe macromolecular strategies in guiding π-assembly.

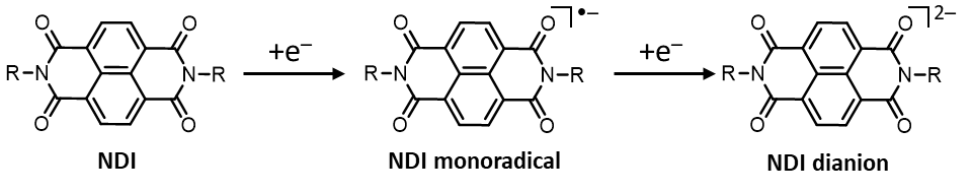

Scheme 1.1. Chemical structures of neutral NDI, which can be readily reduced to form an NDI monoradical which can be subsequently reduced a second time to form an NDI dianion.

NDI undergoes a facile one electron reduction to a monoradical state (i.e., $NDI^{\bullet-}$) which can be further reduced to a dianionic state, (i.e., NDI^{2-}), with both reductions fully reversible (Scheme 1.1). Because of their reduction properties, NDI-functionalised molecules have found applications in charge transport[27,28] and energy storage[29] materials. Non-core substituted NDI molecules typically show three well-resolved absorption bands (Figure 1.6) centred at 380,

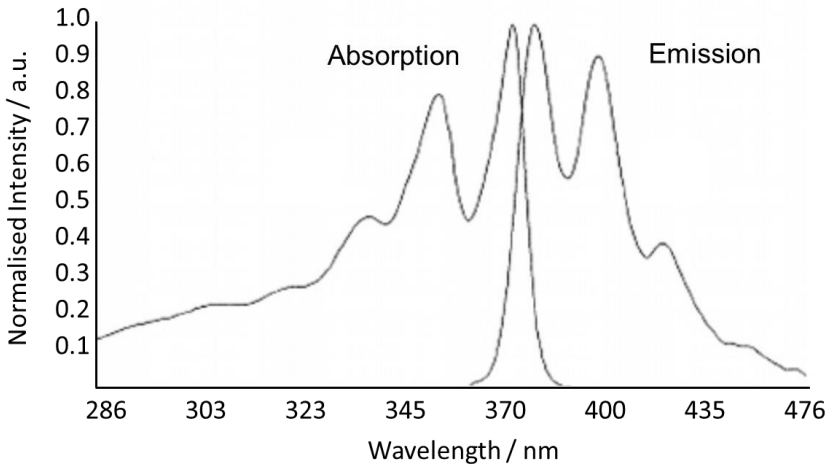

Figure 1.6. Typical normalised absorption and fluorescence emission spectra of an *N*-alkyl substituted NDI. Emission collected following excitation at 356 nm.[97]

360 and 340 nm as a result of the π→π* transitions along the long axis of the chromophore in the non-aggregated state. The corresponding emission profile consists of a mirror-image of the absorption profile that possess a small Stoke's shift.[30,31] NDI units have very low quantum yields ($\Phi_f < 0.02$) and lifetimes which are indicative of the fast deactivation of the S_1 state *via* intersystem crossing (ISC) to the close lying triplet state.[32] Ultimately, the properties of monomeric non-aggregated NDI units are generally well-understood, however, upon aggregation the optical as well as electronic properties can change in various ways that are indicative of specific π-assembly processes.

1.3.1 Neutral NDI Aggregates

As mentioned, NDI units have excellent optical characteristics such as their tendency to absorb in the UV-Vis region that not only allows for easier product isolation (i.e., when used during chromatographic analysis) but also the probing of their aggregation. When NDI units aggregate they typically assemble into *H*- or *J*-aggregates. These assemblies modify the excited state energies and oscillator strengths for the transitions between the ground and excited states. A bathochromic shift and decrease in intensity of the lowest-energy vibronic absorption is commonly referred to as *J*-aggregation, i.e., a thermodynamically favourable aggregation of NDI units *via* packing into slip stacked or head-to-tail assemblies.[33] Conversely, a hypsochromic shift in the absorption energy profile is commonly referred to as *H*-aggregation, i.e., a thermodynamically unfavourable aggregation of NDI units packing head-to-head. The energetic cost for imposing a close, head-to-head interaction is often 'paid for' using other stabilising forces such as hydrogen bonding or through enforcing the geometry of the π-interaction using a covalent framework. In addition to the changes in absorption profile, there are stark differences in the emission of the differing aggregates. *J*-aggregation of NDI units typically results in a featureless emission band (i.e., an excimer) that can be significantly red-shifted in energy. On the other hand, *H*-aggregate emission is typically very weak or not observable. Additionally, hetero-assembly of NDI units with aromatic solvents molecules, i.e., solvent-mediated charge-transfer complexes, can also form which also have significant effects on the absorption and emission profiles. Although these general trends apply to most PAHs, exact molecular structure and aggregation can result in a relaxing of the exciton transition rules.[33]

An example by Banerjee et al. demonstrates how a single NDI system can achieve a variety of different assemblies upon changing the solvent type and polarity.[34] From titrating *n*-octane or toluene in to a solution of **NDIA** in chloroform, *H*-aggregates (Figure 1.7a/d) or *J*-aggregates (Figure 1.7c/e) form, respectively, with clear changes in the absorption and emission spectra profiles. In aromatic solvents, π-interactions between the solvent and the electron deficient NDI

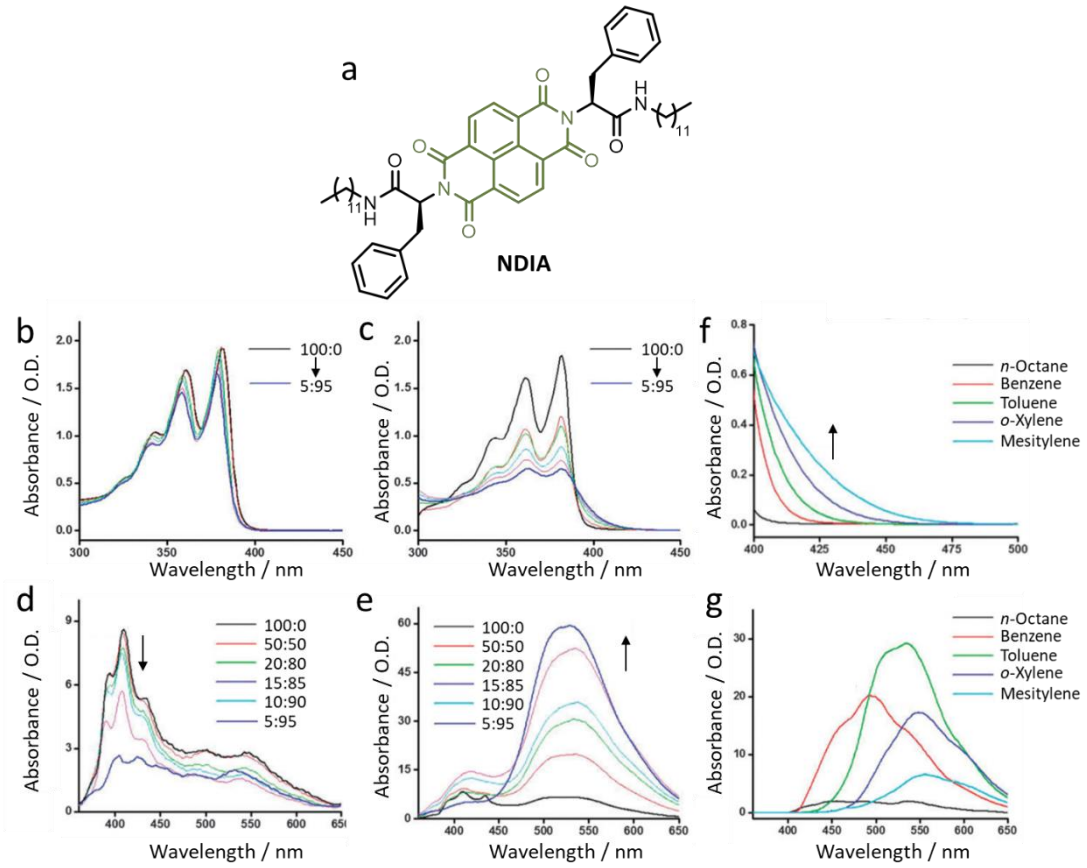

Figure 1.7. a) Structure of dipeptide **NDIA**. UV-Vis absorption spectra at 0.05 mM in $CHCl_3$ with varying % compositions of b) *n*-octane and c) toluene. Emission spectra at 12 mM in $CHCl_3$ with varying % compositions of d) *n*-octane and e) toluene. f) Absorption spectra CT bands and g) emission spectrum of donor–acceptor CT complexes of **NDIA** in various organic solvents at 0.05 mM.

core prevents *H*-aggregation in favour of *J*-aggregate like assemblies.[35] There is an increase in the λ_{onset} (Figure 1.7f) of absorption and a red-shift in $\lambda_{em,max}$ (Figure 1.7g) which is correlated to the electron donating capacity of the solvents, i.e., the extent of aromatic CT in the solvent mediated CT complexes varies from significant (mesitylene) to none (*n*-octane). This example shows an individual NDI molecule can form a mixture of assemblies depending on the solvent polarity or type. However, there are also examples of two-component mixtures used to direct more ordered assembly in supramolecular systems. For instance, Gosh et al. have used

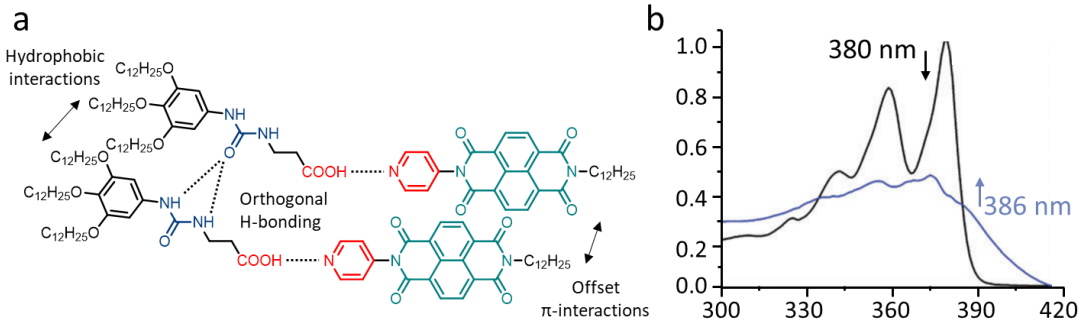

Figure 1.8. a) Gosh's two-component NDI system driven to assembly by hydrophobic and hydrogen bonding interactions. b) In MCH, *J*-aggregation of the NDI units is observable by UV-Vis spectroscopy with a significant red-shift in the onset of absorption.

orthogonal hydrogen bonding to assemble a two-component NDI system (Figure 1.8a).[36] In chloroform, the UV-Vis spectra showed (Figure 1.8b) well-resolved NDI absorption bands that were indicative of a fully dissolved state whereas in methylcyclohexane (MCH) an 18 nm shift in the onset of absorption was observed indicative of *J*-aggregation of NDI units and therefore assembly of the two-component system.

In the solid state, deeper insight into the molecular interactions between NDI units can be obtained using X-ray crystallography, with the morphology of these assemblies observable using microscopy when they are drop cast as thin films. Bhosale et al. have demonstrated[37] the self-assembly of a cholic acid *N*-substituted NDI conjugate (**NDI-DCA**, Figure 1.9a) into various nanostructures depending on the solvent environment. The cholic acid residues instil chirality into **NDI-DCA**, however, only a weak signal is observed from circular dichroism (CD) spectroscopy (Figure 1.9b). Upon molecular self-assembly, the embedded chirality can direct a handedness to the aggregated nanostructures with the chirality transferred to the chromophore—this is known as the Cotton effect and a characteristic signal can be observed depending on the specific aggregation adopted, e.g., anti-parallel β-sheets. A strong cotton effect is observed upon addition of water with two negative signal at 360 and 380 nm and a positive signal at 410 nm observed (Figure 1.9c) for **NDI-DCA**, indicative of right-handed helical aggregates. Scanning electron microscopy (SEM) allowed for visualisation of the aggregates following solvent evaporation. In 30% THF–H_2O, right-handed (*P*-type) helices were observed several microns in length, whereas in 20% THF–H_2O spheres (200–400 nm diameter) were observed exemplifying the sensitivity of the self-assembly process of the NDI-conjugated molecules.

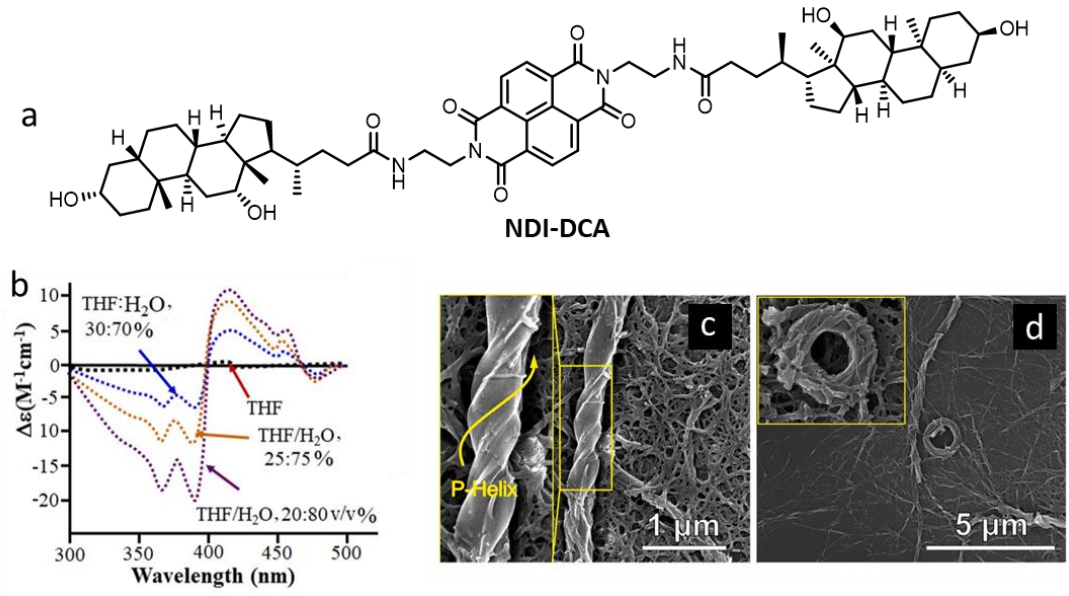

Figure 1.9. a) Molecular structure of **NDI-DCA**. b) CD spectra of **NDI-DCA** (10 μM) in various different THF–H_2O mixtures. SEM images of nanostructures formed by **NDI-DCA** in different THF–H_2O mixtures (10 μM) of c) 70% and d) 80% H_2O in THF.

1.3.2 π-Aggregation of NDI Radicals

The field of NDI assembly was inspired by the early work of Larry Miller.[38–40] He performed an in-depth analysis of how NDI molecules assemble in aqueous media in both the neutral and reduced states. A water soluble bis-sulphonate NDI (**NDIsul**, Figure 1.10a) was prepared and its self-aggregation (i.e. homo-assembly) in various solvents was monitored following complete reduction to the monoradical state (i.e., $NDI^{\bullet-}$) by sodium dithionite.[41] In DMF, characteristic absorptions at 780 and 473 nm were observed in the Vis-NIR spectrum for $\mathbf{NDIsul}^{\bullet-}$, characteristic of a monomerically dissolved NDI radical. However, in water an additional band (Figure 1.10b) was observed at 1140 nm corresponding to the radical anion NDI dimer (i.e., $2\mathbf{NDIsul}^{2(\bullet-)}$). Furthermore, upon the addition of sodium chloride to the aqueous solution containing $\mathbf{NDIsul}^{\bullet-}$, the absorption spectrum (Figure 1.10c) further evolved with a peak at 1700 nm that extended into the IR region (i.e., beyond 2000 nm) as a result of higher order NDI aggregates (i.e., beyond dimer) in the monoradical state.

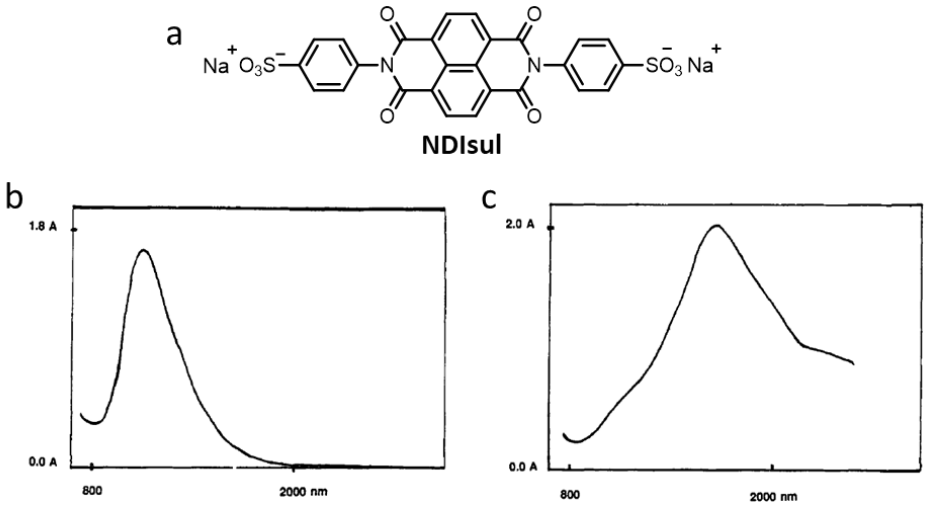

Figure 1.10. a) Chemical structure of **NDIsul**, and the NIR absorption spectra in b) H_2O and c) H_2O with 5.0 mM NaCl.

Radical π-assembly can be difficult to achieve because of the inherent Coulombic repulsion that is experienced between reduced π-systems.[42] Indeed, as demonstrated by Miller, driving forces such as the hydrophobic effect are often required to push together homo-assembly of radical π-systems. A more achievable situation to assemble NDI radicals is through mixed valence systems where an electron rich NDI radical (i.e., $NDI^{\bullet-}$) interacts with an electron-deficient neutral NDI π-system.[43] This has been demonstrated by Stoddart, who showed that π-assembly and electron delocalisation could be observed in discrete NDI systems (i.e., across NDI functionalised oligorotaxanes).[44] Here, NDI macrocycles are threaded (Figure 1.11a) over an ammonium dumbbell and trapped into a MIM following a clipping reaction, i.e., Schiff base formation. The effect of mechanically enforcing the close contact (<3.5 Å) of stoppered NDI

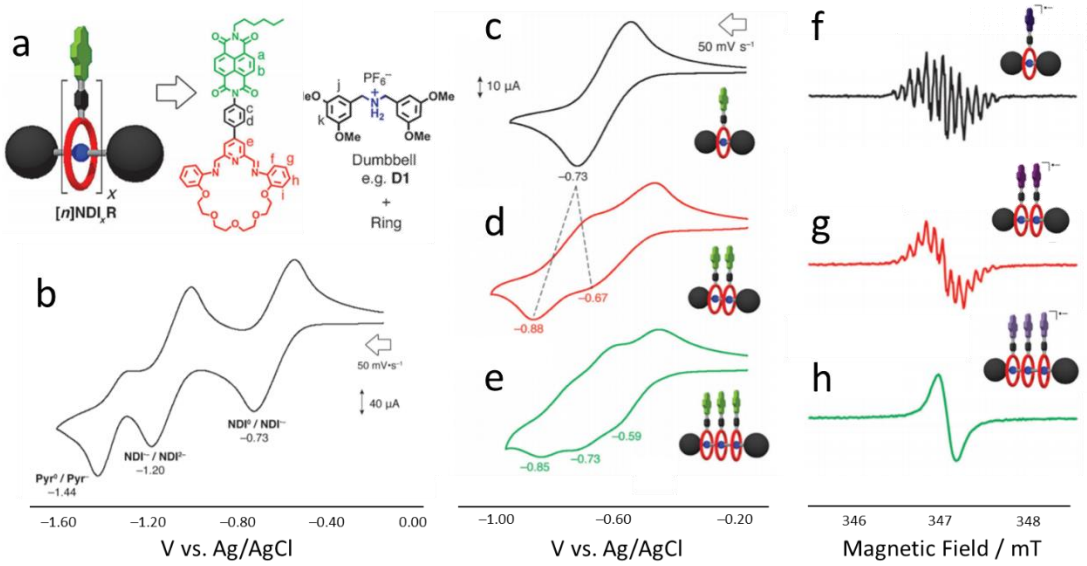

Figure 1.11. a) Oligorotaxane structure with illustrative cartoon, b) voltammogram of **[2]NDI$_1$R** in CH_2Cl_2 at 298 K (1.0 mM, 0.1 M $TBAPF_6$ supporting electrolyte; scan rate = 50 mV s^{-1}). Voltammogram of first-electron reduction for c) **[2]NDI$_1$R** , d) **[3]NDI$_2$R** , e) **[4]NDI$_3$R**, in CH_2Cl_2 at 298 K (1.0 mM, 0.1 M $TBAPF_6$ supporting electrolyte; scan rate = 50 mV s^{-1}). d) EPR spectra for for e) **[2]NDI$_1$R** , f) **[3]NDI$_2$R** , g) **[4]NDI$_3$R** after reduction with $CoCp_2$ (1 equiv.) in CH_2Cl_2 (0.75 mM) at 270 K at X-band (9.5 GHz) with 0.020 mT modulation amplitude.

residues on the electronic properties was probed. For **[2]NDI$_1$R** (i.e., the rotaxane with one clipped NDI units), two characteristic reduction events (Figure 1.8b) at –0.73 V and –1.20 V vs. Ag/AgCl correspond to the formation of the NDI monoradical (i.e., $NDI^{\bullet-}$), and dianion (i.e., NDI^{2-}) species; an additional reduction event observed at –1.44 V corresponds to reduction of the pyridine ring. Owing to π-electronic communication encouraged between two electron-deficient NDI motifs, the first reduction of **[3]NDI$_2$R** (i.e., the rotaxane with two clipped NDI units) takes place at a lower potential (Figure 1.11d) than for **[2]NDI$_1$R**, however, the subsequent reduction is more difficult (–0.88 V) to achieve as a result of adding an electron to a more electron rich π-system. These observations reveal that the intermolecular π-assembly lowers the E_{LUMO}. Furthermore, analysis of the first-wave reduction profiles (Figures 1.11c–e) for a series of **[n]NDI$_1$R** oligorotaxanes reveals increasing separation of the first one-electron reduction process as a result of increasing electronic communication between multiple NDI units, i.e., electronic coupling across all NDI units is observed upon sequential reduction of each NDI unit. In addition, further insight could be gained using electron paramagnetic resonance (EPR) spectroscopy which provides information on thenumber of units involved in a system when radicals are shared. EPR experiments (Figures 1.11f–h) were used to probe the sharing of an electron in the mono-reduced states (i.e., a mixed valence state) with **[4]NDI$_3$R** and **[5]NDI$_4$R**. These results provide additional evidence for electron delocalisation across multiple NDI units with a narrowing of the spectral width as well as a loss in resolution of the hyperfine splitting couplings in the EPR signal.

Although not a supramolecular system, the coupling of reduced NDI units can be further observed in covalent systems that do not allow for disassembly as a result of Coulombic repulsion. Wu et al. reported[45] a rigid NDI cyclophane (**NDIc**) wherein the proximity of the π-surfaces was fixed at 3.5 Å (Figure 1.12a), enforcing strong intramolecular π-orbital coupling of the units. UV-Vis spectroscopy provided initial evidence for strong electronic communication between the NDI units of **NDIc** with a blue shift ($\Delta\lambda_{max}$ = 20 nm) in the lowest-energy vibronic absorption (Figure 1.12b) in comparison to a reference NDI molecule. Upon reducing **NDIc** to the monoradical state, a new absorption band centred at λ_{max} = 1750 nm appears as a result of an intervalence charge transition (IVCT). Simultaneously, the reduction of the EPR-linewidth for **NDIc** by a factor of √2 with respect to the control NDI provided further evidence for delocalisation of the single electron across both NDI units. Further reduction to the dimer anion resulted in a loss of the EPR signal and the disappearance of the IVCT band with the growth of a new band (Figure 1.12b) centred at λ_{max} = 1000 nm for the doubly reduced species (i.e., $NDI^{2(\bullet-)}$). Here, a rigid covalent scaffold has allowed for electrostatically unfavourable radical π-interactions to be observed and characterised with UV-Vis-NIR and EPR spectroscopies.

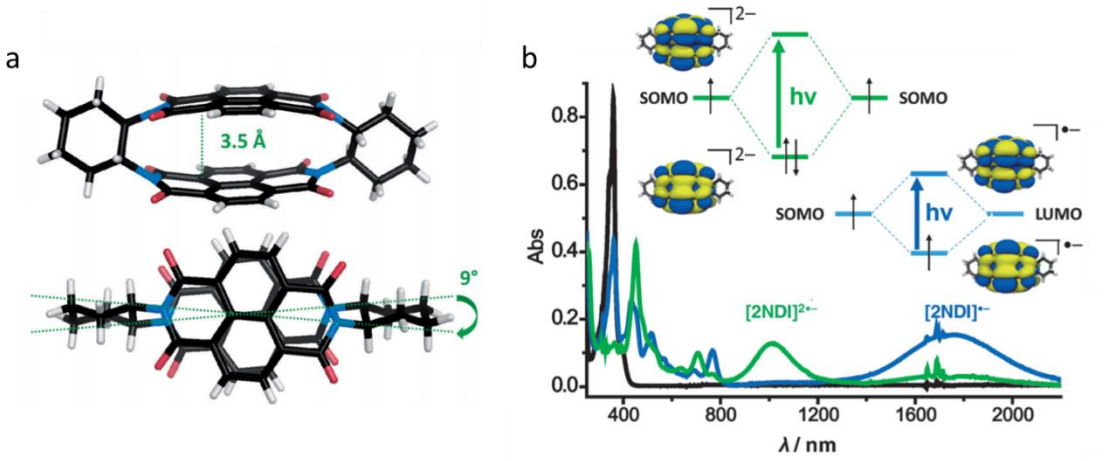

Figure 1.12. a) Plan and side-on views of solid-state structures of **NDIc**, showing the close intramolecular distance and twist angle between the two NDI units. b) Absorption spectra of **NDIc** in the ground state (black trace) and electrochemically mono-reduced (blue trace) and di-reduced (green trace) states with insets showing the mixed orbital interactions and lowest energy electronic transitions of the resulting absorption spectra.

NDI molecules, and related rylene diimides, have been heavily explored and it has been demonstrated that we are able to control—to some extent—and observe interactions in the neutral as well as reduced states. Despite the many success stories, it is still a fundamental challenge to dictate the interactions between π-conjugated molecules and thus the properties of organic materials for electronic applications. An understanding of the processes that drive π-assembly and how it can be enhanced through either structural modification, solvent or redox-control, will pave the way for novel materials with emergent properties. Ultimately, although mediating π-assembly using macromolecular systems may have increased synthetic

difficulty, the benefits of i) high fidelity materials, ii) increased stability (i.e., to stress, temperature, etc.), and iii) nanoscale hierarchical ordering, make it an attractive strategy for the ultimate control over π-assembly processes. The following sections summarise the background and state of the art in two strategies that are central to my PhD thesis: i) macromolecular 3D scaffolds and ii) macromolecular 1D foldamers, for π-assembly.

1.4 Fullerenes as Three-Dimensional Scaffolds

The tendency of rylene diimides—and most planar aromatic molecules—to undergo thermodynamically-governed π-stacking interactions means that they will often lend themselves to the formation of 1D supramolecular π-assemblies and nanostructures (*vide infra*, Section 1.5) that are primed for facilitating unidirectional energy and charge transport processes. However, there is growing interest to understand the fundamental nature of aromatic interactions in 3D space, as this tends to mimic the 3D organisation of natural systems in biology and introduces 'dimensionality' as a novel design consideration, i.e., with respect to developing organic π-conjugated molecules for advanced optoelectronic applications. In order to overcome the electrostatic dictation on π-assembly, covalent scaffolds are generally required to realise precise, 3D spatial arrangements of aromatic units. To this end, hexakis-substituted fullerenes have emerged as a viable scaffold for studying and manipulating the through-space electronic processes that take place between 3D organised aromatic molecules. This section outlines the rather versatile Bingel and 'click' strategies for functionalising fullerenes with up to 12 aromatic units and surveys literature examples that exemplify the role of 3D scaffolds on mediating aromatic assembly and through-space energy transfer events.

Fullerenes are attractive candidates for mediating π-assembly within charge-transport and catalysis applications as they combine three-dimensionality with unique photoelectric and electrochemical properties. Since 1990, the large scale availability[46] of fullerenes has allowed for the development of many synthetic strategies that can modify or functionalise the conjugated fullerene surface. These molecules, and their functionalised derivatives, have received—and continue to receive—a lot of attention owing to their promise in the preparation of advanced materials. Indeed, [6,6]-phenyl-C_{61}-butyric acid methyl ester (**PCBM**) is a fullerene derivative widely used as an electron acceptor[47] in bulk-heterojunction organic solar cells, a promising alternative technology to inorganic solar cells. Fullerene scaffolds offer a globular design, akin to proteins, for the synthesis of multivalent, multifunctional molecules. Owing to these unique properties associated with fullerenes, the synthesis of many bis-[48,49], tris-[50], tetrakis-[51], pentakis-[52] and higher substituted functionalised C_{60} derivatives has been

demonstrated following well-optimised synthetic protocols such as Bingel cycloproponation[53], 1,3-dipolar additions[54] and Diels-Alder[55] reactions (Scheme 1.2). The controlled 3D spatial arrangement of π-functional moieties in space, not only allows for a fundamental understanding of globular three-dimensional carbon structures, but also for the construction of novel multifunctional nanomaterials. To date, only a few examples of aromatic functionalised fullerene derivatives exist in the literature. Their structure dictates a scaffold of high integrity and thus can be used to mediate both intra- and intermolecular π-assembly for the study of fundamental π-interactions and the design of novel organic electronic materials.

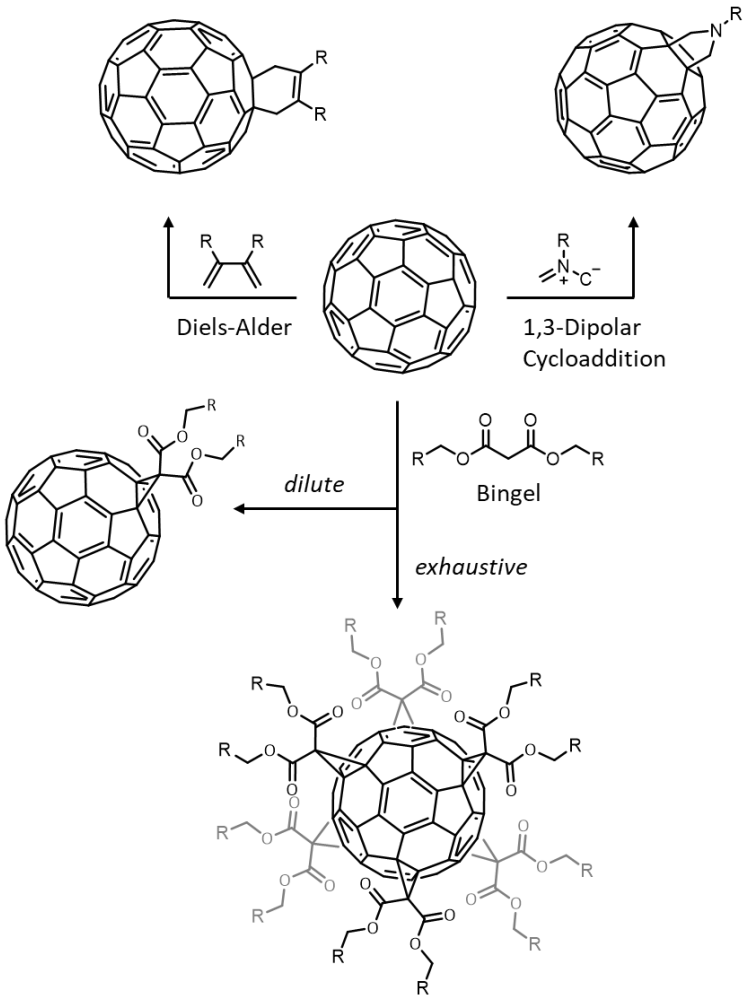

Scheme 1.2. Examples of some of the most popular strategies for functionalisation of fullerene. The Bingel reaction can be employed under dilute or concentrated conditions to target either a mono-adduct or hexakis-adduct, respectively.

Although the chemistry in pursuit of fullerene adducts is vast, this discussion will focus only on derivatives attained using [2+1] cycloaddition reactions, i.e., through a Bingel–Hirsch reaction. The shortest and most reactive π-bonds on the surface of C_{60} are those between two fused six-membered rings. Owing to their electron deficient nature, these sites are susceptible to nucleophilic addition and thus reacting here allows for straightforward access to mono as well as highly substituted fullerenes; there are six [6,6] sites that are distributed in an octahedral

pattern across C_{60}. Generally, functionalisation of fullerenes increases their solubility in common organic solvents and thus aids with the analysis and processability of such materials. However, this in turn can be detrimental to the electrochemical properties of the fullerene core as it disrupts conjugation as well as molecular symmetry and so a balanced approach to the functionalisation of fullerene is required in order to preserve these properties.

The modified Bingel reaction has risen as a key strategy in functionalising fullerenes; it can produce reactive intermediates which can be generated *in situ*, as well as high yields and tolerability to various functional groups. For example, when pursuing a fully functionalised fullerene hexakis-adduct, the reaction is typically carried out in *o*-dichlorobenzene or toluene with C_{60} (1 equiv) added to a bismalonate (10 equiv), tetrabromomethane (100 equiv) and DBU (20 equiv). The reaction involves the use of tetrabromomethane, a bromination source for the *in situ* formation of the bromo malonate which is necessary for cyclopropanation to occur. Here, the bromide is a much greater leaving group than a proton in the ring closing step that links the malonate to the fullerene surface. Traditionally, the yields for this reaction were very low until it was 'modified', with the optimisation leading to previously unattainable high yielding syntheses of many hexakis-adducts. Conversely, selective mono-adduct formation can be achieved upon changing the relative equivalences of the reagents and performing the reaction under high dilution. These methods can therefore provide efficient routes to 3D molecules that vary in their valency, functionality and fundamental properties.

Whilst the modified Bingel reaction provides a one-pot regioselective route to hexakis-adducts, the use of bulkier and structurally more complicated malonates *via* this route is often low yielding and requires extensive and difficult purification methods. The Nierengarten group were the first to use a key intermediate fullerene that was poised for 'click' functionalisation in accessing hexakis-adducts with high levels of structural complexity and functionality.[56] The researchers synthesised an azido functionalised hexakis-fullerene (**12Az**, Scheme 1.3) from which further functionalisation could easily be conducted using Cu(I)-catalysed azide-alkyne cycloaddition (CuAAC) 'click' reactions. A biphasic reaction mixture of dichloromethane–water, containing copper sulphate pentahydrate as the source of copper and sodium ascorbate as the reducing agent, allowed for a range of highly substituted fullerenes—even with bulky peripheral groups,—to be synthesised with yields ranging from 56 to 91%. The CuAAC functionalisation strategy has since provided access to multivalent fullerene hexakis-adducts that have useful functions, .e.g, for inhibition of artificial Ebola virus as well as glycosidase inhibition.[57,58] In addition, the Nierengarten group provided another route (Scheme 1.3) towards hexakis-adduct functionalised fullerenes capitalising on the use of trimethylsilyl-protected alkyne groups. They synthesised **12TMSY** (Scheme 1.3), bearing 12 alkyne groups

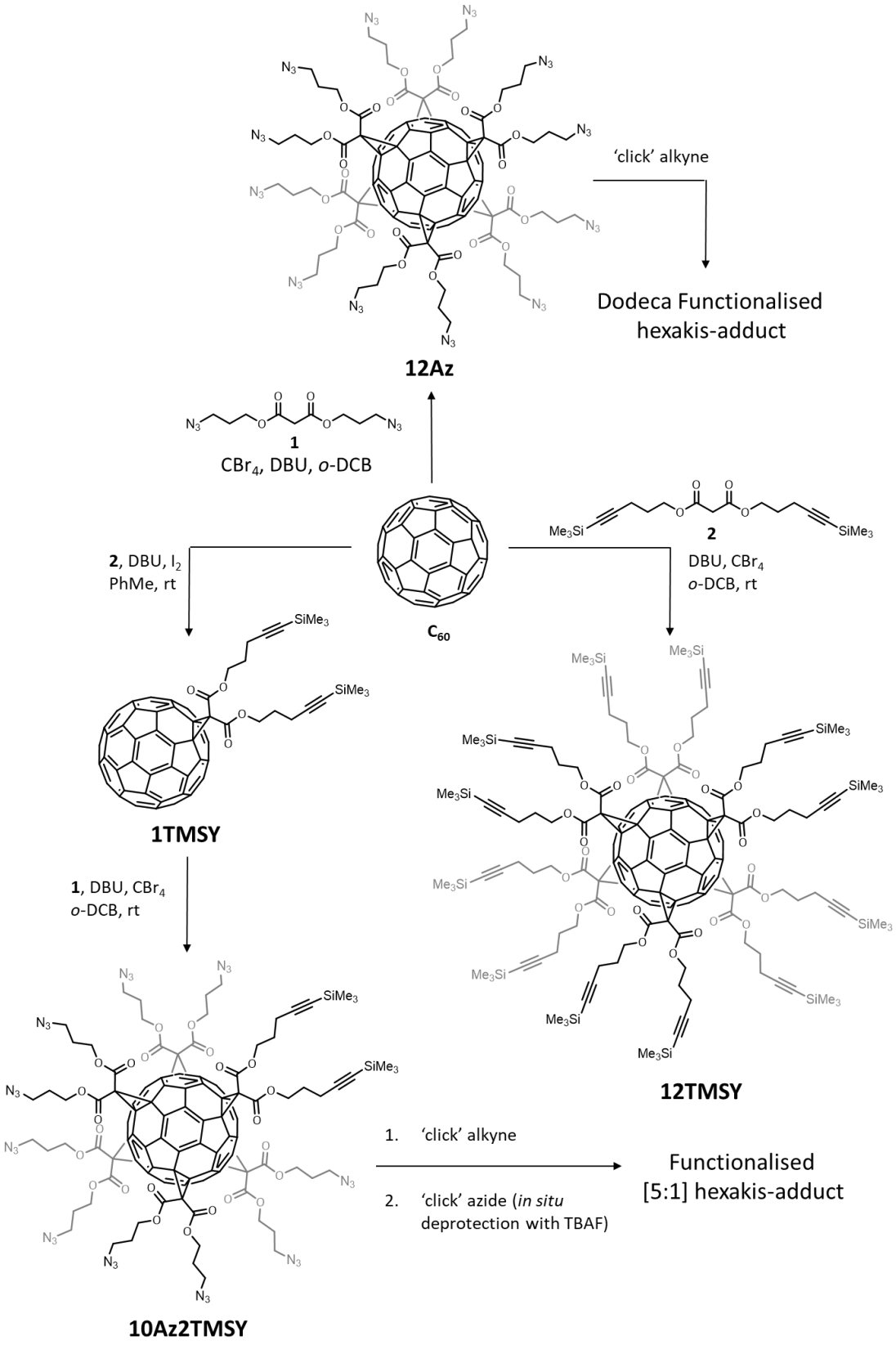

Scheme 1.3. The synthesis of of hexakis-adduct **12Az**, bearing 12 azide groups serves as a key intermediates for the click functionalisation syntheses of dodeca-functionalised fullerenes. Trimethylsilyl-protected alkyne hexakis-adduct **12TMSY** allows for the synthesis of [5:1] fullerene hexakis-adducts following the selective synthesis of **1TMSY** from **1** and $\mathbf{C_{60}}$ under similar conditions under high dilution

that could be functionalised with azide-bearing molecules following *in situ* trimethylsilyl (TMS) deprotection using tetrabutylammonium fluoride (TBAF). Furthermore, capitalising on both synthetic approaches (i.e., varying dilution) towards mono- as well as hexakis-adduct fullerenes, they provided a route towards [5:1] non-symmetrical fullerene derivatives. Here, varying functionality can be appended around the fullerene core and thus a unique situation arises to study redox- and photophysical intramolecular processes between appended functional units as well as the fullerene core. These methods are now widely accepted as the go-to-strategy for synthesising multivalent fullerene hexakis-adducts owing to the ease of reaction, tolerance to a wide range of functional groups, high yields and straight forward purification.

Varying adducts from mono- to hexa-substituted fullerene derivatives are synthetically possible. Yet, owing to the complications in controlling selectivity and purification of different adducts, only singularly functionalised and fully functionalised fullerene adducts are commonly reported in the literature, i.e., mono-adducts and hexakis-adducts. With respect to rylene diimides, there have been some examples of functionalised fullerenes with PDI to probe the interaction between the appended chromophore and the fullerene core. Köhler et al. recently investigated[59] the light-harvesting properties of PDI antennas covalently linked to C_{60}. PDI motifs have a tendency to form strong π-interactions that greatly alter their photophysical properties—this is unwanted with respect to designing light-harvesting materials based on PDI derivatives as energy is not transferred, i.e., to the fullerene in this case. Following the modified Bingel reaction, under high dilution they were able to selectively synthesise **A_2-F** (Figure

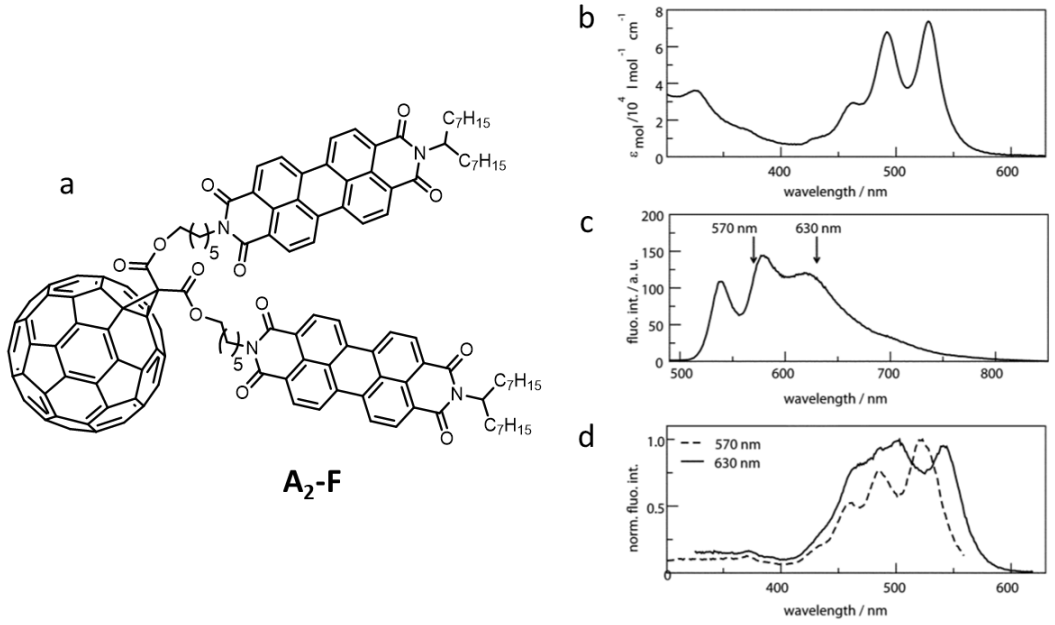

Figure 1.13. a) Chemical structure of **A_2-F**. UV-Vis absorption b) and emission c) spectra of **A_2-F** in $CHCl_3$ [10 µM], with arrows indicating selected wavelengths for generation of d) excitation spectra.

1.13a) in a yield of 47%. With long chain flexible linkers to attach the PDI units covalently to the fullerene surface, they observed a moderate (60%) amount of intramolecular π-interactions. The emission spectrum (Figure 1.13c) shone light on the distribution of non-interacting and interacting PDI units with the excitation spectra (Figure 1.13d) revealing the origin of the lower-energy emission (630 nm) came from *J*-aggregating PDI units. Ultimately, for the design of light harvesting PDI derivatives, the researchers concluded that longer, more-rigid antennas were required to prevent PDI units from aggregating (i.e., to increase performance efficiency) around a fullerene core. Although unwanted for light-harvesting applications with PDI, a fully decorated fullerene, e.g., from a hexakis-adduct, could increase the amount of intramolecular π-assembly for extended stacking of functional units to facilitate properties such as charge transport.

1.4.1 π-Functionalised Fullerene Hexakis-Adducts

To date, there are no examples of rylene diimide functionalised hexakis-adducts of fullerene and this provides an open territory for new research to take place (see Chapter 2). However, the homo-functionalisation of hexakis-adducts has allowed for investigations into the effect of the 3D scaffold on the π-interactions of the appended units. This has been demonstrated by Martín and co-workers who synthesised an electron-rich hexakis-adduct and investigated its interaction with graphene. Whereas surface modification of graphene can negatively impact

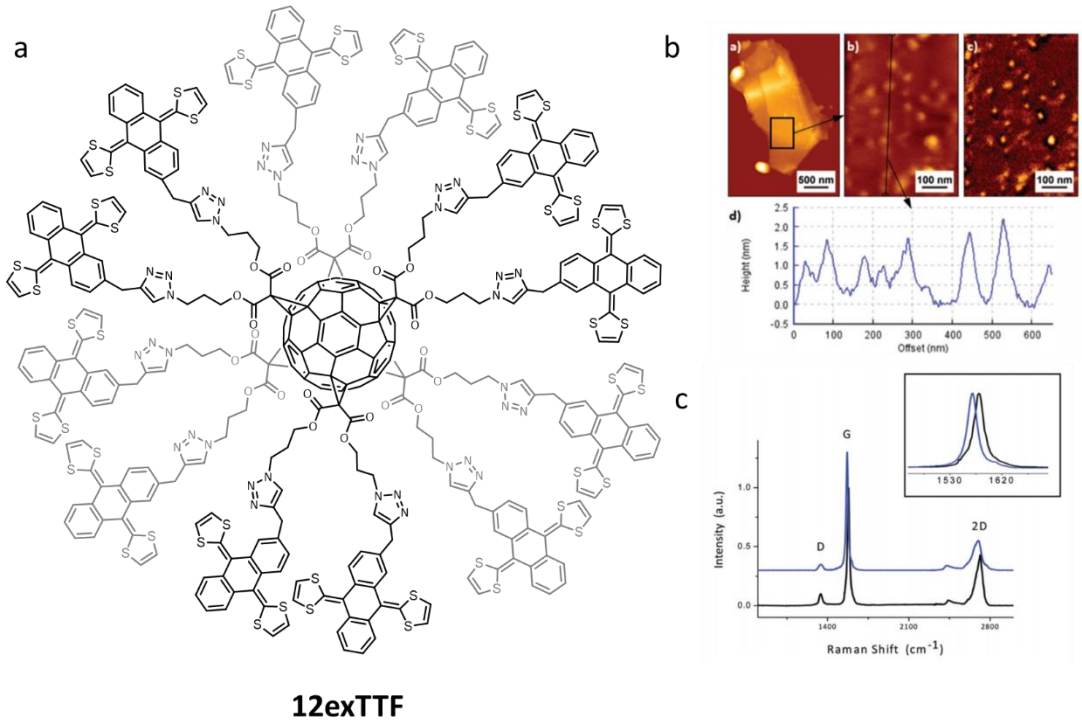

Figure 1.14. Molecular structure of **12exTTF**, bearing 12 π-exTTF moieties. AFM topography images of **12exTTF**–graphene composite showing detail of the surface of a platlet and small aggregates, including the resulting phase change around aggregates. Height profile along the black line shown, identifying aggregate heights of up to 2 nm.

some of its properties such as the band gap, non-covalent interactions can also be used in a manner that is non-destructive; π-interactions are commonly used to interact with the surface of graphene, carbon nanotubes, etc. The 'clicking' of 12 curved π-exTTF groups to deprotected **12TMSY** allowed for the straightforward synthesis of **12exTTF** (Figure 1.14a). Initially, UV-Vis spectroscopy was used to probe the interaction of graphene and a monomeric π-exTTF unit with no interaction observed between the two. Yet, when grafted to the hexakis-adduct scaffold, an interaction with the graphene sheets was observed providing evidence for enhanced binding *via* a 'multivalent'[57] effect of having the 12 groups attached to the 3D scaffold. Furthermore, analysis of the **12exTTF**–graphene composites with atomic force microscopy (AFM) confirmed the presence of graphene platelets (Figure 1.14b) with a high density of **12exTTF** agglomerates, roughly 3–6 nm in diameter and 1–2 nm in height. Additionally, Raman spectroscopy observed (Figure 1.14c) no change to the defect band (D) with a change to the G band, confirming the non-destructive injection of electron density from the **exTTF** moieties to the graphene surface. Although this study did not delve into the alteration of the electronic properties of graphene, it provides evidence for a change in the properties of a π-functionalised motif when it is appended to a multivalent scaffold in the presence of a functional material.

As well as facilitating intermolecular interactions with 2D substrates such as graphene, the hexakis-adduct fullerene core also provides a means to study intramolecular processes. For instance, Iehl et al. decorated[60] **12Az** with 12 conjugated *E*-stilbene (A) oligomers to make **12A** (Figure 1.15a) and investigated its light-harvesting properties; model compounds were synthesised to aid understanding of the properties: **12Ph** (Figure 1.15b) and a 'clicked' *E*-stilbene **A** (Figure 1.15c). Upon collecting the emission spectrum of **12A** they observed that the A-centred fluorescence (ca. 400 nm) was largely quenched, (Figure 1.15d) in comparison to **A**. In addition, a broad band centred ca. 600 nm was observed. Further emission experiments using a 550 nm cut-off filter revealed the presence of an almost quantitative energy transfer process *via* a Förster resonance energy transfer (FRET) mechanism—the fluorescence profile of **A** has significant overlap with the absorption profile of the C_{60} core and thus the emission energy is re-absorbed by the core. The excitation spectrum collected at 670 nm also matched exactly with the absorption spectrum of **A**, confirming the FRET process. Here, photophysical experiments reveal **12A** to be an extremely efficient light-harvester, capable of channelling the absorbed energy from the periphery to the fullerene core by singlet–singlet energy transfer. Furthermore, the authors also suggest that the decorating of a hexakis-adduct with potent electron-donating motifs may allow for electron transfer from the periphery to the acceptor core. These observations provided early evidence that fullerene hexakis-adducts can have

photo- and/or redox-active light-harvesting properties. Indeed, careful selection of the pendant aromatic unit can be used to enhance or avoid these energy transfer properties.

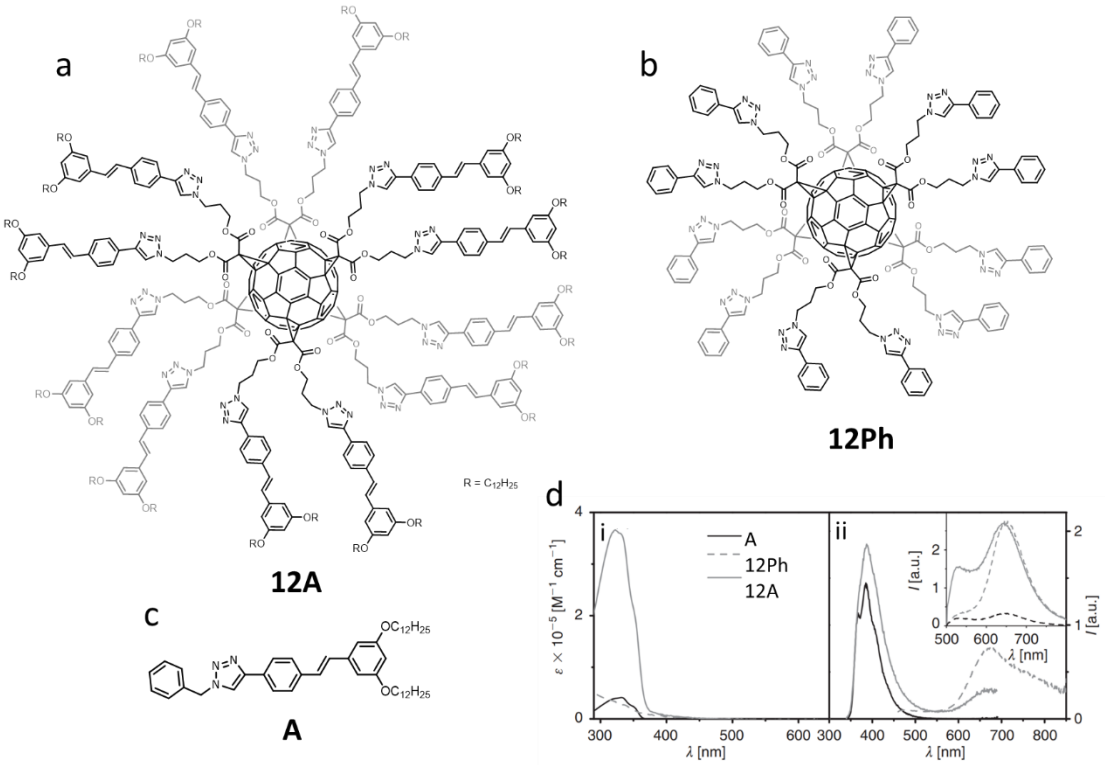

Figure 1.15. Molecular structures of a) hexakis-adduct **12A**, b) hexakis-adduct model compound **12Ph** and c) reference **A**. d) i) Absorption and ii) emission spectra of **A** (black line), **12A** (grey line) and **12Ph** (grey dashed line) collected in CH_2Cl_2; inset shows emission spectra collected using a 550 nm cut-off filter of **12A** (grey line), **12Ph** at the same optical density (grey dashed line) and concentration (dashed black line) as of **12A**. Emission spectra were collected following excitation at 335 nm.

The energy transfer capabilities of fullerene hexakis-adducts has been further demonstrated by the Nierengarten group who designed[61] a [5:1] system that allowed for energy-migration over long distances in a similar way to that which occurs in natural arrays. They chose to functionalise the hexakis-adducts with boron dipyrromethene (BODIPY) dyes; these chromophores are highly fluorescent, easily functionalised and readily facilitate charge transfer.[62] To provide a gradient for energy transfer across a [5:1] system, they sequentially 'clicked' two dyes, a yellow and blue BODIPY, to make **10Y2B** (Figure 1.16a), with each dye differing in its conjugation and therefore optical properties and energy levels. They were able to selectively irradiate the blue BODIPY of **10Y2B** and observe emission similar to that of control **2B10Ph**. However, irradiation at 490 nm (95% selective for the yellow BODIPY) resulted in a very weak emission corresponding to the yellow BODIPY, with a concomitant increase in emission corresponding to blue BODIPY. Drawing comparisons with an equimolar mixture of the control compounds, this related to a quenching of roughly 85%. Excitation, variable-temperature and time-resolved emission spectroscopy experiments confirmed this was as a result of energy migration between the dyes for **10Y2B**. Here, the fullerene hexakis-

scaffold provides a means for charge and energy transfer in a universal direction. When immersing mixtures of the yellow BODIPY-functionalised (**10Y**, Figure 1.16b) and hybrid dye-functionalised (**10Y2B**) fullerenes in a poly(methyl methacrylate) matrix, results confirm fast energy migration between **10Y** molecules followed by the subsequent trapping of excitons by the blue BODIPY fragments of neighbouring **10Y2B** molecules. Here, the migration of energy over long distances (ca. 70 Å) before concentrating at a reactive centre is highly reminiscent of natural light-harvesting systems seen in nature. Despite the synthetically challenging targets, the intricate design of the multivalent system has allowed for the supressing of unwanted intramolecular charge-transfer processes with the fullerene core in favour of intermolecular long-range communication between the different pendant aromatic units. As a proof-of-concept study, this paves the way for the design of analogues and materials that may increase efficacy when used in photovoltaic applications. It is clear that the tailoring of each system can hone in on or sequester the involvement of the fullerene core in optoelectronic processes. Indeed, when necessary the fullerene's use can be concentrated as a scaffold for the

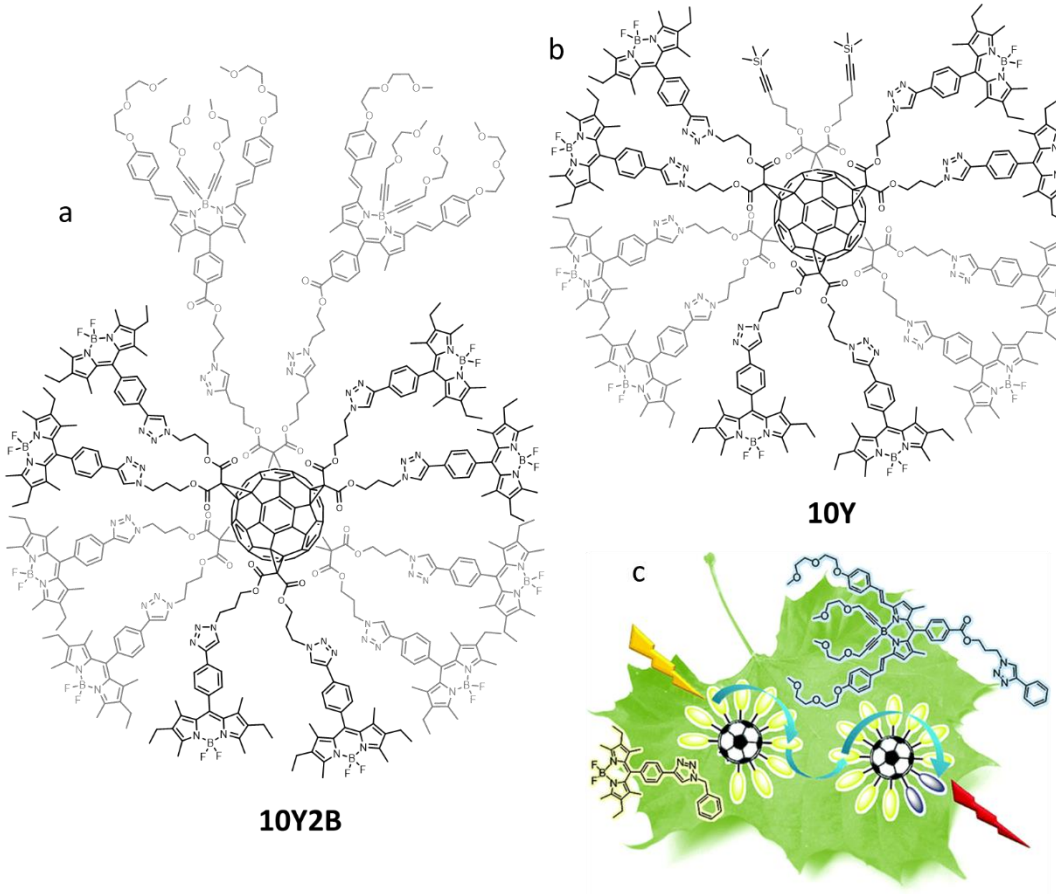

Figure 1.16. Chemical structure of a) [5:1] hexakis **10Y2B**, functionalised with 10 yellow absorbing dyes and 2 blue absorbing dyes and b) [5:1] hexakis **10Y** functionalised with 10 yellow dyes and 2 protected alkynyl moieties. c) Illustrative figure of model dye compounds, and the pathway for energy migration from the absorbing yellow dyes of **10Y** to the blue dye moieties of **10Y2B**.

3D arrangement of not only one chromophore, but also complementary chromophores for charge and/or energy migration.

Energy transfer across fullerene hexakis-adducts has also be manifested in the form of electron migration. Indeed, installation of redox-active pendant units allows for insights into the 3D crowding of said units. The Nierengarten group grafted ten redox-active ferrocene units and two 1,2-dithiolane moieties onto a [5:1] hexakis-adduct to investigate charge-migration in the organic–inorganic hybrid molecules (**10Fer**, Figure 1.17a).[63] With a high affinity for metals, the dithiolane moieties allowed for the anchoring of molecules onto a gold electrode *via* the formation of a submonolayer. Ultrafast CV experiments allowed the researchers to probe the dynamic exchange of electron across the grafted molecules. Various scan rates revealed oxidation processes primarily occur at the close-contact ferrocene–gold electrode surface, before subsequent hole-hopping between ferrocenium residues at further distances from the electrode surface; at faster scan rates the CV signal broadens (836 Vs^{-1}, Figure 1.17b; 55,700 Vs^{-1}. Figure 1.17c), indicating that only a fraction of the ferrocene units are oxidised. Here, charge-migration from one component to another (i.e., $Fc + Fc^{+} \rightarrow Fc^{+} + Fc$) can be observed which allows for fundamental understanding of the processes involved in charge transport e.g., through organic molecular wires and at molecular junctions. In a similar manner, electron migration across the pendant aromatic units was also observed for **12ZnP** (Figure 1.17a), a fullerene hexakis-adduct decorated with 12 porphyrin units.[64] The fluorescence quantum yield was much lower for **12ZnP** (Φ = 0.3%) than the control individual porphyrin

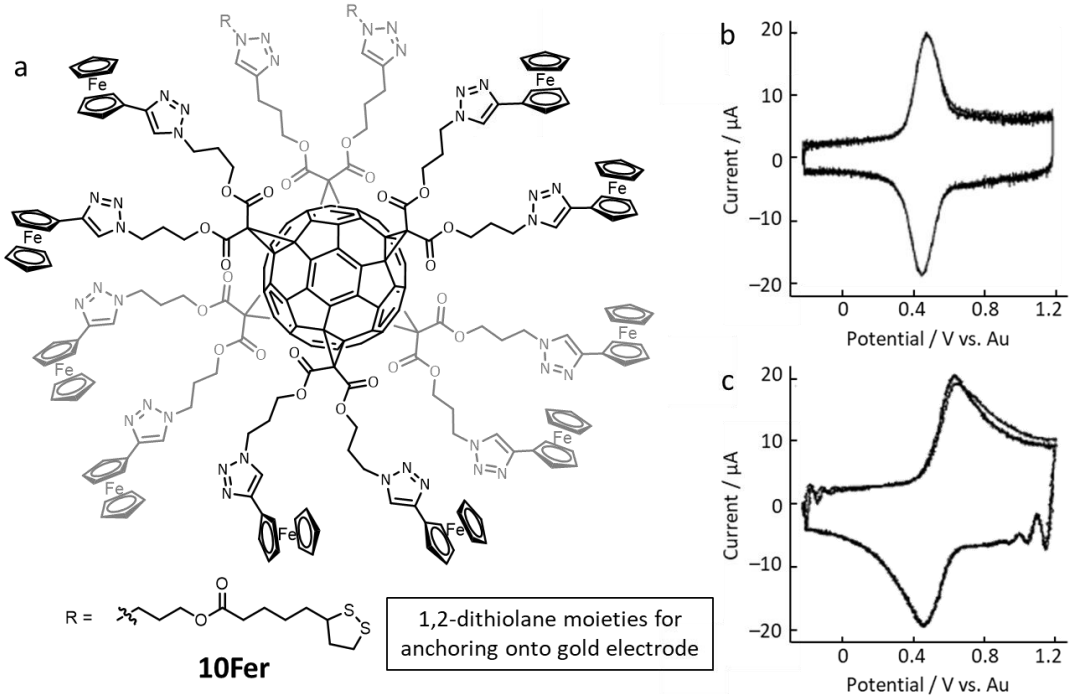

Figure 1.17. a) Chemical structure of mixed [5:1] fullerene hexa-adduct **10Fer**. b) Voltammogram of **10Fer** adsorbed onto a gold electrode in MeCN containing 0.1 M $TBABF_4$ as supporting electrolyte; scan rate of b) 836 Vs^{-1} and c) 55,700 Vs^{-1}.

unit **ZnP** (Φ = 1.7%). In this case, FRET was ruled out with the reduced emission of **12ZnP** associated with extensive intramolecular π-assembly of the peripheral ZnP units. With confirmation of no photo-induced processes occurring between the ZnP units and the fullerene core, the researchers further investigated their system probing the supramolecular binding (Figure 1.18a) of a monofunctionalized pyrrolidinofullerene derivative, **F1**. They found that cooperative binding was at play; following the coordinative binding of the pyrrol unit to a peripheral ZnP, the sandwiching of the fullerene (of **F1**) was initiated by a different porphyrin ring. Nanosecond transient absorption also observed a shoulder at 630 nm and a band at 990 nm which emerged (Figure 1.18b) upon photoexcitation, relating to the porphyrin cation and fullerene **F1** radical, respectively. Unexpectedly, the lifetime of the charge-separated state was calculated to be 300 ns, i.e., very long lived, resulting as a consequence of hole-hopping between Zn^{2+}-porphyrin groups around the periphery of [**12ZnP(F1)$_n$**]. With multiple ZnP chromophores of **12ZnP** able to harvest light from the visible region, and the association of **F1** allowing for photoinduced electron transfer, the fullerene hexakis-adduct has served as a model system mimicking the primary events of photosynthesis.

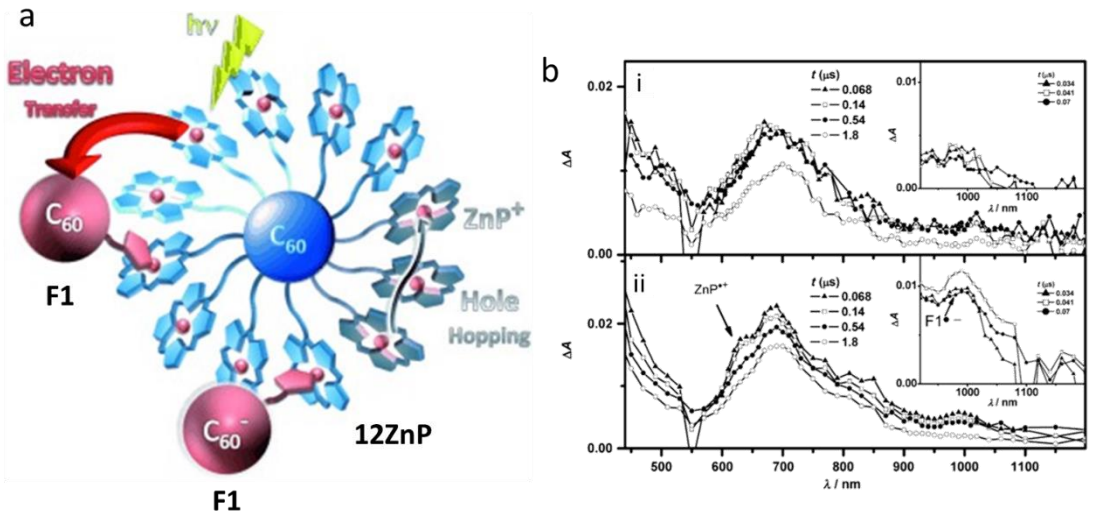

Figure 1.18. a) Schematic representation of photoinduced electron transfer between peripheral ZnP units of **12ZnP** and coordinated **F1**, with subsequent hole-hopping around the periphery. b) Nanosecond transient absorption of **12ZnP** in the presence of **F1** in i) toluene and ii) benzonitrile, excited at 560 nm.

In addition to observing electronic processes across and between fullerene hexakis-adducts there have also been examples that use the pendant functionality to manipulate the 3D scaffold. Stoddart and co-workers have published a canonical example that uses a fullerene scaffold to control the dimerisation process of redox-active viologen units. This work is particularly relevant to Chapter 2 where we use similar techniques to study the redox controlled assembly of NDI units around a fullerene hexakis-adduct. A highly charged species, **12V**$^{24+}$ exists in an 'open' charge-repelled state wherein the viologen units (Figure 1.19a) are at distances >3.5 Å and therefore, non-interacting. Viologen radicals (Figure 1.19b)—when at high concentrations,

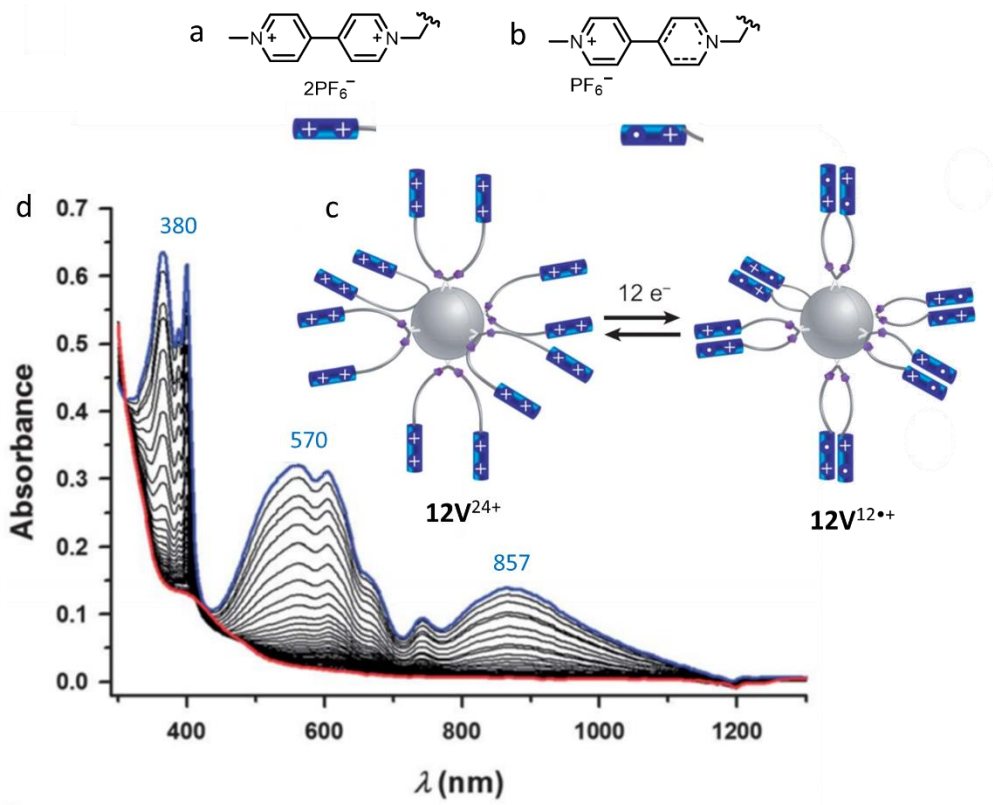

Figure 1.19. a) Viologen unit and b) viologen radical cation unit. c) Illustration of the redox-mediated contraction of a viologen-appended hexakis-adduct of C_{60} *via* π-dimerisation of viologen pairs in the radical state. d) Time resolved UV-Vis spectra of **12V**$^{24+}$ in DMF (0.1 M $TBAPF_6$) with potential held at –0.50 V.

in polar solvents or in covalently enforced close proximity—can dimerse with a characteristic absorption profile centred at ca. λ_{max} = 850 nm. Both by chemical reduction using zinc dust and electrochemically from holding a solution of **12V**$^{24+}$at a potential of –0.50 V vs. Ag/AgCl, **12V**$^{12\bullet+}$ was generated and studied by electrochemistry, UV-Vis (Figure 1.19d) and EPR spectroscopies. With the growth of absorptions bands at λ_{max} = 857 nm the researchers were able to confirm the π-dimerisation of the viologen units, which reverted back to an 'open' state upon oxidation in air. Here, the use of a 3D rigid scaffold with flexible linker chains has allowed for the study of a redox-switchable system that induces molecular reorganisation (Figure 1.19c) upon stimuli (i.e., reduction or oxidation). Whereas only intramolecular (<200 μM) interactions are investigated here, intermolecular investigations of **12V**$^{24+}$a smart material could pave the way for 3D artificial-muscle like molecules (i.e., material contraction and relaxation), in a similar way to that recently described[65] by Barnes and co-workers.

The list of aromatic functionalised hexakis-adducts is not exhaustive in this section but the examples presented demonstrate how the fullerene scaffold can be used to our advantage to look at π-assembly and the associated electronic processes in 3D space. Notably, most of the studies are conducted in the solution state and/or only address fundamental concepts with no implementation in a true device setting. However, devices incorporating fullerene hexakis-adducts as functional molecules are starting to emerge. Völker et al. synthesised[66] a

'super-triarylamine' functionalised hexakis-adduct of fullerene, **FU7** (Figure 1.20a), which was used as an active layer in the design (Figure 1.20b) of a novel perovskite solar cell (PSC). CV experiments of **FU7** confirmed the orbital energies of the HOMO (–5.04 eV) and LUMO (–3.50 eV) to be situated on the triarylamine units and fullerene core respectively. The researchers rationalised that owing to the high conduction band, **FU7** could allow for hole-transporting properties whilst also acting as an efficient electron-blocking material; maintaining carrier transfer to the anode and cathode allows for higher efficiencies to be reached. Additionally, with the apex of the molecule centred around a spherical C_{60} cage, the 3D transport pathways and increased structural ordering in thin films is correlated with a higher device performance (fill factor = 67%), in comparison to a benchmark control spiro-OMeTAD.[67] Indeed, whereas a device based on an active layer of spiro-OMeTAD (fill factor = 20%) required morphology controlling additives such as 4-tert-butylpyridine and lithium bis(trifluoromethane) sulphonimidate to function efficiently, devices based on **FU7** did not. The 3D arrangement of pendant aromatic units likely provides charge transport pathways *via* intra- and intermolecular π-assembly whilst also allowing for a favourable morphology controlled deposition in the device. This study has not only allowed for the synthesis of a functional molecule in a PSC, but has also served as a platform for the next generation of hexakis-adducts that may have improved electrochemical and morphological properties for PSC applications.

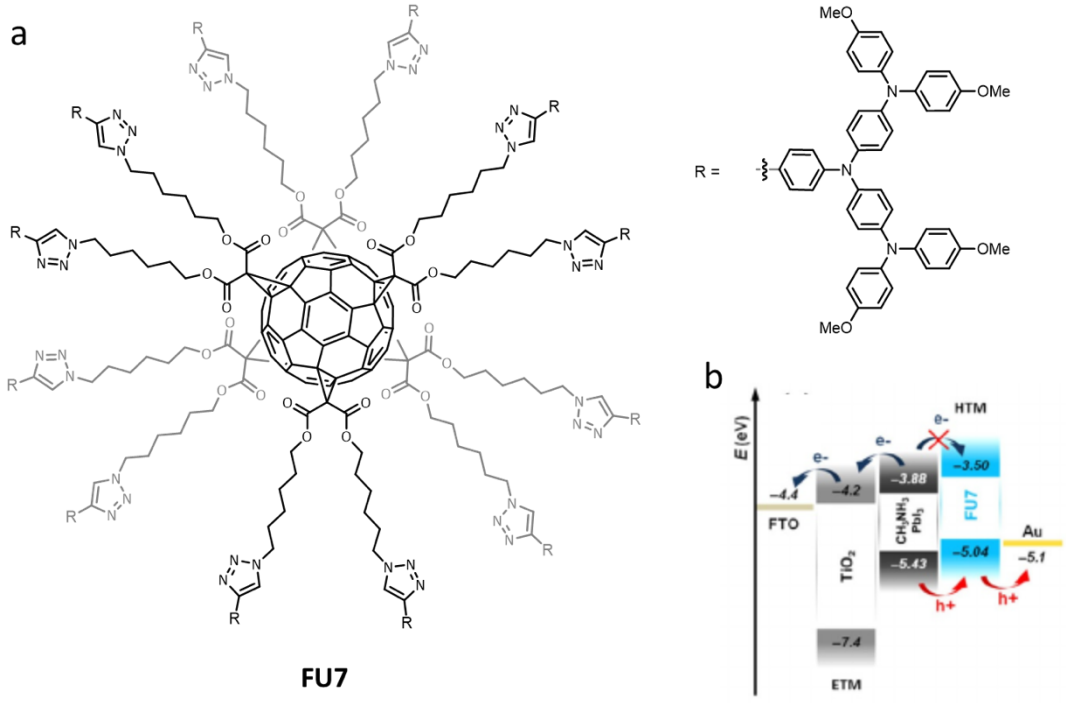

Figure 1.20. a) Chemical structure of hexakis-adduct **FU7**. b) Proposed PSC architecture showing energy level gradients; **FU7** can serve as a *p*-type semiconductor whilst at the same time preventing the backflow of electrons from towards anode.

As demonstrated by the examples presented here, the controlled 3D spatial arrangement of π-functional aromatic units in space provides a unique opportunity to study multivalent photo- and redox-active globular molecules. The fullerene hexakis-adduct structure dictates a scaffold of high integrity and thus can be used to mediate both intra- and intermolecular π-assembly and charge transfer processes for the design of novel organic electronic materials. Indeed, properties such as energy and electron transfer are sought after for photovoltaics, semiconductor materials, etc., and it is only recently that fullerene hexakis-adducts with exploitable properties in devices are starting to emerge. There is a need to synthesise functionalised fullerene hexakis-adducts and study their emergent properties in anticipation of their integration into advanced materials. To this extent we have synthesised redox-active fullerene hexakis-adducts to study radical π-assembly and photoinduced charge transfer in 3D space in Chapters 2 and 3, with the potential applications of these molecules explored in Chapter 4.

1.5 Supramolecular vs. Macromolecular π-Assembly

The study of aromatic interactions in 3D space is still in its nascency because of the challenges associated with the synthesis of 3D scaffolds. 1D assembly remains the most popular and accessible way to achieve long-range ordering of functional aromatic units that is necessary for directing charge, e.g., in a semiconductor device.[68] There are many strategies that have been developed to date that are based primarily on supramolecular chemistry that take advantage of hydrogen bonding, electrostatics, multicomponent assembly, etc. to mediate π-assembly. One of the leading strategies is to use peptide-driven assembly. Here, even short peptides (e.g., dipeptides) can spontaneously assemble to form a range of highly ordered nanoscale architectures such as nanotubes, nanofibrils and nanotapes as well as macroscopic assemblies such as hydrogels.[69–71] From selecting known peptide sequences that have a propensity to form secondary structure motifs such as β-sheets (i.e., that have 1D ordering), the adding or embedding of non-natural motifs in a multicomponent system can allow for the engineering of nanoscale devices with unique functionality. Furthermore, careful design of the peptide system can impose more order towards 1D arrays such as parallel and anti-parallel β-sheet formation, with the latter more stable owing to the alignment of hydrogen bonds.[72] Owing to the properties of individual amino acid building blocks, peptides show the same chemical diversity to that of proteins, however, they lack the stability and robustness of high molecular weight proteins such as fibres. Polypeptide π-assembly could allow for some of these limitations to be overcome in providing materials that have, i) increased stability (i.e., to heat, moisture, pH, stress),

ii) nanoscale ordering (i.e., reminiscent of secondary and tertiary protein structures) and iii) higher performance than the low molecular weight analogue monomers. This section first acknowledges some of the key strategies used in the supramolecular peptide-driven assembly of aromatic units, before discussing how advantages from these systems can be adapted to macromolecular strategies.

1.5.1 Peptide π-Conjugate Assembly

The use of peptides to enforce and direct the assembly of non-specific π-interactions is popular owing to the well-established and known assembly patterns of peptide sequences in natural systems. Chemists exploit such peptide sequences to induce hydrogen bonding that effectively marshals the π-systems of multiple peptide–π conjugates into typical linear arrays. Furthermore, stimuli-responsive properties can be instilled from the integration of amino acids such as lysine that can induce electrostatic repulsion, and therefore disassembly, upon protonation. These assembled supramolecular arrays can be used to study and understand spatio-temporal phenomena that occur between their proximal π-orbitals such as photoinduced electron transfer, long-range electron delocalisation, higher order assembly, and so on.

Exemplifying the self-assembly properties of peptide driven assembly, Parquette et al. have used lysine containing dipeptide NDI-conjugates (Figure 1.21a) to form β-sheet assemblies that have long-range spatial organisation.[73] They showed that the self-assembly of an NDI functionalised dipeptide could be controlled by changing the position of the NDI unit and the free amine along the peptide backbone. As observed by transmission electron microscopy (TEM) and AFM, *N*-protected **DP$_A$** and **DP$_B$** (Figure 1.21a) displayed contrasting self-assembly processes wherein left-handed helical twists with a pitch length of 50 ± 4 nm were observed

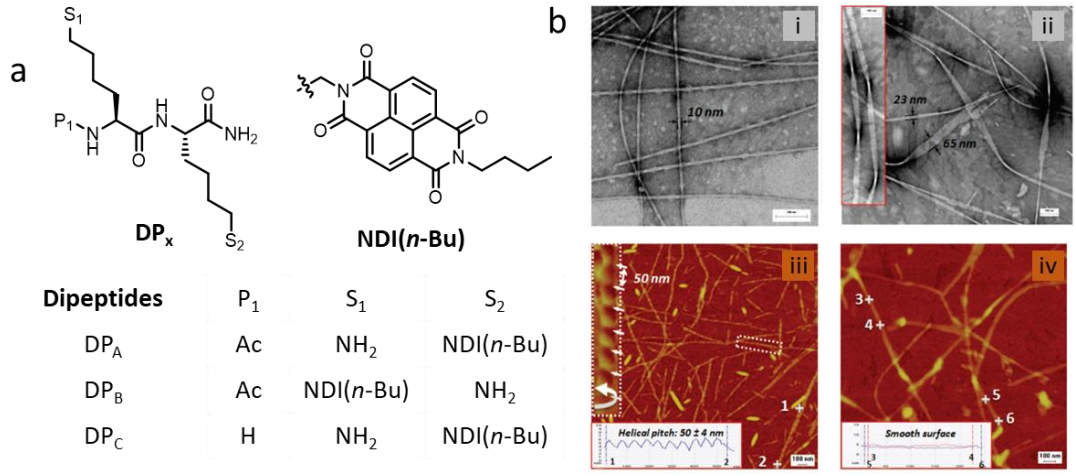

Dipeptides	P_1	S_1	S_2
DP_A	Ac	NH_2	NDI(*n*-Bu)
DP_B	Ac	NDI(*n*-Bu)	NH_2
DP_C	H	NH_2	NDI(*n*-Bu)

Figure 1.21. a) Design of hydrophobic and polar dipeptides, Ac = acetyl. b) The self-assembly of **DP$_A$** in H_2O as visualised by TEM i) and tapping-mode AFM iii) showing left-handed helical fibres with a regular pitch. The self-assembly of **DP$_B$** in H_2O as visualised by TEM ii) and tapping-mode AFM iv) showing left-handed twists that have a smooth surface. No assembly of **DP$_C$** was observed at this concentration (250 μM).

(Figure 1.21b) for **DP$_A$** and flattened, twisted nanoribbons with 20–70 nm in width were observed for **DP$_B$**. In contrast, for the *N*-deprotected **DP$_C$**, no self-assembly was observed at the same concentration (250 μM) owing to the increased electrostatic repulsion between protonated amine groups. Here, a delicate—albeit unpredictable—balance between electrostatic repulsion and hydrophobic interactions are responsible for the self-assembly processes that results in 1D ordering.

Peptide amphiphiles (PAs) can also be used to drive 1D assembly of peptide π-conjugates.[74,75] Here, PAs consists of a hydrophilic head group peptide fragment that is covalently bonded to an aliphatic lipid chain. The incorporation of photo- and redox- units into PAs not only instil optoelectronic properties, but also allows for a synergistic assembly mediated by both hydrogen bonding and π-interactions. Das and co-workers incorporated[76] an NDI unit and a short hydrophilic peptide sequence in a PA (**PC1**, Figure 1.22a) for applications in cell imaging and pH sensing. Their NDI-based hydrogelator self-assembled in aqueous solution, driven by π-stacking, hydrophobic and hydrophilic interactions. Resultantly, a fibrous network formed, with further aggregation over time resulting in the immobilising of water molecules in the formation of a hydrogel, as visualised by TEM (Figure 1.22b).

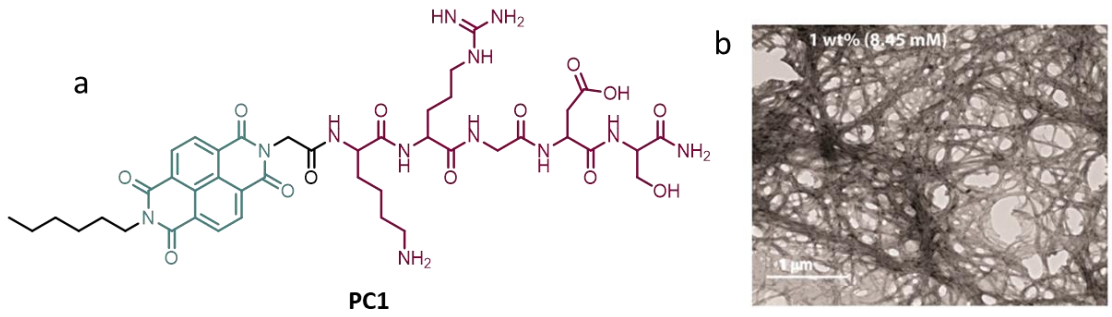

Figure 1.22. a) Chemical structure of **PC1**; π-assembling NDI unit is shown in teal and hydrophilic cell-targeting sequence shown in brown. b) TEM image of the aqueous gel solution of **PC1** taken 72 h from maturation.

Longer peptide sequences that are often synthetically attainable by solid-phase peptide synthesis are more capable of forming highly ordered nanostructures, and as such are used by chemists in designing supramolecular materials that have high fidelity. Inspired by *Bombyx mori silk*, Baurele et al. demonstrated[77] the synthesis and use of peptide-oligothiophene PAs (e.g., **4T-COOH**, Figure 1.23b) to create functional materials with nanoscale structuring also reminiscent of β-sheet formation. They utilised a pentapetide sequence of glycine–alanine (**GAGAG**) to drive assembly of a conjugated thiophene aromatic unit *via* hydrogen bond formation. Signals at 1630 cm^{-1} and 1680 cm^{-1} in the FTIR spectrum (Figure 1.23a) suggested anti-parallel β-sheet organisation of the peptide fragments in the diblock-oligomer, comparable to that of the control **GAGAG** which naturally exhibits β-sheet organisation. However,

disordered linear strands (3.5–4.0 nm in length) were observed (Figure 1.23c) by scanning tunnelling microscopy (STM), presumed to be from head-to-tail assemblies. These observations exemplify the difficulty in enforcing desired—often face-to-face—π-interactions when there are multiple non-covalent interactions present that have the potential to direct self-assembly.

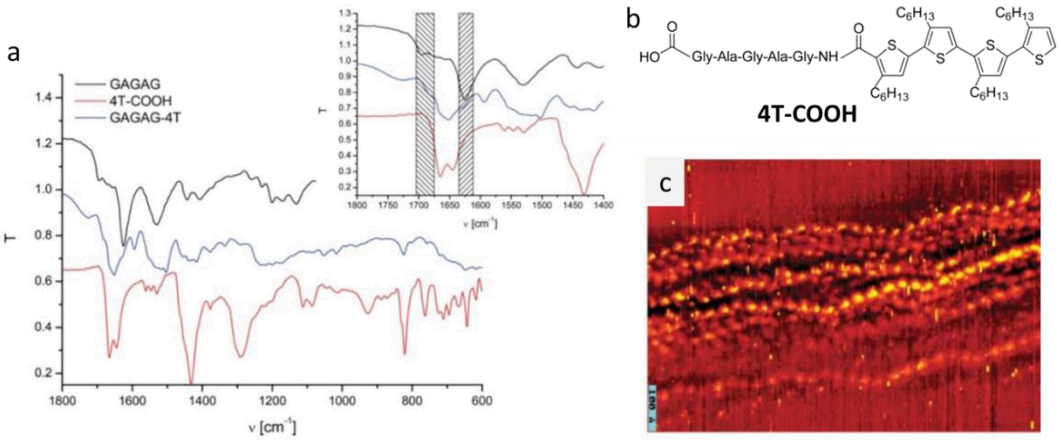

Figure 1.23. a) ATR-FTIR spectra of **GAGAG** (black curve), **4T-COOH** (red curve), and **GAGAG-4T** (blue curve), indicating β-sheet conformation in the peptide hybrid. b) Chemical structure of peptide-oligothiophene conjugate **4T-COOH**. c) STM height image of **GAGAG-4T** on HOPG (62 × 100 nm^2, bias voltage = −600 mV, sample is negative, tunnel current = 68 pA) indicating H-bonded directed assembly in the formation of 2D-organisation.

1.5.2 π-Embedded Peptide Assembly

It is still a challenge to enforce the orientation and through-space interactions of π-functional moieties as they have a propensity to π-stack in a geometry that is energetically favourable, often as head-to-tail assemblies. In peptide assemblies, steric interference induced by large aromatic chromophores can often prevent the desired peptide secondary structures from forming. Whereas PAs allow for access to various nanostructures, another strategy to predictably controlling the π-assembly processes of peptide π-conjugates is through embedding the aromatic units within peptide chains.[78] Although this can be more synthetically challenging, this strategy provides a more predictable level of control over π-interactions during the assembly process. This approach has been utilised to great effect in designing peptide-based organic electronic materials that have 1D ordering.

For instance, Stupp et al. have prepared[79] 1D nanostructured gels using oligothiophene-embedded peptide derivatives in pursuit of functional optoelectronic materials. Breaking their design (Figure 1.24a) strategy into four segments they used: i) a semiconducting oligothiophene core, ii) β-sheet forming amino acids to drive self-assembly, iii) an alkyl spacer chain for molecular flexibility and iv) amino acids for enhanced solubility i.e. lysine. TEM (Figure 1.24b) and AFM imaging confirmed intertwined networks of 1D nanostructures of both

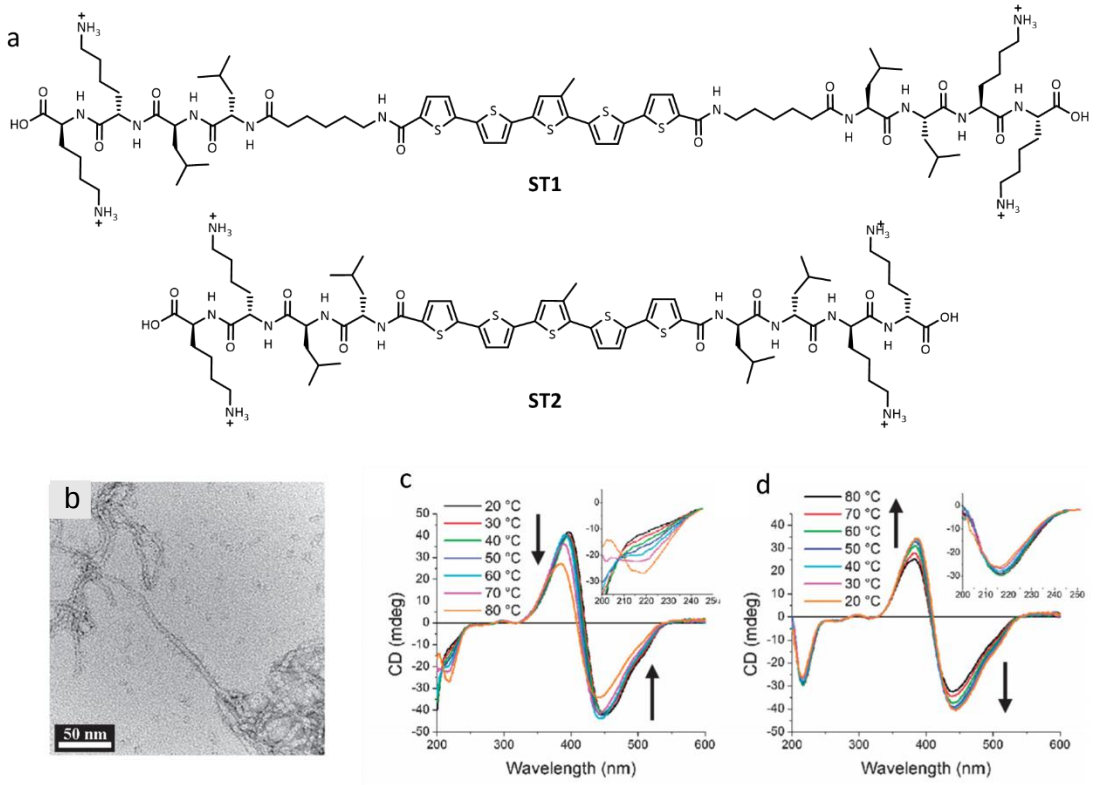

Figure 1.24. a) Molecular structures of oligothiophene-embedded peptides 5TAHxLLKK (**ST1**) and 5TLLKK (**ST2**), differing from the incorporation of a flexible alkyl chain in **ST1**. b) TEM image of **ST1** showing 1D nanostructures with a width of 6.30 ± 0.85 nm. c) Variable-temperature CD spectra of **ST1** upon heating in water and methanol at room temperature. d) Variable-temperature CD spectra of **ST1** upon cooling.

ST1 and **ST2**, with gelation occurring at concentrations ranging from 1–3 wt% in water over the course of 12 h to 5 days. Variable-temperature CD spectroscopy was used to investigate the conformation of the peptide fragment in the 1D structures they observed. Upon heating **ST1**, a minimum at 219 nm was observed in the CD spectrum (inset, Figure 1.24c) indicative of β-sheet assemblies within the gel. Initially, the CD spectrum showed a lack of order (inset, Figure 1.24c) at ambient temperature, suggesting that π-interactions are the dominant force in the aggregates. Following a second round of heating, the assembly does not return to its original state as the β-sheet ordering remains present in the CD spectrum, i.e., once formed the β-sheet assemblies are strong. Interestingly, **ST2** does not show any bands in the peptidic region (200–250 nm) of its CD spectrum (Figure 1.24d), at all temperatures tested, with only a small Cotton effect observed correlating to the thiophene units. The additional flexibility of **ST1** is necessary in facilitating hydrogen bonding between the peptide fragments and without the linker, the uncontrolled π-assembly processes dominate aggregate formation over β-sheet ordering. Despite observing self-sustaining hydrogels for both π-embedded peptides, these investigations show that other factors, such as the addition of spacers and the spatial alignment of hydrogen bonds are vital in controlling nanoscale ordering.

In another example, Hodgkiss[80] et al. capitalised on the complementarity of an antiparallel β-strand interface that exists between the two subunits of the protein dimer peroxiredoxin. By embedding PDI units between the peptide sequences (Ile-Lys-His-Leu-Ser-Val-Asn) from the two interfaces, they were able to direct 1D assembly (Figure 1.25a). Furthermore, a series of embedded PDI peptide-conjugates were synthesised to compare the effect of the number of peptide substituents and the directionality of their connectivity. Sequences were also terminated with a trimer of glutamic acid residues that were used to aid solubility of the molecule as well as providing a means to invoke pH-triggered assembly of the π-embedded peptide. The material with the peptides oriented in the *N*-terminal to *C*-terminal direction away from PDI resulted in strong intermolecular π-couplings and long range ordering visualised by TEM and CD experiments (Figure 1.25a/b). Although this example demonstrates a highly order one-dimensional assembly of PDI units, it is synthetically quite demanding as it uses a non-repetitive 20 amino acid sequence. A route towards highly order 1D assembly that only makes use of repetitive amino acids or dipeptide sequences is an attract alternative.

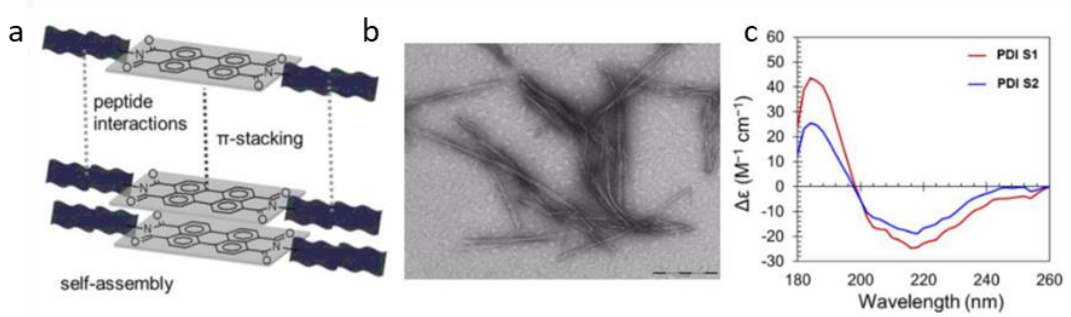

Figure 1.25. a) Illustration of self-assembly between PDI-embedded peptide conjugates, confirmed to be 1D assemblies, i.e., β-sheets, by b) TEM and c) CD spectroscopy experiments.

For all of the fundamental progress achieved in the synthesis of peptide–π conjugates and demonstration of emergent properties, it is still uncommon for such self-assembled materials to be investigated for fundamental energy transfer processes—though there are a handful of examples. Tovar et al. have used[81] both embedded and side-chain aromatic motifs for the peptide-driven supramolecular polymerisation of π-conjugated electron donor–acceptor molecules. Electron-donating oligothiophene motifs were embedded in a β-sheet forming peptide sequence (Gly-Gly-Val-Glu-Lys), with electron-accepting NDIs installed *via* imidation at site-specific lysine residues (Figure 1.26a). Stacking of the π-conjugated peptides under aqueous conditions afforded 1D nanostructures (Figure 1.26b) that were confirmed by CD and TEM experiments. The transfer of charge between the peptidic platforms was confirmed using dynamic photospectroscopy (Figure 1.26c/d) with long lived charge-separated species observed in the assembled state. Altering the pH of the medium allowed for control of the assembly process and the degree of charge transfer by modulating charged states and the degree of Coulombic repulsion between peptide chains.

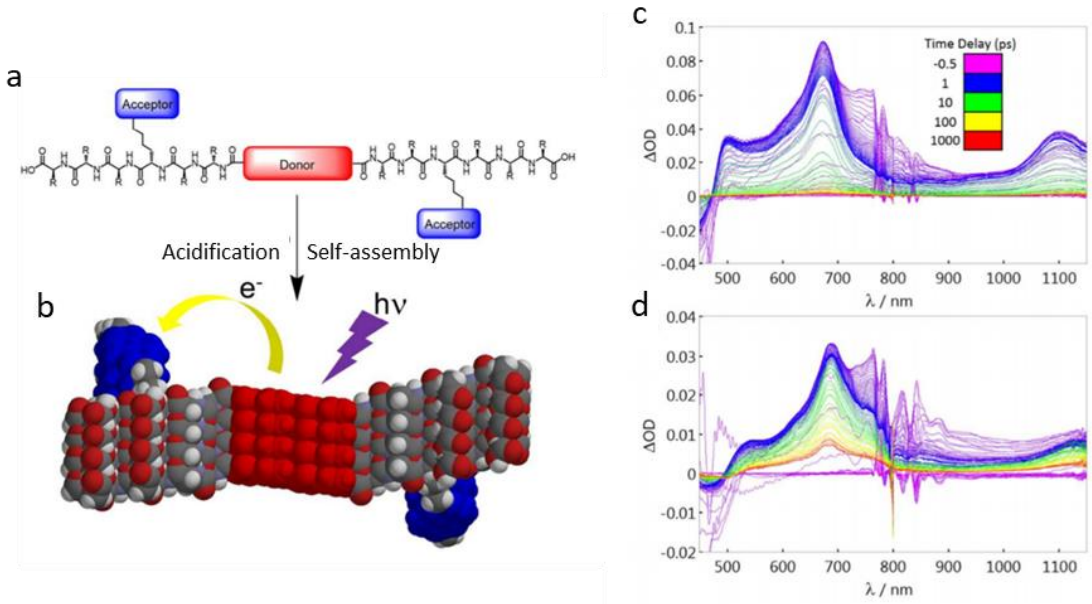

Figure 1.26. a) Molecular design and b) illustration of self-assembly and electron transfer of the donor-acceptor π-peptide hybrid. Spectral dynamics following excitation of the designed system (**DA-2**) in a c) non-assembled and (d) assembled state, showing two photo induced responses including excitation of oligothiophene and oxidation of NDI.

Additionally, charge transport properties have been demonstrated[82] through self-assembled nanostructures of oligothiophene-embedded peptides (Figure 1.27a). Tovar and co-workers used highly charged peptide sequences, i.e., glutamic and aspartic amino acids, to increase the solubility of their peptide π-conjugates whilst instilling a means to drive self-assembly upon changing pH. At pH = 6 (i.e., when Coulombic repulsion is no longer present), UV-Vis and CD spectroscopies identified that the monomeric units self-assembled into *H*-like aggregates (Figure 1.27b). TEM was used to characterise the nanostructure morphologies

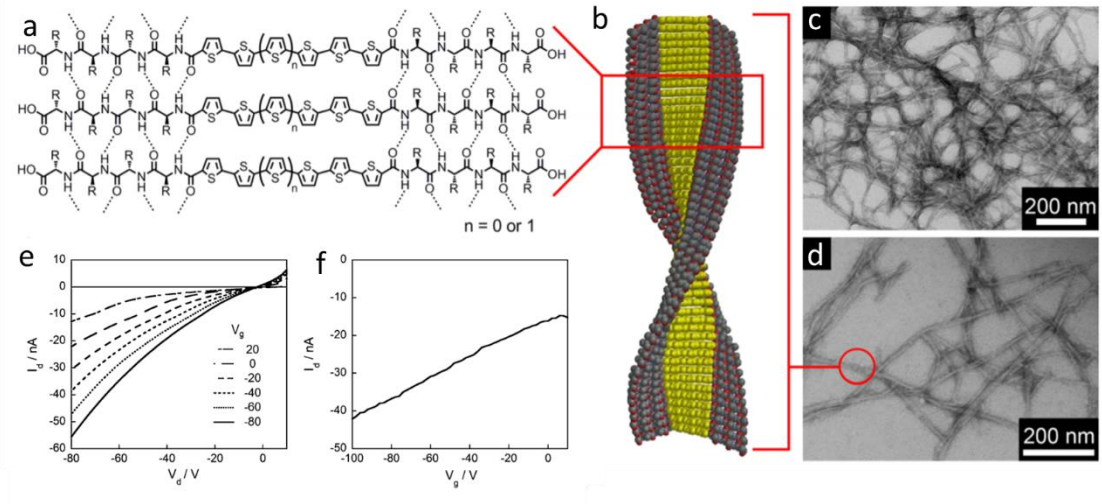

Figure 1.27. a) Chemical structure of a general oligothiophene peptide conjugate including the intermolecular hydrogen bonding network and b) a space-filling model to illustrate the assemblies. c–d) TEM images of 1D nanostructures formed following self-assembly. Current–voltage plots for field-effect transistor of an oligothiophene peptide conjugate at e) gate voltages of 20 V to –80 V and d) at an applied drain voltage of –80 V, with varied gate voltage.

(Figures 1.27c/d) confirming that 1D assemblies in micrometre length were formed. To demonstrate the electrical properties, the self-assembled nanostructures were incorporated into the active layer of a field effect transistor. The current–voltage output (Figure 1.27e/f) allowed for a hole mobility of the nanostructures to be calculated (3.8×10^{-5} cm^2 V^{-1} s^{-1}) confirming that charge could be transported through the networks of self-assembled structures. As demonstrated by these examples, multicomponent supramolecular assemblies involving the propagation of individual 'monomer' molecules presents an elegant, straightforward route to accessing nanotopologies of high structural ordering. Indeed, with a vast library of protein structures available, there is breadth for the inspiration of newly designed nanotechnologies driven to assemble using established peptide sequences. However, the use of peptides in multi-component self-assembly is not without drawbacks as, i) their assembly to desired nanostructures is often hard to predict and ii) the low molecular weight building blocks can be sensitive to temperature changes and acidic or alkali environments, sometimes hampering their structural integrity and ability to function in device applications.

1.5.3 Mediating π-Assembly with Macromolecular Architectures

Beyond supramolecular multicomponent assembly, researchers have looked at other strategies to achieve aromatic interactions within discrete molecules. These pre-configured systems are in many ways more synthetically demanding, however, they provide a situation from which fundamental π-interactions can be fully interrogated (e.g., by CV, UV-Vis and PL

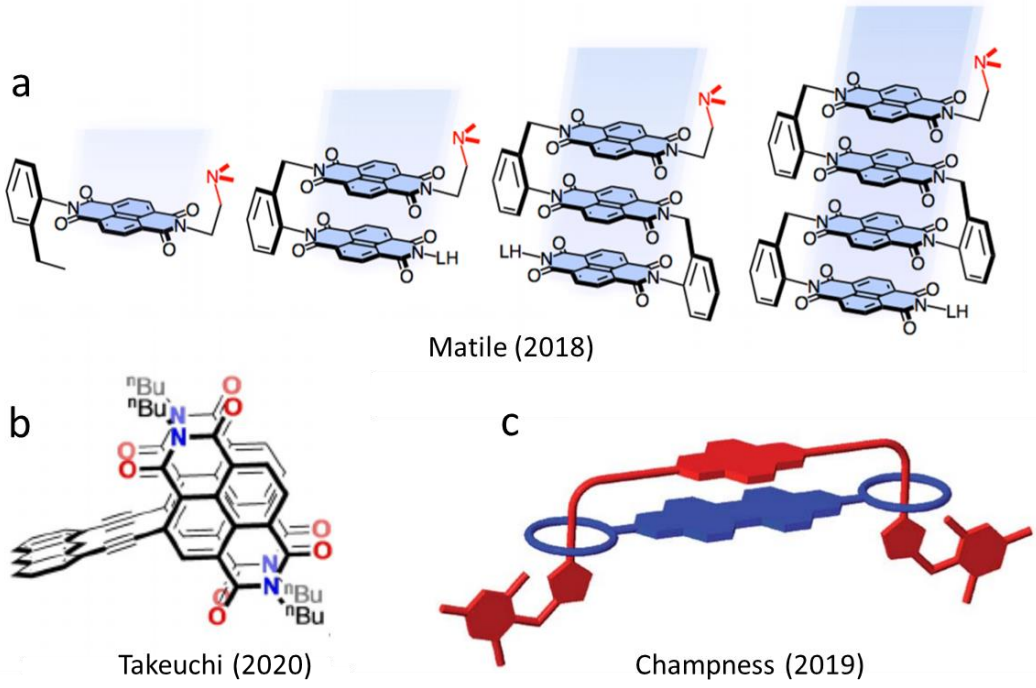

Figure 1.28. Structures of a) Matile's NDI foldamers, b) Takeuchi's tweezer-shaped NDI–anthracene conjugate and c) illustration of Champness' NDI–PDI mechanically interlocked handcuff.

spectroscopy, etc.) For instance, macrocycles such as the NDI cofacial dimer[45] (*vide supra*, Figure 1.12) as well as rigid oligomers of NDI from the Matile[83] (Figure 1.28a) and Takeuchi[84] groups (Figure 1.28b) have provided platforms to observe NDI interactions in the neutral as well as reduced state. Even MIMs, such as those presented by the Champness group (Figure 1.28c), where now the π-systems are more dynamic with respect to one another but are still confined to a discrete space allow for fundamental investigations into aromatic interactions between rylene diimides.[85] These examples are valuable because they allow understanding of electronic processes across well-defined distances between a discrete number of functional aromatic units which is difficult to achieve in supramolecular systems (i.e., where the number of interacting units is not possible to control). However, it is synthetically quite demanding to prepare these small molecular systems and ideally, higher length scales want to be achieved so that these materials can be potentially developed for applications in organic electronic devices. This section is going to describe the current state of the field with regards to using macromolecular strategies to organise aromatic units in long-range 1D assemblies. Ultimately, macromolecular approaches to guiding π-assembly have not yet demonstrated the successful self-assembly properties displayed by peptide-driven assembly, however, the field is beginning to move towards this target.

Iverson et al. have demonstrated[86,87] the extent to which π-interactions can be directed using foldamer assembly. Comprising of a flexible amphiphilic backbone of alternating asparagine and leucine amino acids, the Iverson foldamers[86] (Figure 1.29a) adopt a folded conformation in which electron-rich 1,5-dialkoxynaphthalene (DAN) and NDI units are stacked upon each other, owing to the favourable aromatic CT interactions between π-surfaces. These polymeric structures display characteristic CT absorbance in the visible region, giving rise to a purple colour in aqueous solution.

Whereas hetro-assembly of donor–acceptor aromatics is relatively straight forward because of the favourable electrostatics between the units, homo-assembly is much more challenging to achieve. Following their initial foldamer work, Iverson et al. revealed[87] the conformational switching of the stacked foldamer into a fibril aggregate, driven by homo-assembly, i.e., by intermolecular NDI–NDI aggregation. Upon heating the stacked foldamer, the researchers observed the disappearance of the NDI–DAN CT band (λ_{max} = 526 nm) by UV-Vis spectroscopy with chiral assemblies, i.e., fibril formation, confirmed by CD spectroscopy and TEM (Figure 1.29b). They proposed that the formation of 1D ribbons was driven by the amphilicity of the unravelled foldamer, with hydrophobic leucine surfaces coming in close contact to form a pseudo-bilayer. Proposing that this could also be a fundamental driving force in amyloid fibre formation this example demonstrates the use of foldamers to not only understand secondary structure formation, but also hierarchical ordering.

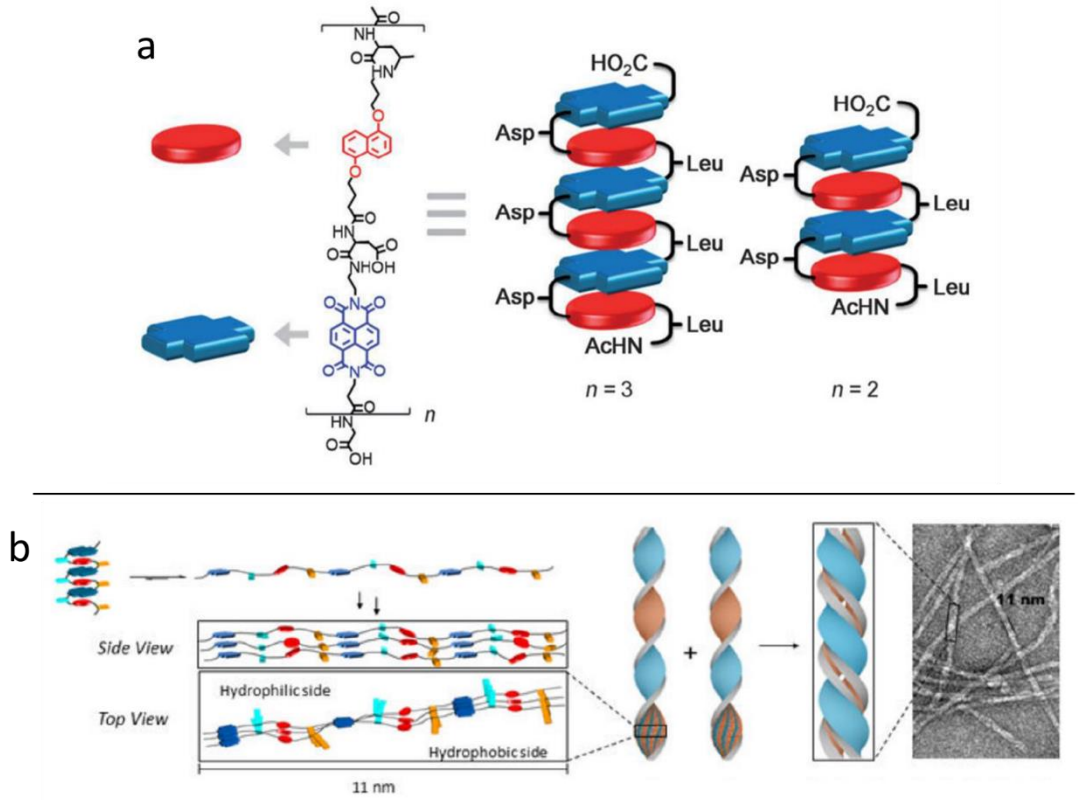

Figure 1.29. a) Iverson et al. synthesised a range of foldamers based on their initial design of alternating DAN and NDI residues in a flexible chain, overserving self-assembly driven by the hydrophobic effect and aromatic CT interactions. b) Upon heating, the unfolded amphiphilic foldamer form 1D fibres, driven to assembly by off-set NDI–NDI stacking with dimerisation to sequester the hydrophobic leucine residues.

The conformation switching properties of diaminonaphthalene–viologen (**NP1**) foldamers has been exemplified by the Li group.[72] Here, instead of using heat to switch between macromolecular conformations, they used redox chemistry (i.e., reduction with Zinc dust) to cause a switch between CT-stabilised hetro-assembly and homo-assembly (Figure 1.30) of viologen units. Unlike in discrete supramolecular systems that are less dynamic, these macromolecular system still possesses a degree of dynamic behaviour that allows for the switching of conformations and different types of aromatic assembly in the same system.

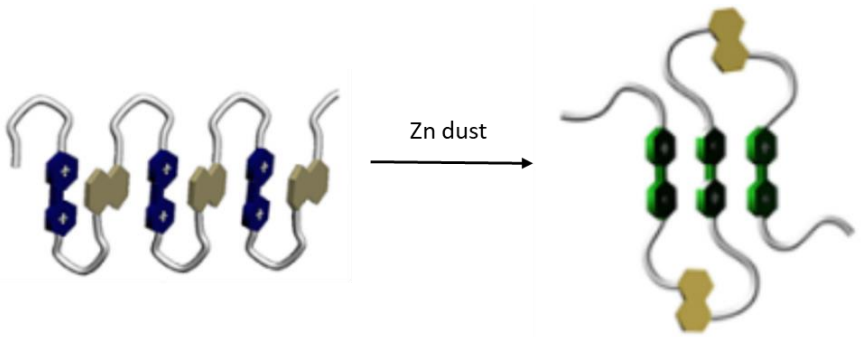

Figure 1.30. Polymer **NP1** is stabilised by intramolecular aromatic charge-transfer π-interactions, i.e., hetro-assembly of viologen (dark blue) and diaminonaphthalene (beige) units. Upon reduction of the viologen units, the polymer changes conformation to allow for aggregation of the viologen radical cations (green).

It is not necessary to use such complex systems to achieve homo-assembly of aromatic units with redox-controlled assembly possible in homo-polymers of viologen units. This has been demonstrated again by the Li group who showed that oligo (ethylene glycol)-linked viologen radical cation polymers (**L1–4**, Figure 1.31a) can form pleated secondary structures driven by radical stacking. Owing to Coulombic repulsion between viologen units, the polymers exist in an extended state. Upon reducing their polymers of differing linker length between viologen units (V), they observed an absorption band at 650 nm corresponding to the monomer bipyridium radical cation ($V^{\bullet+}$) as well as a band at 1020 nm (Figure 1.33c) corresponding to the radical cation dimer $(V^{\bullet+})_2$. At the same concentration, no absorption for $(V^{\bullet+})_2$ was observed in the spectrum for **LM1** (Figure 1.31b), indicating that positive cooperativity was at play between $V^{\bullet+}$ in the polymers of greater chain length. Subsequently, the addition of lithium and sodium cations to the polymers allowed for coordination to the glycol chains and the reinforcing of the pleated structure (Figure 1.31d), as confirmed with an increase in absorption corresponding to the $(V^{\bullet+})_2$ dimer. Li et al. found that the linker between strands of a folding polymer play an important role in directing intermolecular π-assembly. Indeed, for **L1** (shortest linker) intermolecular dimerisation of $V^{\bullet+}$ was favoured over intramolecular folding whereas the longer linkers resulted in a looser folded state with the absorption corresponding to $(V^{\bullet+})_2$ weakening from **L2**, to **L3** to **L4**. These observations confirm that the shape and length of linkers in π-embedded foldamers are very important in enhance 1D nanostructures such as pleated sheets with the Li group demonstrating these findings further in multiple examples.[88,89]

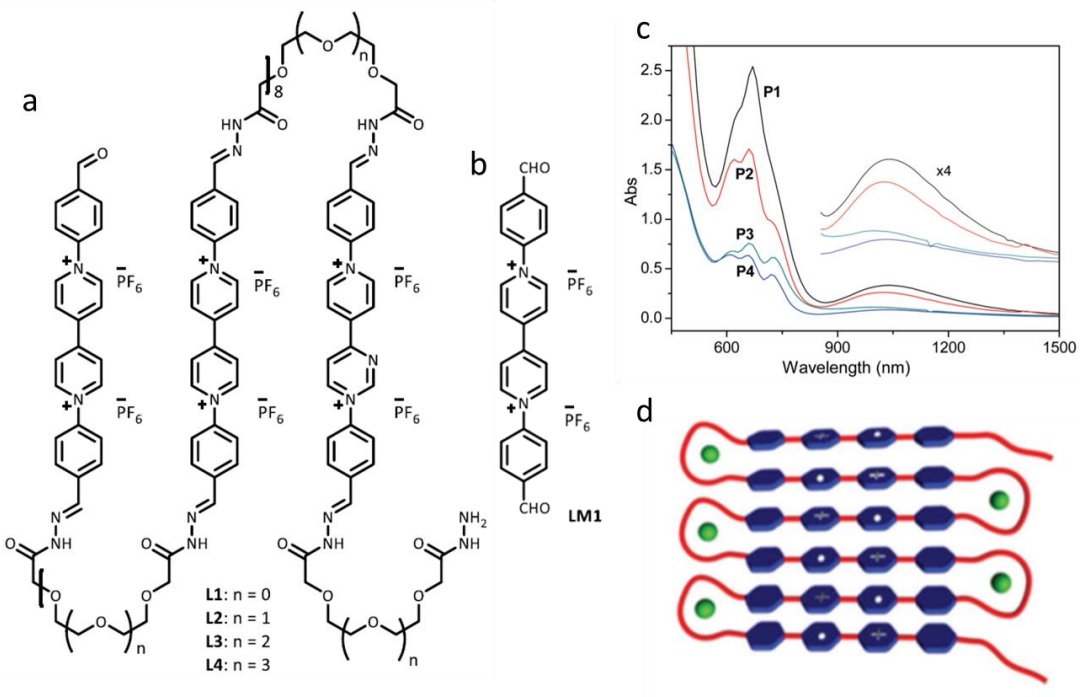

Figure 1.31. Molecular structures of a) the viologen polymers (**L1–4**) of differing glycol space length and b) control monomer **LM1**, and viologen monomer. c) UV-Vis spectra of the reduced polymers. d) Illustration of the proposed pleated foldamers driven by the dimerisation of V•+ units and stabilisation of structure by ether–cation binding.

Macromolecular systems that mediate π-assembly in the context of a device are currently uncommon. However, Ikeda has demonstrated that an understanding of the self-assembly process of such systems can be realised in a device setting. Ikeda published[90,91] a series of papers on the hierarchical self-assembly of a synthetic polymer that forms supramolecular 2D nanosheets for applications in OEDs. Their design adopted a phenyl-capped bithiophene (Ph_2TPh) as a rigid, functional π-motif, terminated with ethylene glycol chains. Utilising azide and alkyne end groups, they polymerised their macromonomer to **poly(Ph_2TPh-OEG)** (Figure 1.32) *via* CuAAC chemistry. In the polymeric form, the UV-Vis spectrum showed aggregation of the Ph_2TPh motifs in organic solvent, indicating the folding of the copolymer and close-proximity of the bithiophene units. TEM and dynamic light scattering (DLS) revealed, however, the formation of nanosheets (Figure 1.32) instead of the proposed 1D fibres. The UV-Vis spectrum of the monomeric species did not show any indication of self-assembly (i.e., π-aggregation) which shows that nanosheet formation required the folding of the copolymer. These observations identify the importance of pre-inducing the folding of the polymer chains in directing interactions between embedded π-units.

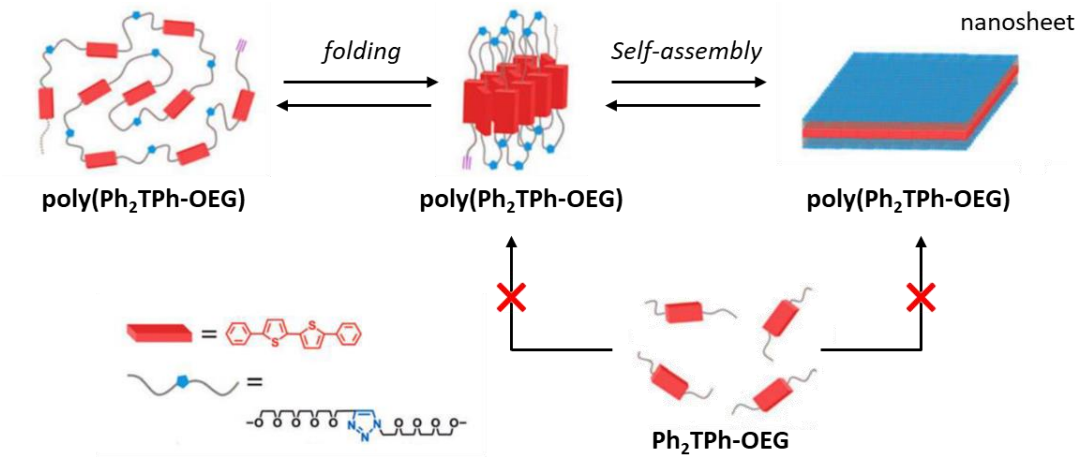

Figure 1.32. Illustration of the potential mechanism to nanosheet assembly including folding of **poly(Ph_2TPh-OEG)** into aggregated states that self-assemble, whilst monomeric **Ph_2TPh-OEG** does not self-assemble.

Recently, these ultrathin nanosheets of **poly(Ph_2TPh-OEG)** have been demonstrated[92] as high performance pseudo capacitors for potential new concept thin-film energy storage devices. Stacked in a film consisting (Figure 1.33a) of a gold-coated polyethylene terephthalate (PET) substrate and electrochemically exfoliated graphene (EG), the **poly(Ph_2TPh-OEG)** nanosheets were tested for their use as all-solid-state supercapacitors (ASSSs). An ultrahigh energy density of 13 mWh cm^{-3} was attained for TP/EG-ASSSs with uptake of the energy at 4.5 mWh cm^{-3} for TP/EG-ASSSs indicating very fast recharge times. Functionally, the capacitive performance of TP/EG-ASSSs under deformation was tested and showed no decrease in performance

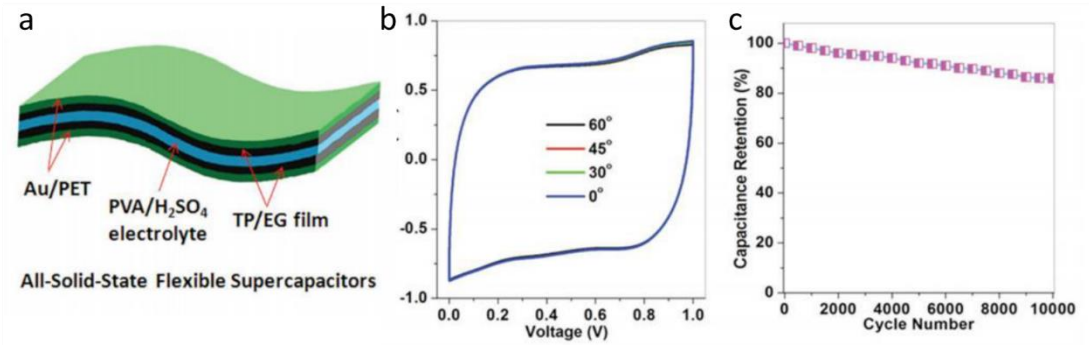

Figure 1.33. a) The device architecture of flexible **poly(Ph2TPh-OEG)**/EG-ASSSs. b) voltammogram of **poly(Ph2TPh-OEG)**/EG-ASSSs tested under different bending degrees. c) The cycling stability of the **poly(Ph2TPh-OEG)**/EG-ASSSs measured at a scan rate of 100 mV s^{-1}.

(Figure 1.33b), with only a slight degradation in performance over 1000 cycles (Figure 1.33c). Although not using biomimetic assembly to induce hierarchical formation, this work demonstrates an example of hierarchical assembly of a macromolecule in functional nanomaterials that bare exceptional performance. Additionally, this work further implies that π-interactions on their own cannot yield 1D structures predictably. In fact, a macromolecular assembly approach is key to accessing this topology.

As has been noted, π-assembly within a macromolecular architecture offers the opportunity to develop robust materials that exhibit high levels of structural hierarchy. Although not in pursuit of 1D assemblies with embedded photo- and/or redox-active properties, an approach by Guan and co-workers on synthetic β-sheet forming polypeptides provides an attractive route to accessing polymers exhibiting 1D and hierarchical ordering.[93] They employed CuAAC to polymerise a peptide macromonomer (**GM1**, Figure 1.34a) composed of a hexapeptide sequence of alternating alanine and glycine residues, similar to the repeating amino acid sequences of β-sheet forming polypeptides found in spider silks. Their use of CuAAC

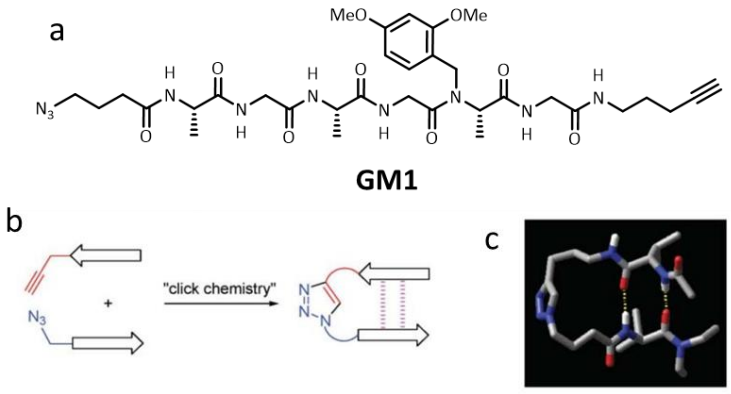

Figure 1.34. a) A protected hexapeptide macromonomer (**GM1**) with azide and alkyne moieties, synthesised by Guan et al. b) β-turn mimic as described by Burgess et al. utilising CuAAC 'click' chemistry, and c) an energy minimised structure showing hydrogen bond formation between the strands; a three carbon linker chain between the triazole and the proximal amide residues maximises the interactions between strands, similar to that observed in anti-parallel β-sheet formation in amyloid fibres.

chemistry not only allowed a convergent synthetic route to high molecular weight polymers, but also embedded a synthetic β-turn (Figure 1.34b/c) regularly throughout the macromolecule.[94] Although not mediating π-assembly, this method of polymer assembly could be applied towards organising photo- and redox-active embedded macromolecules into nanoscale structures sought after for accessing unique and interesting optoelectronic properties.

By utilising directed hydrogen bonding networks between antiparallel peptide chains, specific cofacial 1D-alignment of functional aromatic surfaces can be enforced and exploited for their emergent optical and electron conducting properties. The synthetic achievement's[93] by Guan serve as the ideal platform to tailor a macromolecular system for the design of functional optoelectronic materials. Peptide driven assembly has been used[76,77,95,96] to guide π-interactions, in pursuit of materials exhibiting optoelectronic properties. However, macromolecular-polypeptide assembly *via* the formation of synthetic β-sheets offers an unparalleled level of control in directing π-assembly processes, and thus will be worth the additional synthetic challenge in successfully making high molecular weight functional polymers. In doing so, we may achieve access to novel materials for fundamental structure–property investigations as well as for the development of advanced organic electronic devices.

1.6 Overview

With the emergence of nanotechnology and the 'bottom up' approach to designing materials, supramolecular strategies are poised to deliver unrivalled performance from a means that is tuneable, low cost and from a renewable source. Controlling the π-assembly of photo- and/or redox-active aromatic units is not only on fundamental importance to supramolecular chemistry, but also for the design of functional materials in a device setting. There are various strategies that exist to control the assembly of functional aromatic molecules. In this chapter, we have explored the current state-of-the-art for two main strategies in controlling the π-assembly of aromatic systems. 3D scaffolding that takes advantage of fullerene hexakis-adducts has been shown to facilitate electronic processes, energy transfer and even redox-controlled aromatic assemblies in 3D space. The 3D approach to organising aromatic molecules is still in its nascency and therefore much less developed than 1D strategies. We have explored the attractive supramolecular approaches that have been in pursuit of 1D ordering and seen how these strategies have evolved for π-assembly mediated by macromolecular architectures. Supramolecular materials have inherent limitations such as their sensitivity to pH, moisture, temperature, stress, etc. and their propensity to aggregate into non-desirable nanoscale ordering. Macromolecular scaffolds can help to overcome some of these issues by providing access to: i) more robust materials, ii) materials that have hierarchical ordering (i.e., multiple levels of assembly) and iii) materials that have advanced functioning. Moreover, macromolecular π-assembly is not an extensively studied approach towards guiding the assembly of π-surfaces and therefore opportunities exist to further scientific understanding through fundamental investigations.

Photo- and redox-active molecules that have useful optoelectronic properties are important for the design of advanced organic materials. Strategies that can control and exploit how these functional molecules interact in homo- as well as hetro-assemblies will pave the way for materials with emergent properties that have the potential to be used in many applications such as photovoltaics, semiconductor materials, advanced displays, and many more.

1.7 References

1 M. Iwane, T. Tada, T. Osuga, T. Murase, M. Fujita, T. Nishino, M. Kiguchi and S. Fujii, *Chem. Commun.*, 2018, **54**, 12443–12446.

2 J. Idé, R. Méreau, L. Ducasse, F. Castet, Y. Olivier, N. Martinelli, J. Cornil and D. Beljonne, *J. Phys. Chem. B*, 2011, **115**, 5593–5603.

3 T. Okamoto, S. Kumagai, E. Fukuzaki, H. Ishii, G. Watanabe, N. Niitsu, T. Annaka, M. Yamagishi, Y. Tani, H. Sugiura, T. Watanabe, S. Watanabe and J. Takeya, *Sci. Adv.*, 2020, **6**, eaaz0632.

4 S. Chen, S. M. Lee, J. Xu, J. Lee, K. C. Lee, T. Hou, Y. Yang, M. Jeong, B. Lee, Y. Cho, S. Jung, J. Oh, Z. G. Zhang, C. Zhang, M. Xiao, Y. Li and C. Yang, *Energy Environ. Sci.*, 2018, **11**, 2569–2580.

5 S. K. Hong, J. H. Sim, I. G. Seo, K. C. Kim, S. Il Bae, H. Y. Lee, N. Y. Lee and J. Jang, *J. Disp. Technol.* 2010, **6**, 601-606.

6 Y. Chen and C. Wang, *Acc. Chem. Res.* 2020, **53**, 2636–2647.

7 C. K. Mc Laughlin, G. D. Hamblin and H. F. Sleiman, *Chem. Soc. Rev.*, 2011, **40**, 5647–5656.

8 D. W. Ussery, in *Encyclopedia of Life Sciences*, John Wiley & Sons, Ltd, Chichester, UK, 2002.

9 M. T. Dang, L. Hirsch and G. Wantz, *Adv. Mater.*, 2011, **23**, 3597–3602.

10 M. Vanjinathan, H. C. Lin and A. S. Nasar, *Macromol. Chem. Phys.*, 2011, **212**, 849–859.

11 D. Basak, A. Das and S. Ghosh, *RSC Adv.*, 2014, **4**, 43564–43571.

12 T. M. Gianga, E. Audibert, A. Trandafir, G. Kociok-Köhn and G. D. Pantoş, *Chem. Sci.*, 2020, **11**, 9685–9690.

13 M. B. Upama, M. A. Mahmud, G. Conibeer and A. Uddin, *Sol. RRL*, 2020, **4**, 1900342.

14 C. J. Traverse, R. Pandey, M. C. Barr and R. R. Lunt, *Nat. Energy*, 2017, **2**, 849–860.

15 G. Li, W. H. Chang and Y. Yang, *Nat. Rev. Mater.*, 2017, **2**, 17043.

16 J. Vrbancich and G. L. D. Ritchie, *J. Chem. Soc. Faraday Trans. 2.*, 1980, **76**, 648–659.

17 C. R. Martinez and B. L. Iverson, *Chem. Sci.*, 2012, **3**, 2191–2201.

18 J. Hernández-Trujillo and A. Vela, *J. Phys. Chem.*, 1996, **100**, 6524–6530.

19 Y. Geng, H. Bin Li, S. X. Wu and Z. M. Su, *J. Mater. Chem.*, 2012, **22**, 20840–20851.

20 A. Sugie, W. Han, N. Shioya, T. Hasegawa and H. Yoshida, *J. Phys. Chem. C*, 2020, **124**, 9765–9773.

21 K. Takimiya, S. Shinamura, I. Osaka and E. Miyazaki, *Adv. Mater.*, 2011, **23**, 4347–4370.

22 J. T. E. Quinn, J. Zhu, X. Li, J. Wang and Y. Li, *J. Mater. Chem. C*, 2017, **5**, 8654–8681.

23 J. Choi, H. Song, N. Kim and F. S. Kim, *Semicond. Sci. Technol.*, 2015, **30**, 064002.

24 C. Wang, H. Dong, W. Hu, Y. Liu and D. Zhu, *Chem. Rev.*, 2012, **112**, 2208–2267.

25 A. A. J. Aquino, I. Borges, R. Nieman, A. Köhn and H. Lischka, *Phys. Chem. Chem. Phys.*, 2014, **16**, 20586–20597.

26 S. Quinn, E. S. Davies, C. R. Pfeiffer, W. Lewis, J. McMaster and N. R. Champness, *ChemPlusChem*, 2017, **82**, 489–492.

27 H. C. Wentz, G. Skorupskii, A. B. Bonfim, J. L. Mancuso, C. H. Hendon, E. H. Oriel, G. T. Sazama and M. G. Campbell, *Chem. Sci.*, 2020, **11**, 1342–1346.

28 N. Kumari, S. Naqvi and R. Kumar, *J. Mater. Sci.*, 2018, **53**, 4046–4055.

29 S. Maniam, K. Oka and H. Nishide, *MRS Commun.*, 2017, **7**, 967–973.

30 N. Nandi, S. Basak, S. Kirkham, I. W. Hamley and A. Banerjee, *Langmuir*, 2016, **32**, 13226–13233.

31 S. Maniam, H. F. Higginbotham, T. D. M. Bell and S. J. Langford, *Chem. Eur. J.*, 2019, **25**, 7044–7057.

32 P. Ganesan, X. Yang, J. Loos, T. J. Savenije, R. D. Abellon, H. Zuilhof and E. J. R. Sudhölter, *J. Am. Chem. Soc.*, 2005, **127**, 14530–14531.

33 F. Würthner, T. E. Kaiser and C. R. Saha-Möller, *Angew. Chem. Int. Ed.*, 2011, 50, 3376–3410.

34 S. Basak, N. Nandi, A. Baral and A. Banerjee, *Chem. Commun.*, 2015, **51**, 780–783.

35 S. Ghosh, X. Q. Li, V. Stepanenko and F. Würthner, *Chem. Eur. J.*, 2008, **14**, 11343–

11357.

36 H. Kar, M. R. Molla and S. Ghosh, *Chem. Commun.*, 2013, **49**, 4220–4222.

37 S. M. Wagalgave, S. D. Padghan, M. D. Burud, M. Al Kobaisi, D. D. La, R. S. Bhosale, S. V. S. V. Bhosale and S. V. S. V. Bhosale, Sci. Rep. 2019, **9**, 12825.

38 V. W. S. Kwan, V. Cammarata, L. L. Miller, M. G. Hill and K. R. Mann, *Langmuir*, 1992, **8**, 3003–3007.

39 C. J. Zhong, W. S. V. Kwan and L. L. Miller, *Chem. Mater.*, 1992, **4**, 1423–1428.

40 L. L. Miller, T. Hashimoto, I. Tabakovic, D. R. Swanson and D. A. Tomalia, *Chem. Mater.*, 1995, **7**, 9–11.

41 J. F. Penneau, B. J. Stallman, L. L. Miller and P. H. Kasai, *Chem. Mater.*, 1991, **3**, 791–796.

42 K. Cai, L. Zhang, R. D. Astumian and J. F. Stoddart, *Nat. Rev. Chem.*, 2021, **5**, 447–465.

43 R. Murase, C. F. Leong and D. M. D'Alessandro, *Inorg. Chem.*, 2017, **56**, 14373–14382.

44 A. J. Avestro, D. M. Gardner, N. A. Vermeulen, E. A. Wilson, S. T. Schneebeli, A. C. Whalley, M. E. Belowich, R. Carmieli, M. R. Wasielewski and J. F. Stoddart, *Angew. Chem. Int. Ed.*, 2014, **53**, 4442–4449.

45 Y. Wu, M. Frasconi, D. M. Gardner, P. R. McGonigal, S. T. Schneebeli, M. R. Wasielewski and J. F. Stoddart, *Angew. Chem. Int. Ed.*, 2014, **53**, 9476–9481.

46 W. Krätschmer, L. D. Lamb, K. Fostiropoulos and D. R. Huffman, *Nature*, 1990, **347**, 354–358.

47 V. D. Mihailetchi, J. K. J. Van Duren, P. W. M. Blom, J. C. Hummelen, R. A. J. Janssen, J. M. Kroon, M. T. Rispens, W. J. H. Verhees and M. M. Wienk, *Adv. Funct. Mater.*, 2003, **13**, 43–46.

48 F. Cardinali, J. L. Gallani, S. Schergna, M. Maggini and J. F. Nierengarten, *Tetrahedron Lett.*, 2005, **46**, 2969–2972.

49 T. M. Figueira-Duarte, V. Lloveras, J. Vidal-Gancedo, B. Delavaux-Nicot, C. Duhayon, J. Veciana, C. Rovira and J. F. Nierengarten, *Euro. J. Org. Chem.*, 2009, **2009**, 5779–5787.

50 I. Lamparth and A. Hirsch, *J. Chem. Soc. Chem. Commun.*, 1994, 1727–1728.

51 C. Fuertes-Espinosa, C. García-Simón, M. Pujals, M. Garcia-Borràs, L. Gómez, T. Parella, J. Juanhuix, I. Imaz, D. Maspoch, M. Costas and X. Ribas, *Chem*, 2020, **6**, 169–186.

52 Y. Matsuo, A. Muramatsu, R. Hamasaki, N. Mizoshita, T. Kato and E. Nakamura, *J. Am. Chem. Soc.*, 2004, **126**, 432–433.

53 C. Bingel, *Chem. Ber.*, 1993, **126**, 1957–1959.

54 M. Prato, Q. C. Li, F. Wudl and V. Lucchini, *J. Am. Chem. Soc.*, 1993, **115**, 1148–1150.

55 F. Diederich, U. Jonas, V. Gramlich, A. Herrmann, H. Ringsdorf and C. Thilgen, *Helv. Chim. Acta*, 1993, **76**, 2445–2453.

56 J. Iehl, R. Pereira De Freitas, B. Delavaux-Nicot and J. F. Nierengarten, *Chem. Commun.*, 2008, 2450–2452.

57 A. Muñoz, D. Sigwalt, B. M. Illescas, J. Luczkowiak, L. Rodríguez-Pérez, I. Nierengarten, M. Holler, J. S. Remy, K. Buffet, S. P. Vincent, J. Rojo, R. Delgado, J. F. Nierengarten and N. Martín, *Nat. Chem.*, 2016, **8**, 50–57.

58 F. Stauffert, A. Bodlenner, T. M. Nguyet Trinh, M. I. García-Moreno, C. Ortiz Mellet, J. F. Nierengarten and P. Compain, *New J. Chem.*, 2016, **40**, 7421–7430.

59 C. C. Hofmann, S. M. Lindner, M. Ruppert, A. Hirsch, S. A. Haque, M. Thelakkat and J. Köhler, *Phys. Chem. Chem. Phys.*, 2010, **12**, 14485–14491.

60 J. Iehl, M. Holler, J. F. Nierengarten, K. Yoosaf, J. M. Malicka, N. Armaroli, J. M. Strub, A. Van Dorsselaer and B. Delavaux-Nicot, *Aust. J. Chem.*, 2011, **64**, 153–159.

61 J. Iehl, J. F. Nierengarten, A. Harriman, T. Bura and R. Ziessel, *J. Am. Chem. Soc.*, 2012, **134**, 988–998.

62 M. M. Ravikanth, L. Vellanki and R. Sharma, *Reports Org. Chem.*, 2016, **6**, 1.

63 P. Fortgang, E. Maisonhaute, C. Amatore, B. Delavaux-Nicot, J. Iehl and J. F. Nierengarten, *Angew. Chem. Int. Ed.*, 2011, **50**, 2364–2367.

64 K. Yoosaf, J. Iehl, I. Nierengarten, M. Hmadeh, A. M. Albrecht-Gary, J. F. Nierengarten and N. Armaroli, *Chem. Eur. J.*, 2014, **20**, 223–231.

65 A. F. Greene, M. K. Danielson, A. O. Delawder, K. P. Liles, X. Li, A. Natraj, A. Wellen and J. C. Barnes, *Chem. Mater.*, 2017, **29**, 9498–9508.

66 S. F. Völker, M. Vallés-Pelarda, J. Pascual, S. Collavini, F. Ruipérez, E. Zuccatti, L. E. Hueso, R. Tena-Zaera, I. Mora-Seró and J. L. Delgado, *Chem. Eur. J.*, 2018, **24**, 8524–8529.

67 Z. Hawash, L. K. Ono and Y. Qi, *Adv. Mater. Interfaces*, 2018, **5**, 1700623.

68 G. Shen and D. Chen, *Front. Optoelectron. China*, 2010, **3**, 125–138.

69 J. J. Panda and V. S. Chauhan, *Polym. Chem.*, 2014, 5, 4418–4436.

70 S. Lee, T. H. T. Trinh, M. Yoo, J. Shin, H. Lee, J. Kim, E. Hwang, Y. B. Lim and C. Ryou, *Int. J. Mol. Sci.*, 2019, **20**, 5850.

71 Y. Lan, M. Lv, S. Guo, P. Nasr, V. Ladizhansky, R. Vaz, M. G. Corradini, T. Hou, S. M. Ghazani, A. Marnangoni and M. A. Rogers, *Soft Matter*, 2019, **15**, 9205–9214.

72 A. Perczel, Z. Gáspári and I. G. Csizmadia, *J. Comput. Chem.*, 2005, **26**, 1155–1168.

73 H. Shao, T. Nguyen, N. C. Romano, D. A. Modarelli and J. R. Parquette, *J. Am. Chem. Soc.*, 2009, **131**, 16374–16376.

74 M. P. Hendricks, K. Sato, L. C. Palmer and S. I. Stupp, *Acc. Chem. Res.*, 2017, **50**, 2440–2448.

75 H. Cui, M. J. Webber and S. I. Stupp, *Biopolymers*, 2010, **94**, 1–18.

76 N. Singha, P. Gupta, B. Pramanik, S. Ahmed, A. Dasgupta, A. Ukil and D. Das, *Biomacromolecules*, 2017, **18**, 3630–3641.

77 H. A. Klok, A. Rösler, G. Götz, E. Mena-Osteritz and P. Bäuerle, *Org. Biomol. Chem.*, 2004, **2**, 3541–3544.

78 J. D. Tovar, *Acc. Chem. Res.*, 2013, **46**, 1527–1537.

79 D. A. Stone, L. Hsu and S. I. Stupp, *Soft Matter*, 2009, **5**, 1990–1993.

80 G. L. Eakins, R. Pandey, J. P. Wojciechowski, H. Y. Zheng, J. E. A. Webb, C. Valéry, P. Thordarson, N. O. V. Plank, J. A. Gerrard and J. M. Hodgkiss, *Adv. Funct. Mater.*, 2015, **25**, 5640–5649.

81 A. M. Sanders, T. J. Magnanelli, A. E. Bragg and J. D. Tovar, *J. Am. Chem. Soc.*, 2016, **138**, 3362–3370.

82 A. M. Sanders, T. J. Dawidczyk, H. E. Katz and J. D. Tovar, *ACS Macro Lett.*, 2012, **1**, 1326–1329.

83 A. B. Bornhof, A. Bauzá, A. Aster, M. Pupier, A. Frontera, E. Vauthey, N. Sakai and S. Matile, *J. Am. Chem. Soc.*, 2018, **140**, 4884–4892.

84 S. K. Keshri, W. Nakanishi, A. Takai, T. Ishizuka, T. Kojima and M. Takeuchi, *Chem. Eur. J.*, 2020, **26**, 13288–13294.

85 L. Yang, P. Langer, E. S. Davies, M. Baldoni, K. Wickham, N. A. Besley, E. Besley and N. R. Champness, *Chem. Sci.*, 2019, **10**, 3723–3732.

86 J. K. Klosterman, M. Fujita and Y. Yamauchi, *Chem. Soc. Rev.*, 2009, **38**, 1714–1725.

87 C. Peebles, R. Piland and B. L. Iverson, *Chem. Eur. J.*, 2013, **19**, 11598–11602.

88 L. Chen, H. Wang, D.-W. Zhang, Y. Zhou and Z.-T. Li, *Angew. Chemie*, 2015, **127**, 4100–4103.

89 Q. Qi, B. Yang, C. G. Xi, X. Yang, D. W. Zhang, S. Liu and Z. T. Li, *ChemistrySelect*, 2016, **1**, 6792–6796.

90 Y. Zheng, H. Zhou, D. Liu, G. Floudas, M. Wagner, K. Koynov, M. Mezger, H. J. Butt and T. Ikeda, *Angew. Chem. Int. Ed.*, 2013, **52**, 4845–4848.

91 T. Ikeda, *Langmuir*, 2015, **31**, 667–673.

92 Z. S. Wu, Y. Zheng, S. Zheng, S. Wang, C. Sun, K. Parvez, T. Ikeda, X. Bao, K. Müllen and X. Feng, *Adv. Mater.*, 2017, **29**, 1602960.

93 T. Bin Yu, J. Z. Bai and Z. Guan, *Angew. Chem. Int. Ed.*, 2009, **48**, 1097–1101.

94 K. Oh and Z. Guan, *Chem. Commun.*, 2006, 3069–3071.

95 C. J. C. Edwards-Gayle and I. W. Hamley, *Org. Biomol. Chem.*, 2017, **15**, 5867–5876.

96 W. S. Horne, N. Ashkenasy and M. R. Ghadiri, *Chem. Eur. J.*, 2005, **11**, 1137–1144.

97 S. Alp, Ş. Erten, C. Karapire, B. Köz, A. O. Doroshenko and S. Içli, *J. Photochem. Photobiol. A Chem.*, 2000, **135**, 103–110.

Chapter 2| Self-Assembly Properties of a Multi-Electron Acceptor Fullerene

Synopsis

Inherently spherical, fullerenes can serve as molecular scaffolds for the organisation of functional units in three-dimensional (3D) space. We envisaged that combining the structural offerings of a T_h-symmetrical hexakis-adduct of fullerene with 12 redox-active NDI electron acceptors would allow us to construct a molecule that could serve as a platform to monitor and control their aromatic assembly in 3D space. In doing so, there would be potential to exploit these interactions for applications related to organic electronics where dimensional charge delocalisation and electron transfer processes are sought after. Theoretical and experimental observations indicate the presence of favourable, extended and dynamic intramolecular NDI–NDI π-interactions around the periphery of **12NDI** in the NDI neutral state. Notably, we observed the unexpected assembly of NDI radical anions in the reduced states of **12NDI**—evidenced by strong low-energy (IR) absorption bands—despite considerable Coulombic repulsive forces and the inherent flexibility of the covalent linkages to the fullerene core. Additionally, insights into electron delocalisation around their periphery are provided by variable temperature EPR spectroscopy. Previously, mixed-valence and electron sharing between NDI residues has been observed through covalent or mechanically-interlocked assemblies as well as through supramolecular systems. However, the findings in this study highlight this is not a prerequisite in accessing these properties and that dynamic scaffolds can impose electron-sharing in 3D space. As electroactive materials these molecules have the potential to percolate charge in an organic electronic device such as a photovoltaic.

Acknowledgements

The following people are gratefully acknowledged for their contributions to this Chapter: Dr Krishnamurthy Munusamy (visiting researcher under the British Council Newton–Bhabha scheme) for conceptualising this project and demonstrating the initial synthesis of **12NDI**, **1** and **2NDI**. Dr V. Suresh Mothika at the University of York for performing dynamic light scattering experiments. Professor Mark R. Wilson at Durham University for performing molecular dynamics simulations. Professor Victor Chechik at the University of York for performing EPR spectroscopy experiments and EPR data simulations. In addition, Dr Marc K. Etherington at Northumbria University is acknowledged for his helpful discussions relating to photophysical measurements.

2.1 Introduction

Throughout the last decade, electroactive organic molecules that have semiconductor properties have received increasing attention owing to their advantages to viably replace traditional metal-based electronic materials.[1–3] Yet, it is still a challenge to design, control and exploit the assembly of functional aromatic molecules in which the orientation and alignment of typically intermolecular π-systems ultimately dictate bulk properties such as charge transport. Naphthalene diimide (NDI) is a staple π-electron acceptor whose electrochemical and self-assembly behaviour is well understood.[4] As a result of a strong molecular quadrupole moment (as with other members of rylene diimide family), non-polar NDI molecules have a propensity to aggregate in an uncontrolled fashion. Aggregation patterns that reduce or eliminate π-orbital overlap are undesired when developing materials that require charge delocalisation and conductivity properties; here, one-dimensional (1D) alignment of planar molecules is important for high levels of performance. Many strategies have been developed to encourage and/or direct the assembly of these valued motifs.[5] Electron delocalisation between close-contact rylene diimide motifs has been observed by the Stoddart and Wasielewski groups in highly rigid NDI cyclophanes[6] that are model compounds for the 1D alignment of NDI molecules (Figure 2.1a). Additionally, methods to stabilise the radical anion of NDI have been developed in order to pursue advanced paramagnetic and NIR-absorbing materials. The Mukhopadhyaya group have successfully used chemical modification (Figure 2.1b) to access NDI radicals[7,8] that have air, light and chromatographic stability, whereas the Liu (Figure 2.1c) and Li, Stoddart and Wasielewski groups (Figure 2.1d) have used encapsulation methods to enhance the stability of reduced NDI species.[9,10] Recently, the Champness group have used flexible, mechanically-interlocked systems, wherein loose 1D

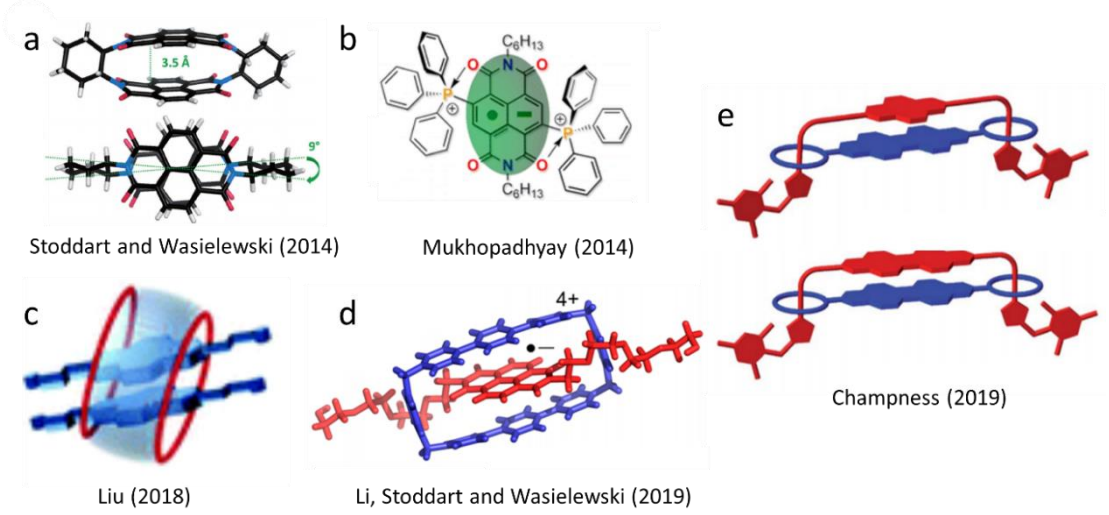

Figure 2.1. Stabilising rylene diimide radicals in a, a) rigid NDI cofacial dimer, b) phosphonium-substituted NDI, c) cucurbit[n]uril host, d) in a tetracationic cyclophane and e) molecular handcuffs.

alignment of rylene diimides is imposed; these unique 'molecular handcuffs' have allowed for the observation of rare and unusual π-radical interactions (Figure 2.1e).[11] To date, a dynamic scaffold that allows for the observation of NDI radical π-interactions precedes us.

Another family of excellent *n*-type acceptor are that of the fullerenes; they can exhibit high levels of charge mobility (i.e. PCBM[12], $\mu_e = 2 \times 10^{-7}$ $m^2 V^{-1} s^{-1}$) and have therefore been popularly exploited in organic electronics applications, including photovoltaics.[13,14] Inherently spherical, fullerenes can serve as molecular scaffolds for the organisation of other functional units in 3D space; this endows properties such as molecular recognition, ligand binding (e.g., in a MOF) and energy harvesting.[15] Functionalisation not only increases the solubility of fullerenes, but also allows for the creation of dynamic, multivalent macromolecules that are akin to globular proteins. The Nierengarten group have provided a key strategy for the design and high-yielding synthesis of various hexakis C_{60} adducts using Cu(I)-catalysed azide–alkyne cycloaddition (CuAAC, See Chapter 1 Section 1.4.1 for discussion) chemistry.[16,17] Indeed, their work has allowed for the synthesis of highly T_h-symmetrical fullerene derivatives that possesses various electrochemical and photochemical properties thanks to their pendant functionalities, whilst at the same time providing an opportunity to study the synergy of the 3D 'multivalent effect'[18]. To this extent, C_{60} has been decorated with redox-active viologen units[19] to study intramolecular π-dimerisations as well as porphyrin[20] and BODIPY[21] dyes for the construction of photosynthetic models and artificial light-harvesting arrays, respectively. However, despite the diverse developments in designing and characterising functionalised fullerene hexakis-adducts, there are surprisingly few examples that fully explore the effect of 3D crowding on the redox-active properties of appended units in anticipation of rationalising high performance in organic electronics. We envisaged that combining the structural offerings of a T_h-symmetrical octahedral fullerene with an NDI electron acceptor would allow us to construct a molecule that could serve as a platform to monitor and control interactions between two-dimensional (2D) planar aromatic units for potential applications in organic electronics where charge delocalisation and electron transfer processes are sought after.

Here, we investigate the intramolecular self-assembly and charge delocalisation properties between NDI units that are decorated in 3D space around a fullerene hexakis-adduct, **12NDI**, drawing comparisons with a model NDI compound **2NDI** that represents the 'ungrafted' arm of the fullerene species. Owing to the high local concentration of NDI motifs around the periphery of **12NDI**, the assembly of NDI radical anions in the reduced states is evidenced by strong low-energy (IR) absorption bands despite considerable Coulombic repulsive forces and the inherent flexibility of the covalent linkages to the fullerene core.

2.2 Results and Discussion

2.2.1 Synthesising a NDI-Functionalised C_{60} Hexakis-Adduct

NDI functionalisation of the azido-fullerene core (**12Az**, *vide infra* Scheme 2.2) enables access to a multivalent redox-active species that is capable of accumulating at least 24 electrons, i.e., two per NDI. In order to install NDI motifs to the fullerene core, an asymmetric NDI bearing alkyne functionality (**1**) was prepared according to Scheme 2.1. High yields of asymmetric *N,N'*-substituted NDIs can be accessed through a variety of methods. For instance, one-pot reactions are attractive, however, they usually result in poor selectivity that results in statistical mixtures of desired and undesired products. Owing to the success of pH-controlled protocols for synthesising NMIs in aqueous solution, this route (Scheme 2.1) was used to prepare the desired NDI monoalkyne **1** *via* the NMI diacid intermediate **3**. NDA was first suspended in H_2O and treated with 1 M KOH to form the tetracarboxylic acid. The pH was then adjusted to 6.3 before the addition of one equivalent of hexylamine to the reaction mixture, which was subsequently heated at reflux overnight. The initially transparent solution gradually became cloudy as the poorly soluble NMI diacid **3** began to precipitate out of solution as a beige solid. Upon cooling the mixture to room temperature, an excess of acetic acid was added to fully precipitate NMI **3**, which was isolated by filtration in 92% yield and could be used in the next step without further purification. Subsequently, NMI diacid **3** was subjected to typical imide condensation conditions with propargylamine to obtain the asymmetric NDI **1**. Specifically, propargylamine was added to a solution of **3** in dry DMF and heated under a N_2 atmosphere at 140 °C overnight. Precipitation of the crude product in 1 M HCl, followed by purification by flash column chromatography (SiO_2: 30–80% CH_2Cl_2 in *n*-hexanes), afforded pure **1** in 70% yield. The straightforward, and scalable (up to 10 g), synthesis of NDI **1** allowed for sufficient quantities that were utilised in the 12-fold functionalization of **12Az**.

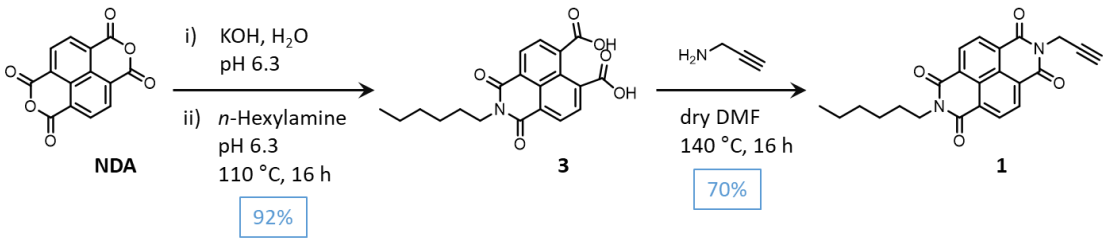

Scheme 2.1. Conventional solution-phase synthesis of alkyne bearing NDI 1; high selectivity for the synthesis of **3** was achieved using a pH-controlled aqueous reaction.

With the alkyne **1** in hand, **12Az** could be functionalized using CuAAC chemistry to finally produce the **12NDI**. Following a similar protocol (Scheme 2.2) as described by Nierengarten et al. (see Chapter 1, Scheme 1.3), an excess of alkyne **1** (1.25 equiv. per azide) was added to

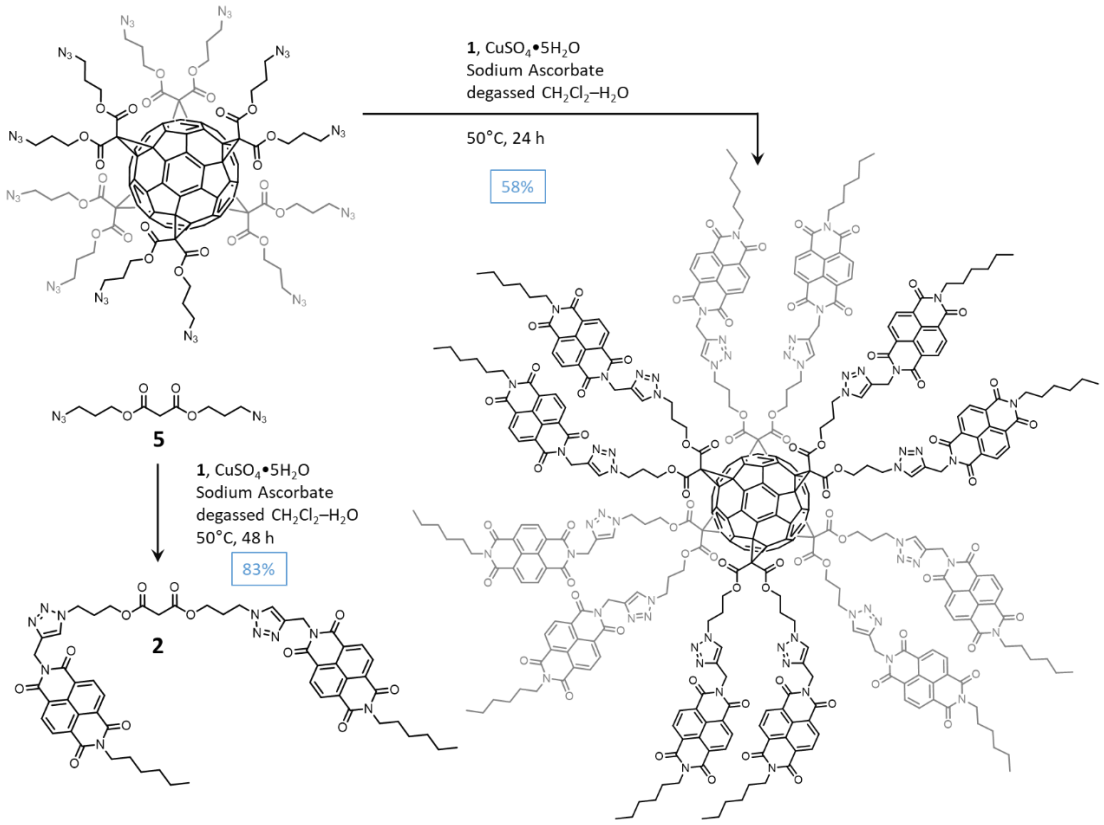

Scheme 2.2. The synthesis of **12NDI**; NDI **1** can be clicked onto **12Az** up to 12 times following CuAAC 'click' chemistry in a biphasic mixture of CH_2Cl_2–H_2O with $CuSO_4$ and sodium ascorbate present as the source of Cu and reducing agent respectively. Control malonate **2NDI** can be synthesised using similar conditions from the azido malonate **5**.

a solution of **12Az** in CH_2Cl_2. Screening of reaction conditions allowed us to identify 1.25 equiv. of alkyne per azide as being optimal, yet still resource efficient, for ensuring all azides would react to afford a monodisperse **12NDI** product. A solution of $CuSO_4$ (0.3 equiv) and sodium ascorbate (0.9 equiv.) in H_2O was subsequently added to the reaction mixture, which was immediately degassed by three cycles of freeze-pump-thaw to ensure the active Cu(I) species was maintained over the course of the reaction. The reaction mixture was stirred under Ar atmosphere at 50 °C until the azide stretch (ca. 2100 cm^{-1}) was no longer detectable by IR spectroscopy—typically after 24 h. The solvent was then removed and the crude product purified by flash column chromatography (SiO_2: 0–6.5% MeOH in CH_2Cl_2) to give **12NDI** in 58% yield. ^{1}H NMR analysis showed (Figure 2.2) broad peaks for all environments, indicative of a multivalent species, with peaks at δ_H 8.52 (10, 11, Figure 2.2) and 2.20 ppm (19, Figure 2.2)—corresponding to the NDI aromatic and fullerene methylene protons, respectively—integrating in a 2:1 ratio (i.e., 48 and 24 protons), thus confirming the addition of 12 total NDI motifs to fullerene core. MALDI-TOF analysis (Figure 2.27, appendix) confirmed the generation of a completely functionalised and monodisperse **12NDI** product, displaying only a single peak at 6969.4 *m*/z (6991.0 *m*/z calculated for $[M+H]^+$ = $C_{390}H_{312}N_{60}O_{72}$); no other adducts relating to partially reacted fullerene adducts were observed.

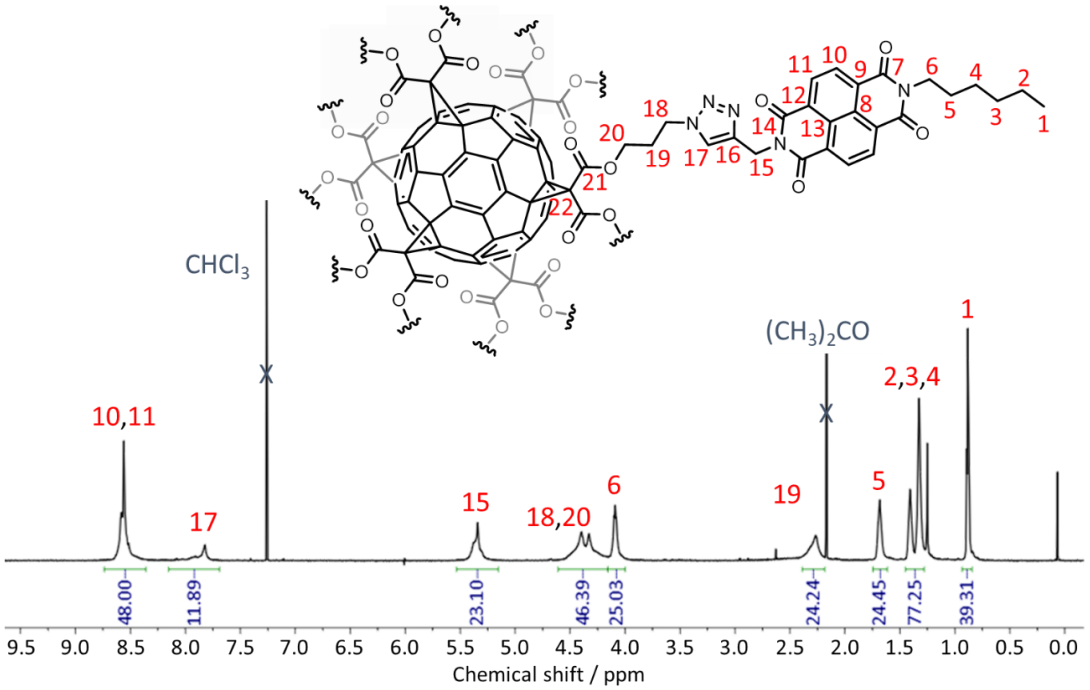

Figure 2.2. ^{1}H NMR ($CDCl_3$, 700 MHz, 298 K) spectrum of **12NDI**.

In order to aid the characterisation and interpretation of data collected for **12NDI**, an NDI control compound (**2NDI**) was prepared (Scheme 2.2). Starting from the malonate **5**[22], a key intermediate in the synthesis of **12Az**, similar CuAAC reaction conditions were applied to install two equivalents of **1**, thereby generating **2NDI** in 83% yield (see Experimental Section 2.5.1 for full synthetic details). Without the effect of tethering to a three-dimensional fullerene surface, control compound **2NDI** is expected to observe different self-assembly properties, both in solution and the solid state. Control **2NDI** can adopt more conformations in comparison to when covalently bound to the fullerene surface (as in **12NDI**). Therefore, intramolecular π-interactions should not be as enforced as conformational freedom remains unrestricted. On the other hand, we surmise that the 3D globular architecture imposed by the fullerene core will enforce a degree of directionality towards intramolecular NDI assembly of **12NDI**.

2.2.2 Neutral-State Assembly Properties of **12NDI** and **2NDI**

With the compounds in hand, UV-Vis and photoluminescence studies were conducted to investigate the intramolecular self-assembly properties of the pendant NDI units of **12NDI**. Sample solutions were surveyed initially at low concentrations to only consider contributions from intramolecular NDI assembly. Briefly, a concentration study of **12NDI** was performed in dry CH_2Cl_2 (Figure 2.29, appendix) to confirm the maximum working concentration (0.5 mM) for which a linear dependence Beer–Lambert law was still observed. Furthermore, dynamic light scattering (DLS) experiments were conducted to confirm the UV-Vis spectra were representative of primarily non-aggregated molecules. In CH_2Cl_2, at 0.3 mM there was little

evidence of any intermolecular aggregation of the hexakis-adduct, with a mean particle diameter of 3.99 nm observed (Figure 2.33, appendix) which correlates to one molecule (as estimated by the MD simulations in CH_2Cl_2, *vide infra*). Indeed, no aggregates correlating to assemblies of more than one individual molecule were observed up to 120 h later (Figures 2.34/35, appendix). Control samples (i.e., of **2NDI** and **1**) for all solution-state studies herein were consistently prepared at equimolar concentrations with respect to NDI units of the **12NDI** solution to ensure results could be genuinely compared.

Solvent-dependent absorption analysis of **12NDI** (1 μM; 12 μM with respect to NDI units) was performed in a range of solvent polarities to monitor the solvatochromic effects on intramolecular NDI assembly. The 12 NDI units of **12NDI** exist in close proximity to one another as a result of steric crowding arising from the multivalent substitution of the fullerene core. Ground-state aggregation effects (see Chapter 1, Section 1.3.1 for discussion on NDI aggregation) should therefore result in more exaggerated red-shifting and broadening effects to reflect a higher degree of assembly than in **1** and **2NDI**. In CH_2Cl_2, **12NDI** shows (Figure 2.3a) well-resolved sharp absorption bands between 300–400 nm as a result of the π–π* transition across the long axis of the NDI chromophore; this absorption feature is suggestive of a monomeric, non-aggregated state.[23,24] Yet, for compounds **1** and **2NDI**, the ratio ($A_{380\ nm}/A_{360\ nm}$) between the two lowest-energy absorptions (i.e., 381 and 360 nm) is greater in CH_2Cl_2 (**1** = 1.26, **2NDI** = 1.25, **12NDI** = 1.08, Figure 2.30, appendix for **1**, Figure 2.3b for **2NDI**), which indicates that even in a solvent known for its high solubility of planar aromatics, there is still some intramolecular aggregation of NDI units in **12NDI**. In comparison to CH_2Cl_2, there is significant red shifting observed in all other solvents (i.e., THF, dioxane, PhMe, *o*-DCB and DMSO) which is in accord with the formation of *J*-aggregates and/or solvent mediated aromatic charge-transfer complexes, both orienting the NDI chromophores into co-facial, presumably slip-stacked arrangements that are thermodynamically stabilised

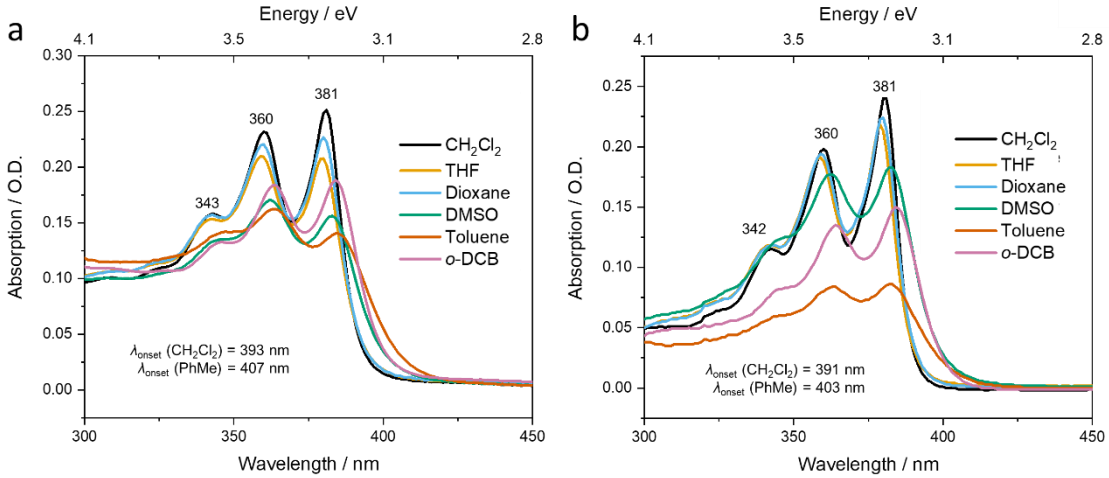

Figure 2.3. Solvent-dependent UV-Vis spectra of a) **12NDI** [1 μM] and b) **2NDI** [6 μM].

relative to the monomerically dissolved state.[25,26] Specifically, the ratio between the 381 and 360 nm absorptions of **12NDI** is inverted in comparison to **1** and **2NDI** in THF (0.96), DMSO (0.92) and PhMe (0.86), indicating extensive intramolecular NDI aggregation is present in these solvents; this ratio is decreased significantly in all solvents in comparison to **2NDI** and **1**. The absorption spectrum of divalent species **2NDI** appear similar to those of **1**, with an earlier onset of absorption (391 > 388 nm) in CH_2Cl_2 and PhMe (403 > 401 nm) that may be indicative of enhanced intramolecular π-interactions between the two NDI units of **2NDI**. These spectral changes between **12NDI**, **2NDI** and **1** confirm the fullerene scaffold instils a propensity for NDI units to intramolecularly aggregate in the neutral state in all solvents.

Solvent-dependent emission profiles of **12NDI** reveal (Figure 2.4a) that excited-state aromatic dimers ('excimer') between co-facially interacting NDI units and/or excited-state aromatic complexes ('exciplexes') between π-electron-deficient NDI units and π-electron-rich solvent molecules are present. Indeed, excimer emission is observed in CH_2Cl_2 at 490 nm, confirming the ground state intramolecular NDI aggregation in all solvents for **12NDI**. Excimer-like emission was also observed (Figure 2.4b) for **2NDI** at 487 nm, in a relatively similar intensity to the molecularly dissolved state emission, observable at 386 nm; this suggests there is a mixture of conformations for the control **2NDI**, one with intramolecular NDI aggregation, and one without. The excimer emission is not present for **1** in CH_2Cl_2 (Figure 2.21, appendix), confirming that the molecular scaffolds of **12NDI** and **2NDI** are important in pre-organising their respective NDI units in space. Additionally, the solvent mediated charge-transfer interactions observed by absorption experiments in PhMe and *o*-DCB are confirmed by broad, featureless emission at wavelengths >425 nm (i.e., PhMe: $\lambda_{em,max}$ = 492 nm: *o*-DCB: $\lambda_{em,max}$ = 464 nm for **12NDI**) owing to energetically favourable solvent π-interactions.[27,28] Both UV-Vis and emission spectroscopy unequivocally confirm intramolecular NDI aggregation in

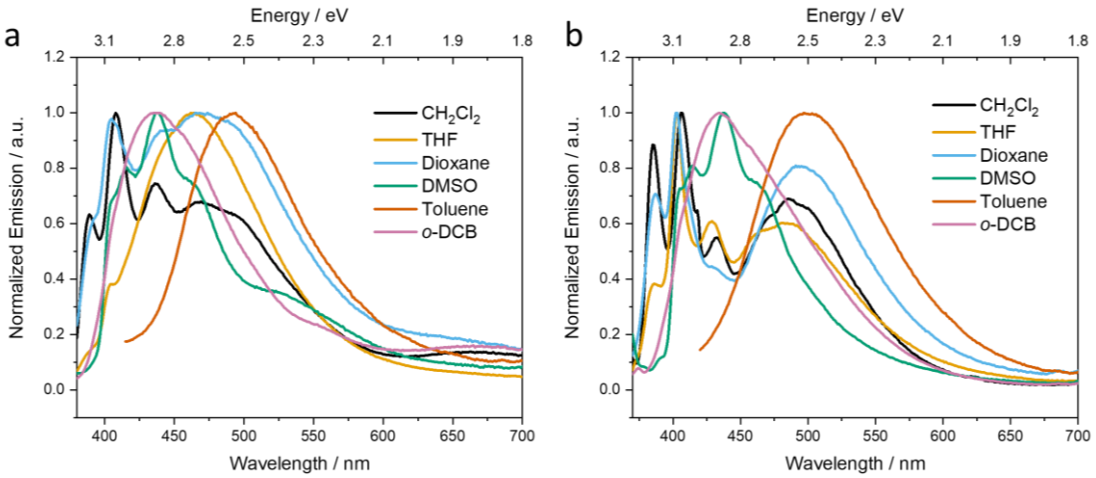

Figure 2.4. Solvent-dependent normalized emission data of a) **12NDI** [1 µM] and b) **2NDI** [6 µM].

12NDI in all solvents, i.e., intramolecular NDI aggregation is inherent because of the steric crowding of the NDI units in 3D space.

Although this work is primarily geared towards understanding the intramolecular interactions of NDI around a spherical core in the solution state, investigations of these interactions in the solid state would also allow us to develop insights for implementing **12NDI** in the context of device active layers (see Chapter 4). Therefore, thin films of **2NDI** and **12NDI** were prepared at 1 wt% in 3 different polymer matrices (ZEONEX®: a cyclic olefin copolymer (COC), PS: polystyrene; PMMA: polymethylmethacrylate, Figure 2.5c) for photoluminescence experiments. Here, dispersions at 1 wt% focus on mainly intramolecular interactions and therefore provide insight into the intramolecular NDI aggregation in the solid state. Additionally, this would allow us to modulate the interaction of polymer side chains—if any—with the NDI units. The polymers were first solubilised in *o*-DCB, with overnight mixing at room temperature to ensure complete dissolution. Aliquots of **2NDI** and **12NDI** were added to the polymer solutions to create 1 wt% mixtures that were subsequently cast onto quartz and dried overnight under vacuum (<0.1 mbar). The solid-state emission profiles of **12NDI** (Figure 2.4b) and **2NDI** (Figure 2.5a) display a broad featureless emission band at ca. 460 nm that is reminiscent of excimer-like emission that was observed in the steady-state experiments—this was correlated to NDI dimer aggregation. Unlike in the steady-state emission spectrum, however, a second broad featureless emission band (i.e., >500 nm) is present. This observation suggests that higher order intramolecular NDI assemblies[29] can be facilitated in the solid state by both **2NDI** and **12NDI**. The non-aggregated state emission (459 nm) of **2NDI** is relatively unchanged with respect to **12NDI** in all three matrices, with a Stoke's shift of ca. 10 nm towards 467 nm. However, the lower energy emission is broad, up to—and encompassing—700 nm; this is not observed for **2NDI**. Additionally, this NIR emission band observes clear differences in each of the polymer matrices, with varying ratios between the higher energy (467 nm) and the two main lower energy (581 and 639 nm) absorptions; these differences can be attributed to the 3D multivalency of **12NDI**. PS is poised for intermolecular π-interactions, with **12NDI**, that can facilitate extended NDI aggregation around the periphery of individual molecules. Indeed, as observed in the steady-state experiments, PS (Figure 2.5) is conducive to excited-state aromatic charge transfer interactions. The NIR emission band is less pronounced in PMMA (Figure 2.5) and ZEONEX® (Figure 2.5) in which the purely aliphatic or polar polymer chains clearly have little effect on the intramolecular assembly. Together, the steady- and solid-state results highlight the dynamic pre-organisation of NDI units afforded by the three-dimensional multi-substituted **12NDI**, akin to a multivalent globular protein interacting within an extracellular matrix.

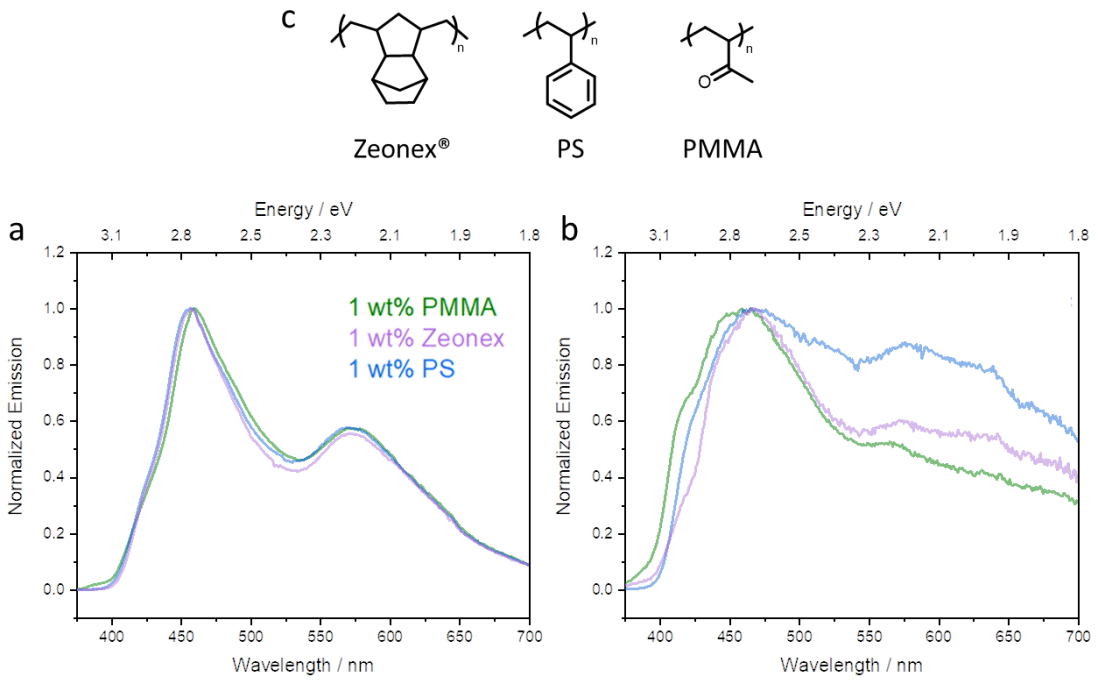

Figure 2.5. Solid-state emission spectra of a) **2NDI** and b) **12NDI**, prepared from drop casting a solution (1 mg/mL) of compound from o-DCB, with vacuum drying; 1 wt% embedded within different polymer matrices, PMMA (green), ZEONEX® (pink) and PS (blue) was also investigated.

Molecular dynamics (MD) simulations were conducted in order to gain insight into the likely conformations adopted by the neutral states of **2NDI** and **12NDI** in CH_2Cl_2 solution that in turn relate to the ground state intramolecular NDI aggregation (see appendix, Section 2.5.9 for full discussion on calculations). Given the size and complexity of the **12NDI** structure, restrained electrostatic potential atomic partial (RESP) charges needed to be obtained in a two-stage process, by first calculating separately the RESP partial charges of the much simpler dimer **2NDI** and a hexakis-substituted fullerene core (not prepared synthetically, see Figure 2.44, appendix for structure), and then matching these by hand to the fully constructed **12NDI** molecule).

Using the reference atoms (shown in Figure 2.43, appendix) intra- and interbranch distances between NDI units were monitored over t = 800 and t = 500 ns for **2NDI** and **12NDI**, respectively, where π-interactions were assumed at distances $d_{NDI} \leq 3.5$ Å.[30] As the free (i.e., untethered) 'arm' of **12NDI**, flexible dimer **2NDI** (Figure 2.6a) is able to adopt more conformations (i.e., 35–180° vs. 37–165° for **12NDI**, see Figure 2.49, appendix for probability distribution over MD simulation) in solution that ultimately range between i) a 'bound' state in which its two neutral NDI units are co-facially oriented within 3.5 Å of one another and ii) an 'open' non-interacting or 'unbound' state. From the simulation data, an equilibrium constant $K = N_{bound}/N_{unbound}$—corresponding to the ratio of 'bound' (defined at cut-off distance of 0.55 nm) and 'unbound' states (Figure 2.6b) of neutral dimer **2NDI**—has been calculated as 4.39. By applying the relationship between Gibb's free energy and the equilibrium constant (i.e., ΔG

= $-RT \ln K$) a free energy of binding (ΔG_{bound}) for **2NDI** is estimated to be –3.7 kJ mol^{-1}. This ΔG_{bound} value is not too dissimilar to that of a weak strength hydrogen bond (2.1–6.3 kJ mol^{-1})[31], however, it is moderately strong for a π-interaction and is similar to that of benzene dimers (6.2–10.4 kJ mol^{-1})[32], and—as predicted by the MD simulation—at room temperature the dominant conformation will likely be the 'bound' state. On the other hand, ground-state absorption studies did indicate a monomeric i.e. 'unbound' state, whereas excited-state studies revealed a mixture of pre-aggregated excimer-like emission as well as monomerically solvated emission—it is likely a mixture of 'unbound' and 'bound' conformations are present at room temperature in CH_2Cl_2.

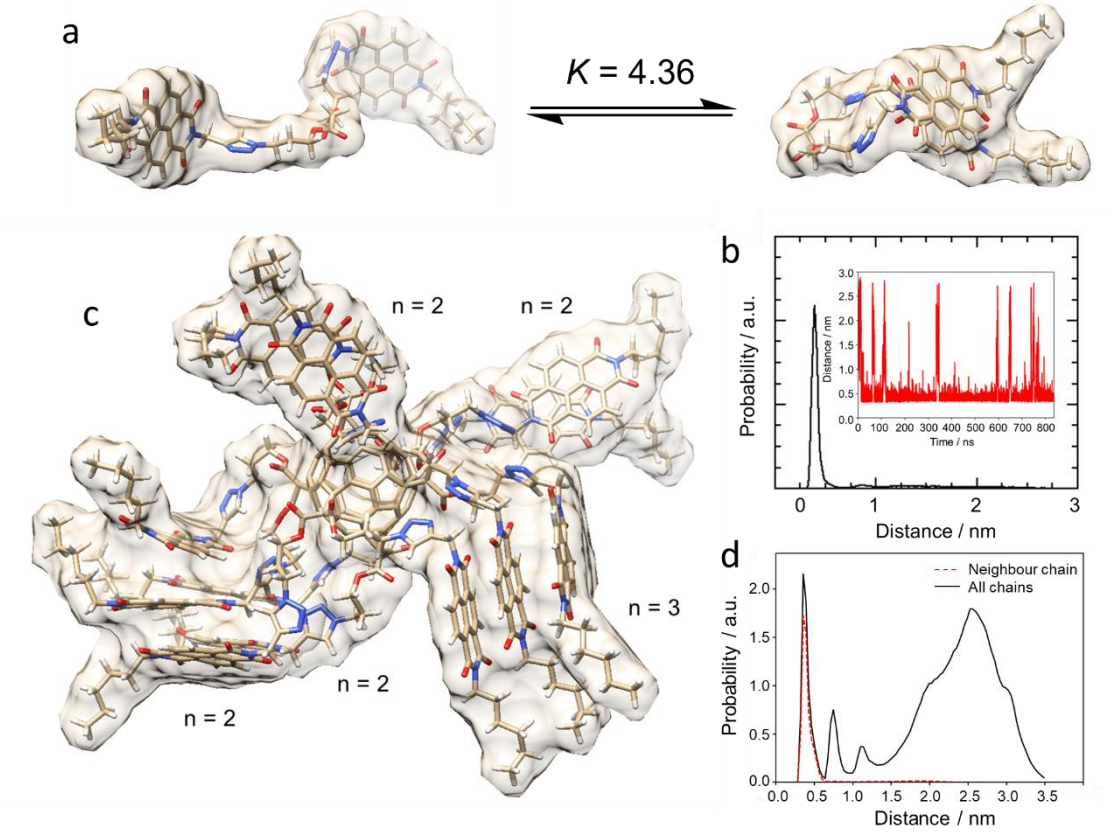

Figure 2.6. a) Snapshot MD simulation image of **2NDI** in 'unbound' and 'bound' conformations. The molecule is fluxional between unbound and bound states at room temperature. b) Histogram of NDI–NDI distances for **2NDI** monitored over 800 ns in CH_2Cl_2; inset shows NDI distances over duration of the simulation. Based on a cut-off for binding of 0.55 nm, the equilibrium constant, $K = N_{bound} / N_{unbound} = 4.39$ and the free energy of binding = –3.7 kJ mol^{-1}. c) Snapshot MD simulation image (taken at 123 ns) of **12NDI** revealing the molecular conformation as well as multiple NDI–NDI close distanced stacks of n = 2 or 3. d) Most probable NDI–NDI distances for neighbouring, as well as all other chains, around the periphery of the molecule over the duration of the simulation for **12NDI**.

Similar MD simulations carried out on **12NDI** over 200 ns reveal a similar propensity for neutral NDI units to dimerise, but indicate that these can do so either with a neighbouring NDI unit attached to i) the same 'arm' or ii) a separate 'arm' tethered to the fullerene core. Moreover, owing to the mutivalent substitution of **12NDI**, each of the 12 NDI units are able to form assemblies beyond dimers, such that the number of NDI units in an intramolecular cluster or aggregate is greater than two (e.g., see Figure 2.6c where $n = 2$ and 3 at 123 ns). These situations

are encouraged by the fact that NDI–NDI distances ($d_{NDI} \leq 3.5$ Å) are observed persistently over the course of the simulation for NDI–NDI interactions on i) the same 'arm' and ii) neighbouring 'arms'. Indeed, NDI stacks, i.e., dimer, trimer and tetramer assemblies, are observed at d_{NDI} = 3.5, 7.0 and 10.5 Å, respectively (Figure 2.6d). The NDI units can move freely to become non-interacting or aggregate with a different neighbouring NDI unit—this is expected owing to the low binding energy (ΔG_{bound} –3.7 kJ mol^{-1}) for dimerisation, as calculated for **2NDI**. These calculations are in accord with the ground-state absorption data, corroborating the observations that suggested extended intramolecular NDI aggregation. These observations suggest **12NDI** could demonstrate both intramolecular electron delocalisation in a single molecule as well as intermolecular long-range electron delocalisation in a highly dense state such as in the active layer of a device where charge mobility through the material is required (see Chapter 4 for space-charge-limited diode study with **12NDI**).

2.2.3 Redox-Induced Assembly of **12NDI** and **2NDI**

With clear observations of ground-state and excited-state NDI intramolecular aggregation, attention was then turned towards probing the electronic couplings in reduced states, i.e., the occurrence of electrostatically-driven 'mixed valence'[33] interactions, for example between a relatively π-electron-dense NDI$^{\bullet-}$ monoradical anion and an electron-deficient surface of neutral NDI^0. These 'mixed valence' species are readily characterised by the appearance of an intervalence charge transfer (IVCT) in the NIR region of the corresponding absorption spectrum, as well as by electron paramagnetic resonance (EPR) spectroscopy which provides information on the number of units involved in the system when radicals are shared.[34] Additionally, strong electronic couplings in the reduced states can also be visualised by cyclic voltammetry (CV) experiments, with the resolving of sequential redox processes when molecular orbitals are coupled. Table 2.1 summarises the energy level and band gap parameters derived from solution-state UV-Vis and CV experiments.

Table 2.1. Optoelectronic properties calculated by UV-Vis spectroscopy and cyclic voltammetry

Compound	λ_{abs}[a] [nm]	E_{gap}[b] [eV]	E_{red} [V]	LUMO[c] [eV]	HOMO[d] [eV]
1	380, 359	3.20	–0.50	–3.77	–6.96
2NDI	380, 360	3.19	–0.47	–3.79	–6.98
12NDI	381, 360	3.17	–0.43	–3.84	–7.01

[a] solution, [b] Onset of absorption, [c] $E_{LUMO} = -(E_{red} + 4.75)$ eV, [d] $E_{HOMO} = E_{LUMO} - E_{gap}$ eV

Previous photophysical investigations (see Section 2.2.1) by UV-Vis and emission spectroscopy were completed at low concentrations (i.e., <12 μM of NDI units) in order to

highlight contributions from intramolecular interactions. With the following techniques (i.e., CV, SEC, EPR) requiring higher concentrations of compound for the collection of spectra that has respectable signal to noise ratio, experiments in CH_2Cl_2 were deliberately conducted at concentrations of 0.3 mM thereby encouraging intramolecular NDI interactions. CV was carried out on samples of **12NDI** in dry, degassed CH_2Cl_2 solutions containing 0.1 M $TBAPF_6$ as the supporting electrolyte, and the data compared to samples of **1** and **2NDI** prepared at equimolar concentrations with respect to NDI units. Briefly, NDI monomer **1** undergoes two well-defined single-electron reduction events (Figure 2.7d) at –0.65 and –1.02 V vs. Ag/AgCl to generate the NDI radical anion ($\mathbf{1}^{\bullet-}$) and dianion ($\mathbf{1}^{2-}$) states, respectively, in a stepwise fashion. Additionally, both reduction events are similar in nature, as observed by SWV (Figure 2.7a). Unsurprisingly, this behaviour of **1** is consistent with the NDI literature.[32] It is the cyclic voltammogram of **2NDI**, however, that begins to provide us with insights into how intramolecular NDI assembly can influence molecular electrochemical properties.

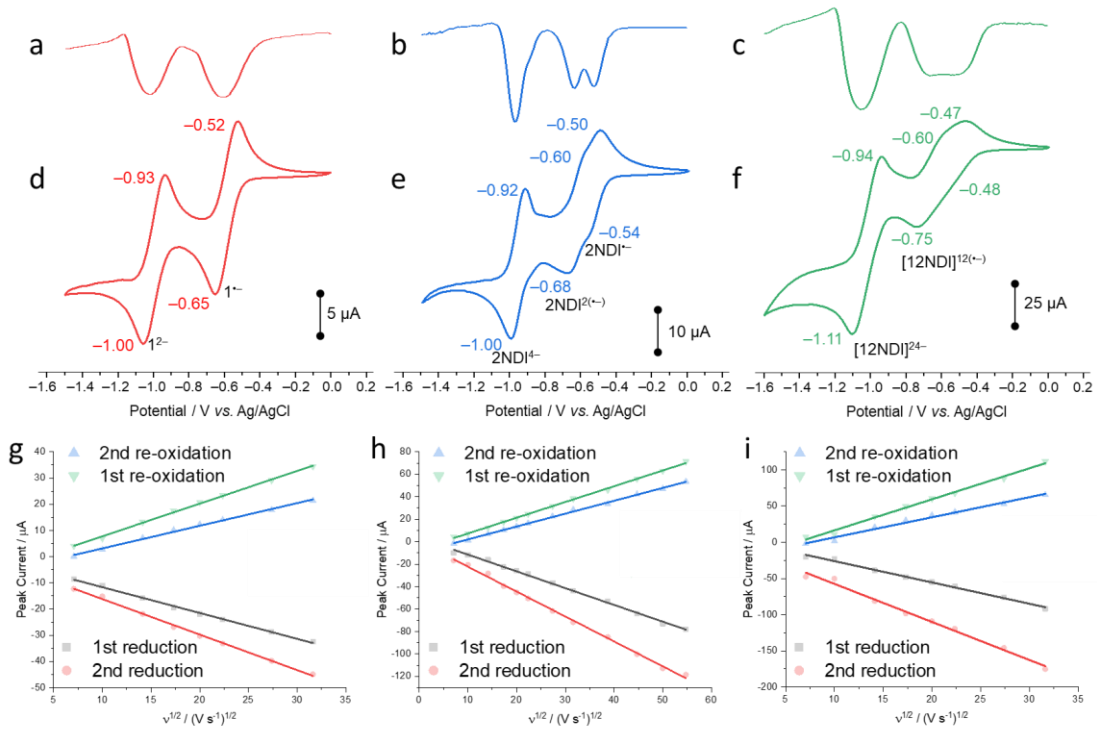

Figure 2.7. Square-wave voltammograms of a) **1**, b) **2NDI** and c) **12NDI** ([0.3 mM with respect to NDI units] in degassed CH_2Cl_2 containing 0.1 M $TBAPF_6$ as supporting electrolyte; scan rate range 50–1000 mV s^{-1} for **1** and **12NDI**, 50–3000 mV s^{-1} for **2NDI**. Cyclic voltammogram (50 mVs^{-1}, 298 K) of d) **1**, e) **2NDI** and f) **12NDI** ([0.3 mM with respect to NDI units] in degassed CH_2Cl_2 containing 0.1 M $TBAPF_6$. Line plots of current peak versus the square root of the scan rate confirming the excellent electrochemical reversibility of the exhaustive first-wave and second-wave cathodic/anodic processes for g) **1**, h) **2NDI** and i) **12NDI**.

The first notable observation (Figures 2.7b/e) is that dimer **2NDI** undergoes reduction at less negative potentials than **1** (–0.46 vs. –0.51 V), which is indicative of a more energetically accessible NDI LUMO (E_{LUMO}) for the population of **2NDI** with a single electron, i.e., for the generation of $\mathbf{2NDI}^{\bullet-}$. Given the fact that similar *N*-substitution of NDI units has little influence

on the π-electronics, the reduced E_{LUMO} can confidently be attributed to the preferable intramolecular ground-state interactions (ΔG_{bound} –3.7 kJ mol^{-1}) of neutral NDI units, i.e., within the 'bound' state of **2NDI**. In other words, the π-orbital overlap between co-facially oriented NDI units in **2NDI** affords an energetically stabilised extended LUMO that can more easily receive electron density. Upon lowering the potential further, a second first-wave reduction leading to the generation of **2NDI**$^{2(\bullet-)}$ is observed, clearly demonstrating the favourable electronic coupling between NDI^{0} and NDI$^{\bullet-}$ units, later confirmed by spectroelectrochemistry (SEC) to be an intramolecular mixed-valence state (see discussion on SEC, *vide infra*). Subsequent reduction of both NDI$^{\bullet-}$ units of **2NDI**$^{2(\bullet-)}$ to their dianionic states occurs simultaneously, as evidenced by a single two-electron reduction event that is also scan-rate independent between 50–1000 mV s^{-1} (Figure 2.7h). We take this to mean that Coulombic interactions within **2NDI**$^{4-}$ causes reconfiguration to an 'unbound' state quickly on the timescale of these experiments, such that the presence of a theoretical NDI$^{\bullet-}$/NDI^{2-} mixed-valence intermediate state is unlikely. Square-wave voltammetry (Figure 2.7b) provides further evidence to describe the transition from the 'bound' to 'unbound' state with two singularly resolved processes for the formation of **2NDI**$^{\bullet-}$ and **2NDI**$^{2(\bullet-)}$ at –0.53 and –0.64 V, respectively, in addition to the single process for the formation of **2NDI**$^{4-}$ at –0.98 V. Furthermore, molecular dynamics simulations were also conducted on the partially reduced species **2NDI**$^{\bullet-}$ in an attempt to visualise the 'mixed valence' state. In an approach similar to that for preparing the neutral state MD simulations, quantum mechanically-derived RESP charges of **1**$^{\bullet-}$ were used to approximate π-electrostatic interactions in **2NDI**$^{\bullet-}$ with d_{NDI} = 3.5 Å confirming the persistence of a π-interaction from the neutral to the mixed-valence state (Figure 2.48, appendix). Owing to the conformational switching of **2NDI**$^{\bullet-}$ towards full reduction, increased scan rates of up to 3 Vs^{-1} were used to try and resolve electronic couplings of the higher states in the 'bound' conformations, i.e. mixed-valence states such as **2NDI**$^{\bullet-}$/**2NDI**$^{2-}$, however, no individual processes could be resolved. Nonetheless, collecting CV data at variable scan rates allowed us to confirm the electrochemical reversibility of each NDI redox process *via* the Randles–Ševčík equation (eq. 1) and rule out any instances of irreversible chemical reactions taking place.

$$i_p = 2.69 \times 10^5 \times A \times D^{\frac{1}{2}} \times n^{\frac{3}{2}} \times v^{\frac{1}{2}} \times C \qquad \text{at } 25°\text{C} \qquad \text{(eq. 1)}$$

where i_p = current max, A = electrode area, D = diffusion coefficient, n = number of electrons transferred, v = scan rate, C = concentration

Here, the relationship between redox peak current and square root of the scan rate is correlated *via* eq. 1, with a linearly proportional relationship indicating reversibility. As expected, variable scan rate CV analysis shows (Figure 2.7g–i) that both reductions are fully reversible for **2NDI**

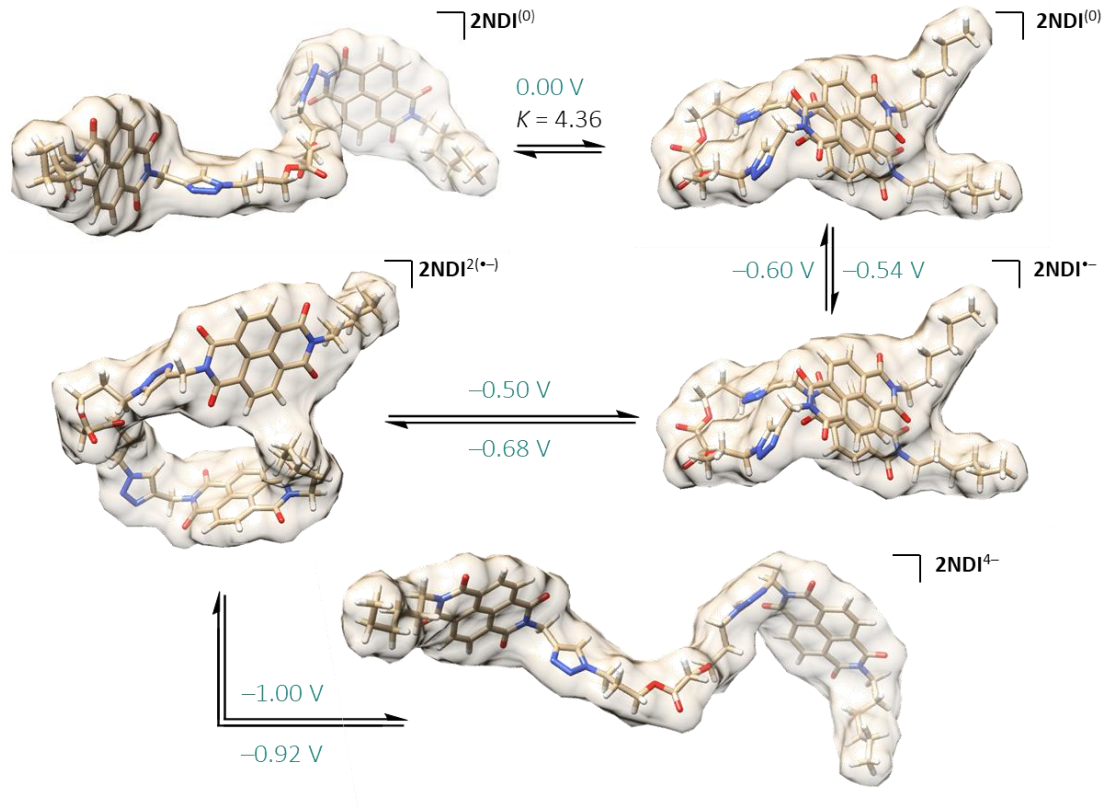

Figure 2.8. Illustration to demonstrate the conformational switching for **2NDI** in the neutral as well as multiply reduced states.

as well as **1**, indicating no chemical modification upon generating the multiply charged species. Rationalised by the MD simulations, charge transport pathways around the periphery of **12NDI** are possible owing to the dynamic nature of the T_h-symmetrical octahedral scaffold; the reduced conformational freedom (37–165°, see Figure 2.49, appendix) of the arms ensures that NDI–NDI π-interactions are maintained. Upon reduction, evidence (Figure 2.7f) of favourable and potentially extended π-interactions and stacks emerges with a further decrease in the onset of reduction (ΔV = –50 mV) in comparison to **2NDI**; the LUMO is further stabilised for **12NDI** than for **2NDI**, i.e., –3.84 vs. –3.79 eV. A notably lower peak reduction potential (–0.75 V) is required to generate [**12NDI**]$^{12(\bullet-)}$, in which all NDI units have been electrochemically converted to 12 NDI radical anions. Unlike during the first reduction wave of **2NDI**, it is more difficult to resolve the overlapping single-electron reductions for each of the 12 NDI units within **12NDI**. However, there is indication by square-wave voltammetry that the first-wave reduction process can be at least viewed (Figure 2.7c) as two distinct groupings that collectively represent of all of the NDI interactions around the fullerene hexakis adduct, albeit each still broad due to electronic fluctuations experienced by NDI units that can now participate in dynamic ensembles involving more than two NDI units. These observations are in accord with seminal work by Larry Miller on NDI radical aggregation within a multivalent dendrimer.[35] As the cathodic sweep begins, the initial reduced NDI interact with neighbouring neutral NDI and form mixed-valence stacks. The broadness of the first reduction event is indicative of different

radical stacks that are not in equilibrium—with 12 NDI units per molecule, there are likely varying degrees of NDI aggregation during the course of the CV experiment. Indeed, the presence of mixed-valence interactions was further supported (Figure 2.46, appendix) by MD simulations of [**12NDI**]$^{6(\bullet-)}$, that were prepared in a similar manner to simulations of **2NDI**$^{\bullet-}$. Here, extended NDI stacks (i.e., dimers, trimers and tetramers) were observed to form around the periphery of the molecule providing some evidence for extended delocalisation of radicals in the mixed-valence state. Indeed, [**12NDI**]$^{6(\bullet-)}$ still adopts a broad range of interbranch conformations (i.e., 33–110°, see Figure 2.50, appendix for probability distribution over MD simulation) in solution that facilitates extended NDI stacks. An idealised cartoon graphic is offered in Figure 2.10.

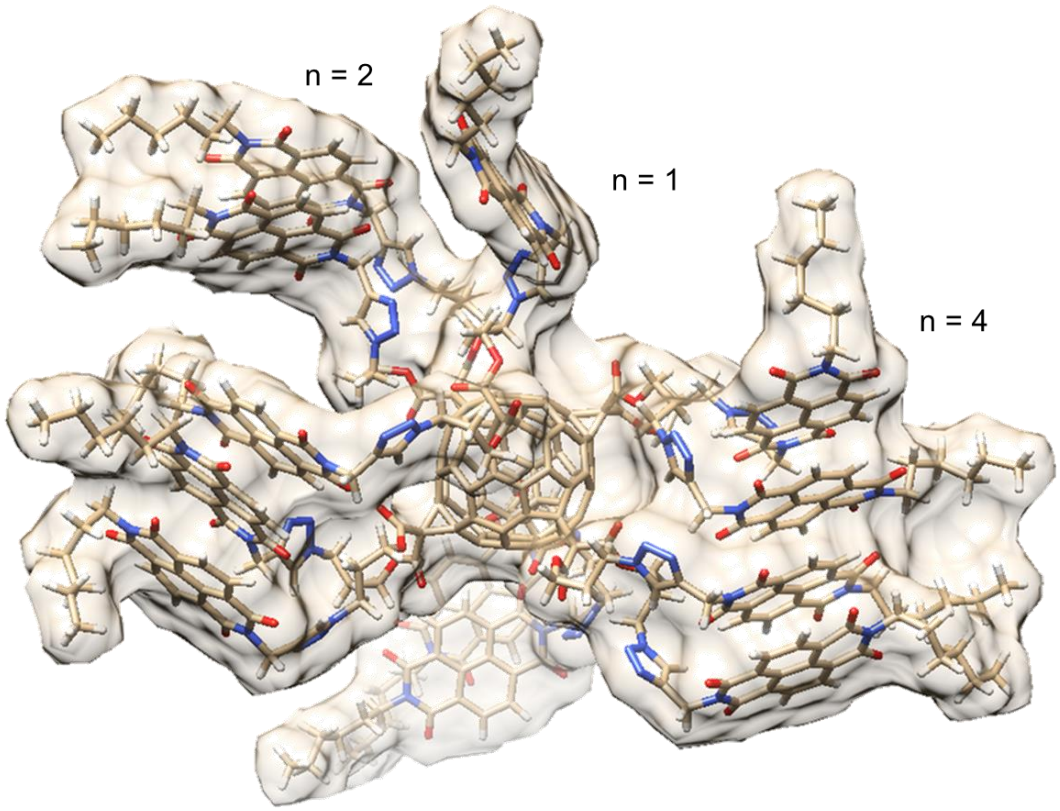

Figure 2.9. Snapshot MD simulation image (95 ns) of [**12NDI**]$^{6(\bullet-)}$ revealing molecular conformation as well as multiple NDI close distanced stacks of n = 1, 2, 3 or 4.

We hypothesised that the reduced conformational freedom of the grafted 'arms' might allow us to observe additional mixed valence states i.e., for [**12NDI**]$^{18(\bullet-)}$, wherein stacks of NDI$^{2(\bullet-)}$ and NDI$^{\bullet-}$ are forced in to close proximity despite the Coulombic repulsion that was shown to to 'open up' **2NDI**$^{4-}$. Variable scan rates (50–1000 mVs^{-1}, Figure 2.7h) did not allow for any resolution of the second-reduction wave towards [**12NDI**]$^{24-}$, despite the addition of 12 electrons. Clearly, the electrostatic repulsion between the NDI^{2-} states is too great to resolve any interactions over the duration of the CV experiment. However, the full reduction of the molecule occurs at a significantly lower potential, i.e. ΔV = 70 mV in comparison to **2NDI**$^{4-}$,

which indicated that Coulombic effects are much greater for **12NDI** during the second reduction to the dianionic state of each NDI unit. Additionally, the single-electron reduction of the hexakis-adduct fullerene core is not observed as a result of signal overlap (–1.15 V) with the second reduction process towards [**12NDI**]$^{24–}$. Despite the use of flexible scaffolds, clearly, electronic communication in the multiply reduced states of both **2NDI** and **12NDI** is observed.

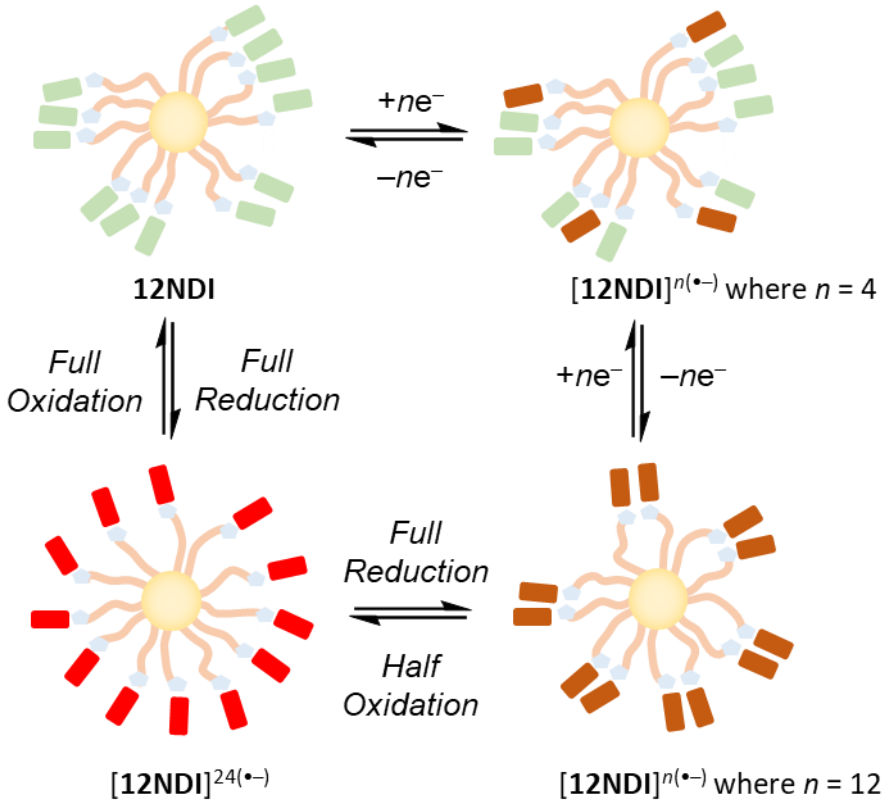

Figure 2.10. Cartoon depicting sequential reduction of **12NDI**: neutral (green), radical (brown) and dianionic (red) NDI. The favourable interactions i.e. neutral–neutral, radical–neutral and radical–radical, are observed during the CV experiment whereas the Coulombic repulsion of dianion–dianion NDIs results in a single reduction event.

Spectroelectrochemistry was subsequently employed to confirm the presence of mixed-valence interactions as well as to gain further insight into other higher order interactions present in the multiply reduced state. Spectroelectrochemical measurements were conducted in dry, degassed CH_2Cl_2 solutions with 0.1 M $TBAPF_6$ as the supporting electrolyte. The samples were added to an Ar-purged, air-tight optically transparent thin-layer electrochemical (OTTLE) cell (Pt/Pt/Ag wire configuration; path length ca. 0.2 mm). OTTLE cells are a convenient tool for electrochemically generating oxygen-sensitive species *in situ* for real-time spectroscopic analysis; the cell is designed to be easily accommodated by most FTIR and UV-Vis absorption spectrometers. The absorption spectra of reduced NDI units, i.e., $NDI^{\bullet-}$ and NDI^{2-}, are characteristic in a monomeric, non-aggregated state. Predictably, subjecting NDI **1** to a constant potential of –0.80 V vs. Ag generates the radical anion $\mathbf{1}^{\bullet-}$ which displays (Figure 2.11) characteristic absorption bands centred at 476 and 754 nm. A further reduction in the applied

potential to –1.10 V results in the diminishing of the radical absorptions in favour of the dianion $\mathbf{1}^{2-}$ spectrum, with the new bands centred at 423 and 604 nm. Noticeably, no absorption bands were observed between 800–3000 nm. These observations were as expected as no significant electronic couplings were identified by CV experiments. On the other hand, the CV and SWV of **2NDI** in CH_2Cl_2 identified significant orbital couplings were present in the reduced state, i.e., a mixed-valence state was likely present for $\mathbf{2NDI}^{\bullet-}$.

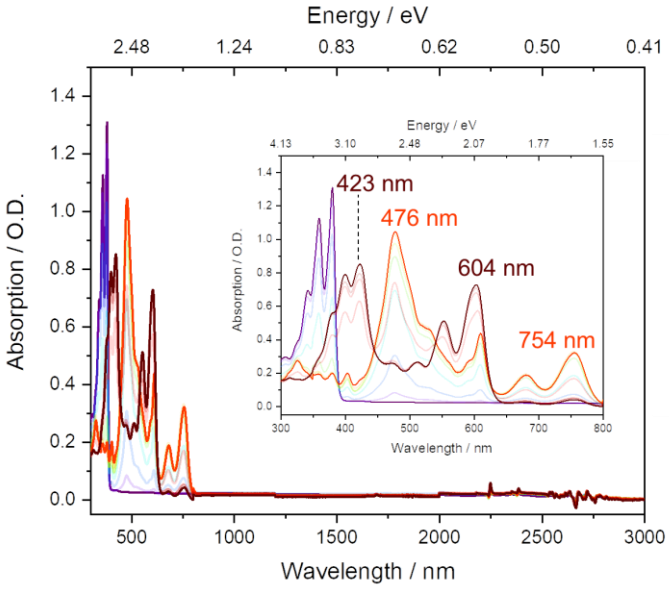

Figure 2.11. UV-Vis-NIR absorption spectra (1.8 mM of NDI units) of **1** (purple) and upon its sequential electrochemical reduction *in situ* to afford the fully reduced $\mathbf{1}^{2-}$ (orange) *via* $\mathbf{1}^{\bullet-}$ (brown). Spectra were recorded under an argon atmosphere in deaerated anhydrous CH_2Cl_2 solutions containing 0.1 M $TBAPF_6$ as the supporting electrolyte.

Applying a potential of –0.55 V allowed for the generation of the monoreduced $\mathbf{2NDI}^{\bullet-}$. Subsequently, the appearance (Figure 2.12a/b) of an IVCT band centred at 2160 nm confirmed the presence of a mixed-valence state, i.e., the formation of a singularly occupied molecular orbital (SOMO) in which an NDI dimer is populated with one electron ($NDI^0/NDI^{\bullet-}$). Upon forming the diradical $\mathbf{2NDI}^{2(\bullet-)}$ at –0.80 V, this low-energy IR band disappears in favour of a very weak band at 1125 nm. This higher energy absorption can be attributed to a weak interaction between two singularly reduced NDI units, i.e., $NDI^{\bullet-}/NDI^{\bullet-}$, with the remaining profile highly reminiscent to that of $\mathbf{1}^{\bullet-}$. These observations correlate well with those previously published, i.e., water-soluble NDI radicals have been found to dimerise in aqueous solution with the corresponding λ_{max} at 1140 nm.[36] As expected, the full reduction of both NDI units to the dianionic state, i.e., $\mathbf{2NDI}^{4-}$, reveals an absorption profile identical to that of $\mathbf{1}^{2-}$, confirming that no aggregation is present in the higher reduced states. Previously rationalised by the CV and SWV experiments (Figure 2.7), these observations agree with the hypothesised conformational switching of **2NDI** between the 'bound' and 'unbound' states upon sequential reduction of the NDI units.

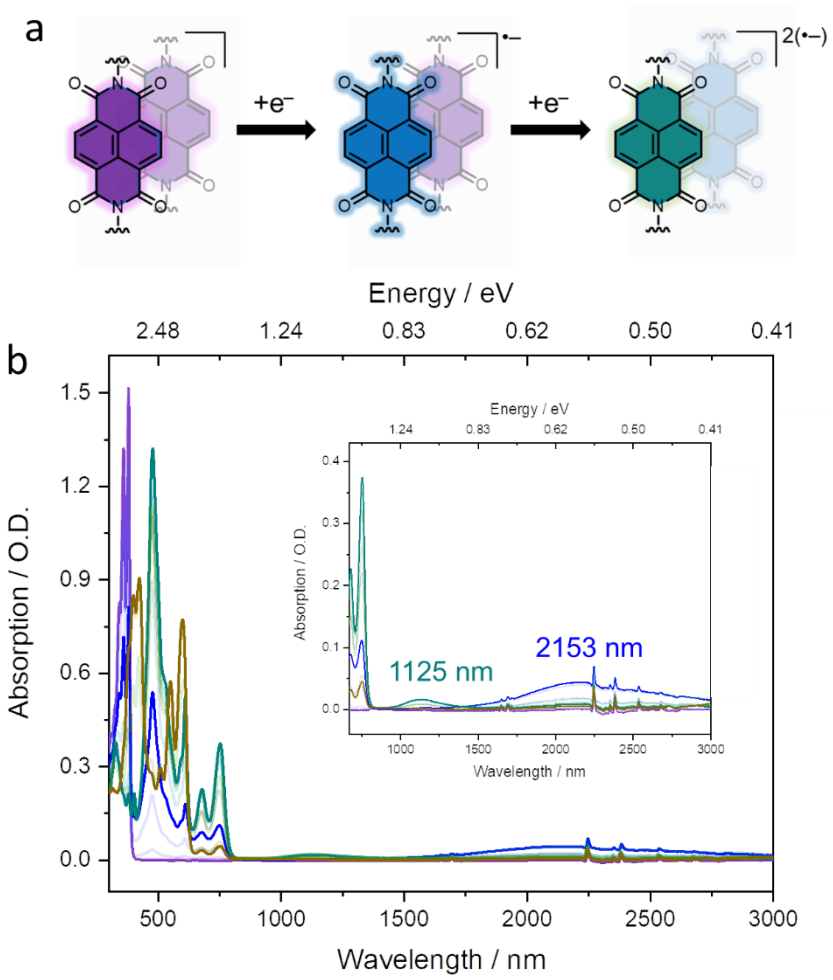

Figure 2.12. a) Illustrative reduction of an NDI dimer stack. b) UV-Vis-NIR absorption spectra of **2NDI** (1.8 mM of NDI units) and upon its sequential electrochemical reduction in situ to afford fully reduced NDI^{2-} units (i.e., $\mathbf{2NDI}^{2(2-)}$ = $\mathbf{2NDI}^{4-}$) species *via* the $NDI^{\bullet-}$ radical anion (i.e., $\mathbf{2NDI}^{2(\bullet-)}$ = $\mathbf{2NDI}^{2-}$). Spectra were recorded under an argon atmosphere in deaerated anhydrous CH_2Cl_2 solutions containing 0.1 M $TBAPF_6$ as the supporting electrolyte.

Whereas the 'ungrafted arms' have the freedom to adopt various conformations, the 'grafted arms' of **12NDI** are much more restricted and the impact of these features should be evident by spectroelectrochemistry upon reduction to the variously reduced states. As expected, subjecting **12NDI** to a potential of –0.45 V resulted in the growth of an IR absorption band centred at 2305 nm (Figure 2.13). This mixed-valence absorption band is similar to that observed for $\mathbf{2NDI}^{\bullet-}$, however, for $\mathbf{12NDI}^{n(\bullet-)}$ (where n = <12) the band is greater in intensity (O.D. = 0.057 vs. 0.044 for $\mathbf{2NDI}^{\bullet}$) and has a shift in the λ_{max}, i.e., 152 nm red shift to that observed for $\mathbf{2NDI}^{\bullet-}$. This corroborates the previous rational that the hexakis C_{60} scaffold directs intramolecular NDI aggregation—both in the neutral as well as reduced state. Indeed, the shift in λ_{max} is indicative of higher order, i.e., beyond dimer, mixed-valence interactions[36]. Previously, these IVCT interactions have only been observed in aqueous media or in very rigid systems wherein the close-proximity of NDI units in the reduced state is enforced.[6,35] Upon further reduction towards $[\mathbf{12NDI}]^{12(\bullet-)}$, the band centred at 2305 nm diminishes in favour of

the higher energy band at 1135 nm that is associated with NDI radical–radical interactions. Notably, the relative intensity of this band in **12NDI**$^{12(\bullet-)}$ is significantly increased (O.D = 0.054) compared to that observed (O.D. = 0.016) for **2NDI**$^{2(\bullet-)}$. These observations confirm that the fullerene hexakis-adduct scaffold pre-organises the NDI units in 3D space in both the neutral as well as multiple reduced states. The broad first reduction event observed in the CV of **12NDI** was indicative of the generation of NDI radicals that were not in equilibrium. However, for [**12NDI**]$^{12(\bullet-)}$ each NDI$^{\bullet-}$ is now in an equilibrated state that is likely as radical dimer pairs; this can be rationalised owing to the similarity with the λ_{max} of **2NDI**$^{2(\bullet-)}$, i.e., $\Delta\lambda_{max}$ = 5 nm. The intensity of the radical interaction is greater than in **2NDI**$^{2(\bullet-)}$ as the 'grafted arms' of [**12NDI**]$^{12(\bullet-)}$ hinder the radicals from disassociating. Indeed, the equilibrated radical state is supported by the sharp second reduction wave as [**12NDI**]$^{24-}$ is generated at –1.30 V. Now, each NDI unit is in the dianionic form and Coulombic effects result in the disassociation of any previous NDI radical pairs. Subsequently, the absorption spectrum of [**12NDI**]$^{24-}$ is highly reminiscent of both **1**$^{2-}$ and **2NDI**$^{4-}$, with no evidence of any additional mixed-valence states observed by variable scan rate (50–1000 mVs^{-1}) experiments. Additionally, during the second reduction wave the single-electron reduction of the C_{60} is observed with a broad and featureless band (see Figure 2.40, appendix) at 943 nm, confirming

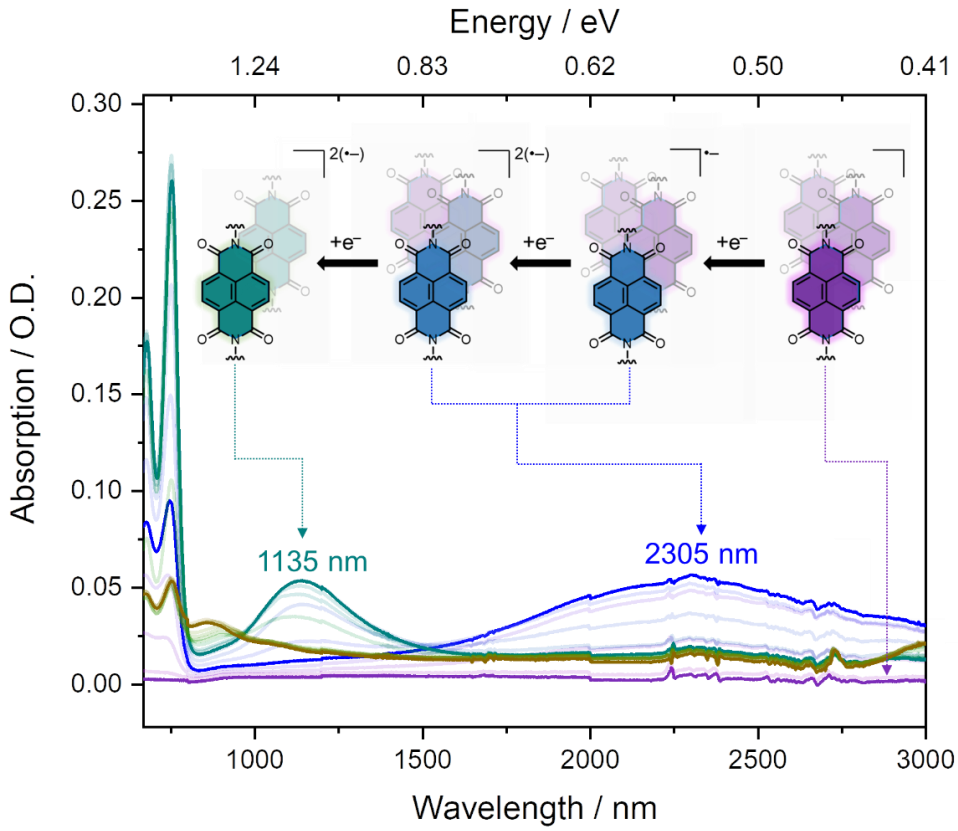

Figure 2.13. UV-Vis-NIR absorption spectra of **12NDI** (1.8 mM of NDI units) and upon its sequential electrochemical reduction *in situ* to afford the NDI$^{\bullet-}$ radical anion (i.e., **12NDI**$^{12(\bullet-)}$ = **12NDI**$^{12-}$) *via* the mixed-valence partially reduced states that are depicted above the spectra. Spectra were recorded under an argon atmosphere in deaerated anhydrous CH_2Cl_2 solutions containing 0.1 M $TBAPF_6$ as the supporting electrolyte.

that the fully reduced species is a twenty-five electron acceptor (i.e., 24 e^- for all NDI units and 1e^- for the fullerene moiety). Additionally, spectroelectrochemical FTIR was conducted however no significant differences (Figures 2.37–39, appendix) between **1**, **2NDI** and **12NDI** were observed that could be indicative of mixed-valence interactions. To gain a deeper understanding of any electron sharing that may be present between the electronically coupled NDI units, EPR spectroscopy was employed for various radicals of **12NDI** as well as **2NDI**.

Radical anion samples (150 µM spin density) for continuous-wave EPR (CW-EPR) spectroscopy were chemically generated in an argon glove box by titrating analyte solutions with cobaltocene ($CoCp_2$) solution; $CoCp_2$ is a single-electron reductant ($E_{1/2}(CoCp_2)$ = –1.3 V vs. Fc^+/Fc) that can allow for the formation of $NDI^{\bullet-}$ but not for over reduction to NDI^{2-}. First, the active concentration of freshly prepared $CoCp_2$ stock solutions was determined (Figure 2.14a) by titrating known volumes of the reductant into a solution of NDI **1** (150 µM), and monitoring for saturation of the signature NDI radical anion absorption (λ_{max} = 476 nm in CH_2Cl_2). Subsequently, the mixed-valence states could be accurately generated, i.e., **2NDI**$^{\bullet-}$, [**12NDI**]$^{\bullet-}$, etc., for CW-EPR analysis. The samples were prepared in glass pasteur pipette in deaerated CH_2Cl_2 and the EPR spectra were recorded at X-band using 0.1 G modulation amplitude. Additionally, any simulated spectra were generated using EasySpin[37] toolbox (MatLab). We simulated the EPR spectrum (Figure 2.14b) of **1**$^{\bullet-}$ assuming that the NDI unit is symmetrical but with the N-CH_2 protons having different hyperfine splitting constants. As a result of this simulation, the hyperfine splitting values were 0.22 (αH), 0.97 (αN), 1.72 (αH)

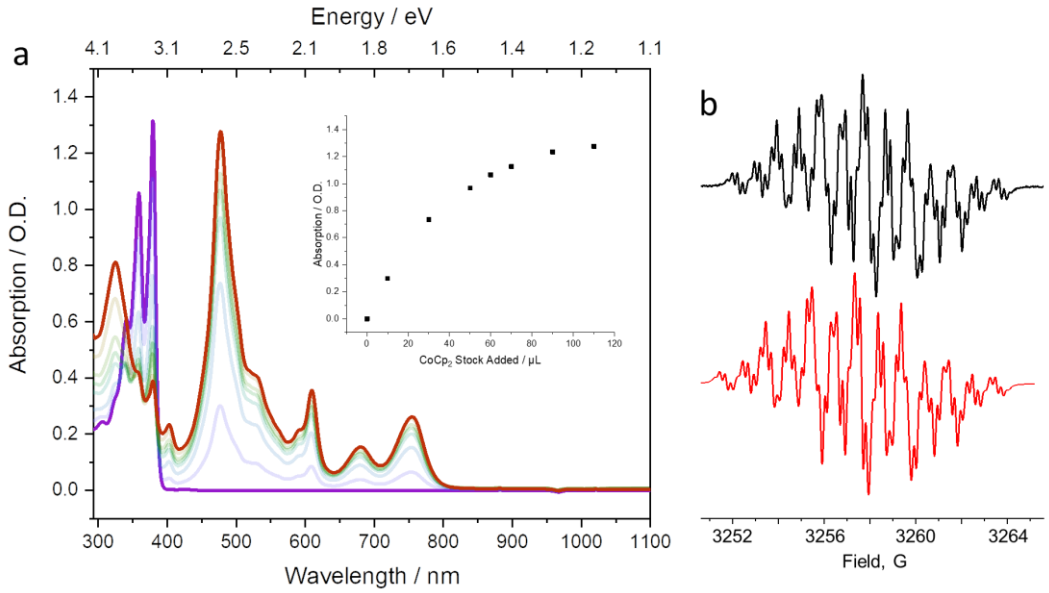

Figure 2.14. a) Titration of **1** [150 µM] in degassed CH_2Cl_2 with a glove-box prepared stock solution of $CoCp_2$ in degassed CH_2Cl_2; no change in absorption is observed between 90 and 110 µL additions. Plot of absorbance at 476 nm after each addition of $CoCp_2$ stock. Stock concentration calculated to be 4.63 mM. b) Room-temperature CW-EPR spectrum of **1**$^{\bullet-}$ (150 µM spin density) in CH_2Cl_2 upon chemical reduction of **1** with 1 (black) equiv. of $CoCp_2$ and the simulated spectrum for **1**$^{\bullet-}$.

and 2.05 (αH), corresponding to the aromatic naphthalene protons, the nitrogen atoms, and the two methylene groups, respectively. These values are similar to previously reported hyperfine splitting constants for monomeric NDI and are consistent with the experimental EPR data for **1**$^{\bullet-}$ (Figure 2.14b).

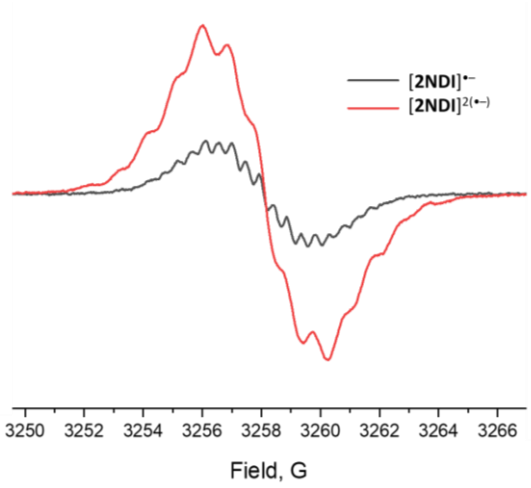

Figure 2.15. Room-temperature CW-EPR spectra of **2NDI**$^{\bullet-}$ (red, 150 μM spin density) and **2NDI**$^{2(\bullet-)}$ in CH_2Cl_2 upon chemical reduction of **2NDI** with 1 and 2 equiv. of $CoCp_2$, respectively.

As identified by SEC, the mixed-valence state for **2NDI**$^{\bullet-}$ should facilitate electron sharing between two NDI units. At ambient temperature, the EPR spectrum (black, Figure 2.15) of **2NDI**$^{\bullet-}$ is clearly different to that of **1**$^{\bullet-}$. Despite the broadness of the EPR spectrum, it can be reproduced by simulation if the coupling of two NDI units is assumed. Here, the hyperfine values of **2NDI**$^{\bullet-}$ are ca. half that of **1**$^{\bullet-}$, i.e., 0.12 (αH), 0.48 (αN), 0.86 (αH) and 0.96 (αH) which confirms the radical is delocalised over two NDI units and that **2NDI**$^{\bullet-}$ exists almost entirely in a 'bound' conformation. These observations—in hand with the results from CV and SEC experiments–unequivocally confirm a mixed-valence interaction. Upon decreasing the temperature of **2NDI**$^{\bullet-}$, the EPR signal (Figure 2.16a) broadens slightly. This broadening likely occurs as a consequence of i) slower molecular tumbling in a more viscous solvent at low temperature, ii) the slowing of a dynamic process (i.e., conformational switching), or iii) a slowing in the radical exchange rate. However, these observations strongly indicate that the dominant conformation is the 'bound' state at ambient temperature, corroborating the intensity of the mixed-valence band that was visualised by UV-Vis spectroscopy. On the other hand, greater intensity mixed valence (λ_{max} = 2305 nm in CH_2Cl_2) and radical dimer NDI$^{\bullet-}$/NDI$^{\bullet-}$, (λ_{max} = 1135 nm in CH_2Cl_2) bands were observed in the spectra for **12NDI** and therefore electron sharing between NDI units should be even greater for the 12-fold decorated hexakis-adduct.

The EPR spectrum of the direduced species, i.e., **2NDI**$^{2(\bullet-)}$, provides further insight into the conformational switching in the direduced state. At ambient temperature, the EPR profile (red, Figure 2.15) of **2NDI**$^{2(\bullet-)}$ is broad with respect to the signal of monoradical **1**$^{\bullet-}$. The

potential mixture of 'unbound' and 'bound' states rationalises the weaker intensity $NDI^{\bullet-}/NDI^{\bullet-}$ interaction that was observed in the $\mathbf{2NDI}^{2(\bullet-)}$ absorption spectra (λ_{max} = 1125 nm in CH_2Cl_2). Upon cooling $\mathbf{2NDI}^{2(\bullet-)}$, there is a significant decrease (Figure 2.16b) in intensity which suggests a diamagnetic species is forming, i.e., an EPR silent conformation. However, the reduced intensity signal has increasingly sharpened lines with the spectrum resembling that of $\mathbf{1}^{\bullet-}$. This strongly suggests that at low temperature the two NDI units become isolated, which is consistent with an EPR active 'unbound' conformation. The mixture of 'unbound' and 'bound' states rationalises the weaker intensity $NDI^{\bullet-}/NDI^{\bullet-}$ interaction that was observed for the $\mathbf{2NDI}^{2(\bullet-)}$ absorption (λ_{max} = 1125 nm in CH_2Cl_2).

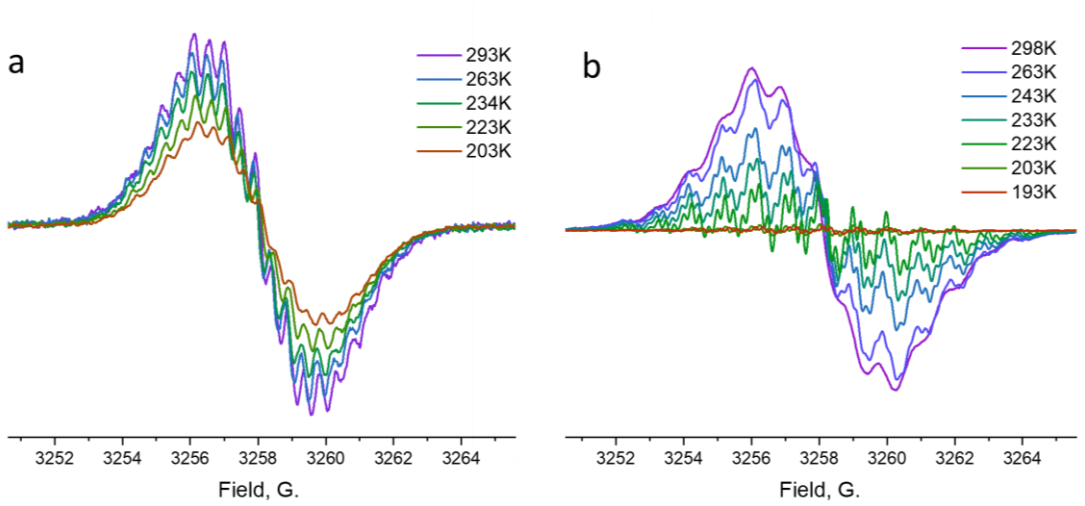

Figure 2.16. Variable-temperature CW-EPR spectra of a) $\mathbf{2NDI}^{\bullet-}$ [150 µM spin density] and b) $\mathbf{2NDI}^{2(\bullet-)}$ [300 µM spin density] in CH_2Cl_2 upon chemical reduction of **2NDI** with 1 equiv. and 2 equiv. of $CoCp_2$, respectively. Spectra were collected between 293–193 K.

EPR samples of $[\mathbf{12NDI}]^{\bullet-}$, $[\mathbf{12NDI}]^{4(\bullet-)}$ and $[\mathbf{12NDI}]^{12(\bullet-)}$ were prepared in order to probe the electron sharing both in the mixed-valence states as well as for the full mono reduction of each NDI unit. In comparison to $\mathbf{2NDI}^{\bullet-}$, the EPR signal corresponding to the monoreduced fullerene, i.e., $[\mathbf{12NDI}]^{\bullet-}$, is broadened (Figure 2.17) and consistent with increased delocalisation of the radical. Indeed, these observations are consistent with the hypothesis rationalised from CV and SEC experiments, i.e., when only a few radicals are present in the system there is greater delocalisation than in the fully monoreduced $NDI^{\bullet-}$ state. For the tetraanionic, $[\mathbf{12NDI}]^{4(\bullet-)}$, the signal increases (Figure 2.17) in intensity and is reminiscent of the monoradical, i.e., no splitting is observed. Here, for $[\mathbf{12NDI}]^{4(\bullet-)}$, there are also $NDI^{\bullet-}/NDI^{\bullet-}$ interactions that can take place. However, there is a clear resolving (Figure 2.17) of the EPR signal for the dodeca-radical $[\mathbf{12NDI}]^{12(\bullet-)}$ in which each NDI unit is mono reduced to $NDI^{\bullet-}$. This change in signal indicates there is less radical exchange present, likely owing to the Coulombic repulsion in the highly reduced state. However, the broadened signal does suggests that dynamic processes are still at play. The change in signal upon formation of the dodeca-radical corroborates the hypothesis that electron sharing capabilities are most prominent in the

mixed-valence state, and it is these states that persist and are observable by other techniques such as CV and SEC.

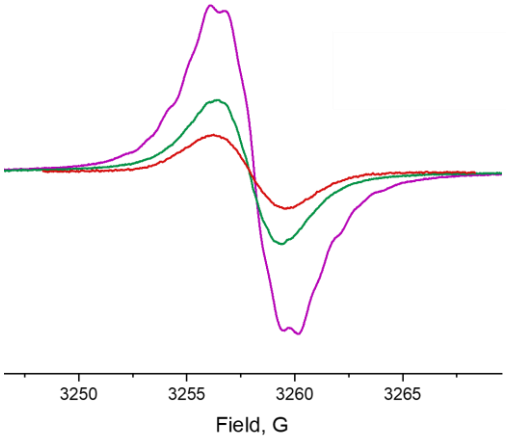

Figure 2.17. Room-temperature CW-EPR spectra of **12NDI** (150 μM spin density) in CH_2Cl_2 upon chemical reduction with 1 (red), 4 (green) and 12 (purple) equiv. of CoCp2, respectively.

Clearly, the extensive intramolecular NDI assembly observed in the neutral-state is maintained upon reduction. These mixed-valence states are rarely observed in organic solvents and therefore this study provides insight into approaches that can be used to enforce radical interactions that have previously not been observed. Currently, work is still on going to gain an even deeper understanding of the π-interactions in the reduced state. Variable-temperature EPR experiments in different solvents, as well as electron-nuclear double resonance (ENDOR) analysis should shine light on the extent of electron sharing in **12NDI** as well as **2NDI**. Additionally, the solid-state assembly of **12NDI** in the reduced state may pave the way for novel fullerene assemblies that have emergent optoelectronic applications.

2.3 Conclusions

Capitalising on an approach developed by the Nierengarten group, we have synthesised a multi-redox hexakis-adduct of C_{60} functionalised with naphthalene diimide moieties (**12NDI**). We have found that the three-dimensional scaffold facilitates NDI–NDI π-interactions in both the neutral and reduced states; these observations are rare in flexible NDI compounds, especially in highly solubilising solvents such as CH_2Cl_2. The control **2NDI** has demonstrated redox-controlled conformational switching between an ‘unbound’ and a ‘bound’ state, *via* formation of a mixed-valence interaction that has been observable by CV, SEC and EPR. Fullerene hexakis-adduct **12NDI** enforces intramolecular NDI aggregation in the neutral state that is maintained upon reduction of the NDI units. Low-energy IVCT absorptions are indicative of mixed-valence states that constitute extended NDI stacks in the reduced state, e.g., $NDI^{\bullet-}/NDI^{0}$.

Indeed, EPR spectroscopy suggests that the monoreduced hexakis-adduct, i.e., [**12NDI**]$^{\bullet-}$ can facilitate radical sharing in higher order assemblies beyond the dimer. It is clear that despite the dynamic nature of the fullerene hexakis-adduct scaffold, the pre-organisation of the pendant NDI units in 3D space allows for the study of fundamental π-interactions in the neutral and reduced states. To gain further insight into the nature of the multivalent states, we are currently employing solvatochromic EPR and ENDOR spectroscopy. Furthermore, we are now looking at the integration of these *n*-type semiconductor molecules in a device setting for potential applications in an organic electron device (see Chapter 4 for discussion on space-charge-limited diodes involving **12NDI**).

2.4 Experimental Details

2.4.1 General Materials & Methods

Materials: All reagents and solvents were purchased from commercial suppliers (Merck, Acros Organics, Alfa Aesar, Fischer Scientific, Tokyo Chemical Industry or Fluorochem) and used without further purification unless stated otherwise. Anhydrous solvents were obtained from a Solvent Purification System (neutral alumina) and stored over activated (>250 °C at 0.01 mbar overnight) 3 Å molecular sieves under a dry Ar atmosphere. Solvents and solutions required for air-sensitive manipulations were degassed thoroughly using a minimum of three freeze–pump–thaw cycles and the flask back-filled under an Ar atmosphere. *N*-Hexyl-1,4,5,8-naphthalenetetracarboxylicacid-1,8-monoimidediacid[38] (**1**), 1,3-bis(3azidopropyl)propanedioate[16] and the azido fullerene hexakis-adduct[16] (**12Az**) were synthesised according to previously published literature procedures.

Product confirmation: Analytical thin-layer chromatography (TLC) was performed on aluminum-backed silica gel 60 plates pre-loaded with F254 indicator (Sigma Aldrich) and visualised either under UV light irradiation (254 and 365 nm) and/or by dip-staining methods. Flash column chromatography was carried out on an automated system (Teledyne Isco Combiflash Rf+) outfitted with a broad range UV–Vis (200–800 nm) absorption detector. Nuclear magnetic resonance (NMR) spectra were recorded using either a Bruker Advance III Ultrashield 400 Plus (working frequencies: ^{1}H and ^{13}C nuclei = 399.975 and 100.603 MHz, respectively), an Appleby VNMRS-600 (^{1}H and ^{13}C nuclei = 599.832 and 150.288 MHz, respectively) or a Varian VNMRS-700 (^{1}H and ^{13}C nuclei = 700.130 and 176.048 MHz, respectively) spectrometer at a constant temperature of 298 K. Operating temperatures of the NMR spectrometers were measured with the aid of a MeOH internal calibrant. All ^{13}C NMR experiments were proton decoupled. Chemical shifts (δ) are reported in parts per million (ppm) relative to the signals corresponding to the residual non-deuterated solvents ($CDCl_3$: δ_H = 7.26, δ_C = 77.16 ppm; DMSO-d_6: δ_H = 2.50, δ_C = 39.52 ppm). Coupling constants (J) are reported in Hertz (Hz) and ^{1}H multiplicities are reported in accordance with the following convention: s = singlet, d = doublet, t = triplet, q = quadruplet, p = pentet, m = multiplet. Assignment of ^{1}H and ^{13}C NMR signals were accomplished with the aid of '**p**ure-**s**hift' **y**ielded **c**hirp **e**xcitation[39] (PSYCHE) and two-dimensional COSY, HSQC and HMBC NMR spectroscopies. NMR spectra were processed using MestReNova software, Version 11. Low-resolution **e**lectro**s**pray **i**onisation (ESI-MS) and **a**tmospheric **s**olids **a**nalysis **p**robe (ASAP-MS) mass spectrometries were performed using a Waters TQD UPLC ES MS/MS spectrometer and a Waters Xevo QTOF spectrometer equipped with an **a**tmospheric **p**ressure **i**onisation (API) source,

respectively. High-resolution mass spectra (HR-MS) were obtained using either a high-resolution Waters LCT Premier XE spectrometer equipped with an ESI source or an accurate mass UPLC ES MS equipped with an API source. Matrix-assisted laser-desorption ionisation time-of-flight (MALDI–TOF) mass spectrometry was carried out on an Autoflex II ToF/ToF mass spectrometer (Bruker Daltonik GmBH). Modes of analysis include reflectron enhanced mass resolution between *m*/z 500 and 5000. Linear above m/z 5000 and MS/MS (LIFT) Elemental analysis was conducted using a Exeter Analytical CE-440 instrument (horizontal furnace, static combustion), which was calibrated with acetanilide reference standard.

Sample analysis: Attenuated total reflectance (ATR) Fourier transform infrared (FTIR) spectroscropy was performed on PerkinElmer Frontier FTIR spectrometer equipped with a Specac Quest ATR accessory with extended range diamond puck. UV-Vis-NIR absorbance data were collected using a Cary 5000 Series UV–Vis–NIR spectrophotometer (Agilent Technologies) at room temperature. The steady-state photoluminescence (PL) of solutions and solid-state films was measured using Jobin Yvon Fluoromax and Horiba Fluorlog3 spectrophotometers, respectively, against machine-specific calibration curves. Cyclic voltammetry (CV) and square-wave voltammetry (SQV) was carried out at room temperature on Ar-purged sample solutions in anhydrous CH_2Cl_2 using a PalmSens EmStat3 potentiostat interfaced to a PC. Tetrabutylammonium hexafluorophosphate ($TBAPF_6$; 0.1 M) was recrystallized from hot EtOH and used as the supporting electrolyte. All solution-state electrochemical experiments were performed using a glassy carbon working electrode (BASi; 0.071 cm^2). The electrode surface was polished routinely with 0.05 μm alumina–water slurry on a felt surface immediately before each use. The counter electrode was a Pt wire and the reference electrode was an Ag/AgCl (sat. KCl) aqueous electrode stored routinely in a 3 M KCl aqueous solution. Spectroelectrochemistry (SEC) experiments were performed at room temperature using an optically transparent thin-layer electrochemical (OTTLE) cell (path length approx. 0.2 mm with two CaF_2 windows separated by PTFE spacers) fitted with a Pt wire mesh working electrode, Pt wire counter electrode and a Ag wire pseudo-reference electrode. All SEC samples were prepared as Ar-purged solutions in anhydrous CH_2Cl_2 or anhydrous THF containing $TBAPF_6$ (0.1 M) as the supporting electrolyte and analysed under an applied voltage sweep. Electron paramagnetic resonance (EPR) spectra were recorded at X-band on a JEOL X320 spectrometer using 0.1 G modulation amplitude. The spectra were simulated using EasySpin[37] toolbox for MatLab. EPR samples (150–400 μmol spins/ L; approximately 200 μM per sample) were prepared and stored in an anaerobic glove box (MBraun UniLab Pro) under a dry Ar atmosphere by titrating cobaltocene as a chemical reductant into anhydrous CH_2Cl_2 or THF solutions. Chemically-generated redox states were routinely confirmed by absorption spectroscopy prior to EPR analysis in borosilicate glass

tubes (O.D 3 mm, thickness ca.1 mm) sealed under an Ar atmosphere. An FEI Helios dual-beam scanning electron microscope (SEM; 3.0 kV) was used to image the morphology of thin-film specimens. SEM samples were prepared by drop-casting 50 µL of a solution (0.1 mg/ mL) in anhydrous *o*-dichlorobenzene onto pristine silicon wafers that were then dried thoroughly overnight under reduced pressure (<0.01 mbar). A Cressington Scientific sputter coater equipped with a Au/Pd target and MTM-10 thickness monitor was used to apply a thin conductive layer (10 nm) to samples immediately before SEM images were taken.

2.4.2 Experimental Procedures

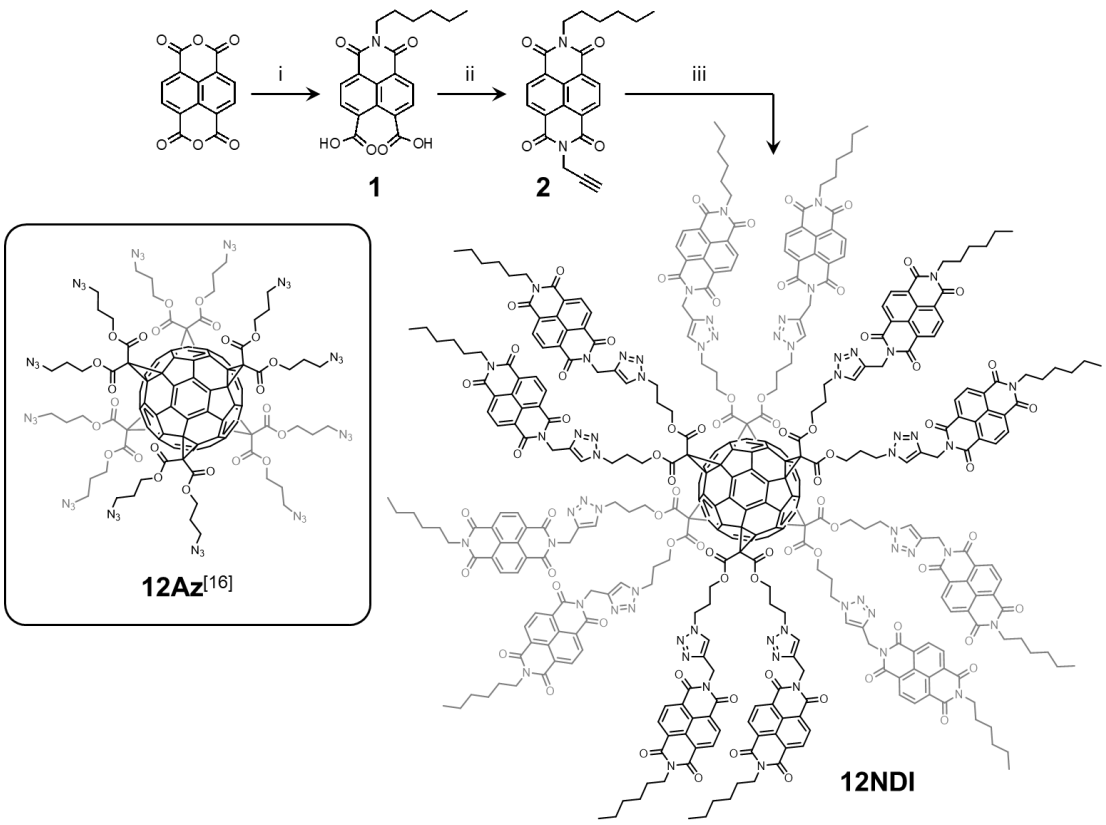

Scheme 2.3. Synthesis of the NDI-functionalised 'click' fullerene hexakis adduct **12NDI**. Reagents and conditions: (i) i) 1 M KOH, H_2O, ii) n-hexylamine, pH 6.3, reflux, 16 h, 91%; (ii) propargylamine, DMF, reflux, 16 h, 71%; (iii) **12Az**[16], $CuSO_4$•$5H_2O$, sodium ascorbate, CH_2Cl_2–H_2O, 50 °C, 16 h, 58%.

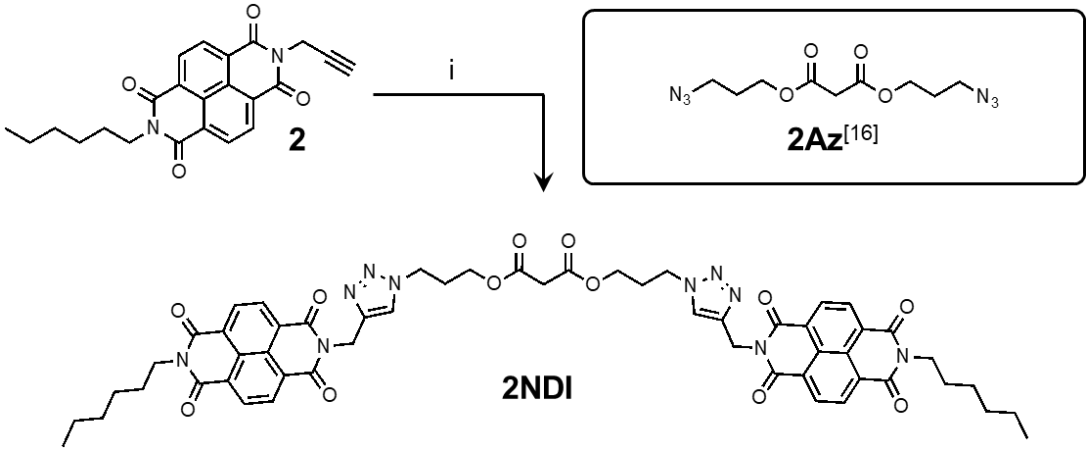

Scheme 2.4. Synthesis of **2NDI**. Reagents and conditions: (i) 1,3-bis(3-azidopropyl)propanedioate[16] (**2Az**), $CuSO_4$•$5H_2O$, sodium ascorbate, CH_2Cl_2–H_2O, 50 °C, 16 h, 83%.

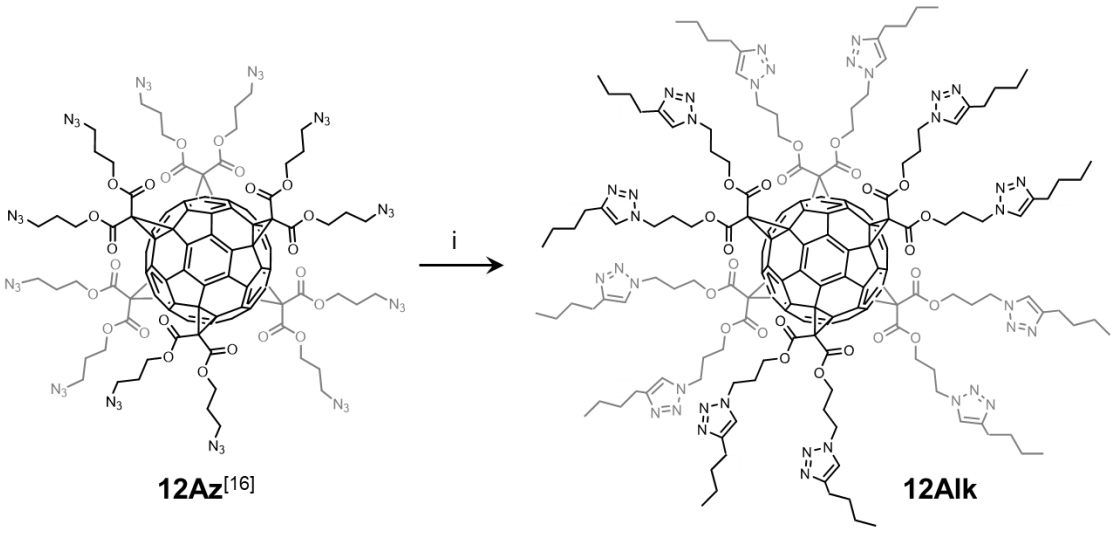

Scheme 2.5. Synthesis of the alkyl-functionalised 'click' fullerene hexakis adduct **12Alk**. Reagents and conditions: (i) **12Az**[16], $CuSO_4$•$5H_2O$, sodium ascorbate, CH_2Cl_2–H_2O, 50 °C, 16 h, 47%.

General Procedure for Cu^I-catalyzed azide–alkyne [3+2] cycloadditions or 'click' reactions:

A freshly prepared solution of $CuSO_4$•$5H_2O$ (0.3 equiv.) as the Cu source and sodium ascorbate (0.9 equiv.) as the reducing agent in Ar-degassed deionised water (11–18 mM with respect to Cu^I) was added to a separately prepared Ar-degassed solution of azide (1.0 equiv.) and requisite alkyne (1.25 equiv. per azide functionality) in CH_2Cl_2 (11–14 mM). The resulting biphasic mixture (i.e., 3:1 *v*/*v* CH_2Cl_2–H_2O) was subjected to further degassing by freeze-pump-thaw before stirring the reaction at 50 °C for 48 h under an Ar atmosphere. The reaction was monitored by FTIR analysis and, upon observing the complete disappearance of the $–N_3$ stretch (ca. 2093 cm^{-1}), the solvents were removed completely by rotary evaporation (<60 mbar at 40 °C) and crude material subjected to automated flash chromatography to afford the desired 'click' product.

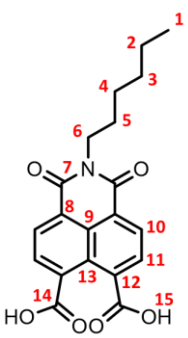

***N*-Hexyl-1,4,5,8-naphthalenetetracarboxylic acid-1,8-monoimide diacid**[38] **(1):** Compound **1** was prepared according to a modified literature[40] procedure. In a 500 mL round-bottomed flask equipped with a magnetic stir bar and air condenser, naphthalene-1,4,5,8-tetracarboxylic acid dianhydride (3.00 g, 11.2 mmol, 1.0 equiv.) was suspended in deionised water (300 mL). A 1 M KOH aqueous solution (50 mL) was added to the stirring solution, resulting in complete dissolution of the starting material as the potassium carboxylate salt. A 1 M H_3PO_4 aqueous solution (ca. 15 mL) was then added to adjust the solution pH to 6.3 by digital meter readout before adding

n-hexylamine (1.47 mL, 11.2 mmol, 1.0 equiv.) to afford a clear yellow solution. The solution pH was readjusted back to 6.3 using a 1 M H_3PO_4 aqueous solution before heating the reaction mixture to reflux (>100 °C) in an open flask overnight (ca. 16 h). Upon cooling the reaction to room temperature, glacial acetic acid (20 mL) was added slowly whilst stirring and the flask was stored at 4 °C overnight to afford complete precipitation of the desired product. The resulting solid was collected by vacuum filtration, washed with copious amounts of 1 M HCl followed by cold MeCN (30 mL), and dried under high vacuum to obtain the title compound **1** (3.78 g, 10.2 mmol, 91%) as a beige powder, which was used directly in subsequent syntheses without further purification.

^{1}H NMR (600 MHz, DMSO-d_6, 298 K): δ_H 8.52 (d, J = 7.5 Hz, 2H^{10}), 8.15 (d, J = 7.5 Hz, 2H^{11}), 4.01 (t, J = 7.5 Hz, 2H^{6}), 1.62 (p, J = 7.4 Hz, 2H^{5}), 1.24–1.38 (m, 6H^{2,3,4}), 0.86 (q, J = 8.1, 6.5 Hz, 3H^{1}). **^{13}C NMR** (150 MHz, $CDCl_3$, 298 K): δ_C 168.7 (C^{14}), 162.8 (C^{7}), 137.6 (C^{9}), 130.1 (C^{10}), 128.9 (C^{11}), 128.5 (C^{8}), 125.5 (C^{13}), 124.2 (C^{12}), 39.9 (C^{6}), 31.0 (C^{3}), 27.3 (C^{5}), 26.2 (C^{4}), 22.0 (C^{2}), 13.9 (C^{1}). **HR-MS** (ESI; MeOH, *ve*$^-$): *m*/z [*M*–H]$^-$ calcd for $C_{20}H_{18}NO_6$ = 368.1134, found: 368.1222.

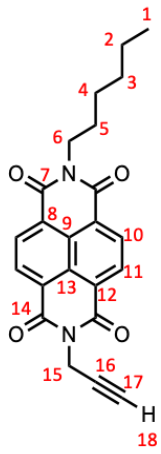

***N*-Hexyl-*N′*-(3-propargyl)-1,4,5,8-naphthalene diimide** (**2**): In a 50 mL round-bottomed flask equipped with a magnetic stir bar and an air condenser, monoimide **1** (1.98 g, 5.37 mmol, 1.0 equiv.) was suspended in anhydrous DMF (20 mL) under an Ar atmosphere, followed by the addition of propargylamine (378µL, 5.91 mmol, 1.1 equiv.). The resulting mixture was stirred at 140 ºC overnight (ca. 16 h). Upon cooling the reaction to room temperature, the solvent was removed completely by rotary evaporation (<7 mbar at 40 °C) to afford a black solid. The solid was dispersed in acetone (30 mL) with the aid of agitation by sonication and the suspension poured into cold 1 M HCl (500 mL) with the precipitate collected by vacuum filtration. The solid was re-dissolved in CH_2Cl_2 (30 mL) and passed through a silica plug followed by additional CH_2Cl_2 (300 mL) to remove any remaining insoluble materials. The solvent was removed from the filtrate completely by rotary evaporation and the crude residue was purified by automated flash column chromatography (Teledyne Isco CombiFlash Rf+ system, SiO_2: 30–80% CH_2Cl_2 in *n*-hexanes) to afford the title compound **2** (1.48 g, 3.81 mmol, 71%) as a pink powder.

^{1}H NMR (700 MHz, $CDCl_3$, 298 K): δ_H 8.80 (d, J = 7.6 Hz, 2H^{11}), 8.77 (d, J = 7.6 Hz, 2H^{10}), 4.98 (d, J = 2.5 Hz, 2H^{15}), 4.17–4.21 (m, 2H^{6}), 2.23 (t, J = 2.4 Hz, 1H^{18}), 1.70–1.78 (m, 2H^{5}), 1.40–1.47 (m, 2H^{4}), 1.30–1.39 (m, 4H^{2,3}), 0.89 (t, J = 7.1 Hz, 3H^{1}). **^{13}C NMR** ($CDCl_3$, 176 MHz, 298 K): δ_C 162.8 (C^{7}), 162.2(C^{14}), 131.5(C^{11}), 131.1(C^{10}), 127.2(C^{12}), 126.9(C^{9}),

126.35(C^{8}), 78.0(C^{15}), 71.3(C^{17}), 41.2(C^{6}), 31.6(C^{3}), 30.0(C^{15}), 28.2(C^{5}), 26.9(C^{4}), 22.7(C^{2}), 14.2(C^{1}). **HR-MS** (ESI; MeOH, *ve*$^{+}$): *m*/z [*M*+H]$^{+}$ calcd for $C_{23}H_{21}N_2O_4$ = 389.1501, found 389.1501. **Elemental analysis**: Anal. calcd for $C_{23}H_{21}N_2O_4$: C, 71.12; H, 5.18; N, 7.21. Anal. found: C, 71.08; H, 5.19; N, 7.15 (–0.04% C, +0.01% H, –0.06% N).

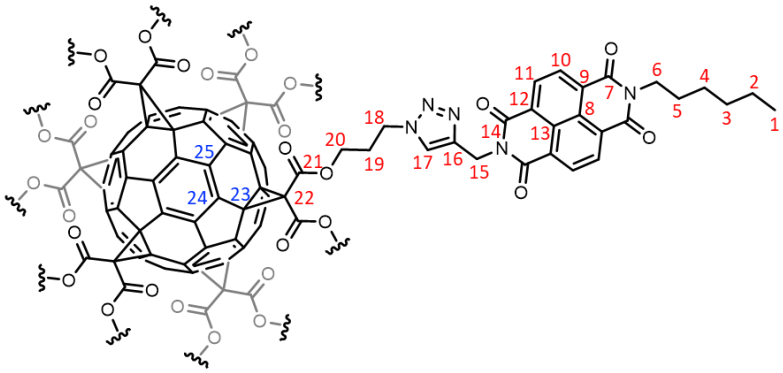

NDI-functionalised 'click' fullerene hexakis-adduct 12NDI: Applying the *General Procedure* for 'click' reactions described above, the title compound **12NDI** was prepared from **12Az** (140 mg, 60.1 µmol, 1.0 equiv.), alkyne **2** (350 mg, 0.90 mmol, 15 equiv), $CuSO_4$•$5H_2O$ (6.7 mg, 27.0 µmol, 0.3 equiv.) and sodium ascorbate (16.0 mg, 81.0 µmol, 0.9 equiv.) in a 3:1 *v*/*v* CH_2Cl_2–H_2O mixture (7 mL). Purification was achieved by automated flash column chromatography (Teledyne Isco CombiFlash Rf+ system, 24 g SiO_2: 0–6.5% MeOH in CH_2Cl_2) to afford pure **12NDI** (243 mg, 34.9 µmol, 58%) as an orange powder.

^{1}H NMR ($CDCl_3$, 700 MHz, 298 K): δ_H 8.33–8.74 (m, 48H^{10,11}), 7.64–8.09 (m, 12H^{17}), 5.20–5.49 (m, 24H^{15}), 4.19–4.60 (m, 48H^{18,20}), 4.00–4.15 (m, 24H^{6}), 2.18–2.45 (m, 24H^{19}), 1.62–1.74 (m, 24H^{5}), 1.27–1.45 (m, 72H^{4,2,3}), 0.81–0.95 (m, 36H^{1}). **^{13}C NMR** ($CDCl_3$, 176 MHz, 298 K): δ_C 163.5 (C^{21}), 162.5 (C^{7or14}), 162.4 (C^{7or14}), 145.9 (C^{24}), 142.9 (C^{16}), 141.3 (C^{25}), 131.1(C^{10}), 130.9 (C^{11}), 126.7 (C^{9}), 126.5 (C^{8+13}), 126.2 (C^{12}), 123.9 (C^{17}), 69.2 (C^{23}), 63.9 (C^{18}), 47.0 (C^{20}), 45.5 (C^{22}), 41.1 (C^{6}), 35.6 (C^{15}), 31.6 (C^{3}), 29.4 (C^{19}), 28.1 (C^{5}), 26.9 (C^{4}), 22.7 (C^{2}), 14.2 (C^{1}). **MALDI–TOF** (*ve*$^{+}$): *m*/z [*M*+H]$^{+}$ calcd for $C_{390}H_{312}N_{60}O_{72}$ = 6991.0, found: = 6969.4. **Elemental analysis**: Anal. calcd for $C_{390}H_{312}N_{60}O_{72}$: C, 65.71; H, 4.75; N, 12.46. Anal. found: C, 65.57; H, 4.47; N, 11.43 (–0.14% C, –0.28% H, –1.03% N).

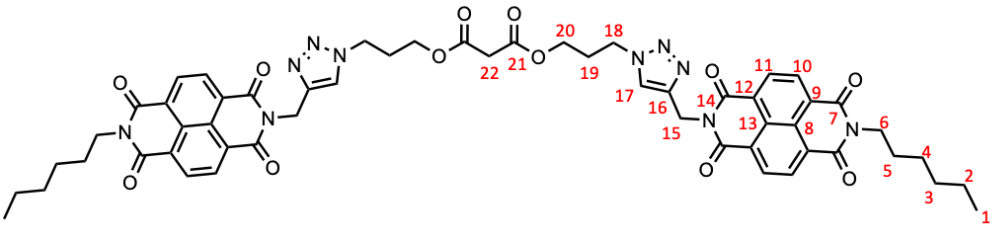

2NDI: Applying the *General Procedure* for 'click' reactions described above, the title compound **2NDI** was prepared from 1,3-bis(3-azidopropyl)propannedioate[16] (**2Az**)

(97 mg, 0.36 mmol, 1.0 equiv.), alkyne **2** (350 mg, 0.90 mmol, 2.5 equiv), $CuSO_4$•$5H_2O$ (27 mg, 0.11 mmol, 0.3 equiv.) and sodium ascorbate (64 mg, 0.32 mmol, 0.9 equiv.) in a 3:1 *v*/*v* CH_2Cl_2–H_2O mixture (31 mL). Purification was achieved by automated flash column chromatography (Teledyne Isco CombiFlash Rf+ system, 24 g SiO_2: 0–3.5% MeOH in CH_2Cl_2) to obtain pure **2NDI** (314 mg, 0.30 mmol, 83%) as a colourless powder.

^{1}H NMR ($CDCl_3$, 700 MHz, 298 K): δ_H 8.68–8.73 (m, 8H[10,11]), 7.76 (s, 2H[17]), 5.48 (s, 4H[15]), 4.44 (t, J = 6.9 Hz, 4H[19]), 4.16 (t, J = 6.5 Hz, 8H[6,20]), 3.36 (s, 2H[22]), 2.27 (p, J = 6.5 Hz, 4H[18]), 1.69–1.75 (m, 4H[5]), 1.42 (p, J = 7.2 Hz, 4H[4]), 1.29–1.38 (m, 6H[2,3]), 0.89 (t, J = 6.9 Hz, 6H[1]). **^{13}C NMR** ($CDCl_3$, 176 MHz, 298 K): δ_C 166.3 (C[21]), 162.8 (C[7]), 162.7 (C[14]), 143.0 (C[16]), 131.3 (C[10]), 131.0 (C[11]), 127.0 (C[9]), 126.9 (C[13]), 126.8 (C[8]), 126.5 (C[12]), 123.9 (C[17]), 62.2 (C[20]), 47.0 (C[18]), 41.4 (C[16]), 41.2 (C[22]), 35.7 (C[15]), 31.6 (C[3]), 29.3 (C[19]), 28.2 (C[5]), 26.9 (C[4]), 22.7 (C[2]), 14.2 (C[1]). **HR-MS** (ASAP; *ve*$^+$): *m*/z [*M*+H]$^+$ calcd for $C_{55}H_{54}N_{10}O_{12}$ = 1047.4041, found: = 1047.4036. **Elemental analysis**: Anal. calcd for $C_{55}H_{54}N_{10}O_{12}$: C, 63.09; H, 5.20; N, 13.38. Anal. found: C, 62.75; H, 5.16; N, 13.25 (–0.34% C, –0.04% H, –0.13% N).

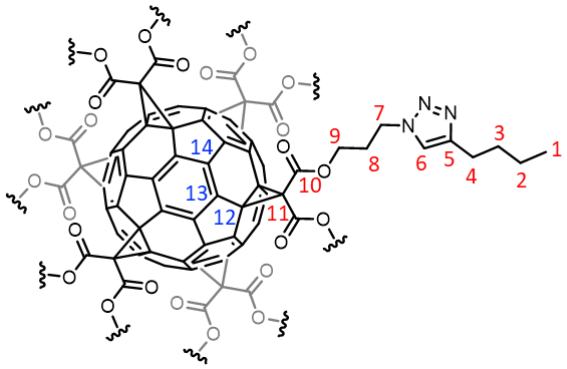

Alkyl-functionalised 'click' fullerene hexakis-adduct 12Alk: Applying the *General Procedure* for 'click' reactions described above, the title compound **12Aalk** was prepared from **12Az** (331 mg, 142 µmol, 1.0 equiv.), 1-hexyne (243 mg, 2.13 mmol, 15 equiv), $CuSO_4$•$5H_2O$ (10.6 mg, 42.6 µmol, 0.3 equiv.) and sodium ascorbate (25.3 mg, 128 mµmol, 0.9 equiv.) in a 3:1 *v*/*v* CH_2Cl_2–H_2O mixture (17 mL). Purification was achieved by automated flash column chromatography (Teledyne Isco CombiFlash Rf+ system, 24 g SiO_2: 0–5% MeOH in CH_2Cl_2) to obtain pure **12Alk** (230 mg, 66.9 µmol, 47%) as a dark orange glassy solid.

^{1}H NMR ($CDCl_3$, 700 MHz, 298 K): δ_H 7.27–7.78 (m, 12H[6]), 4.08–4.67 (m, 48H[9,7]), 2.52–2.85 (m, 24H[4]), 2.13–2.47 (m, 24H[8]), 1.48–1.75 (m, 24H[3]), 1.25–1.46 (m, 24H[2]), 0.90 (t, J = 7.2 Hz, 36H[1]). **^{13}C NMR** ($CDCl_3$, 151 MHz, 298 K): δ_C 163.5 (C[10]), 148.9 (C[5]), 145.9 (C[13]), 141.2 (C[14]), 121.2 (C[6]), 69.2 (C[12]), 63.9 (C[9]), 46.9 (C[7]), 45.4 (C[11]), 31.5 (C[3]), 29.4 (C[8]), 25.5 (C[4]), 22.4 (C[2]), 13.9 (C[1]). **MALDI-TOF** (*ve*$^+$): *m*/z [*M*+H]$^+$ calcd for $C_{186}H_{192}N_{36}O_{24}$ = 3316.7, found

3438.1. **Elemental analysis**: Anal. calcd for $C_{186}H_{192}N_{36}O_{24}$: C, 67.37; H, 5.84; N, 15.21. Anal. found: C, 64.32; H, 5.46; N, 13.74 (–3.05% C, –0.38% H, –1.47% N).

2.5 Appendix of Supplementary Data and Discussion

2.5.1 Structural Assignment by Two-Dimensional (2D) NMR

In order to fully assign the ^{1}H and ^{13}C signals of fullerene hexakis adducts **12NDI** and 1**2Alk**, we employed 2D NMR spectroscopy. Briefly, we first determined peak assignments for the simpler **2NDI** compound through analysis of COSY (Figure 2.18), HSQC (Figure 2.19) and HMBC (Figure 2.20) correlations, which enabled us to confidently assign by comparison the analogous peaks present in **12NDI** and **12Alk**. Process of elimination allowed us to attribute any remaining ^{13}C signals to the naphthalene core.

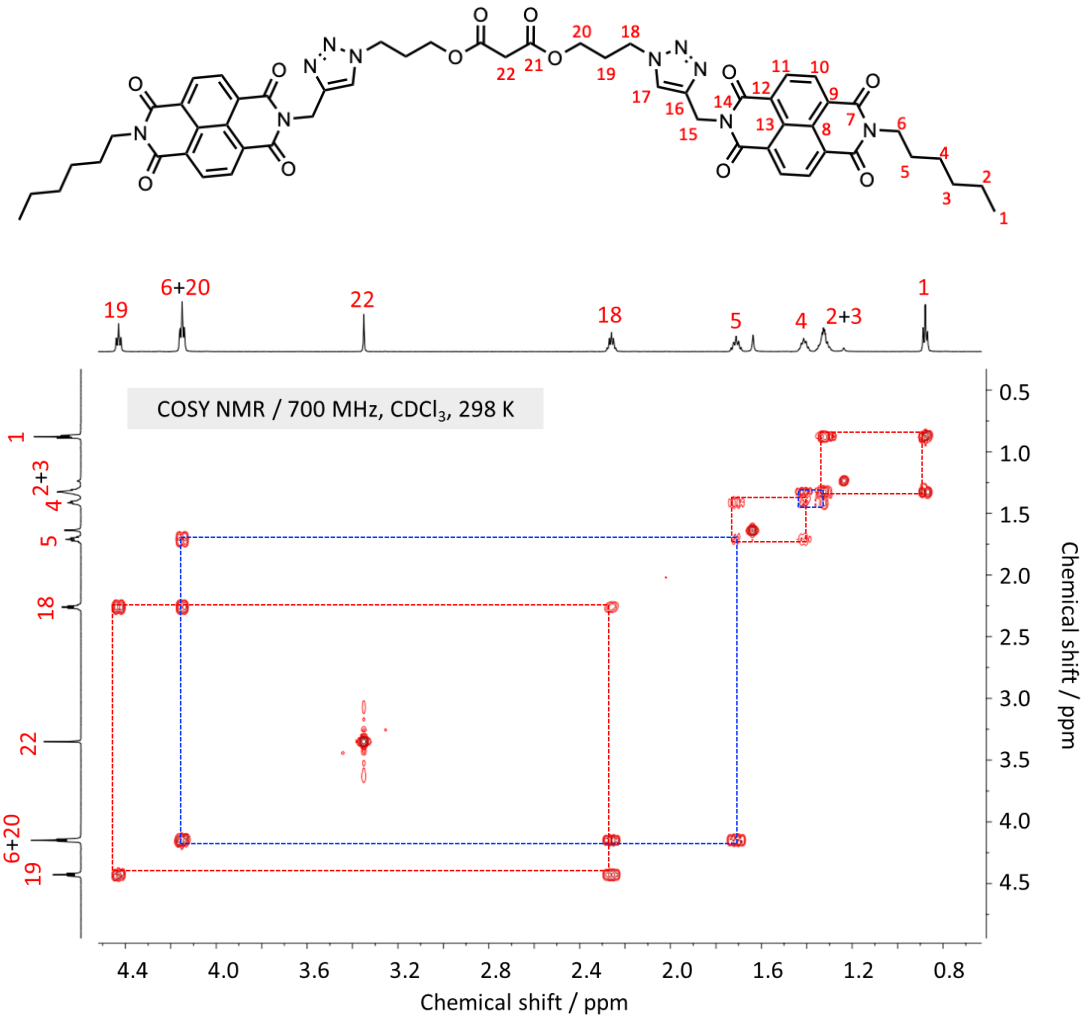

Figure 2.18. Partial ^{1}H–^{1}H COSY NMR spectrum (700 MHz, $CDCl_3$, 298 K) of **2NDI**.

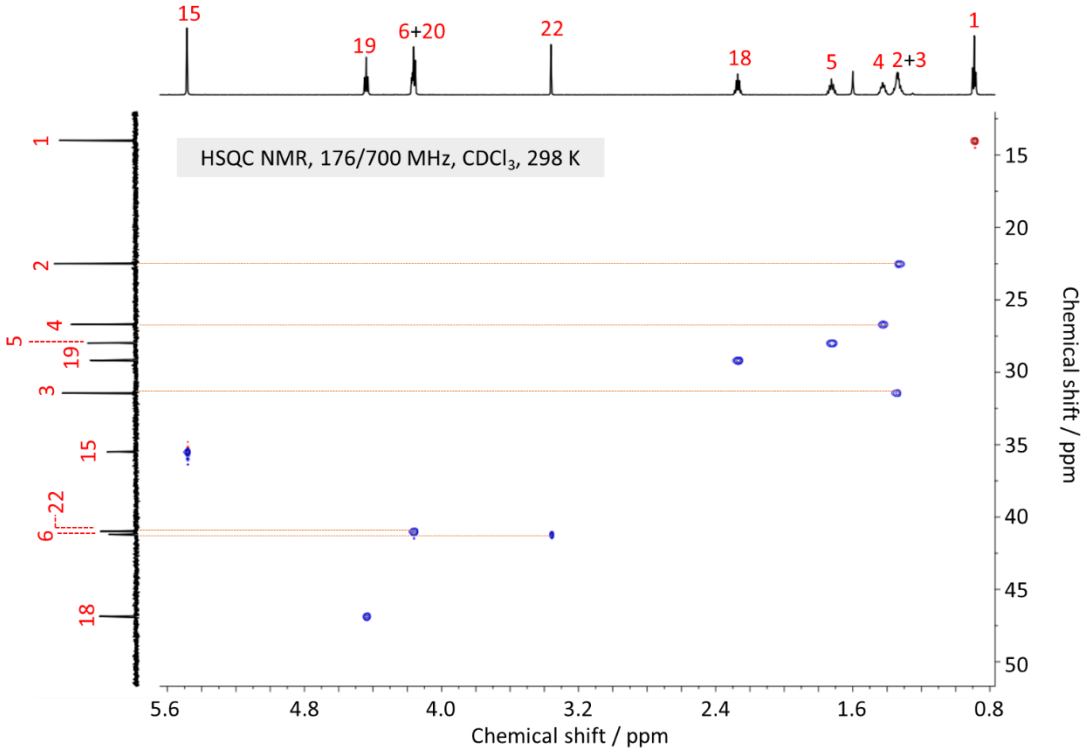

Figure 2.19. Partial HSQC NMR spectrum of **2NDI**. Key assignments are correlated between the ^{1}H and ^{13}C nuclei.

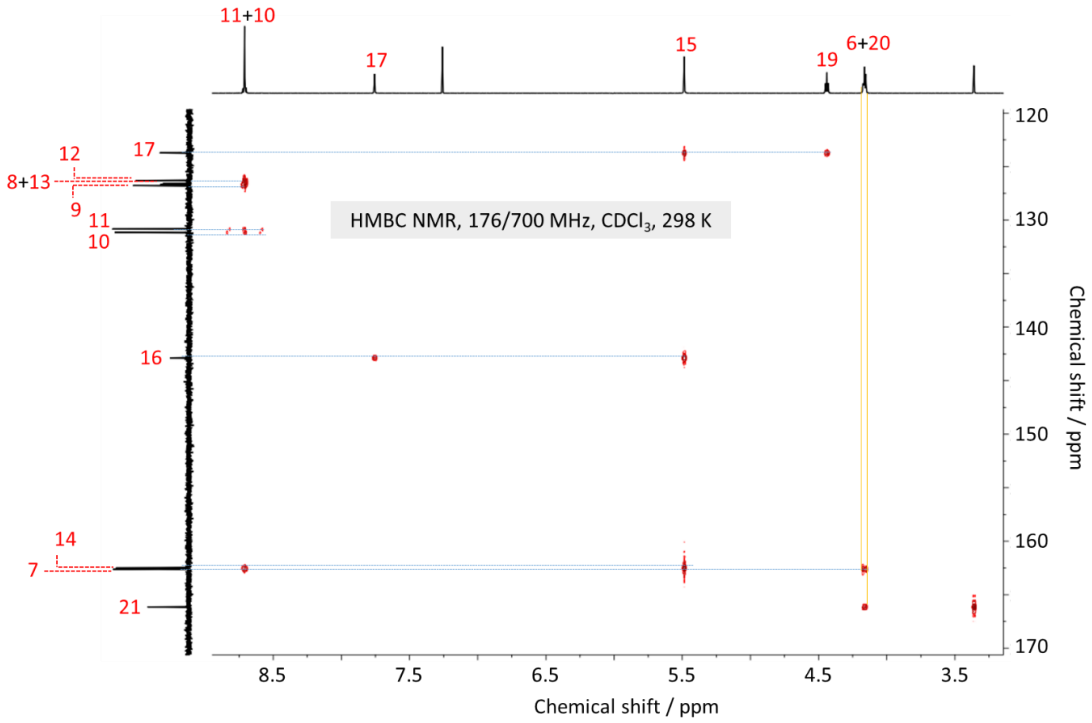

Figure 2.20. Partial HMBC NMR spectrum of **2NDI**. Key assignments are correlated between the ^{1}H and ^{13}C nuclei.

Owing to its octahedral T_h-symmetry, the core of fullerene hexakis-adducts comprises three chemically non-equivalent carbon environments that can be readily distinguished on the basis of chemical shift, i.e., two sp^2-carbon centres (ca. 141 and 145 ppm for **12NDI**) and one sp^3-carbon centre (ca. 70 ppm) associated with the non-conjugated propane ring. We determined peak assignments for **12NDI** compound through analysis of COSY (Figure 2.21), HSQC (Figure 2.22) and HMBC (Figure 2.23) correlations. Similarly, peak assignments for **12Alk** were determined through analysis of COSY (Figure 2.23), HSQC (Figure 2.24) and HMBC (Figure 2.25) correlations.

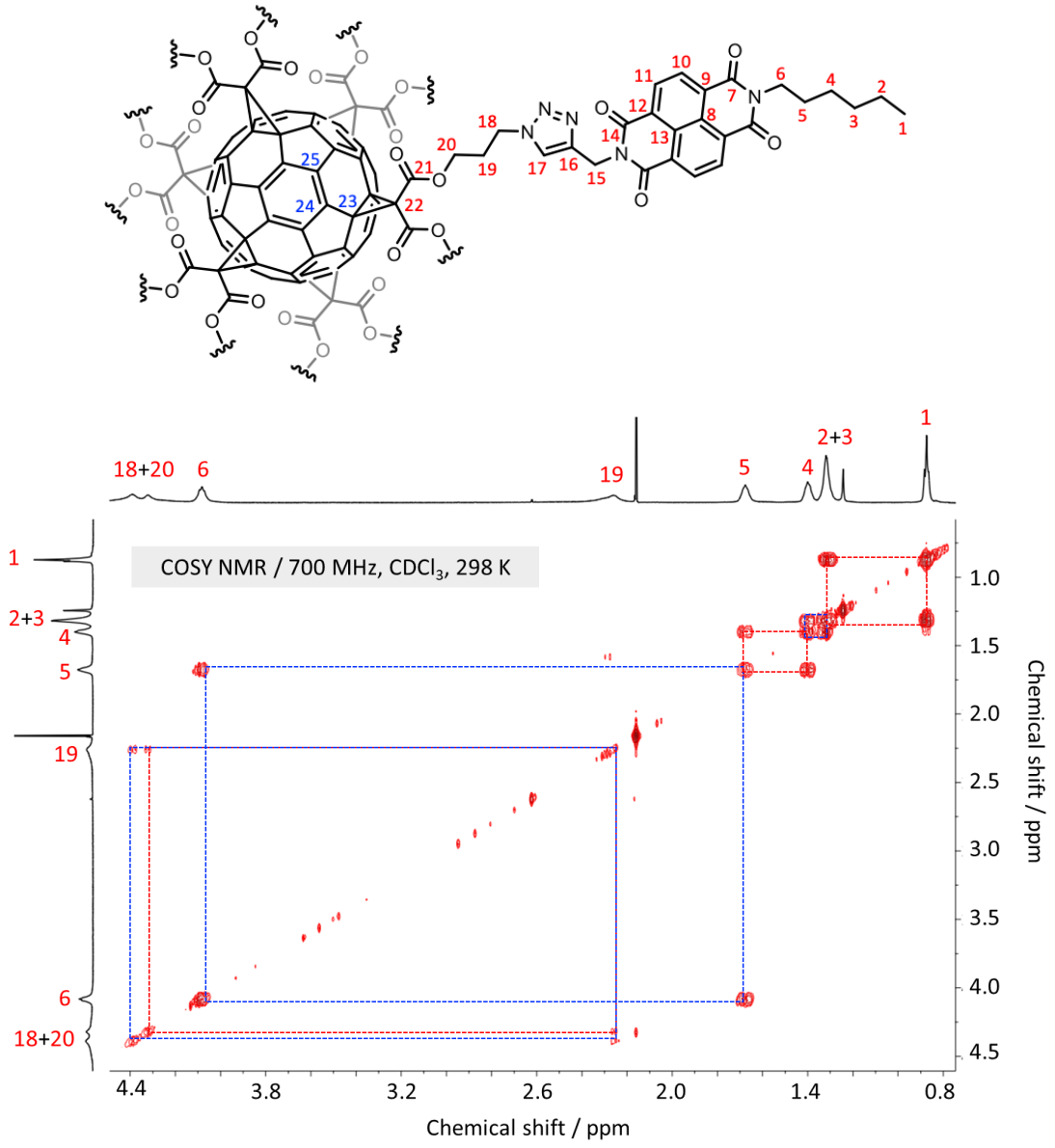

Figure 2.21. Partial ^{1}H–^{1}H COSY NMR spectrum of **12NDI**.

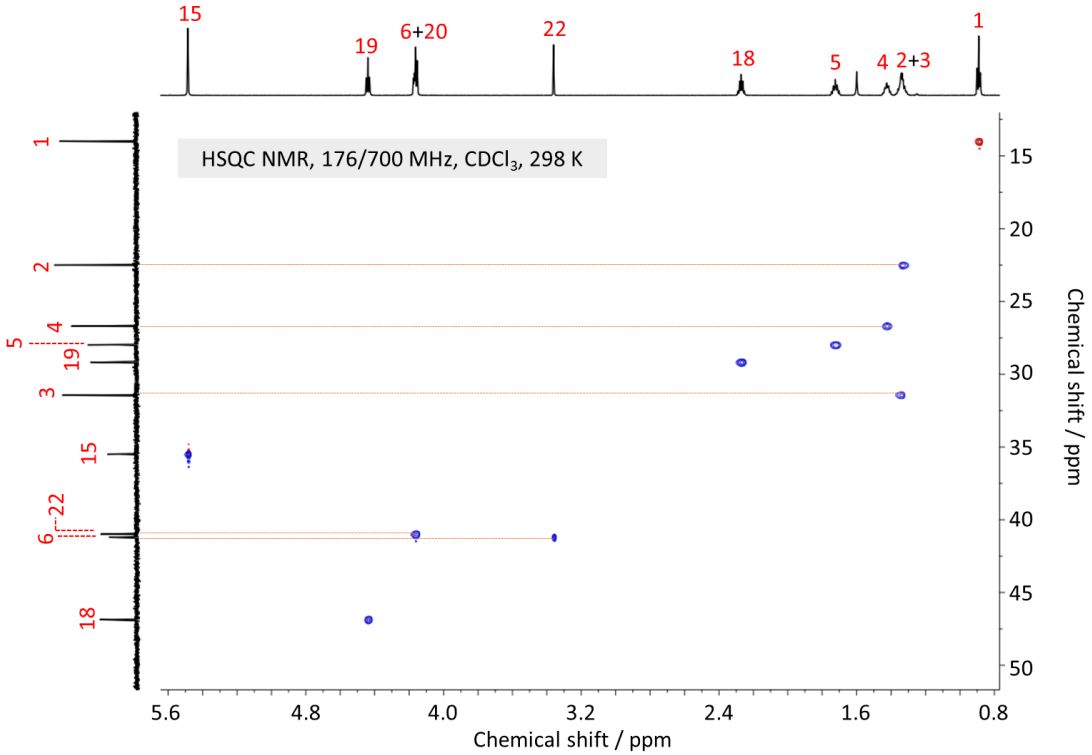

Figure 2.22. Partial HSQC NMR spectrum of **12NDI**. Key assignments are correlated between the ^{1}H and ^{13}C nuclei.

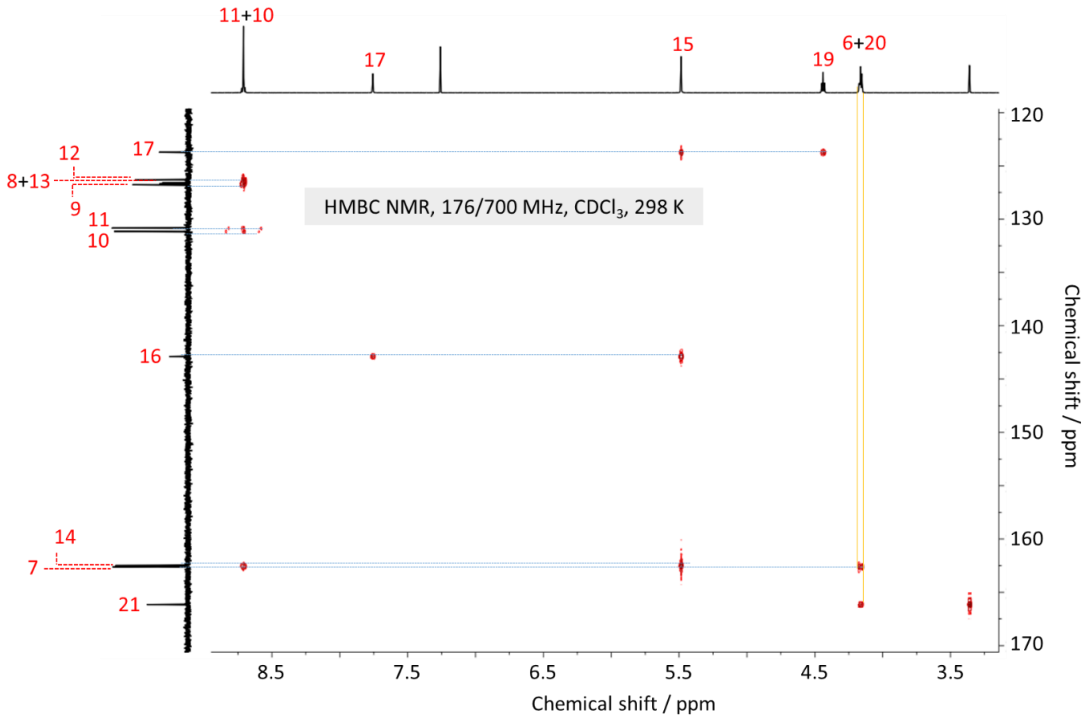

Figure 2.23. Partial HMBC NMR spectrum of **12NDI**. Key assignments are correlated between the ^{1}H and ^{13}C nuclei.

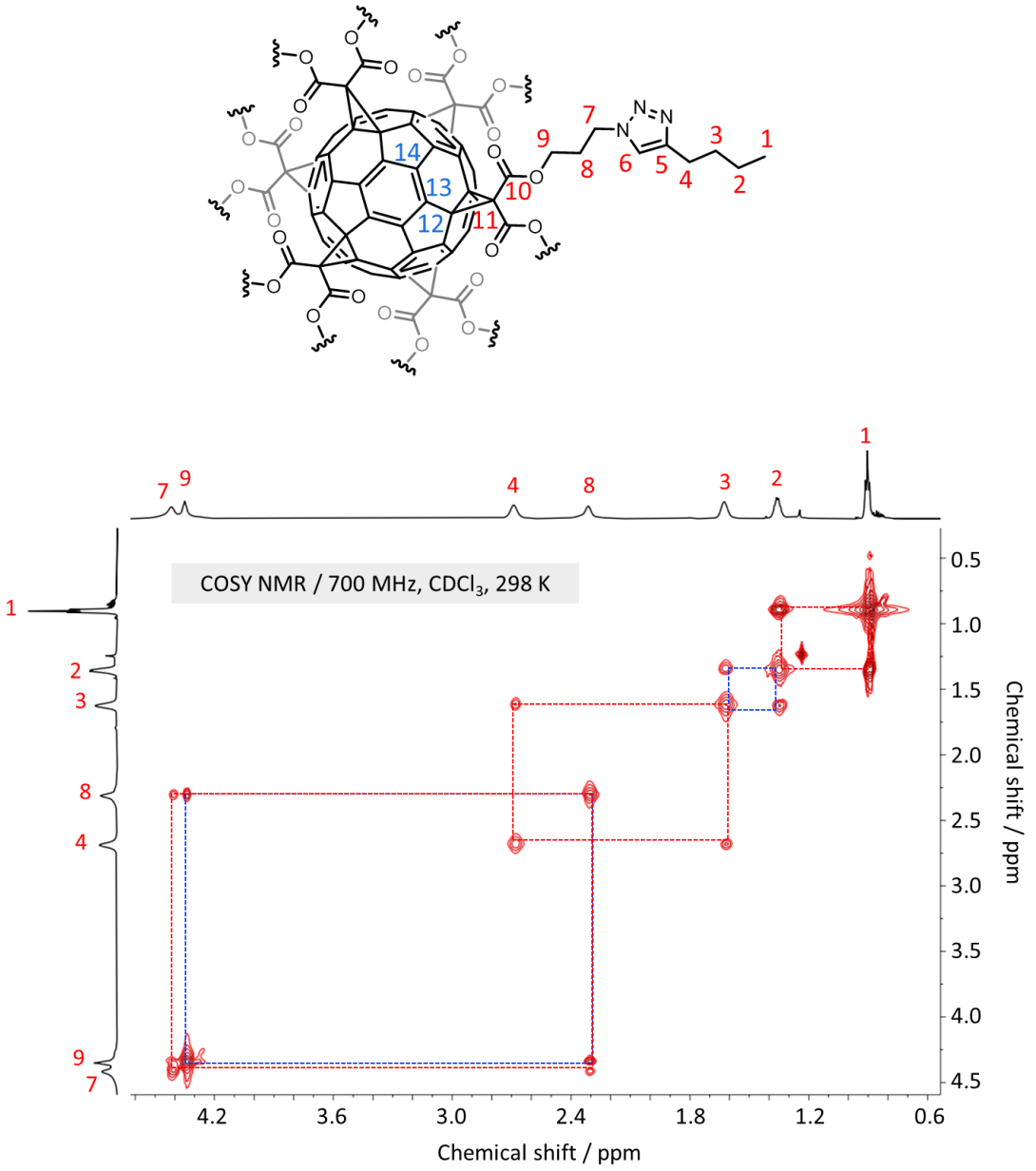

Figure 2.24. Partial ^{1}H–^{1}H COSY NMR spectrum of **12Alk**. Key assignments are correlated between the ^{1}H and ^{13}C nuclei.

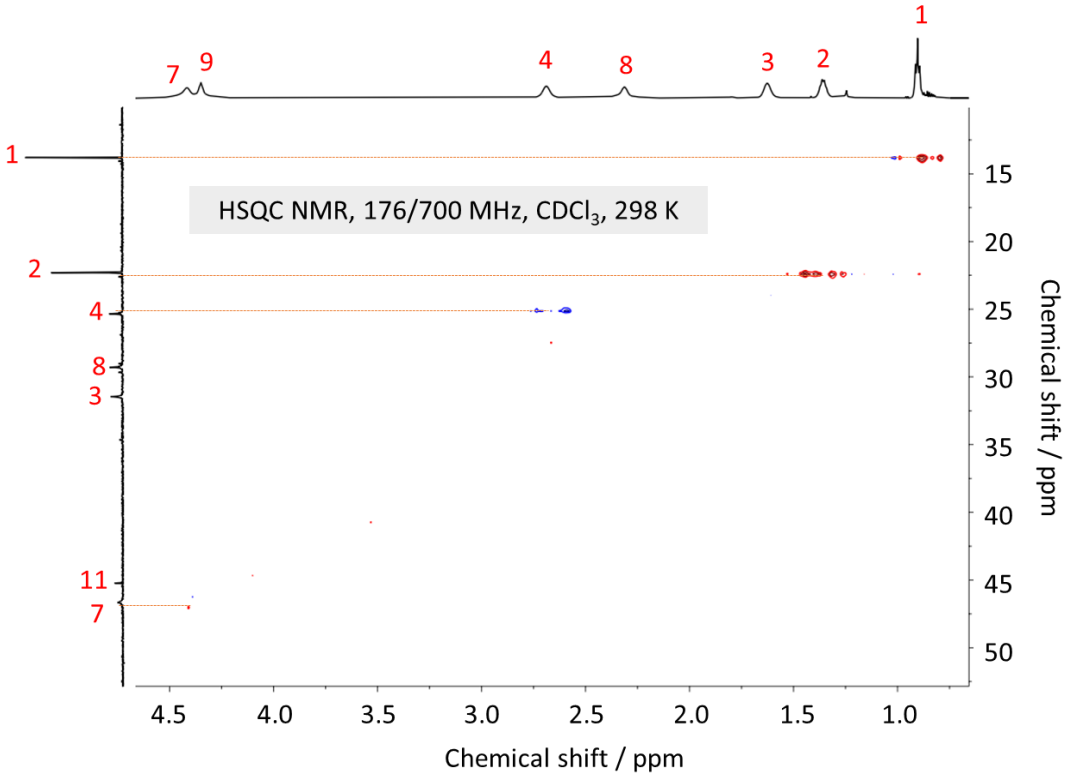

Figure 2.25. Partial HSQC NMR spectrum of **12Alk**. Key assignments are correlated between the ^{1}H and ^{13}C nuclei.

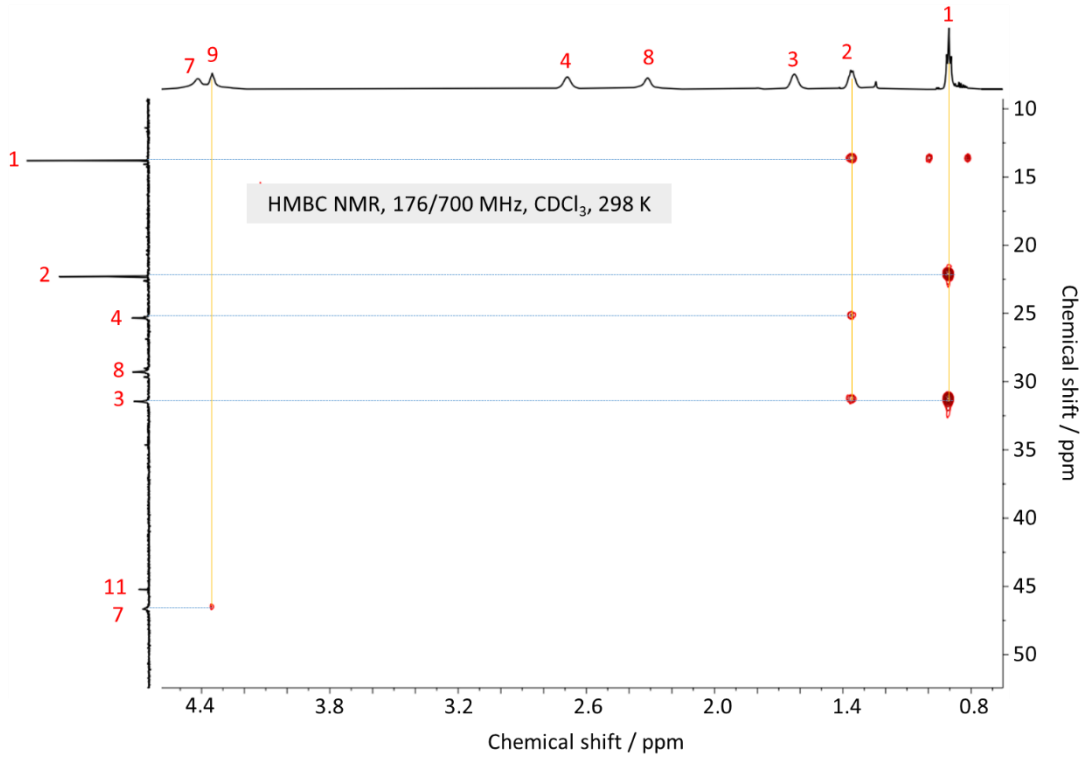

Figure 2.26. Partial HMBC NMR spectrum of **12Alk**. Key assignments are correlated between the ^{1}H and ^{13}C nuclei.

2.5.2 MALDI-TOF

Hexakis-adducts often have high molecular weights, and due to their often multivalent/ dendrimer like structure, it is difficult to structurally confirm these compounds by ^{1}H and ^{13}C NMR. However, MALDI-TOF can provide invaluable information, especially when monitoring the 'click' functionalisation of hexakis-adducts in addition to confirming the number of pendant units. Depending on volatility and fragmentation of compound, signal intensity can be very broadly scattered. Representative examples of **12NDI** (Figure 2.27) and **12Alk** (Figure 2.28) are shown below.

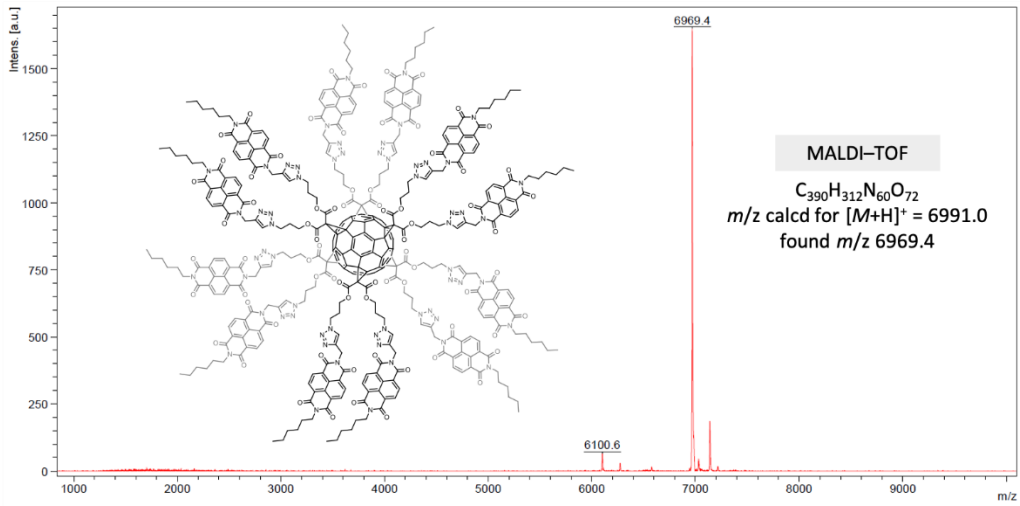

Figure 2.27. MALDI–TOF mass spectrum of TBF-functionalised 'click' fullerene hexakis-adduct **12NDI**.

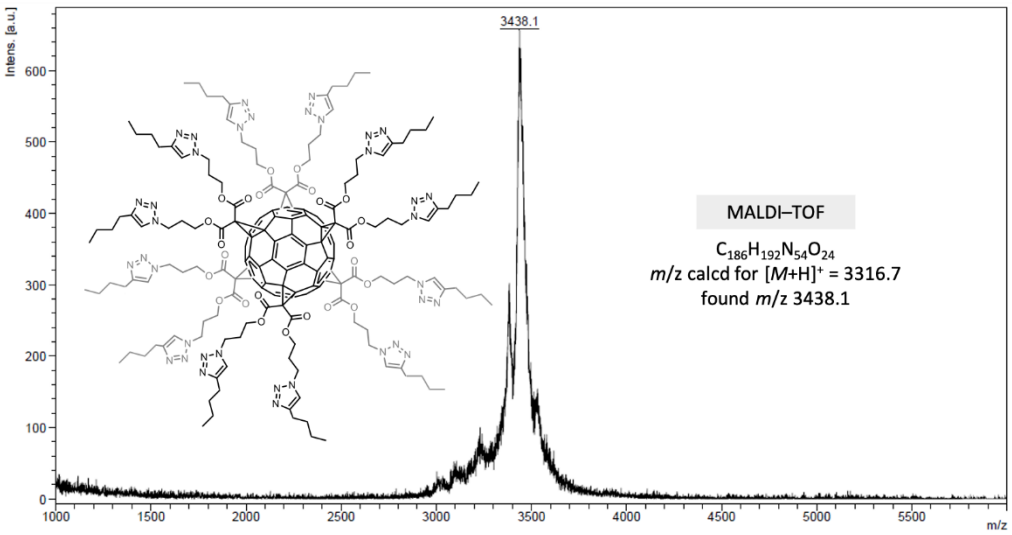

Figure 2.28. MALDI–TOF mass spectrum of alkyl-functionalised 'click' fullerene hexakis-adduct **10Alk**.

2.5.3 Absorption and Emission Spectroscopy

The solution-state optical properties of NDI derivatives serve as excellent tools to probe the intra- and intermolecular organisation of their aromatic quadrupoles. Samples were prepared containing equimolar concentrations of NDI units for direct comparison of results in anhydrous, spectroscopic grade solvents and with the aid of sonication to afford complete dissolution. Steady-state absorption and fluorescence emission spectra were recorded at room temperature (25 ºC) in quartz cuvettes (10 mm and 10 × 10 mm path lengths, respectively) and corrected with respect to the pure solvent. All fluorescence samples were excited at 360 nm and spectra recorded using either a standard 90º detector set up or, in the case of samples with optical densities >0.3 O.D, front-facing detection. The molar absorptivity (ε) was calculated using the following equation:

$$\epsilon = \frac{A \times l}{c}$$

where A is measured absorption (O.D.), c is concentration, and l is pathllength of cuvette.

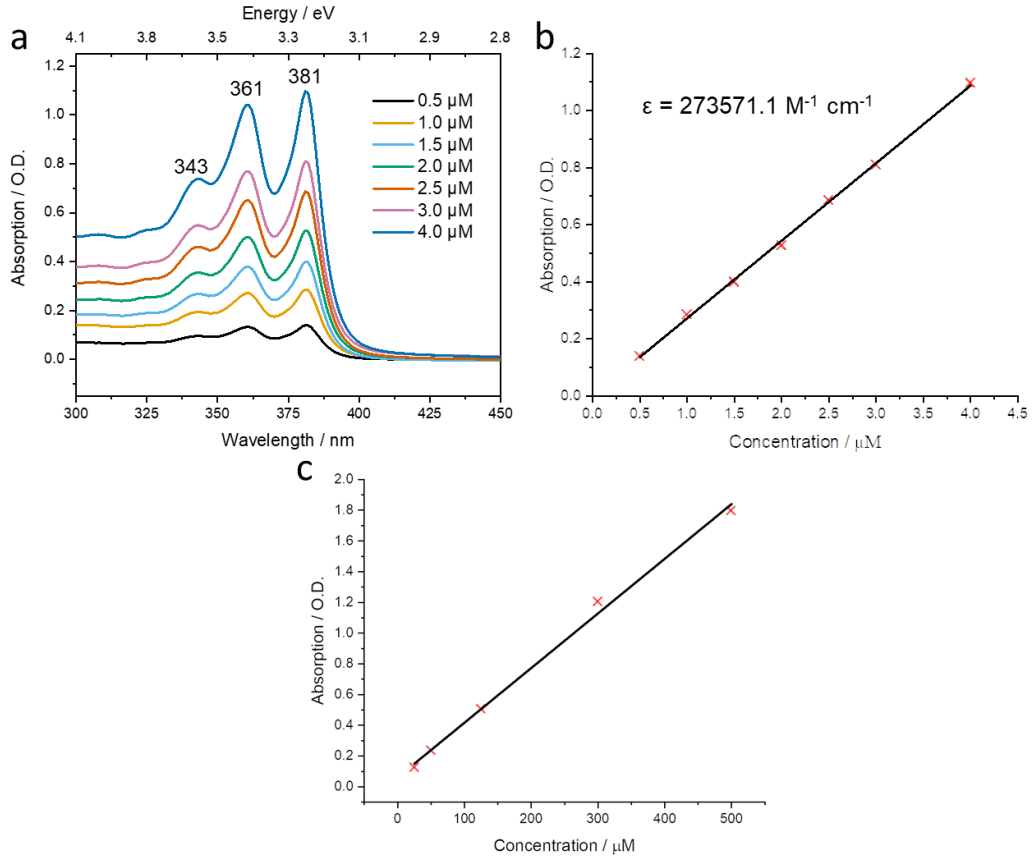

Figure 2.29. a) Concentration-dependent absorption spectra of **12NDI** in $CHCl_3$ (298 K). Cuvette path length = 10 mm. Absorbance at 381 nm for **12NDI** at varying concentration b) 0.5–4.0 µM; ε shown on graph in M^{-1} cm^{-1} and c) at 25–500 µM where a cuvette with path length ca. 0.2 mm was used.

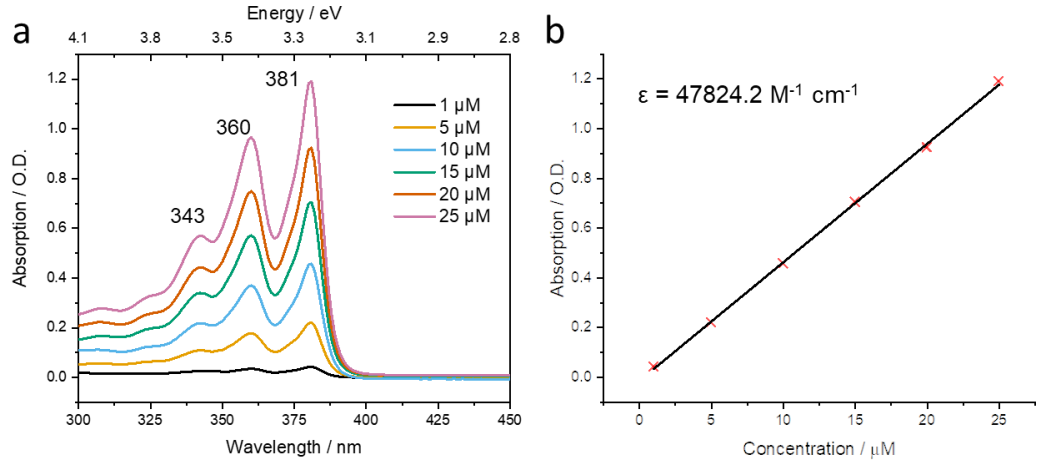

Figure 2.30. a) Room-temperature concentration-dependent absorption spectra of **2NDI** in $CHCl_3$. Cuvette path length = 10 mm. b) Absorbance at 381 nm for **2NDI** at varying concentration 1–25 μM; ε shown on graph in M^{-1} cm^{-1}.

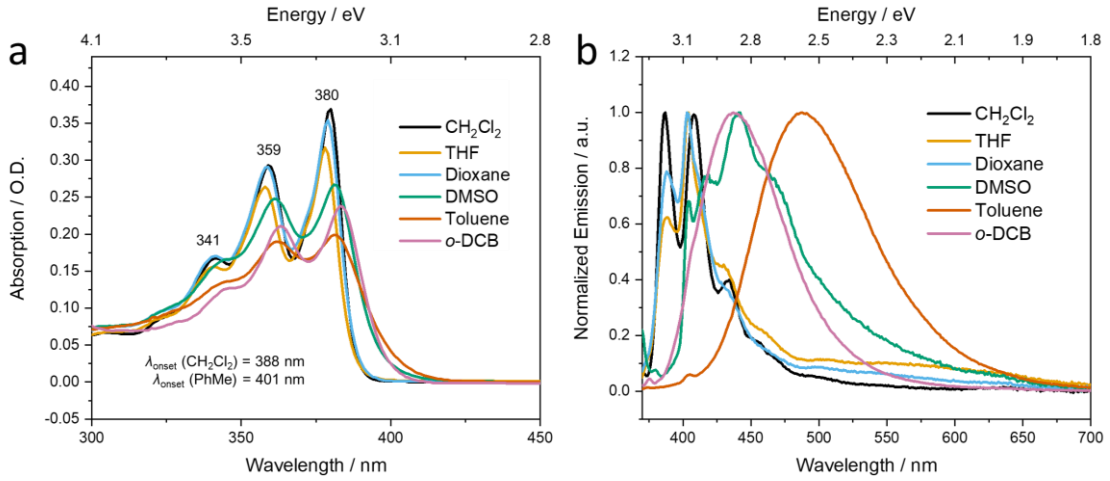

Figure 2.31. Room-temperature solvent-dependent absorption spectra of **1** [12 μM]. Cuvette path length = 10 mm. Room-temperature solvent-dependent emission spectra of **1**. Samples were prepared at 0.1–0.3 O.D. and excited at 360 nm. Cuvette path length = 10 mm.

We also investigated the ability of **12NDI** and **2NDI** to form solid-state intra- and intermolecular NDI interactions using absorption and emission spectroscopies. Intramolecular NDI interactions were encouraged by drop-casting *o*-dichlorobenzene solutions containing each analyte (0.05 mg/ mL) and polymer (5 mg/ mL) onto quartz substrates, resulting in 'diluted' thin films as 1 wt% dispersions of analyte in a polymer matrix. A selection of polymers—poly(methylmethacrylate) (PMMA), polystyrene (PS) and Zeonex® (a proprietary cycloolefin polymer)—were considered in order to modulate the interaction of polymer side chains with NDI units. Thin films were allowed to cure by slow evaporation of the solvent under ambient conditions before drying films completely under vacuum at 0.1 mbar overnight. Quartz substrates were routinely cleaned prior to preparation of thin films by rinsing in concentrated aqueous H_2SO_4 followed by water then acetone before drying in an oven at

100 °C for at least 1 h. The observation of higher order aggregates in **12NDI** suggests the presence of other higher-order NDI assemblies[29] that can take place intramolecularly. It is apparent from comparing the ratios of the two emission band intensities that the flexible, multivalent nature of **12NDI** lends itself better to the formation of long-range networked ensembles in neat thin films compared to **2NDI**, which we envision could manifest (Figure 2.32) *via* the intercalation of several NDI units originating from multiple separate fullerene molecules. While **2NDI** is also capable of participating in similar interactions (albeit divalent), its propensity to already pre-organise NDI units co-facially into a 'bound conformation in solution may ultimately limit the extent of higher-order assembly observed the solid state.

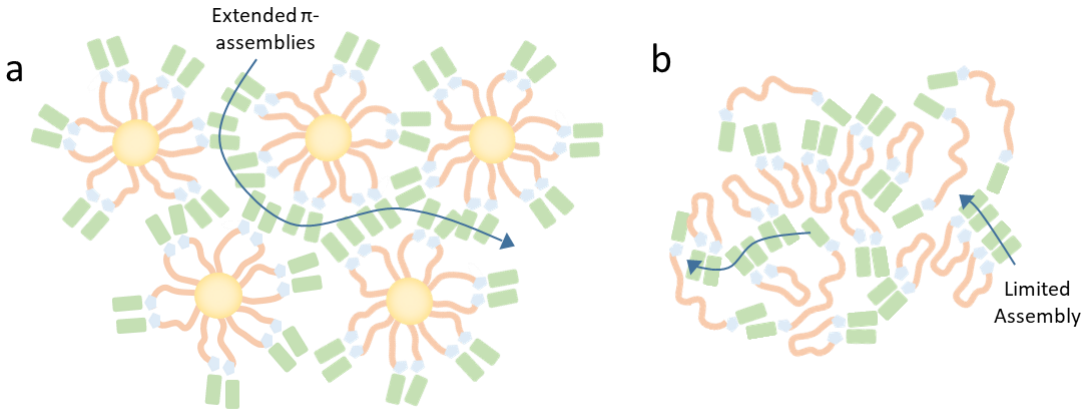

Figure 2.32. Potential intra- and intermolecular NDI assembly pathways of (a) **12NDI** and (b) **2NDI**.

2.5.4 Dynamic Light Scattering (DLS)

As a multivalent molecule, we rationalised that **12NDI** may aggregate into larger assemblies *via* aromatic π-interactions, i.e., there is potential for intermolecular interactions. DLS was conducted in order to find a working concentration for all experiments that would home in on the properties of individual molecules where there are no contributions from molecules interacting. A working concentration of 0.3 mM for **12NDI** was hypothesised; this is a concentration where good signal-to-noise ratio should be maintained for analysis by CV, SEC (OTTLE), EPR spectroscopy, etc. Samples were prepared in CH_2Cl_2 [0.3 mM] and filtered using an Acrodisc 0.45 µm filter immediately after dissolution of the material, before addition to a quartz cuvette (10 mm path length). Data collected at 298 K. Mean particle diameter = 4.48 nm, SD = 4.0%.

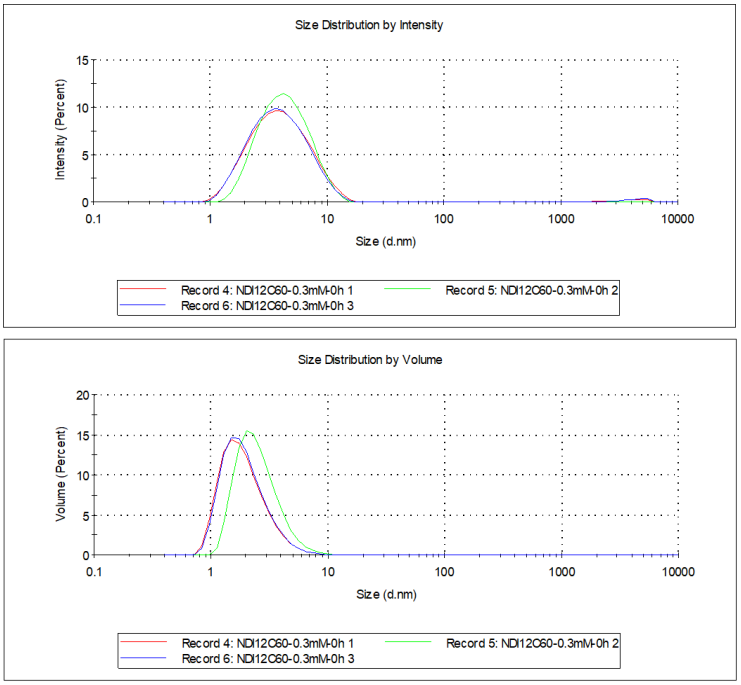

Figure 2.33. DLS data for a freshly prepared solution of **12NDI** in CH_2Cl_2 [0.3 mM]. The sample was filtered using an Acrodisc 0.45 µm filter before addition to a quartz cuvette (10 mm path length). Data collected at 298 K. Mean particle diameter = 4.51 nm, SD = 4.1%.

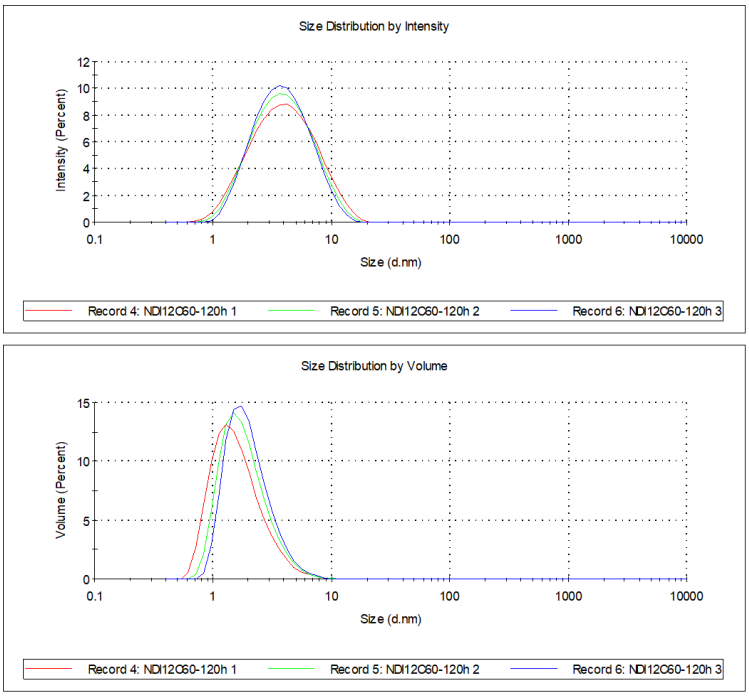

Figure 2.34. DLS data for an aged solution of **12NDI** in CH_2Cl_2 [0.3 mM], t = 120 h. The sample was filtered at t = 0 h using an Acrodisc 0.45 µm filter before addition to a quartz cuvette (10 mm path length). Data collected at 298 K. Mean particle diameter = 4.48 nm, SD = 4.0%.

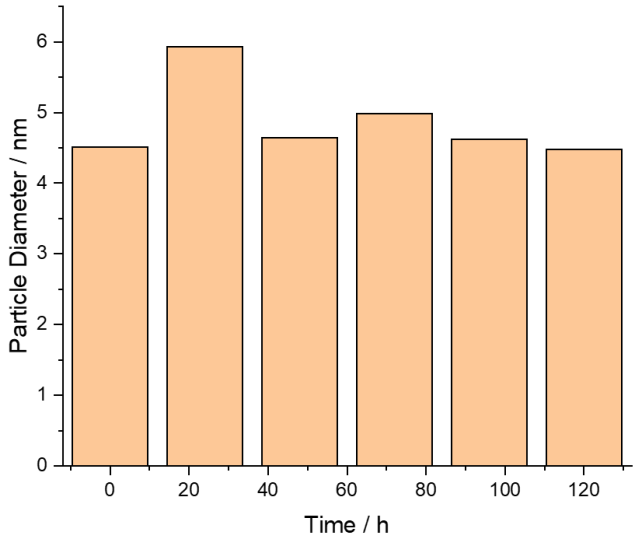

Figure 2.35. Average particle diameter (3 runs) of **12NDI** in CH_2Cl_2 [0.3 mM] as measured by DLS every 24 hours. No aggregation into larger particles was observed.

2.5.5 Electrochemical Analysis

Cyclic voltammograms of **1**, **2NDI** and **12NDI** were recorded at room temperature in deaerated CH_2Cl_2 solutions (3.6 mM with respect to NDI units; 0.1 M $TBAPF_6$ supporting electrolyte) under an argon atmosphere using a standard three-electrode set up. See Section 2.4.1 (Materials and Methods) for full experimental details. The current intensity is directly proportional to the square-root of the scan rate for each CV experiment which reveals that all first- and second-wave cathodic/anodic processes are highly reversible. We further note that, while the π-conjugation compared to pristine C_{60} has indeed been disrupted, hexakis-substituted fullerene

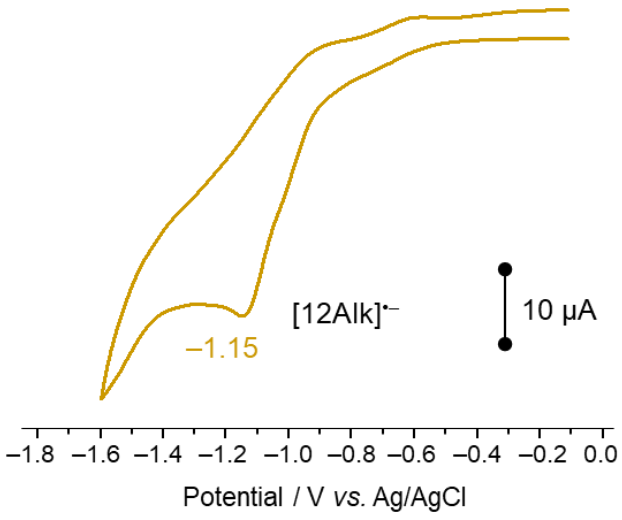

Figure 2.36. Cyclic voltammogram (50 mVs^{-1}, 298 K) of **12Alk** ([0.3 mM] in degassed CH_2Cl_2. The irreversible one-electron reduction is observed at –1.15 V and therefore coincides with the second reduction event of **12NDI**.

cores are not electrochemically inert and undergo electrochemically irreversible single-electron reduction themselves[16], i.e., –1.15 V vs Ag/AgCl for the model fullerene hexakis adduct **12Alk** (Figure 2.36), which is coincident with the second-wave NDI reductions of **12NDI**.

2.5.6 SEC–FTIR Analysis

Spectroelectrochemical measurements were conducted on dearated anhydrous CH_2Cl_2 solutions (3.6 mM with respect to NDI units) containing 0.1 M $TBAPF_6$ as the supporting electrolyte in an air-tight optically transparent thin-layer electrochemical (OTTLE) cell (path length ca. 0.2 mm) under an argon atmosphere. See Section 2.4.1 (Materials and Methods) for full details. Neutral NDI molecules are typically characterised by strong FTIR vibrational bands associated with the symmetric and asymmetric stretching of the imide carbonyls (1650–1725 cm^{-1}) and aromatic C–C bonds (<1600 cm^{-1}) of the naphthalene core.[11]

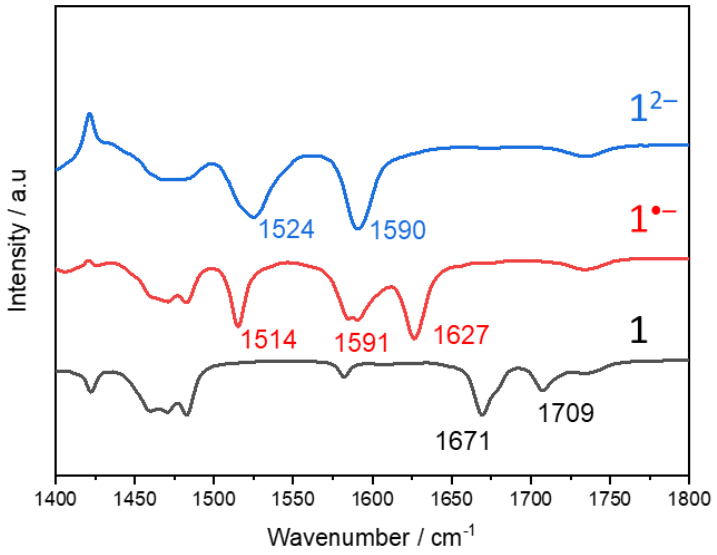

Figure 2.37. Partial FTIR spectra of **1** in deaerated anhydrous CH_2Cl_2 under argon atmosphere before and during the application of a constant voltage to generate step-wise the radical anion $\mathbf{1}^{\bullet-}$ (–0.6 V vs. Ag) and dianion $\mathbf{1}^{2-}$ (–1.1 V). TBAPF6 (0.1 M) was used as the supporting electrolyte.

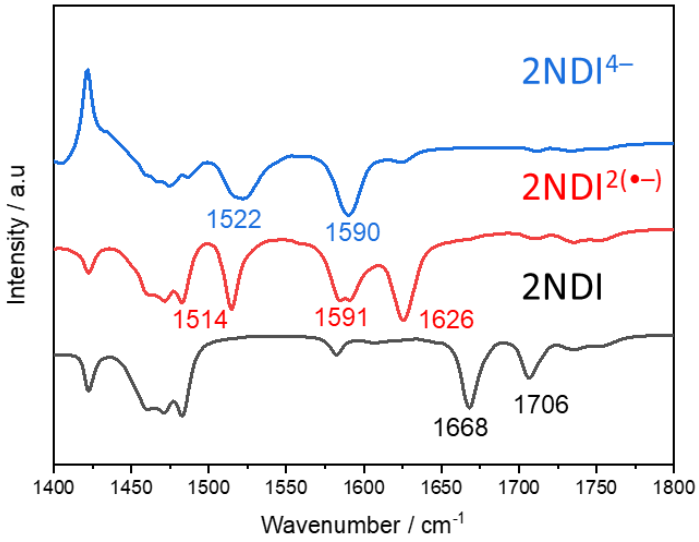

Figure 2.38. Partial FTIR spectra of **2NDI** in deaerated anhydrous CH_2Cl_2 under argon atmosphere before and during the application of a constant voltage to generate step-wise the diradical **2NDI**$^{2(\bullet-)}$ (–0.7 V vs. Ag) and tetranionic **2NDI**$^{4-}$ (–1.3 V). TBAPF6 (0.1 M) was used as the supporting electrolyte.

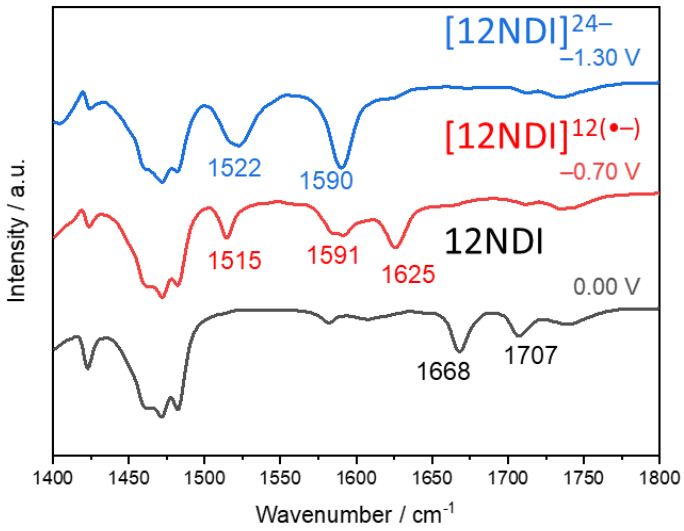

Figure 2.39. Partial FTIR spectra of **12NDI** in deaerated anhydrous CH_2Cl_2 under argon atmosphere before and during the application of a constant voltage to generate step-wise [**12NDI**]$^{12(\bullet-)}$ (–0.7 V vs. Ag) and [**12NDI**]$^{24-}$ (–1.3 V). TBAPF6 (0.1 M) was used as the supporting electrolyte.

2.5.7 SEC–UV-Vis-NIR Analysis

Spectroelectrochemical measurements were conducted on dearated anhydrous CH_2Cl_2 solutions (3.6 mM with respect to NDI units) containing 0.1 M $TBAPF_6$ as the supporting electrolyte in an air-tight optically transparent thin-layer electrochemical (OTTLE) cell (path length ca. 0.2 mm) under an argon atmosphere. See Section 2.4.1 (Materials and Methods) for full experimental details. Upon applying a voltage of –0.90 V to **12NDI**, an absorption correlating to the reduction of the C_{60} core grows in at 945 nm (Figure 2.40). The C_{60} hexakis radical can also be generated with control compound **12Alk**. The absorption profile of **12Alk**$^{\bullet-}$ is similar in profile (Figure 2.41) to that observed for **12NDI**, however, there is a slight red shift in energy (i.e., λ_{max} = Δ50 nm), potentially arising from an interaction between an NDI$^{\bullet-}$ and $C_{60}^{\bullet-}$.

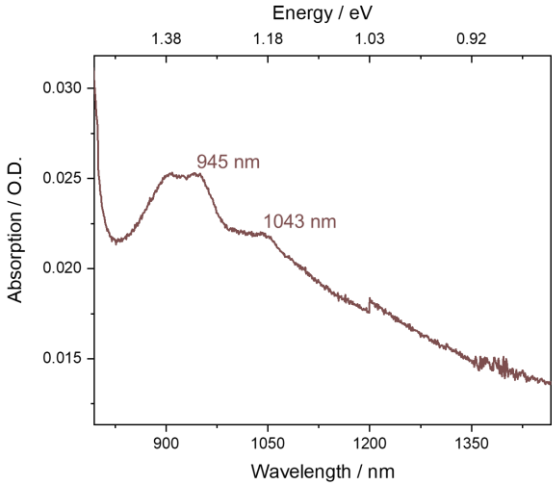

Figure 2.40. Partial absorption window of **12NDI** (1.8 mM of NDI units) following the exhaustive and electrochemical irreversible reduction in deaerated anhydrous CH_2Cl_2 containing 0.1 M $TBAPF_6$ as the supporting electrolyte. Profile is correlated to the reduction of the C_{60} core. A constant potential –0.90 V was applied.

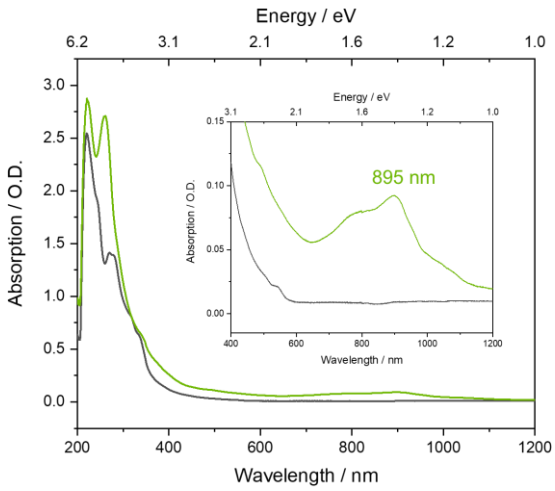

Figure 2.41. UV-Vis-NIR absorption spectra of **12Alk** (1.0 mM) in deaerated anhydrous CH_2Cl_2 containing 0.1 M $TBAPF_6$ as the supporting electrolyte. A constant potential –1.10 V was applied.

2.5.8 Chemical Reductions by Cobaltocene Titrations

All chemical reduction experiments were performed in an argon glove box (<0.1 ppm O_2 and H_2O content) by controlled titration of cobaltocene ($CoCp_2$) as a single-electron reductant ($E_{1/2}(CoCp_2)$ = –1.3 V vs. Fc^+/Fc) into analyte solutions prepared using well-deaerated anhydrous solvents. The active concentration of freshly prepared $CoCp_2$ stock solutions was determined *via* Equation 2 by titrating known volumes of the reductant into a solution of NDI **1** (150 µM), a well-established electron acceptor available in our laboratory, and monitoring for saturation of the signature NDI radical anion absorption (λ_{max} = 478 nm in CH_2Cl_2).

$$[CoCp^A] = [CoCp^T] \times (A^T/A^A)^{-1} \qquad \text{(eq.2)}$$

$CoCp^A$ = active $CoCp_2$ concentration µM, $CoCp^T$ = theoretical $CoCp_2$ concentration µM, A^T = theoretical amount for 1 equiv. in µL, A^A = actual amount for 1 equiv. in µL.

2.5.9 CW-EPR Spectra

EPR (CW-EPR) spectra were recorded at X-band on a JEOL X320 spectrometer using 0.1 G modulation amplitude. The spectra were simulated using EasySpin[37] toolbox for MatLab. CW-EPR spectra were collected between 293–193K in a glass pasteur pipette in deaerated anhydrous solvents. Radical anion samples (150 µM spin density) were chemically generated in an argon glove box (<0.1 ppm O_2 and H_2O content) by titrating analyte solutions with known equivalents of $CoCp_2$ stock solution. All samples were confirmed by absorption spectroscopy prior to EPR analysis.

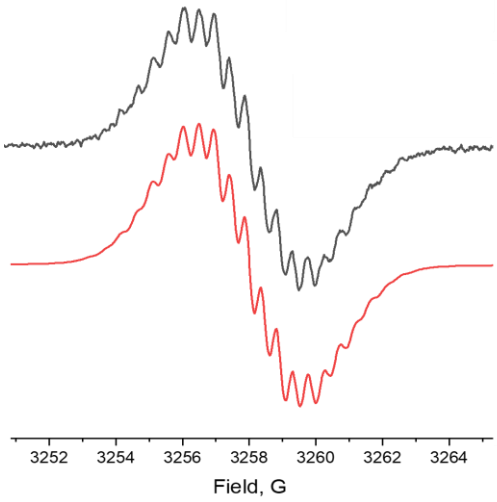

Figure 2.42. Room-temperature CW-EPR spectra of a) **2NDI**$^{\bullet-}$ (black, 150 µM spin density) and b) **2NDI**$^{2(\bullet-)}$ (red, simulated spectra) in CH_2Cl_2.

2.5.10 Molecular Dynamics (MD) Simulations

Molecular dynamics (MD) simulations were conducted in order to gain insight into the likely conformations adopted by the neutral states of **2NDI** and **12NDI** in CH_2Cl_2 solution that in turn relate to the ground state intramolecular NDI aggregation. **2NDI** and **12NDI** structures were initially built in the SCIGRESS molecular modelling package[41] and energy minimised by first employing the MM3 force field[42–44], followed by the AM1 semiempirical Hamiltonian[45]. Force fields were then constructed using the GAFF (Generalized Amber Force Field)[46] and RESP charges using the antechamber tool of the AmberTools 18 package[47]. RESP (restrained electrostatic potential atomic partial charges), were obtained from Gaussian 09 Hartree-Fock calculations with a 6-31G* basis set, with charges fitted to the electrostatic potential at points selected according to the Merz-Singh-Kollman scheme[48]. GAFF topologies and coordinate files were converted into the GROMACS format using the ACPYPE script[49].

Given the size and complexity of the **12NDI** structure, RESP charges needed to be obtained in a two stage process, by first calculating separately the restrained electrostatic potential atomic (RESP) partial charges of the much simpler dimer **2NDI** and a hexakis-substituted fullerene core (not prepared synthetically, see Figure 2.44 for structure), and then matching these by hand to the fully constructed **12NDI** molecule. The minimum energy conformations were then obtained using GAFF-RESP in the GROMACS 2018.7 package. These conformations were solvated with CH_2Cl_2 solvent and added PF_6^- and TBA^+ ions. These configurations were then used as the starting point for the molecular dynamics simulations.. The systems were first compressed to liquid state densities at 298 K and 1 bar, using a modified Berendsen thermostat and a Berendsen barostat. The systems were then equilibrated using a Nosé-Hoover thermostat and a Parrinello-Rahman barostat (over 200 ps). These runs used thermostat and barostat relaxation times of 1 ps and 2 ps respectively and a 1 fs time step. Production runs with the same thermostat and barostat were carried out for >800 ns for **2NDI** and >500 ns for **12NDI**. Using the reference atoms (shown in Figure 2.43) intra- and interbranch distances between NDI units were monitored over t = 800 ns and t = 500 ns for **2NDI** and **12NDI**, respectively, where π-interactions were assumed at distances $d_{NDI} \leq 3.5$ Å.[30] As the free (i.e., untethered) 'arm' of **12NDI**, flexible dimer **2NDI** (Figure 2.5a) is able to adopt more conformations in solution that ultimately range between i) a 'bound' state in which its two neutral NDI units are co-facially oriented within 3.5 Å of one another and ii) a non-interacting or 'unbound' state.

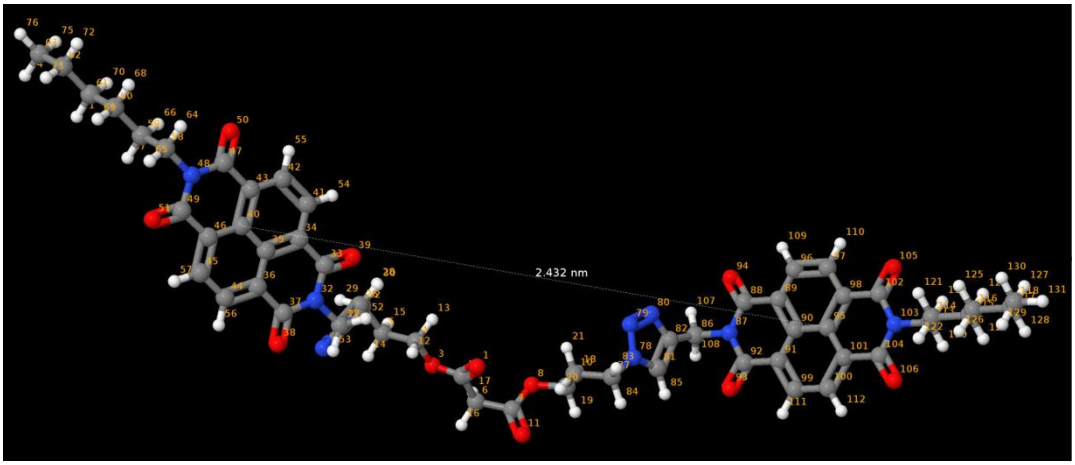

Figure 2.43. 2NDI model used for calculating restrained charges on 'arms' (HF/6-31G*, Gaussian 9). NDI–NDI distance is shown here in the 'open' form, i.e., at 2.4 nm

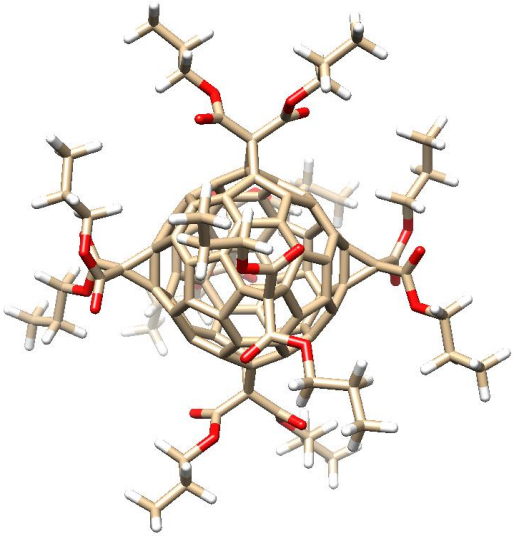

Figure 2.44. Fullerene model 'cage' used for calculating respiratory charges on C_{60} core (HF/6-31G*, Gaussian 9).

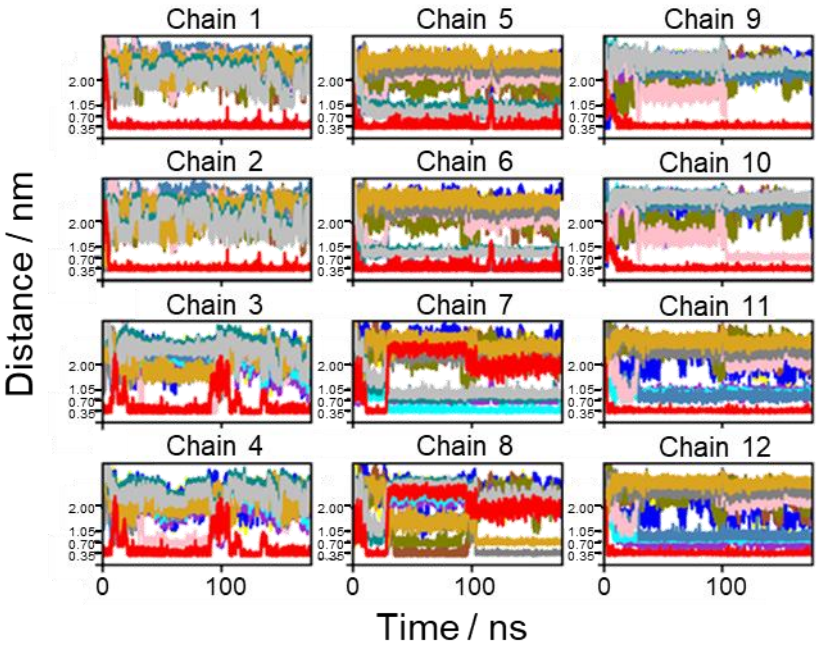

Figure 2.45. Distances between NDI units across **12NDI**, monitored over 200 ns in CH_2Cl_2.

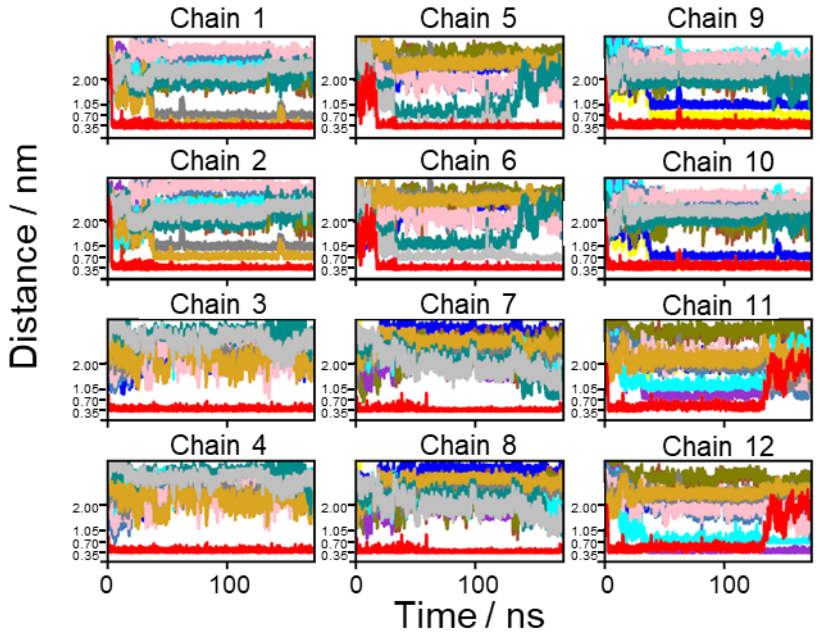

Figure 2.46. Distances between NDI units across [**12NDI**]$^{6(\bullet-)}$, monitored over 200 ns in CH_2Cl_2

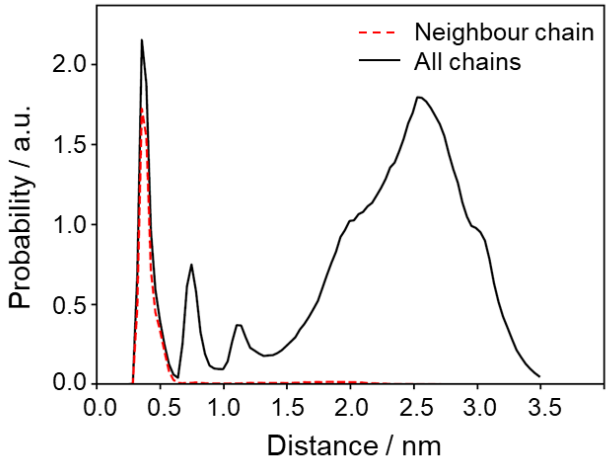

Figure 2.47. Histogram of NDI–NDI distances on a) intra branch (red line) and b) all branches (black line) of [**12NDI**]$^{6(\bullet-)}$, monitored over 200 ns in CH_2Cl_2.

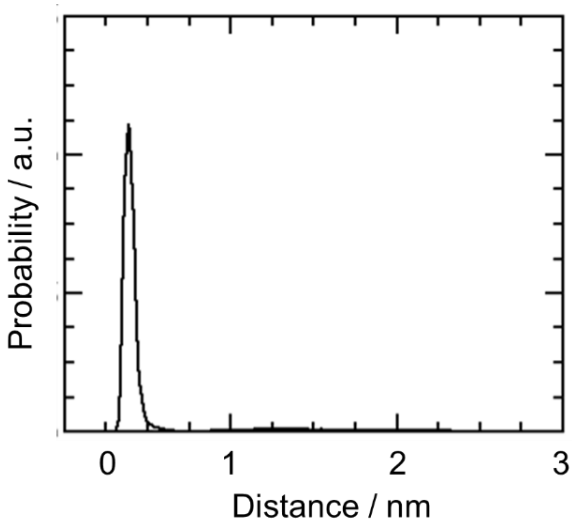

Figure 2.48. Histogram of NDI–NDI distance for **2NDI**$^{(\bullet-)}$ monitored over 200 ns in CH_2Cl_2.

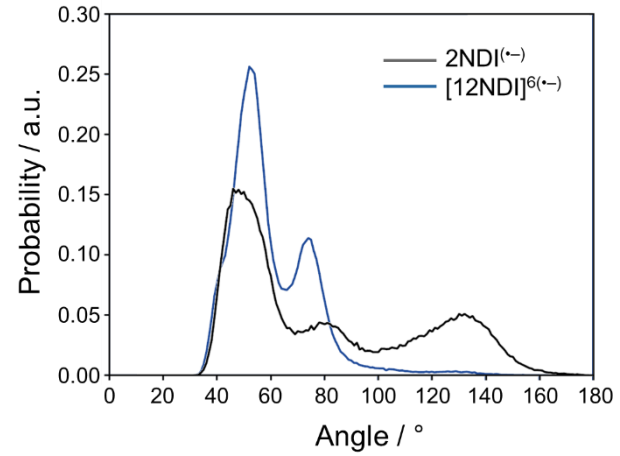

Figure 2.49. Interbranch angle distribution of **2NDI**$^{\bullet-}$ (black) and one 'arm' of [**12NDI**]$^{6(\bullet-)}$ (blue), monitored over the duration of the MD simulations following simulated annealing. Hexakis-adduct data is averaged over the six arms.

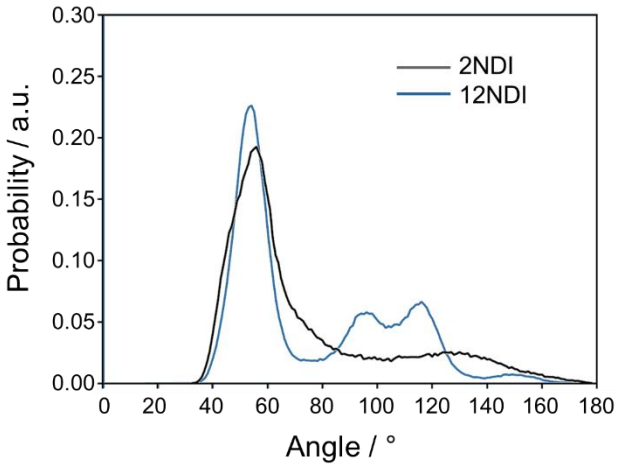

Figure 2.50. Interbranch angle distribution of **2NDI** (black) and one 'arm' of **12NDI** (blue), monitored over the duration of the MD simulations following simulated annealing. Hexakis-adduct data is averaged over the six arms.

2.6 References

1 H. Bronstein, C. B. Nielsen, B. C. Schroeder and I. McCulloch, *Nat. Rev. Chem.*, 2020, **4**, 66–77.

2 G. P. Neupane, W. Ma, T. Yildirim, Y. Tang, L. Zhang and Y. Lu, *Nano Mater. Sci.*, 2019, **1**, 246–259.

3 G. Schweicher, G. Garbay, R. Jouclas, F. Vibert, F. Devaux and Y. H. Geerts, *Adv. Mater.*, 2020, **32**, 1905909.

4 M. Al Kobaisi, S. V. Bhosale, K. Latham, A. M. Raynor and S. V. Bhosale, *Chem. Rev.*, 2016, **116**, 11685–11796.

5 C. Fu, H. P. Lin, J. M. Macleod, A. Krayev, F. Rosei and D. F. Perepichka, *Chem. Mater.*, 2016, **28**, 951–961.

6 Y. Wu, M. Frasconi, D. M. Gardner, P. R. McGonigal, S. T. Schneebeli, M. R. Wasielewski and J. F. Stoddart, *Angew. Chem. Int. Ed.*, 2014, **53**, 9476–9481.

7 Y. Kumar, S. Kumar, K. Mandal and P. Mukhopadhyay, *Angew. Chem. Int. Ed.*, 2018, **57**, 16318–16322.

8 S. Kumar, M. R. Ajayakumar, G. Hundal and P. Mukhopadhyay, *J. Am. Chem. Soc.*, 2014, **136**, 12004–12010.

9 X. Zhao, F. Liu, Z. Zhao, H. Karoui, D. Bardelang, O. Ouari and S. Liu, *Org. Biomol. Chem.*, 2018, **16**, 3809–3815.

10 T. Jiao, K. Cai, J. N. Nelson, Y. Jiao, Y. Qiu, G. Wu, J. Zhou, C. Cheng, D. Shen, Y. Feng, Z. Liu, M. R. Wasielewski, J. F. Stoddart and H. Li, *J. Am. Chem. Soc.*, 2019, **141**, 16915–16922.

11 L. Yang, P. Langer, E. S. Davies, M. Baldoni, K. Wickham, N. A. Besley, E. Besley and N. R. Champness, *Chem. Sci.*, 2019, **10**, 3723–3732.

12 V. D. Mihailetchi, J. K. J. Van Duren, P. W. M. Blom, J. C. Hummelen, R. A. J. Janssen, J. M. Kroon, M. T. Rispens, W. J. H. Verhees and M. M. Wienk, *Adv. Funct. Mater.*, 2003, **13**, 43–46.

13 D. M. Guldi, B. M. Illescas, C. Mª Atienza, M. Wielopolski and N. Martín, *Chem. Soc. Rev.*, 2009, **38**, 1587–1597.

14 C. J. Brabec, S. Gowrisanker, J. J. M. Halls, D. Laird, S. Jia and S. P. Williams, *Adv.*

Mater., 2010, **22**, 3839–3856.

15 W. Yan, S. M. Seifermann, P. Pierrat and S. Bräse, *Org. Biomol. Chem.*, 2015, **13**, 25–54.

16 J. Iehl, R. Pereira De Freitas, B. Delavaux-Nicot and J. F. Nierengarten, *Chem. Commun.*, 2008, 2450–2452.

17 J. Lehl and J. F. Nierengarten, *Chem. Eur. J.*, 2009, **15**, 7306–7309.

18 F. Stauffert, A. Bodlenner, T. M. Nguyet Trinh, M. I. García-Moreno, C. Ortiz Mellet, J. F. Nierengarten and P. Compain, *New J. Chem.*, 2016, **40**, 7421–7430.

19 J. Iehl, M. Frasconi, H. P. J. de Rouville, N. Renaud, S. M. Dyar, N. L. Strutt, R. Carmieli, M. R. Wasielewski, M. A. Ratner, J. F. Nierengarten and J. F. Stoddart, *Chem. Sci.*, 2013, **4**, 1462–1469.

20 K. Yoosaf, J. Iehl, I. Nierengarten, M. Hmadeh, A. M. Albrecht-Gary, J. F. Nierengarten and N. Armaroli, *Chem. Eur. J.*, 2014, **20**, 223–231.

21 J. Iehl, J. F. Nierengarten, A. Harriman, T. Bura and R. Ziessel, *J. Am. Chem. Soc.*, 2012, **134**, 988–998.

22 Y. Xu, Y. Suzuki and M. Komiyama, *Angew. Chem. Int. Ed.*, 2009, **48**, 3281–3284.

23 M. Kumar and S. J. George, *Chem. Eur. J.*, 2011, **17**, 11102–11106.

24 H. Shao, J. Seifert, N. C. Romano, M. Gao, J. J. Helmus, C. P. Jaroniec, D. A. Modarelli and J. R. Parquette, *Angew. Chem. Int. Ed.*, 2010, **49**, 7688–7691.

25 S. Basak, J. Nanda and A. Banerjee, *Chem. Commun.*, 2013, **49**, 6891–6893.

26 M. R. Molla and S. Ghosh, *Chem. Mater.*, 2011, **23**, 95–105.

27 S. Basak, N. Nandi, A. Baral and A. Banerjee, *Chem. Commun.*, 2015, **51**, 780–783.

28 C. Kulkarni, G. Periyasamy, S. Balasubramanian and S. J. George, *Phys. Chem. Chem. Phys.*, 2014, **16**, 14661-14664.

29 S. Basak, N. Nandi, S. Paul and A. Banerjee, *ACS Omega*, 2018, **3**, 2174–2182.

30 M. Y. Yeh and H. C. Lin, *Phys. Chem. Chem. Phys.*, 2014, **16**, 24216–24222.

31 J. Emsley, *Chem. Soc. Rev.*, 1980, **9**, 91–124.

32 Y. C. Park and J. S. Lee, *J. Phys. Chem. A*, 2006, **110**, 5091–5095.

33 R. Murase, C. F. Leong and D. M. D'Alessandro, *Inorg. Chem.*, 2017, 56, 14373–

14382.

34 T. S. Navale, K. Thakur, V. S. Vyas, S. H. Wadumethrige, R. Shukla, S. V. Lindeman and R. Rathore, *Langmuir*, 2012, **28**, 71–83.

35 I. Tabakovic, L. L. Miller, R. G. Duan, D. C. Tully and D. A. Tomalia, *Chem. Mater.* 1997, **9**, 736–745.

36 J. F. Penneau, B. J. Stallman, L. L. Miller and P. H. Kasai, *Chem. Mater.*, 1991, **3**, 791–796.

37 S. Stoll and A. Schweiger, *J. Magn. Reson.*, 2006, **178**, 42–55.

38 J. Liang, L. N. Soucie, D. R. Blechschmidt, A. Yoder, A. Gustafson and Y. Liu, *Org. Lett.* 2019, **21**, 513–518.

39 M. Foroozandeh, R. W. Adams, N. J. Meharry, D. Jeannerat, M. Nilsson and G. A. Morris, *Angew. Chem. Int. Ed.*, 2014, **53**, 6990–6992.

40 W. S. Horne, N. Ashkenasy and M. R. Ghadiri, *Chem. Eur. J.*, 2005, **11**, 1137–1144.

41 SCIGRESS, https://www.fqs.pl/en/chemistry/products/scigress, (accessed 28 June 2021).

42 J. H. Lii, N. L. Allinger, Y. H. Yuh and J. H. Lii, *J. Am. Chem. Soc.*, 1989, **111**, 8551–8566.

43 J. H. Lii and N. L. Allinger, *J. Am. Chem. Soc.*, 1989, **111**, 8576–8582.

44 J. H. Lii and N. L. Allinger, *J. Am. Chem. Soc.*, 1989, **111**, 8566–8575.

45 M. J. S. Dewar, E. G. Zoebisch, E. F. Healy and J. J. P. Stewart, *J. Am. Chem. Soc.*, 1985, **107**, 3902–3909.

46 GAFF, http://ambermd.org/antechamber/gaff.html, (accessed 28 June 2021).

47 D. A. Case, T. E. Cheatham, T. Darden, H. Gohlke, R. Luo, K. M. Merz, A. Onufriev, C. Simmerling, B. Wang and R. J. Woods, *J. Comput. Chem.*, 2005, **26**, 1668–1688.

48 U. C. Singh and P. A. Kollman, *J. Comput. Chem.*, 1984, **5**, 129–145.

49 A. W. Sousa Da Silva and W. F. Vranken, *BMC Res. Notes*, 2012, **5**, 367.

Chapter 3| Charge-Transfer Properties of a Donor–Acceptor Fullerene

Synopsis

Inherently spherical, fullerenes can serve as molecular scaffolds for the organisation of functional units in three-dimensional space. We envisaged that combining the structural offerings of a T_h-symmetrical hexakis-adduct of fullerene with 12 redox-active tetrabenzo[*a*,*c*,*g*,*i*]fluorene (TBF) units would allow us to construct a molecule from which photoinduced energy and/or electron transfer processes could take place between the pendant donor units and acceptor core. Here, charge transfer processes are of fundamental interest to artificial light-harvesting systems as well as the active components of donor–acceptor molecules and junctions in organic electronic devices such as solar cells. Facilitated by the close proximity of TBF units around the fullerene scaffold, extended π-stacks of TBF are observed in the neutral as well as radical state of **12TBF**. Notably, we observe Förster resonance energy transfer (FRET) between the TBF and fullerene units of **12TBF**. Indeed, for twice decorated **2TBF**, much greater FRET is observed for the fully decorated **12TBF** which provides some initial evidence of a 'multivalent' effect. In addition, TBF halide derivatives (**18-Cl**, **18-Br** and **18-I)** were isolated whilst in pursuit of **12TBF**. This small family of α-substituted TBF compounds allowed for a systematic study of the inherent optoelectronic properties of TBF units. Ultimately, the substituent effect did not greatly alter the optoelectronic properties of the TBF unit with no evidence of a through-space interaction between the halide and TBF π-system. The three TBF halides have different packing's in the solid state which require different helical pitches; **18-Cl** has the closest intermolecular π–π-interactions and the smallest torsional angle. The multi-redox and light-harvesting molecule **12TBF** is explored as a photocatalyst for the degradation of waste water textile dyes and is described later in Chapter 4.

Acknowledgements

The following people are gratefully acknowledged for their contributions to this chapter: Dr. Krishnamurthy Munusamy, P. Ramar, Dr. A.A Boopathi, Assistant Professor Srinivasan Sampath and Dr. Debasis Samanta for conceiving the project and preparing **12TBF**. Dr. Chunyong Li at Durham University for fsTA sample measurements. Dr Marc K. Etherington at Northumbria University for his help with data interpretation relating to photophysical measurements.

3.1 Introduction

Multivalent fullerenes, such as those discussed in Chapters 1 and 2, have shown to serve as scaffolds for supporting aromatic assemblies and electronic processes. The fullerene hexakis-adduct scaffold was exploited in Chapter 2 to pre-organise redox-active naphthalene diimide (NDI) units in three-dimensional (3D) space from which electronic couplings could be observed. The decoration of fullerene hexakis-adducts with donor motifs provides a platform to study artificial light-harvesting and artificial photosynthetic systems. To this extent, Iehl et al. have demonstrated[1] the light-harvesting properties of an *E*-stilbene functionalised hexakis-adduct, and the Martín group have probed the enhanced binding of a π-extended tetrathiafulvalene[2] unit with graphene when decorated on a fullerene hexakis-adduct *via* a 'multivalent'[3] effect. Depending on the photo- and redox-active properties of the appended donor molecules, the resulting applications of said donor–acceptor hexakis-adducts can vary, e.g., materials for energy migration[4]. A relatively unexplored donor that has the potential to be integrated into a fullerene hexakis-adduct is tetrabenzo[*a*,*c*,*g*,*i*]fluorene (TBF), i.e., a π-extended derivative of photo- and redox-active fluorene. We envisaged that a dodeca-functionalised TBF fullerene (**12TBF**, Figure 3.3) would provide an ideal platform to study the three-dimensional (3D) precise arrangement of TBF units in close proximity of an acceptor unit, in this case, a fullerene core.

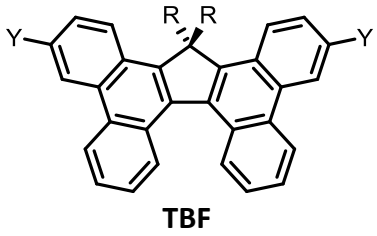

Figure 3.1. Chemical structure of tetrabenzo[*a*,*c*,*g*,*i*]fluorene.

The photoactive donor properties of TBF derivatives have not been fully explored with regards to electron/charge-transfer processes. However, the parent molecule fluorene has been extensively studied for its optoelectronic properties for materials such as light-emitting diodes[5] and photovoltaics[6,7] and TBF should facilitate similar optoelectronic properties, with the additional benefits of a π-extended system (e.g., a change in band gap). The supramolecular assembly of fluorene derivatives is key in accessing useful properties such as charge transport[8], and it is anticipated TBF-based materials will also require a high degree of control over TBF-assembly. A rigid 3D scaffold based on a fullerene hexakis-adduct scaffold provides an ideal opportunity to study TBF assembly as well as probe the photo- and/or redox-relationship with an acceptor, i.e., a fullerene.

Kawase and co-workers have explored the optoelectronic properties of TBF derivatives. Substituting at positions R and Y (Figure 3.1) with alkyl chains (Figure 3.2a)[9] and electron donating/withdrawing groups (Figure 3.2b)[10,11], respectively, allowed for tuneable emission properties as a result of aggregation and extended conjugation. The self-assembly properties of TBF (Y = H) derivatives have also been explored (Figure 3.2c) by Sampath et al.[12] Varying morphologies for the self-assembled TBF derivatives were observed by scanning (SEM) and transmission (TEM) electron microscopy upon changing the solvent conditions; cuboid shape nanocrystals and vesicles were formed from solutions of toluene and THF–H_2O mixtures, respectively.[13] Assali et al. have exploited TBF in functional materials for e.g., its use as an anchor—owing to its electron rich nature and ability to partake in non-covalent π-interactions—to interact with carbon nanotubes (Figure 3.2d).[14] Researchers at the University of Oxford and Lancaster University have also capitalised on the high-affinity of TBF to anchor porphyrin single-molecule transistors on graphene (Figure 3.2e).[15,16] Both of these strategies for installing the TBF anchoring unit make use of an alkyne functionalised TBF **1** (Figure 3.3), either using Cu(I)-catalysed azide–alkyne cycloaddition (CuAAC) or palladium-catalysed Sonogashira cross-coupling reactions to create higher order TBF derivatives.

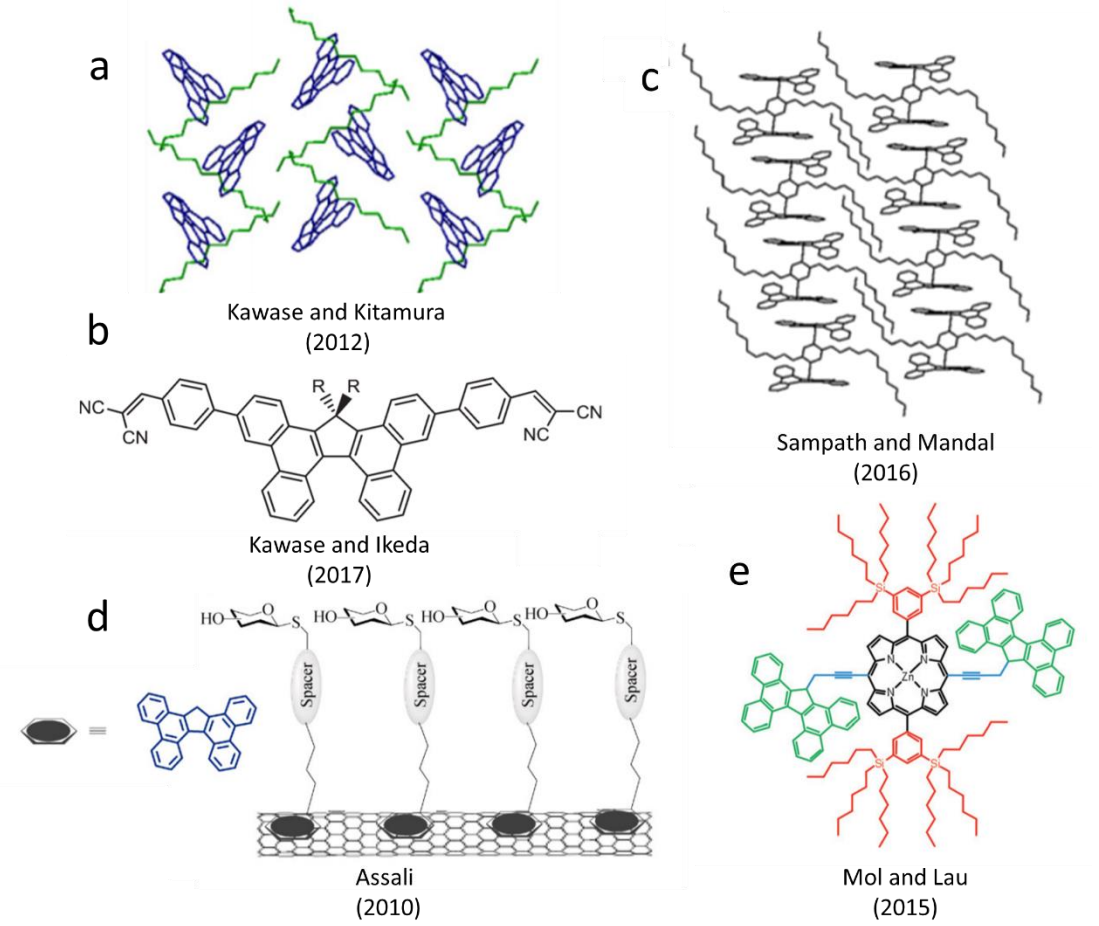

Figure 3.2. TBF optoelectronic and assembly studies. a) dialkyl-substituted TBF, b) electron-withdrawing extended TBFs, c) self-assembling TBFs. TBFs as an anchor for d) carbon nanotubes and e) graphene.

Here, we investigate the self-assembly and photo-induced energy transfer properties of a multi-redox-active fullerene hexakis-adduct, **12TBF**. Owing to the high local concentration of TBF units around the periphery of **12TBF**, thermodynamically favourable π-interactions are observed between pendant TBF units. Energy transfer between the TBF unit and the fullerene core is observed *via* a Förster resonance energy transfer (FRET) mechanism with greater FRET observed for **12TBF** in comparison to control **2TBF**, i.e., a twice TBF decorated hexakis-adduct (Figure 3.3). Following the discussion on **12TBF**, a small family of TBF halides (i.e., Cl, Br and I) that were isolated as intermediates for **12TBF** have provided an opportunity to study the optoelectronic properties of TBF in a systematic manner. Ultimately, the optoelectronic properties do not vary with substituent, however, differences in the individual molecular structures have a significant effect on the packing as elucidated by single-crystal X-ray analysis.

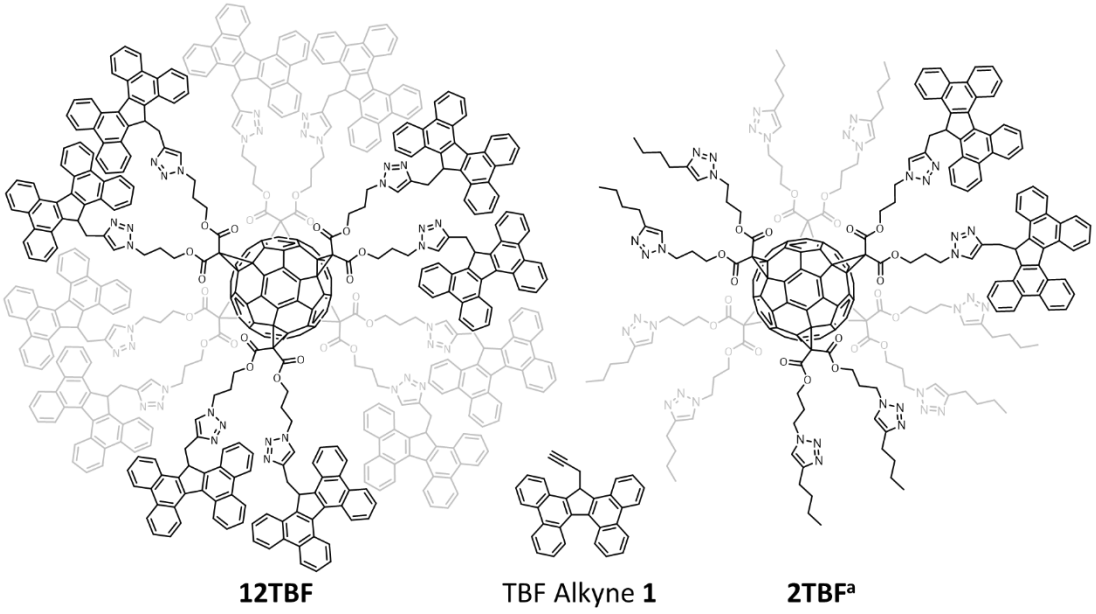

Figure 3.3. Dodeca-functionalised hexakis-adduct **12TBF** and envisaged [5:1] fullerene hexakis-adduct **2TBF[a]**, accessible from TBF alkyne **1**.

3.2 Results and Discussion

3.2.1 Synthesising TBF-Functionalised C_{60} Hexakis-Adducts

A TBF-functionalised hexakis fullerene adduct **12TBF** was produced by carrying out CuAAC chemistry on **12Az** with alkyne-functionalised TBF **1**, following the same methodology as applied to the synthesis of **12NDI** in Chapter 2. The preparation[14] of TBF **1** is shown in Scheme 3.1. Briefly, 9-bromophenanthrene (**2**) was subjected to Grignard conditions in the presence of Mg and ethyl formate (**3**) to form TBF dimer **4** which was isolated in 77% yield. Treatment of alcohol **4** with TFA induced formation of the cationic intermediate that readily undergoes cycloaromatisation to form a mixture of tautomers **5** that were pure in 93% yield following washings with *n*-hexanes. A solution of **5** in dioxane at 120ºC with nBu_4NOH (tetrabutylammonium hydroxide, TBAOH) results in the immediate precipitation the TBF tetrabutylammonium salt **6** as a bright yellow solid. Although this salt has moderate stability in organic solvents, owing to its high sensitivity to moisture, the precipitate was collected, washed with anhydrous dioxane and anhydrous Et_2O and used in subsequent reactions immediately. Upon re-suspending the yellow solid in anhydrous dioxane, the addition of propargyl bromide **7** results in a high conversion to TBF **1**, which can be isolated (85% yield) following simple trituration with MeOH. Although the S_N2 reaction using TBF **6** seems facile, the salt is highly basic—even at low temperatures—and therefore electrophiles that do not allow for proton abstraction are necessary in achieving successful S_N2 reactions, e.g., **7**.

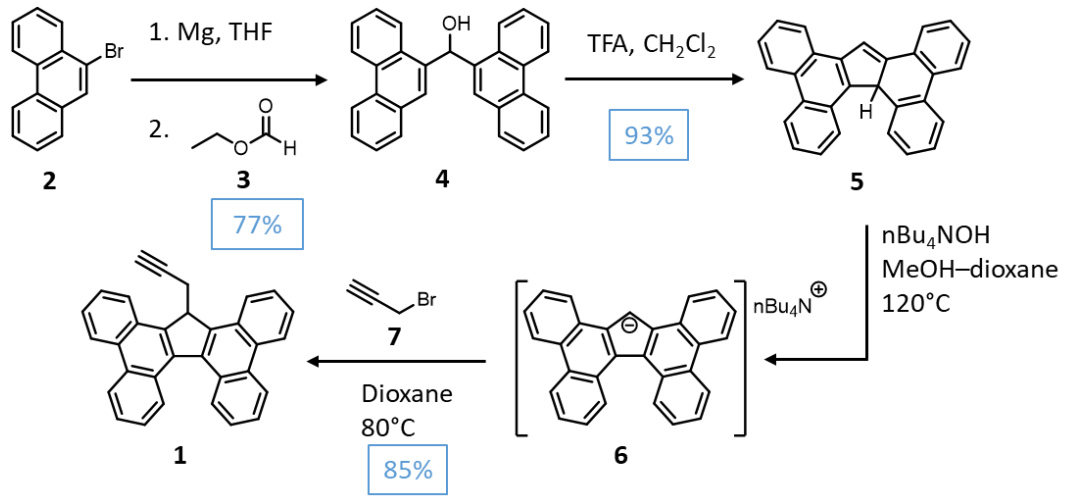

Scheme 3.1. Synthesis route towards TBF alkyne **1**, formed from reacting TBF **6** with propargyl bromide **(7)**.

With alkyne **1** in hand, **12Az** could be functionalized using CuAAC chemistry to produce **12TBF**. Following a similar protocol (Scheme 3.2) as described by Nierengarten et al.[17] (see Chapter 1, Scheme 1.3), an excess of alkyne **1** (1.25 equiv. per azide) was added to a solution of **12Az** under CuAAC conditions. The reaction mixture was stirred under Ar atmosphere at

40 °C until the azide stretch (ca. 2100 cm^{-1}) was no longer detectable by FTIR spectroscopy—typically after 24 h. The solvent was then removed and the crude product purified by flash column chromatography (SiO_2: 0–5.0% MeOH in CH_2Cl_2) to give **12TBF** in 46% yield. Owing to the low solubility of **12TBF** in common deuterated solvents such as $CDCl_3$ and DMSO-d_6, full 2D NMR structural analysis could not be obtained. However, ^{1}H NMR analysis showed (Figure 3.22, appendix) broad peaks for all environments, indicative of a multivalent species, with peaks at δ 7.3–8.8 ppm corresponding to the aromatic TBF and triazole protons. MALDI-TOF analysis further confirmed the generation of a functionalised **12TBF** product, displaying (Figure 3.24, appendix) a broad peak at 7211.7 *m*/z (7178.4 *m*/z calculated for $[M+K]^+$ =

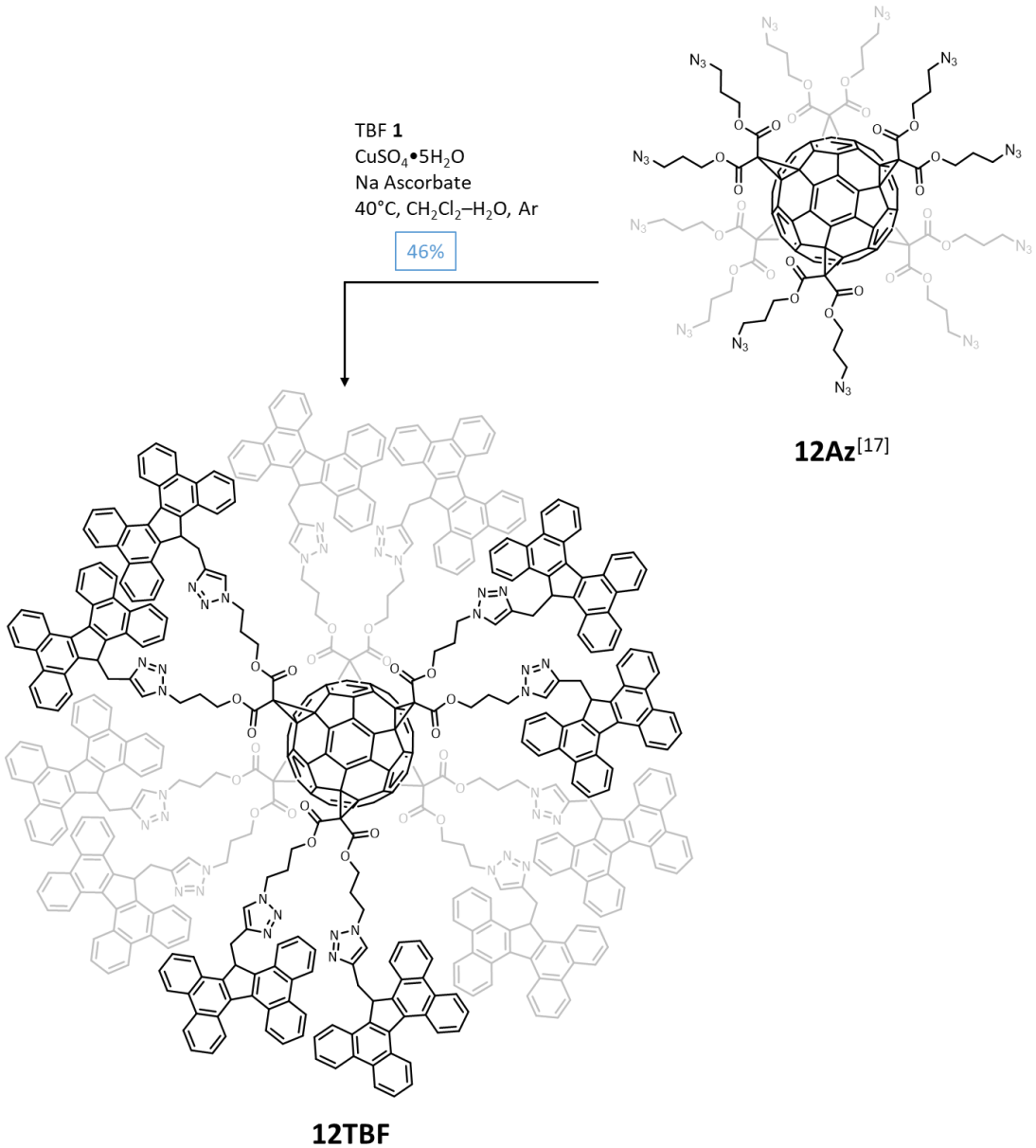

Scheme 3.2. The synthesis of **12TBF**; TBF **1** can be clicked onto **12Az** up to 12 times following CuAAC 'click' chemistry in a biphasic mixture of CH_2Cl_2–H_2O with $CuSO_4$ and sodium ascorbate present as the source of Cu^{2+} and reducing agent respectively.

$C_{498}H_{312}N_{36}O_{24}$) for a fully substituted species. Owing to the low volatility and high fragmentation of the dodeca-functionalised fullerene other peaks were observed in the MALDI-TOF spectrum, however, FTIR spectroscopy confirmed no unreacted azide groups were present (ca. 2100 cm^{-1}) in **12TBF**.

In order to make the [5:1] fullerene hexakis-adduct **2TBF^a**, a different fullerene scaffold was required.[18] We envisaged that **2TBF^a** would be synthetically achievable from fullerene monoadduct **8** (Figure 3.4) that bears azide functionality; this would be complementary to reacting with the in-hand TBF alkyne **1** with a subsequent Bingel reaction allowing for full functionalisation of the remaining reactive sites on the fullerene surface. Unfortunately, mono-adduct **8** was found to be highly reactive with extensive intra- and intermolecular by-product formation *via* 1,3-dipolar cycloaddition reactions between the azide groups and fullerene molecules, ultimately hampering its purification and use.[19] Instead, a route (*vide infra*, Scheme 3.3) towards **2TBF** *via* the alkyne mono-adduct (**9**, Figure 3.4) was selected. Consequently, a complimentary TBF azide derivative—that could be 'clicked'—required synthesising.

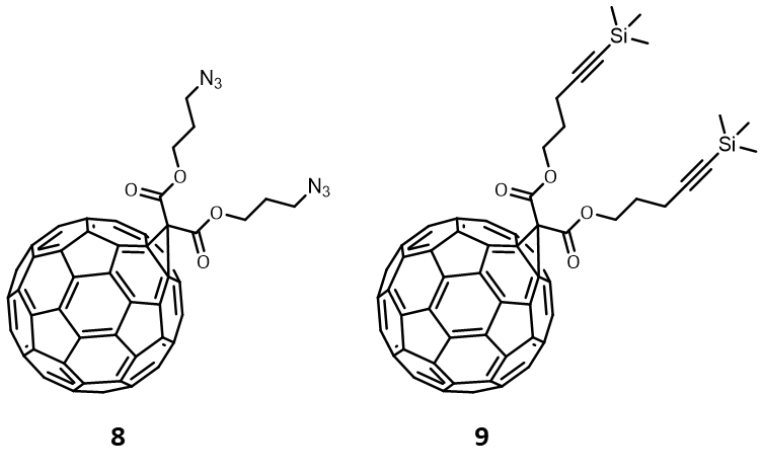

8 **9**

Figure 3.4. Chemical structure of azido mono-adduct (**8**) and the protected alkyne mono-adduct (**9**) both accessible from C_{60}.

It was envisaged that a TBF azide derivative could be readily achieved (Figure 3.5a) following treatment of a TBF halide with a source of azide anion, e.g., NaN_3. Unfortunately—despite numerous attempts involving changing reagents and conditions—the direct conversion to the azide derivative was not possible. Despite the low basicity of N_3^- (pK_b = 9.2), upon addition to one of the TBF halides, immediate abstraction of the bridged proton was observed. This unwanted reaction is highly favourable as the resulting aromatic species is fully conjugated. Other strategies such as i) attaching the halide–alkyl chain before engaging with azide S_N2 reactions and ii) using Grignard/organolithium chemistry in conjunction with an electrophilic source of azide, were also unsuccessful. Attention was then turned towards synthesising TBF azide **10** (Figure 3.5b) with the retrosynthesis suggesting that the reaction of TBF salt **6** with

1-(azidomethyl)-4-(bromomethyl)benzene (**12**) should not allow for any unwanted elimination reactions to occur.

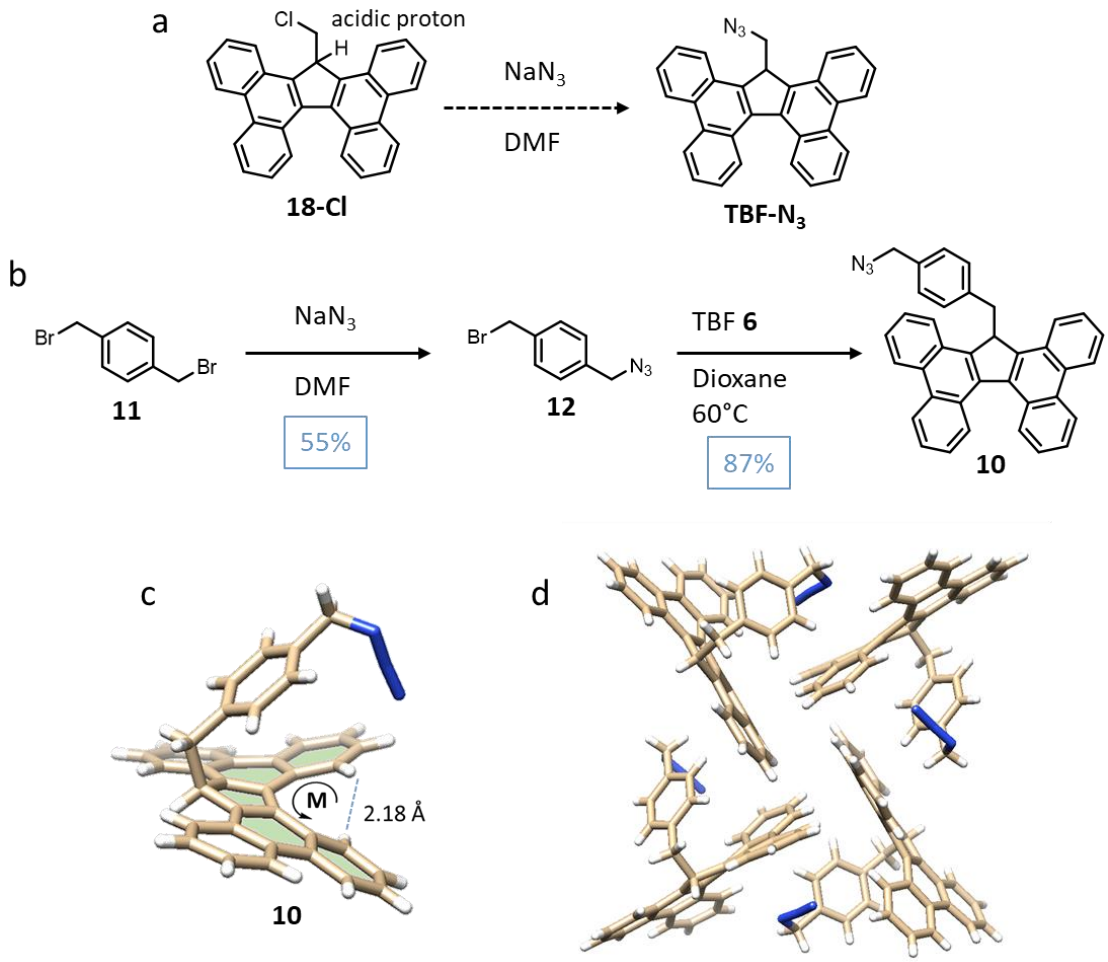

Figure 3.5. a) Unsuccessful synthesis of **TBF-N3**, showing problematic acidic proton on TBF chloride (**18-Cl**). Synthesis of 1-(azidomethyl)-4-(bromomethyl)benzene (**12**) from **11**, and subsequent reaction with TBF **6** to form TBF azide **10**. d) Solid-state structure of *M*-**10** and c) unit cell packing of **10** as enantiomer pairs of *M*- and *P*-isomers.

Compound **12** was first prepared from the addition of NaN_3 to 1,4-bis(bromomethyl)benzene (**11**), with the reaction monitored by TLC (SiO_2: 100% *n*-hexanes) until the monosubstituted product was the dominant species. Following purification by chromatography (SiO_2: 100% *n*-hexanes), **12** was isolated in 55% yield. Azide **12** was then coupled to freshly prepared tetrabutylammonium salt **6**, with TBF azide **10** isolated by filtration in a yield of 87%. Single-crystals of **10** were grown from a mixture of CH_2Cl_2–*n*-hexanes with **10** packing as racemic pairs of *P*-**10** and *M*-**10** (Figure 3.5c) enantiomers with a pitch of 2.18 Å that pack into a pseudo-herringbone array (Figure 3.36, appendix). Notably, the phenyl spacer was situated above the TBF framework at ca. 3.5–3.9 Å, i.e., a weak intramolecular π-interaction may be present. No intermolecular π–π interactions between the aromatic units were observed (Figure 3.5d) in the packing, however, multiple CH–π interactions were present. With TBF **10** in hand,

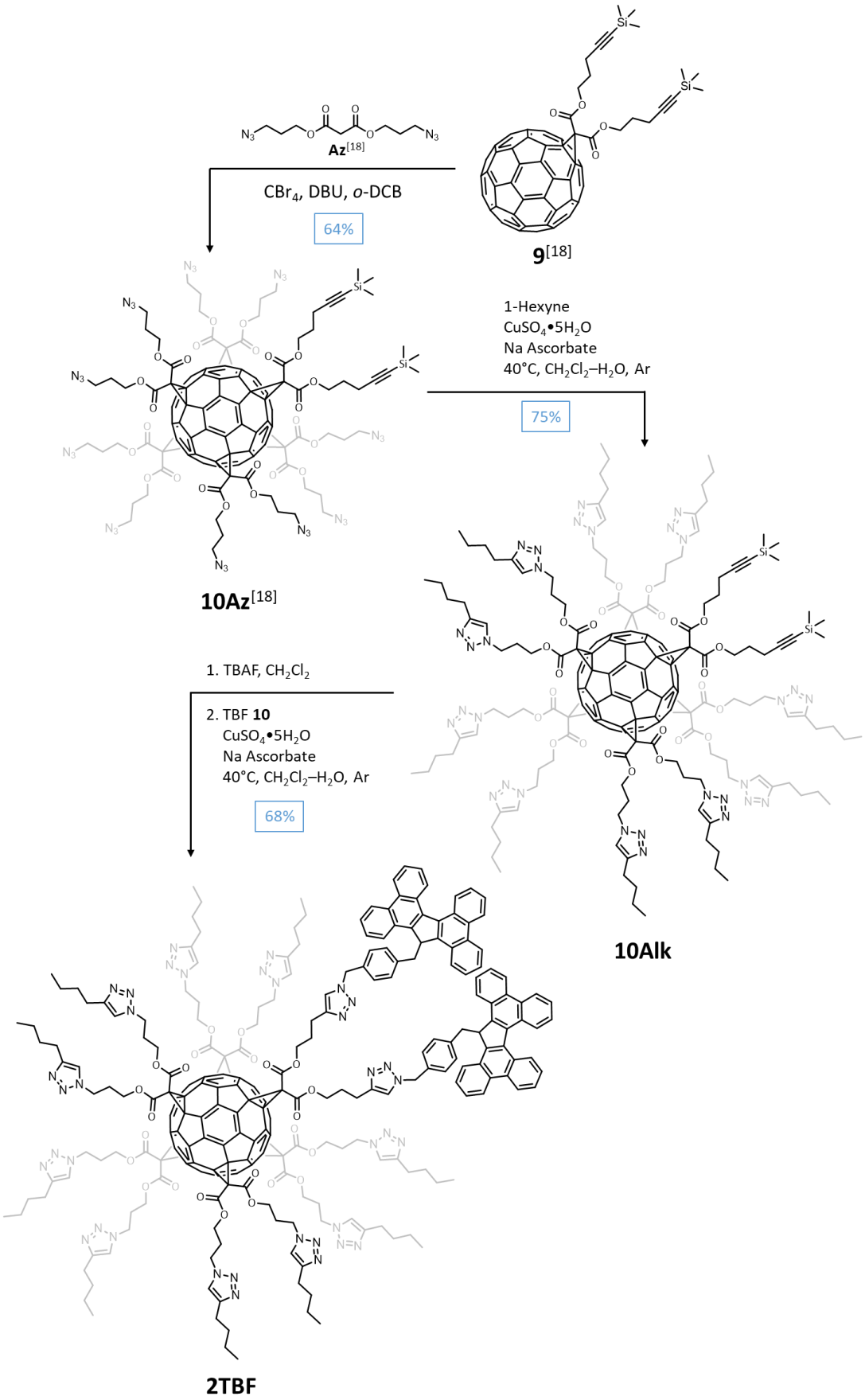

Scheme 3.3. The synthesis of **2TBF**; sequential CuAAC 'click' reactions can be used to construct the non-symmetrical [5:1] hexakis-adduct.

attention was then turned towards constructing an appropriate [5:1] hexakis-adduct from C_{60} mono-adduct **9**.

With azide **10** in hand, a [5:1] hexakis-adduct that was poised for CuAAC chemistry to produce **2TBF** was required. Following a similar protocol (Scheme 3.3) as described by Nierengarten et al. (see Chapter 1, Scheme 1.3), **10Alk** was targeted, i.e., a [5:1] hexakis-adduct bearing 10 *n*-butyl groups and two protected alkyne moieties. The azido hexakis-adduct **10Az** was prepared from fullerene mono-adduct **9**, with both compounds synthesised following modified literature procedures.[18] Following similar CuAAC reaction conditions that were used to generate **12TBF**, pendant alkyl groups were installed on to **10Az** using 1-hexyne (see Experimental Section 3.4.2 for full synthetic details), with **10Alk** isolated in 75% yield. Subsequently, **10Alk** was deprotected *in situ* following treatment with TBAF, to cleave the TMS groups and liberate the free alkyne units. Following CuAAC conditions at ambient temperature, two TBF azide **10** were installed, thereby generating **2TBF** in 68% yield (see Experimental Section 3.4.2 for full synthetic details). Despite the high molecular weight and multivalent nature of the compound, ^{1}H NMR analysis showed (Figure 3.6) good agreement between the integration of the two TBF, the *n*-butyl chains, and the C_{60} scaffold, with peaks at δ_H 8.25 and 8.75 (5+4 and 1+8, Figure 3.6) and 4.30 ppm (10+13, Figure 3.6)—corresponding to TBF aromatic and fullerene methylene protons, respectively—integrating in a 1:3 ratio (i.e., 16 and 48 protons), thus confirming the addition of two TBF units to the fullerene. MALDI-TOF analysis also confirmed the monodisperse **2TBF** species was present with a peak (Figure 3.26, appendix) for $C_{252}H_{226}N_{36}O_{24}$ found at 4182 *m/z*; no fragments were

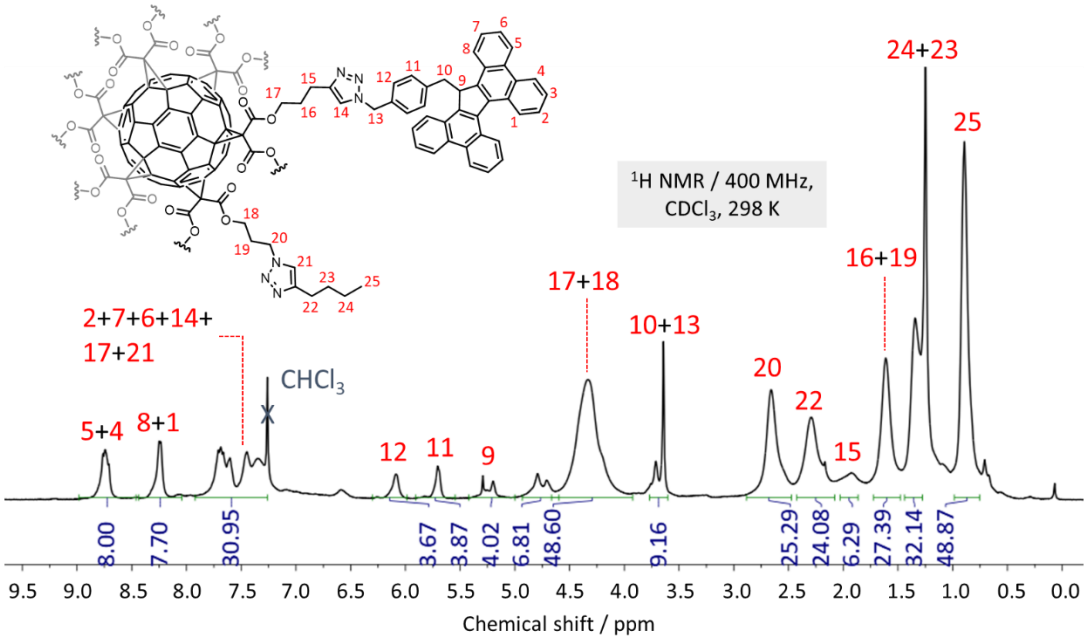

Figure 3.6. ^{1}H NMR ($CDCl_3$, 400 MHz, 298 K) spectrum of **2TBF**.

found for the monoTBF-substituted derivatives or unreacted starting materials **10Alk**, confirming the addition of two TBF motifs.

3.2.2 Redox- and Charge-Transfer Properties of **12TBF**

The fullerene hexakis-scaffold for electron acceptor **12NDI** (see Chapter 2, Section 2.2.2 for discussion) pre-organised the NDI units such that electronic couplings were observable by electrochemical techniques such as cyclic voltammetry (CV). The electronic coupling between donor motifs, e.g., when fixed at proximal distance in a macrocycle, has been shown to facilitate a significant change in the redox properties of the individual units.[20] For the TBF donor functionalised fullerene, **12TBF**, we envisaged electronic couplings between TBF units upon the oxidation to the corresponding radical cation and dicationic species. Fluorene itself is a two-electron oxidant that typically shows reversible CV behaviour upon formation of its radical cation **14** (Scheme 3.4) and its dication **15**.[21,22] In the presence of base or a basic solvent (e.g., DMSO, Scheme 3.4) radical cation **14** can readily undergo proton abstraction to form **16** (Scheme 3.4) which can dimerise to form **17**. This irreversible chemical transformation to **17** can be observed by CV with a non-reversible oxidation process in addition to the reversible formation of **14** and **13**.[22]

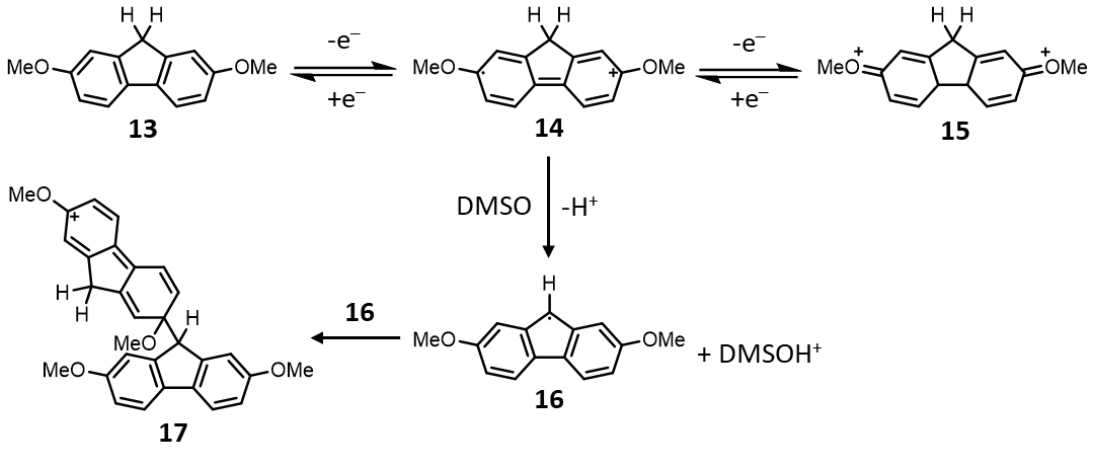

Scheme 3.4. Fluorene derivatives can undergo two reversible oxidation processes to form, e.g., **14** and then **15**. In the presence of base or a basic solvent dimerization can occur, e.g., from **16** to **17**.

In CH_2Cl_2, the CVs (Figure 3.39, appendix) of TBF alkyne **1** and azide **10** showed only one oxidation event, +1.24 and +1.22 V vs. Ag/AgCl, respectively, that was fully reversible. The full reversibility of the oxidation processes shows there is no irreversible dimerization of the TBF units as seen for, e.g., **13** (Scheme 3.4). Furthermore, the extended conjugation on each side of the fluorene unit significantly increases the E_{HOMO} to ca. –5.22 eV in comparison to the parent fluorene[23] (–6.16 eV) and therefore the TBF units will have quite different redox-properties to fluorene so should not be expected to be entirely the same. In DMF, the voltammograms (Figure 3.7) of alkyne **1** and azide **10** show two separate oxidation processes

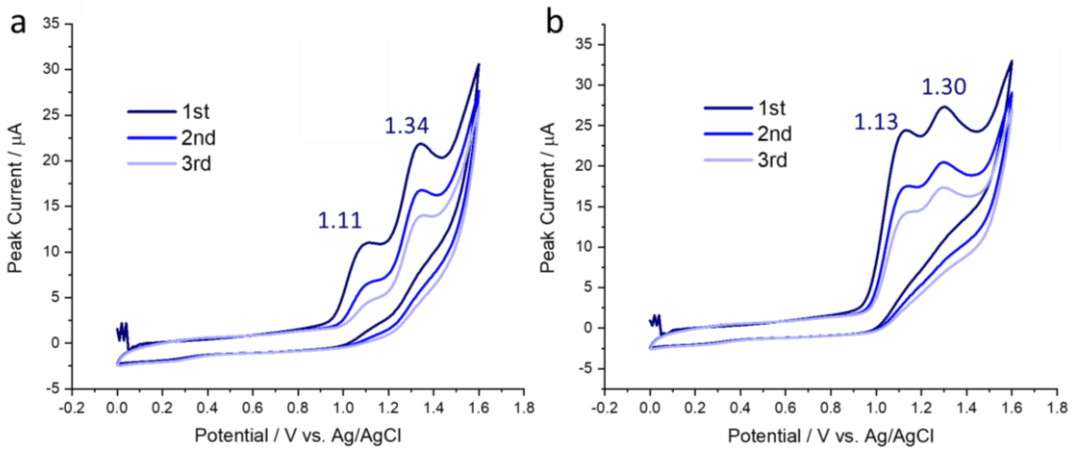

Figure 3.7. Cyclic voltammograms (100 mVs^{-1}, 298 K) of a) TBF alkyne **1** and b) TBF azide **10** collected at [1.0 mM] in degassed DMF containing 0.1 M $TBAPF_6$ as supporting electrolyte; a decrease in current is observed between the first (black line), second (blue line) and third scan (grey line).

at ca. +1.11 V ($TBF^{+\bullet}$) and ca. +1.34 V (TBF^{2+}) for both compounds. These oxidation events are also observed to be quasi-reversible, i.e., the oxidised species is not fully reduced during the time scale (100 mVs^{-1}) of the CV experiment. Furthermore, the current peak drops between subsequent scans. Initially, these observations suggested dimerisation of the radical species (Scheme 3.4). However, for TBF azide **10**, spectroelectrochemistry shows almost complete regeneration (Figure 3.41, appendix) of the neutral TBF state upon reduction of the fully oxidised states (i.e., TBF^{2+}) confirming that no chemical modification/dimerisation had taken place. The resolving of the oxidation events and the reduction in peak current between scans are likely as a result of slower electron transfer between the TBF molecules and the electrode surface in DMF.[24] Additional CV experiments in solvents of various polarity and viscosity may shine light on the redox-properties of **1** and **10** in CH_2Cl_2. Owing to the low solubility of **12TBF** and **2TBF** in organic solvents such as CH_2Cl_2, CV experiments were conducted in DMF at 0.2 mM and 0.5 mM, respectively.

The hexakis-adduct scaffold should facilitate intramolecular TBF aggregation around the periphery of the globular scaffold. The oxidation behaviour of **2TBF** is not dissimilar to what was observed for TBF **1** and **10**, undergoing two oxidation events (Figure 3.8a) at +1.13 and +1.34 V to generate $\mathbf{2TBF}^{4+}$. However, it is the voltammogram of **12TBF** that provides insight (Figure 3.8b) into how intramolecular TBF aggregation can influence the electrochemical properties. A notable higher oxidation potential (+1.24 V vs. +1.13 V for **2TBF**) is required to generate the first oxidised species, presumably $\mathbf{12TBF}^{12(\bullet+)}$. The increased difficulty in oxidation can be rationalised owing to the likely thermodynamically favourable electronic π-couplings between neutral TBF units that are proximal to $TBF^{\bullet+}$ radicals, i.e., the electrons in neutral TBF units are attracted to $TBF^{\bullet+}$ and more difficult to oxidise. Indeed, this is further evidenced by an even higher potential (+1.41 V vs. +1.32 V for **2TBF**) for the full oxidation

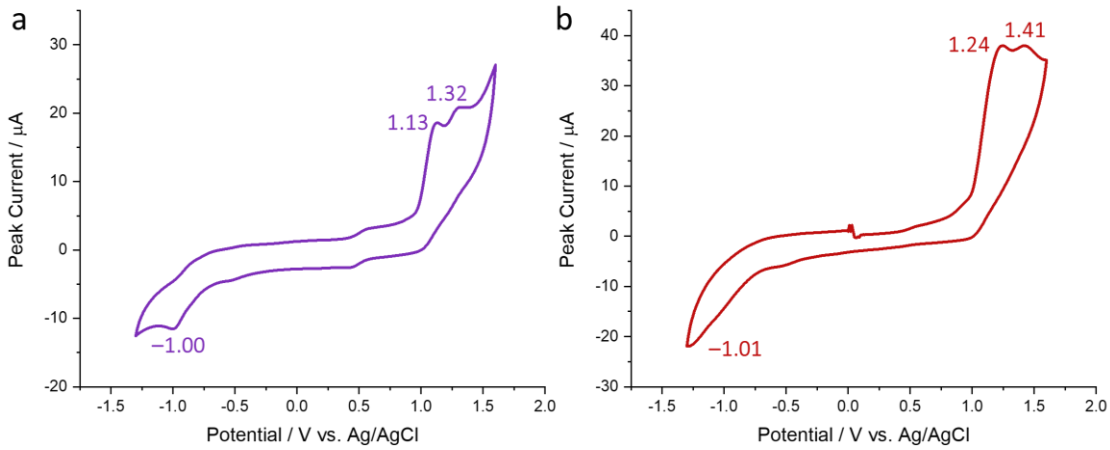

Figure 3.8. Cyclic voltammograms (100 mVs^{-1}, 298 K) of a) **2TBF** [0.5 mM] and b) **12TBF** [0.2 mM] collected in degassed DMF containing 0.1 M $TBAPF_6$ as supporting electrolyte.

of each TBF unit in forming **12TBF**$^{24+}$. Additionally, the irreversible reduction of the C_{60} core is observed at –1.00 and –1.01 V for **2TBF** and **12TBF**, respectively, at a slightly lower potential than the core reduction of control **12Alk** (–0.94 V vs. Ag/AgCl, see Chapter 2 Section 2.5.4)—potentially as a result of an interaction between the electron rich TBF units and the acceptor core. With the multi-redox behaviour of **12TBF** confirmed, attention was then turned towards characterising any intramolecular TBF couplings as well as any photo-induced energy and/or charge transfer processes with the fullerene core.

Typically, TBF units show an absorption band centred at λ_{max} = 368 nm, with a smaller shoulder at 380 nm, that occur as a result of the π–π* transition.[12] As anticipated, in both CH_2Cl_2 and DMF, the UV-Vis spectra of TBF alkyne **1** and azide **10** are almost identical (Figure 3.9a), with the two lowest-energy absorptions at 371 and 379 nm. Additionally, the emission spectra (Figure 3.9a) are also similar for both compounds in DMF and CH_2Cl_2 with $\lambda_{em,max}$ = 424 nm. These observations suggest there is no ground-state or excited-state (i.e., excimer) aggregation

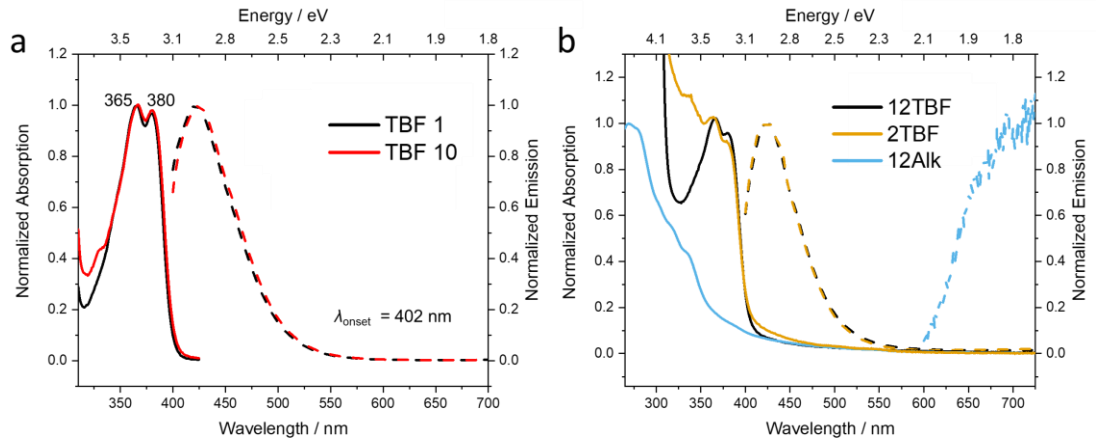

Figure 3.9. a) UV-Vis (solid line) and emission spectra (dashed line) of TBF alkyne **1** (black) and azide **10** (red) in DMF. b) Normalised UV-Vis (solid line) and emission spectra (dashed line) of **12TBF** (black), **2TBF** (gold) and **12Alk** (blue) in DMF; data is normalized at different wavelengths to illustrate comparison. Emission spectra collected after excitation at 390 nm.

present in **1** and **10**. However, when the TBF units are attached to the hexakis-adduct scaffold, there are small but noticeable differences in the optical properties (Figure 3.9b). Notably, in DMF (Figure 3.9b) there is a red-shifted onset of absorption for **2TBF** (402 nm) and **12TBF** (405 nm) in comparison to TBF **1** (400 nm) and **10** (401 nm). Additionally, there is a blue-shift in the λ_{max} to 366 nm for **2TBF** and **12TBF**. These observations suggest there is ground-state electronic intramolecular coupling of the TBF units on **2TBF** and **12TBF**. The absorption of the C_{60} core is weak in the visible region, with a shoulder extending out towards 600 nm. The low extinction coefficient of the fullerene core conceals the absorption to the baseline for **2TBF** and **12TBF**, however, it can be observed from the absorption spectrum of **12Alk**. For **12Alk**, the emission profile observes a maxima ($\lambda_{em,max}$ >700 nm) in the NIR region that is correlated to the C_{60} core. For **2TBF** and **12TBF** the emission from the fullerene core is not observed as the spectra is dominated by the highly emissive TBF units ($\lambda_{em,max}$ = 426 nm). However, with significant spectral overlap (i.e., between 150–400 nm) between the emission of the TBF fragments and the absorption of the C_{60} core, it is possible for energy transfer to take place between the donor–acceptor fragments *via* a Förster resonance energy transfer (FRET) mechanism.[25]

Any energy and/or electron transfer processes that may be possible between the TBF units and fullerene core in the solid state is important in the context of device implementation. Therefore, photophysical investigations were employed on thin films of **2TBF**, **12TBF**, TBF **1** and **12Alk** which were prepared on quartz substrates at 1 wt% in ZEONEX®, a cyclic olefin polymer (COP) that has high optical transparency. Here, dispersions at 1 wt% would hone in on mainly intramolecular interactions in the solid state. The absorption band correlating to the TBF units of **2TBF** shows a red shift (i.e., $\Delta\lambda_{max}$ = 14 nm) to 393 nm when embedded in the polymer matrix, whereas **12TBF** shows a red shift to 396 nm (i.e., $\Delta\lambda_{max}$ = 15 nm) in the polymer as opposed to in DMF (Figure 3.10a). This data suggests that in the solid state there is increased TBF aggregation around the fullerene scaffold, and to a greater extent in **12TBF** where beyond dimer intramolecular stacks of TBF units are possible. The lowest-energy absorption for alkyne **1** (Figure 3.10a) also bathochromically shifts ($\Delta\lambda_{max}$ = 9 nm, vs. DMF) when embedded in the polymer, suggesting some intermolecular TBF aggregation is still facilitated at 1 wt%. The fullerene control, **12Alk**, also absorbs and emits in a similar manner to when solvated by DMF, i.e., a NIR emission $\lambda_{em,ax}$ >700 nm is observed (Figure 3.10c) which suggests that **12Alk** is likely in the same (i.e., non-aggregated) environment when solvated by DMF and when at 1 wt%. It is the emission spectrum of **12TBF**, however, that provides some initial evidence of FRET with a NIR emission observable (Figure 3.10c) at $\lambda_{em,max}$ >700 nm. A low energy emission ($\lambda_{em,max}$ = ca. 650 nm) is also observed (Figure 3.10c) for **2TBF**, however, in a relatively lower intensity in comparison to its TBF centred ($\lambda_{em,max}$ = 420 nm) emission. These

observations suggest that the hexakis-adduct scaffold facilitates extended TBF intramolecular aggregation as well as FRET in the solid state, which is greater for the fully decorated hexakis-adduct **12TBF**.

We hypothesised that neat films, i.e., 100 wt%, would allow us to probe the inclusion of extended intermolecular interactions on the energy transfer processes. Neat films of **12TBF**, **2TBF**, **12Alk** and TBF alkyne **1** were prepared in a similar manner to the embedded polymer samples from drop cast solution in DMF [0.1 mg/ mL]. Additionally, a [1:12] mixture of **12Alk**: **1** was prepared to investigate the effect of tethering the TBF units covalently to the fullerene scaffold. For hexakis-adducts **2TBF** and **12TBF**, there is slight blue shift (i.e., $\Delta\lambda_{max}$= –8 and –4 nm, respectively) in absorption (Figure 3.10b) in contrast to when dispersed in the polymer. This increase in energy could arise from intermolecular aggregation of TBF units in a slightly thermodynamically destabilising assembly that is not enforced when in a monodisperse state. A broad and featureless emission—that is significant in intensity—is observed (Figure 3.10d)

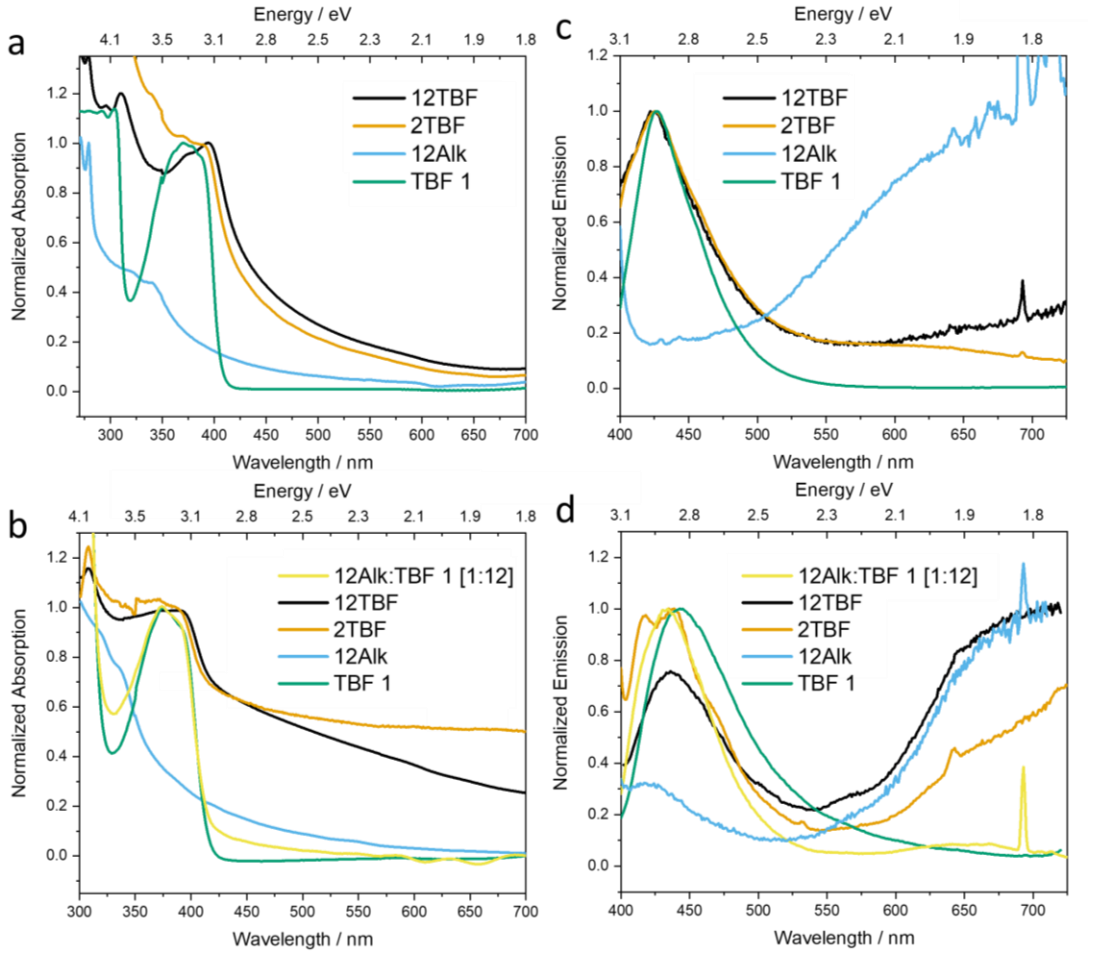

Figure 3.10. Solid-state a) absorption and c) emission of compounds dispersed at 1 wt% in ZEONEX matrix; samples were prepare from *o*-DCB solutions. Control non covalent mixture **12Alk**:TBF **1** (yellow), **12TBF** (black), **2TBF** (orange), **12Alk** (blue) and TBF alkyne **1** (green). Solid-state absorption b) and emission d) of thin films of compounds drop cast from solutions of DMF [0.1 mg/ mL]. Emission spectra collected after excitation at 390 nm. Control **12Alk** is normalized to show comparable intensity.

for **12TBF** at $\lambda_{em,max}$ = 650–700 nm, which is similar to the emission profile of **12Alk**. The C_{60} core emission is observed for **2TBF**, but at a much lower intensity relative to the TBF centred emission at 440 nm. The emission profile (Figure 3.10d) of the non-covalent mixture **12Alk**:TBF **1** was highly reminiscent of TBF **1**, however, a weak emission ($\lambda_{em,max}$ = 646 nm) from the C_{60} core is observed i.e. a small amount of FRET takes place. Clearly, the covalent linkage of the TBF units and the C_{60} core enhances FRET between the TBF units and the fullerene core with the ratio between the C_{60} ($\lambda_{em,\ max}$ =700 nm) and TBF ($\lambda_{em,\ max}$ =420 nm) emission at 1.13, 0.53 and 0.09 for **12TBF**, **2TBF** and the non-covalent mixture **12Alk**:TBF **1**, respectively. Furthermore, solid-state excitation experiments (Figure 3.11) of **12TBF** neat films carried out at 435 and 700 nm produced identical excitation profiles that resembled the TBF donor absorption, consistent with the notion of an active FRET process. The FRET process within **12TBF** is similar to that observed by Iehl et al., who decorated a hexakis-adduct with stilbene oligomers.[1] The researchers also proposed that photoinduced electron transfer (PET) between strong donors and the C_{60} core could also be possible in appropriately designed systems.

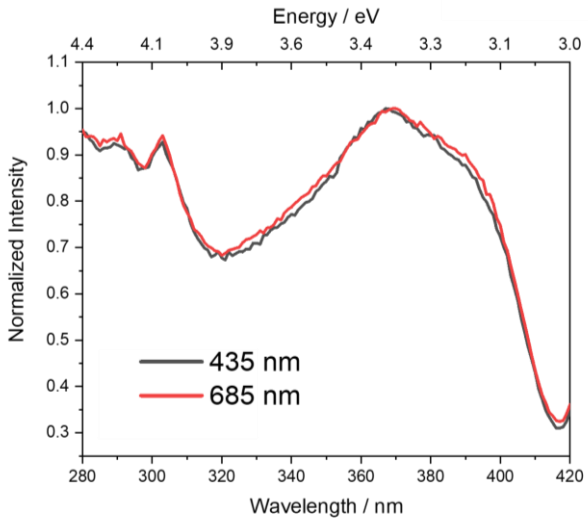

Figure 3.11. Excitation spectra of **12TBF** collected after monitoring emission at 435 (black) and 685 (red) nm.

Following excitation of a sample, measuring the absorption spectra overtime provides information that relates to the evolution and/or decaying of intermediate excited or charge-separated species; femtosecond transient absorption analysis (fsTA) is useful for observing photo-induced electron and energy transfer processes. fsTA spectra (Figures 3.12a–d) were collected following excitation at 343 nm; all samples were prepared at 100 µM in DMF using a 1 mm path length cuvette (See section 3.5.8 for full fsTA details). The decay times for **12TBF**, **2TBF**, TBF **1** and **12Alk** at energies of interest, i.e., 568 nm for C_{60}* and 695 nm for TBF*, are presented in Table 3.1 (for exponential decay fitting see Figures 3.44–47, appendix).

Table 3.1. Absorption lifetimes of main absorptions for C_{60} (568 nm) and TBF (695 nm) excited states.

	568 nm		695 nm	
	τ_1	τ_2	τ_1	τ_2
12Alk	71 ± 11 ps	1.19 ± 0.01 ns	–	–
TBF **1**	–	–	3.05 ± 0.01 ns	–
2TBF	92 ± 3 ps	1.07 ± 0.01 ns	109 ± 1 ps	1.01 ± 0.01 ns
12TBF	80 ± 3 ps	1.48 ± 0.02 ns	12 ± 1 ps	1.79 ± 0.03 ns

Exciting a sample of **12TBF** in DMF at 343 nm generates the 12TBF* excited state (695 nm) followed by rapid decay over 1.79 ± 1 ps and a long decay over 1.79 ± 0.03 ns. The shorter decay is 250-fold faster than the excited-state decay of free TBF alkyne **1**, suggesting the role of the C_{60} in facilitating through-space energy transfer. Indeed, decay of TBF* excited state in **12TBF** is concomitant with the generation of a C_{60}* absorption band at 570 nm. Meanwhile, the absence of any new absorption bands that could correspond to the charge-separated $TBF^{\bullet+}$ species (verified *in situ* by spectroelectrochemistry; Figure 3.42, appendix) in the fsTA spectra

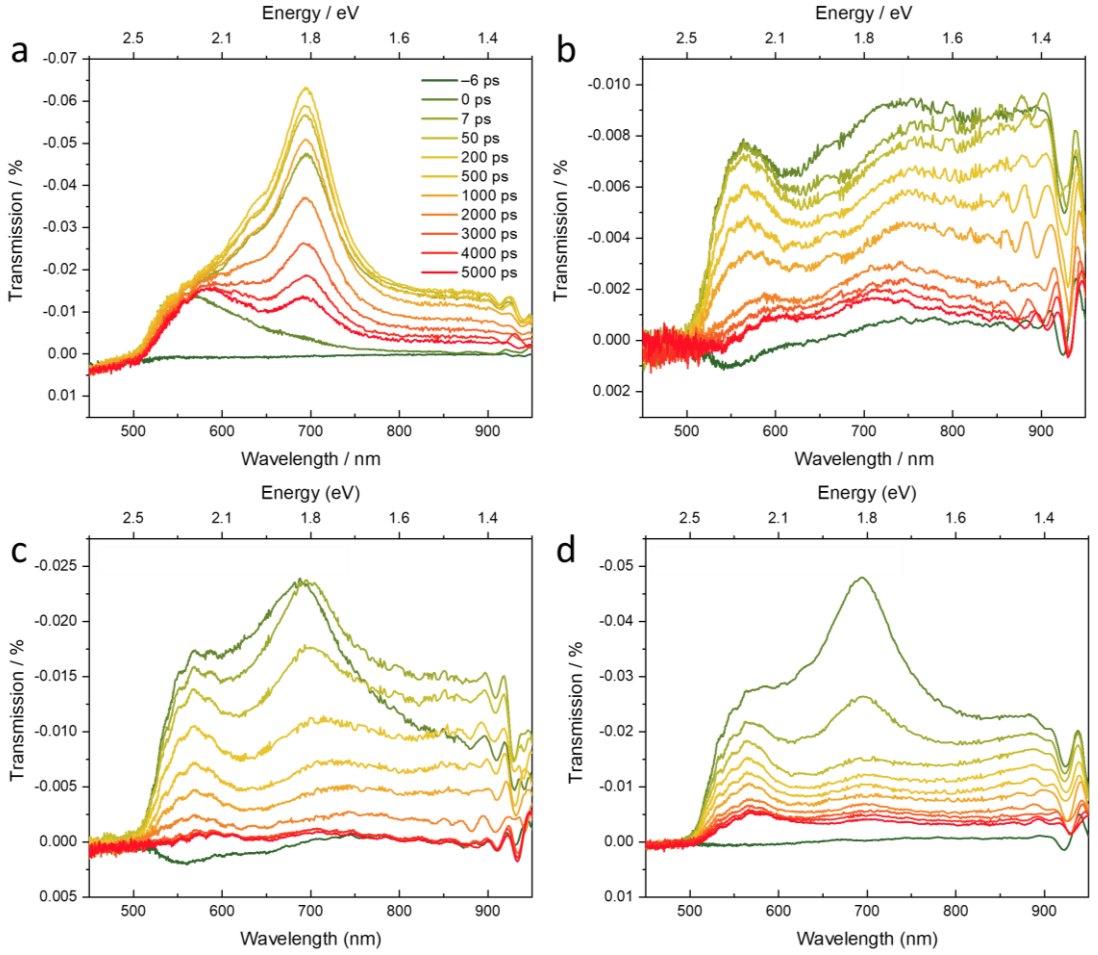

Figure 3.12. Absorption spectra of a) TBF **1**, b) **12Alk**, c) **2TBF** and d) **12TBF** monitored following pulse at 343 nm. Spectra shown are from pre-pulse (–6 ps) to 5000 ps. All samples were prepared in DMF [100 μM].

of **12TBF** rules out PET in favour of the FRET hypothesis. This is supported with the absence of $C_{60}^{\bullet-}$ in the fsTA spectra, however, the absorption is weak and broad between 700–900 nm (verified *in situ* by spectroelectrochemistry; Figure 3.43, appendix), and therefore this signal could not be easily detected by fsTA. Meanwhile, the fsTA spectra of **2TBF** demonstrate similar features to that of **12TBF** but notably experiences a longer-lived TBF* excited-state over 109 ± 1 ps. Furthermore, the C_{60}* core has a longer decay of τ_1 = 80 ps and τ_2 = 1.48 ns for **12TBF** in comparison to **12Alk** (τ_1 = 92 ps and τ_2 = 1.07 ns). These data indicate that energy from the TBF* is dissipated faster for the fully decorated **12TBF**, either as a result of increased FRET with the C_{60} core that prolongs the C_{60}* state, or from intramolecular TBF aggregation.[26]

Both donor–acceptor hexakis-adducts **12TBF** and **2TBF** are of very similar size and shape, and both are dynamic in nature owing to the hexakis-adduct scaffold that allows for molecular rearrangement. Comparing all compounds, there is evidence for a 'multivalent'[27] effect i.e., the crowding of functional units in a given space has allowed access to more FRET in the fully decorated **12TBF** as opposed to **2TBF**. Molecules such as **12TBF** that are highly efficient at absorbing light in the visible region and focusing it at an active centre are highly desirable when it comes to studying natural light-harvesting systems as well as designing photo-active functional molecules. There is potential for these molecules to have applications in photo-active catalysis, however, further fundamental studies could also enable the observation of other intra- and intermolecular processes such as PET. The photocatalytic properties of **12TBF** are explored in Chapter 4.

3.2.3 Optoelectronic Properties of α-Functionalised TBF Halides

During the early stages of this research, we also generated a small number of intermediate TBF halide derivatives i.e., **18-Cl**, **18-Br** and **18-I** (Figure 3.13, see Experimental 3.4.2 for synthetic details) that although they were not used directly in the synthesis of **12TBF**, allowed for the probing of fundamental optoelectronic and solid-state TBF assembly properties. This small section summarises our findings through, absorption and emission spectroscopies, cyclic voltammetry and single crystal X-ray analysis.

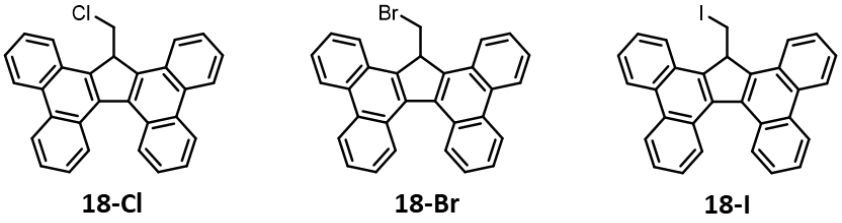

Figure 3.13. Chemical structures of TBF halides, **18-Cl, 18-Br and 18-I.**

UV-Vis absorption spectra of **18-Cl**, **18-Br** and **18-I** were collected in CH_2Cl_2, THF, DMF, PhMe and *o*-DCB (Figure 3.14a for **18-I**, see Figure 3.37, appendix for **18-Cl** and **18-Br**) in order to probe any ground-state aggregation and solvatochromism. All three compounds show spectra reminiscent[9,11] of (structurally similar) TBF derivatives in non-polar and aromatic solvents, with λ_{max} = ca. 370 nm. Unexpectedly, in DMF, extensive bathochromic shifts were observed for TBF halides **16** with a decrease in the absorption at 370 nm in place of an absorption at 455 nm. Additionally, a new well-resolved transition appears at 328 nm. In THF, similar red-shifted features—albeit much lower in intensity–were observed for TBF **18-Br** and TBF **18-I**. The bathochromic shifts are most prominent in polar solvents and indicate positive solvatochromism. Furthermore, the non-polar TBF molecules may aggregate in more polar solvents which could result in bathochromic shifts and therefore emission studies were employed on **18-Cl**, **18-Br** and **18-I** in order to probe any excimer-like emissive aggregation in DMF and THF.

Initially, observations identify a similar emission spectra—a featureless emission at $\lambda_{em,max}$ = 430 nm—in all solvents, including in DMF for which ground state aggregation was hypothesised (Figure 3.14b for **18-I**, see Figure 3.37, appendix for **18-Cl** and **18-Br**). Notably, for TBF **18-I**, a vibronic emission with peaks at 476 and 466 nm was observed in *o*-DCB, suggesting a π-interaction between the TBF unit and the electron poor aromatic solvent that results in a more order TBF state.[28] No low energy excimer-like emission was observed for **18-Cl**, **18-Br** and **18-I**, ruling out aggregation as the likely cause of the bathochromic shift in the absorption profile. Further experiments (dynamic light scattering and photoluminescence quantum yields) are required to rule out the formation of any non-emissive aggregates.[29] Additionally, computational calculation (i.e., DFT) of the dipole moments in the ground and excited states will help rationalise the insensitivity of the emission spectra to

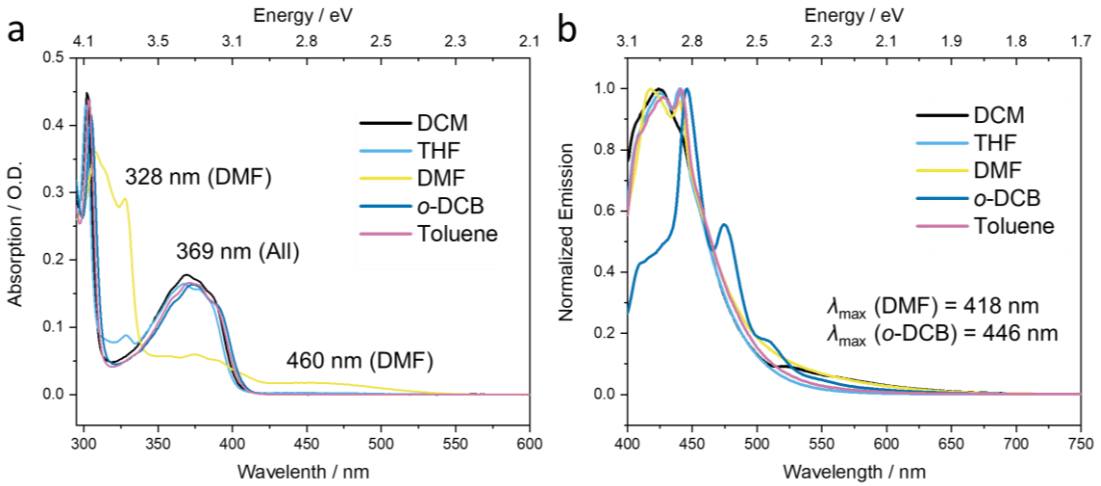

Figure 3.14. a) UV-Vis and b) emission spectra of TBF **18-I**, in various solvents: DCM (black), THF (light blue), DMF (yellow), *o*-DCB (dark blue) and Toluene (pink). Emission spectra were collected after excitation at 390 nm.

solvatochromism.[30,31] Ultimately, the halide substituent effect does not greatly alter the absorption and emission properties of the TBF halides, however, solvatochromic properties have been observed which are useful for stimuli-responsive materials.[32]

Cyclic voltammetry was employed to further explore if the halide substituent effect changed the electronic properties of the donor TBF molecules. CV was carried out in degassed CH_2Cl_2 solutions using 0.1 M $TBAPF_6$ as the supporting electrolyte. Notably, TBF derivatives **18-Cl**, **18-Br** and **18-I** all undergo oxidations (Figure 3.15) at similar potentials, i.e., –1.29, –1.30 and –1.27 V vs. Ag/AgCl to form the dications **18-Cl**$^{2+}$, **18-Br**$^{2+}$ and **18-I**$^{2+}$, respectively. Each oxidation event is fully reversible with the relationship between the square of the variable scan rate and peak current directionally proportional for all oxidation and reduction processes (Figure 3.40, appendix). These observations suggest that the halide substituent does not greatly alter the electronic properties of the TBF units. Indeed, the calculated E_{HOMO} levels (Table 3.4, appendix) range between –5.39 to –5.43 eV which are of similar energy to the TBF alkyne **1** and azide **10** derivatives (Table 3.2, appendix) Additionally, the E_{HOMO} are similar to non-functionalised aromatic hydrocarbons such as dibenzo[*g*,*p*]chrysenes (DBC, –5.25 to –5.65 eV)[33]. Nevertheless, the TBF halide derivatives **18-Cl**, **18-Br** and **18-I** all show a reversible two-electron oxidation in CH_2Cl_2 and therefore they could find use as *p*-type organic semiconductor molecules in an organic electronic device, e.g., in a photoactive donor–acceptor bulk heterojunction system.

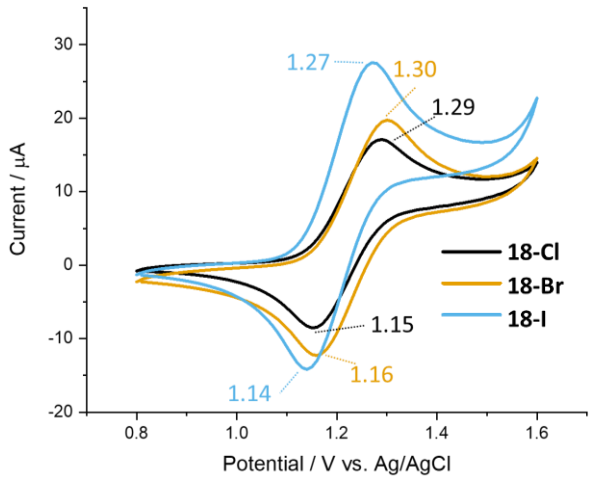

Figure 3.15. Cyclic voltammograms (100 mVs^{-1}, 298 K) of **18-Cl** (black), **18-Br** (gold) and **18-I** (blue) collected at [1.0 mM] in degassed CH_2Cl_2 containing 0.1 M $TBAPF_6$ as supporting electrolyte.

Single crystals of the TBF halides **18** were grown by slow evaporation of CH_2Cl_2–hexanes solutions. TBF **18-Cl** crystallised (Figure 3.16a) as enantiomeric pairs of *P*-**18-Cl** and *M*-**18-Cl** in space group *P*21/*n* whereas **18-Br** (Figure 3.16b) and **18-I** (Figure 3.33, appendix) crystallised as enantiomeric pairs (i.e., *P*-**18-Br**/**I** and *M*-**18-Br**/**I**) in space group *P*-1. TBF **18-Cl** packs into a sandwiched herringbone array whereas both **18-Br** and **18-I** pack in highly

ordered arrays of sheets. Notably, the torsional angles were ±18.09 for *P*- and *M*-**18-Cl** which are considerably low in comparison to dialkyl-substituted TBF derivatives published[9] by Kawase et al. The torsional angles for *P*- and *M*-**18-Br** and *P*- and *M*-**18-I** were 24.93º and 25.29º, respectively, confirming a large increase in pitch between **18-Cl** and **18-Br**/**18-I**. The bond angle between the TBF framework and the halide also increases linearly from **18-Cl** to **18-Br** and then **18-I** (111.76°, 112.87° and 113.09°). Multiple intermolecular interactions (i.e., π–π, C-H–π, Cl/Br/I–H-C) are present in the packing of the molecules. However, the enantiomeric pair of *P*- and *M*-**18-Cl** pack with the shortest intermolecular π–π distances (3.39 Å), around the sum of the Van der Waals radii. Additionally, the chloride atom has close contacts between 2.84–3.41 Å with aromatic protons whereas the bromide and iodide's are at a longer distance of 3.02–3.41 Å. These observations suggest that the additional and shorter intermolecular interactions between **18-Cl** molecules allows for a smaller helical pitch. The E_{HOMO} for **18-Cl**, **18-Br** and **18-I** lends the molecules to similar oxidation potentials, however,

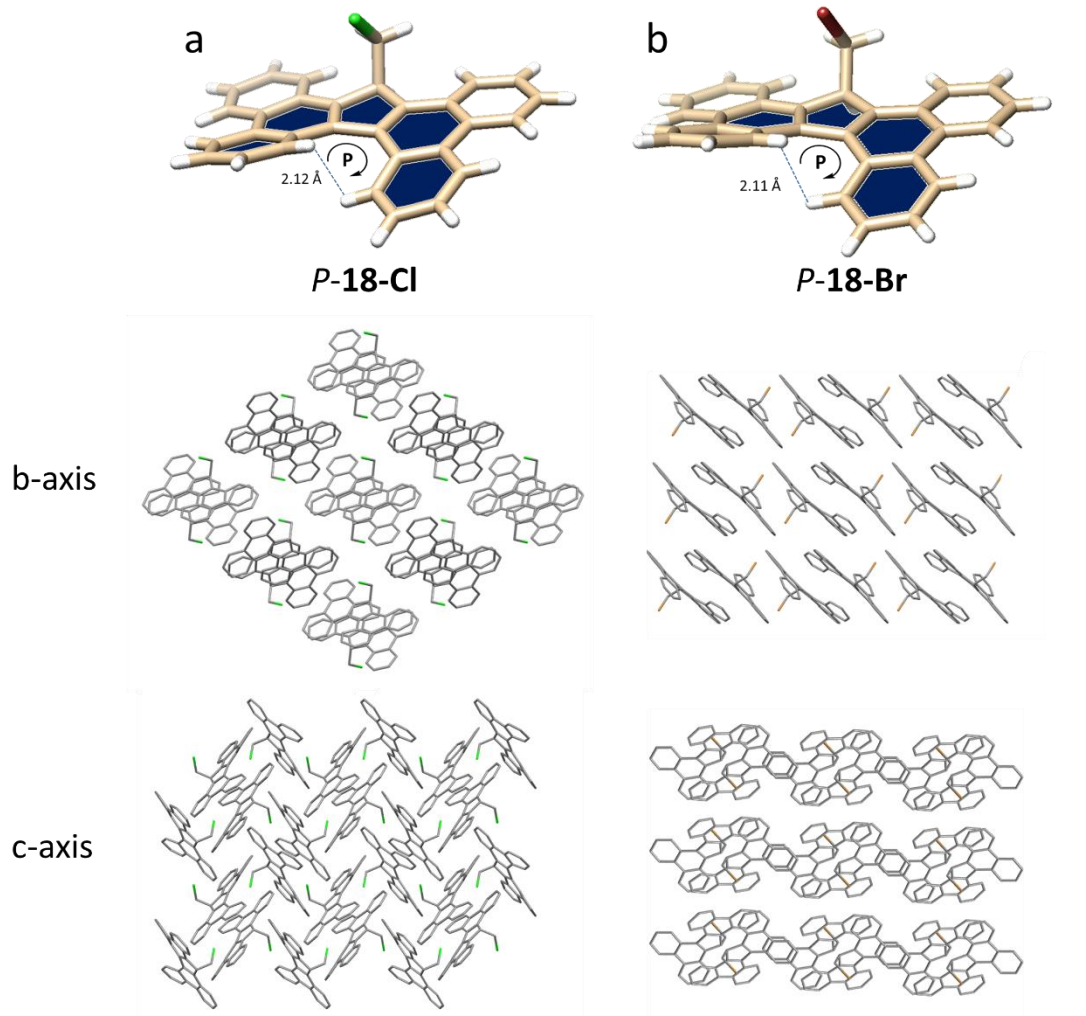

Figure 3.16. Solid-state structure of a) *P*-**18-Cl** and b) *P*-**18-Br**. Crystal packing of molecules in **18-Cl** and **18-Br** showing sandwiched herringbone and sheet-like arrays of interacting molecules, respectively. Crystal packing is viewed along the b-axis and c-axis with hydrogens omitted for clarity.

the different packing arrangements will likely result in different charge mobilities in say a device where the TBF halides could act as *p*-type semiconductor materials.

3.3 Conclusions

Capitalising on an approach developed by the Nierengarten group, we have synthesised a hexakis-adduct of C_{60} functionalised with TBF units (**12TBF**). We have found that the 3D scaffold facilitates intramolecular TBF π-interactions in both the neutral and reduced states which are observable by UV-Vis and PL spectroscopies as well as CV experiments. The donor–acceptor fullerene **12TBF** facilitates FRET. The energy transfer process is confirmed with emission and excitation spectroscopic measurements that confirm the TBF centred emission is quenched in favour of NIR-emission from the fullerene core. FRET is also observed for twice decorated hexakis-adduct **2TBF**, however, the relative amount is much less than for the fully decorated **12TBF**. fsTA spectroscopy confirms the FRET process, with photo-induced electron transfer between the donor and acceptor units not observed. In addition, a small family of TBF halide derivatives (**18-Cl**, **18-Br** and **18-I**) have been investigated for their optoelectronic and structural characterisation. We have observed the TBF halides to have solvatochromic behaviour by UV-Vis spectroscopy with extensive bathochromic shifts observed in DMF. In the solid state, the molecular conformation and packing is dictated by the various halogen and π–π interactions which are not present for all three halides. With light-harvesting properties confirmed, **12TBF** has potential applications in organic electronic materials such as organic light-emitting diodes or solar cells.[34] Chapter 4 details the investigation of **12TBF** as a potential photo-active catalyst for the light-induced degradation of waste dyes.

3.4 Experimental Details

3.4.1 General Materials and Methods

Materials: All reagents and solvents were purchased from commercial suppliers (Merck, Acros Organics, Alfa Aesar, Fischer Scientific, Tokyo Chemical Industry or Fluorochem) and used without further purification unless stated otherwise. Anhydrous solvents were obtained from a Solvent Purification System (neutral alumina) and stored over activated (>250 °C at 0.01 mbar overnight) 3 Å molecular sieves under a dry Ar atmosphere. Solvents and solutions required for air-sensitive manipulations were degassed thoroughly using a minimum of three freeze–pump–thaw cycles and the flask back-filled under an Ar atmosphere. Compounds **1**[14], **4**[35], **5**[35], **9**[18], **12**[36], **10Az**[18], **12Az**[17] and **19**[37] were synthesised according to previously published literature procedures.

Product confirmation: Analytical thin-layer chromatography (TLC) was performed on aluminum-backed silica gel 60 plates pre-loaded with F254 indicator (Sigma Aldrich) and visualised either under UV light irradiation (254 and 365 nm) and/or by dip-staining methods. Flash column chromatography was carried out on an automated system (Teledyne Isco Combiflash Rf+) outfitted with a broad range UV–Vis (200–800 nm) absorption detector. Nuclear magnetic resonance (NMR) spectra were recorded using either a Bruker Advance III Ultrashield 400 Plus (working frequencies: ^{1}H and ^{13}C nuclei = 399.975 and 100.603 MHz, respectively), an Appleby VNMRS-600 (^{1}H and ^{13}C nuclei = 599.832 and 150.288 MHz, respectively) or a Varian VNMRS-700 (^{1}H and ^{13}C nuclei = 700.130 and 176.048 MHz, respectively) spectrometer at a constant temperature of 298 K. Operating temperatures of the NMR spectrometers were measured with the aid of a MeOH internal calibrant. All ^{13}C NMR experiments were proton decoupled. Chemical shifts (δ) are reported in parts per million (ppm) relative to the signals corresponding to the residual non-deuterated solvents ($CDCl_3$: δ_H = 7.26, δ_C = 77.16 ppm; DMSO-d_6: δ_H = 2.50, δ_C = 39.52 ppm). Coupling constants (J) are reported in Hertz (Hz) and ^{1}H multiplicities are reported in accordance with the following convention: s = singlet, d = doublet, t = triplet, q = quadruplet, p = pentet, m = multiplet. Assignment of ^{1}H and ^{13}C NMR signals were accomplished with the aid of '**p**ure-**s**hift' **y**ielded **c**hirp **e**xcitation[38] (PSYCHE) and two-dimensional COSY, HSQC and HMBC NMR spectroscopies. NMR spectra were processed using MestReNova software, Version 11. Low-resolution **e**lectro**s**pray **i**onisation (ESI-MS) and **a**tmospheric **s**olids **a**nalysis **p**robe (ASAP-MS) mass spectrometries were performed using a Waters TQD UPLC ES MS/MS spectrometer and a Waters Xevo QTOF spectrometer equipped with an **a**tmospheric **p**ressure **i**onisation (API) source, respectively. High-resolution mass spectra (HR-MS) were obtained using either a

high-resolution Waters LCT Premier XE spectrometer equipped with an ESI source or an accurate mass UPLC ES MS equipped with an API source. Matrix-assisted laser-desorption ionisation time-of-flight (MALDI–TOF) mass spectrometry was carried out on an Autoflex II ToF/ToF mass spectrometer (Bruker Daltonik GmBH). Modes of analysis include reflectron enhanced mass resolution between *m*/z 500 and 5000 and linear above *m*/z 5000 and MS/MS (LIFT).

Sample analysis: The X-ray single crystal data for TBF **10**, **18-Cl**, **18-Br** and **18-I** were collected at temperature 120.0(2) K, maintained by Cryostream (Oxford Cryosystems) open-flow nitrogen cryostats. Data for all compounds were collected using λMoKα radiation (λ =0.71078Å). The SXRD experiments were performed on the Bruker D8Venture (Photon III MM C14 CPAD detector, IμS-III-microsource, focusing mirrors - for TBF **10**; Photon100 CMOS detector, IμS-microsource, focusing mirrors - for all other compounds) diffractometers. Numerical (**18-I**) or multi-scan (all other compounds) absorption correction was applied. The structures were solved by direct method (intrinsic phases method for **18-I**) and refined by full-matrix least squares on F^2 for all data using Olex2[39] and SHELXTL[40] software. All non-hydrogen atoms were refined in anisotropic approximation, hydrogen atoms in structures **18-Cl** polymorph A were refined freely with isotropic a.d.p.'s, hydrogen atoms in other compounds were placed in the calculated positions and refined in riding mode. Crystal structure **18-Cl** polymorph B contains severely disordered solvent molecules (most probably 0.5 DCM and 0.5 hexane, 36 symmetry-independent electrons) in partially occupied positions. These molecules could not be modelled reliably and their contribution was taken into account by applying the MASK procedure of Olex2 program package. Attenuated total reflectance (ATR) Fourier transform infrared (FTIR) spectroscopy was performed on PerkinElmer Frontier FTIR spectrometer equipped with a Specac Quest ATR accessory with extended range diamond puck. UV-Vis-NIR absorbance data were collected using a Cary 5000 Series UV–Vis–NIR spectrophotometer (Agilent Technologies) at room temperature. The steady-state photoluminescence (PL) of solutions and solid-state films was measured using Jobin Yvon Fluoromax and Horiba Fluorlog3 spectrophotometers, respectively, against machine-specific calibration curves. Cyclic voltammetry (CV) was carried out at room temperature on Ar-purged sample solutions in anhydrous CH_2Cl_2 or DMF using a PalmSens EmStat3 potentiostat interfaced to a PC. Tetrabutylammonium hexafluorophosphate ($TBAPF_6$; 0.1 M) was recrystallized from hot EtOH and used as the supporting electrolyte. All solution-state electrochemical experiments were performed using a glassy carbon working electrode (BASi; 0.071 cm^2). The electrode surface was polished routinely with 0.05 μm alumina–water slurry on a felt surface immediately before each use. The counter electrode was a Pt wire and the reference electrode was an Ag/AgCl (sat. KCl) aqueous electrode stored routinely in a 3 M KCl

aqueous solution. Spectroelectrochemistry (SEC) experiments were performed at room temperature using an optically transparent thin-layer electrochemical (OTTLE) cell (path length approx. 0.2 mm with two CaF_2 windows separated by PTFE spacers) fitted with a Pt wire mesh working electrode, Pt wire counter electrode and a Ag wire pseudo-reference electrode. All SEC samples were prepared as Ar-purged solutions in anhydrous CH_2Cl_2 or anhydrous DMF containing $TBAPF_6$ (0.1 M) as the supporting electrolyte and analysed under an applied voltage sweep. For fsTA setup and individual component details see Section 3.5.8.

3.4.2 Experimental Procedures

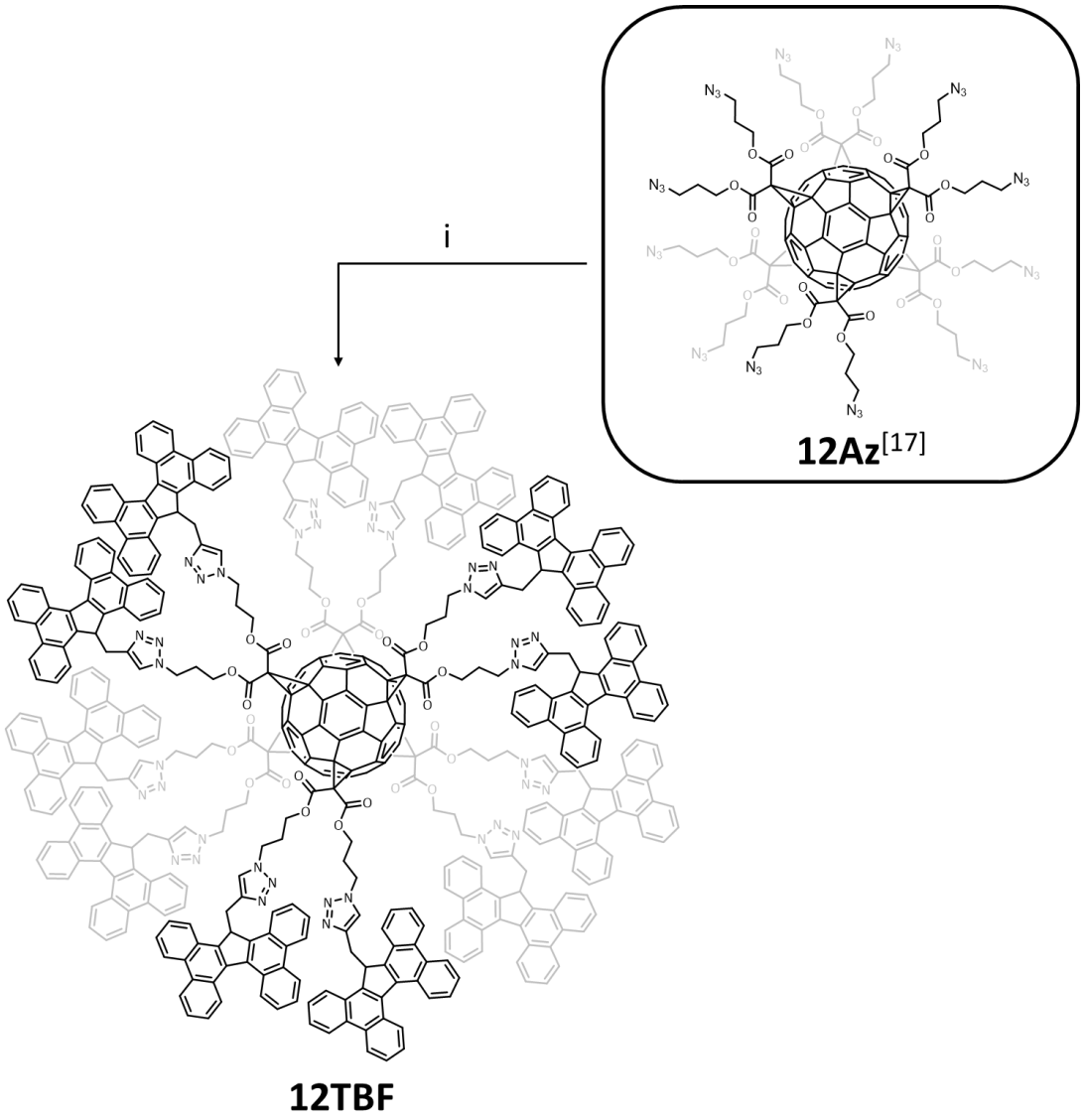

Scheme 3.5. Synthesis of the TBF-functionalised 'click' fullerene hexakis-adduct **12TBF**. Reagents and conditions (i) **12Az**[17], **12**[12], $CuSO_4 \cdot 5H_2O$, sodium ascorbate, CH_2Cl_2–H_2O, 40 °C, 24 h, 46%.

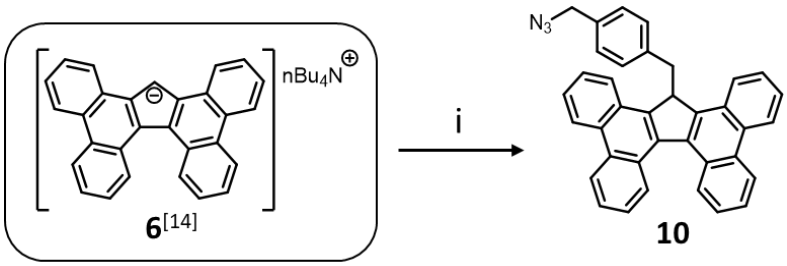

Scheme 3.6. Reagents and conditions (i) **12**[12], dioxane, 60 °C, 3 h, 86%.

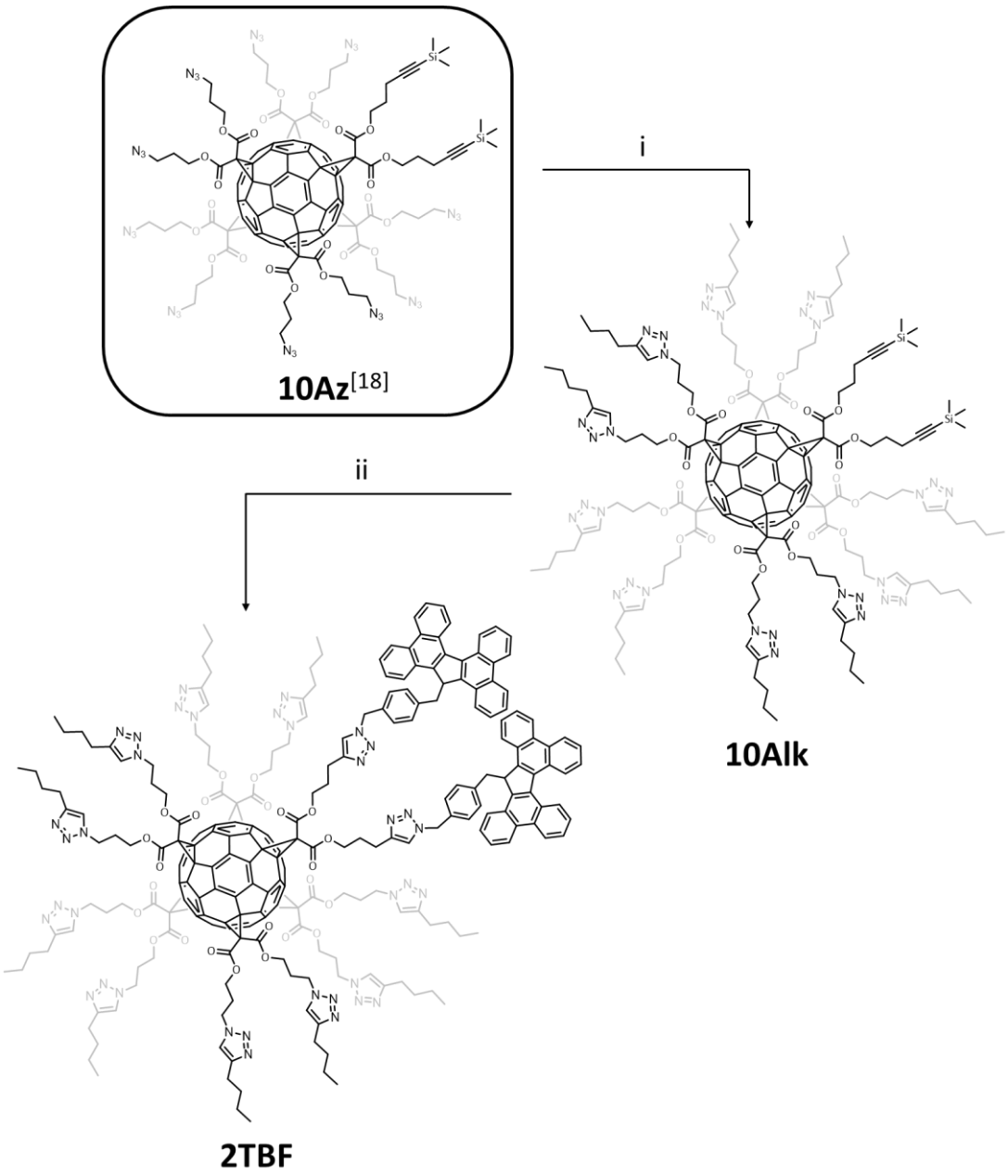

Scheme 3.7. Synthesis of the TBF-functionalised 'click' fullerene hexakis adduct **2TBF**. Reagents and conditions (i) 1-Hexyne, $CuSO_4$•$5H_2O$, sodium ascorbate, CH_2Cl_2–H_2O, 50 °C, 24 h, 75%. (ii) **10**, $CuSO_4$•$5H_2O$, sodium ascorbate, CH_2Cl_2–H_2O, rt, 24 h, 68%.

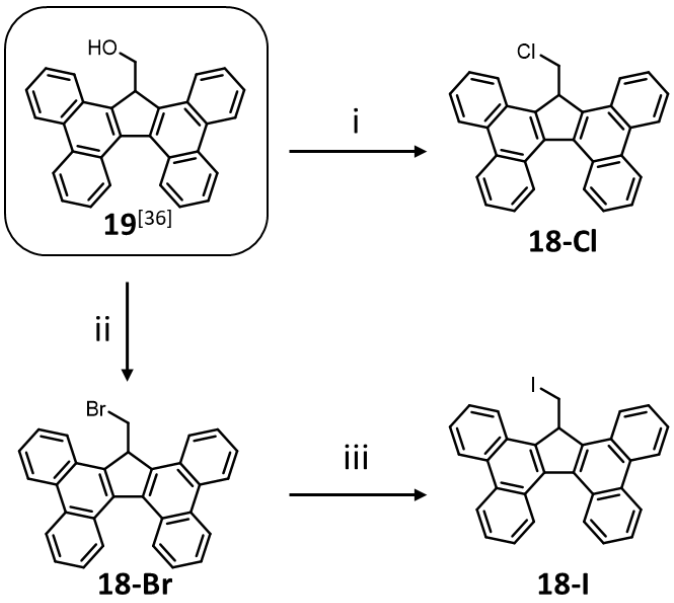

Scheme 3.8. Synthesis of the TBF halide derivatives. Reagents and conditions: (i) $SOCl_2$, CH_2Cl_2, reflux, 2 h, 66%; (ii) PBr_3, THF, 0°C–rt, 1 h, 72%; (iii) NaI, acetone, reflux, 16 h, 99%.

General Procedure for Cu(I)-catalysed azide–alkyne [3+2] cycloadditions (or 'click' reactions):

A freshly prepared solution of $CuSO_4 \bullet 5H_2O$ (0.5 equiv.) as the Cu(I) source and sodium ascorbate (1.5 equiv.) as the reducing agent in degassed water (10 mM with respect to Cu(I)) was added to separately prepared and degassed solution of either fullerene hexakis-adduct **12Az, 10Az** or **10Alk** (1 equiv.) and the desired alkyne or azide (1.25 equiv. per azide or alkyne) in CH_2Cl_2 (22 mM). The resulting biphasic mixture was subjected to a further round of degassing before back-filling the flask with Ar gas and stirring the reaction vigorously at 40 °C (or rt for **10Az**)) for 24 h. The reaction was monitored by FT-IR analysis and worked up upon observing the complete disappearance of the $–N_3$ stretch (2093 cm^{-1}). The crude product was extracted into CH_2Cl_2 and the solvent removed by rotary evaporation. The pure product was isolated by column chromatography.

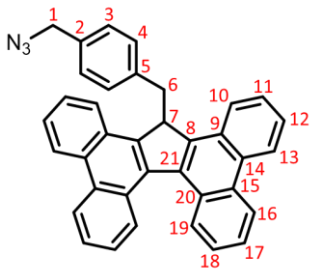

TBF-N_3 (10): In a 50 mL round-bottomed flask equipped with a magnetic stir bar and a reflux condenser, TBF **6** (762 mg, 1.25 mmol, 1.0 equiv.) was added to anhydrous dioxane (20 mL) under Ar. The reaction mixture was then heated to 110 °C to dissolve **6** and form a clear solution. nBu_4NOH in MeOH (1.26 mL, 1 M, 1.0 equiv.) was added to the reaction mixture upon which a bright yellow precipitate formed immediately. After 20 minutes stirring at 110°C, the precipitate was collected by vacuum filtration and washed with warm anhydrous dioxane (12 mL) and then Et_2O (15 mL). The yellow solid was then immediately transferred to a 20 mL

round-bottomed flask equipped with a magnetic stir bar and under Ar. The solid was re-suspended in anhydrous dioxane (10 mL) and the reaction mixture heated to 60°C. Compound **12** (340 mg, 1.50 mmol, 1.2 equiv.) was added to the reaction mixture, which was subsequently stirred for 3 hours at 60 °C during which time a beige solid precipitated out of the reaction mixture. The reaction mixture was concentrated and the precipitate collected by vacuum filtration. After washing the solid with MeOH (15 mL), the desired compound TBF azide **10** (558 mg, 1.09 mmol, 87%) was isolated as a beige powder.

^{1}H NMR ($CDCl_3$, 599 MHz, 298 K): δ_H 8.79–8.83 (m, 2H[13]), 8.75–8.78 (m, 2H[16]), 8.32–8.35 (m, 2H[19]), 8.29–8.32 (m, 2H[10]), 7.73–7.78 (m, 2H[12]), 7.68–7.73 (m, 2H[11]), 7.61–7.66 (m, 2H[18]), 7.47–7.52 (m, 2H[17]), 6.24–6.28 (m, 2H[3]), 5.80–5.84 (m, 2H[4]), 5.27 (t, J = 4.7 Hz, 1H[7]), 3.79 (d, J = 4.7 Hz, 2H[6]), 3.76 (s, 2H[1]). **^{13}C NMR** ($CDCl_3$, 151 MHz, 298 K): δ_C 143.3 (C[8]), 137.5 (C[21]), 135.9 (C[5]), 132.7 (C[2]), 131.4 (C[20]), 130.6 (C[14]), 129.1 (C[4]), 129.0 (C[9]), 128.1 (C[15]), 127.4 (C[19]), 127.1 (C[12]), 126.5 (C[3]), 126.1 (C[11]), 125.8 (C[18]), 125.2 (C[16]), 124.7 (C[10]), 123.9 (C[13]), 123.6 (C[17]), 54.3 (C[1]), 48.2 (C[7]), 39.9 (C[6]). **HRMS** (ESI; MeOH, *ve*$^+$): *m*/z $[M+H]^+$ calcd for $C_{37}H_{26}N_3$ = 512.2127, found 512.2126.

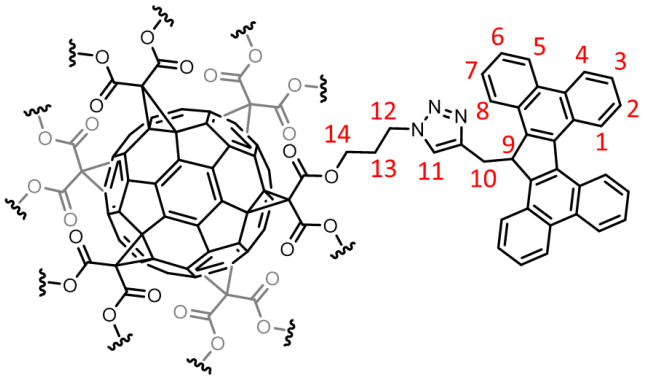

TBF-functionalised 'click' fullerene hexakis-adduct TBF: Applying the *General Procedure* described above, the TBF-functionalised fullerene hexakis-adduct **12TBF** was prepared from **12Az** (231 mg, 0.1 mmol, 1.0 equiv.), TBF alkyne **1** (604 mg, 1.49 mmol, 15 equiv), $CuSO_4$•$5H_2O$ (12 mg, 0.05 mmol, 0.5 equiv.) and sodium ascorbate (30 mg, 0.15 mmol, 1.5 equiv.) in CH_2Cl_2–H_2O (1:1, 10 mL). Purification was achieved by column chromatography (SiO_2: 0–5% MeOH in CH_2Cl_2) to obtain pure **12TBF** (350 mg, 0.05 mmol, 46%) as a dark red powder.

^{1}H NMR ($CDCl_3$, 400 MHz, 298 K): δ_H 8.37–8.53 (m, 72H), 7.81–8.37 (m, 24H), 7.26–7.75 (m, 96H), 4.95–5.16 (m, 12H), 3.40–3.67 (m, 72H), 1.61–1.62 (m, 24H). **^{13}C NMR** ($CDCl_3$, 100 MHz, 298 K): δ_C 161.4, 143.8, 143.8, 142.8, 136.6, 136.6, 131.3, 130.3, 128.5, 127.80, 127.1, 127.0, 126.1, 125.9, 125.2, 125.1, 124.7, 123.6, 123.5, 121.1, 63.0, 62.9, 46.8, 45.1, 44.8, 30.9, 29.3. **FT-IR**; 3080, 2960, 2923, 2853, 1742, 1602, 1499, 1452, 1362, 1259, 1219,

1082, 1017, 965, 907, 772, 753, 724, 617, 527, 433 cm^{-1}. **MALDI–TOF** (ve^+): *m*/z $[M+H]^+$ calcd for $C_{498}H_{312}N_{36}O_{24}$ = 7178.4, found: = 7211.7 $[M+K]^+$.

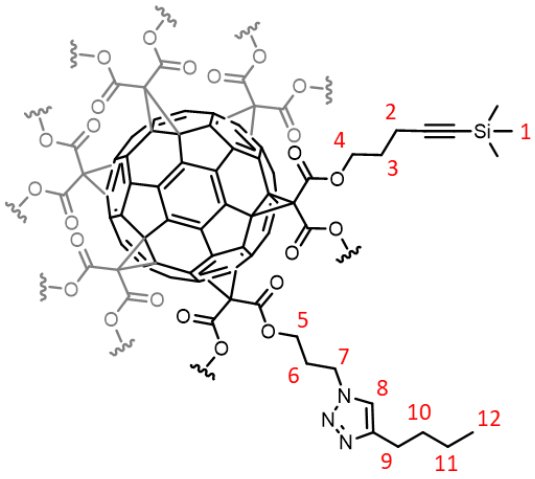

Alkyl-functionalised 'click' fullerene hexakis-adduct 10Alk: Applying the *General Procedure* described above, the Alkyl-functionalised fullerene hexakis-adduct **10Alk** was prepared from **10Az** (368 mg, 0.15 mmol, 1.0 equiv.), 1-hexyne (215 µL, 1.89 mmol, 12.5 equiv), $CuSO_4$•$5H_2O$ (18 mg, 0.07 mmol, 0.5 equiv.) and sodium ascorbate (45 mg, 0.23 mmol, 1.5 equiv.) in CH_2Cl_2–H_2O (1:1, 6 mL). Purification was achieved by column chromatography (SiO_2: 0–5% MeOH in CH_2Cl_2) to obtain pure **10Alk** (369 mg, 0.11 mmol, 75%) as a dark red powder.

^{1}H NMR ($CDCl_3$, 400 MHz, 298 K): δ_H 7.28–7.54 (m, $10H^5$), 4.11–4.60 (m, $48H^{4+5}$), 2.53–2.83 (m, $20H^7$), 2.14–2.42 (m, $24H^9$), 1.82–2.01 (m, $4H^2$), 1.54–1.71 (m, $36H^{3+6+10}$), 1.27–1.46 (m, $30H^{11}$), 0.81–1.00 (m, $9H^{12}$), -0.07–0.21 (m, $8H^1$). **^{13}C NMR** ($CDCl_3$, 100 MHz, 298 K): δ_C 163.4, 163.4, 145.9, 145.8, 145.7, 141.3, 141.1, 141.0, 141.0, 130.5, 127.8, 121.1, 105.0, 85.9, 69.2, 69.0, 65.9, 63.8, 46.6, 45.2, 31.5, 29.3, 27.5, 25.4, 22.3, 16.5, 13.9, 0.1. **MALDI–TOF** (ve^+): *m*/z $[M+H]^+$ calcd for $C_{184}H_{190}N_{30}O_{24}Si_2$ = 3261.8, found: = 3263.4 $[M+H]^+$.

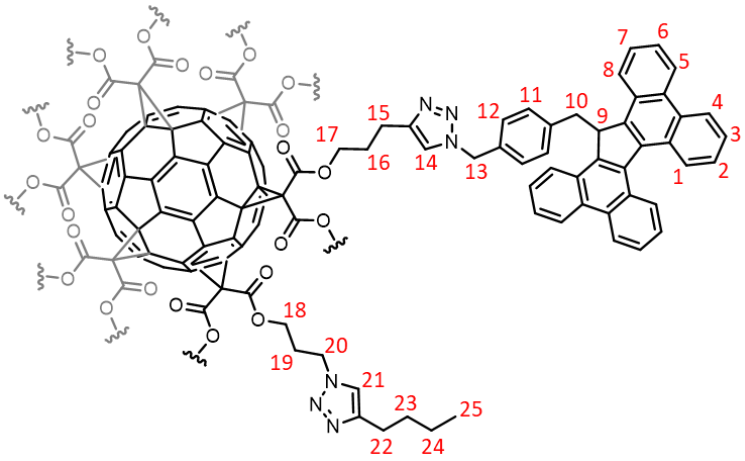

TBF-functionalised 'click' fullerene hexakis-adduct 2TBF: Applying the *General Procedure* described above, the TBF-functionalised fullerene hexakis-adduct **2TBF** was prepared from **10Alk** (45 mg, 13.8 µmol, 1.0 equiv.), TBF azide **10** (18 mg, 34.5 µmol, 2.5 equiv), $CuSO_4$•$5H_2O$ (2 mg, 6.9 µmol, 0.5 equiv.) and sodium ascorbate (4 mg, 20.7 µmol, 1.5 equiv.) in CH_2Cl_2–H_2O (1:1, 500 µL) with TBAF (35 µL, 34.5 µmol, 2.5 equiv.). Purification was achieved by column chromatography (SiO_2: 0–5% MeOH in CH_2Cl_2) to obtain pure **2TBF** (39 mg, 9.4 µmol, 68%) as a dark red solid.

^{1}H NMR ($CDCl_3$, 400 MHz, 298 K): δ_H 8.58–8.89 (m, 8H^{5+4}), 8.17–8.37 (m, 8H^{8+1}), 7.28–7.82 (m, 28H$^{2+6+7+14+17+21}$), 6.01–6.19 (m, 4H^{12}), 5.56–5.77 (m, 4H^{11}), 5.11–5.34 (m, 2H^{9}), 3.98–4.58 (m, 46H^{17+18}), 3.60–3.78 (m, 8H^{10+13}), 2.46–2.80 (m, 24H^{20}), 2.11–2.43 (m, 20H^{22}), 1.82–2.06 (m, 4H^{15}), 1.50–1.75 (m, 24H^{16+19}), 1.13–1.42 (m, 30H^{24+23}), 0.73–0.97 (m, 30H^{25}). **^{13}C NMR** ($CDCl_3$, 151 MHz, 298 K): δ_C 163.6, 148.7, 146.0, 143.2, 141.2, 137.2, 131.3, 130.4, 129.2, 128.9, 127.9, 127.2, 127.1, 126.2, 125.9, 125.1, 124.6, 123.8, 123.7, 121.1, 70.7, 64.0, 48.1, 46.7, 39.8, 32.0, 31.6, 29.48, 25.4, 22.8, 22.5, 14.2, 14.0. **MALDI–TOF** (*ve*$^+$): *m*/z $[M+H]^+$ calcd for $C_{252}H_{226}N_{36}O_{24}$ = 4142.7, found: = 4181.8 $[M+K]^+$.

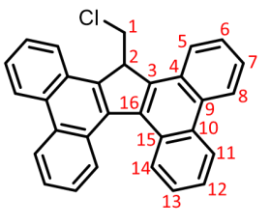

TBF **16-Cl**: In a 10 mL round-bottomed flask equipped with a magnetic stir bar, alcohol **19** (348 mg, 0.88 mmol, 1.0 equiv.) was added to CH_2Cl_2 (3.5 mL). The reaction mixture was cooled to 0 °C before the addition of thionyl chloride (120 µL, 1.66 mmol, 2.0 equiv.). The reaction mixture was then heated to reflux for 2 hours. Upon cooling, the solvent was removed by rotary evaporation. The resulting solid was re-dissolved in CH_2Cl_2 (10 mL) and precipitated by the addition of MeOH (50 mL). The solid was collected by vacuum filtration to yield the desired compound **18-Cl** (241 mg, 0.58 mmol, 66%) as a yellow powder.

^{1}H NMR ($CDCl_3$, 599 MHz, 298 K): δ_H δ 8.81–8.85 (m, 4H^{8+11}), 8.65–8.71 (m, 2H^{14}), 8.21–8.25 (m, 2H^{5}), 7.67–7.76 (m, 6H^{6+7+13}), 7.61–7.66 (m, 2H^{12}), 5.25 (t, J = 3.6 Hz, 1H^{2}), 4.52 (d, J = 3.7 Hz, 2H^{1}). **^{13}C NMR** ($CDCl_3$, 151 MHz, 298 K): δ_C 141.2 (C^{3}) , 138.1 (C^{16}), 131.9 (C^{15}), 130.9 (C^{9}), 128.5 (C^{4}), 128.0 (C^{10}), 127.8 (C^{14}), 127.3 (C^{7}), 126.4 (C^{6}), 126.3 (C^{13}), 125.4 (C^{12}), 124.2 (C^{11}), 123.9 (C^{8}), 123.8 (C^{5}), 49.1 (C^{2}), 47.5 (C^{1}). **HRMS** (ESI; MeOH, *ve*$^{+}$): *m*/z [*M*+H]$^{+}$ calcd for $C_{30}H_{20}Cl$ = 415.1254, found 415.1255.

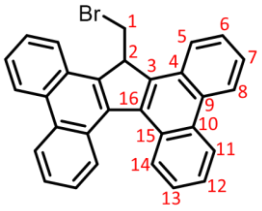

TBF **18-Br**: In a 10 mL round-bottomed flask equipped with a magnetic stir bar and under Ar, alcohol **17** (793 mg, 2.0 mmol, 1.0 equiv.) was added to anhydrous THF (3 mL). The reaction mixture was cooled to 0 °C and PBr_3 (76 µL, 0.8 mmol, 0.4 equiv.) was added dropwise. The reaction mixture was stirred at 0 °C for 1 hour, during which the reaction went from suspension of white solid to a clear amber solution. Upon warming to room temperature, the solvent was remove by rotary evaporation. H_2O (20 mL) and CH_2Cl_2 (20 mL) were added to the reaction mixture and the crude product was extracted into CH_2Cl_2 (3 x 40 mL). The organic fractions were combined and then washed with saturated $NaHCO_3$ (3 × 10 mL), H_2O (3 × 10 mL) and brine (2 × 10 mL). The solvent was removed by rotary evaporation to afford a yellow solid that was triturated with hexanes (3 × 10 mL). The solid was collected by vacuum filtration to yield the desired compound **18-Br** (662 mg, 1.44 mmol, 72%) as a yellow powder.

^{1}H NMR ($CDCl_3$, 599 MHz, 298 K): δ_H δ 8.79–8.86 (m, 4H^{8+11}), 8.65–8.74 (m, 2H^{14}), 8.19–8.25 (m, 2H^{5}), 7.68–7.76 (m, 6H^{6+7+13}), 7.61–7.66 (m, 2H^{12}), 5.26 (t, J = 3.5 Hz, 1H^{2}), 4.47 (d, J = 3.5 Hz, 2H^{1}). **^{13}C NMR** ($CDCl_3$, 151 MHz, 298 K): δ_C 141.5 (C^{3}), 138.1 (C^{16}), 131.9 (C^{15}), 130.9 (C^{9}), 128.5 (C^{4}), 128.0 (C^{10}), 127.9 (C^{14}), 127.4 (C^{7}), 126.4 (C^{6}), 126.3 (C^{13}), 125.4 (C^{12}), 124.0 (C^{11}), 123.9 (C^{5}), 123.8 (C^{8}), 47.9 (C^{2}), 36.2 (C^{1}). **HRMS** (ESI; MeOH, *ve*$^{+}$): *m*/z [*M*+H]$^{+}$ calcd for $C_{30}H_{20}Br$ = 459.0748, found 459.0746.

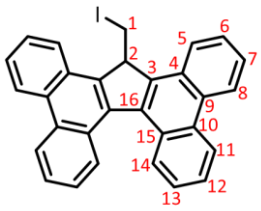

TBF **18-I**: In a 10 mL round-bottomed flask equipped with a magnetic stir bar and under Ar, TBF **18-Br** (206.7 mg, 0.45 mmol, 1.0 equiv.) and NaI (270 mg, 1.80 mmol, 4 equiv.) were added to $(CH_3)_2CO$ (2 mL). The reaction mixture was heated to reflux and stirred overnight. Upon cooling, H_2O (10 mL) and CH_2Cl_2 (30 mL) were added to the reaction mixture and the crude product was extracted into CH_2Cl_2 (3 x 40 mL). The organic fractions were combined and then washed with $Na_2S_2O_3$ (3 × 10 mL), H_2O (3 × 10 mL) and brine (3 × 10 mL). The solvent was removed by rotary evaporation. The desired compound **18-I** (223 mg, 0.44 mmol, 99%) was isolated as an orange powder.

^{1}H NMR ($CDCl_3$, 599 MHz, 298 K): δ_H δ 8.78–8.85 (m, 4H^{8+11}), 8.66–8.73 (m, 2H^{14}), 8.10–8.17 (m, 2H^{5}), 7.68–7.76 (m, 6H^{6+7+13}), 7.61–7.66 (m, 2H^{12}), 4.83 (t, J = 3.6 Hz, 1H^{2}), 4.37 (d, J = 3.5 Hz, 2H^{1}). **^{13}C NMR** ($CDCl_3$, 151 MHz, 298 K): δ_C 142.5 (C^{3}), 137.9 (C^{16}), 131.8 (C^{15}), 130.9 (C^{9}), 128.4 (C^{4}), 128.0 (C^{10}), 127.9 (C^{14}), 127.3 (C^{7}), 126.4 (C^{6}), 126.3 (C^{13}), 125.4 (C^{12}), 124.0 (C^{11}), 123.8 (C^{8}), 123.6 (C^{5}), 46.4 (C^{2}), 11.5 (C^{1}). **HRMS** (ESI; MeOH, ve^+): m/z $[M+H]^+$ calcd for $C_{30}H_{20}I$ = 507.0610, found 507.0611.

3.5 Appendix of Supplementary Data and Discussion

3.5.1 Structural Assignment by Two-Dimensional (2D) NMR

In order to fully assign the ^{1}H and ^{13}C signals of the TBF derivatives **18-Cl**, **18-Br**, **18-I** and TBF azide **10** we employed 2D NMR spectroscopy. We determined peak assignments through analysis of COSY (Figures 3.17), HSQC (Figures 3.18) and HMBC (Figures 3.19) correlations, as demonstrated for TBF **18-I**.

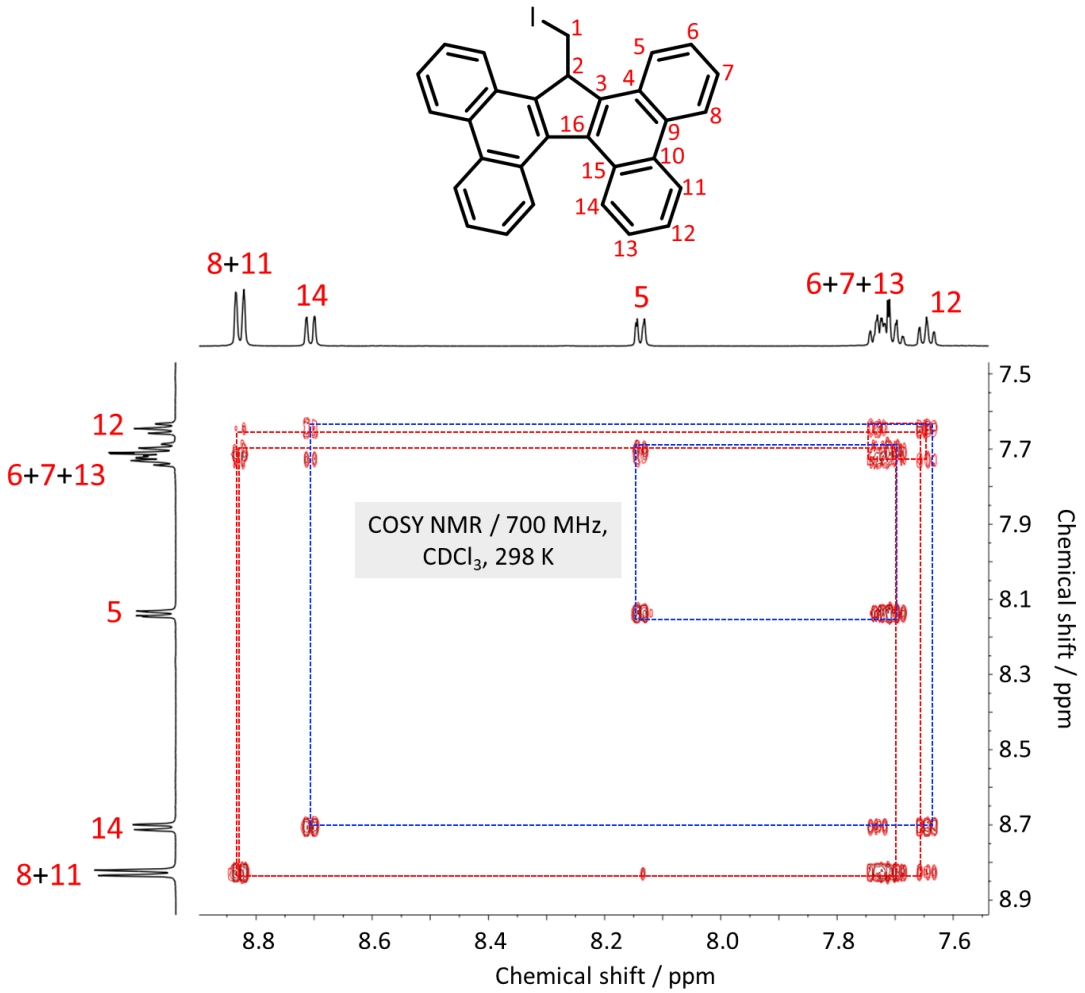

Figure 3.17. Partial ^{1}H–^{1}H COSY NMR spectrum (700 MHz, $CDCl_3$, 298 K) of **18-I**.

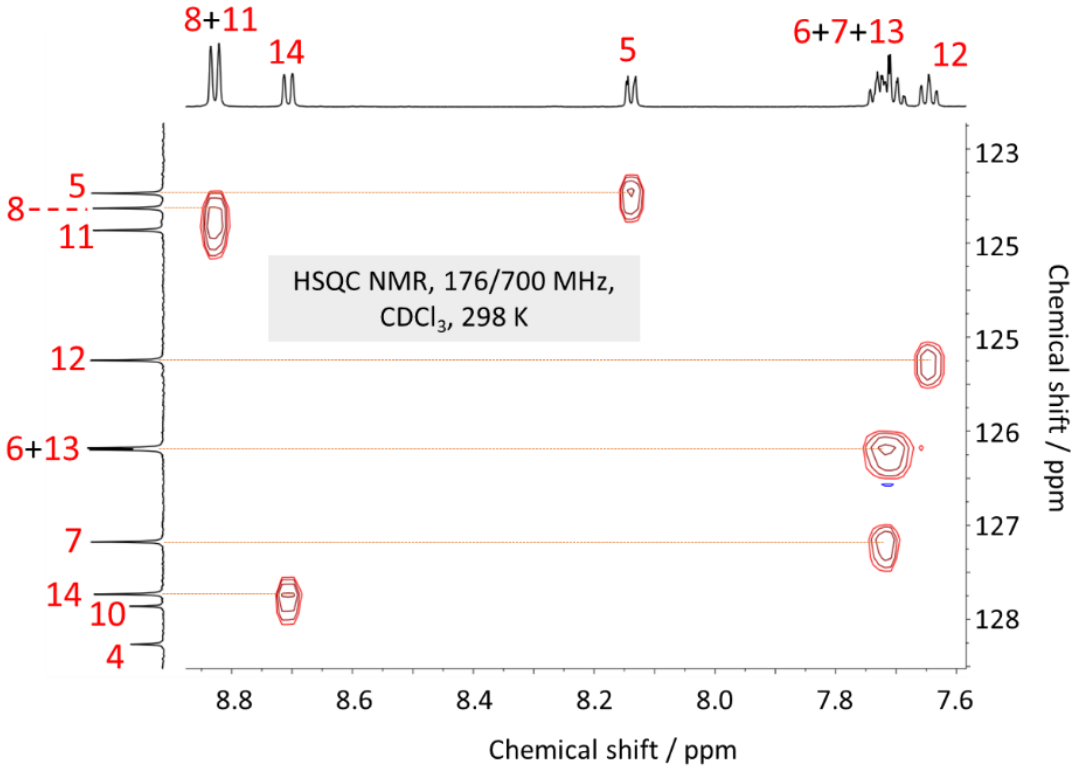

Figure 3.18. Partial HSQC NMR spectrum of **18-I**. Key assignments are correlated between the ^{1}H and ^{13}C nuclei.

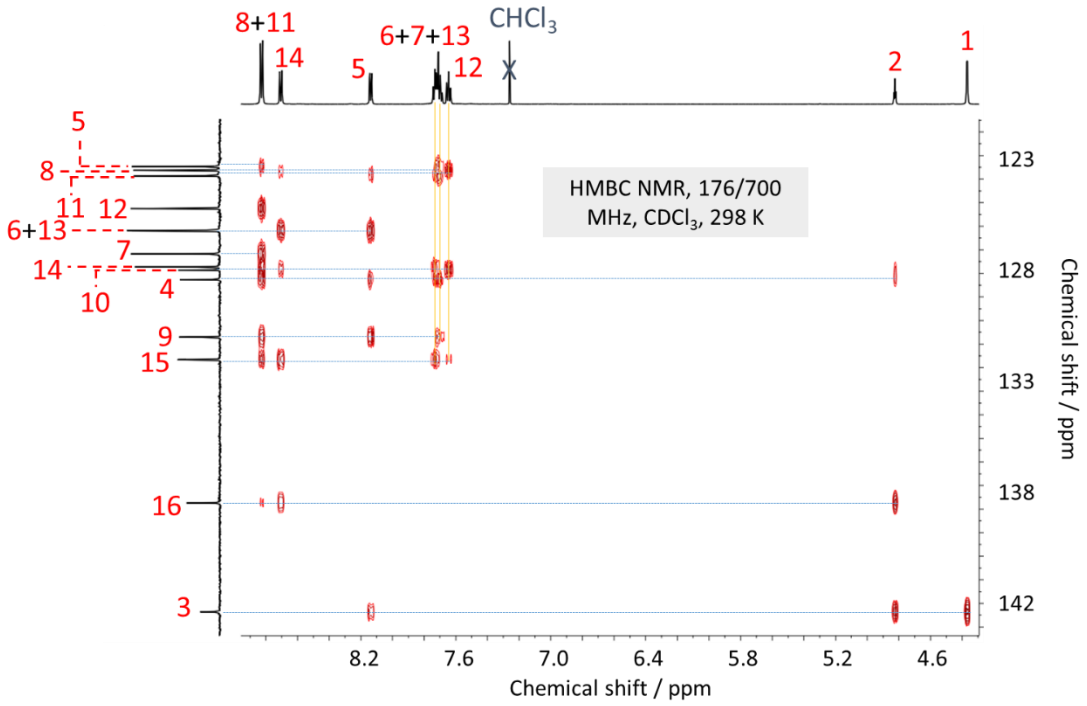

Figure 3.19. Partial HMBC NMR spectrum of **18-I**. Key assignments are correlated between the ^{1}H and ^{13}C nuclei.

Owing to its octahedral T_h-symmetry, the core of fullerene hexakis-adducts, i.e., **12TBF**, **12Az** and **12Alk**, comprises three chemically non-equivalent carbon environments that can be readily distinguished on the basis of chemical shift, i.e., two sp^2-carbon centres (ca. 141 and 145 ppm) and one sp^3-carbon centre (ca. 70 ppm) associated with the non-conjugated propane ring. In practice, the chemically non-equivalent carbon environments in C_{2v}-symmetrical [5:1] fullerene hexakis-adducts, i.e., **2TBF**, **10Az**, **10Alk**, appear at similar chemical shifts to the hexakis-adducts. Owing to the low solubility, and the complex functionality of the hexakis-adducts, only partial assignment of the ^{1}H NMR proton environments was possible. A representative assignment of the ^{1}H (Figure 3.20) and ^{13}C (Figure 3.21) environments of **10Alk** is shown. The low solubility of **12TBF** in $CDCl_3$ makes full ^{1}H assignment difficult (Figure 3.22).

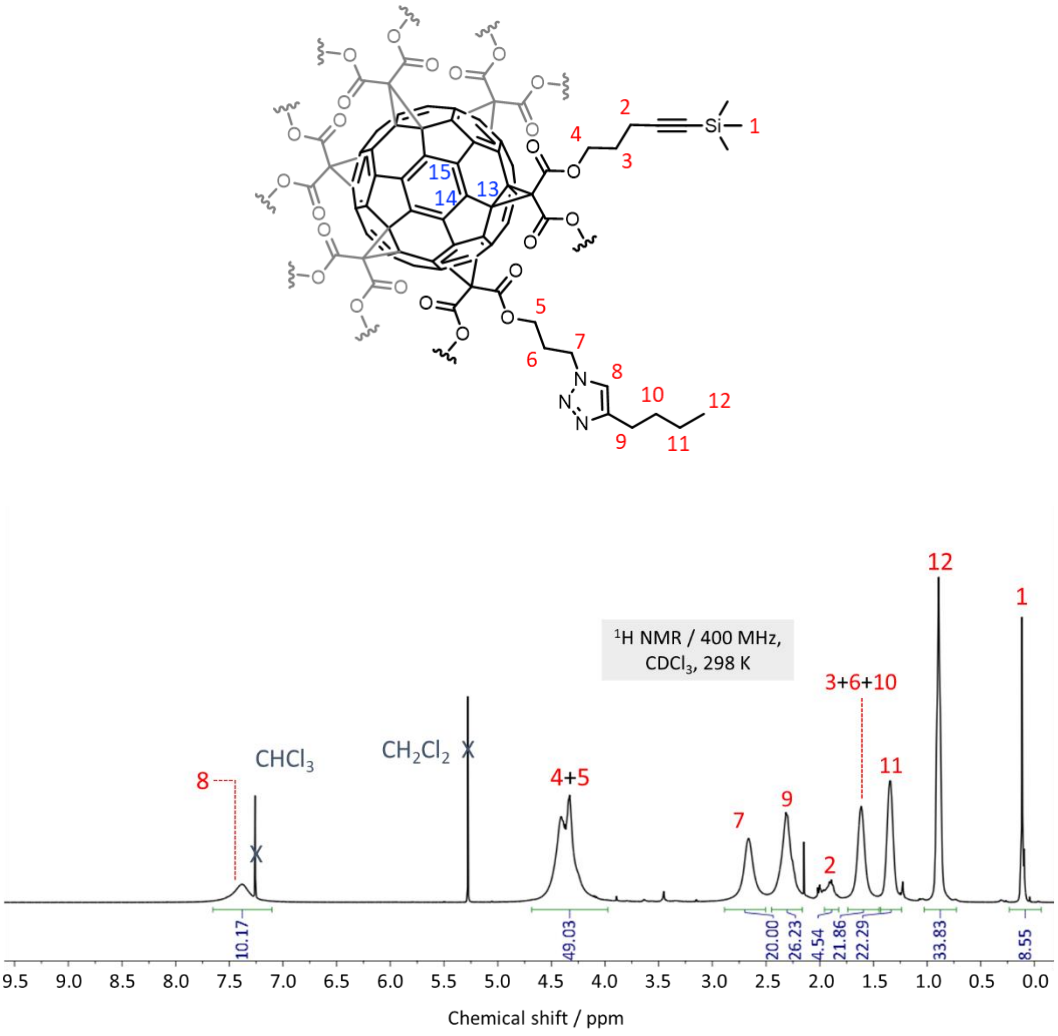

Figure 3.20. ^{1}H NMR ($CDCl_3$, 400 MHz, 298 K) spectrum of **10Alk**.

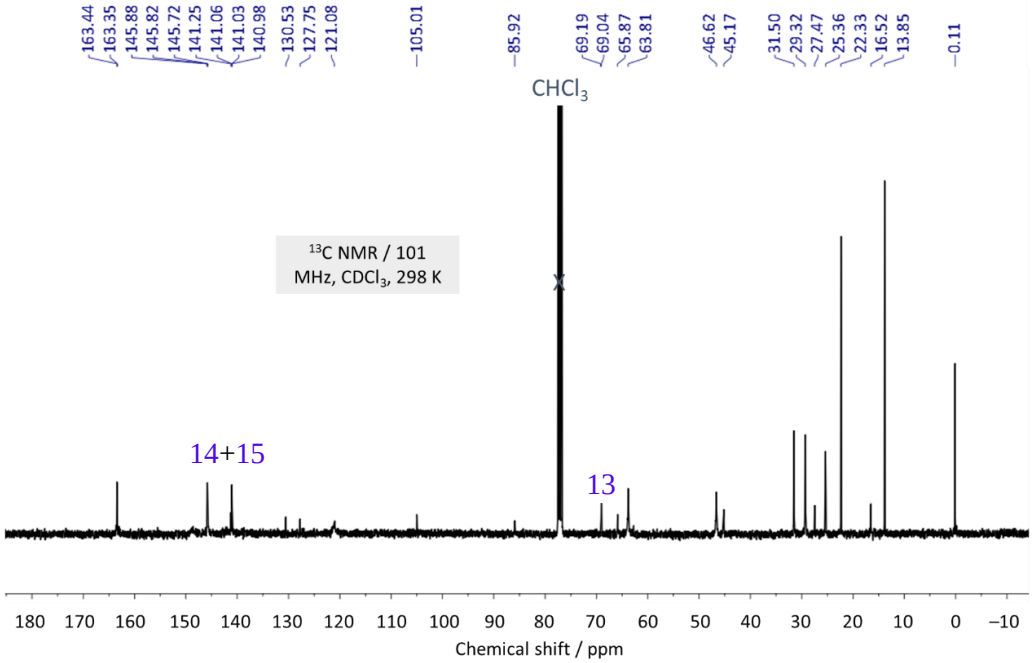

Figure 3.21. ^{13}C NMR ($CDCl_3$, 101 MHz, 298 K) spectrum of **10Alk**; fullerene core environments are assigned.

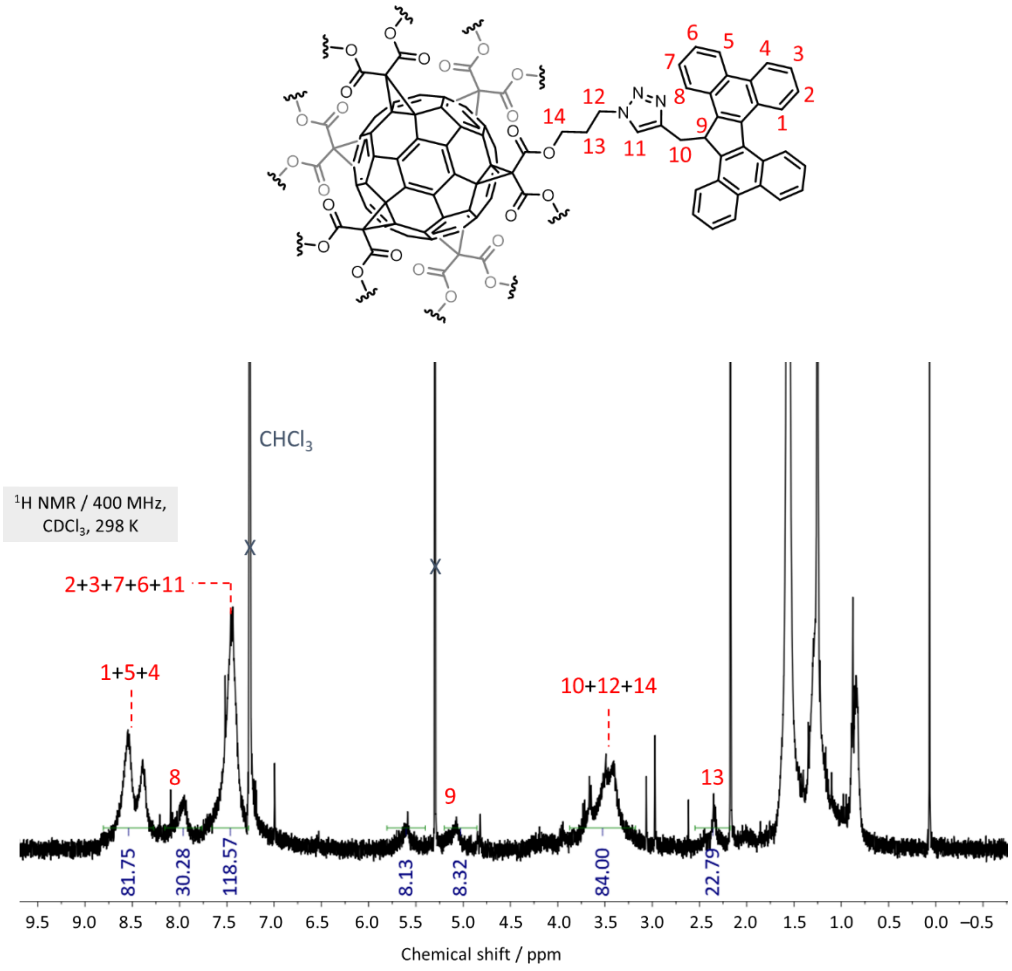

Figure 3.22. ^{1}H NMR ($CDCl_3$, 400 MHz, 298 K) spectrum of **12TBF**.

3.5.2 NMR Spectroscopy

The ^{1}H NMR spectra of the halide derivatives does not change dramatically for the series. The most significant changes occur at the bridged proton and methylene groups. For the weakly electronegative **18-I**, the iodine atom is less shielding and there is a concomitant upfield shift (Figure 3.23) for environments.

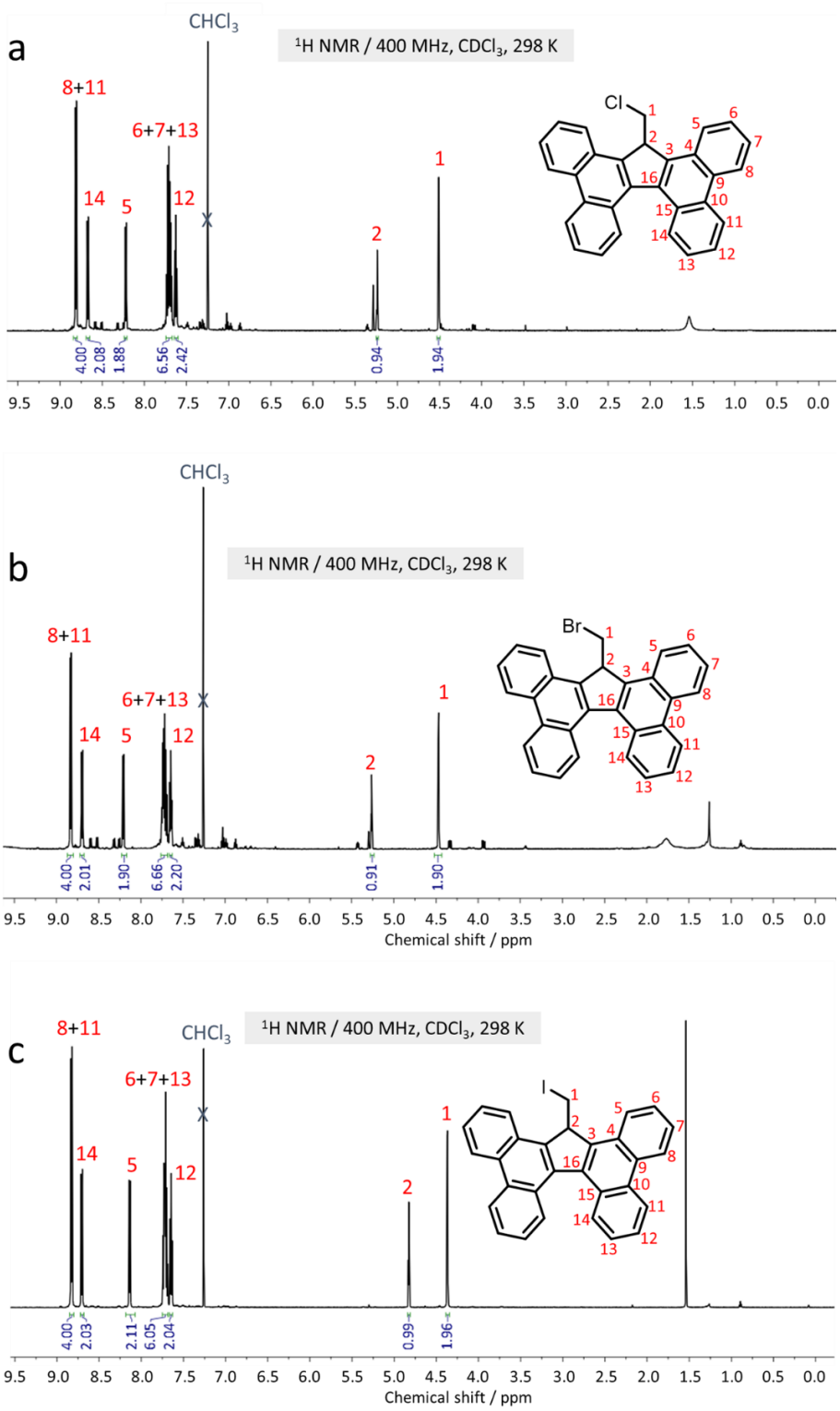

Figure 3.23. ^{1}H NMR ($CDCl_3$, 400 MHz, 298 K) spectrum of a) **18-Cl**, b) **18-Br** , c) **18-I**.

3.5.3 MALDI-TOF

Hexakis-adducts often have high molecular weights, and owing to their often multivalent/ dendrimer like structure, it is difficult to structurally confirm these compounds by ^{1}H and ^{13}C NMR. However, MALDI-TOF can provide invaluable information, especially when monitoring the 'click' functionalisation of hexakis-adducts in addition to confirming the number of pendant units. Depending on volatility and fragmentation of compound, signal intensity can be very broadly scattered. Representative examples of **12TBF** (Figure 3.24), **10Alk** (Figure 3.25) and **2TBF** (Figure 3.26) are shown below.

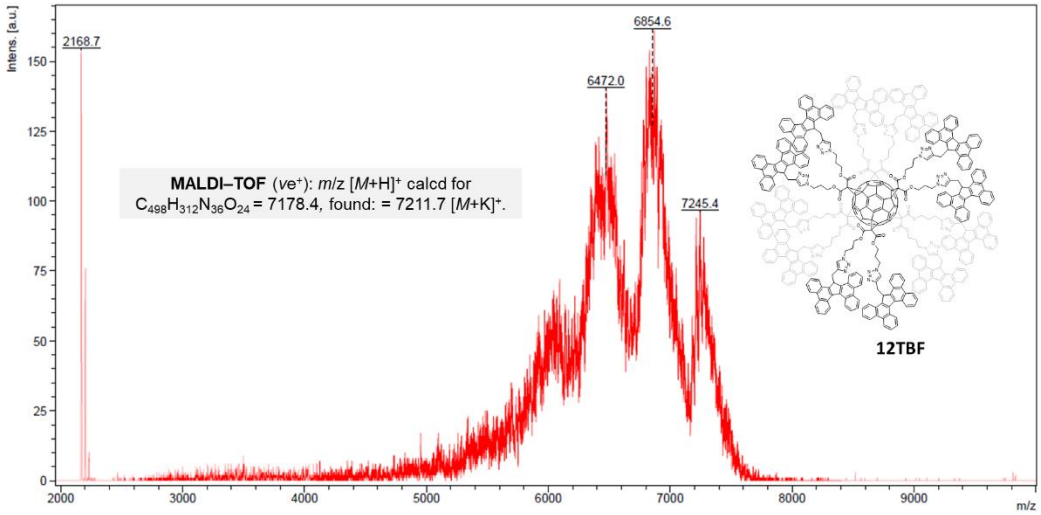

Figure 3.24. MALDI–TOF mass spectrum of TBF-functionalised 'click' fullerene hexakis-adduct **12TBF**. Peaks centred at *m*/z = 6855 and 6472 correspond to fragmentations of one and two TBF units lost at the triazole position.

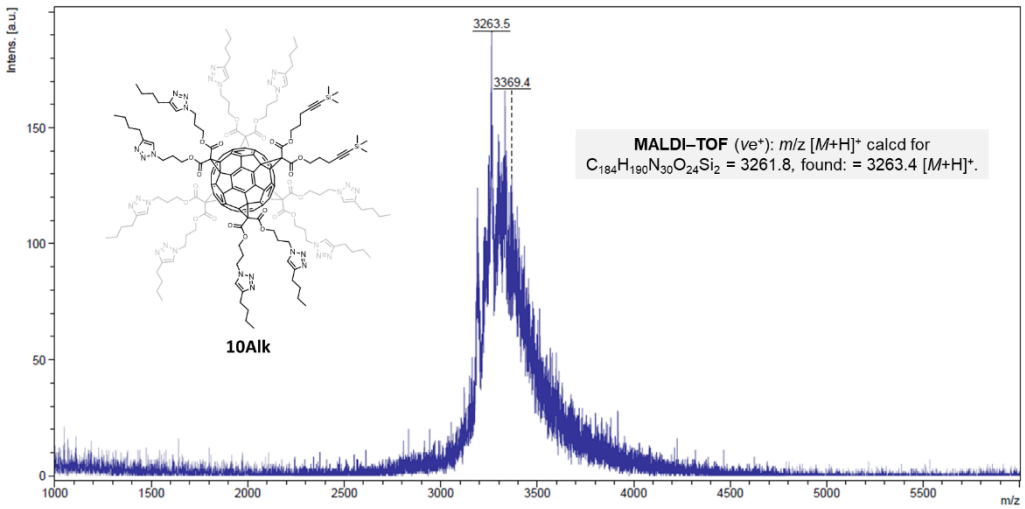

Figure 3.25. MALDI–TOF mass spectrum of alkyl-functionalised 'click' fullerene hexakis-adduct **10Alk**.

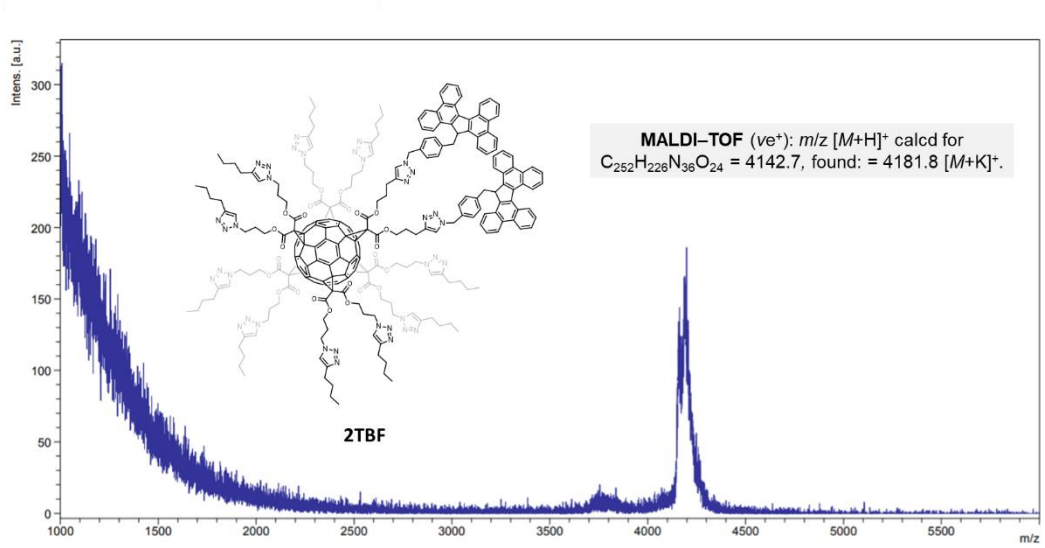

Figure 3.26. MALDI–TOF mass spectrum of alkyl-functionalised ‘click’ fullerene hexakis-adduct **2TBF**.

3.5.4 X-Ray Crystallographic Analysis

Analysis of all crystal structures are shown (Figure 3.27–33) with the crystal system, space group, unit cell parameters reported below. TBF **18-Cl** crystallised into two different polymorphs, A and B that were both grown by slow evaporation of a mixture of CH_2Cl_2–hexanes. Polymorph B of **18-Cl** could not be properly modelled.

TBF **18-Cl** Polymorph A

Crystal system: monoclinic

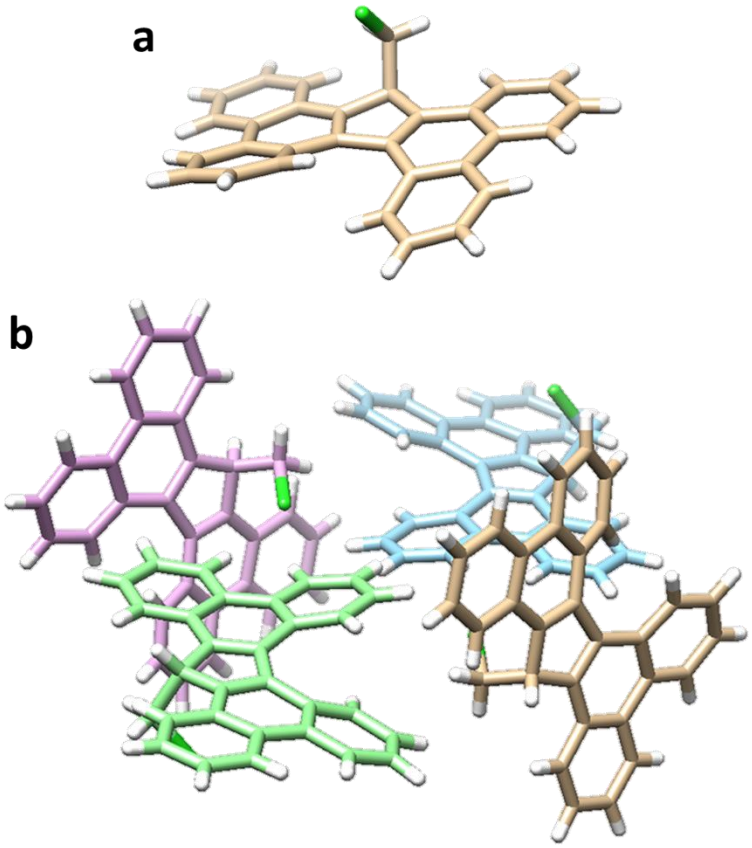

Figure 3.27. a) Solid-state structure of TBF **18-Cl** and b) packing of **18-Cl** molecules in polymorph A.

Space group: $P2_1/n$

Unit Cell Parameters: a = 11.0349(5) Å, b = 12.4222(6) Å, c = 14.3785(7) Å, α = 90°, β = 91.2370(18)°, γ = 90°, volume = 1970.51(16) $Å^3$, ρ_{cal} g/cm^3 = 1.399, Z = 4, R = 1%.

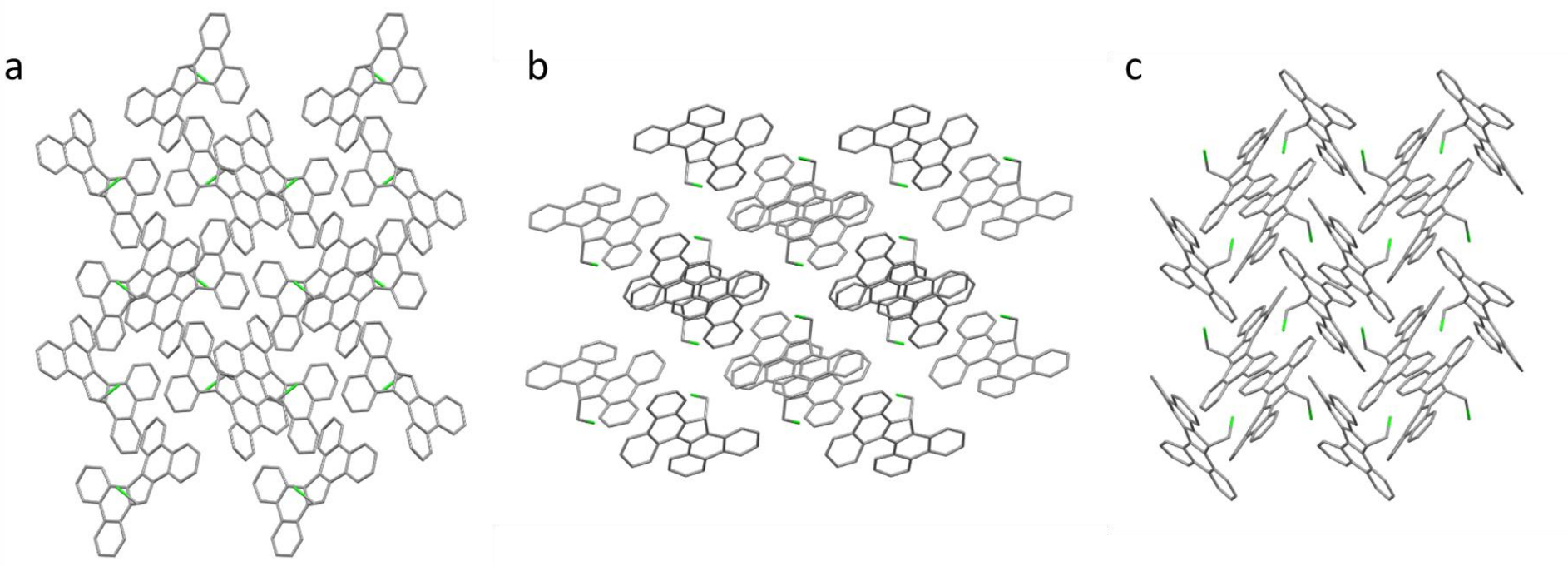

Figure 3.28. Solid-state superstructure of TBF **16-Cl** in polymorph A. Lattice is made up of 2×2×2 unit cells in order to illustrate the crystal packing. Projections are viewed along the crystallographic a) a-, b) b-, and c) c-axes. Hydrogen atoms are emitted for clarity.

TBF **16-Cl** Polymorph B

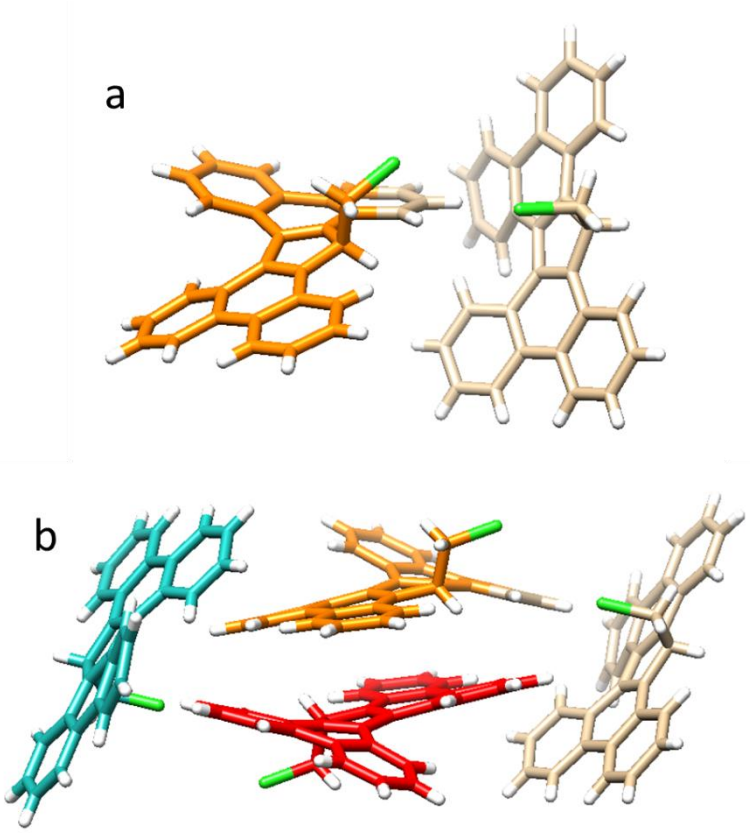

Figure 3.29. a) Solid-state structure of TBF **18-Cl** and b) packing of **18-Cl** molecules in polymorph B.

Crystal system: triclinic

Space group: P-1

Unit Cell Parameters: a = 10.7011(11) Å, b = 12.3864(12) Å, c = 18.2367(17) Å, α = 97.338(4)°, β = 95.758(3)°, γ = 114.094(3)°, volume = 2157.3(4) $Å^3$, ρ_{cal} g/cm^3 = 1.277, Z = 4, R = 17%.

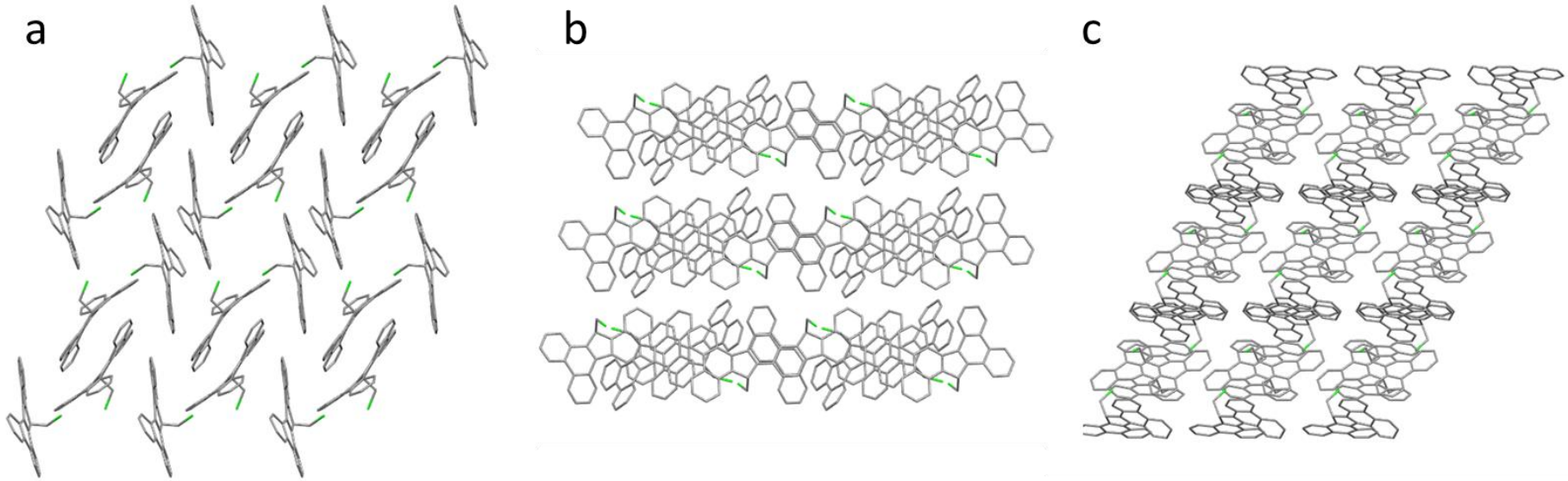

Figure 3.30. Solid-state superstructure of TBF **16-Cl** in polymorph B. Lattice is made up of 3×3×2 unit cells in order to illustrate the crystal packing. Projections are viewed along the crystallographic a) a-, b) b-, and c) c-axes. Hydrogen atoms are emitted for clarity.

TBF **18-Br**

Crystals of TBF **18-Br** suitable for X-ray diffraction were grown by slow evaporation of a mixture of CH_2Cl_2–hexanes.

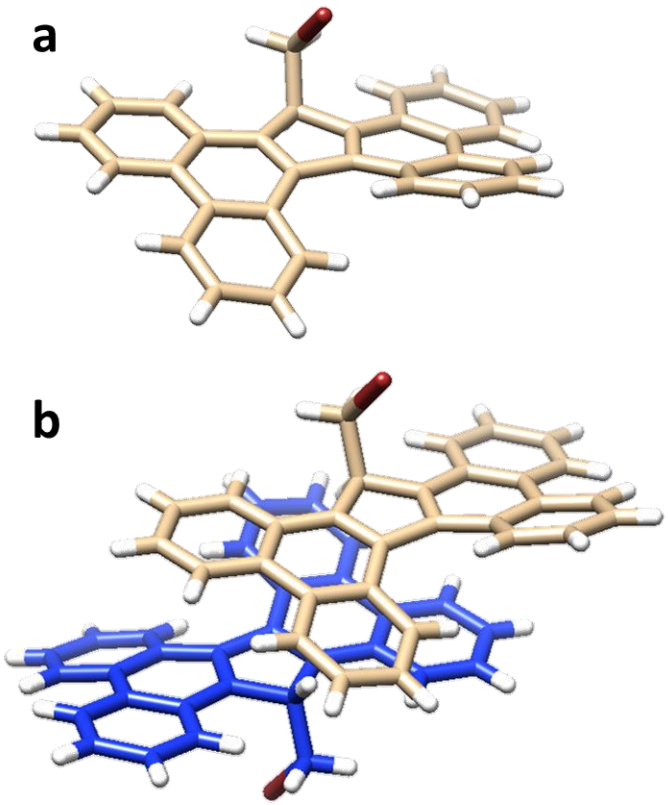

Figure 3.31. a) Solid-state structure of TBF **18-Br** and b) packing of **18-Br** molecules.

Crystal system: triclinic

Space group: P-1

Unit Cell Parameters: a = 8.4143(4) Å, b = 10.5591(6) Å, c = 11.8568(6) Å, α = 104.559(2)°, β = 94.001(2)°, γ = 91.502(2)°, volume = 1016.09(9) $Å^3$, ρ_{cal} g/cm^3 = 1.501, Z = 2, R = 8%.

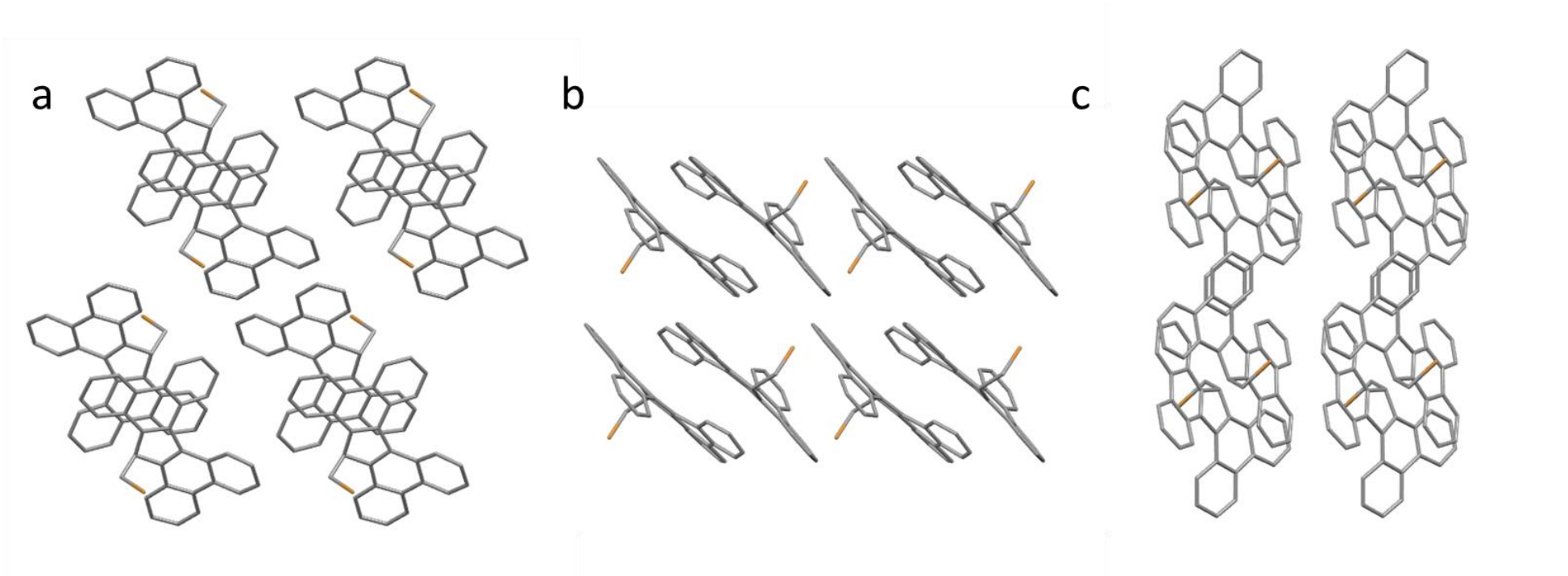

Figure 3.32. Solid-state superstructure of TBF **16-Br**. Lattice is made up of 2×2×2 unit cells in order to illustrate the crystal packing. Projections are viewed along the crystallographic a) a-, b) b-, and c) c-axes. Hydrogen atoms are emitted for clarity.

TBF-I

Crystals of TBF **18-I** suitable for X-ray diffraction were grown by slow evaporation of a mixture of CH_2Cl_2–hexanes.

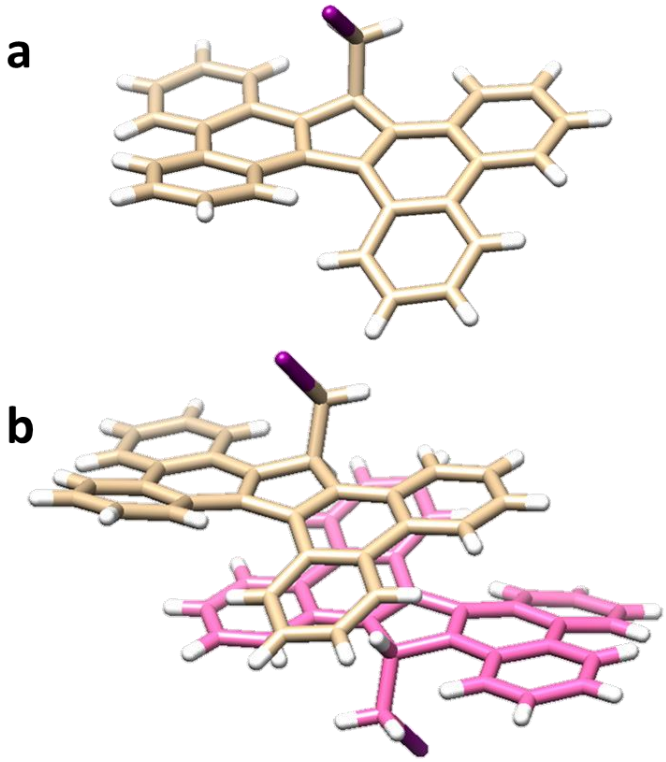

Figure 3.33. a) Solid-state structure of TBF **18-I** and b) packing of **18-I** molecules.

Crystal system: triclinic

Space group: P-1

Unit Cell Parameters: a = 8.5929(4) Å, b = 10.6641(5) Å, c = 11.8010(5) Å, α = 102.913(2)°, β = 93.960(2)°, γ = 91.642(2)°, volume = 1050.45(8) $Å^3$, ρ_{cal} g/cm^3 = 1.601, Z = 2, R = 5%.

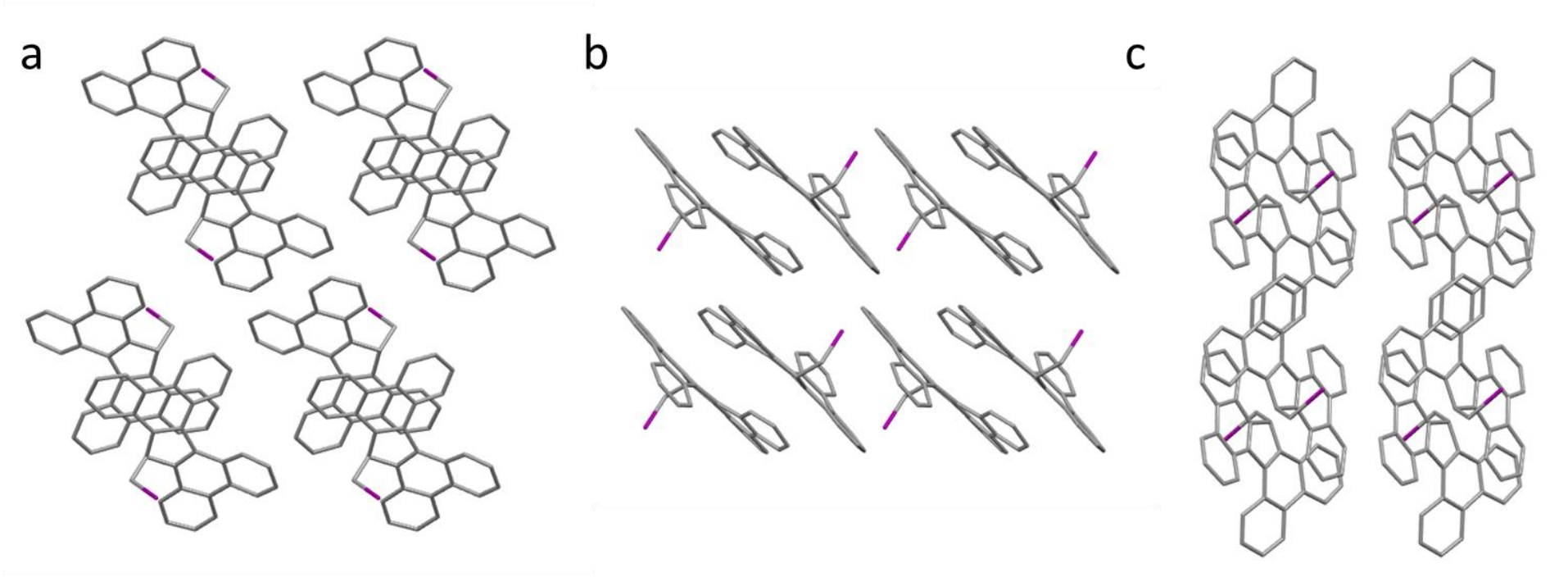

Figure 3.34. Solid-state superstructure of TBF **16-I**. Lattice is made up of 2×2×2 unit cells in order to illustrate the crystal packing. Projections are viewed along the crystallographic a) a-, b) b-, and c) c-axes. Hydrogen atoms are emitted for clarity.

TBF **10**

Crystals of TBF azide **10** suitable for X-ray diffraction were grown by slow evaporation of a mixture of CH_2Cl_2–hexanes.

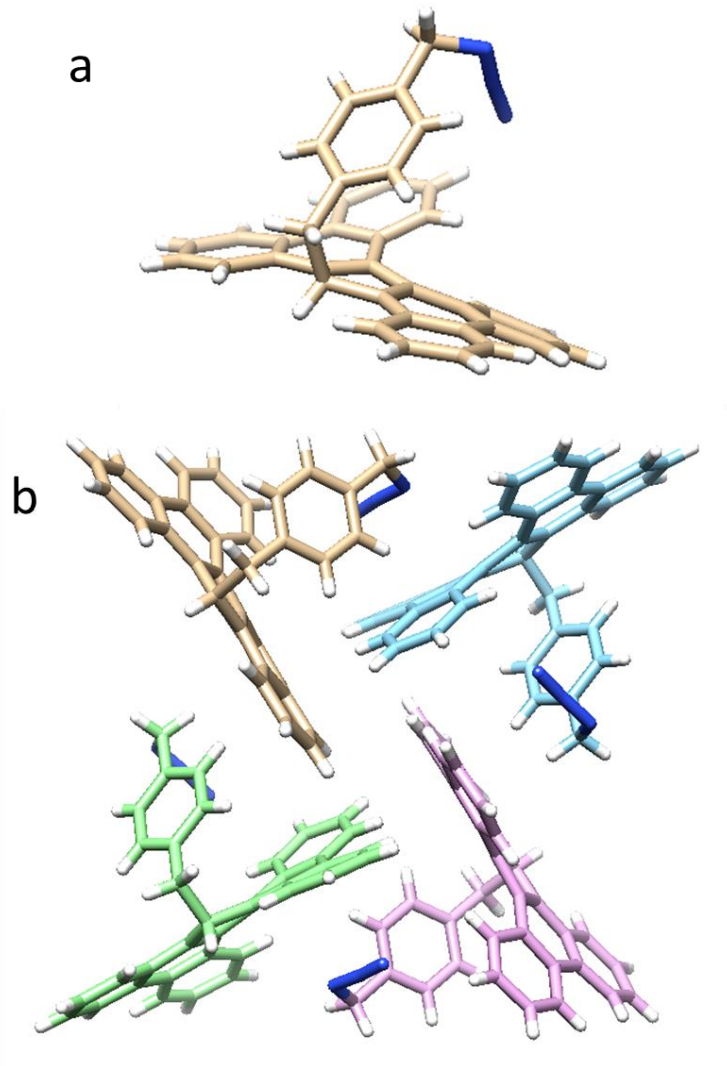

Figure 3.35. a) Solid-state structure of TBF **10** and b) packing of TBF **10** molecules.

Crystal system: monoclinic

Space group: $P2_1/n$

Unit Cell Parameters: a = 11.2354(4) Å, b = 14.5637(6) Å, c = 15.6833(6) Å, α = 90°, β = 91.251(2)°, γ = 90°, volume = 2565.63(17) $Å^3$, ρ_{cal} g/cm^3 = 1.324, Z = 4. R = 12%.

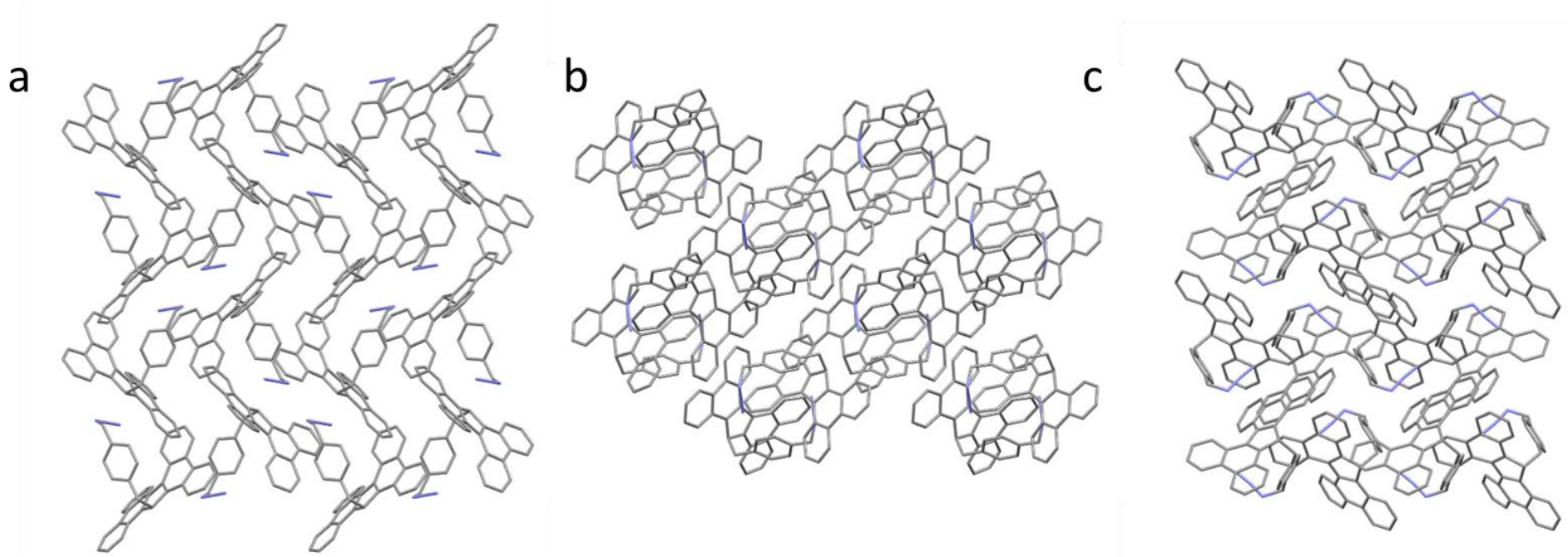

Figure 3.36. Solid-state superstructure of TBF **10**. Lattice is made up of 2×2×2 unit cells in order to illustrate the crystal packing. Projections are viewed along the crystallographic a) a-, b) b-, and c) c-axes. Hydrogen atoms are emitted for clarity.

3.5.5 Absorption and Emission Spectroscopy

Samples were prepared in anhydrous, spectroscopic grade solvents and with the aid of sonication to afford complete dissolution. Steady-state absorption and fluorescence emission spectra were recorded at room temperature (298 K) in quartz cuvettes (10 mm and 10 ×10 mm path lengths, respectively) and corrected with respect to the pure solvent. All fluorescence samples were excited at 390 nm and spectra recorded using a standard 90º detector set.

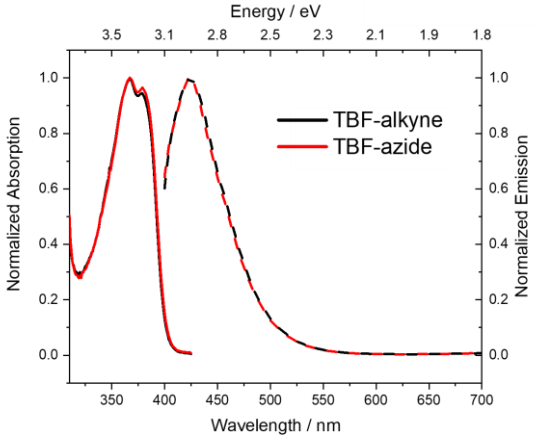

Figure 3.37. Normalized UV-Vis (solid line) and emission (dashed line) spectra of TBF alkyne **1** (black) and TBF azide **10** (red) in CH_2Cl_2. Spectra measured at 298 K. Excitation at 390 nm.

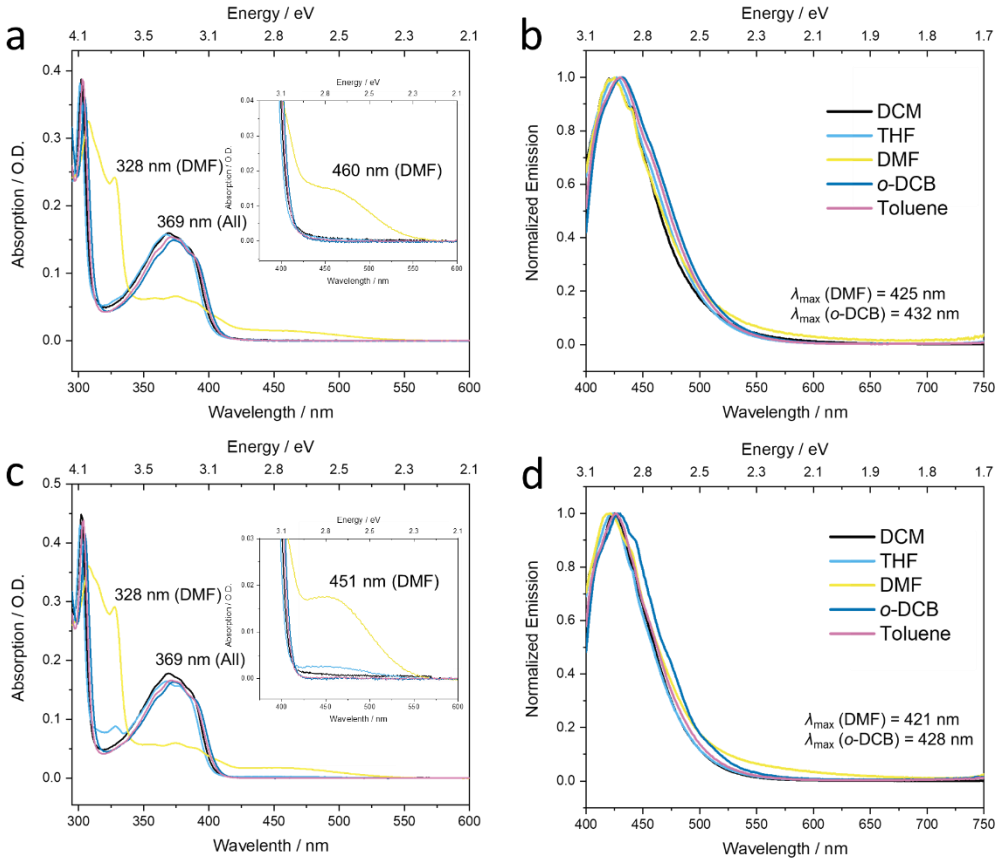

Figure 3.38. a) UV-Vis and b) emission spectra of TBF **18-Cl** and c) UV-Vis and d) emission spectra of TBF **18-Br** in various solvents: DCM (black), THF (light blue), DMF (yellow), *o*-DCB (dark blue) and Toluene (pink). Spectra measured at 298 K. Excitation at 390 nm

3.5.6 Cyclic Voltammetry

Cyclic voltammograms of TBF **1**, **10**, **18-Cl**, **18-Br** and **18-I** were recorded at room temperature in deaerated CH_2Cl_2 solutions with 0.1 M $TBAPF_6$ as supporting electrolyte under an argon atmosphere using a standard three-electrode set up. See Experimental section 3.4.1 for full experimental details. Table 3.2 (CH_2Cl_2) and Table 3.3 (DMF) summarises energy level and band gap parameters derived from solution-state experiments. The current intensity is directly proportional to the square-root of the scan rate for each CV experiment which reveals that all first- and second-wave cathodic/anodic processes are highly reversible.

Table 3.2. Optoelectronic properties calculated by UV-Vis spectroscopy and cyclic voltammetry in CH_2Cl_2

Compound	λ_{abs}[a] [nm]	E_{gap}[b] [eV]	E_{ox} [V]	HOMO[c] [eV]	LUMO[d] [eV]
TBF **1**	379, 367	3.08	+1.11	–5.37	–2.29
TBF **10**	379, 367	3.08	+1.07	–5.33	–2.25

[a] solution, [b] Onset of absorption, [c] $E_{HOMO} = -(E_{ox}+4.75)$ eV, [d] $E_{LUMO} = E_{HOMO} + E_{gap}$ eV

Table 3.3. Optoelectronic properties calculated by UV-Vis spectroscopy and cyclic voltammetry in DMF

Compound	λ_{abs}[a] [nm]	E_{gap}[b] [eV]	E_{ox} [V]	HOMO[c] [eV]	LUMO [eV]
TBF **1**	380, 365	3.09	+0.96	–5.22	–2.13[d]
TBF **10**	381, 367	3.08	+0.96	–5.22	–2.14[d]
2TBF	380, 364	2.13	+0.99	–5.21	–3.47[e]
12TBF	381, 366	2.11	+0.82	–5.04	–3.45[e]

[a] solution, [b] Onset of absorption, [c] $E_{HOMO} = -(E_{ox} + 4.75)$ eV, [d] $E_{LUMO} = E_{HOMO} + E_{gap}$ eV
[e] $E_{LUMO} = -(E_{red} + 4.75)$ eV

Table 3.4. Optoelectronic properties calculated by UV-Vis spectroscopy and cyclic voltammetry in CH_2Cl_2.

Compound	λ_{abs}[a] [nm]	E_{gap}[b] [eV]	E_{ox} [V]	HOMO[c] [eV]	LUMO[d] [eV]
18-Cl	369	3.08	+1.15	–5.44	–2.34
18-Br	369	3.08	+1.17	–5.43	–2.36
18-I	371	3.08	+1.13	–5.39	–2.32

[a] solution, [b] Onset of absorption, [c] $E_{HOMO} = -(E_{ox} + 4.75)$ eV, [d] $E_{LUMO} = E_{HOMO} + E_{gap}$ eV

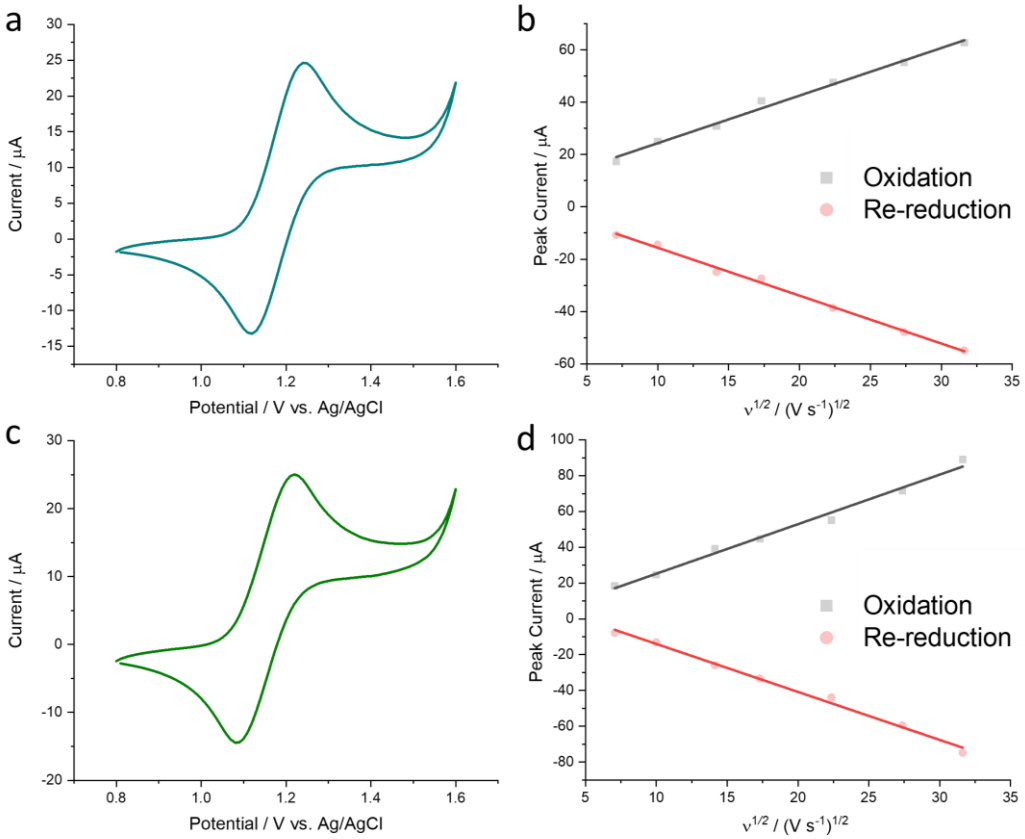

Figure 3.39. Cyclic voltammograms (100 mVs^{-1}, 298 K) of a) TBF alkyne **l** and c) TBF azide **10** ([1.0 mM] in degassed CH_2Cl_2 containing 0.1 M $TBAPF_6$ as supporting electrolyte. CV also collected at variable scan rates: 50–1000 mVs^{-1} and current peak against the square root of the scan rate has been plotted showing a linear relationship that indicates redox-reversibility for both b) TBF **1** and d) **10**.

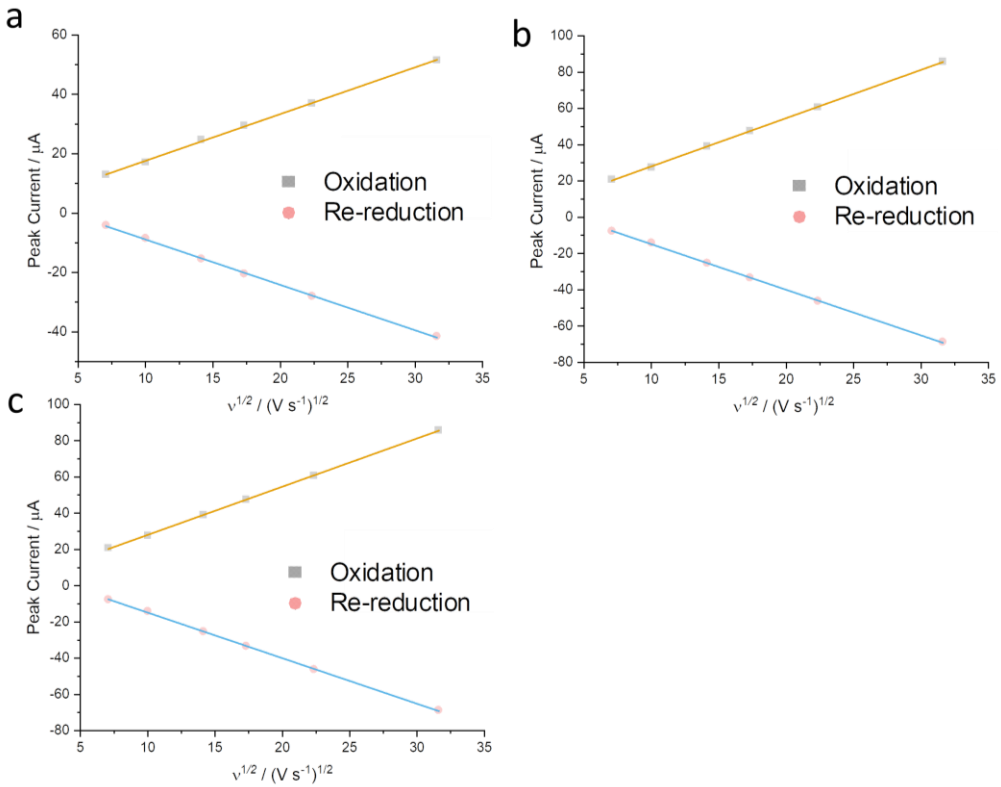

Figure 3.40. Current peak against the square root of the scan rate for a) **18-Cl**, b) **18-Br** and c) **18-I** shows a linear relationship that indicates a fully reversible oxidation process for all three compounds.

3.5.7 SEC–UV-Vis-NIR Analysis

Spectroelectrochemical measurements were conducted on dearated anhydrous CH_2Cl_2 or DMF solutions containing 0.1 M $TBAPF_6$ as the supporting electrolyte in an air-tight optically transparent thin-layer electrochemical (OTTLE) cell (path length ca. 0.2 mm) under an argon atmosphere at 298 K. See Experimental Section 3.4.1 for full experimental details. Upon re-applying a voltage of +0.2 V towards TBF $\mathbf{1}^{2+}$ (itself generated by applying a potential of +1.2 V) the characteristic TBF band (i.e., for neutral TBF) returns, confirming no degradation upon oxidation (Figure 3.41). In CH_2Cl_2 the absorption profile (Figure 3.42) of TBF $\mathbf{1}^{2+}$ is much more resolved. The C_{60} hexakis radical can also be generated with control compound **12Alk** from applying a voltage of –1.1 V (Figure 3.43).

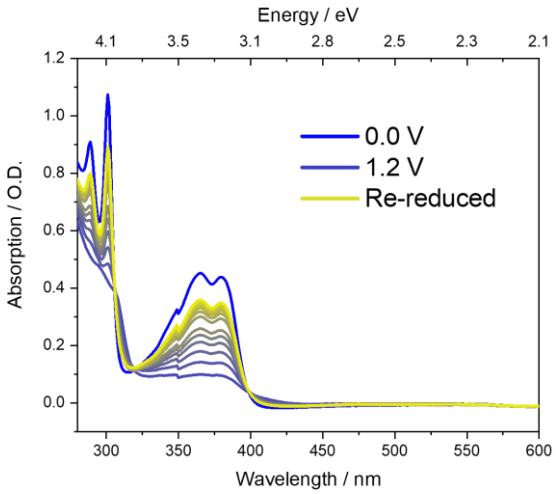

Figure 3.41. UV-Vis absorption spectra of TBF alkyne **1** [1.0 mM] in deaerated anhydrous DMF containing 0.1 M $TBAPF_6$ as the supporting electrolyte at 0.0 V (blue line) and 1.2 V (dark blue line). A constant potential +0.2 V was applied to re-reduce the compound (yellow line).

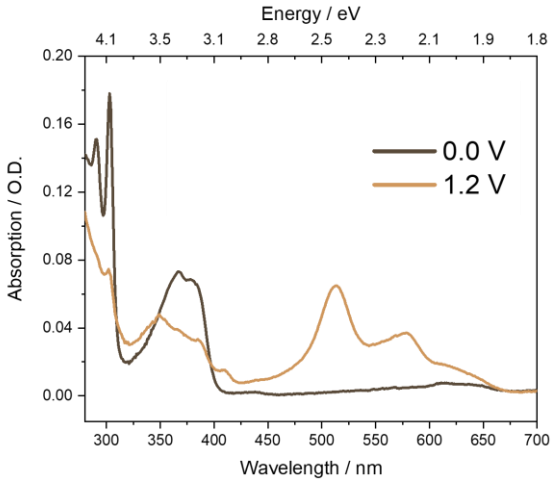

Figure 3.42. UV-Vis absorption spectra of TBF alkyne **1** [1.0 mM] in deaerated anhydrous CH_2Cl_2 containing 0.1 M $TBAPF_6$ as the supporting electrolyte at 0.0 V (black line) and 1.2 V (brown line).

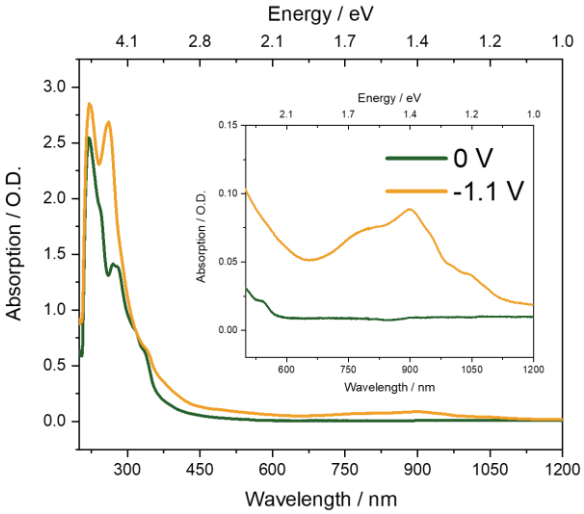

Figure 3.43. UV-Vis spectrum of **12Alk** [1.0 mM] in in deaerated anhydrous CH_2Cl_2 containing 0.1 M $TBAPF_6$ as the supporting electrolyte at 0.0 V (black line) and at –1.15 V (orange line) when the sample has been fully reduced. Inset shows low intensity absorptions between 400–1200 nm.

3.5.8 Femtosecond Transient Absorption Spectroscopy (fsTA)

Set up for fsTA was as follows; the laser is PHAROS from Light Conversion (wavelength: 1030 nm, pulse duration: 180 fs, repetition rate: 1 KHz, power: 0.6 W). Part of the output is used to do third harmonic generation (THG), which produces 343 nm output that is used to pump the sample at a power of 0.5 mW. Another part of the output is used to pump a 2 mm sapphire plate to generate white light continuum (WLC), which is used to probe the dynamics of the excited states. The polarization of the pump is vertical to the optical table, while the polarization of the probe is parallel to the optical table. The spot sizes (Full Width @ $1/e^2$) of the pump and probe are 270 μm and 200 μm, respectively. The time delay between the pump and the probe is controlled by a 1 meter motorized translation stage (Zaber Technologies Inc. A-LST1000AKT07G06SU), which can generate a 6 ns delay. The pump is modulated by an optical chopper (Thorlabs Inc. MC2000B-EC) that is locked to the half frequency of the laser repetition rate to create an iterated pump on / pump off situation. The WLC goes through a spectrometer and the intensities at different wavelengths are monitored by a camera (Imaging Solutions Group LightWise LW-ELIS-1024A-1394). The camera is synchronized with the laser pulse to ensure it captures the spectrum of WLC pulse by pulse. The transient absorption spectrum at one fixed time delay is calculated by eq.1.

$$\Delta T/T = (\sum_{i=1}^{N} (Spectrum_{pump-on} - Spectrum_{pump-off})/Spectrum_{pump-off})/N$$

(eq. 1)

where N is average number, in our case N=500. By changing the time delay between pump and probe, we obtain the whole transient absorption spectra. All data was collected following excitation at 343 nm; all samples prepared at 100 uM in DMF using a 1 mm path length cuvette.

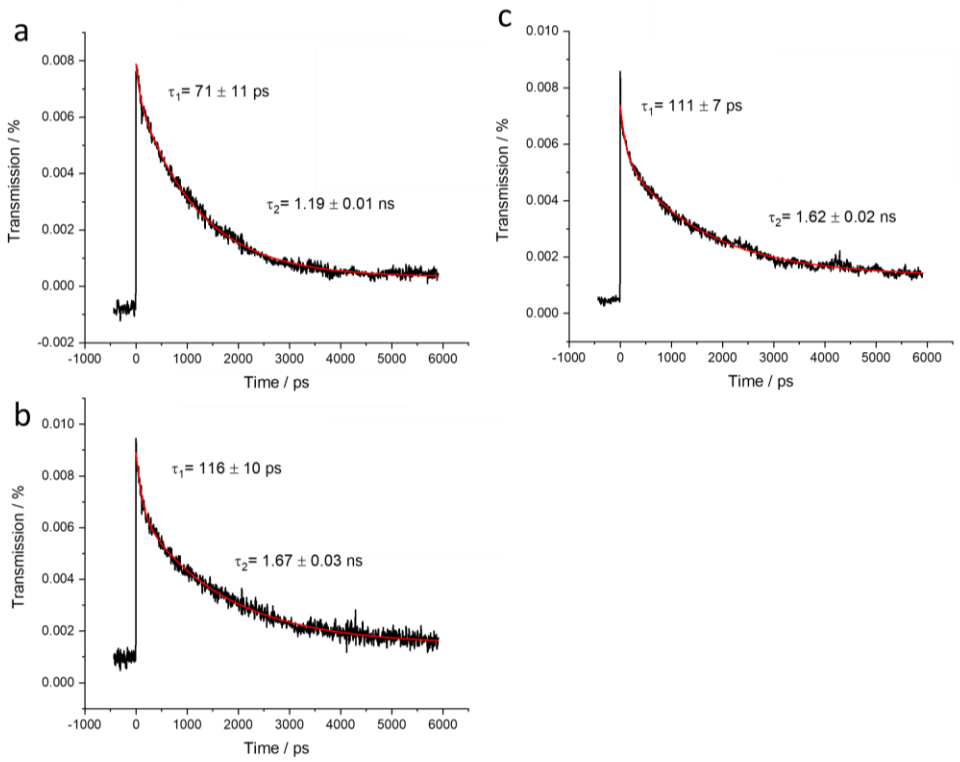

Figure 3.44. Decay measured at a) 568 nm, b) 740 nm and c) 695 nm for **12Alk** following excitation at 343 nm. Decay is fit to exponential decay.

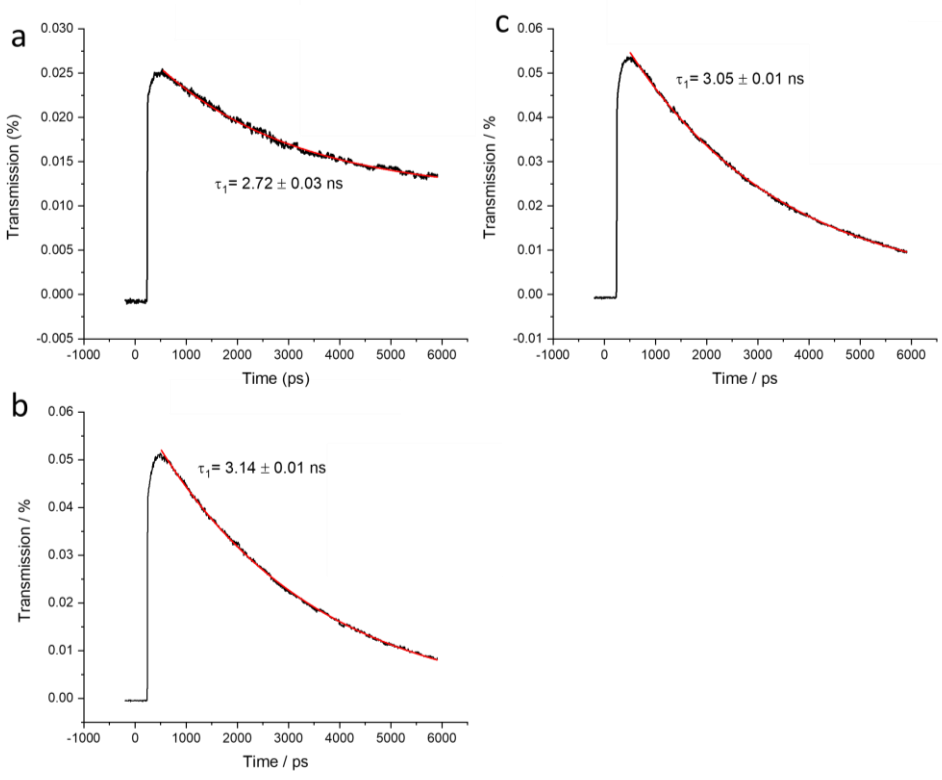

Figure 3.45. Decay measured at a) 568 nm, b) 740 nm and c) 695 nm for TBF alkyne **1** following excitation at 343 nm. Decay is fit to exponential decay.

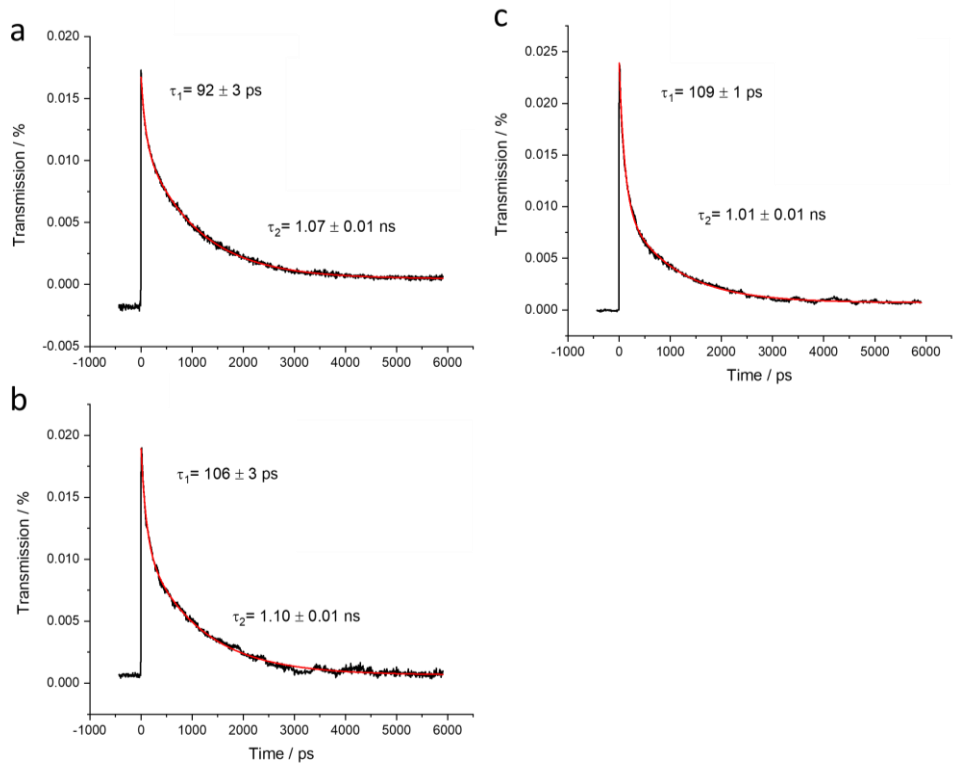

Figure 3.46. Decay measured at a) 568 nm, b) 740 nm and c) 695 nm for hexakis-adduct **2TBF** following excitation at 343 nm. Decay is fit to exponential decay.

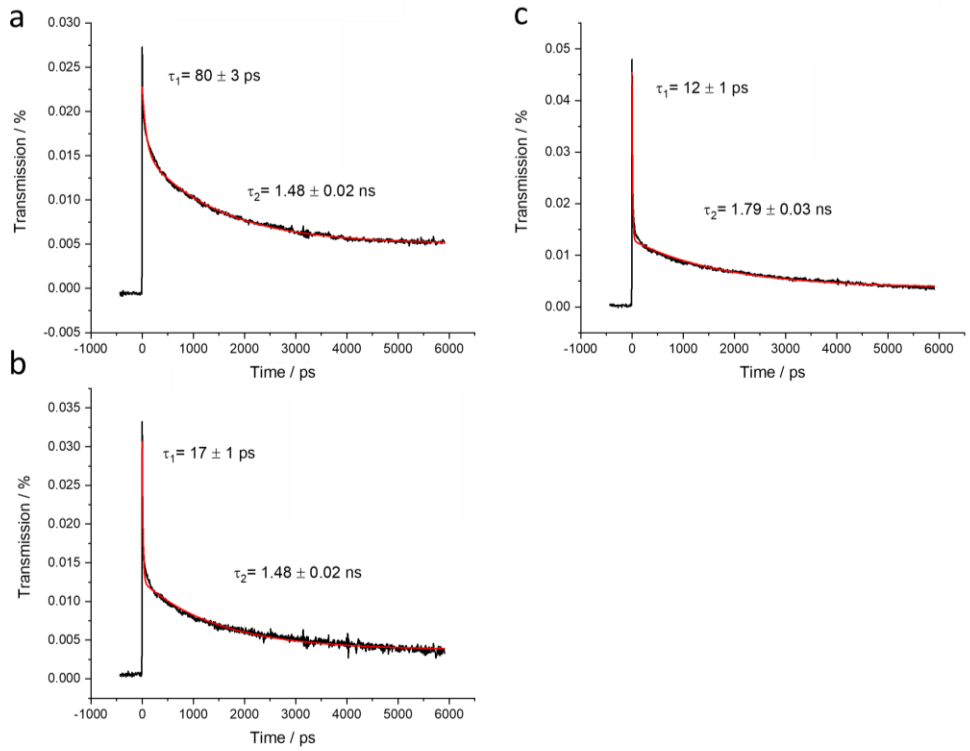

Figure 3.47. Decay measured at a) 568 nm, b) 740 nm and c) 695 nm for hexakis-adduct 1**2TBF** following excitation at 343 nm. Decay is fit to exponential decay.

3.6 References

1 J. Iehl, M. Holler, J. F. Nierengarten, K. Yoosaf, J. M. Malicka, N. Armaroli, J. M. Strub, A. Van Dorsselaer and B. Delavaux-Nicot, *Aust. J. Chem.*, 2011, **64**, 153–159.

2 A. Muñoz, L. Rodríguez-Pérez, S. Casado, B. M. Illescas and Nazario Martín, *J. Mater. Chem. C*, 2019, **7**, 8962-8968.

3 A. Muñoz, D. Sigwalt, B. M. Illescas, J. Luczkowiak, L. Rodríguez-Pérez, I. Nierengarten, M. Holler, J. S. Remy, K. Buffet, S. P. Vincent, J. Rojo, R. Delgado, J. F. Nierengarten and N. Martín, *Nat. Chem.*, 2016, **8**, 50–57.

4 J. Iehl, J. F. Nierengarten, A. Harriman, T. Bura and R. Ziessel, *J. Am. Chem. Soc.*, 2012, **134**, 988–998.

5 A. Donat-Bouillud, I. Lévesque, Y. Tao, M. D'Iorio, S. Beaupré, P. Blondin, M. Ranger, J. Bouchard and M. Leclerc, *Chem. Mater.*, 2000, **12**, 1931–1936.

6 S. L. Lee, H. S. Kim, J. W. Ha, H. J. Park and D. H. Hwang, *Bull. Korean Chem. Soc.*, 2020, **41**, 143–149.

7 S. Ma, Y. Fu, D. Ni, J. Mao, Z. Xie and G. Tu, *Chem. Commun.*, 2012, **48**, 11847–11849.

8 R. Abbel, A. P. H. J. Schenning and E. W. Meijer, *J. Polym. Sci. Part A Polym. Chem.*, 2009, **47**, 4215–4233.

9 C. Kitamura, Y. Tanigawa, T. Kobayashi, H. Naito, H. Kurata and T. Kawase, *Tetrahedron*, 2012, **68**, 1688–1694.

10 Y. Ueda, Y. Tanigawa, C. Kitamura, H. Ikeda, Y. Yoshimoto, M. Tanaka, K. Mizuno, H. Kurata and T. Kawase, *Chem. Asian J.*, 2013, **8**, 392–399.

11 Y. Kimura, I. Kawajiri, M. Ueki, T. Morimoto, J. I. Nishida, H. Ikeda, M. Tanaka and T. Kawase, *Org. Chem. Front.*, 2017, **4**, 743–749.

12 S. Sampath, A. A. Boopathi and A. B. Mandal, *Phys. Chem. Chem. Phys.*, 2016, **18**, 21251–21258.

13 A. A. Boopathi, S. Sampath and T. Narasimhaswamy, *New J. Chem.*, 2019, **43**, 9500–9506.

14 M. Assali, M. P. Leal, I. Fernández, P. Romero-Gomez, R. Baati and N. Khiar, *Nano Res.*, 2010, **3**, 764–778.

15 J. A. Mol, C. S. Lau, W. J. M. Lewis, H. Sadeghi, C. Roche, A. Cnossen, J. H. Warner, C. J. Lambert, H. L. Anderson and G. A. D. Briggs, *Nanoscale*, 2015, **7**, 13181–13185.

16 B. Limburg, J. O. Thomas, G. Holloway, H. Sadeghi, S. Sangtarash, I. C. Y. Hou, J. Cremers, A. Narita, K. Müllen, C. J. Lambert, G. A. D. Briggs, J. A. Mol and H. L. Anderson, *Adv. Funct. Mater.* 2018, **28**, 1803629.

17 J. Iehl, R. Pereira De Freitas, B. Delavaux-Nicot and J. F. Nierengarten, *Chem. Commun.*, 2008, 2450–2452.

18 J. Lehl and J. F. Nierengarten, *Chem. Eur. J.*, 2009, **15**, 7306–7309.

19 I. Nierengarten and J. F. Nierengarten, *Chem. Rec.*, 2015, **15**, 31–51.

20 A. Nafady, P. J. Costa, M. J. Calhorda and W. E. Geiger, *J. Am. Chem. Soc.*, 2006, **128**, 16587–16599.

21 T. Nishinaga, R. Inoue, A. Matsuura and K. Komatsu, *Org. Lett.*, 2002, **4**, 4117–4120.

22 F. G. Bordwell, J. P. Cheng and M. J. Bausch, *J. Am. Chem. Soc.*, 1988, **110**, 2867–2872.

23 F. G. Bordwell, J. P. Cheng, S. E. Seyedrezai and C. A. Wilson, *J. Am. Chem. Soc.*, 1988, **110**, 8178–8183.

24 N. G. Tsierkezos, *J. Solution Chem.*, 2007, **36**, 289–302.

25 M. Calçada, J. T. Lunardi, L. A. Manzoni, W. Monteiro and M. Pereira, *Front. Phys.*, 2019, **7**, 100.

26 K. Yoosaf, J. Iehl, I. Nierengarten, M. Hmadeh, A. M. Albrecht-Gary, J. F. Nierengarten and N. Armaroli, *Chem. Eur. J.*, 2014, **20**, 223–231.

27 J. Ramos-Soriano, J. J. Reina, B. M. Illescas, N. De La Cruz, L. Rodríguez-Pérez, F. Lasala, J. Rojo, R. Delgado and N. Martín, *J. Am. Chem. Soc.*, 2019, **141**, 15403–15412.

28 D. Zheng, X. A. Yuan, H. Ma, X. Li, X. Wang, Z. Liu and J. Ma, *R. Soc. Open Sci.* 2018, **5**, 171928.

29 J. Sturala, M. K. Etherington, A. N. Bismillah, H. F. Higginbotham, W. Trewby, J. A. Aguilar, E. H. C. Bromley, A. J. Avestro, A. P. Monkman and P. R. McGonigal, *J. Am. Chem. Soc.*, 2017, **139**, 17882–17889.

30 M. R. Ceba, C. C. Blanco and F. G. Sánchez, *J. Photochem.*, 1985, **30**, 353–362.

31 W. Liptay, R. Wortmann, R. Böhm and N. Detzer, *Chem. Phys.*, 1988, **120**, 439–448.

32 J. P. Peterson and A. H. Winter, *Org. Lett.*, 2020, **22**, 6072–6076.

33 X. Zhang, Z. Xu, W. Si, K. Oniwa, M. Bao, Y. Yamamoto and T. Jin, *Nat. Commun.*, , 2017, **8**, 15073.

34 J. M. Cole, *J. Chem. Inf. Model.*, 2020, **60**, 6095–6108.

35 A. M. Hay, S. Hobbs-Dewitt, A. A. MacDonald and R. Ramage, *Synthesis.*, 1999, **11**, 1979–1985.

36 T. Vašíček, V. Spiwok, J. Červený, L. Petrásková, L. Bumba, D. Vrbata, H. Pelantová, V. Křen and P. Bojarová, *Chem. Eur. J.*, 2020, **26**, 9620–9631.

37 R. . Ramage and G. . Raphy, *Tetrahedron Lett.*, 1992, **33**, 385–388.

38 M. Foroozandeh, R. W. Adams, N. J. Meharry, D. Jeannerat, M. Nilsson and G. A. Morris, *Angew. Chem. Int. Ed.*, 2014, **53**, 6990–6992.

39 O. V. Dolomanov, L. J. Bourhis, R. J. Gildea, J. A. K. Howard and H. Puschmann, *J. Appl. Crystallogr.*, 2009, **42**, 339–341.

40 G. M. Sheldrick, *Acta Crystallogr. Sect. A Found. Crystallogr.*, 2008, **64**, 112–122.

Chapter 4| Emergent Applications of Hexakis-Adduct Fullerenes

Synopsis

The implementation of functionalised C_{60} hexakis-adducts in photo- and electro-active materials is an emergent area of research. The selective functionalisation of fullerene scaffolds instils bespoke properties that can be exploited for high performing devices and materials. We envisaged that a T_h-symmetrical hexakis-adduct of fullerene with 12 redox-active naphthalene diimide (NDI) electron acceptors could direct charge as an active layer in an organic electronic device. Solid-state self-assembly investigations by UV-Vis and PL spectroscopies provide evidence of varying intermolecular aggregation (i.e., potential charge-transport pathways) between a small family of novel acceptor molecules. Space-charge-limited diodes have been fabricated to calculate the electron-only mobility of the acceptor materials. Contrary to our initial hypothesis, for non-optimised devices we observe greater charge mobility (μ_e) in the model compounds of the hexakis-adduct system, with the fullerene species shown to be a poor electron transporting material. We also hypothesised a tetrabenzo[*a*,*c*,*g*,*i*]fluorene (TBF) hexakis-adduct of fullerene could be used as an organic dopant to increase the photocatalytic dye degradation properties of a semiconductor catalyst, i.e., ZnO. Solid-state analyses by FTIR and UV-Vis spectroscopies provides evidence for the integration of the hexakis-adduct and ZnO in a composite. An increase in dye degradation efficacy is observed for the composite in comparison to undoped ZnO. Additionally, the composite has wide applicability as it is effective against several types of dye and has high recyclability, which will serve it well in applications beyond the lab. As photo- or redox-active materials, these first-generation functionalised molecules should pave the way for fullerene hexakis-adducts to be viable candidates for various useful applications.

Acknowledgements

The following people are gratefully acknowledged for their contributions to this Chapter: Dr. Krishnamurthy Munusamy, P. Ramar, Dr. A.A Boopathi, Assistant Professor Srinivasan Sampath and Dr. Debasis Samanta for performing all solid-state analyses of the ZnO composites as well as the dye degradation studies involving TBF-based materials. David Palacios-Gomez is thanked for fabricating all space-charge-limited diode devices and calculating the mobility of all NDI-based materials. Professor Chris Groves is acknowledged for space-charge-limited diode device design and data interpretation.

4.1 Introduction

Classically, the synthesis of higher-order fullerene derivatives—especially those with T_h-symmetry—was not possible until the fullerene azido-functionalisation strategy[1] was developed by the Nierengarten group in 2008. Capitalising on Sharpless's CuAAC (Cu(I) azide-alkyne cycloaddition) 'click' reaction[2], the Nierengarten group have pioneered the synthesis, characterisation and properties analysis of functionalised fullerene hexakis-adducts. Indeed, they have designed many derivatives that have useful applications in biological systems. For instance, carbohydrate functionalised fullerenes 'sugar balls'[3] have been found to be anti-adhesive against bacterial infection whereas polycationic hexakis-adducts have gene delivery capabilities.[4] The successful application of these fullerene derivatives depends not only on the embedded 'clicked' functionality, but also on the precise three-dimensional (3D) arrangement of said pendant units. However, the applications of such systems in organic electronic materials are still limited, even though the controlled functionalisation of fullerene hexakis-adducts has enabled the study of fundamental redox- and photo-controlled processes. To this extent, viologen[5], BODIPY[6] and polycyclic aromatic hydrocarbon (PAH)[7] functionalised fullerenes have been studied (for full discussion see Chapter 1, Section 1.4.2). There is one example from Völker et al. who have integrated (Figure 4.1) a triaryl-amine functionalised hexakis-adduct into a perovskite with the fullerene species having a dual role,

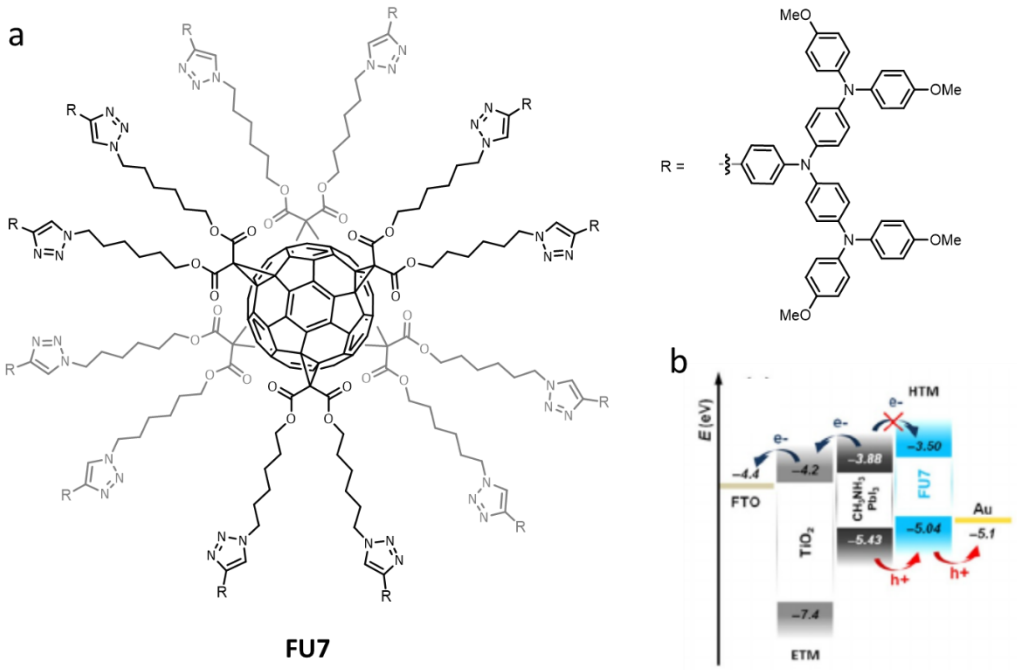

Figure 4.1. a) Chemical structure of fullerene hexakis-adduct **FU7**. b) Proposed PSC architecture showing energy level gradients; **FU7** can serve as a *p*-type semiconductor whilst also preventing the backflow of electrons towards the anode.

i.e., acting as an electron-blocking unit and providing a means for hole-transport—these properties are facilitated by the C_{60} core and the pendant aromatic units, respectively.[8]

Clearly, there is an untapped potential in the implementation of fullerene hexakis-adducts in organic electronic materials for real-life applications. With the growing need for functional organic molecules that allow for more tuneable, compact and cheaper nanotechnologies, fullerene derivatives are poised to emerge as functional organic molecules that have applications in a multitude of fields.

The progress so far in regards to the development of functional fullerene hexakis-adducts for optoelectronic applications has been discussed in Chapter 1. Despite the benefits of constructing 3D macromolecules that have tailored redox properties, integration of such molecules into devices for, e.g., organic electronics, is still rare. Here, two different applications of fullerene hexakis-adducts **12NDI** (Figure 4.2, see Chapter 2) and **12TBF** (see Chapter 3) are discussed. Capable of accepting a minimum of 24 electrons, i.e., two per NDI unit, **12NDI** has the potential to serve as an electron-transporting material for conductivity applications. The solid-state assembly of **12NDI**, and the constituent compounds that are used to form the fullerene species, is investigated by UV-Vis and PL (photoluminescence) spectroscopies as well as scanning electron microscopy (SEM). Space-charge-limited diodes have been fabricated containing an active layer of the novel acceptor compounds, with carrier mobility calculated using the space-charge-limited-current model. In the non-optimised devices, we observe the structurally less complex acceptors, i.e., **2NDI** ($\mu_e = 0.8 \times 10^{-6}\ m^2\ V^{-1}\ s^{-1}$) and **1NDI** ($\mu_e = 1.5 \times 10^{-8}\ m^2\ V^{-1}\ s^{-1}$), to have the greatest charge mobility capabilities and these molecules could function as active layers in semiconductor devices. Likewise, we can tailor the properties of functionalised hexakis-adducts by installing electron-rich pendant donor units. These donor–acceptor hybrid fullerene derivatives display light-harvesting properties that are reminiscent of natural photosynthetic systems. Donor–acceptor fullerene **12TBF** exhibits multi-redox and light-harvesting properties, as identified by cyclic voltammetry (CV) experiments and UV-Vis and PL spectroscopies (see Chapter 2). When combined with zinc oxide (ZnO), a common inorganic photocatalyst, **12TBF** is shown to mitigate the high h^+ and e^- recombination rates that limit the use of ZnO in practical dye photodegradation applications. To this end, a composite of **12TBF** with ZnO has been prepared and characterised by FTIR and UV-Vis spectroscopies, as well as powder X-ray diffraction (PXRD) which confirms a change to the optical properties upon composite formation but no change in the crystalline form of the ZnO nanoparticles. The organic–inorganic composite has been investigated as a photocatalyst for dye degradation with increased efficacy observed for the composite, in comparison to lone ZnO, for five industrially relevant dyes. A mechanism has been proposed to rationalise the increased efficacy with our

current understanding that efficient h^+ transfer from the TBF units to ZnO prevents h^+ and e^- recombination on the inorganic catalyst. There is promise for both **12NDI** and **12TBF** to find use as functional molecules in two very different, but important applications. These studies were primarily conducted by collaborators, and presented here is my interpretation of the data.

4.2 NDI–Fullerene Hybrids as Electron Transport Materials

To date, there are ample examples of *p*-type semiconductors with excellent charge carrier mobilities whereas there are far lower performance comparable *n*-type organic semiconductor materials[9]. For injection charge to be facilitated by *n*-type organic materials, electron-deficient molecules that have low energy LUMOs (i.e., lowest unoccupied molecular orbital) are required. In addition, for the material to be stable in air, its LUMO energy ideally falls below that of water and oxygen, where –4 eV tends to be favourable. Fullerene acceptors (FAs)[1] and their derivatives have been extensively studied as electron acceptor materials owing to their high electron affinity, mobility and their ability to percolate charge in thin films as well as in

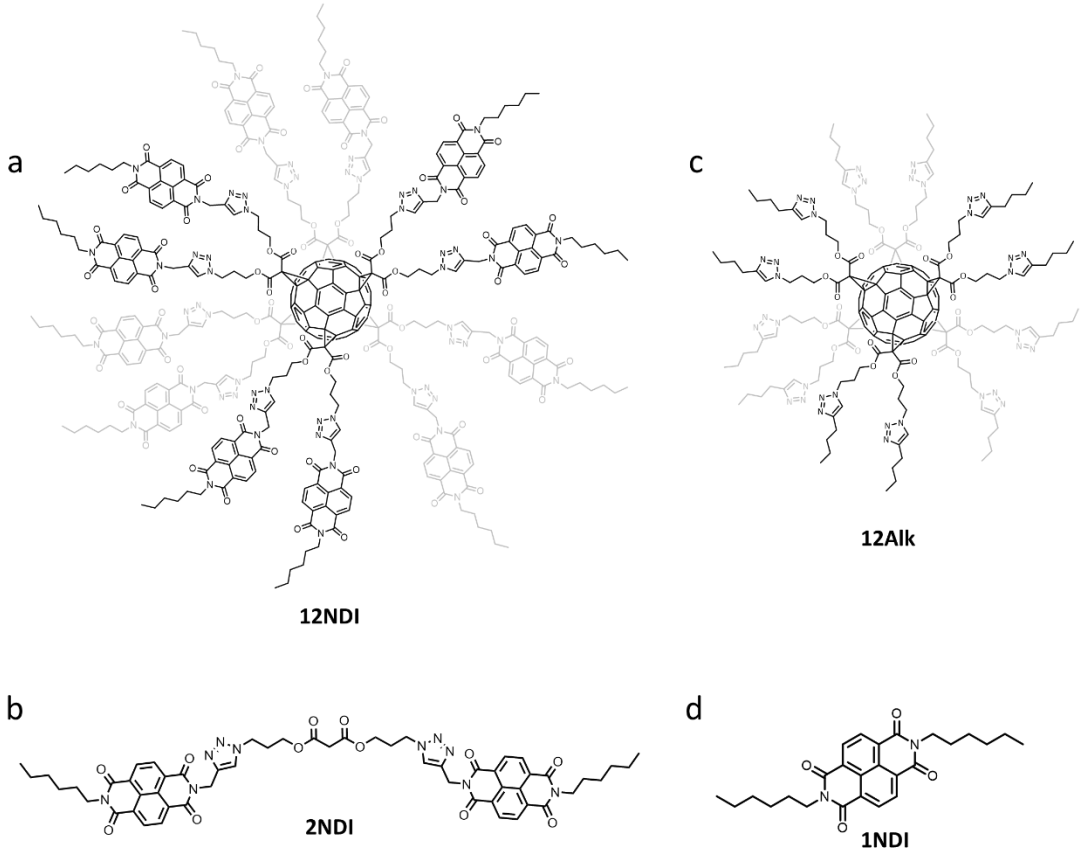

Figure 4.2. Chemical structure of a) fullerene hexakis-adduct **12NDI**, b) divalent **2NDI**, c) fullerene hexakis-adduct **12Alk** as well as d) monovalent **1NDI**.

binary material mixes (e.g., bulk hetrojunction organic solar cells). However, FAs have inherent limitations with their poor synthetic flexibility, as well as their high propensity to degradation. Consequently, new classes of electron acceptor materials, prosaically termed non-fullerene acceptors (NFAs), have come about as alternatives to traditional FAs. Specifically, rylene imide dyes such as perylene diimide (PDI) and naphthalene diimide (NDI) have emerged as promising candidates to replace traditional FA-based materials. As electron-deficient molecules, PDI and NDI have low energy LUMOs and thus are capable of behaving as *n*-type organic semiconductors. We rationalised that the electron sharing capabilities of **12NDI** and **2NDI** (Figure 4.2b) would allow them both to mediate charge in an organic electronic device (OED). Whereas **12NDI** has the potential to form extended charge-transport pathways in 3D space (Figure 4.3a), divalent **2NDI** (Figure 4.3b) shares similar photophysical properties yet different self-assembly properties. In addition to **12NDI** and **2NDI**, the synthesis of electronically active control compounds, i.e., a fullerene core bearing no NDI units, **12Alk** (Figure 4.2c), and a monomer NDI species *bis*-hexyl NDI (**1NDI**, Figure 4.2d) has allowed for the study of charge mobility in a small family of FA/NFA and FA–NFA hybrids.

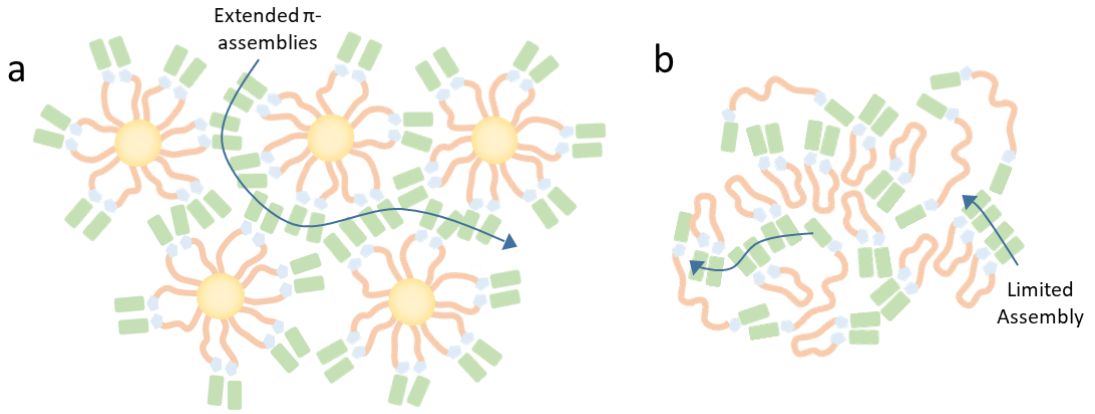

Figure 4.3. Potential intra- and intermolecular NDI assembly pathways of a) **12NDI** and b) **2NDI** that may lend themselves to charge-transport pathways in the active layer of device.

4.2.1 Solid-State Self-Assembly of Acceptor Molecules

First, we investigated the solid state intramolecular NDI π-interactions of the acceptor molecules using absorption and emission spectroscopies. Neat thin films were prepared by drop-casting *o*-dichlorobenzene solutions onto quartz substrates that were dried overnight under vacuum (<0.1 mbar). *o*-Dichlorobenzene (*o*-DCB) is a common solvent used in organic electronic device fabrication as it can solubilise fullerene derivatives, however, it was also chosen to encourage[10] intramolecular NDI π-interactions during evaporation of the solvent.

Optical absorption analysis is important in identifying aggregation and the presence of potential charge transport pathways between molecules. The thin-film absorption spectra of **1NDI**, **2NDI**

and **12NDI** (solid lines, Figure 4.4) all display the characteristic NDI peaks (i.e., ca. 360 and 380 nm) between 300–400 nm. In the solid state, **1NDI** shows a peak at 369 nm with a λ_{max} at 392 nm. However, the ratio (A_{380}/A_{360}) between the two absorptions is inverted in **2NDI** and **12NDI** (**1NDI** = 1.09, **2NDI** = 0.95 and **12NDI** = 0.95). These observations indicate there is greater propensity for NDI intermolecular aggregation in **2NDI** and **12NDI**. However, the onset of absorption is lower in energy for **1NDI** (λ_{onset} = 417 nm) and **2NDI** (λ_{onset} = 424 nm) in comparison to **12NDI** (λ_{onset} = 409 nm) which also indicates that NDI aggregation is present for the model acceptor molecules **1NDI** and **2NDI**.

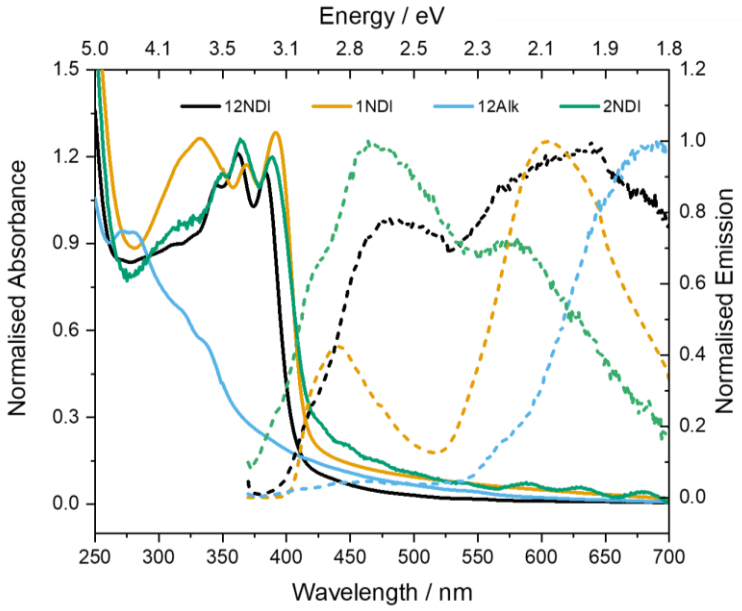

Figure 4.4. Solid-state absorption spectra of **12NDI** (black line), **12Alk** (blue line), **2NDI** (green line) and **1NDI** (gold line); samples were prepared by drop-casting *o*-DCB solutions onto quartz before drying overnight under vacuum. Solid-state emission profiles of **12NDI** (black dotted line), **12Alk** (blue dotted line), **2NDI** (green dotted line) and **1NDI** (gold dotted line).

The NDI aggregates can be further identified with a loss of vibronic structure in their emission profiles that is concomitant with the rigidification of closely coupled NDI units in the electronically excited state. Extensive excimer-like emission (i.e., <450 nm) is observed (dotted lines, Figure 4.4) for all NDI compounds. For **1NDI**, a significant contribution from lower energy emission ($\lambda_{em.max}$ = 606 nm) is observed in comparison to higher energy excimer-like emission ($\lambda_{em.max}$ = 439 nm). The lower energy emission suggests extensive intermolecular NDI aggregation is present for **1NDI**, thus confirming the ground state observations by UV-Vis spectroscopy.[11,12,13] On the other hand, the intensity of these emission bands at ca. 460 and 580 nm are inverted for **2NDI** and broadened which indicates extensive intermolecular NDI aggregation is present in what is likely a different packing arrangement to that observed for **NDI1**.[14] Similarly, a different packing arrangement is rationalised from the emission profile of **12NDI**, in which the higher energy emission ($\lambda_{em.max}$ = 479 nm) is further red shifted ($\Delta\lambda$ = 19 nm) than **2NDI**. Additionally, the emission profile shows a significant

contribution in the NIR region between 525 and 700 nm. The lower-energy emission could arise from intramolecular NDI aggregation around the hexakis-adduct, however, it is likely that both inter- and intramolecular NDI aggregation is present between the fullerene molecules. For **12Alk**, emission from the fullerene core is observed at ($\lambda_{em.max}$ = 700 nm), significantly lower in energy from that of the excimer-like NDI aggregates. Ultimately, the broadened emission profiles indicate there is different aggregation—and potential charge transport pathways—between the NDI units for **12NDI**, **2NDI** and **1NDI**.

SEM analysis was then conducted to investigate the morphologies of the thin films. Whereas the morphology is not a direct indication of the bulk aggregation, it can identify highly crystalline or amorphous aggregation patterns that may in turn relate to the self-assembly of the organic molecules. The resulting intermolecular forces that drive molecular assembly into highly ordered aggregates can be very important in forming close contacts between conjugated sites that provide efficient pathways for the delocalisation of charge. SEM samples were prepared on silicon wafers from solutions in *o*-DCB. The dried organic deposit was coated in gold nanoparticles (10 nm) before imaging with an FEI Helios dual-beam scanning electron microscope (see Experimental Section 4.4.1 for full substrate preparation details and Figures 4.19–21, appendix for additional images). The surface morphology of **1NDI** reveals a highly crystalline state (Figure 4.5a) wherein long-range ordering is present, i.e., plates of up to

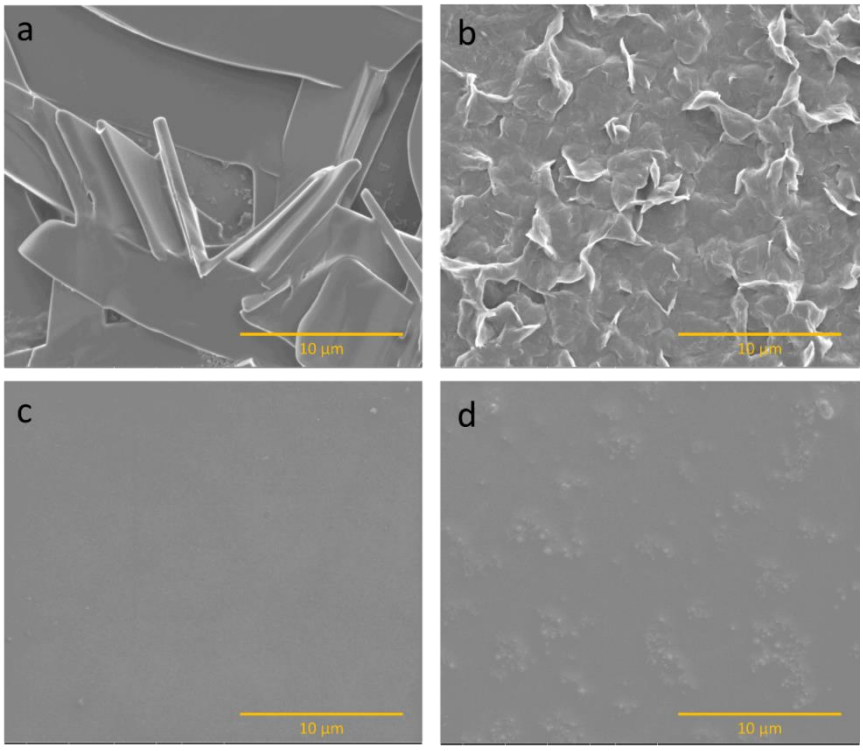

Figure 4.5. Scanning electron micrographs of a) **1NDI**, b) **2NDI**, c) **12NDI** and d) **12Alk**, drop-cast from *o*-DCB solutions (1 mg/ mL) onto pristine silicon wafers. Magnification: 10000x.

30 μM in length are observed. Observations are significantly different for divalent compound **2NDI** wherein fibrillar aggregates (Figure 4.5b) are most common. Additionally, some areas of monodisperse spherical aggregates (4 μm in diameter, see Figure 4.20e, appendix) are observed, likely forming as a result of concentration gradients upon the drying of the films. In comparison to **2NDI**, the increased molecular flexibility (i.e., intramolecular folding) may allow for the controlled assembly into spherical aggregates. However, the main morphology observed is the fibrillar aggregation. In contrast, no noticeable morphology is observed (Figure 4.5c) from drop-cast solutions of **12NDI**, with what is most likely an amorphous thin film of compound. This loss in ordered assembly (in comparison to **2NDI**) is expected owing to the spherical molecular shape that should hinder packing of aggregates into crystalline domains. The formation of the thin film may provide a controlled 3D network of favourable π-interactions between NDI units on neighbouring **12NDI** molecules. This controlled morphology is evidenced by analysis of **12Alk** where with areas of much greater disorder and varying particulate sizes are present (Figure 4.5d). As there are only non-directional interactions between neighbouring **12Alk** molecules, there is no aid to forming a uniform thin film as demonstrated with the aromatic interactions that can drive assembly of **12NDI**. With evidence of varying self-assembly processes, likely dictated by intermolecular NDI aggregation in the solid state, attention was turned to fabricating space-charge-limited diode devices. As electron only devices, the electron transport in the bulk materials can be calculated. This work was completed by a fellow PhD student in the Department of Engineering at Durham University—David A. Palacios-Gomez, under the supervision of Professor Chris Groves.

4.2.2 Charge Mobility Studies of Acceptor Molecules

The field effect transistor (FET) and space-charge-limited current (SCLC) methods are both widely used to measure the charge mobilities of organic semiconductor materials.[15–17] One of the advantages of using the SCLC model is that the properties can be measured using thin films, with a device fabrication that is similar to that of an organic photovoltaic (OPV). To focus on the electron-only properties of the FA/NFA and FA–NFA hybrids, the devices (Figure 4.6a) were sandwiched between PEDOT:PSS (Figure 4.6c) and LiF electrodes; PEDOT:PSS has a work function of 5.2 eV and therefore hole injection into the HOMO of the novel acceptors is supressed (Figure 4.6b). The synthesised materials were tested for electron transport in electron-only devices by the SCLC method, with a device configuration of glass/ITO/PEDOT:PSS/**active layer**/LiF/Al (see Appendix and Supplementary Information Section 4.3.3 for full device preparation details). Following active layer deposition, the devices were thermally annealed at 120 °C for 10 minutes.

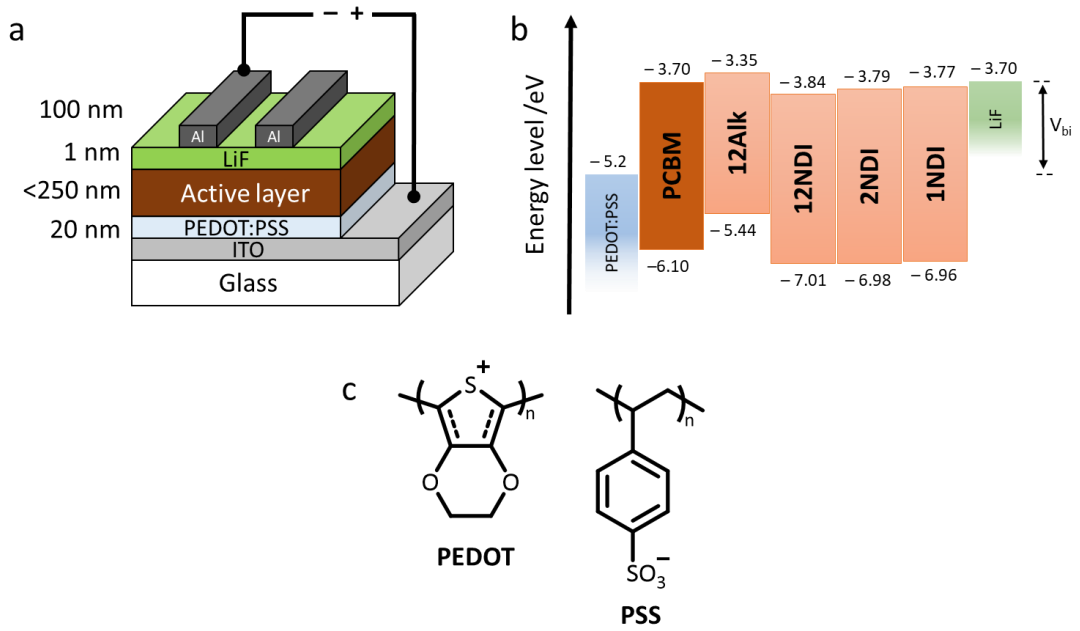

Figure 4.6. a) Schematic of the device architecture. b) HOMO and LUMO energy levels of the materials used to construct the active layer of the devices as well as HOMO energy levels for PEDOT:PSS and LiF (V_{bi} = 1.5*V*). c) Chemical structures of macromolecular salt PEDOT:PSS.

Generally, the thicker an active layer, the more likely disorder may be present resulting in increased h^+ and e^- recombination and therefore a lower carrier mobility.[18,19] However, we fabricated devices with thin (ca. 100 nm) and thick (ca. 250 nm) active layers to determine if performance was limited by injection currents or space-charge currents, with the latter allowing for the performance of the semiconductor material to be calculated. A quadratic relationship between voltage (*V*) and the current density (*J*) reveals that current is dominated by carriers injected from the contacts and that performance correlates to space-charge currents. Hence, the current is only dependent on mobility which in turn can be estimated from *J*–*V* measurements, e.g., *via* the Mott–Gurney (eq. 1) method. High charge carrier mobility would be expected from materials that have high conductivity such as a metal or highly doped semiconductor and this is beyond the scope of the Mott–Gurney method—a linear relationship between *V* and *J* is observed in this situation.

$$J = \frac{9}{8}\varepsilon_0\varepsilon_r\mu\frac{(V_{app}-V_{bi})^2}{d^3} \qquad \text{(eq. 1)}$$

J = current density, d = thickness of active layer, V_{app} = applied potential, V_{bi} = built-in potential, ε_0= vacuum permittivity, ε_r = permittivity of active layer, μ = electron mobility of material.

Devices were fabricated with active layers of the NDI compounds **12NDI**, **2NDI** and **1NDI**. In addition, devices containing an alkyl-substituted fullerene hexakis-adduct **12Alk** and **PCBM** were also fabricated as controls with inefficient and efficient charge mobility performance, respectively. The charge mobility results are summarised in Table 4.1.

Table 4.1. Summary of charge mobility described by SCLC model for devices constructed as glass/ITO/PEDOT:PSS/**active layer**/LiF/Al; V_{bi} of 1.5V.

Active Layer	Thickness (nm)	$\mu_{electron}$ mobility ($m^2\ V^{-1}\ S^{-1}$)
PCBM	240	2.90×10^{-6}
12Alk	200	1.03×10^{-11}
12Alk	145	1.43×10^{-11}
1NDI	248	0.73×10^{-8}
1NDI	100	1.50×10^{-8}
2NDI	220	0.80×10^{-6}
12NDI	189	2.47×10^{-11}
12NDI	139	0.82×10^{-11}
12NDI;**2NDI** [1:1]	191	3.00×10^{-9}
12NDI;**2NDI** [1:2]	167	1.75×10^{-8}

A SCLC diode comprising **PCBM** was characterised to validate the working device architecture and provide a benchmark for assessing the performing of devices involving novel active materials. **PCBM** is a well-known, and well-studied, electron-acceptor material that has a mobility of $\mu_e = 2 \times 10^{-7}\ m^2\ V^{-1}\ s^{-1}$.[20] Although thin-film (120 mm) devices comprising

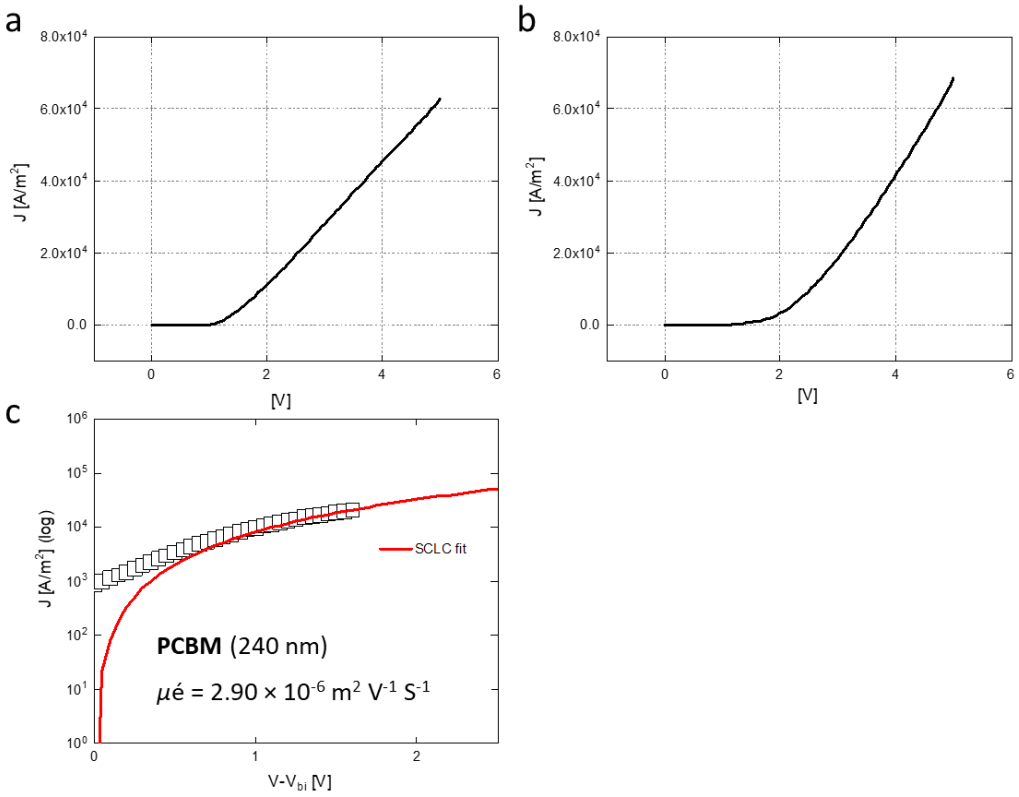

Figure 4.7. *J–V* dark characteristics of electron-only devices based on glass/ITO/PEDOT:PSS/**PCBM**/LiF/Al for a) thin (120 nm) and b) thick (240 nm) films. c) Experimental electron transport (square) measured by SCLC (solid line) with a mobility of $2.90 \times 10^{-6}\ m^2\ V^{-1}\ S^{-1}$ using V_{bi} of 1.5 *V*. *Electron mobility not measured for the thin film due to the linear *J–V* behaviour which is not characteristic of the SCLC model.

PCBM did not display charge mobility behaviour within the space-charge regime (i.e., characterised by a linear *J–V* curve; Figure 4.7a), thicker devices (240 mm; Figure 4.7b) allowed us to determine by eq. 1 a charge mobility of 2.90×10^{-6} m^2 V^{-1} S^{-1} using V_{bi} of 1.5 *V*. This value is similar to that observed in the literature[20] and therefore confirms the integrity of the device architecture.

Attention was then turned towards characterising the charge mobility of the NDI derivatives. Absorption and emission studies of **1NDI** suggested there was extensive intermolecular NDI aggregation and therefore the presence of extended charge-transport pathways. SEM analysis of **1NDI** also identified highly crystalline domains that were representative of a highly ordered morphology. Thin-film (100 mm) and thicker (248 nm) devices comprising of **1NDI** displayed charge mobility behaviour within the space-charge regime (i.e., characterised by a quadratic *J–V* curve; Figure 4.8a), allowing us to determine by eq. 1 charge mobilities of 1.50×10^{-8} m^2 V^{-1} S^{-1} and 0.73×10^{-8} m^2 V^{-1} S^{-1} using V_{bi} of 1.5 *V* for the 100 and 248 nm films, respectively. These modest charge carrier mobilities for **1NDI** are 1–2 orders of magnitude lower than those of similar NDI derivatives,[21] however, for a non-optimised device, these values are promising. Kumar et al. have shown[21] that annealing the active layers at high temperatures (200 °C) can enforce greater structural order and high carrier mobility for simple

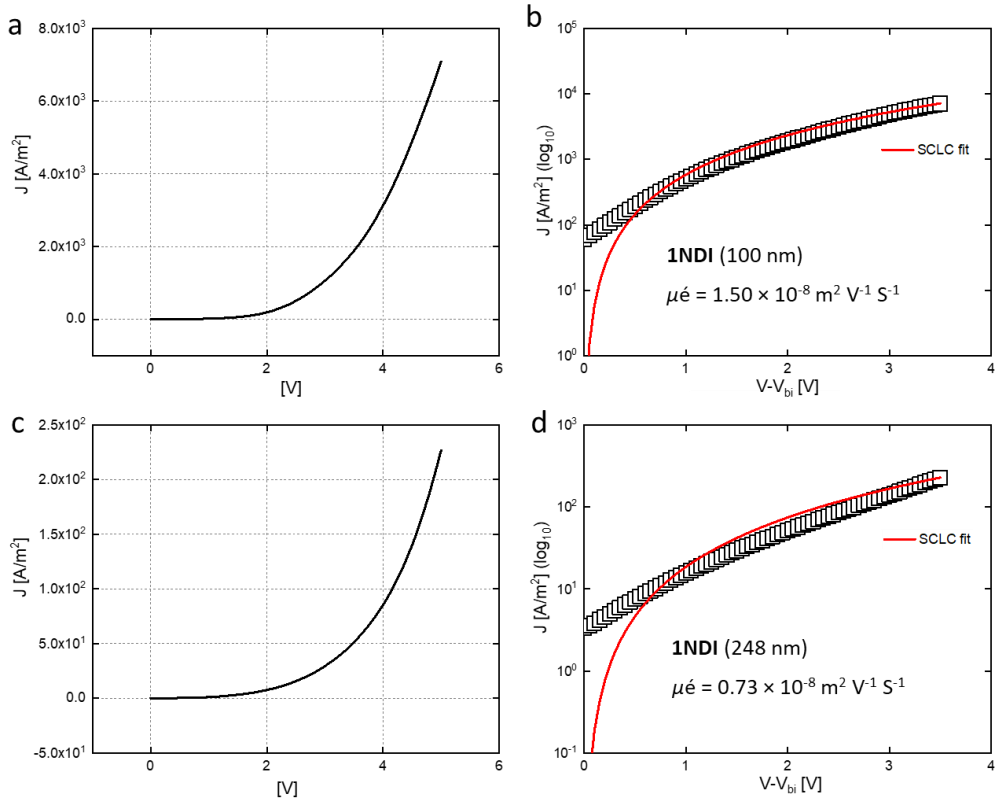

Figure 4.8. *J–V* dark characteristics of electron-only devices prepared with glass/ITO/PEDOT:PSS/**1NDI**/LiF/Al for a) 100 and c) 248 nm films. Experimental electron transport (square) as described by SCLC measurement (solid line) with a mobility of 1.50×10^{-8} m^2 V^{-1} S^{-1} at 100 nm b) and 0.73×10^{-8} m^2 V^{-1} S^{-1} at 248 nm d) using, V_{bi} of 1.5V.

alkyl-substituted NDI derivatives. They also rationalised the improved charge transport properties were as a result of long range π-aggregation and reduced orientation disorder, in a similar manner to that also discussed by Avinash et al.[22]

For the divalent NDI species **2NDI**, the photophysical, as well as morphology studies, suggested a significantly different assembly of NDI units in comparison to **1NDI**. Extensive NDI intermolecular aggregation was confirmed by emission spectroscopy with SEM analysis revealing a morphology that was dominated by fibrillar assembly, i.e., a more amorphous morphology than that of **1NDI**. Thin-film (83 mm) devices comprising **2NDI** displayed linear *J*–*V* behaviour not within the space-charge regime indicating that charge mobility is high for the divalent molecule. Thicker devices (220 nm; Figure 4.8b) allowed us to determine by eq. 1 a charge mobility of 0.8×10^{-6} m^2 V^{-1} S^{-1} using V_{bi} of 1.5 *V*. This relatively high mobility is 1–2 orders of magnitude greater than that observed for **1NDI**, and is likely facilitated by greater long-range assembly of NDI units. The SEM morphology analysis showed less order for **2NDI** (than the crystalline **1NDI**), however, the fibrillar networks may provide more extensive charge-transport pathways that can govern increased charge mobility. With optimisation *via* various annealing temperatures and potentially the addition of morphology

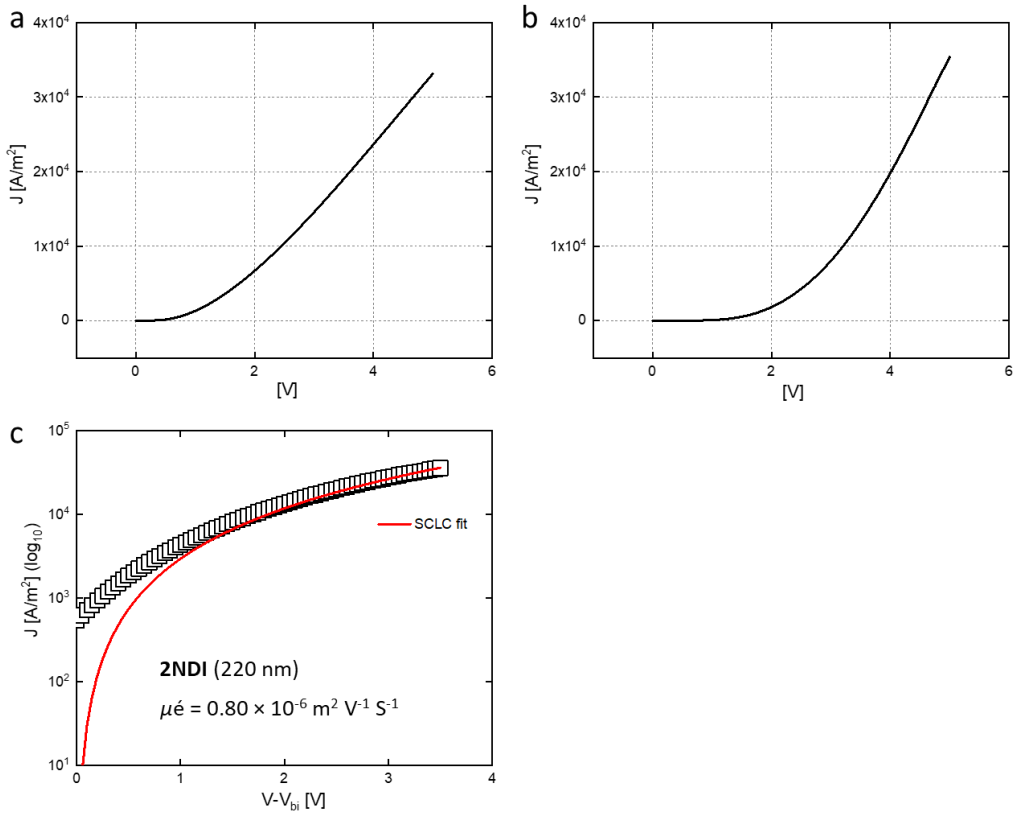

Figure 4.9. *J*–*V* dark characteristics of electron-only devices based on glass/ITO/PEDOT:PSS/**2NDI**/LiF/Al for a) thin (83 nm) and b) thick (220 nm) films. c) Experimental electron transport (square) measured by SCLC (solid line) with a mobility of 0.8×10^{-6} m^2 V^{-1} S^{-1} using V_{bi} of 1.5 *V*. *Electron mobility not measured for the thin film due to the linear *J*–*V* behaviour which is not characteristic of the SCLC model.

controlling additives, the enhanced electronic properties of **2NDI** could lead it to be a promising candidate for implementation into an organic electronic device.

The FA–NFA hybrid **12NDI** is functionalised with 12 NDI units that are distributed in 3D space. If the molecular packing is in a similar manner to that observed for **2NDI**—the closely related 'ungrafted' arm of **12NDI**—then extended charge transport pathways may be possible throughout the thin film. Thin-film (139 mm) and thicker devices (189 nm) comprising **12NDI** displayed quadratic *J*–*V* behaviour within the space-charge regime allowing us to determine charge mobilities of 0.82 and 2.47 × 10^{-11} m^2 V^{-1} S^{-1} using V_{bi} of 1.5 *V* for the 139 and 189 nm films, respectively. The low carrier mobilities are similar to alkyl-substituted fullerene hexakis-adduct control **12Alk** (1.43 × 10^{-11} and 1.03 × 10^{-11} m^2 V^{-1} S^{-1} using V_{bi} of 1.5 *V* for 145 and 200 nm thick films, respectively; Figure 4.23, appendix). These data suggest the percolation of charge is not being facilitated by the NDI units in **12NDI**, but by the fullerene hexakis-adduct core which itself is an ineffective material for charge transport. Comparing the molecular design of **12NDI** to Völker's fullerene **FU7** (*vide supra*, Figure 4.1), it is possible that increased linker length between the C_{60} core and the NDI residues, as well as increasing the density of NDI residues on each arm, may facilitate higher levels of charge mobility. The

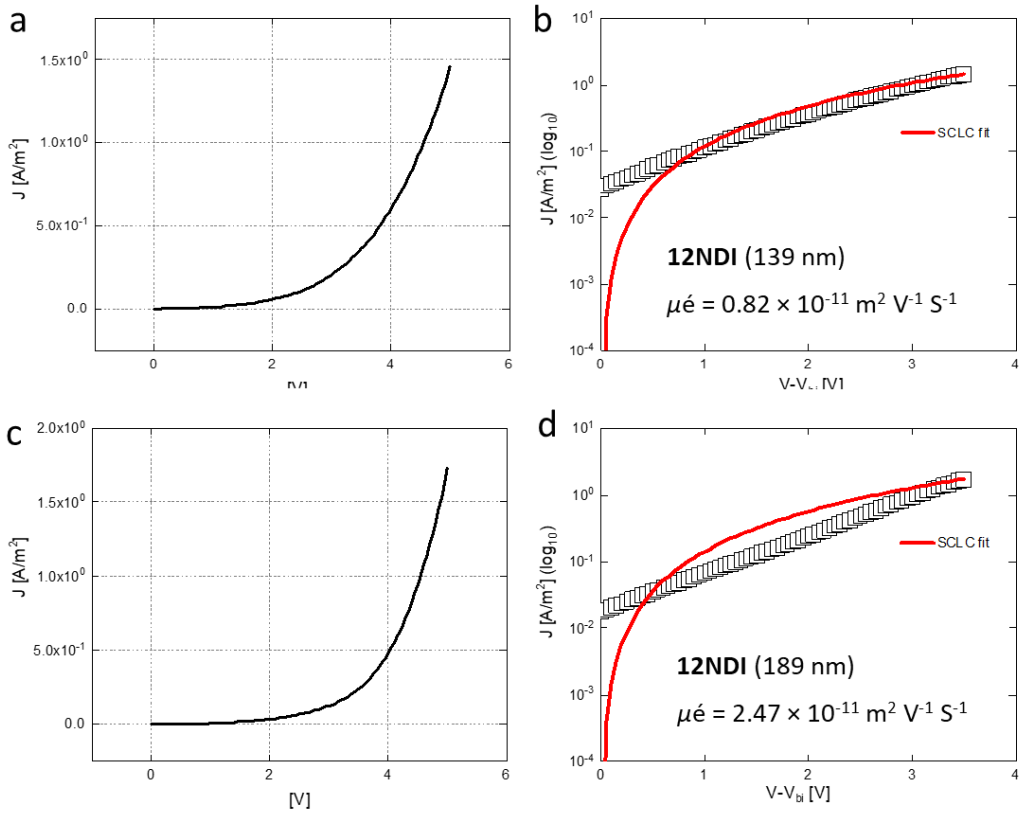

Figure 4.10. *J*–*V* dark characteristics of electron-only devices prepared with glass/ITO/PEDOT:PSS/**12NDI**/LiF/Al for a) 139 and c) 189 nm film. Experimental electron transport (square) as described by SCLC measurement (solid line) with a mobility of 0.82 × 10^{-11} m^2 V^{-1} S^{-1} at 139 nm b) and 2.47 × 10^{-11} m^2 V^{-1} S^{-1} at 189 nm d) using, V_{bi} of 1.5 *V*.

increased molecular flexibility may promote the formation of long-range charge transport pathways between NDI residues as observed for **2NDI**. In order to probe if incomplete NDI–NDI charge-transport pathways were the cause of the low mobility observed for **12NDI**, blends of **12NDI** and **2NDI** were fabricated. Here, the mobility (Figures 4.24/25, appendix) rose linearly with increasing amount of **2NDI** in the blend, suggesting that **12NDI** and **2NDI** were not intercalating to form extended charge transport pathways.

We have implemented our novel acceptor molecules into the fabrication of space-charge-limited diodes. The devices have been used to calculate the charge mobility of the materials as electron-only devices using the space-charge-limited current model. In conjunction with their photophysical as well as morphology studies, the observed carrier mobilities can be rationalised and understood. The best performing device is that with an active layer of **2NDI** that has a charge mobility of $0.80 \times 10^{-6}\,m^2\,V^{-1}\,S^{-1}$; a high mobility such as this suggests that **2NDI** could find use in an organic electronic device. Following device optimisation from, e.g., annealing the active layers at various temperatures or from the addition of additives, the formation of more ordered charge-transport pathways may be realised. These preliminary charge mobility studies indicate there is promise for NDI-functionalised fullerene hexakis-adducts to be used as functional organic materials for applications in charge delocalisation and conductivity. Increasing the local concentration of NDI units may provide more complete charge-transport pathways for high levels of charge mobility, whilst maintaining the advantages of having a processable and morphology-controlled material for organic electronic materials. Additionally, an NDI-substituted hexakis-adduct with increased molecular flexibility may facilitate a 3D network for charge delocalisation in a manner that is currently not possible for **12NDI**. Device optimisation and the synthesis of these compounds is currently underway.

4.3 A Donor–Acceptor Fullerene for Water Remediation

Depending on the functional unit, fullerene hexakis-adducts can have applications as, e.g., diodes, transistors or photovoltaics. However, organic electronic materials are not the only potential application when hexakis-adducts are functionalised with redox-active units. For instance, fullerene hexakis-adducts can be integrated into inorganic composites to alter the properties of functional semiconductor materials. Specifically, photocatalysis using metal oxides (MOs) is an area of research that currently strives for increased efficacies by composite formation with organic dopants. Here, we explore a composite of **12TBF** with the aim of overcoming some of the current limitations with the use of ZnO a photocatalyst. Donor–acceptor hexakis-adduct **12TBF** has light harvesting applications, multi-redox activity and

potential binding affinity with two-dimensional (2D) substrates that may aid h^+ and e^- recombination on ZnO thereby increasing the photocatalytic efficacy with regards to dye degradation applications.

Water pollution is a global problem that is growing in severity. Rapid population growth, as well as the boom of the textiles industries, has fuelled water pollution with organic materials that are extremely harmful to not only humans, but aquatic life and animals too.[23] Over the past 20 years, researchers have developed various strategies for treating water polluted with waste organic dyes with photocatalysis emerging as a front-runner. MOs such as TiO_2 and ZnO have been extensively investigated as semiconductor photocatalysts; they are low-cost, resistant to erosion and non-toxic.[24,25] Upon sunlight irradiation, TiO_2/ZnO form charge carriers as h^+ and e^- pairs. Subsequently, a series of chemical reactions (Scheme 4.1) can occur that generate species such as $^{\bullet}OH$ (eq. 2), H_2O_2 (eq. 2) and $^{\bullet}O_2^-$ (eq. 3), that are responsible for degrading organic pollutants in water.

$$2H_2O \xrightarrow{4h^+} 4\,^{\bullet}OH \longrightarrow 2H_2O_2 \qquad \text{(eq. 2)}$$

$$O_2 \xrightarrow{e^-} {}^{\bullet}O_2^- \xrightarrow{H^+} {}^{\bullet}HO_2 \xrightarrow{H^+ + e^-} H_2O_2 \qquad \text{(eq. 3)}$$

Scheme 4.1. Upon photoirridation, h^+ and e^- pairs form on MO nanoparticles; these are the sites upon which O_2 and H_2O ultimately form reactive species such as $^{\bullet}O_2^-$, $^{\bullet}OH$ and H_2O_2 that degraded organic pollutants such as dyes.

However, one of the major drawbacks in accessing high levels of photocatalytic activity for ZnO and titanium dioxide (TiO_2) is the rapid recombination of the h^+ and e^- pairs. The large band gaps for MO also limit their absorption from the visible-light region of solar energy.[25] In order to generate high concentrations of reactive species such as hydrogen peroxide (H_2O_2), organic additives such as electron acceptor materials, e.g., graphene, can be used to prevent recombination on the MO by trapping the charge carriers and increasing the amount of solar energy that can be harvested by the catalyst.[26–30] Additionally, fullerenes such as C_{70}[31] and C_{60}[32] have also been explored as acceptor materials that increase the photocatalytic efficacy of ZnO and TiO_2, respectively. To date, the use of fullerene hexakis-adducts has not been explored for increasing the efficacy of MOs with regards to dye degradation applications. Yet, these systems could offer electron-acceptor, light-harvesting and anti-photocorrosive properties that would increase the device performance of semiconductor photocatalysts.

Fullerene hexakis-adduct **12TBF** (Scheme 3.2, see Chapter 3 for synthesis and optoelectronic characterisation) is as a multi-redox molecule that possesses light-harvesting properties. We envisaged that **12TBF** could enhance the photocatalytic efficiency of ZnO by participating in redox reactions that prevent recombination of h^+ and e^- on ZnO and ultimately the generation of degrading radical species. In addition, interaction of **12TBF** with the inorganic nanoparticles

could also modify the band gap and therefore increase the extinction coefficient of absorbed solar energy, i.e., in the visible region, to further increase photocatalytic efficacy.

4.2.1 Preparation of a TBF-Fullerene–ZnO Composite

To make (Scheme 4.2) the organic–inorganic composite, ZnO was first dispersed in ethanol by sonication (see Appendix and Supplementary Information Section 5.3.5 for full synthetic details). The organic compound was then added to the ZnO suspension and the components were mixed in the dark before drying.

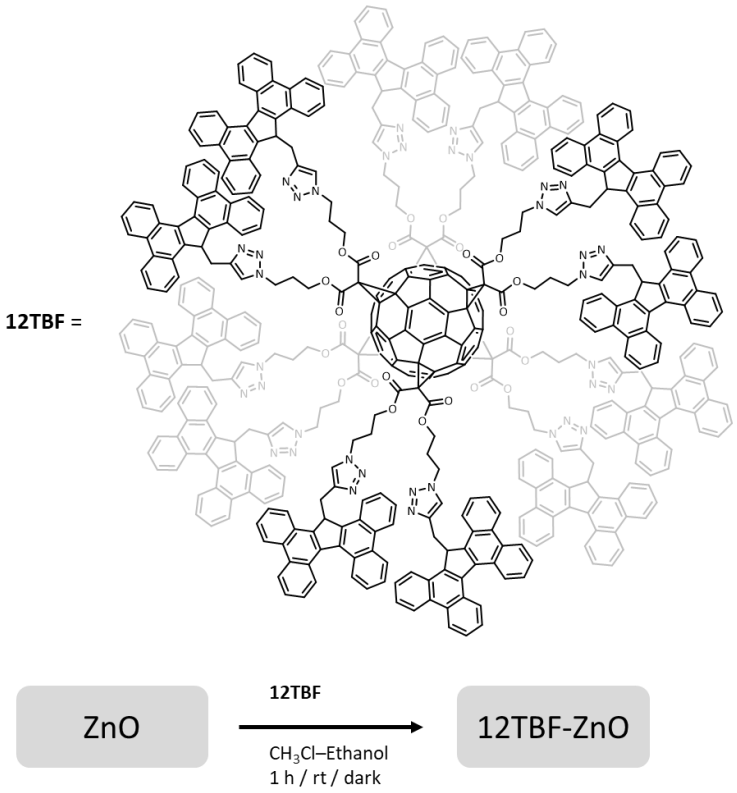

Scheme 4.2. Preparation of **12TBF**-ZnO composite. The ZnO was initially dispersed using sonication for 1 hr.

Initially, a composite containing 1wt% **12TBF** was prepared with FTIR spectroscopy used to confirm the presence of **12TBF** in the composite. ZnO is typically identified by a band (Figure 4.11) at ca. 520 cm^{-1} in the FTIR spectra.[33] Additionally, bands at 3400 cm^{-1} and between 1300–1750 cm^{-1} correspond to surface interactions with air, i.e., water and carbon dioxide. For the composite, these bands (Figure 4.11) arising from surface interactions are diminished significantly, suggesting that **12TBF** is decorated as a layer across the surface of the ZnO nanoparticles. The band at 520 cm^{-1} has also shifted to a lower wavenumber which suggests a lengthening of the Zn–O bond and an interaction with **12TBF**. The aromatic C–H stretches of the TBF units are observed in the composite at ca. 3000 cm^{-1}, however, no significant shifts are observed in comparison to bare **12TBF**.

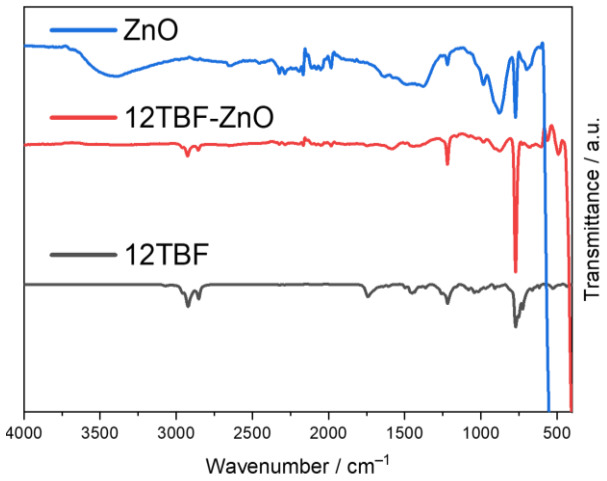

Figure 4.11. FTIR spectra of individual components ZnO (blue) and **12TBF** (black), and composite **12TBF**-ZnO (red).

PXRD patterns were then collected in order to probe any change to the crystalline structure and size of ZnO upon composite formation. The PXRD pattern of bare ZnO (Figure 4.29, appendix) indexed to the well-established (100), (002), (101), (102), (110), (103), (200), (112), (201), (004), (202) crystal planes of its hexagonal lattice geometry.[34] The diffraction patterns are relatively unchanged for the ZnO-C_{60} and ZnO-**12TBF** composites suggesting there is no significant change to the crystalline structure of ZnO following composite preparation. The ZnO particle size was calculated for each composite using the Debye–Scherrer equation using 2θ = 35.9.

$$D = \frac{K\lambda}{\beta_{hkl} cos\theta} \qquad \text{(eq.4)}$$

where β_{hkl} is the integral half width, K is a constant equal to 0.9, k is the wave length of the incident X-ray (k = 1.5406 Å), D is the crystallite size, and θ is the Bragg angle.

The crystallite sizes were found to be 30.4, 32.6 and 31.4 nm for ZnO, C_{60}-ZnO and **12TBF**-ZnO, respectively, confirming that the preparation of the composites did not alter ZnO particle sizes. Furthermore, the similar crystallite sizes confirms that the surface area of the ZnO nanoparticles will be of similar size and therefore the number of reactive sites available for dye degradation processes should be the same throughout, with the change in efficacy directly correlated to the organic dopant.

To probe any changes to the band gap of ZnO, UV-Vis diffuse-reflectance spectroscopy (DRS) was conducted (Figure 4.27, appendix) for the composite materials and Tauc plots, which allow for the direct band gap energy, were generated (Figure 4.12 and see Figure 4.28, appendix). ZnO was calculated to have an apparent band gap of 3.08 eV, which is similar to that previously reported for ZnO nanoparticles.[35] For C_{60}-ZnO and **12TBF**-ZnO, the apparent band gap is

increased to 3.14 and 3.19 eV, respectively. Here, a blue shift in absorption could be evidence of Burstein–Moss (BM) effect[36], i.e., if the conductance band of ZnO is populated with electrons, the e^- excited from the valence band will be forced to occupy a higher energy band. Consequently, a blue shift in absorption and an increase in the band gap occurs.With evidence that the properties of ZnO are modified—even at 1 wt%—attention was then turned towards dye degradation experiments with a staple dye, Rhodamine B (RhB).

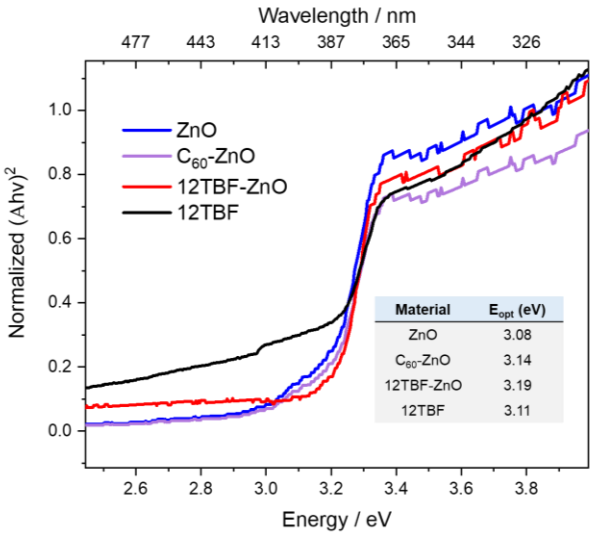

Figure 4.12. Tauc plots i.e., plot of $(Ahv)^2$ vs. energy (eV) for ZnO (blue), C_{60}-ZnO (purple), **12TBF**-ZnO (red) and **12TBF** (black); A = absorption, hv = incidence photon energy. Inset shows calculated optical band gap (E_{opt}) taken from x-axis intercept.

4.3.2 Dye Degradation Properties of a TBF-Fullerene–ZnO Composite

With the **12TBF**-ZnO composite in hand, dye degradation studies were initially performed in aqueous solutions of RhB dye at varying concentrations of RhB. In order to fully understand the donor–acceptor fullerenes role, control composites were prepared and analysed alongside with all composites at 1wt % dopant. All experiments were carried out under irradiation of light for 120 minutes and the concentration of dye in solution was monitored by steady-state UV-Vis spectroscopy. The dye removal efficacy of composites was calculated using eq. 5 below.

$$\text{Removal of Dye (\%)} = (C_i\text{-}C_f)\,/C_i \times 100 \qquad \text{(eq. 5)}$$

C_i = initial concentration of dye and C_f = final concentration of dye.

Initially, composites were screened for their photocatalytic activities to degrade RhB dye at 1 wt% doping of organic material. UV-Vis spectroscopy was used to monitor the removal of dye from solution, i.e., the degradation efficacy. Composite **12TBF**-ZnO outperforms (Figure 4.13) all other control composites, as well as ZnO, for all experiments at various

starting concentrations of dye. At 12 ppm of dye, the **12TBF**-ZnO composite still removes 75% of dye from solution whereas the performance of ZnO drops to 34%. All other controls perform at 52–61% at 12 ppm, significantly less than that of **12TBF**-ZnO; this confirms it is necessary to have the TBF units situated in a 3D space at a high local concentration around the fullerene. Generally, as the concentration of dye increases in solution there is a drop in efficacy. This behaviour is in line with other dye degrading semiconductor catalysts and is caused by the overcrowding of ZnO by dye and by-product molecules, in addition to the dye molecules blocking transmission of energy to ZnO.[37]

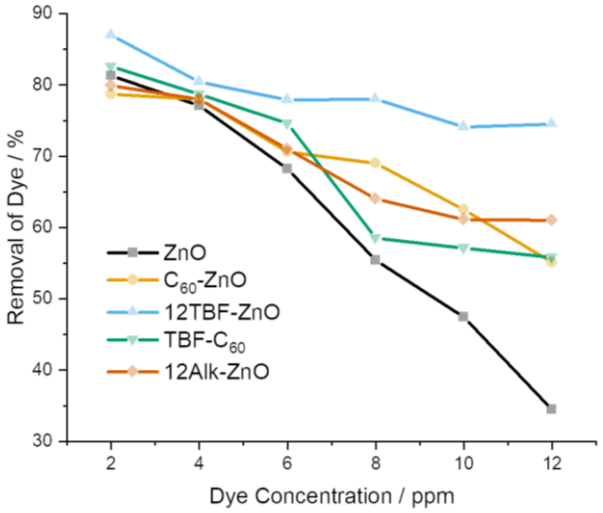

Figure 4.13. Removal of RhB from solution at varying initial concentrations (2–12 ppm). **12TBF**-ZnO composite (blue line) consistency outperforms all other controls for each experiment.

All composites were tested at 1 wt% doping of organic material, however, in order to optimise the performance of the **12TBF**-ZnO composite, various loading wt% of **12TBF** were explored. At the lowest starting concentration of dye (2 ppm) there is an improvement in performance for the 3.0 wt% and 5.0 wt% composites, with 96% and 97% removal of dye, respectively (Figure 4.14a/b). However, at greater concentrations of dye (12 ppm) the performance of the 5 wt% composite decreases to 67% whereas the 3.0 wt% composite still performs above 80%. This type of behaviour is in line with previously published organic–ZnO composites that have deteriorating performance at high levels of organic doping.[30] The photocatalytic performance decreases with excessive amounts of **12TBF** as direct irradiation of ZnO is diminished with **12TBF** covering the surface and forming large, light-absorbing aggregates.

The instability of ZnO under UV irradiation can hinder its implementation as an effective photocatalyst. However, UV absorbing barriers–such as graphene oxide sheets—can increase the durability of ZnO by supressing photo-corrosion and therefore increasing its photocatalytic efficiency.[38] In order to test the recyclability of the **12TBF**-ZnO composite, repeat tests with

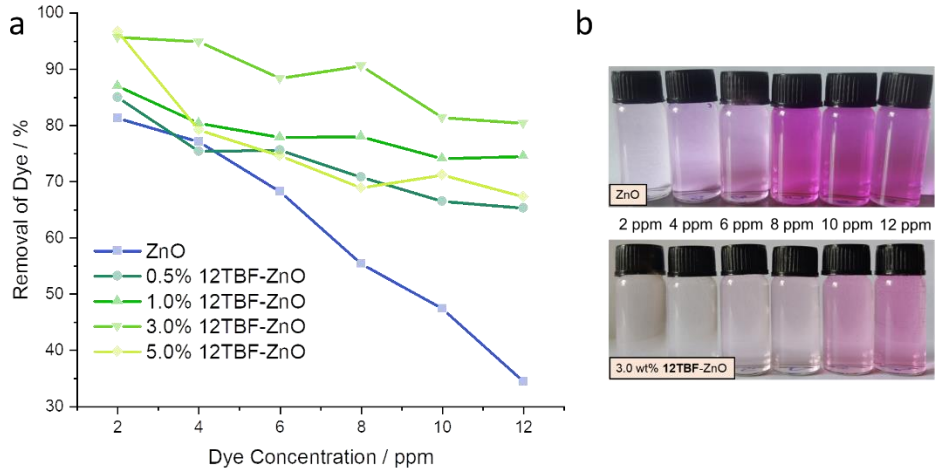

Figure 4.14. a) Removal of Rhodamine B from solution using **12TBF**-ZnO composite at varying wt% loading of **12TBF**. b) Sample images of the best performing composite 3 wt% **12TBF**-ZnO vs. **ZnO**.

the same composite were completed for the degradation of RhB (12 ppm) solutions. The 3 wt% **12TBF**-ZnO composite had an efficacy of 80% for the first dye degradation experiment. After 5 cycles, 62% of dye is still removed (Table 4.2) from solution by the composite, which is 77% reproducible in comparison to the efficacy of the first experiment. This high level of reproducibility serves **12TBF**-ZnO as a genuine candidate for a hybrid photocatalyst with high efficacy.

Table 4.2. Recyclability of **12TBF**-ZnO (3 wt%) catalyst; after 5 cycles, 61.8% of dye is still removed from solution.

Cycle	Removal of Dye / %
1	80.4
2	73.5
3	65.6
4	65.0
5	61.8

To demonstrate the diverse use of the composite, degradation studies were then conducted on a range of industrially relevant dyes. Here, dyes of differing molecular structure will have varying susceptibilities to degradation, however, the composite should always outperform ZnO when working as an efficient photocatalyst. The photocatalytic efficacy of the **12TBF**-ZnO composite was compared against undoped ZnO for Reactive Blue 4 (RB4, 50 ppm), Quinoline Yellow (QY, 12 ppm), Methylene Blue (MB, 20 ppm) and Safranin (SO, 20 ppm); all degradation was monitored by UV-Vis spectroscopy (Figure 4.15). Although the concentration is varied for each dye, the **12TBF**-ZnO composite consistently outperforms ZnO (Figure 4.15). Indeed, for MB the composite approaches near 100% removal of dye from solution, in comparison to just 64% for ZnO.

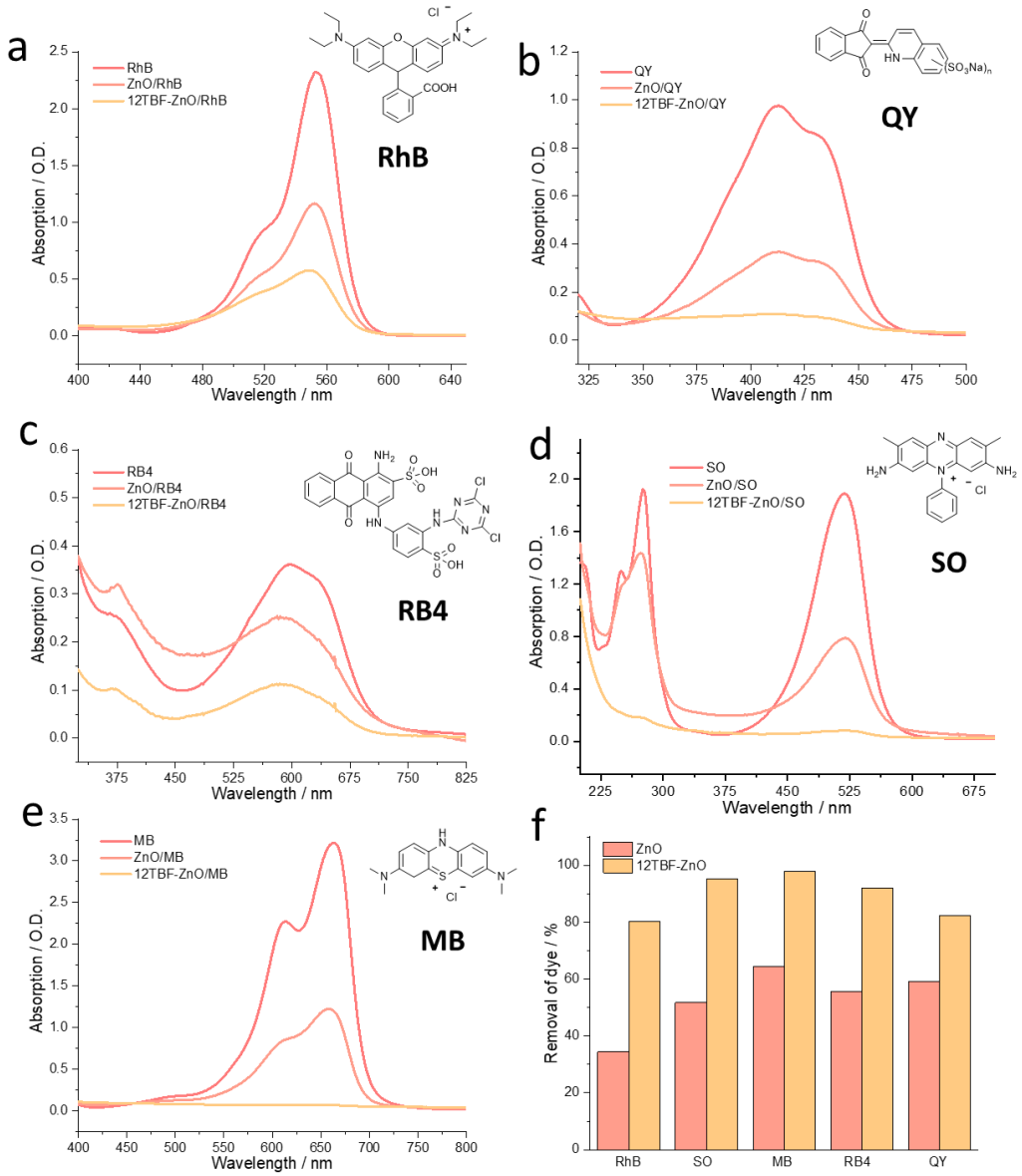

Figure 4.15. UV-Vis absorption spectra for dye degradation studies on a) RhodamineB, b) Quinoline Yellow, c) Reactive Blue 4, d) Safranin Orange and e) Methylene Blue; red line = before treatment, pink like = ZnO treatment, orange line = **12TBF**-C_{60} treatment. Bar chart shows comparison between the two treatments for each dye.

In order to quantify the rate of dye degradation for the best performing composite, the removal of RhB from solution was monitored over time using the 3 wt% composite. A solution of RhB (12 ppm) was mixed with the 3 wt% **12TBF**-ZnO composite and aliquots were taken every 30 minutes (for 180 minutes) with the concentration of dye remaining calculated by UV-Vis spectra measurements (Figure 4.16a and see Figure 4.30, appendix for spectra). The reaction was found to follow a Langmuir–Hinshelwood mechanism for catalysis at the surface of ZnO, i.e., a heterogeneous catalytic process.[37,39] The photocatalytic degradation reaction followed pseudo first-order kinetics with respect to irradiation time (Figure 4.15b) and the rate constant values were estimated by the pseudo first-order eq.5:

$$\ln(C_i/C_f) = kt \qquad \text{(eq. 5)}$$

K = pseudo first order rate constant for degradation of dye (in min^{-1}), t = irradiation time (in min.), C_i = initial concentration of dye and C_f = final concentration of dye.

To compare the efficacy, the rate of dye degradation was also quantified using bare ZnO (see Supporting Table 4.3, appendix). Plotting $\ln(C_i/C_f)$ against irradiation time allowed for the calculation of the rate constants, with $k = 6 \times 10^{-3}$ and $k = 15 \times 10^{-3}$ for ZnO and **12TBF**-ZnO, respectively. With a confirmed enhancement in efficacy, i.e., 2.5 × increase in rate, attention was then turned towards deciphering the likely mechanism for the increased performance.

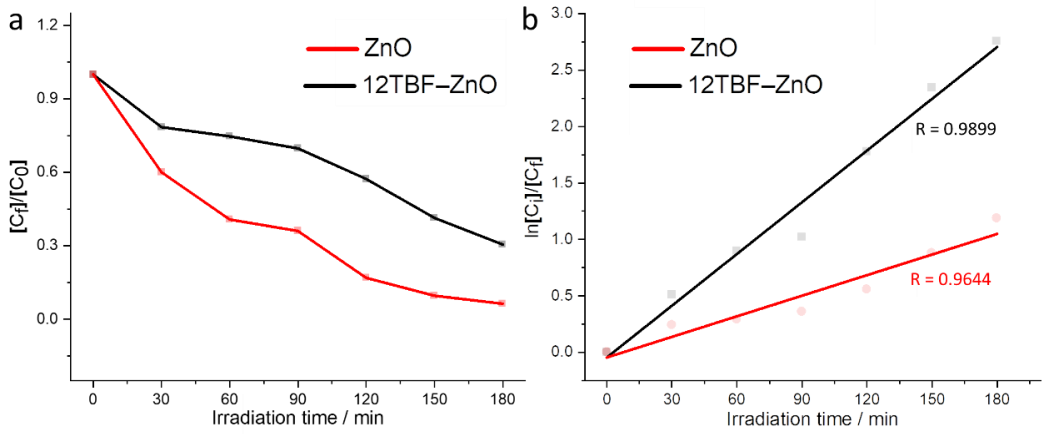

Figure 4.16. a) Ratio of final concentration of dye (C_f) vs. initial concentration (C_i) of Rhodmaine B dye throughout duration of experiment for both **ZnO** (red line) and 3wt% **12TBF**-ZnO (black line). b) Plot of $\ln(C_i/C_f)$ vs. irradiation time allows for the calculation of the rate constant for dye degradation; the behaviour is pseudo first order. ZnO = –0.006 min^{-1}, **12TBF**-ZnO (3 wt%) = –0.015 min^{-1}.

The optical bands gaps that were calculated for the composites (DRS UV-Vis spectroscopies) indicated that there were no significant changes to the amount of sunlight irradiation that could be absorbed and therefore this reasoning behind the increased efficacy in comparison to ZnO is unlikely. However, an increase in the apparent band gap of the **12TBF**-ZnO composite was indicative of a BM effect which could be evidence for less h^+ and e^- recombination in ZnO. As a donor–acceptor hybrid, **12TBF** is bestowed with oxidative as well as reductive units. Owing to the poor electron affinity of the fullerene hexakis-adduct core of **12TBF** (E_{LUMO} = –3.5 eV) it is not thermodynamically feasible for photoexcited electrons in ZnO (conductance band = –4.1 eV) to be transferred to the LUMO of **12TBF**. On the other hand, h^+ transfer between a photogenerated h^+ on ZnO and a TBF unit on **12TBF** is thermodynamically favourable as the valence band for ZnO is –7.8 eV whereas the E_{HOMO} of TBF is –5.1 eV. With **12TBF** adsorbed at the surface of the ZnO nanoparticles, there is a high local concentration of TBF units and therefore multiple h^+ transfer reactions can occur simultaneously for separate TBF units of **12TBF**. With efficient h^+ transfer taking place, the recombination of photogenerated h^+ and e^- on ZnO could be significantly reduced. Subsequently, the concentration of dye degrading species (i.e., $^{\bullet}O_2^-$, $^{\bullet}OH$, H_2O_2) at the surface of ZnO is increased, which ultimately results in a greater removal of dye from solution. This proposed mechanism

would agree with the blue-shift in absorption for the **12TBF**-ZnO composite in comparison to pure ZnO that might arise from the BM effect. Furthermore, the **TBF**-ZnO composite i.e., with a monomeric TBF unit, only showed 55% efficacy for the degredation of RhB in comparison to 3 wt% **12TBF**-ZnO (75%) which suggests that crowing of TBF units in 3D space is required to access the higher performing composites. The mechanistic processes are depicted in Figure 4.17.

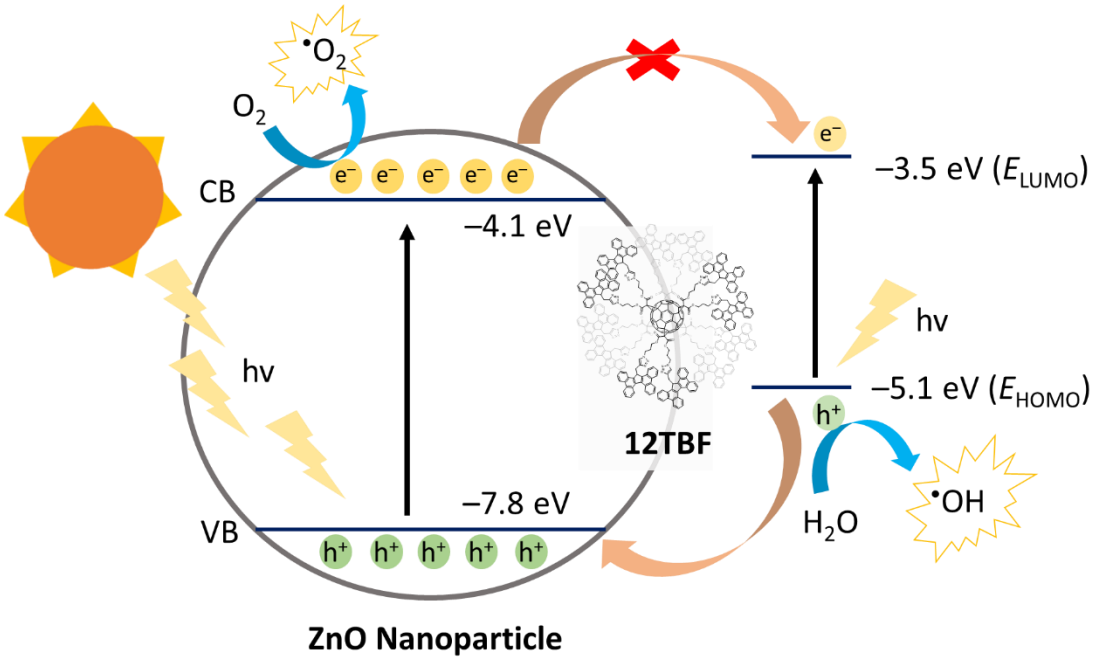

Figure 4.17. Suggested mechanism for photocatalytic degradation of dye molecules. The recombination of photo generated h^+ and e^- on ZnO is lowered thanks to effective h^+ transfer from the TBF moieties of **12TBF**. Electron transfer from the conductance band of ZnO to the LUMO of C_{60} is thermodynamically unfavourable.

In summary, these results show that the organic–inorganic composite, i) can increase the efficacy of ZnO for dye degradation applications and ii) has increased photo-stability owing to the ZnO surface shielding by **12TBF** molecules. With a clear observation that the donor-acceptor C_{60} hexakis-adduct increases the performance of ZnO, further photophysical investigations could help elucidate and gain further insight into the mechanism behind the increased efficacy. Whereas the performance has been demonstrated for 3 wt% **12TBF**-ZnO, we are currently investigating the 'multivalent'[40] effect that is bestowed on the fullerene scaffold from the full decoration with 12 TBF units. A second fullerene hexakis-adduct, **2TB** (Chapter 3), that bears only two TBF units, has been used to form a new ZnO composite from which a comparison can be made with **12TBF**-ZnO. Currently, dye degradation experiments are being conducted on the **2TBF**-ZnO composite. If there is an unprecedented increase in performance between the di- and dodeca-decorated fullerenes, this could be evidence of a synergy that relates to a multivalent effect.

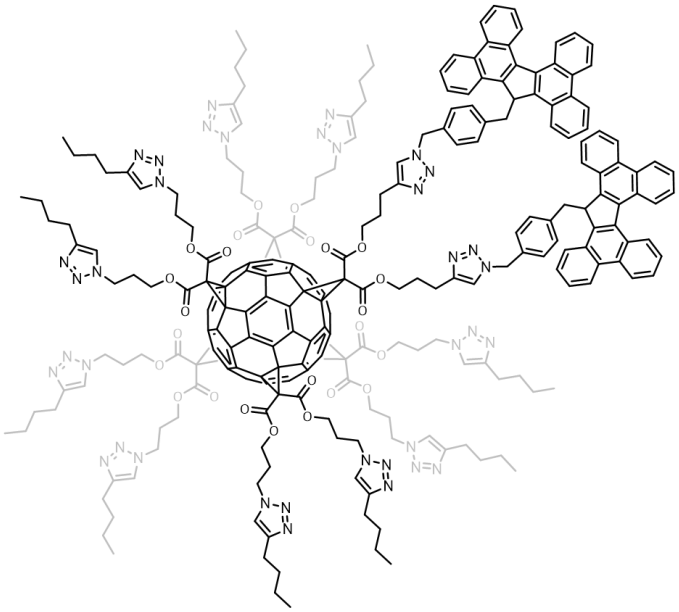

2TBF

Figure 4.18. Chemical structure of [5:1] hexakis-adduct **2TBF**, functionalised with only two TBF units.

4.5 Conclusions

Following the fundamental properties analysis of the key molecules in Chapters 2 (**12NDI**) and 3 (**12TBF**), we rationalised that our hexakis-adduct fullerene molecules could have applications in organic electronic and photocatalytic materials. We have implemented our novel acceptor molecules into diodes and have calculated the charge mobility as electron-only devices using the space-charge-limited current model. The non-optimised devices calculate a charge mobility of ca. 1×10^{-11} m^2 V^{-1} S^{-1} for **12NDI**, significantly less than for model compound **2NDI** (1×10^{-6} m^2 V^{-1} S^{-1}). Indeed, alike **12Alk**, the observed charge mobility is extremely low. These data suggest that despite the decoration of NDI units in 3D space, sufficient charge-transport pathways are not formed between molecules to mediate charge throughout the active layer. Device optimisation from, e.g., annealing the active layers at various temperatures or from the addition of additives, should improve the performance of the devices. However, the changing of the pendant aromatic unit (e.g., to a PDI unit) and/or quantity of the pendant units (e.g., in branched system) may also facilitate greater charge mobilities for fullerene hexakis-adducts. Hexakis-adduct **12TBF** is poised for further investigations that could help explain the increased dye degradation efficacy of ZnO when used as a composite. Currently, h^+ transfer from the TBF units to a vacant h^+ site on ZnO is rationalised as the main contributor for the increased efficacy. The recyclability of the composite has been demonstrated with high levels of degradation still observed after five

cycles. Additionally, the degradation of five industrially relevant dye has shown the wide applicability of the composite, i.e., it is a versatile photocatalyst for degradation. Currently, we are investigating the dye degradation efficacy of a [5:1] hexakis-adduct composite, i.e., **2TBF**-ZnO, that may not only help deduce the mechanism behind the increased performance for **12TBF**, but also provide evidence for a 'multivalency'[41] effect. Here, proving a multivalent effect is responsible for the increased device performance could inspire the design of bespoke fullerene hexakis-adducts that have emergent properties in photo- and redox-active materials.

4.6 Experimental Details

4.6.1 General Materials and Methods

Materials: All reagents and solvents were purchased from commercial suppliers (Merck, Acros Organics, Alfa Aesar, Fischer Scientific, Tokyo Chemical Industry or Fluorochem) and used without further purification unless stated otherwise. Compounds **2NDI**, **12NDI**, **12Alk** were synthesised following procedures described in Chapter 2) and **12TBF**, **2TBF**, **TBF** were synthesised following procedures described in Chapter 3. Anhydrous solvents were obtained from a Solvent Purification System and stored over activated (>250 °C at 0.01 mbar overnight) 3 Å molecular sieves under an Ar atmosphere. Solvents and solutions required for air-sensitive manipulations were degassed thoroughly using a minimum of three freeze–pump–thaw cycles and the flask back-filled under an Ar atmosphere.

Product confirmation: Analytical thin layer chromatography (TLC) was performed on aluminium-backed silica gel 60 plates pre-loaded with F254 indicator (Sigma-Aldrich) and visualised under UV light irradiation (254 and 365 nm). Nuclear magnetic resonance (NMR) spectra were recorded using a Varian VNMRS-700 (^{1}H and ^{13}C nuclei = 700.130 and 176.048 MHz, respectively) spectrometer at a constant temperature of 298 K. Operating temperatures of the NMR spectrometers were measured with the aid of a MeOH internal calibrant. All ^{13}C NMR experiments were proton decoupled. Chemical shifts (δ) are reported in parts per million (ppm) relative to the signals corresponding to the residual non-deuterated solvents ($CDCl_3$: δ_H = 7.26, δ_C = 77.16 ppm). Coupling constants (J) are reported in Hertz (Hz) and ^{1}H multiplicities are reported in accordance with the following: s = singlet, d = doublet, t = triplet, q = quadruplet, p = pentet, m = multiplet. NMR spectra were processed using MestReNova software, Version 11.

Sample analysis: UV-Vis absorbance data were collected using a Cary 5000 Series UV–Vis–NIR spectrophotometer (Agilent Technologies) at room temperature. UV-Vis DRS spectra were collected on a UV 2600, Shimadzu spectrometer. The steady-state photoluminescence (PL) of films were measured using Jobin Yvon Fluoromax and Fluorlog spectrophotometers, respectively, against machine-specific calibration curves. An FEI Helios dual-beam scanning electron microscope (SEM; 3.0 kV) was used to image the morphology of thin-film specimens. SEM samples were prepared by drop-casting 50 µL of a solution in *o*-dichlorobenzene (0.1 mg/ mL) onto pristine silicon wafers that were dried thoroughly overnight under reduced pressure (<0.01 mbar). A Cressington Scientific sputter coater equipped with a Au/Pd target and MTM-10 thickness monitor was then used to coat samples with a thin conductive layer (10 nm) immediately before SEM images were taken. PXRD data was

collected on a Rigaku mini flex-II Desktop X-Ray diffractometer. PXRD scans were collected between 5 to 80 degrees, with Cu Kα radiation.

Space-charge-limited Diode Device Preparation: ITO coated glass substrates (VisionTek systems LTD) with sheet film resistance of 7 Ω and 19.5 mm by 16.5 mm were first cleaned by ultrasonic bath in 2-propanol, acetone, Decon 90 and de-ionised water for 15 min each. After cleaning, substrates were blown dry with nitrogen gas and then treated with UV-oxygen plasma, 100W, for 10 min. Using a Laurell spin coater, a layer of 200 µL of poly(3,4-ethylenedioxythiophene): poly styrenesulfonate PEDOT:PSS (Heraeus CLEVIOStm P VP AI 4083) was spin coated (after passing through 0.2 µL syringe filter) at 2500 rpm for 45 s on top of the ITO before thermally annealing all substrates at 140 °C for 10 min. Substrates were then moved into a glovebox to spin coat active layers. Solutions of [6,6]-phenyl-C60-butyric-acid-methyl-ester (PCBM) and **12NDI** were prepared with a combination of $CHCl_3$ and *o*-DCB (90:10 ratio, dissolved in 600 µL) containing 18 mg and 10 mg to produce thick (~250 nm) and thin (~100 nm) films respectively. Compounds **1NDI** and **12Alk** were prepared only with $CHCl_3$ containing 18 mg and 10 mg to produce thick (~250 nm) and thin (~100 nm) films respectively. Compound **2NDI** was prepared with $CHCl_3$ using 18 mg dissolved in 1200 µL. **12NDI**, **12Alk**, **2NDI**, and **1NDI** solutions were heated in a hot plate at 50 °C while stirring for 4 hours before film deposition. A 100 µL of active layer was spin coated at 1000 rpm for 60 s on top of the PEDOT:PSS layer. For **1NDI**, 2000 rpm for 60 s were used (both for 18 mg and 10 mg) and for **2NDI** 1000 rpm for thin devices and 500 rpm for thick devices. Thermal annealing for 10 min at 120 °C was carried out prior to vacuum deposition (6.0×10^{-6} torr). A 1 nm layer of lithium fluoride and 100 nm of aluminium were thermally evaporated through a shadow mask with an active area of 3.53×10^{-6} m^2.

4.6.2 Experimental Procedures

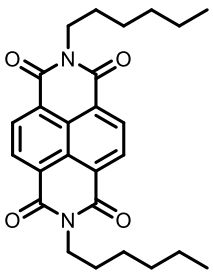

***N,N′*-Bis(hexyl)naphthalene diimide** (**1NDI**): Compound **1NDI** was prepared according to a literature[42] procedure without further modification. The product was recrystallised from hot DMF and dried thoroughly under high vacuum prior use in device studies. Spectroscopic data were consistent with those previously published.[42]

^{1}H NMR ($CDCl_3$, 700 MHz, 298 K): δ_H 8.76 (s, 4H), 4.20 (t, J = 7.5 Hz, 4H), 1.75 (p, J = 7.2 Hz, 4H), 1.36–1.45 (m, 12H), 0.91 (t, J = 6.9 Hz, 6H).

4.7 Appendix of Supplementary Data and Discussion

4.7.1 Solid-State Thin Film Absorption and Emission

We investigated the ability of **12NDI**, **2NDI** and **1NDI** to form solid-state intra- and intermolecular NDI interactions using absorption and emission spectroscopies. Intramolecular NDI interactions were encouraged by drop-casting *o*-DCB solutions containing each analyte (0.1 mg/ mL) onto quartz substrates. Thin films were allowed to cure by slow evaporation of the solvent under ambient conditions before drying films completely under vacuum at 0.1 mbar overnight. Quartz substrates were routinely cleaned prior to preparation of thin films by rinsing in concentrated aqueous sulphuric acid followed by water then acetone before drying in an oven at 100 °C for at least 1 h.

4.7.2 Scanning Electron Microscopy (SEM) Images

SEM analysis was used to gain insight into the morphology of the acceptor compounds in the solid state. All SEM samples were drop cast from solutions (0.1 mg/ ml) of *o*-DCB onto pre-cut silicon wafers before drying under high vacuum (<0.01 mbar for 16 h at 25 °C).

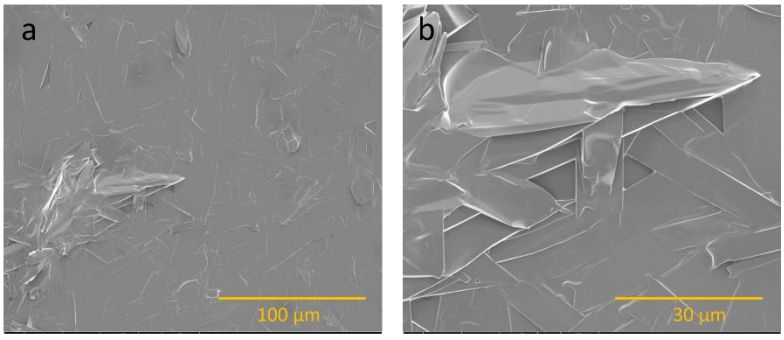

Figure 4.19. Scanning electron micrographs of **1NDI** drop-cast from *o*-DCB (0.1 mg/ mL) onto pristine silicon wafers. Magnification: a) 1000x and b) 3500x.

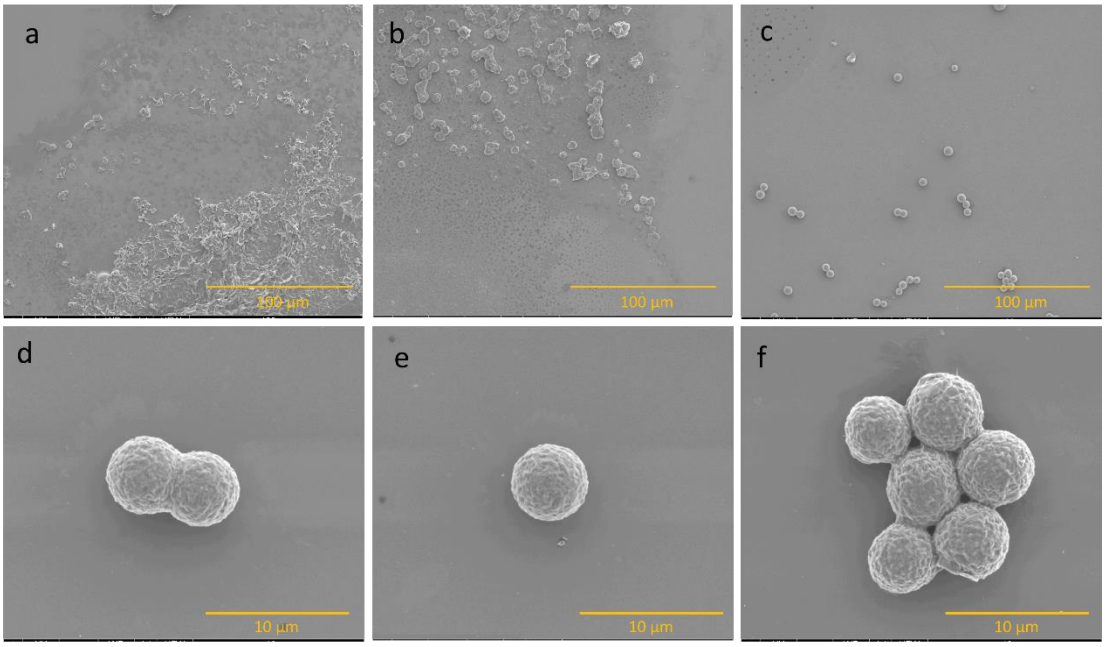

Figure 4.20. Scanning electron micrographs of **2NDI**, drop-cast from *o*-DCB (0.1 mg/ mL) onto pristine silicon wafers. Magnification: (a–c) 10000x and (d–f) 3500x.

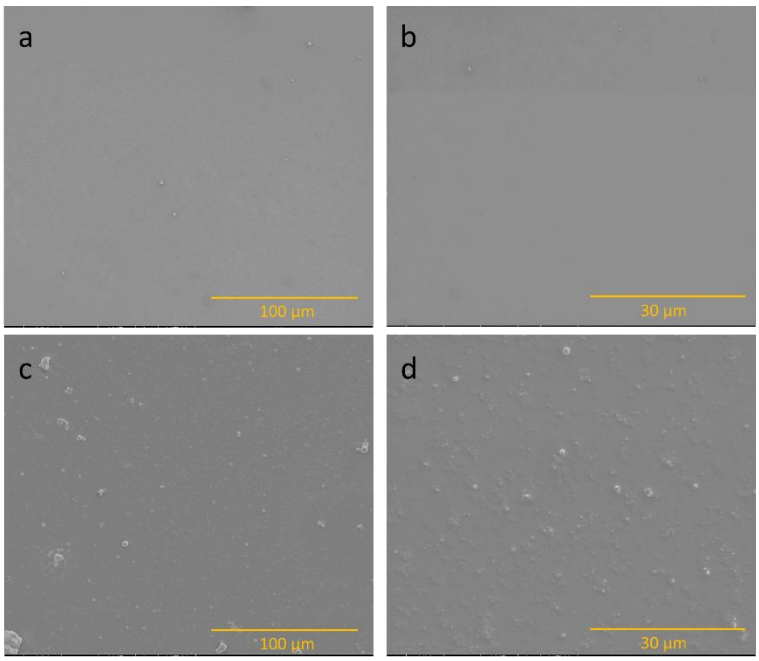

Figure 4.21. Scanning electron micrographs of (a,b) **12NDI** and (c,d) **12Alk** drop-cast from *o*-DCB solutions (0.11 mg/ mL) onto pristine silicon wafers. Magnification: 1000x and 3500x show a thin film with irregular sized aggregates throughout, providing evidence for thin-film formation of **12NDI** driven by favourable π-interactions between molecules.

4.7.3 Charge Mobility in Space-Charge-Limited Diode (SCLC) Device

The acceptor materials were tested for electron transport in electron-only devices by the SCLC method, with a device configuration of glass/ITO/PEDOT:PSS/**active layer**/LiF/Al (see Experimental Section 4.4.1 for full device preparation details). A total of 264 devices were fabricated (Figure 4.22).

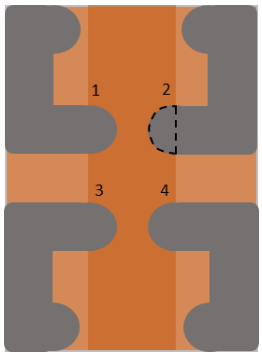

Figure 4.22. The substrate configuration with diode area (dashed line) of 3.53×10^{-6} m^2).

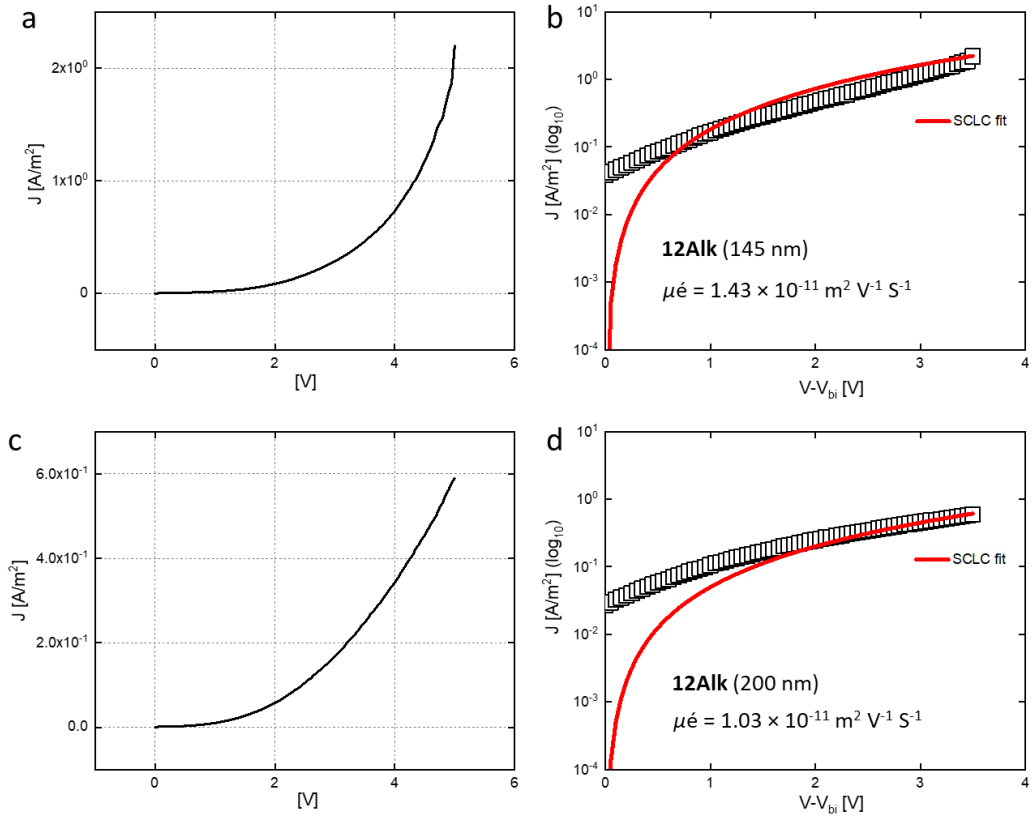

Figure 4.23. *J–V* dark characteristics of electron-only devices prepared with glass/ITO/PEDOT:PSS/ **12Alk**/LiF/Al for a) 145 nm and c) 200 nm film. Experimental electron transport (square) as described by SCLC measurement (solid line) with a mobility of 1.43×10^{-11} m^2 V^{-1} S^{-1} at 145 nm b) and 1.03×10^{-11} m^2 V^{-1} S^{-1} at 200 nm d) using, V_{bi} of 1.5*V*.

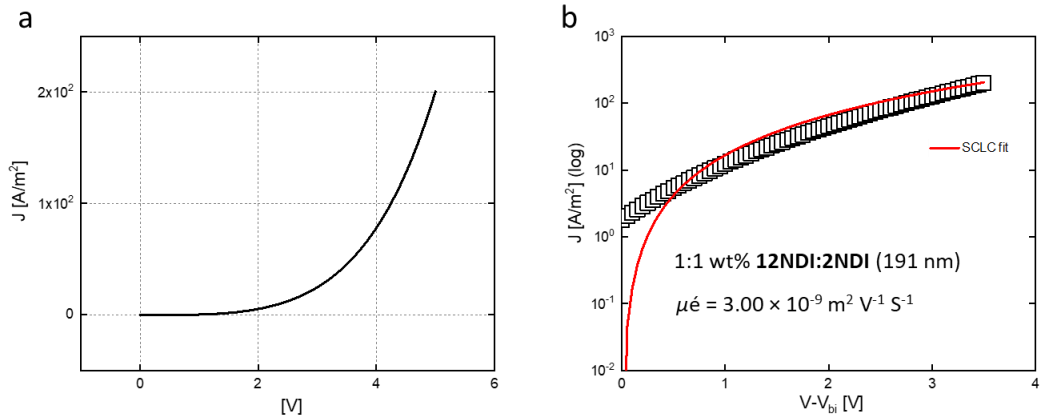

Figure 4.24. a) *J–V* dark characteristics of electron-only devices for binary mixture of **12NDI**:**2NDI** with a 1:1 ratio prepared with glass/ITO/PEDOT:PSS/**active layer**/LiF/Al with film thickness of 191 nm film. b) Experimental electron transport (square) as described by SCLC measurement (solid line) with a mobility of 3.00×10^{-9} m^2 V^{-1} S^{-1} using V_{bi} of 1.5*V*, for this blend.

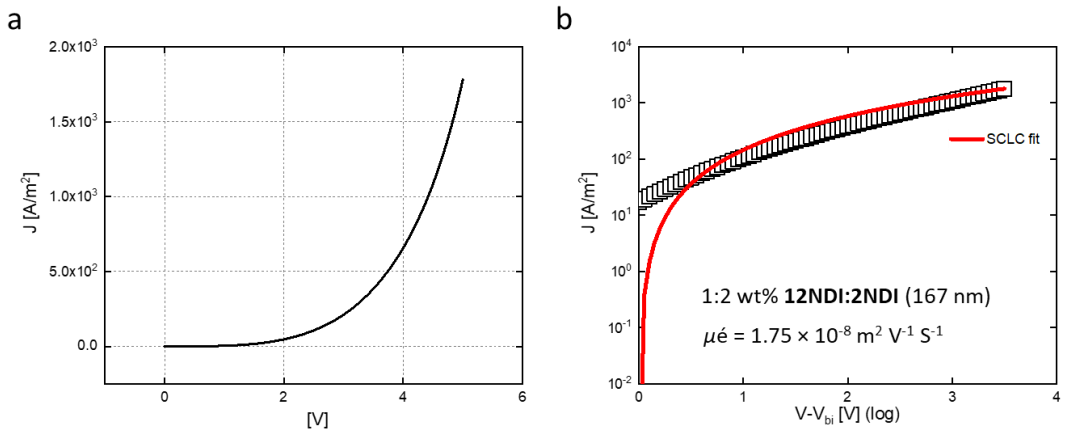

Figure 4.25. a) *J–V* dark characteristics of electron-only devices for binary mixture of **12NDI**:**2NDI** with a 1:2 ratio prepared with glass/ITO/PEDOT:PSS/**active layer**/LiF/Al with film thickness of 167 nm film. b) Experimental electron transport (square) as described by SCLC measurement (solid line) with a mobility of 1.75×10^{-8} m^2 V^{-1} S^{-1} using V_{bi} of 1.5*V*, for this blend.

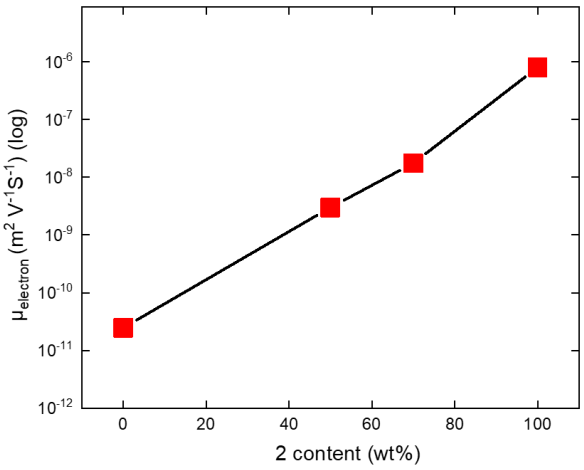

Figure 4.26. Dimer **2NDI** doping in a **12NDI**:**2NDI** blend and its effect on electron transport.

4.7.4 Composite Preparation

General Procedure for the preparation of ZnO composites:

ZnO (500 mg) was dispersed in ethanol (50 ml) and sonicated for 1 hour at rt. The dispersed ZnO was taken in a 100 ml single neck round-bottom flask. The organic compound (5 mg) was dissolved in $CHCl_3$ (5 mL). The organic solution was then added dropwise into the dispersed ZnO solution over 5 minutes away from light. After complete addition, the cloudy reaction mixture was stirred vigorously for 1 h under dark conditions. The reaction mixture solvent was removed by rotary evaporation and the composite was dried for 12 h under high vacuum oven at 65 ºC to obtain solid powders. The prepared composites e.g., **12TBF-ZnO**, were used as photocatalysts for the degradation of Rhodamine B (RhB) dye. Similarly, the TBF-ZnO, C_{60}-ZnO, and **12Alk**-ZnO composites were also prepared in this manner. In the case of C_{60}-ZnO, C_{60} (5 mg) was dissolved in toluene (5 ml) prior to addition to the dispersed ZnO mixture. The composites were used as control compounds in the dye degradation studies.

4.7.5 UV-Vis Diffuse Reflectance Spectroscopy (DRS)

The UV-Visible spectroscopy studies were conducted on UV 2600, Shimadzu spectrometer, with a scan speed of 200 nm/ min. A tauc plot (i.e., $(Ahv)^2$ vs. hv, Figure 4.27) was used to determine the optical band gap of the materials.

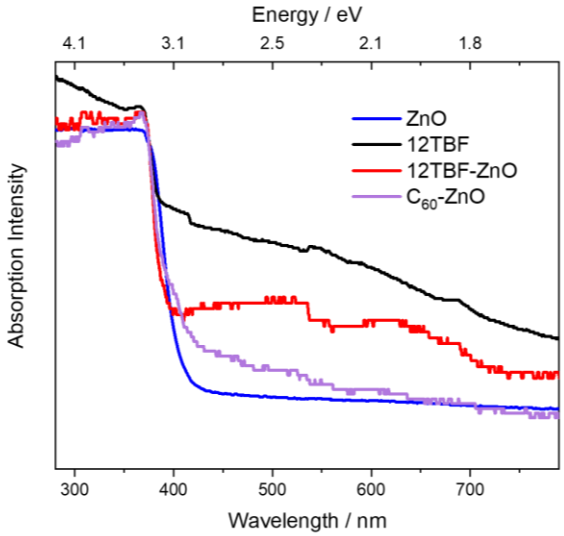

Figure 4.27. UV-Vis DRS spectra of ZnO (blue), **12TBF** (black), composites **12TBF**-C_{60} (red) and C_{60}-ZnO (purple).

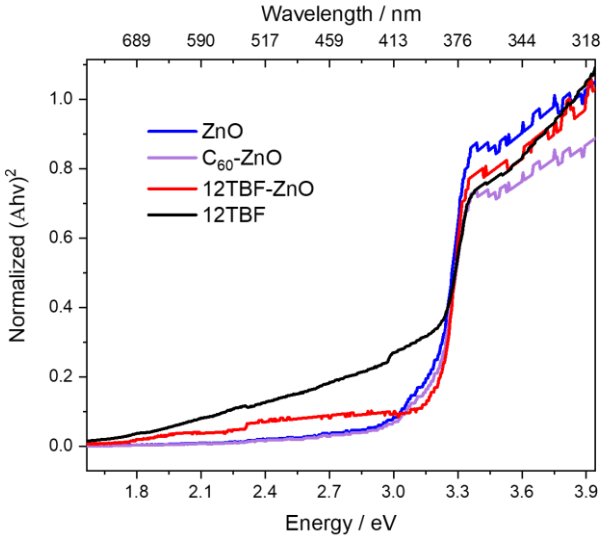

Figure 4.28. Tauc plot $(Ahv)^2$ vs. hv) used to determine the optical band gap of ZnO (blue), **12TBF** (black), composites **12TBF**-C_{60} (red) and C_{60}-ZnO (purple).

4.5.6 Powder X-Ray Diffraction (PXRD)

Powder X-ray diffractions were conducted on a Rigaku mini flex-II Desktop X-Ray diffractometer. Scans were conducted between 5 to 80 degrees, with Cu Kα radiation. The PXRD pattern of bare ZnO was 2θ = 31.40°, 34.06°, 35.92°, 47.24°, 56.32°, 62.54°, 66.04°, 67.6°, 68.76°, 72.76° and 76.74°

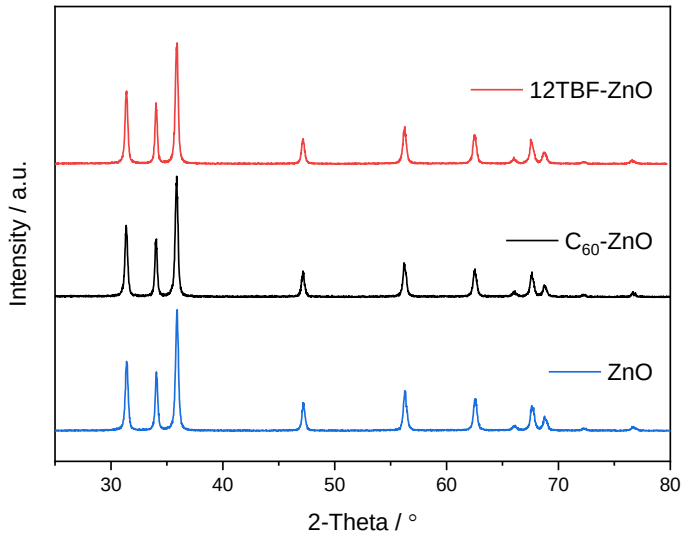

Figure 4.29. Powder X-ray diffraction patterns for ZnO (blue), and composites (1 wt%) of C_{60}-ZnO (black) and **12TBF**-ZnO (red). Typical diffraction paterrn for pure ZnO is: 31.37° (100), 34.03° (002), 35.86° (101), 47.16° (102), 56.21° (110), 62.51° (103), 66.08° (200), 67.58° (112), 68.74° (201), 72.23° (004), 76.71° (202). No significant diffraction peak shifting is observed for the composites.

4.7.6 Photocatalytic Degradation Studies

Rhodamine B (RhB) was used as a model dye to estimate the photocatalytic dye degradation capability of the composites. The prepared photocatalysts were studied systematically for degradation of RhB under sunlight in different experimental conditions. The degradation of RhB dye was calculated in terms of percentage by using the equation:

$$\text{Percentage removal} = (C_i\text{-}C_f)\ /C_i \times 100$$

C_i = initial concentration of dye and C_f = final concentration of dye

Initially, the photodegradation of RhB solution was monitored at different concentrations ranging from 2 ppm to 12 ppm with ZnO, C_{60}-ZnO, **12TBF**-ZnO, **12Alk**-ZnO, and **TBF**-ZnO photocatalyst under 120 min irradiation of sunlight to confirm molecular design principle and optimise the photocatalytic activity of catalyst. After that, the concentration of dye solution was fixed (12 ppm) and the irradiation time of sunlight was varied ranging from 30 to 180 min with 20 mg of ZnO and **12TBF**-ZnO. Generally, the photocatalytic degradation reaction followed pseudo first order reaction with respect to irradiation time and the rate constant values were estimated by the pseudo first order equation:

$$\ln (C_i/C_f) = kt$$

k = pseudo first order rate constant for degradation of dye (in min^{-1}) and t = irradiation time in min.)

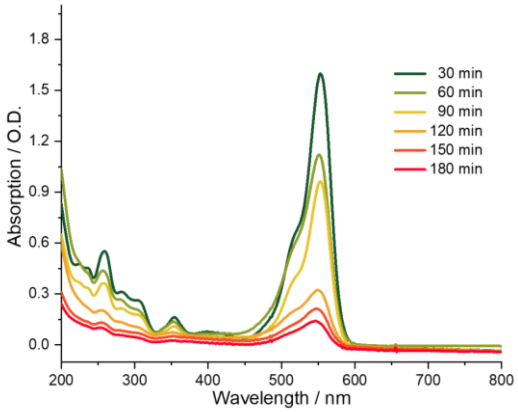

Figure 4.30. UV-Vis absorption spectra of RhB solution (12 ppm) and its sequential degradation using 3 wt% **12TBF**-ZnO over 180 min at rt.

Table 4.3. Removal of RhB (12 ppm) dye from solution over time following catalyst treatment

Irradiation time / min	Removal of Dye / %	
	ZnO	**12TBF**-ZnO
30	21.5	40.1
60	25.2	51.7
90	30.1	66.4
120	42.6	78.6
150	58.5	91.2
180	69.4	97.0

4.8 References

1 J. Iehl, R. Pereira De Freitas, B. Delavaux-Nicot and J. F. Nierengarten, *Chem. Commun.*, 2008, 2450–2452.

2 V. V. Rostovtsev, L. G. Green, V. V. Fokin and K. B. Sharpless, *Angew. Chem. Int. Ed.*, 2002, **41**, 2596–2599.

3 I. Nierengarten and J. F. Nierengarten, *Chem. Asian J.*, 2014, **9**, 1436–1444.

4 D. Sigwalt, M. Holler, J. Iehl, J. F. Nierengarten, M. Nothisen, E. Morin and J. S. Remy, *Chem. Commun.*, 2011, **47**, 4640–4642.

5 J. Iehl, M. Frasconi, H. P. J. de Rouville, N. Renaud, S. M. Dyar, N. L. Strutt, R. Carmieli, M. R. Wasielewski, M. A. Ratner, J. F. Nierengarten and J. F. Stoddart, *Chem. Sci.*, 2013, **4**, 1462–1469.

6 J. Iehl, J. F. Nierengarten, A. Harriman, T. Bura and R. Ziessel, *J. Am. Chem. Soc.*, 2012, **134**, 988–998.

7 A. Muñoz, L. Rodríguez-Pérez, S. Casado, B. M. Illescas and N. Martín, *J. Mater. Chem. C*, 2019, **7**, 8962–8968.

8 S. F. Völker, M. Vallés-Pelarda, J. Pascual, S. Collavini, F. Ruipérez, E. Zuccatti, L. E. Hueso, R. Tena-Zaera, I. Mora-Seró and J. L. Delgado, *Chem. Eur. J.*, 2018, **24**, 8524–8529.

9 A. F. Paterson, S. Singh, K. J. Fallon, T. Hodsden, Y. Han, B. C. Schroeder, H. Bronstein, M. Heeney, I. McCulloch and T. D. Anthopoulos, *Adv. Mater.*, 2018, **30**, 1801079.

10 S. Schlisske, C. Rosenauer, T. Rödlmeier, K. Giringer, J. J. Michels, K. Kremer, U. Lemmer, S. Morsbach, K. C. Daoulas and G. Hernandez-Sosa, *Adv. Mater. Technol.*, 2021, **6**, 2000335.

11 S. Basak, N. Nandi, S. Paul and A. Banerjee, *ACS Omega*, 2018, **3**, 2174–2182.

12 N. V. Ghule, R. S. Bhosale, S. V. Bhosale, T. Srikanth, N. V. S. Rao and S. V. Bhosale, *ChemistryOpen*, 2018, **7**, 61–67.

13 X. Liang, L. Tan, Z. Liu, Y. Ma, G. Zhang, L. Wang, S. Li, L. Dong, J. Li and W. Chen, *Chem. Commun.*, 2017, **53**, 4934–4937.

14 M. Pandeeswar, H. Khare, S. Ramakumar and T. Govindaraju, *RSC Adv.*, 2014, **4**,

20154–20163.

15 C. Groves, *Rep. Prog. Phys.*, 2017, **80**, 026502.

16 F. Schauer, in *Sol. Energy Mater. Sol. Cells*, 2005, **87**, 235–250.

17 Y. Li, R. G. Clevenger, L. Jin, K. V. Kilway and Z. Peng, *J. Mater. Chem. C*, 2014, **2**, 7180–7183.

18 J. Vlahović, M. Stanojević, J. Gojanović, J. Melancon, A. Sharma and S. Živanović, *Opt. Express*, 2021, **29**, 8710.

19 S. Foster, F. Deledalle, A. Mitani, T. Kimura, K. B. Kim, T. Okachi, T. Kirchartz, J. Oguma, K. Miyake, J. R. Durrant, S. Doi and J. Nelson, *Adv. Energy Mater.*, 2014, **4**.

20 V. D. Mihailetchi, J. K. J. Van Duren, P. W. M. Blom, J. C. Hummelen, R. A. J. Janssen, J. M. Kroon, M. T. Rispens, W. J. H. Verhees and M. M. Wienk, *Adv. Funct. Mater.*, 2003, **13**, 43–46.

21 N. Kumari, S. Naqvi and R. Kumar, *J. Mater. Sci.*, 2018, **53**, 4046–4055.

22 M. B. Avinash and T. Govindaraju, *Adv. Funct. Mater.*, 2011, **21**, 3875–3882.

23 B. Lellis, C. Z. Fávaro-Polonio, J. A. Pamphile and J. C. Polonio, *Biotechnol. Res. Innov.*, 2019, **3**, 275–290.

24 G. Malekshoar, K. Pal, Q. He, A. Yu and A. K. Ray, *Ind. Eng. Chem. Res.*, 2014, **53**, 18824–18832.

25 M. A. Mohd Adnan, N. M. Julkapli and S. B. Abd Hamid, *Rev. Inorg. Chem.*, 2016, **36**, 77–104.

26 X. Pan, M. Q. Yang, Z. R. Tang and Y. J. Xu, *J. Phys. Chem. C*, 2014, **118**, 27325–27335.

27 D. Fu, G. Han, Y. Chang and J. Dong, *Mater. Chem. Phys.*, 2012, **132**, 673–681.

28 R. Lv, X. Wang, W. Lv, Y. Xu, Y. Ge, H. He, G. Li, X. Wu, X. Li and Q. Li, *J. Chem. Technol. Biotechnol.*, 2015, **90**, 550–558.

29 S. Gayathri, P. Jayabal, M. Kottaisamy and V. Ramakrishnan, J. *Appl. Phys.*, 2014, **115**.

30 V. R. Posa, V. Annavaram, J. R. Koduru, V. R. Ammireddy and A. R. Somala, *Korean J. Chem. Eng.*, 2016, **33**, 456–464.

31 H. Fu, T. Xu, S. Zhu and Y. Zhu, *Environ. Sci. Technol.*, 2008, **42**, 8064–8069.

32 S. Wang, C. Liu, K. Dai, P. Cai, H. Chen, C. Yang and Q. Huang, *J. Mater. Chem. A*, 2015, **3**, 21090-21098.

33 G. Nagaraju, Udayabhanu, Shivaraj, S. A. Prashanth, M. Shastri, K. V. Yathish, C. Anupama and D. Rangappa, *Mater. Res. Bull.*, 2017, **94**, 54–63.

34 W. Muhammad, N. Ullah, M. Haroon and B. H. Abbasi, *RSC Adv.*, 2019, **9**, 29541–29548.

35 A. Murali and H. Y. Sohn, *J. Nanosci. Nanotechnol.*, 2019, **19**, 4377–4386.

36 G. Tang, H. Liu and W. Zhang, *Adv. Mater. Sci. Eng.*, *Adv. Mater. Sci. Eng.* 2013, **2013**.

37 Z. Jia, J. Miao, H. B. Lu, D. Habibi, W. C. Zhang and L. C. Zhang, *J. Taiwan Inst. Chem. Eng.*, 2016, **60**, 267–274.

38 Y. Zhang, Z. Chen, S. Liu and Y. J. Xu, *Appl. Catal. B Environ.*, 2013, **140**–**141**, 598–607.

39 A. Modwi, M. A. Abbo, E. A. Hassan, O. K. Al-Duaij and A. Houas, *J. Environ. Chem. Eng.*, 2017, **5**, 5954–5960.

40 J. Ramos-Soriano, J. J. Reina, B. M. Illescas, N. De La Cruz, L. Rodríguez-Pérez, F. Lasala, J. Rojo, R. Delgado and N. Martín, *J. Am. Chem. Soc.*, 2019, **141**, 15403–15412.

41 F. Stauffert, A. Bodlenner, T. M. Nguyet Trinh, M. I. García-Moreno, C. Ortiz Mellet, J. F. Nierengarten and P. Compain, *New J. Chem.*, 2016, **40**, 7421–7430.

42 G. S. Vadehra, R. P. Maloney, M. A. Garcia-Garibay and B. Dunn, *Chem. Mater.*, 2014, **26**, 7151–7157.

Chapter 5|
A Macromonomer Route Towards an NDI-Embedded Polypeptide

Synopsis

Peptide recognition provides a highly versatile and tuneable strategy to direct aromatic assembly and afford the preparation of functional, one-dimensional (1D) organic materials comprising higher-order nanostructures. The wide availability and programmability of amino acids to generate self-assembling peptide sequences and their sensitivity to changes in their environment allows for the predictable construction of artificial β-sheets with stimuli responsive properties. By utilising directed hydrogen bonding networks between parallel or antiparallel peptide chains, specific cofacial 1D-alignment of functional aromatic surfaces can be enforced and exploited for their emergent optical and electron conducting properties. In doing so, we may achieve access to novel materials for fundamental structure–property investigations as well as for the development of advanced organic electronic devices.

Relatively unexplored, macromolecular peptide assembly offers arguably the opportunity to effect controlled nanoarchitectures with i) greater stability over their energetically-limited supramolecular counterparts on account of their kinetic trapping as well as ii) more advanced structural hierarchy. Here, an NDI-embedded polypeptide (**P1**$^{\mathbf{DMB}}$) is targeted *via* a convergent synthetises of a peptide macromonomer that is poised for Cu(I)-catalysed azide–alkyne cycloaddition (CuAAC) polymerisation. **P1**$^{\mathbf{DMB}}$ has stimuli responsive behaviour with the acid-labile dimethoxybenzyl (DMB) group acting as hydrogen bond blocking motif. Upon removal of the DMB group, the deprotected polymer (**P1**) should self-assemble with the macromolecular architecture promoting antiparallel β-sheet formation. *J*-aggregation of NDI units in the DMB protected polymer **P1**$^{\mathbf{DMB}}$ is observed by UV-vis spectroscopy. Additionally, CD spectroscopy shows exciton coupling of NDI units *via* a Cotton effect, which arises owing to the formation of chiral assemblies. These NDI couplings are not pronounced in the protected macromonomer **M1**$^{\mathbf{DMB}}$ providing evidence for π-assembly that is mediated by macromolecular folding directed by a β-turn mimic. CV experiments show that the NDI units within **P1**$^{\mathbf{DMB}}$ are easier to reduce than for **M1**$^{\mathbf{DMB}}$ as a consequence of favourable interactions between the electron-deficient NDI units in the partially folded polypeptide. Additionally, the full reduction of each NDI unit in the protected polymer to the dianionic state is achieved at a lower potential than for **M1**$^{\mathbf{DMB}}$, providing evidence for a hydrogen bond stabilised macromolecular architecture that can partially counteract electrostatically repulsive π-interactions between the embedded NDI units. Preliminary self-assembly studies by FTIR spectroscopy of deprotected polymer **P1** suggest the desired 1D alignment of the polymer chains, i.e., the formation of β-sheet assemblies, can be facilitated following TFA-assisted DMB removal.

As a result of COVID, this project could not be completed, however, all synthetic targets have been made and self-assembly and optoelectronic characterisation is currently being completed in the group.

Acknowledgements

The following people are gratefully acknowledged for their contribution to this Chapter: Dr Alyssa-Jennifer Avestro and Charlotte Wright for their contributions to peptide macromonomer synthesis and characterisation during the initial stages of project development.

5.1 Introduction

Artificial β-sheet assemblies offer access to 1D nanoscale geometries that open the door to materials with novel optoelectronic properties. Well-understood β-sheet-forming peptide sequences have been used to direct/enforce assembly of functionally-attractive aromatic units, most commonly *via* multicomponent supramolecular assembly of small peptide–π conjugates (e.g., π-peptide amphiphiles and π-embedded peptides).[1–4] (See Chapter 1, Section 1.5.1 for discussion). Mediating π-assembly *via* a peptide-inspired macromolecular design is a relatively unexplored approach towards guiding the assembly of π-surfaces into 1D assemblies. Yet, the macromolecular strategy offers advantages such as i) stabilised/robust materials owing to the high molecular weight building blocks ii) more reliable assembly processes and iii) nanoscale structures of high fidelity. The nanoscale topologies of macromolecular self-assembled systems are often challenging to predict. However, Guan et al. have recently provided a strategy[4] to β-sheet-forming macromolecules *via* a convergent synthetic approach utilising a 'macromonomer'. They used CuAAC[5,6] to polymerise a peptide macromonomer (**G1^{DMB}**, Figure 5.1,) composed of a hexapeptide sequence of alternating alanine and glycine residues, similar to the repeating amino acid sequences of β-sheet forming polypeptides found in spider silks.[7] Furthermore, the polymerisation instilled a folding of the polypeptide *via* a 1,4-substituted triazole β-turn mimic[8]. Guan and co-workers were able to apply[9] their strategy to the convergent synthesis of a synthetic polypeptide **PG1^{DMB}** that folds into well-defined β-sheets and further assembles into hierarchical nanofibrils.

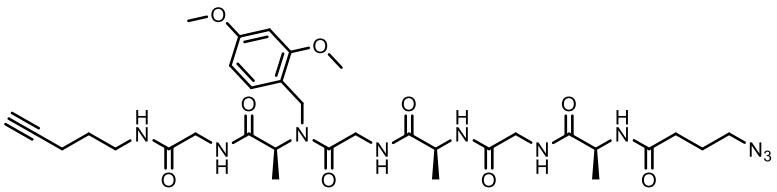

G1^{DMB}

Figure 5.1. The DMB-protected hexapeptide macromonomer **G1^{DMB}** ( ) with azide and alkyne terminal moieties, synthesised by Guan et al.[9]

An acid-cleavable 2,4-dimethoxybenzyl (DMB) amide protecting group increases the solubility of **PG1^{DMB}** and inhibits premature assembly until it is removal with TFA. Following DMB deprotection of **PG1^{DMB}**, the polymer (**PG1**, Figure 2) self-assembles into a fibrous 1D material with inherent β-sheet assemblies. This was confirmed by the presence of a minimum at λ = 206 nm and a maximum at λ = 105 nm in the CD spectrum, which is indicative of a β-sheet conformation. [10] Both TEM and AFM imaging identified that the β-sheets assemble into hierarchical amyloid-like nanofibrils, with widths of 3.8 ± 0.4 nm corresponding to the length of a single β-sheet and heights of 1.7–7 nm indicating the stacking of one to four layers

of β-sheet bilayers in individual fibrils. Although not functional with respect to optoelectronic properties, the polymer was able to form 1D nanoscale structures with inherent hierarchical ordering.

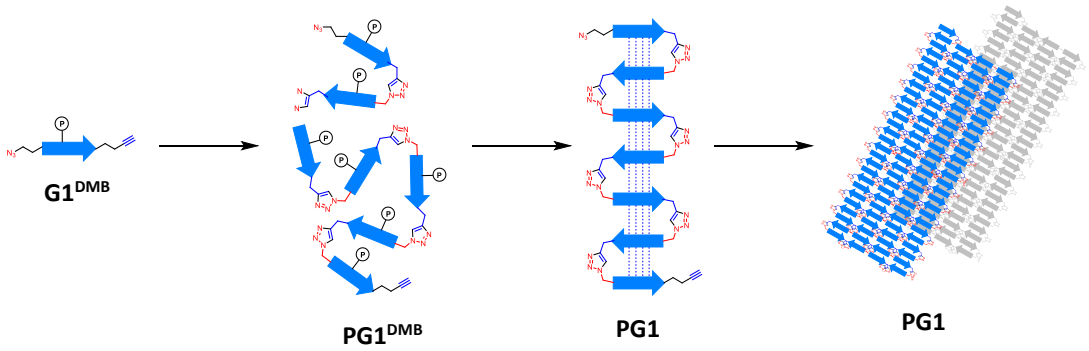

Figure 5.2. Following polymerisation of a protected macromonomer, *via* CuACC chemistry, self-assembly into β-sheets and then nanofibers could be induced *via* acid treatment to remove the protecting group.

The approach on synthetic β-sheet forming polypeptides provides a predictable route to accessing polymers exhibiting high levels of structural order, both at the nanoscale in the formation of β-sheets and macroscopic scale *via* the formation of hierarchical nanofibrils. The work in this Chapter describes synthetic efforts to prepare naphthalene diimide (NDI)-embedded polypeptide foldamers inspired by a macromonomer strategy. DMB-protected alanine–glycine $(AlaGly)_n$ macromonomers containing a main-chain NDI unit are C- and N-terminated with reactive azide and alkyne groups, respectively, to enable 'click' polymerisation by CuAAC chemistry. The C–N sequence of the macromonomer will allow for anti-parallel β-strand formation in the polymer, wherein the intramolecular hydrogen bonding interactions are fully aligned between main chain –NH and –CO groups. Here, the enhanced alignment of the amino acid residues should also facilitate coplanar aggregation of NDI units for more efficient charge delocalisation to occur, i.e., for materials with high conductivity. Owing to the large π-surface of NDI and the potential for these units to participate in hydrogen bonding interactions, a route that mediates intramolecular NDI assembly should be applicable to other functional redox-active units such as pyromellitic and perylene diimide.

5.2 Results and Discussion

5.2.1 Convergent Synthesis of Macromonomers **M1^{DMB}** and **C1^{DMB}**

The synthesis of DMB-protected peptide macromonomers for subsequent 'click' polymerisation was approached using a convergent methodology. Retrosynthetic analysis of desired macromonomer **M1^{DMB}** allowed for the identification of three key intermediates (Scheme 5.1) required for its convergent synthesis: two complementary CuAAC 'clickable' peptide end fragments, **AlkyneGA^{DMB}** and **AzideAG^{X}** (x = *C*-activation group), and an asymmetric NDI amino acid, **H$_2$N-NDI-COOH**.[9]

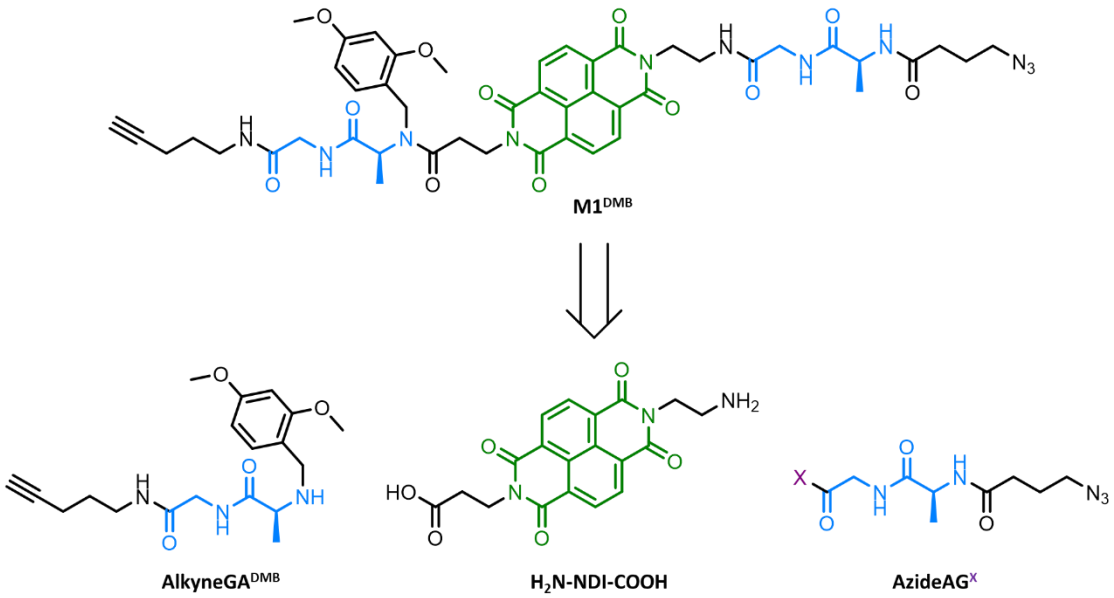

Scheme 5.1. The convergent synthesis of macromonomer **M1^{DMB}** requires the synthesis of an asymmetric NDI amino acid (**H$_2$N-NDI-COOH**), a *C*-activated alanine-glycine azide fragment (**AzideAG^{X}**, **X** = activating group), and a 2,4-dimethoxybenzene (DMB) protected alanine-glycine alkyne fragment (**AlkyneGA^{DMB}**).

The NDI 'amino acid' **H$_2$N-NDI-COOH** was easily accessed (Figure 5.3) from 1,4,5,8-naphthalenetetracarboxylic acid dianhydride (NDA) by pH-mediated synthesis[11] of an asymmetric naphthalene monoimide carboxylic acid **β-Ala-NMI** (98% yield) followed by its condensation *N*-Boc-ethylenediamine (**4**) to generate **Boc-NDI-COOH** (85% yield). Product NDI **5** was confirmed by ^{1}H NMR spectroscopy (Figure 5.3) in which the peaks associated with NDI aromatic protons at δ_H 8.62 (7, 11, Figure 5.3) exhibit an AB pattern indicative of the asymmetric *N*,*N*-substitution. In addition, peaks at δ_H 4.17 (3, Figure 5.3) and 4.28 ppm (12, Figure 5.3) corresponding to two chemically-distinct α-imide proton environments confirm the asymmetric substitution of NDI **5**. Mass spectrometry further confirmed NDI **5**, with a peak at 481.1485 *m*/z (481.1472 *m*/z calculated for $[M\text{-H}]^-$ = $C_{24}H_{23}N_3O_8$).

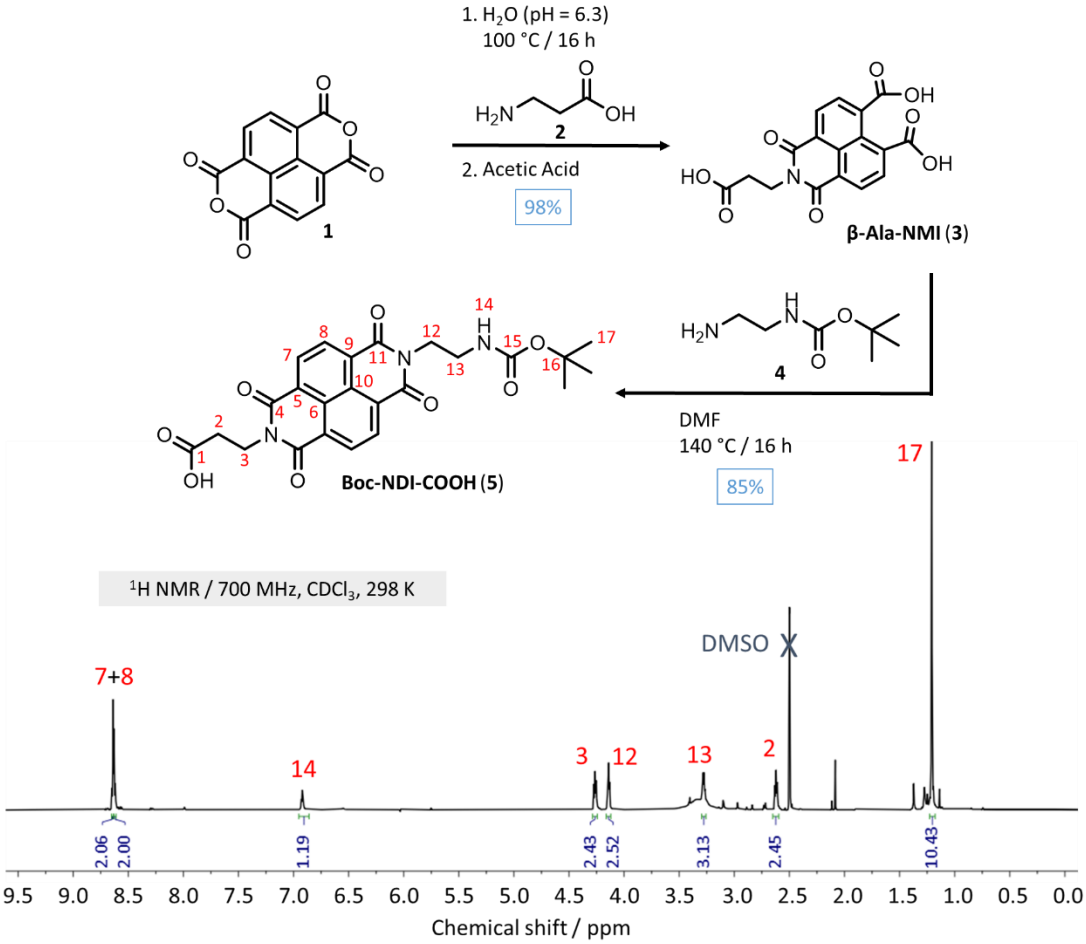

Figure 5.3. Synthesis of **β-Ala-NMI** *via* the controlled condensation of β-alanine (**9**) and **NDA** (**1**) and subsequent synthetic step towards **Boc-NDI-COOH** (**5**) from condensation with *N*-Boc-ethylenediamine at 140 °C in anhydrous DMF. ^{1}H NMR (DMSO-d_6, 700 MHz, 298 K) spectrum of **Boc-NDI-COOH**.

The *N*-terminal peptide fragment **11** bearing the alkyne end group and a DMB protecting group was initially synthesised according to a modified literature procedure[4] (Scheme 5.2). An EDC•HCl/HOBt-mediated amide coupling between *N*-Boc-glycine (**6**) and 1-amino-4-pentyne (**7**) in CH_2Cl_2, provided alkyne intermediate peptide **8** in 94% yield. Boc-deprotection of **8** in 1:1(*v/v*) TFA–CH_2Cl_2, followed by a second EDC•HCl/HOBt coupling with *N*-Boc-alanine (**9**) yielded dipeptide **AlkyneGA^{Boc}** in 86% yield. The TFA salt of **10** was then subjected directly to reductive amination with 2,4-dimethoxybenzaldehyde using $NaCNBH_3$ to afford the desired *N*-terminal fragment **AlkyneGA^{DMB}** in 74% yield. An alternative high-yielding preparation of **AlkyneGA^{Boc}** (82% yield) was also achieved by carrying out an EDC•HCl/HOBt-mediated amide coupling of the TFA ammonium salt of 1-amino-4-pentyne with dipeptide **12** (Figure 5.4)—a common intermediate that is additionally used for the synthesis of *N*-terminal fragment **AzideAG^{X}** (*vide infra*, Scheme 5.4). Approaching the synthesis of **AlkyneGA^{DMB}** in this manner means the use of precursors like dipeptide **12** (for preparation, see Scheme 5.4, *vide infra*) is maximised, encouraging a more efficient synthesis overall.

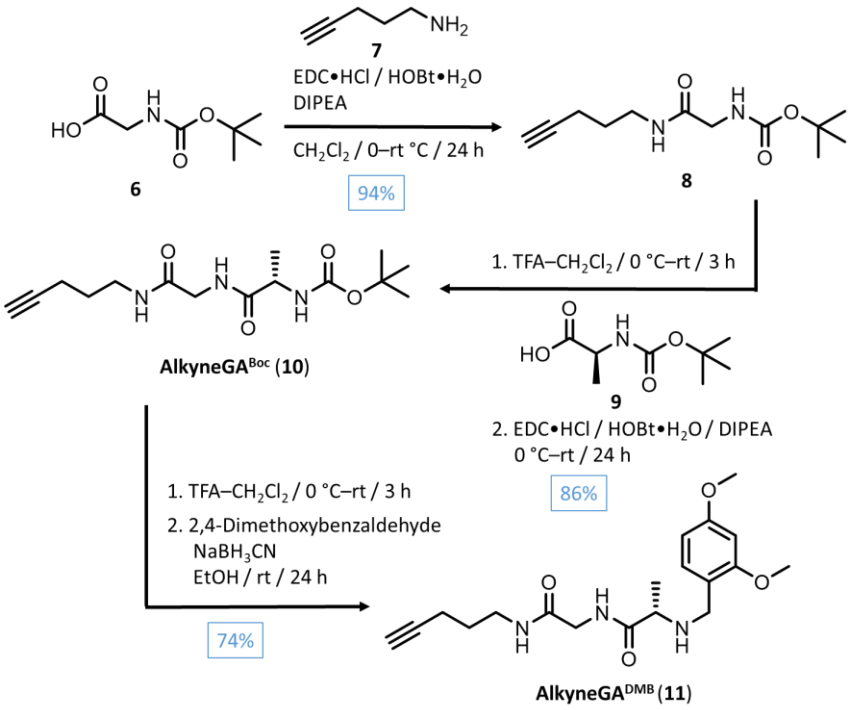

Scheme 5.2. Synthesis of alkyne functionalised peptide fragment **AlkyneGA^{DMB}** using an orthogonal group protecting strategy.

The synthesis of fragment **17** (*vide infra*, Scheme 5.4) was originally envisaged using conventional orthogonal protecting group strategies involving a *C*-terminal ester functionality followed by saponification to free the *C*-terminus for peptide coupling. However, in our hands, the strong hydroxide conditions required to saponify said ester resulted in unwanted degradation products that could not be identified by NMR spectroscopy. Therefore, a *C*-activation route involving highly electron-withdrawing perfluorophenyl (Pfp) esters was

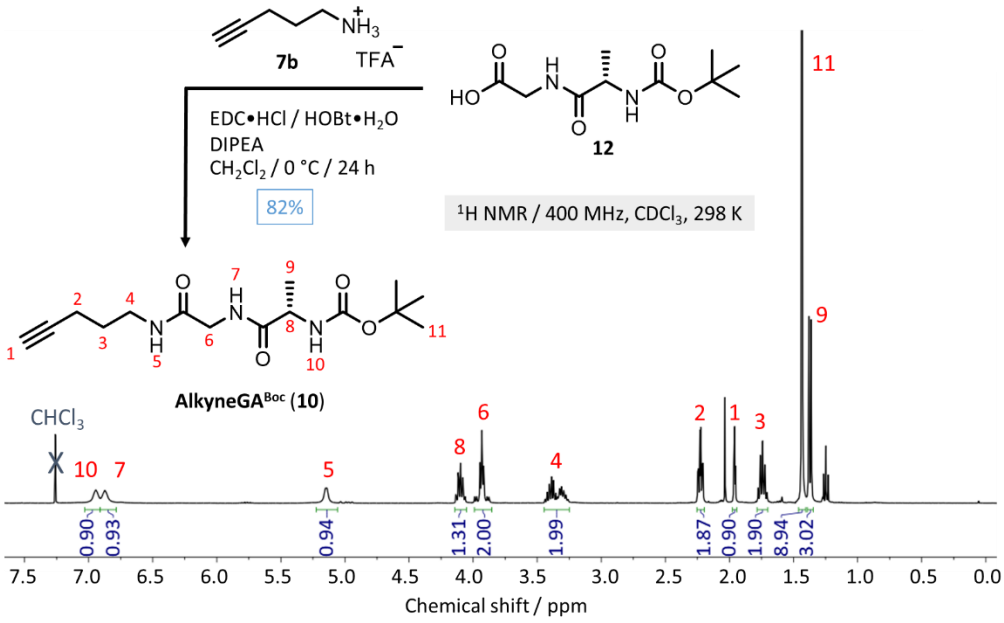

Figure 5.4. ^{1}H NMR ($CDCl_3$, 400 MHz, 298 K) of **AlkyneGA^{Boc}**, synthesised from dipeptide intermediate **19**. Amine **14b** was used as the TFA salt, prepared and stored from the addition of 1 mole equivalence of TFA.

instead used to avoid the need for base-mediated saponification and afford amide coupling to **20** by straightforward nucleophilic attack. *N*-Boc-alanine (**9**) was Pfp-activated by DCC-mediated coupling with pentafluorophenol to afford **13** in 75% yield (Scheme 5.3). The rapid precipitation of the dicyclohexylurea (DCU) by-product is observed which is mostly removed from the reaction mixture by filtration. To remove trace amounts of DCU, the crude residue was subjected to reverse-phase column chromatography (C18: 0–100% H_2O in MeOH) giving pure *C*-activated **13** in 75% yield. The Pfp-activated alkyl azide (**15**) was prepared and purified in a similar manner from **14** in 72% yield (Scheme 5.3).

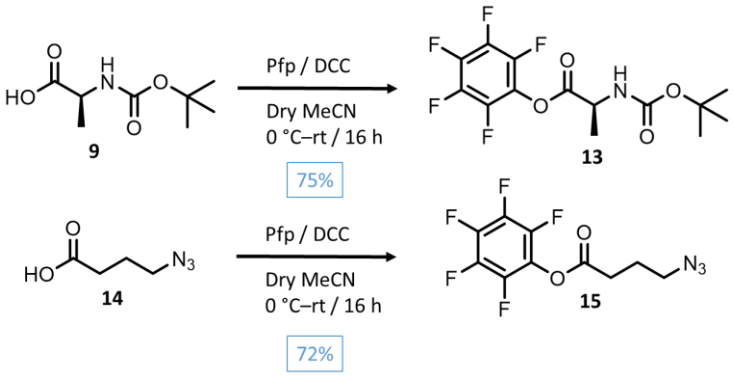

Scheme 5.3. Reaction scheme for the synthesis of Pfp-activated alanine **13**, and of Pfp-activated alkyl azide **15**, following the same procedure and work up.

C-activated **13** and glycine (**16**) were coupled (Scheme 5.4) to form dipeptide **12**, introduced previously as a common intermediate to DMB-protected alkyne **11**. Partitioning the crude mixture between H_2O and CH_2Cl_2 allowed for the removal of pentaflurophenol and excess **13** from the organic phase with the crude dipeptide **12** purified by crystallisation from hot H_2O to

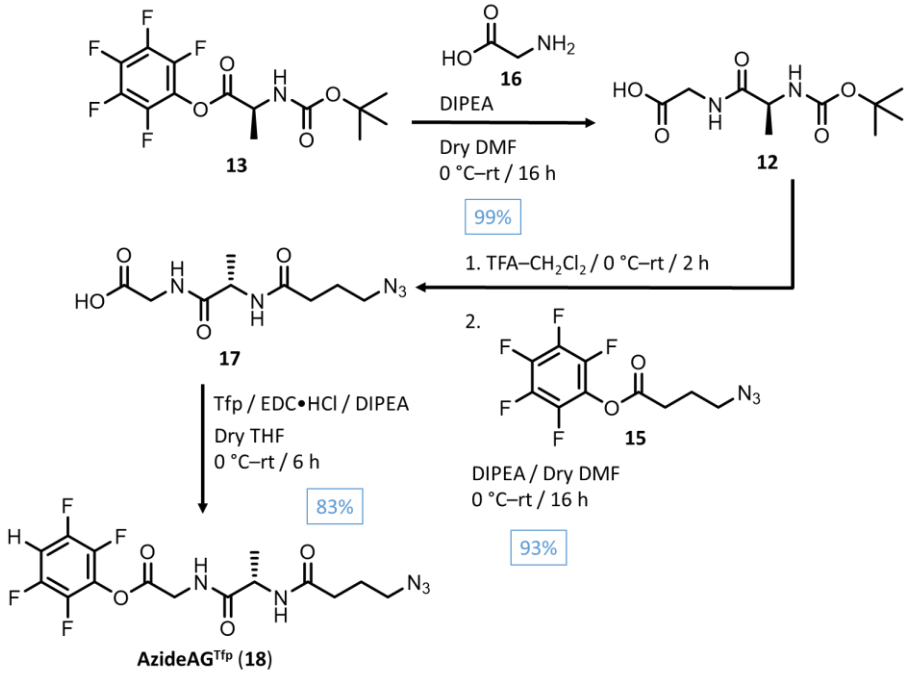

Scheme 5.4. Synthesis of **AzideAG^{Tfp}** *via* alanine-glycine intermediate **12**, utilising Pfp- and Tfp-activated peptide coupling methods.

afford a final 99% yield. Single-crystal X-ray analysis (Figure 5.5) confirmed the absolute stereochemistry (*S*) of the key alanine-glycine intermediate. Indeed, multiple hydrogen bonds were observed between molecules in a pleated ordering (see Figure 5.35, appendix), boding well for the self-assembly properties of the repeat unit.

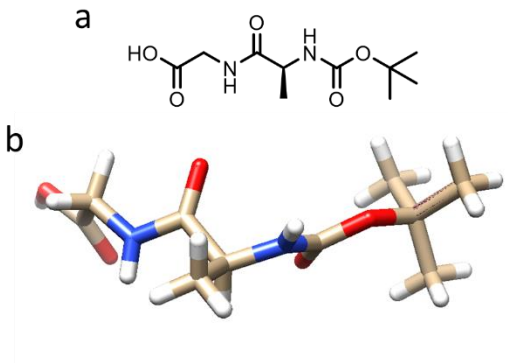

Figure 5.5. a) Chemical structure and b) solid-state structure of dipeptide **12**.

Dipeptide **12** was then deprotected (1:1 *v/v* TFA–CH_2Cl_2) to yield the TFA ammonium salt (97% yield), which was subsequently coupled (Scheme 5.4) to **15** to give the desired *N*-terminal peptide fragment **17** in 93% yield. Successful purification of **17** was achieved using reverse-phase chromatography (C18: 0–100% MeOH in H_2O), with the addition of 0.1% TFA essential to keep the acid moiety protonated and prevent co-elution with DIPEA. The *C*-activated Pfp ester of **17** (**AzideAG^{Pfp}**) was initially pursued by DCC-mediated coupling of **17** with pentafluorophenol. ^{1}H NMR analysis confirmed the reaction had gone to completion, however, the Pfp ester was found to have poor stability in water, as evidenced by recovery of **17** in large quantities from the aqueous layer. To reduce unwanted side reactions of the *C*-terminus of **AzideAG^{Pfp}**, the less reactive tetrafluorophenyl (Tfp) ester group was pursued instead, resulting

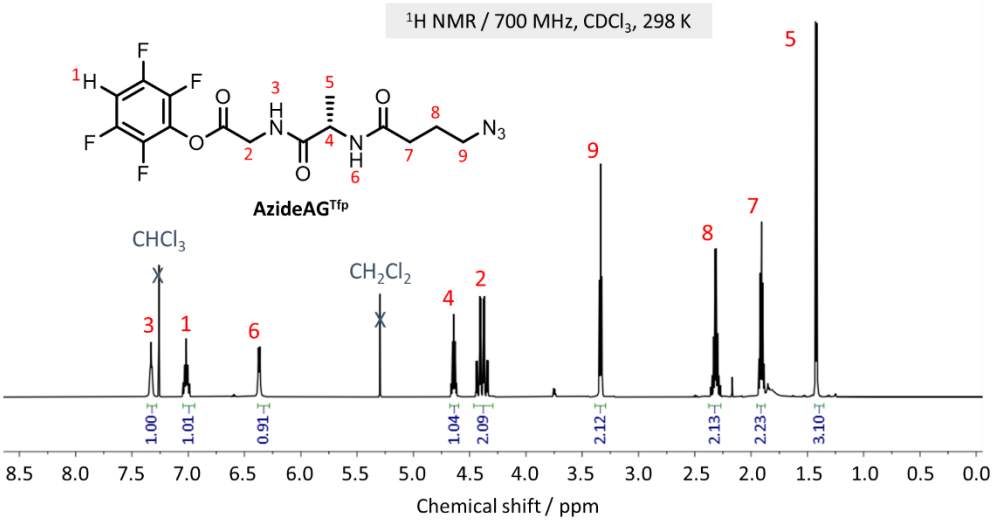

Figure 5.6. Partial ^{1}H NMR ($CDCl_3$, 700 MHz, 298 K) of **AzideAG^{Tfp}**, synthesised from **17** using EDC coupling reagent.

in **AzideAG^{Tfp}** (**18**, Figure 5.6). In this case, a combination of EDC•HCl and DIPEA was required to carry out the transformation of acid **17** to *C*-activated **18** in anhydrous THF. Following purification by normal-phase chromatography (SiO_2: 100% EtOAc), the *C*-activated **18** peptide fragment was successfully isolated in 83 % yield with no apparent side reactivity involving the Tfp ester observed this time. ^{1}H NMR spectroscopy (Figure 5.6) confirmed the successful *C*-activation, with the aromatic proton at δ_H 6.98 ppm (1, Figure 5.6) and glycine protons at δ_H 4.38 ppm (2, Figure 5.6) integrating to 1 and 2, respectively. Furthermore, the glycine amide proton at δ_H 6.98 ppm (3, Figure 5.6) is significantly downfield shifted in comparison to the alanine amide proton at δ_H 6.37 ppm (3, Figure 5.6) which suggests that some intramolecular hydrogen bonding is present involving the glycine residue of **AzideAG^{Tfp}**.

With **AlkyneGA^{DMB}**, **AzideAG^{Tfp}** and **Boc-NDI-COOH** available, the target protected macromonomer **M1^{DMB}** could be finally prepared in addition to control macromonomer **C1^{DMB}** (i.e., bearing no alanine–glycine residues) following a convergent synthetic approach (Scheme 5.5).

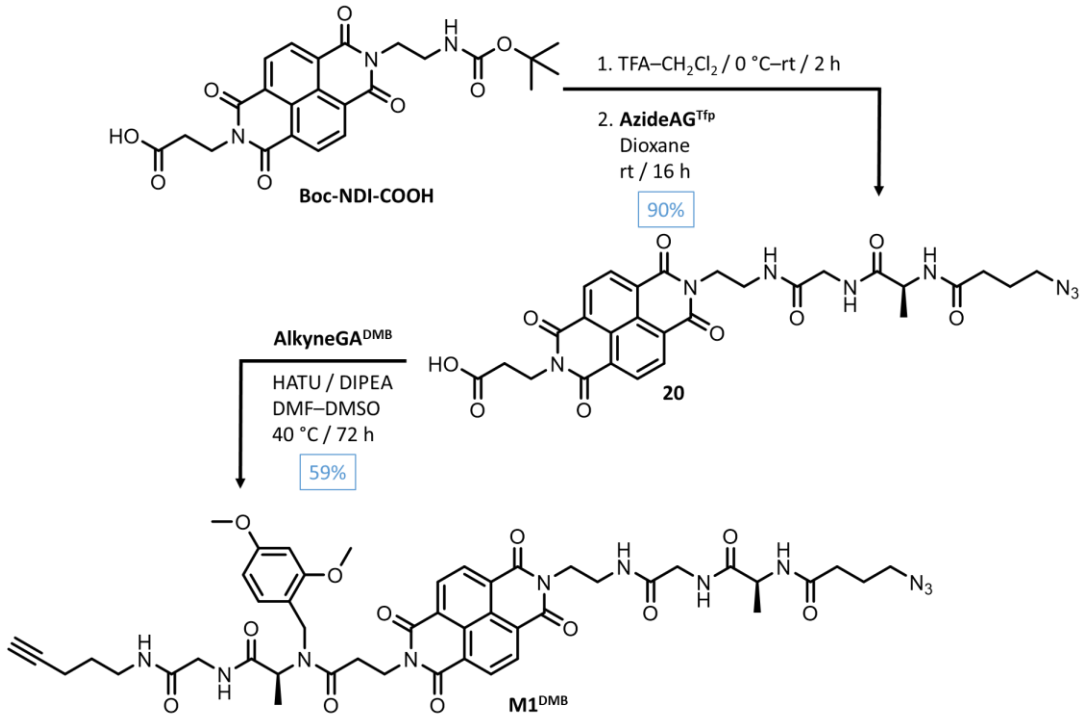

Scheme 5.5. High yielding synthesis of **M1^{DMB}** using both *C*-activation and orthogonal protecting group chemistry.

In pursuit of **M1^{DMB}**, **Boc-NDI-COOH** was Boc-deprotected in 1:1(*v*/*v*) TFA–CH_2Cl_2 before coupling to **AzideAG^{Tfp}**. Following removal of the reaction mixture solvent, the solid was triturated with EtOAc to remove excess **AzideAG^{Tfp}** and 1 M HCl to remove DIPEA, allowing NDI tripeptide **20** to be obtained in 90% yield. For the subsequent coupling with **AlkyneGA^{DMB}**, complete dissolution of tripeptide **20** was only possible at dilute concentrations (<0.01 M) in a mixture of DMF:DMSO 1:0.1(*v*/*v*), with the presence of DMSO also useful for

increasing the yield of peptide coupling reactions that induce molecular aggregation.[12] A coupling of the two fragments with HATU at 40 °C allowed for the target macromonomer **M1^{DMB}** to be isolated by column chromatography (SiO_2: 0–15% EtOH in CH_2Cl_2) in respectable yield (59%) given the coupling of a hindered secondary amine with a poorly soluble carboxylic acid peptide fragment.[4] The product was confirmed by ^{1}H NMR spectroscopy in which an AB quartet centred at δ_H 8.74 (18, 19, Figure 5.7) ppm was observed, indicative of an asymmetric *N*-substituted NDI system. Other proton peaks at δ_H 6.26 (27, Figure 5.7), 6.69 (7, Figure 5.7), 6.88 (24, Figure 5.7), 6.98 (22, Figure 5.7) and 7.12 (5, Figure 5.7) ppm were indicative of the amide proton environments, showing evidence of five peptide bonds in the macromonomer. Peaks associated with the 2,4-dimethoxybenzyl group were also present at δ_H 6.45 (12, 13, Figure 5.7) and 7.12 ppm (11, Figure 5.7), confirming the successful coupling. On closer inspection, geminal protons 4, 6, 10, 23 (Figure 5.7) are all split, e.g., J = 140 Hz for 10, with the presence of chiral centres in **M1^{DMB}** resulting in diastereotopic methylene proton environments. The significant splitting of the glycine methylene signals (6*, J = 286 Hz and 23*, J = 124 Hz, Figure 5.7) indicates a pre-folding of the peptide chains in $CDCl_3$, i.e., there are 'two faces' and geminal protons have differing chemical shifts.[19] The pre-folding on **M1^{DMB}** is likely driven by hydrogen bonds with the intramolecular folding further evidenced by the downfield shifting of the glycine amide signals (δ_H 6.70 and 6.92 ppm)[13], with respect to the alanine amide proton (δ_H 6.32 ppm). In addition, the compound was further confirmed by mass spectrometry with a peak at 964.3976 m/z (964.3953 m/z calculated for $[M+H]^+$ = $C_{47}H_{54}N_{11}O_{12}$).

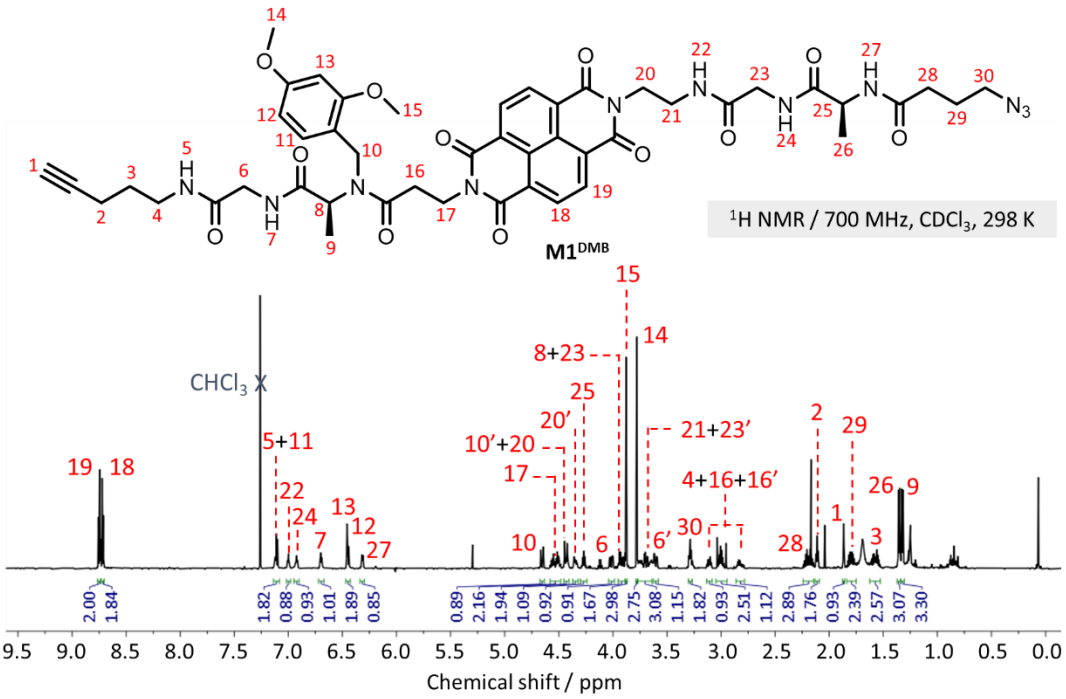

Figure 5.7. ^{1}H NMR ($CDCl_3$, 700 MHz, 298 K) spectrum of **M1^{DMB}**.

The π-embedded design of macromonomer **M1^{DMB}** is such that CuAAC click polymerisation will generate an artificial β-turn mimic *via* a 1,4-triazole that is expected to promote polymer folding into anti-parallel β-sheets upon removal of the DMB protecting group. The formation of 1D fibres is expected to marshal NDI units into co-facial (presumably *H*-type)[14,15] aggregates that lend themselves to investigations of through-space electron delocalisation events across hierarchically ordered π-stacks. A control macromonomer (**C1^{DMB}**, Scheme 5.6) bearing no alanine–glycine peptide residues was also prepared in order to distinguish the critical role of the peptide sequence in stabilising aromatic foldamer assembly. Control NDI macromonomer **C1^{DMB}** was synthesised in a manner similar to macromonomer **M1^{DMB}**, making use of already available intermediates and precursors. Requisite DMB-protected alkyne amine **22** (Scheme 5.6) was prepared in 63% yield by subjecting 1-amino-4-pentyne (**7**) to reductive amination conditions in the presence of 2,4-dimethoxybenzaldehyde using $NaCNBH_3$. The synthesis of **C1^{DMB}** (66%, Scheme 5.6) was then achieved by coupling amine **22** with the azide-terminated NDI **21** (prepared from **Boc-NDI-COOH** and Pfp-activated azide **15**; see

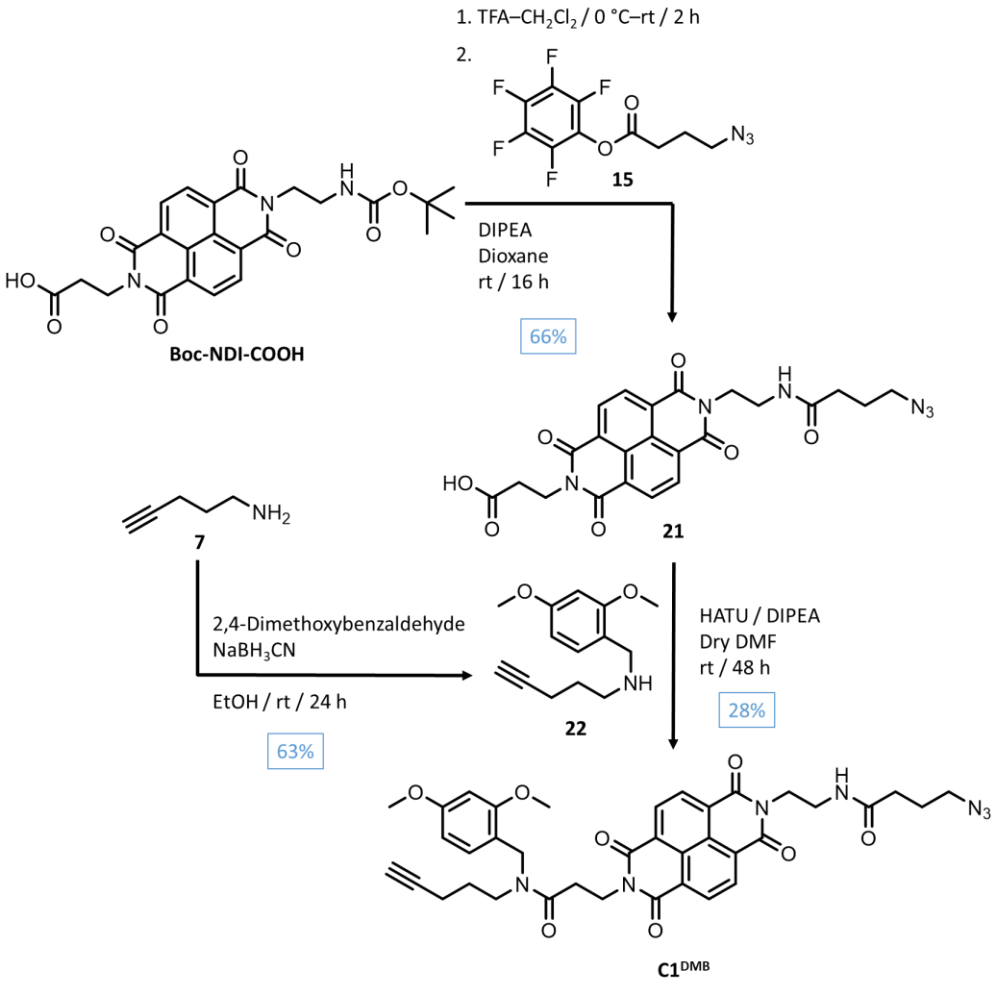

Scheme 5.6. Synthesis of control macromonomer **C1^{DMB}** from NDI **21** and DMB protected alkyne **22** which was synthesised from **7.**

Experimental section for details) with coupling agent HATU in DMF. The protected macromonomer **C1^{DMB}** was isolated by column chromatography (SiO_2: 40–100% EtOAc in *n*-hexanes) in a yield of 28%.

The ^{1}H NMR and NOESY (Figure 5.8) analysis of **C1^{DMB}** in $CDCl_3$ revealed the presence of two different conformers (i.e., rotamers) in solution. Peaks at δ_H 1.89 (1*, Figure 5.8) and 1.94 (1*, Figure 5.8) ppm, as well as peaks at δ_H 6.98 (6*, Figure 5.8) and 7.17 ppm (6*, Figure 5.8) both showed NOESY correlations indicating exchange between both conformers. Environments proximal to the tertiary amine inversion centre are split the most (e.g., 6, 5 and 11, Figure 5.8), with respect to other environments such as the propargyl azide chain which is situated on the opposite termini of **C1^{DMB}**. A stabilised conformation is hypothesised in which the electron-rich DMB group forms an aromatic charge-transfer interaction with the electron poor NDI unit that facilitates the electrostatically stabilised conformer, i.e., the conformer with the greatest population for 6, 5, 11 etc. at roughly 7:3. Indeed, there is a solvent dependency for **C1^{DMB}** to exist as rotamers with the ^{1}H NMR spectrum of **C1^{DMB}** in DMSO-d_6 showing (see

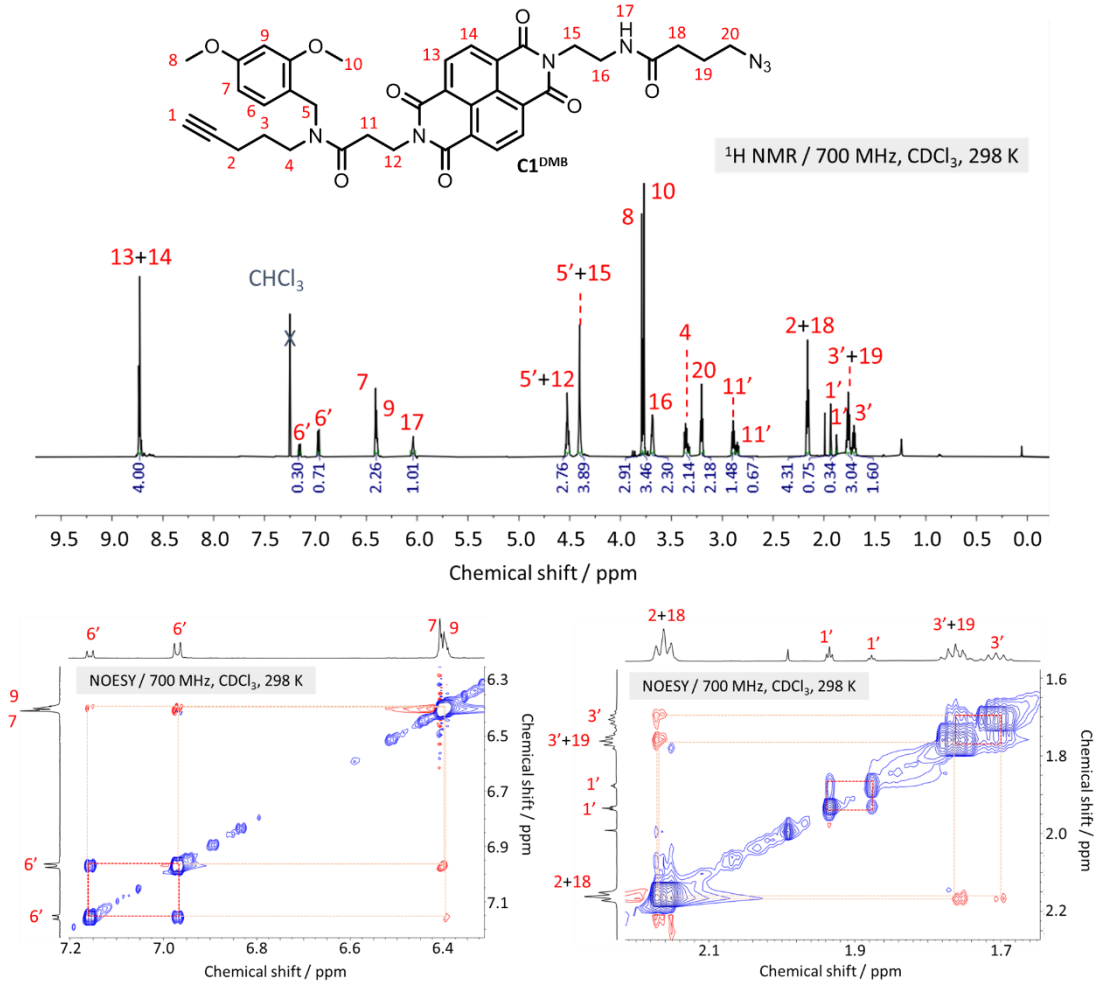

Figure 5.8. Partial ^{1}H NMR ($CDCl_3$, 700 MHz, 298 K) spectrum of **C1^{DMB}** with assignments (top), and partial NOESY spectra between 6.3–7.2 ppm and 1.6–2.2 ppm showing exchange (blue) and COSY (red) correlations.

Figure 5.34, appendix) only one conformation is present. Further, solvent-dependence and variable-temperature NMR analysis will elucidate further insight into the **C1^{DMB}** rotamer dynamics.

Whereas a mixture of conformers is observed for **C1^{DMB}**—which likely form as the result of a weak aromatic CT interaction between the DMB group and the NDI unit—a single conformer is observed for **M1^{DMB}** stabilised by multiple intramolecular hydrogen bonds. These observations bode well for the envisioned self-assembly of the polypeptide. Indeed, with both macromonomers in hand, attention was turned towards preliminary polymerisation reactions.

5.2.2 CuAAC 'Click' Polymerisation of **M1^{DMB}**

The CuAAC (Figure 5.9a) reaction installs an artificial β-turn whilst propagating the length of the polypeptide chain. Typically, macromonomer polymerisations are carried out at high concentrations (0.1 M) in order to maximise the degree of polymerisation (DP) according to Carother's equation[16] for step-growth bifunctional (AB, here, A = azide and B = alkyne) polymerisations. Additionally, a high concentration reduces the formation of cyclic oligomers.[17,18] First, **M1^{DMB}** was dissolved in DMF with TBTA (**30**, Figure 5.9b). As a ligand for Cu(I), TBTA coordinates to and stabilises the active Cu^+ species for catalysing the cycloaddition reaction. The reaction mixture was deoxygenated *via* three cycles of freeze-pump-thaw under Ar before the Cu^+ source (CuOAc) was added and the reaction mixture heated to 80 °C. TLC analysis (SiO_2: 12% ethanol in CH_2Cl_2) indicated the full reaction of the macromonomer after 1 h, however, in an attempt to increase the polymer length, the reaction

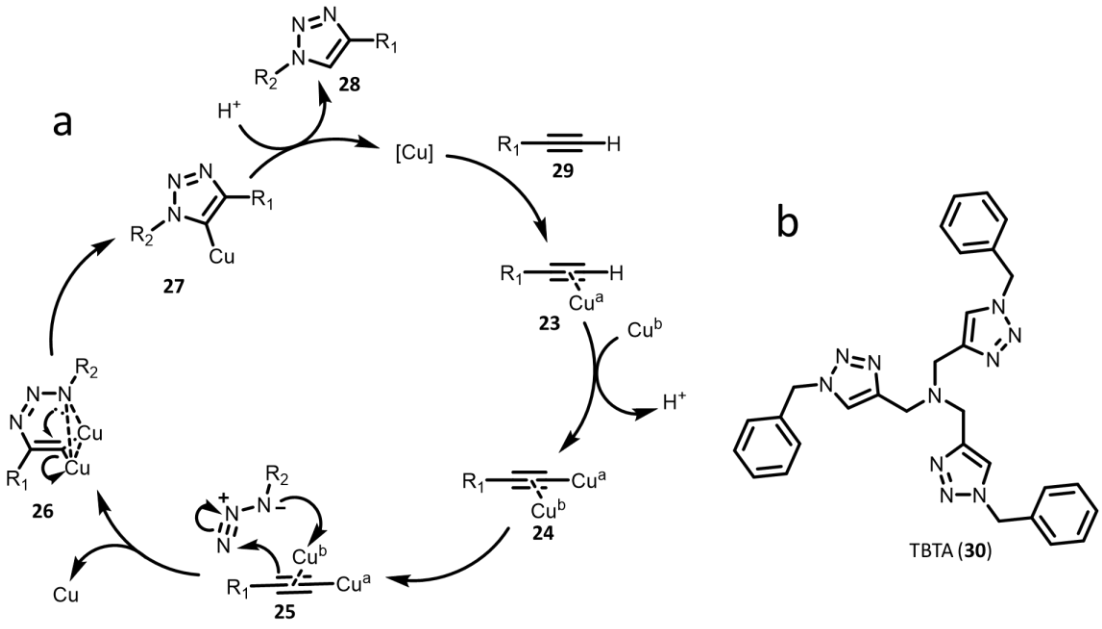

Figure 5.9. Most recently proposed mechanism for CuAAC, as described by Fokin.[47]

was continued overnight. Upon cooling the reaction mixture, MeOH was added to quench the polymerisation and precipitate polymer **P1^{DMB}**, which was subjected to multiple washings in MeOH by centrifugation. As expected, polymer **P1^{DMB}** was less soluble in solvents such as CH_2Cl_2 and THF. **P1^{DMB}** was fully soluble in solvents such as a DMF and DMSO, as well as HFIP, which is known to solubilise hydrogen bond-acceptor molecules such as polyamides; solubility of **P1^{DMB}** in chlorinated solvents (i.e., CH_2Cl_2, $CHCl_3$) could be achieved by introducing 10% *v*/*v* MeOH.

Analysis of the ^{1}H NMR spectrum of **P1^{DMB}** confirms the polymeric nature of this high-molecular weight product: extensive peak broadening is observed for all proton environments compared to the sharper ^{1}H NMR spectrum of monomer **M1^{DMB}**. Peaks at δ_H 8.53 (5, 6, Figure 5.10) and 6.55 (3, 4, Figure 5.10) ppm correspond to the NDI aromatic protons and the aromatic DMB protons, respectively, with the newly formed triazole proton observable at δ 7.50 (7, Figure 5.12). As a result of the broad and overlapping peaks, no end-group analysis could be performed on the alkynyl hydrogen or terminal methylene groups, to estimate the DP.

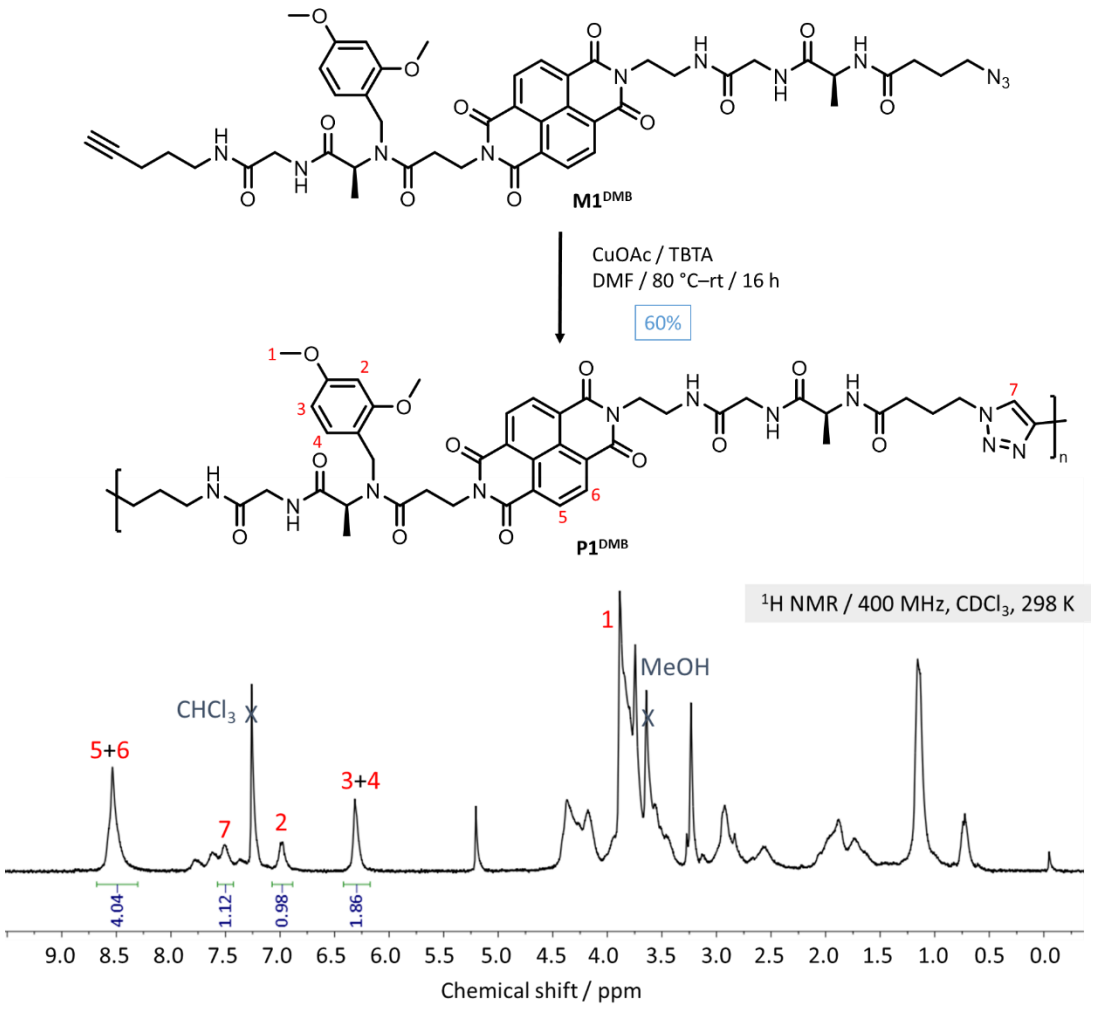

Figure 5.10. CuAAC polymerisation of **P1^{DMB}** using CuOAc in the presence of TBTA. ^{1}H NMR ($CDCl_3$:MeOD 0.9:0.1(*v*/*v*)), 400 MHz, 298 K) spectrum of **P1^{DMB}** with partial assignment. Broadening of all environments indicates a polymeric species is present.

Owing to the low amount of sample isolated, no ^{13}C spectrum could be collected, however, it is anticipated that the disappearance of the alkynyl carbons and the formation of the triazole carbons will further confirm the successful polymerisation of **M1^{DMB}** to **P1^{DMB}**. As a means to quantify the extent of polymerisation and the average mass of the polymers present, attention was then turned towards GPC and MALDI-TOF MS.

The polymer is observed by MALDI-TOF MS as a sodiated adduct, which is common[19] for polyamides (See Figure 5.36, appendix). As MALDI-TOF is not implicitly quantitative the number average molecular weight (M_N) cannot be estimated, however, up to a heptamer of **P1^{DMB}** is observed. To complement the MALDI-MS data, GPC analysis of **P1^{DMB}** was also conducted; sample measurements were calibrated against polystyrene in DMF (0.1 M LiCl). GPC analysis (see Figure 5.37, appendix) of **P1^{DMB}** revealed a retention volume of 13.55 mL which correlated to an M_N of 9,869 g mol^{-1}, weight average molecular weight (M_W) of 24,169 g mol^{-1} and a polydispersity index (PDI) of 2.45. These data are comparable with previously reported[9] CuAAC polymerisations with GPC characterisation of Guan's polymer confirming a M_N of 11,500 g mol^{-1}, M_W of 21,800 g mol^{-1} and a PDI of 1.84.[21] Both GPC and MALDI-MS therefore complement the finding of at least several macromonomers joined together following the CuAAC polymerisation and thus confirm the synthesis of a high molecular weight π-embedded polypeptide.

5.2.3 Optoelectronic Properties of a π-Embedded Polymer, **P1^{DMB}**

The solubility of protected polymer **P1^{DMB}** and protected monomer **M1^{DMB}** was limited in organic solvents, however, solubility of **P1^{DMB}** in DMF and HFIP allowed for some preliminary steady-state characterisation of the DMB-protected polymer by UV-Vis and CD spectroscopy, as well as by cyclic voltammetry. In addition, solid-state analyses have been performed using FTIR spectroscopy.

The optical properties of rigid chromophores such as NDI endow them with properties that are sensitive to their neighbouring environment; the absorption profile varies extensively between monomeric and highly aggregated or coupled states. Samples of **M1^{DMB}** were prepared at 50 μM, i.e., O.D of 1.0 (l = 1 cm). In order to draw genuine comparisons with the monomer, samples of **P1^{DMB}** were prepared at the same O.D. In HFIP, **M1^{DMB}** shows (Figure 5.11a) well-resolved sharp absorption bands between 300–400 nm, i.e., λ_{max} = 342, 360 and 382 nm, as a result of the π–π* transition across the long z-axis of the NDI chromophore; this implies a monomeric, non-aggregated state.[20,21] The spectrum of **P1^{DMB}** in HFIP is almost identical (Figure 5.11a) to the macromonomer profile indicating that the artificial β-turn mimic does not induce folding of the polymer that results in ground-state intramolecular NDI aggregation. In contrast, there is change between the profiles of the macromonomer and the polymer in DMF.

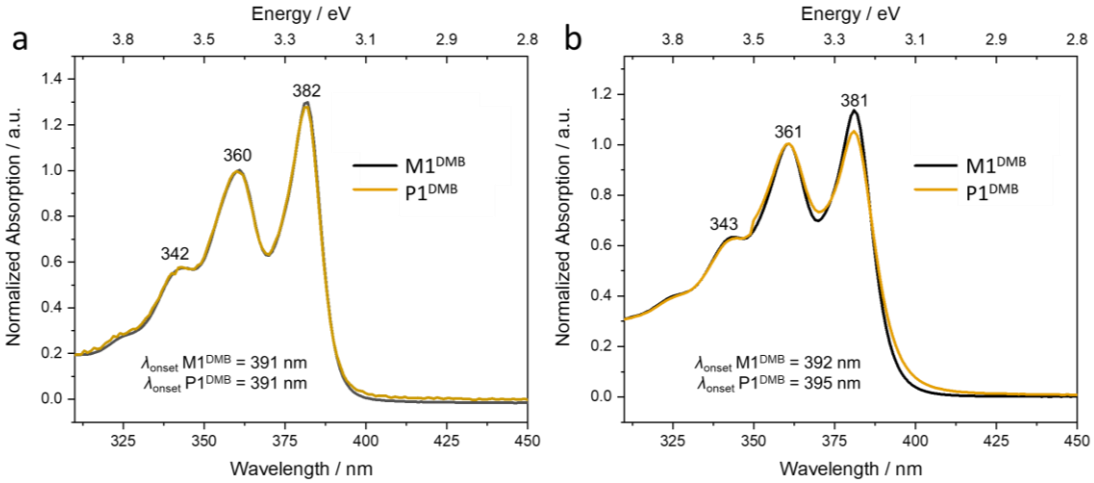

Figure 5.11. Normalised UV-Vis absorbance spectra of monomer **M1^{DMB}** (black) and **P1^{DMB}** (gold) in a) HFIP and b) DMF.

The absorption profile of **M1^{DMB}** in DMF (Figure 5.11b) is highly reminiscent of the profile in HFIP, with peaks at λ_{max} = 381, 361 and 343 nm corresponding to the three main absorptions. However, in DMF, the ratio between the two lowest-energy vibronic absorptions at 381 and 363 nm is decreased, i.e., from 1.13 for **M1^{DMB}** to 1.05 for **P1^{DMB}**. Additionally, the λ_{onset} of **P1^{DMB}** is bathochromically shifted to 395 nm (vs. 392 nm for **M1^{DMB}**). These spectral changes are in accord with the formation of *J*-aggregates, i.e., the orienting of NDI chromophores into co-facial, presumably slip-stacked arrangements that are thermodynamically stabilised relative to the monomerically dissolved state[22,23] These observations also provide evidence that the artificial β-turn facilitates some foldamer assembly wherein NDI units are positioned in close proximity (≤3.5 Å) and electronically coupled.

To gain further insight into the nature of the assembly processes, CD spectroscopy was employed. CD spectroscopy is integral to characterising chiral molecules and nanostructures; chiral structures interact with circularly polarised light, enabling the detection of enantiomers (i.e., *R/S* configurations or *P/M*-helical isomers) that will typically display mirrored CD signals as well as assemblies such as β-sheets (i.e., a maximum and a minimum at 195 nm and 216 nm, respectively[24]). CD analysis in HFIP is useful in identifying a change in the peptidic region of the polymer.[25,26] On the other hand, DMF is useful as a solvent to monitor any changes in the Cotton effect region, while at the same time not inducing any specific conformation as in HFIP. For all CD spectra recorded, the high-tension voltage (HT) was kept under 500 V throughout the measurement in order to not oversaturate the detector.

The far-UV (260–195 nm, Figure 5.12a) CD spectrum for **M1^{DMB}** in HFIP indicates a random coil-like assembly[27] is present with a minimum at 198 nm. Additionally, a negative Cotton effect is observed between 320–420 nm, i.e., λ_{max} = 381 and 357 nm—associated with the ground-state absorption of an NDI unit. For the polymerised species **P1^{DMB}**, in which the

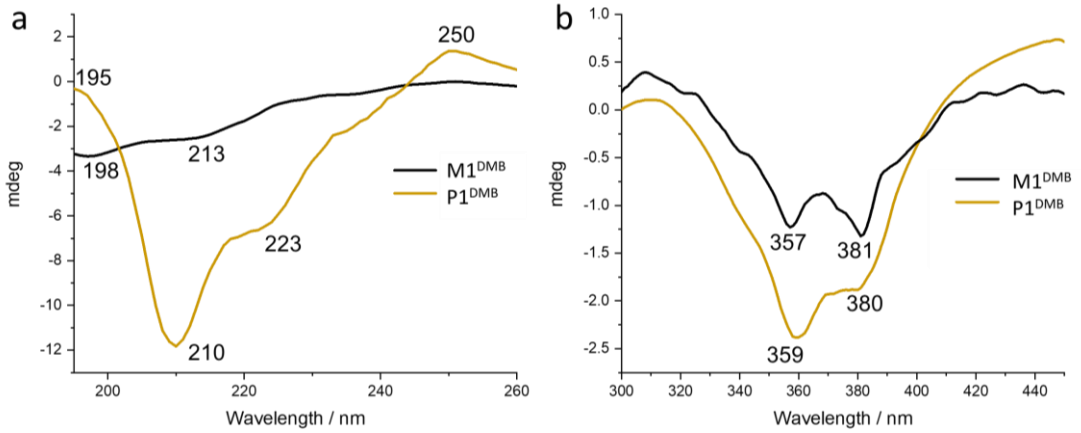

Figure 5.12. CD spectra for **M1^{DMB}** [50 µM] (black) and **P1^{DMB}** [1.0 mg/ mL] (gold) in the a) far-UV and b) low-UV region; collected in HFIP.

artificial β-turn mimic is installed into the backbone, there is a significant change in the far- and low-UV regions (i.e., 190–450 nm). Negative Cotton effects are observed for **P1^{DMB}** (λ_{max} = 380 and 359 nm) in HFIP (Figure 5.12b), with an inversion between the two bands (381 and 357 nm) in comparison to **M1^{DMB}**. Additionally, for **P1^{DMB}** a maximum at 250 nm is indicative of another NDI transition along the short axis of the chromophore, in an assembled state.[28] Whereas ground-state absorption data did not show any signs of NDI aggregation for both **M1^{DMB}** and **P1^{DMB}**, the observations from CD analysis suggest that both molecules assemble into chiral assemblies, likely driven by the high polarity of the HFIP solvent molecules. In the far-UV region, an α-helical conformation of the peptide backbone in **P1^{DMB}** is most prominent with a minima at λ = 223 and 210 nm, although, there is evidence for a random coil conformation with a maximum at λ = 195 nm.[29] The observations can be rationalised owing to the conformational inducing effects of solvents such as HFIP; the solvent molecules interact strongly with peptide regions which simultaneously promote extended helical conformations over more compact, hydrogen bond driven assemblies such as β-sheets.[30] Nevertheless, in HFIP the different CD spectra of **M1^{DMB}** and **P1^{DMB}** show that the macromolecular scaffold facilitates a change in the self-assembly properties with chiral assemblies formed for both the macromonomer and polymer.

On the other hand, in DMF assembly should be unaffected by any solvent-induced conformation that may be present in HFIP. In DMF, for **M1^{DMB}**, there is no Cotton effect observed (Figure 5.13) which suggests that the molecule has not aggregated into any chiral nanostructures. This is in contrast to the behaviour in HFIP that showed assembly of **M1^{DMB}** which suggests that the less polar solvent molecules do not drive assembly. In DMF a positive Cotton effect (Figure 5.13) clearly arises for **P1^{DMB}** between 300–425 nm, (i.e., λ_{max} = 390 and 378 nm), providing evidence that the introduction of the β-turn mimic facilitates foldamer assembly in to nanoscale assemblies that have NDI–NDI couplings. Furthermore, the sign of

the Cotton effect is opposite to that observed in HFIP suggesting a change in helicity of the assemblies from *M*- in HFIP) to *P*- in DMF. Ultimately, analysis of the ground state UV-Vis and CD spectroscopic data suggests that polar solvent molecules of HFIP induces assembly of the peptide fragments of both **M1^{DMB}** and **P1^{DMB}** into chiral assemblies whereas in DMF assembly is dependent on the macromolecular scaffold. Unfortunately, the incompatibility of DMF in the far-UV region (i.e., <270 nm) for CD spectroscopy makes it impossible to rationalise any secondary structure conformation in the assembled polymer. Nevertheless, the polymerisation of **M1^{DMB}** into **P1^{DMB}** has resulted in a change of the electronic couplings of the embedded NDI units that are likely facilitated by an ordered peptide backbone. The UV-Vis and CD spectra strongly support the notion that the artificial β-turn facilitates folding of the polymer to encourage NDI interactions in the ground state—indeed, it is likely that only the partial folding of the macromolecular is possible because of the DMB group. To further investigate any secondary structure formation in **P1^{DMB}**, solid-state FTIR spectroscopy was performed on **M1^{DMB}** and **P1^{DMB}**. Here, the Cotton effect observed in α-helical assemblies provides evidence for anticipated properties such as long range electron transport.[31]

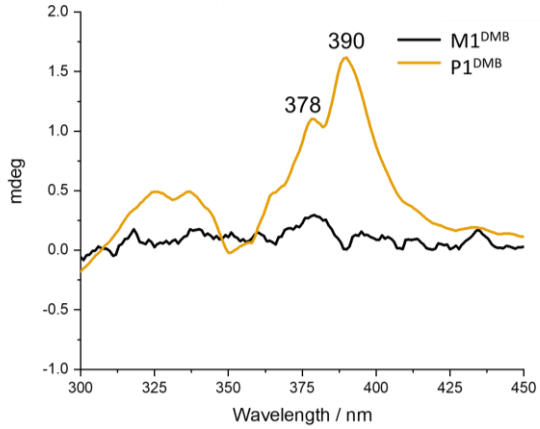

Figure 5.13. CD spectra for **M1^{DMB}** [50 µM] (black) and **P1^{DMB}** [0.5 mg/ mL] (gold) between 450–300 nm; collected in DMF.

FTIR spectroscopy is a powerful tool for assessing secondary structure conformations of polypeptides such as β-sheets and α-helices.[32] There are two amide bands (I and II) that can be used to decipher peptide backbone conformation in FTIR spectra. The easiest to decipher is that of the amide I region; this vibration results from the C=O stretching of the amide group coupling to the bending of the N–H and the stretching of the C–N bonds.[33] The amide I band is found between 1,700–1,600 cm^{-1} and is the site from which β-sheet structures can be observed. Indeed, insights such as the presence of β-turns, parallel and anti-parallel ordering can all be rationalised from the amide I band region and therefore it is an essential technique for probing the assembly of both **M1^{DMB}** and **P1^{DMB}** in the solid state.[34] The FTIR spectrum of **M1^{DMB}** (Figure 5.14a) identifies an easily recognisable $–N_3$ stretch at 2105 cm^{-1}. Upon

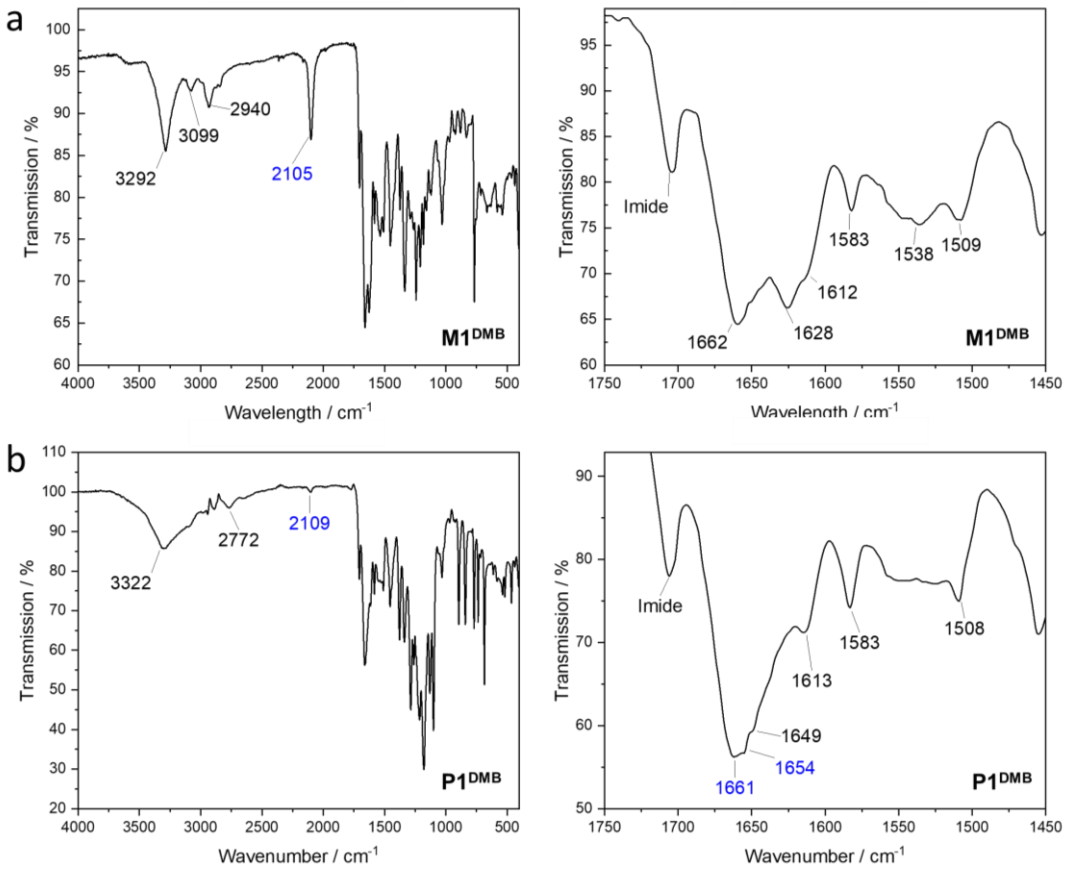

Figure 5.14. FTIR spectrum of a) **M1^{DMB}** with resolution of the amide I and amide II region; the azide stretch is highlighted at 2105 cm^{-1}. FTIR spectrum of b) **P1^{DMB}** with resolution of the amide I and amide II region; the azide stretch is highlighted as well as the frequencies relating to random coil formation.

polymerisation to **P1^{DMB}**, the relative intensity of the azide stretch is diminished significantly, however, it is still present; this is expected owing to the unreacted terminal azide residues in the polydisperse product. Analysis of the amide I region of **M1^{DMB}** suggests a mixture of aggregated states involving the amide residues are present, with absorbances at 1628 and 1162 cm^{-1} indicative of β-sheet and random coil assemblies, respectively. Analysis of the amide I region of **P1^{DMB}** (Figure 5.14b) reveals two key absorptions at 1661 and 1654 cm^{-1} that are characteristic of a random coil conformation[35] with a disappearance of the absorption at 1628 cm^{-1} that was observed for **M1^{DMB}**. These observations are consistent with the CD data of **P1^{DMB}** collected in HFIP that suggested both random coil and helical-like conformations were present. Furthermore, the FTIR spectrum of **P1^{DMB}** is reminiscent to the DMB-protected polypeptide **PG^{DMB}** synthesised by Guan and co-workers who also deduced random coil[9] formation with an absorbance at 1655 cm^{-1}. In conjunction with UV-Vis and CD spectroscopies, FTIR spectroscopy provides further evidence that the artificial β-turn facilitates greater order of the macromolecule that in turn mediates greater π-assembly of NDI stacks. To investigate the resulting effects on the redox-properties of the NDI units, cyclic voltammetry experiments were employed in DMF.

The reduction properties of NDI units are highly sensitive to aggregation with favourable π-interactions between electron-deficient NDI units facilitating easier reductions (see Chapter 1.3).[36] To probe the reduction properties in the NDI-embedded molecules, cyclic voltammetry was carried out on samples of **M1^{DMB}** [0.5 mM] and **P1^{DMB}** [0.5 mg/ mL] in dry, degassed DMF solutions containing 0.1 M $TBAPF_6$ as the supporting electrolyte. Briefly, **M1^{DMB}** undergoes two well-defined single-electron reduction events (Figure 5.15a) at –0.46 and –0.84 V vs. Ag/AgCl to generate stepwise the NDI radical anion (i.e., $NDI^{\bullet-}$) and dianion (i.e., NDI^{2-}) states, respectively; the voltammogram is highly reminiscent of a non-aggregating NDI species.[37] However, the voltammogram of **P1^{DMB}** (Figure 5.15b) provides evidence of electronic coupling of the NDI units with an earlier onset of reduction (ΔV = –80 mV) which is indicative of a more accessible NDI to generation $NDI^{\bullet-}$ for each NDI unit within the polymer chains. As the local environment, i.e., *N*-substitution, of the NDI units in **M1^{DMB}** and **P1^{DMB}** are identical, this observation can be confidently attributed to the pre-folding of the polypeptide chain that facilitates intramolecular NDI aggregation. Additionally, the broadness of the first reduction wave of **P1^{DMB}** is indicative of various redox-states of NDI units that are sequentially reduced over the CV experiment, i.e., in a multivalent species.[38] These observations agree with some assembly of the peptide chains facilitated by the polymer backbone. Additionally, a more negative reduction peak potential (–0.89 V) is required to generate the NDI^{2-} state of **P1^{DMB}**, in which all NDI units have been fully reduced to the dianionic state. The change in potential (ΔV = +50 mV) likely arises owing to increased Coulombic repulsion effects in the partially assembled polymer. Indeed, the lower reduction potential suggests that the partially folded macromolecular scaffold provides a platform for extended $NDI^{\bullet-}$–$NDI^{\bullet-}$ interactions. Upon full reduction to the NDI^{2-} state for each unit, the electronically disfavoured π-interactions between NDI units is ultimately what triggers disassembly of **P1^{DMB}** in a similar manner to the pH controlled disassembly of protonated peptide–π conjugates.[39] These observations suggest that

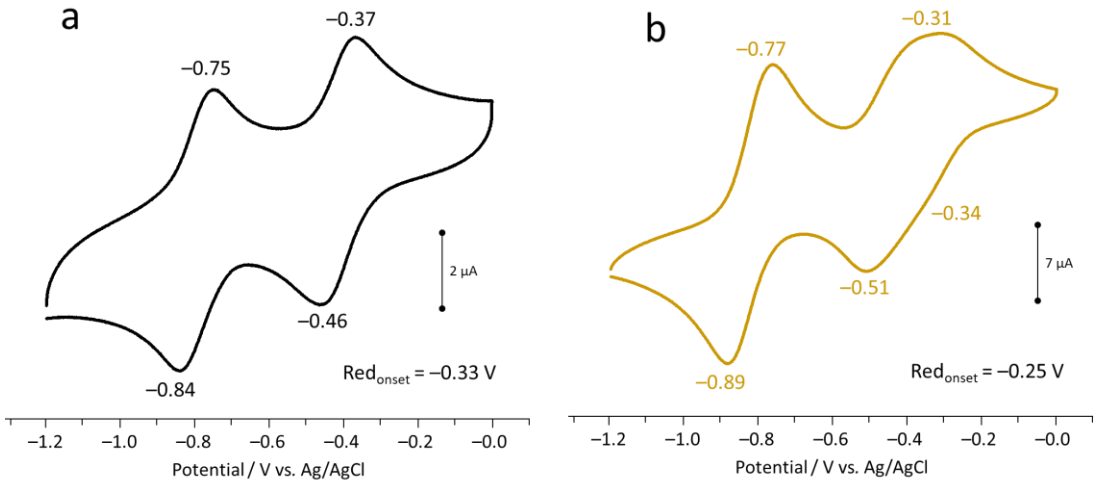

Figure 5.15. Cyclic voltammograms (50 mVs^{-1}, 298 K) of a) **M1^{DMB}** and b) **P1^{DMB}** in degassed DMF containing 0.1 M $TBAPF_6$ as supporting electrolyte.

the macromolecular approach to π-assembly is providing access to properties that are emergent because of the molecular design, i.e., from i) folding facilitated by the β-turn mimic and ii) the intramolecular hydrogen bonding complementarity enforced by anti-parallel β-strand positioning.

Table 5.1. Optical and electrochemical properties of **M1^{DMB}** and **P1^{DMB}** collected in DMF

Compound	λ_{abs}[a] [nm]	E_{gap}[b] [eV]	E_{red} [V]	LUMO[c] [eV]	HOMO[d] [eV]
M1^{DMB}	381, 361	3.16	–0.33	–7.03	–3.87
P1^{DMB}	381, 361	3.14	–0.25	–7.09	–3.95

[a] solution, [b] Onset of absorption, [c] $E_{LUMO} = -(E_{red} + 4.75)$ eV, [d] $E_{HOMO} = E_{LUMO} - E_{gap}$ eV

Although further characterisation of **M1^{DMB}** and **P1^{DMB}** by PL, SEC, AFM and TEM is necessary for a complete understanding of the optoelectronic as well as self-assembly properties, test DMB-deprotections have been conducted on **P1^{DMB}**, in pursuit of the deprotected polymer, **P1**. Indeed, preliminary characterisation of the deprotected polymer may aid the understanding and allow for further insights into the structural and self-assembly properties of **P1^{DMB}**.

5.2.4 Stimuli-Responsive Folding of a π-Embedded Polypeptide

We hypothesised that the integration of the DMB group into the polymer backbone would have benefits such as i) preventing premature aggregation that decreases solubility and ii) installing stimuli-responsive behaviour. Following the removal of the DMB group, a free amide is liberated that can readily participate in hydrogen bonding interactions, i.e., intramolecular interactions that are necessary to fold the polypeptides into 1D β-sheets. When desired, the protecting group can be cleaved following treatment with TFA/TIPS/H_2O (95:2.5:2.5).[9] Following treatment of **P1^{DMB}** with the acidic solution (see Experimental 5.4.2 for full synthetic details), the deprotected polymer **P1** could be isolated by centrifugation with washings of MeOH. Reaction completion was indicated by TLC analysis (SiO_2: 0–12% EtOH in CH_2Cl_2) with disappearance of the **P1^{DMB}** spot, with replacement by another ninhydrin- and UV-active (365 nm) spot on the baseline. With the artificial β-turn directing antiparallel β-sheet assembly, the now freely available alanine residue can participate in hydrogen bonding to allow complete alignment of the monomer strands through successive H-bond donor and acceptor interactions.

FTIR spectroscopy was employed to gain some initial insight into any changes in the peptide backbone conformation upon deprotection. In an attempt to mediate the desired self-assembly of the deprotected polymer **P1**, the time-controlled precipitation of the polymer was initiated from adding H_2O (50%) to a dilute [0.1 mM] solution of **P1** in HFIP (50%).[40] The mixture was left overnight, during which a white cotton-like solid precipitated (66% yield) from solution. The assembled polymer **P1** was isolated by filtration and used for FTIR spectroscopy. Analyses of the amide I region for the non-assembled DMB-protected polymer $\mathbf{P1^{DMB}}$ indicated a random coil conformation was likely present (Figure 5.16a). However, for the assembled polymer **P1**, absorptions (Figure 5.16b) at 1696 and 1628 cm^{-1} in the amide I region were indicative of β-sheet assemblies with the absorption at 1661 cm^{-1} no longer present. Furthermore, absorptions at 1528 and 1577 cm^{-1} in the amide II region of **P1** were indicative of β-turns. These observations provide evidence for an anti-parallel β-sheet conformation in the deprotected polymer **P1**.[9,35] As polypeptide structures are highly dependent on pH, ionic strength and temperature, there is scope to modify the assembly of the deprotected polymer **P1** that may lead to even high order aggregates.[40] Owing to the very low solubility of **P1**, solid-state techniques such as AFM, TEM and WAXS will be key in characterising the assemblies in both the assembled as well as non-assembled polymer. The spectral changes following deprotection demonstrate the validity of our design to enable acid-responsive polymer assembly into anti-parallel β-sheets in the presence of a relatively large chain-embedded NDI π-system. Although these results are preliminary, it is clear that the changing of properties between $\mathbf{M1^{DMB}}$, $\mathbf{P1^{DMB}}$ and **P1** provides some initial evidence of macromolecular assembly that results in β-sheet forming assemblies.

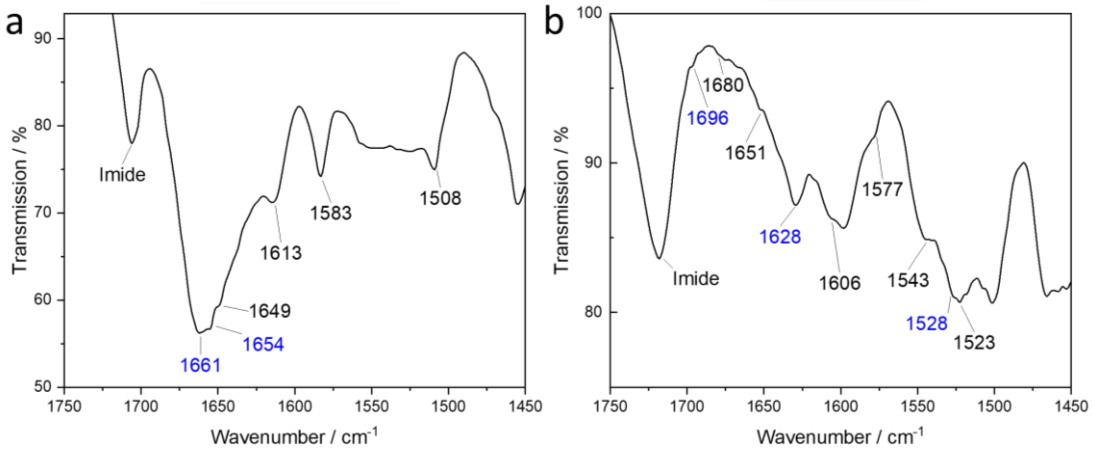

Figure 5.16. FTIR spectra of a) $\mathbf{P1^{DMB}}$ and b) **P1** between 1450–1750 cm^{-1}; the peaks associated with a) random coil and b) β-sheet formation, are highlighted (blue).

Unfortunately, as a result of COVID, this project could not be completed however work is currently being undertaken in the Avestro group to complete all remaining analyses on not only **M1^{DMB}**, **P1^{DMB}** and **P1,** but also **C1^{DMB}**, **CP1^{DMB}** and **CD1** (Figure 5.17). It is anticipated that AFM and TEM will be necessary in characterising the highly ordered nanostructures which will have 1D ordering, i.e., β-sheet assemblies. The proximal positioning of the NDI units in the foldamers should support electron sharing properties and therefore spectroelectrochemistry (SEC) and electron paramagnetic resonance (EPR) spectroscopy will be integral to observing and quantifying the radical delocalisation properties. These charge delocalisation properties are important for assessing conductivity applications in organic electronic materials. The remaining analyses will reinforce the design rational behind a π-embedded polypeptide that allows for functional materials that are reminiscent of biomaterials such as spider silk.

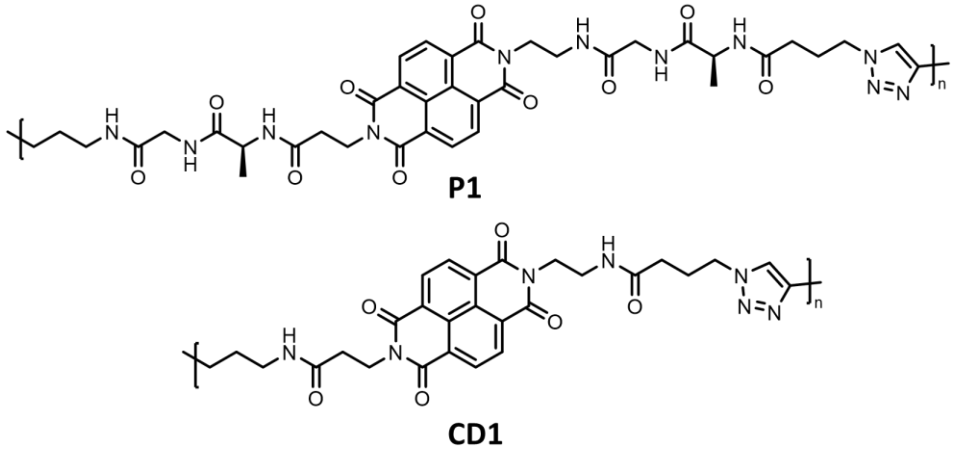

Figure 5.17. Structures of DMB-deprotected polymers **P1** and **CD1**.

5.3 Conclusions

We have designed and synthesised a π-embedded macromonomer that can be 'click' polymerised using CuAAC chemistry providing a route towards high molecular weight polypeptides whilst also installing an artificial β-turn that promotes macromolecular folding. As a proof-of-concept, we have embedded an NDI electron-acceptor motif, a staple π-electron acceptor. The embedded redox-unit has allowed for the monitoring of π-assembly in the macromolecule **P1^{DMB}**. In DMF, NDI π-interactions are observed by UV-Vis spectroscopy which confirms *J*-aggregation of NDI units in the protected polymer **P1^{DMB}** but not for the parent macromonomer **M1^{DMB}**. Additionally, CD spectroscopy of **P1^{DMB}** in DMF shows exciton coupling of NDI units *via* a Cotton effect in the polymer providing evidence for π-assembly that is mediated by macromolecular folding, which in turn is directed by a β-turn mimic. CV experiments show that the NDI units within **P1^{DMB}** are easier to reduce as a

consequence of favourable interactions between the electron-deficient NDI units in the partially folded polypeptide. Additionally, the full reduction of each NDI unit in **P1^{DMB}** to the dianionic state is achieved at a lower potential than for **M1^{DMB}** providing evidence that the macromolecular scaffold can be used to stabilise NDI radical interactions. Here, maintaining the order macromolecular structure is important for facilitating long range charge delocalisation. Preliminary self-assembly studies by FTIR spectroscopy of deprotected polymer **P1** suggest the desired 1D alignment of the polymer chains, i.e., the formation of β-sheet assemblies, can be facilitated following DMB removal. Moreover, analysis of the amide II band provides evidence for anti-parallel β-strand alignment and therefore the most thermodynamically favoured β-sheet structuring in **P1**. Here, mediating π-assembly through a macromolecular architecture will allow for the precise 1D alignment of redox-active units and will pave the way for molecular wires that have emergent optoelectronic properties. As a proof-of-concept, NDI has been selected as the π-embedded motif, however, this strategy is applicable to various redox- and photo-active units that will have bespoke properties.

5.4 Experimental Details

5.4.1 General Materials & Methods

Materials: All reagents and solvents were purchased from commercial suppliers (Merck, Acros Organics, Alfa Aesar, Fisher Scientific, Tokyo Chemical Industry or Fluorochem) and used without further purification unless stated otherwise. Anhydrous solvents were obtained from a Solvent Purification System (neutral alumina) and stored over activated (>250 °C at 0.01 mbar overnight) 3 Å molecular sieves under a dry Ar atmosphere. Solvents and solutions required for air-sensitive manipulations were degassed thoroughly using a minimum of three freeze–pump–thaw cycles and the flask back-filled under an Ar atmosphere. 1-Amino-4-pentyne[4] (**7**), perfluorophenyl-4-azidobutanoate[41] (**15**) were synthesised according to previously published literature procedures.

Product confirmation: Analytical thin-layer chromatography (TLC) was performed on aluminum-backed silica gel 60 plates pre-loaded with F254 indicator (Sigma Aldrich) and visualised either under UV light irradiation (254 and 365 nm) and/or by dip-staining methods. Flash column chromatography was carried out on an automated system (Teledyne Isco Combiflash Rf+) outfitted with a broad range UV–Vis (200–800 nm) absorption detector. Nuclear magnetic resonance (NMR) spectra were recorded using either a Bruker Advance III Ultrashield 400 Plus (working frequencies: ^{1}H and ^{13}C nuclei = 399.975 and 100.603 MHz, respectively), an Appleby VNMRS-600 (^{1}H and ^{13}C nuclei = 599.832 and 150.288 MHz, respectively) or a Varian VNMRS-700 (^{1}H and ^{13}C nuclei = 700.130 and 176.048 MHz, respectively) spectrometer at a constant temperature of 298 K. Operating temperatures of the NMR spectrometers were measured with the aid of a MeOH internal calibrant. All ^{13}C NMR experiments were proton decoupled. Chemical shifts (δ) are reported in parts per million (ppm) relative to the signals corresponding to the residual non-deuterated solvents ($CDCl_3$: δ_H = 7.26, δ_C = 77.16 ppm; DMSO-d_6: δ_H = 2.50, δ_C = 39.52 ppm). Coupling constants (J) are reported in Hertz (Hz) and ^{1}H multiplicities are reported in accordance with the following convention: s = singlet, d = doublet, t = triplet, q = quadruplet, p = pentet, m = multiplet. Assignment of ^{1}H and ^{13}C NMR signals were accomplished with the aid of '**p**ure-**s**hift' **y**ielded **c**hirp **e**xcitation[42] (PSYCHE) and two-dimensional COSY, HSQC and HMBC NMR spectroscopies. NMR spectra were processed using MestReNova software, Version 11. Low-resolution **e**lectro**s**pray **i**onisation (ESI-MS) and **a**tmospheric **s**olids **a**nalysis **p**robe (ASAP-MS) mass spectrometries were performed using a Waters TQD UPLC ES MS/MS spectrometer and a Waters Xevo QTOF spectrometer equipped with an **a**tmospheric **p**ressure **i**onisation (API) source, respectively. High-resolution mass spectra (HR-MS) were obtained using either a

high-resolution Waters LCT Premier XE spectrometer equipped with an ESI source or an accurate mass UPLC ES MS equipped with an API source. Matrix-assisted laser-desorption ionisation time-of-flight (MALDI–TOF) mass spectrometry was carried out on an Autoflex II ToF/ToF mass spectrometer (Bruker Daltonik GmBH). Modes of analysis include reflectron enhanced mass resolution between *m*/z 500 and 5000. Linear above *m*/z 5000 and MS/MS (LIFT)

Sample analysis: The X-ray single crystal data for **12** was collected using λCuKα radiation (λ =1.54178 Å) at 120.0(2) K which was maintained by a Cryostream (Oxford Cryosystems) open-flow nitrogen cryostat. The SXRD experiments were performed on a Bruker D8Venture (Photon100 CMOS detector, IμS-microsource, focusing mirrors) diffractometer. Multi-scan absorption correction was applied. The structures were solved by direct method and refined by full-matrix least squares on F^2 for all data using Olex2[43] and SHELXTL[44] software. All non-hydrogen atoms were refined in anisotropic approximation, hydrogen atoms in **12** were refined freely with isotropic a.d.p.'s, hydrogen atoms in other compounds were placed in the calculated positions and refined in riding mode. Attenuated total reflectance (ATR) Fourier transform infrared (FTIR) spectroscopy was performed on PerkinElmer Frontier FTIR spectrometer equipped with a Specac Quest ATR accessory with extended range diamond puck. UV-Vis-NIR absorbance data were collected using a Cary 5000 Series UV–Vis–NIR spectrophotometer (Agilent Technologies) at room temperature. Circular dichroism spectroscopy was performed on a Jasco J-1500 spectropolarimeter with a band width of 1 nm and a response time of 1 second. The CD spectra was collected between 450–190 nm, with a data pitch of 0.5 nm at 50 nm/min. For each CD spectrum, 3 accumulations were collected and averaged. Cyclic voltammetry (CV) and square-wave voltammetry (SWV) was carried out at room temperature on Ar-purged sample solutions in anhydrous DMF using a PalmSens EmStat3 potentiostat interfaced to a PC. Tetrabutylammonium hexafluorophosphate ($TBAPF_6$; 0.1 M) was recrystallized from hot EtOH and used as the supporting electrolyte. All solution-state electrochemical experiments were performed using a glassy carbon working electrode (BASi; 0.071 cm^2). The electrode surface was polished routinely with 0.05 μm alumina–water slurry on a felt surface immediately before each use. The counter electrode was a Pt wire and the reference electrode was an Ag/AgCl (sat. KCl) aqueous electrode stored routinely in a 3 M KCl aqueous solution. Molecular weight analysis of polymers was carried out by size exclusion chromatography (SEC) using a Viscotek TDA 302 with a refractive index detector. Two 300 mm PLgel 5 μm mixed C columns were used with a linear molecular weight range of 200–2000000 g mol^{-1}. DMF (0.1 M LiCl) was used as the eluent at a flow rate of 1.0 mL min^{-1} at a temperature of 35 °C.

5.4.2 Experimental Procedures

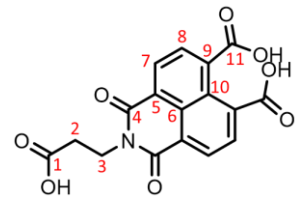

β-Ala-NMI (**3**): To a 500 mL round-bottomed flask was added 1,4,5,8,-naphthalenetetracarboxylic acid anhydride (**1**) (1.19 g, 4.45 mmol, 1.0 equiv.) and H_2O (350 mL). 1 M KOH (40 mL) was added to the suspension. Heating and sonication was used to homogenise the solution before the adjustment to pH 6.35 by the addition of 1 M H_3PO_4. β-Alanine (397 mg, 4.45 mmol, 1.0 equiv.) was added to the reaction mixture which was refluxed at 110 °C overnight. Once cooled, the solution was filtered before glacial acetic acid (6 mL) was added to the filtrate to afford a precipitate that was collected *via* vacuum filtration and washed with H_2O (10 mL). The title compound **β-Ala-NMI** was isolated (1.56 g, 4.36 mmol, 98%) as an off-white solid that did not require further purification.

^{1}H NMR (DMSO-d_6, 700 MHz, 298 K): δ_H 8.47 (d, J = 7.5 Hz, 2H^7), 8.00 (d, J = 7.5 Hz, 2H^8), 4.24 (d, J = 7.4 Hz, 2H,^{3}), 2.58 (t, J = 7.6 Hz, 2H^2). **^{13}C NMR** (DMSO-d_6, 176 MHz, 298 K): δ_C 173.3 (C^1), 169.9 (C^{11}), 163.8 (C^4), 141.9 (C^6), 130.9 (C^7), 129.0 (C^5), 128.4 (C^8), 126.22 (C^9), 123.4 (C^{10}), 36.5 (C^3), 32.8 (C^2). **ESI-HRMS** (MeOH, *ve*$^+$): calcd for $C_{17}H_{11}NO_8$ = 358.0563 *m*/z; found: $[M+H]^+$ = 358.0564.

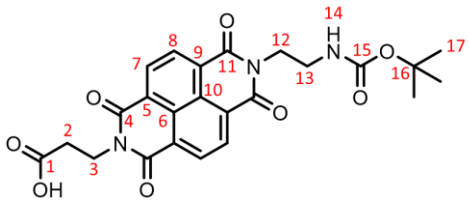

Boc-NDI-COOH (**5**): (a) *Microwave solution-phase synthesis*: To a 20 mL microwave vial, was added β-Alanine (87 mg, 0.98 mmol, 0.8 equiv.), DIPEA (170 µL, 1.22 mmol, 1.0 equiv.), 1,4,5,8,- naphthalenetetracarboxylic acid anhydride (**1**) (328 mg, 1.22 mmol, 1.0 equiv.) and anhydrous DMF (15 mL). The vial was sealed and the suspension was sonicated for 2 mins before being subjected to microwave irradiation for 75 °C for 5 min, followed by 140 °C for 10 min. Upon cooling, *N*-Boc-ethylenediamine (**4**) (193 µL, 1.22 mmol, 1.0 equiv.) and DIPEA (170 µL, 1.20 mmol, 1.2 equiv.) were then added by syringe directly to the reaction mixture, which was then subjected again to microwave irradiation for 5 min at 140 °C. Upon cooling, the solvent was removed under reduced pressure. The resulting residue was taken up into Me_2CO and added to vigorously stirring 1 M HCl solution at 0 °C. The mixture was left to stand in the fridge for 4 h. The precipitate was collected *via* vacuum filtration, washed with water and dried under high vacuum. The crude residue was purified by automated flash column chromatography (Teledyne Isco CombiFlash Rf+ system, 15 g SiO_2: 0 to 20% Me_2CO in CH_2Cl_2). The title compound **Boc-NDI-COOH** was isolated (792 mg, 1.65 mmol, 45%) as a colourless solid.

(b) Conventional solution-phase synthesis: To a 100 mL round-bottomed flask was added **1** (2.53 g, 7.09 mmol, 1.0 equiv.), *N*-Boc-ethylenediamine (**4**) (1.12 mL, 7.09 mmol,

1.0 equiv.) and anhydrous DMF (40 mL). The reaction was left to stir at 140 °C for 18 h. Upon cooling, the solvent was removed under reduced pressure. The residue was taken up in Me_2CO and added to vigorously stirring 1 M HCl solution at 0 °C. The precipitate was collected *via* vacuum filtration and washed with water. The title compound **Boc-NDI-COOH** was isolated (2.90 g, 6.02 mmol, 85%) as a brown solid and did not require any further purification.

^{1}H NMR (DMSO-d_6, 700 MHz, 298 K): δ_H 8.64 (d, J = 7.5 Hz, 2H[7]), 8.63 (d, J = 7.6 Hz, 2H[8]), (t, *J* = 6.2 Hz, 1H[14]), 4.26 (t, *J* = 8.1 Hz, 2H[3]), 4.14 (t, *J* = 5.8 Hz, 2H[12]), 3.26–3.30 (m, 2H[13]), 2.62 (t, *J* = 7.9 Hz, 2H[2]), 1.21 (s, 9H[17]). **^{13}C NMR** (DMSO-d_6, 176 MHz, 298 K): δ_C 172.4 (C[1]), 162.7 (C4[11]), 162.5 (C[4]), 155.8 (C[15]), 130.3 (C[7/8]), 130.2 (C[7/8]), 126.5 (C[5/9]), 126.2 (C[5/9]), 126.0 (C[10/6]), 77.5 (C[16]), 40.3 (C[12]), 37.6 (C[13]), 36.2 (C[3]), 32.2 (C[2]), 28.0 (C[17]); **ESI-HRMS** (MeCN, *ve*$^-$): calcd for $C_{24}H_{23}N_3O_8$ = 481.1472 *m*/z; found: [*M*-H]$^-$ = 481.1485.

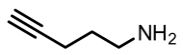

1-Amino-4-pentyne (**7**): 1-phthalimido-4-pentyne (7.64 g, 35.8 mmol, 1.0 equiv.) was suspended in EtOH (70 mL) and hydrazine monohydrate was added dropwise till the mixture became clear. The reaction vessel was fitted with an air condenser and the mixture was stirred at 70 °C for 2 h, during which time a white solid precipitated. After the reaction mixture had cooled, H_2O (50 mL) was added followed by the addition of 2 M HCl to adjust the pH to 3.5. The precipitate was removed by vacuum filtration and the filtrate concentrated by rotary evaporation. The aqueous solution was then cooled to 0 °C and 10 M NaOH (30 mL) was added. The aqueous solution was then extracted with CH_2Cl_2 (3 x 150 mL). The combined organic layer was dried ($MgSO_4$), filtered and concentrated on the rotary evaporator. The title compound **1-Amino-4-pentyne** was isolated (1.25 g, 15.4 mmol, 43%) as a red oil. Spectroscopic data were consistent with those published previously.[9]

^{1}H NMR ($CDCl_3$, 400 MHz, 298 K): δ_H 2.79 (t, *J* = 6.9 Hz, 2H), 2.24 (td, *J* = 7.0, 2.7 Hz, 2H), 1.94 (t, *J* = 2.7 Hz, 1H), 1.65 (p, *J* = 7.0 Hz, 2H).

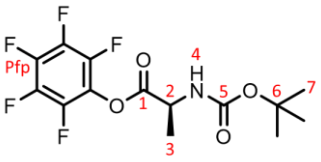

***N*-(tert-butyloxycarbonyl)-(*S*)-alanine pentafluorophenyl ester** (**13**): To a 100 mL round-bottomed flask was added pentafluorophenol (279 mg, 1.52 mmol, 1.0 equiv.), Boc-Ala-OH (**9**) (316 mg, 1.67 mmol, 1.1 equiv.) and anhydrous MeCN (53 mL). The reaction mixture was cooled to 0°C in an ice-bath. A solution of DCC (376 mg, 1.82 mmol, 1.20 equiv.) in anhydrous MeCN (13 mL) was added dropwise to the reaction mixture which was left to stir at rt for 16 h. The precipitate was removed *via* vacuum filtration and the solvent removed under reduced pressure. The residue was triturated further with a small amount of EtOAc (5 mL) to encourage additional precipitation of DCU by-product, which was subsequently removed by vacuum filtration. The filtrate was evaporated

completely under reduced pressure and the resulting residue was purified by automated flash column chromatography (Teledyne Isco CombiFlash Rf+ system, 13.5 g C18: 40 to 100% MeOH in H_2O). The title compound **13** was isolated (404 mg, 1.14 mmol, 75%) as a colourless powder.

^{1}H NMR ($CDCl_3$, 700 MHz, 298 K): δ_H 5.04 (d, J = 7.9 Hz, 1H[4]), 4.66 (m, 1H[2]), 1.58 (d, J = 7.3 Hz, 3H[3]), 1.46 (s, 9H[7]). **^{13}C NMR** ($CDCl_3$, 176 MHz, 298 K): δ_C 169.9 (C[1]), 155.1 (C[5]), 142.0 (C[Pfp]), 140.6 (C[Pfp]), 139.1 (C[Pfp]), 138.8 (C[Pfp]), 137.4 (C[Pfp]), 125.1 (C[Pfp]), 80.7 (C[6]), 49.4 (C[2]), 28.4 (C[7]), 18.4 (C[3]). **^{19}F NMR** ($CDCl_3$, 376 MHz, 298 K): δ_F –152.54 (d, J = 19.7 Hz), –157.52 (t, J = 21.6 Hz), –162.06 (d, J = 20.4 Hz); **ESI-HRMS** (MeOH, ve^+): calcd for $C_9H_7F_5NO_2$ = 256.0397 m/z; found: $[M\text{-Boc}]^+$ = 256.0404.

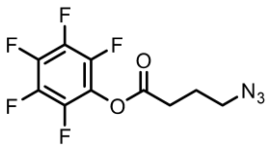

Perfluorophenyl-4-azidobutanoate (**15**): To a 100 mL round-bottomed flask was added pentafluorophenol (1.61 g, 8.51 mmol, 1.1 equiv.), alkyl azide (**14**) (1.01 g, 7.75 mmol, 1.0 equiv.) and anhydrous DMF (310 mL). The reaction mixture was cooled at 0 °C in an ice bath. A solution of DCC (3.20 g, 15.5 mmol, 2.0 equiv.) was added dropwise to the reaction mixture and left to stir at rt for 16 h. The precipitate was removed *via* vacuum filtration and the filtrate concentrated to dryness by rotary evaporation. The residue was triturated in a small amount of EtOAc (5 mL) to encourage the precipitation of DCU by-product, which was subsequently removed by vacuum filtration. The solvent was removed from the filtrate under reduced pressure and the resulting residue was purified by automated flash column chromatography (Teledyne Isco CombiFlash Rf+ system, 40 g C18: 55 to 100 % MeOH in H_2O). To isolate the product, MeOH was removed from the chromatography fractions containing product by rotary evaporation and the product was extracted from the remaining H_2O into EtOAc (4 × 60 mL). The organic fractions were combined, dried over anhydrous $MgSO_4$, filtered and the solvent under reduced pressure. The title compound **15** was isolated (1.65 g, 5.58 mmol, 72%) as colourless liquid. Spectroscopic data were consistent with those published previously.[41]

^{1}H NMR ($CDCl_3$, 600 MHz, 298 K): δ_H 3.46 (t, J = 6.5 Hz, 2H), 2.80 (t, J = 7.2 Hz, 2H), 2.05 (t, J = 6.5 Hz, 2H).

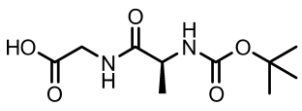

***N*-(tert-butyloxycarbonyl)-(S)-alanylglycine** (**19**): To a 100 mL round-bottomed flask was added glycine (93 mg, 1.24 mmol, 1.0 equiv.) and anhydrous DMF (10 mL). The reaction mixture was cooled at 0 °C in an ice bath. A solution of compound **13** (485 mg, 1.36 mmol, 1.1 equiv.) in anhydrous DMF (10 mL) was added dropwise to the reaction mixture and it was left to stir at rt for 16 h. The solvent was removed under reduced pressure. EtOAc (5 mL) and H_2O (5 mL)

were added to the crude residue. The product was extracted into H_2O (3 x 5 mL). The aqueous fractions were combined and the solvent was removed by reduced pressure. The title compound ***N*-(tert-butyloxycarbonyl)-(S)-alanylglycine** was isolated (302 mg, 1.23 mmol, 99%) as a colourless solid and did not require any further purification. Spectroscopic data were consistent with those published previously.[45]

^{1}H NMR (DMSO-d_6, 700 MHz, 298 K): δ_H 8.00 (t, J = 5.8 Hz, 1H), 6.90 (d, J = 7.8 Hz, 1H), 3.99 (p, J = 7.3 Hz, 1H), 3.66–3.81 (m, 2H), 1.37 (s, 9H), 1.18 (d, J = 7.2 Hz, 3H). **ESI-MS** (MeOH, ve$^+$): calcd for $C_{10}H_{18}N_2O_5$ = 269.343 m/z; found: $[M+Na]^+$ = 269.253.

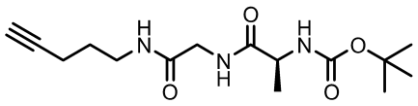

AlkyneGA^{Boc} (**10**): To a 500 mL round-bottomed flask was added **12** (1.20 mg, 4.86 mmol, 1.0 equiv.), DIPEA (1.02 mL, 5.83 mmol, 1.2 equiv.) and CH_2Cl_2 (50 mL). After stirring at rt for 10 min, EDC•HCl (1.02 g, 5.35 mmol, 1.1 equiv.) was added to the reaction mixture. The reaction vessel was then cooled to 0 °C in an ice bath, with additional stirring for 20 mins. A solution of **7b** (1.60 g, 6.33 mmol, 1.3 equiv.) and DIPEA (1.65 mL, 9.50 mmol, 1.5 equiv.) in CH_2Cl_2 (100 mL) was added to the reaction mixture dropwise, which was then allowed to warm to rt and stirred for 48 h. Following this, the reaction mixture was concentrated and washed with 1 M HCl (3 x 50 mL), $NaHCO_3$ sat. (3 x 60 mL) and brine (1 x 50 mL). The organic layer was dried over $MgSO_4$, filtered and concentrated *via* reduced pressure. The crude residue was purified by automated flash column chromatography (Teledyne Isco CombiFlash Rf+ system, 100 g SiO_2: 100% EtOAc) with the title compound **AlkyneGA^{Boc}** isolated (1.24 g, 3.98 mmol, 82%) as a white solid. Spectroscopic data were consistent with those published previously.[9]

^{1}H NMR ($CDCl_3$, 400 MHz, 298 K): δ_H 6.94 (s, 1H), 6.87 (s, 1H), 5.15 (s, 1H), 4.05–4.15 (m, 1H), 3.87–4.00 (m, 2H), 3.24–3.46 (m, 2H), 2.23 (td, J = 7.0, 2.7 Hz, 2H), 1.96 (t, J = 2.7 Hz, 1H), 1.69–1.80 (m, 2H), 1.43 (s, 9H), 1.37 (d, J = 7.1 Hz, 3H).

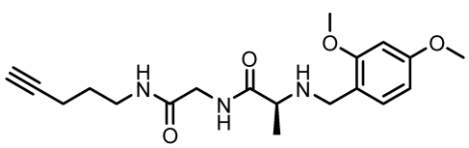

AlkyneGA^{DMB} (**11**): In a 20 mL round-bottomed flask, **10** (437 mg, 1.40 mmol, 1.0 equiv.) was added to CH_2Cl_2 (3 mL) and cooled in an ice bath to 0 °C. TFA (1.07 mL, 14.0 mmol, 10 equiv.) was added to the reaction mixture dropwise and the reaction was left to stir for 2 h. The solvent was removed by rotary evaporation followed by the removal of excess TFA by azeotropic distillation with anhydrous PhMe (3 × 1 mL). MeOH (10 mL) was then added to the reaction vessel. Et_3N (254 µL, 1.82 mmol, 1.3 equiv.) was then added to the reaction mixture, followed by 2,4-dimethoxybenzaldehyde (233 mg, 1.40 mmol, 1.0 equiv.) and then $NaCNBH_3$ (106 mg, 1.68 mmol, 1.2 equiv.). After stirring for 72 h at room temperature, the solvent was removed and the crude reaction mixture was purified by

automated flash column chromatography (Teledyne Isco CombiFlash Rf+ system, 40 g SiO_2: 0 to 5% MeOH in CH_2Cl_2) with the title compound **AlkyneGA^{DMB}** isolated (375 mg, 1.04 mmol, 74 %) as a colourless solid. Spectroscopic data were consistent with those published previously.[9]

^{1}H NMR (400 MHz, DMSO-d_6): δ_H 8.90 (s, 1H), 8.69 (s, 1H), 8.04 (t, J = 5.5 Hz, 1H), 7.30 (d, J = 8.4 Hz, 1H), 6.62 (d, J = 2.4 Hz, 1H), 6.56 (dd, J = 8.4, 2.4 Hz, 1H), 3.96 (s, 2H), 3.79 (d, J = 9.0 Hz, 9H), 3.14 (q, J = 6.6 Hz, 2H), 2.80 (t, J = 2.7 Hz, 1H), 2.17 (td, J = 7.2, 2.7 Hz, 2H), 1.58 (p, J = 7.1 Hz, 2H), 1.38 (d, J = 6.8 Hz, 3H).

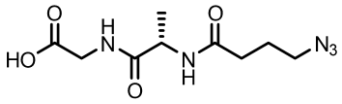

AzideAG (**17**): Compound **19** (251 mg, 1.02 mmol, 1.0 equiv.) was added to CH_2Cl_2 (6 mL) and cooled in an ice bath to 0 °C. TFA (781 µL, 10.2 mmol, 10 equiv.) was added to the reaction mixture dropwise and the reaction was left to stir for 2 h. The solvent was removed by rotary evaporation followed by the removal of excess TFA by azeotropic distillation with anhydrous PhMe (3 × 1 mL). Anhydrous DMF (6 mL) was added to the deprotected amine, followed by the addition of DIPEA (373 µL, 2.14 mmol, 2.1 equiv.) and **15** (361 mg, 1.22 mmol, 1.2 equiv.). After stirring for 16 h the reaction mixture was concentrated by rotary evaporation. The crude product was then partitioned between H_2O (10 mL) and CH_2Cl_2 (15 mL), with the organic soluble impurities washed from the aqueous layer. The aqueous layer was then concentrated before purification using automated flash column chromatography (Teledyne Isco CombiFlash Rf+ system, C18 13.5 g: 10% MeOH–H_2O/0.1% TFA) to yield (244 mg, 0.95 mmol, 93 %) the title compound **AzideAG** as a clear oil. Spectroscopic data were consistent with those published previously.[9]

^{1}H NMR (DMSO-d_6, 700 MHz, 298 K): δ_H 8.12 (t, J = 5.9 Hz, 1H), 8.07 (d, J = 7.7 Hz, 1H), 4.31 (p, J = 7.2 Hz, 1H), 3.69–3.78 (m, 2H), 3.32 (t, J = 6.9 Hz, 2H), 2.20 (td, J = 7.3, 2.3 Hz, 2H), 1.74 (p, J = 7.2 Hz, 2H), 1.19 (d, J = 7.1 Hz, 3H).

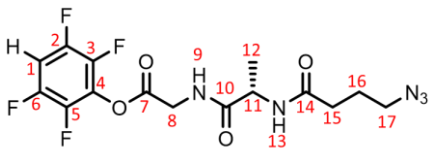

AzideAG^{Tfp} (**18**): Compound **17** (795 mg, 3.09 mmol, 1.0 equiv.) was added to anhydrous THF (20 mL). EDC•HCl (651.6 mg, 3.40 mmol, 1.1 equiv.) and DIPEA (538 µL, 3.09 mmol, 1 equiv.) were then added to the reaction mixture and it was stirred for 15 mins. A solution of tetrafluorophenol (616 mg, 3.71 mmol, 1.2 equiv.) in anhydrous THF (3 mL) was then added to the reaction mixture dropwise which was allowed to stir at rt for 6 h. The reaction solvent was removed under reduced pressure and the residue then dissolved in CH_2Cl_2 (10 mL). The organic layer was washed with 1 M HCL (2 x 30 mL), dried over $MgSO_4$, filtered and the solvent was removed under reduced pressure to isolate (1.04 g, 2.57

mmol, 83 %) the title compound **AzideAG^{Tfp}** as a white solid that did not require any further purification.

^{1}H NMR ($CDCl_3$, 600 MHz, 298K): δ_H 7.33 (t, J = 5.8 Hz, 1H^{9}), 6.98–7.05 (m, 1H^{1}), 6.37 (d, J = 7.5 Hz, 1H^{13}), 4.64 (p, J = 7.1 Hz, 1H^{11}), 4.32–4.46 (m, 2H^{8}), 3.34 (t, J = 6.6 Hz, 2H^{17}), 2.26–2.37 (m, 2H^{15}), 1.91 (p, J = 6.9 Hz, 2H^{16}), 1.42 (d, J = 7.0 Hz, 3H^{12}). **^{13}C NMR** ($CDCl_3$, 150 MHz, 298K): δ_F 173.0 (C^{10}), 172.4 (C^{14}), 166.1 (C^{7}), 147.0 (C^{6}), 145.3 (C^{2}), 141.5 (C^{5}), 139.8 (C^{3}), 129.2 (C^{4}), 103.8 (C^{1}), 50.8 (C^{17}), 48.7 (C^{11}), 40.8 (C^{8}), 33.1 (C^{15}), 24.7 (C^{16}), 17.9 (C^{12}). **ESI-HRMS** (MeCN, *ve*$^{+}$): calcd for $C_{15}H_{16}N_5O_4F_4$ = 406.1138 *m*/z; found: $[M+H]^+$ = 406.1133.

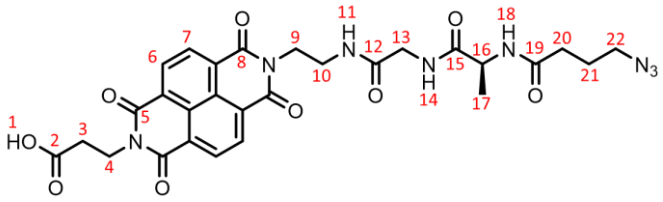

Tripeptide NDI (**20**): To a 20 mL round-bottomed flask was added **Boc-NDI-COOH** (327 mg, 0.68 mmol, 1.0 equiv.) and CH_2Cl_2 (3 mL) and the mixture was cooled to 0 °C in an ice bath. TFA (560 µL, 6.8 mmol, 10 equiv.) was added dropwise to the stirring mixture and allowed to warm to rt over 2 h, in an open reaction vessel to allow for CO_2 release. The solvent was removed under reduced pressure followed by the removal of excess TFA by azeotropic distillation with anhydrous PhMe (3 × 2.5 mL) to produce a brown solid product. Dioxane (10 mL) was added to the reaction vessel. DIPEA (178 µL, 1.0 mmol, 1.5 equiv.) was then added, and the suspension was stirred at rt for 15 mins. A solution of **AzideAG^{Tfp}** (331 mg, 0.82 mmol, 1.2 equiv.) in dioxane (5 mL) was then added to the reaction mixture and it was stirred at rt for 16 h. The solvent was removed by reduced pressure and triturated with EtOAc (3 × 10 mL) and 1 M HCl (3 × 10 mL) to isolate (380 mg, 0.61 mmol, 90 %) the title compound **20** as a brown solid that did not required any further purification.

^{1}H NMR (599 MHz, 298 K, DMSO-d_6): δ_H 12.42 (s, 1H^{1}), 8.51–8.69 (m, 4H^{6+7}), 8.10–8.19 (m, 1H^{18}), 8.05 (t, J = 5.9 Hz, 1H^{14}), 7.94 (t, J = 6.0 Hz, 1H^{11}), 4.24–4.35 (m, 2H^{4}), 4.09–4.21 (m, 2H^{9}), 3.50–3.61 (m, 2H^{13}), 3.39–3.48 (m, 2H^{10}), 3.25–3.33 (m, 2H^{22}), 2.61–2.66 (m, 2H^{3}), 2.10–2.21 (m, 2H^{20}), 1.66–1.77 (m, 2H^{21}), 1.14–1.25 (m, 3H^{17}). **^{13}C NMR** (151 MHz, 298 K, DMSO-d_6): δ_C 174.2, 172.5, 172.4, 171.5, 171.1, 171.1, 169.0, 166.2, 163.2, 162.8, 162.7, 162.5, 130.4, 130.3, 126.4, 126.3, 126.2, 126.1, 126.0, 53.4, 50.2, 50.2, 48.5, 47.4, 42.0, 40.1, 36.3, 36.1, 32.0, 31.9, 31.8, 24.5, 24.3, 18.0, 17.6, 17.1, 16.7. **ESI-HRMS** (MeCN, *ve*$^{+}$): calcd for $C_{28}H_{29}N_8O_9$ = 621.2057 *m*/z; found: $[M+H]^+$ = 621.2047.

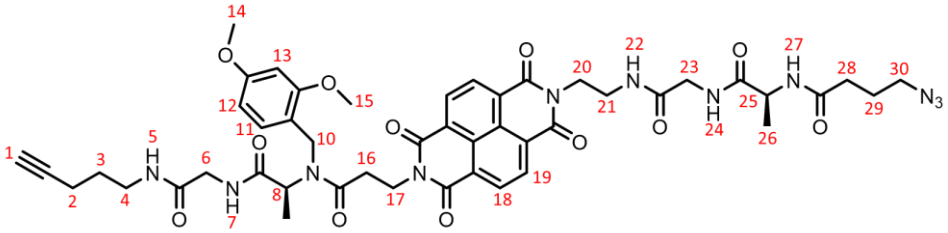

M1^{DMB}: Compound **20** (380 mg, 0.61 mmol, 1.0 equiv.) was added to a mixture of DMF–DMSO 9:1(*v*/*v*) (22 mL). DIPEA (128 µL, 0.73 mmol, 1.2 equiv.) and HATU (278 mg, 0.73 mmol, 1.2 equi.v) were added to the reaction mixture and it was left to stir for 30 mins at 40 °C. **AlkyneGA^{DMB}** (222 mg, 0.67 mmol, 1.1 equiv.) was then added to the reaction mixture and it was left to stir at at 40 °C for 48 h. After 24 h additional HATU (278 mg, 0.73 mmol, 1.2 equiv.) was added to the reaction mixture. Following this, CH_2Cl_2 (20 mL) and then H_2O (10 mL) was added to the reaction mixture. The product was then extracted into CH_2Cl_2 (3 × 20 mL). The organic fractions were combined and washed with 1 M HCl (3 × 50 mL) and brine (1 × 50 mL). The organic layer was dried over $MgSO_4$, filtered and concentrated *via* reduced pressure. The crude residue was purified by automated flash column chromatography (Teledyne Isco CombiFlash Rf+ system, 40 g SiO_2: 0 to 15 % EtOH in CH_2Cl_2) with the title compound **M1^{DMB}** isolated (342 mg, 0.36 mmol, 59 %) as an orange powder.

^{1}H NMR ($CDCl_3$, 700 MHz, 298K): δ_H 8.78 (d, *J* = 7.6 Hz, 2H^{19}), 8.76 (d, *J* = 7.6 Hz, 2H^{18}), 7.11–7.18 (m, 2H^{5+11}), 7.00 (t, *J* = 5.9 Hz, 1H^{22}), 6.90 (t, *J* = 5.9 Hz, 1H^{24}), 6.71 (t, *J* = 6.3 Hz, 1H^{7}), 6.48 (s, 1H^{13}), 6.46 (d, *J* = 2.3 Hz, 1H^{12}), 6.29 (d, *J* = 6.4 Hz, 1H^{27}), 4.69 (d, *J* = 15.6 Hz, 1H,$^{10'}$), 4.50–4.63 (m, 2H^{17}), 4.42–4.49 (m, 2H, $^{10'+20'}$), 4.34–4.41 (m, 1H,$^{20'}$), 4.29 (p, *J* = 7.0 Hz, 1H^{25}), 4.05 (dd, *J* = 17.0, 7.1 Hz, 1H$^{6'}$), 3.92–3.98 (m, 2H$^{8+23'}$), 3.90 (s, 3H^{15}), 3.81 (s, 3H^{14}), 3.67–3.77 (m, 3H$^{21+23'}$), 3.63 (dd, *J* = 17.0, 5.5 Hz, 1H$^{6'}$), 3.31 (td, *J* = 6.6, 1.2 Hz, 2H^{20}), 2.97–3.19 (m, 3H$^{4'+16}$), 2.79–2.89 (m, 1H$^{4'}$), 2.18–2.27 (m, 2H^{28}), 2.13 (td, *J* = 7.1, 2.6 Hz, 2H^{2}), 1.89 (t, *J* = 2.6 Hz, 1H^{1}), 1.76–1.86 (m, 2H^{29}), 1.54–1.65 (m, 2H^{3}), 1.39 (d, *J* = 7.0 Hz, 3H^{26}), 1.35 (d, *J* = 7.0 Hz, 3H^{9}). **^{13}C NMR** ($CDCl_3$, 176 MHz, 298K): δ_C 172.7, 172.3, 171.9, 171.3, 169.4, 169.2, 163.3, 163.0, 161.4, 158.4, 131.0, 130.6, 126.8, 126.5, 126.5, 126.2, 115.6, 104.4, 99.0, 83.7, 77.2, 77.0, 76.8, 68.7, 56.1, 55.4, 50.6, 49.6, 48.4, 43.6, 43.2, 40.4, 38.3, 38.2, 37.4, 32.8, 32.4, 27.8, 24.5, 17.7, 15.9, 13.3. **ESI-HRMS** (MeCN, *ve*$^+$): calcd for $C_{47}H_{54}N_{11}O_{12}$ = 964.3953 *m*/z; found: $[M+H]^+$ = 964.3976.

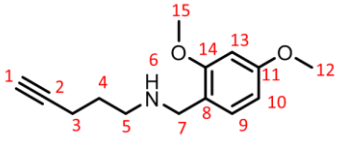

DMB-protected alkyne (**22**): **1-Amino-4-pentyne** (509 mg, 6.12 mmol, 1.0 equiv.) was added to EtOH (30 mL), followed by the addition of $NaCNBH_3$ (500 mg, 7.96 mmol, 1.3 equiv.). A catalytic amount of TFA was added, and the reaction mixture was stirred at rt for 24 h. The solution was then concentrated by rotary

evaporation and the resulting residue purified by column chromatography (20 g SiO_2: 0 to 50% EtOAc in *n*-hexanes) to yield (900 mg, 3.86 mmol, 63%) the title compound **22** as a green oil.

^{1}H NMR ($CDCl_3$, 600 MHz, 298 K): δ_H 7.12 (d, J = 8.0 Hz, 1H[13]), 6.45 (d, J = 2.4 Hz, 1H[9]), 6.42 (dd, J = 8.1, 2.4 Hz, 1H[10]), 3.80 (s, 3H[15]), 3.79 (s, 3H[12]), 3.71 (s, 2H[7]), 2.68 (t, J = 7.1 Hz, 2H[5]), 2.25 (td, J = 7.2, 2.7 Hz, 2H[3]), 1.93 (t, J = 2.7 Hz, 1H[1]), 1.72 (p, J = 7.1 Hz, 2H[4]). ^{13}C NMR ($CDCl_3$, 151 MHz, 298 K): δ_C 160.2 (C[14]), 158.7 (C[11]), 130.5 (C[13]), 121.0(C[8]), 103.8 (C[10]), 98.7 (C[9]), 84.4 (C[2]), 68.5 (C[1]), 55.5 (C[12]), 55.4 (C[15]), 48.8 (C[7]), 48.0 (C[5]), 28.8 (C[4]), 16.5 (C[3]). ESI-HRMS (MeOH, *ve*$^+$): calcd for $C_{14}H_{20}NO_2$ = 234.1494, *m*/z; found: $[M+H]^+$ = 234.1500.

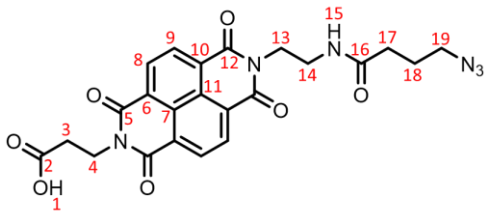

Azide-NDI (**21**): To a 20 mL round-bottomed flask was added **Boc-NDI-COOH** (292 mg, 0.61 mmol, 1.0 equiv.) and CH_2Cl_2 (2 mL) and the mixture was cooled to 0 °C in an ice bath. TFA (467 µL, 6.1 mmol, 10 equiv.) was added dropwise to the stirring mixture and allowed to warm to rt over 2 h, in an open reaction vessel to allow for CO_2 release. The solvent was removed under reduced pressure followed by the removal of excess TFA by azeotropic distillation with anhydrous PhMe (3 × 2.5 mL). DIPEA (266 µL, 1.53 mmol, 2.5 equiv.) were added to DMSO (6 mL) and left to stir for 15 mins. **15** (216 mg, 0.73 mmol, 1.2 equiv.) in DMSO (1 mL) was added dropwise to the reaction mixture which was left to stir overnight. The product was then precipitated in water and collected by vacuum filtration. The excess starting material was removed with washings of EtOAc (3 × 10 mL), isolating the title compound (197 mg, 0.40 mmol, 66%) as a brown solid.

^{1}H NMR (700 MHz, 298 K, DMSO-d_6): δ_H 12.42 (s, 1H[1]), 8.57–8.64 (m, 4H[8+9]), 8.00 (t, J = 6.2 Hz, 1H[15]), 4.26 (t, J = 7.9 Hz, 2H[4]), 4.14 (t, J = 6.0 Hz, 2H[13]), 3.41 (q, J = 6.0 Hz, 2H[14]), 3.21 (t, J = 6.9 Hz, 2H[19]), 2.63 (t, J = 7.8 Hz, 2H[3]), 2.00 (t, J = 7.3 Hz, 2H[17]), 1.61 (p, J = 7.1 Hz, 2H[18]). **^{13}C NMR** (176 MHz, 298 K, DMSO-d_6): δ_C 172.8 (C[2]), 172.0 (C[16]), 163.1 (C[12]), 162.8 (C[5]), 130.8 (C[9]), 130.7 (C[8]), 126.7 (C[10]), 126.6 (C[7]), 126.5 (C[11]), 126.4 (C[6]), 50.6 (C[19]), 40.4 (C[13]), 36.7 (C[14]), 36.5 (C[4]), 32.6 (C[17]), 32.4 (C[3]), 24.8 (C[18]). **HRMS** (ASAP, *ve*$^+$): *m*/z calcd for $[M+H]^+$ 493.1472, found 493.1461.

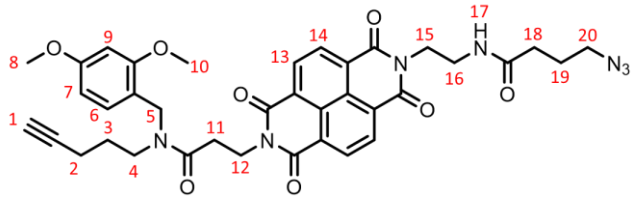

C1^{DMB}: Compound **22** (98 mg, 0.42 mmol, 1.1 equiv.) and **21** (186 mg, 0.38 mmol, 1.0 equiv.) were added to anhydrous DMF (4 mL) and cooled to 0 °C. DIPEA (80 µL, 0.46 mmol, 1.2 equiv.) was added to the reaction mixture. After 5 min of stirring at 0 °C, HATU (175 mg, 0.46 mmol, 1.2 equiv.) was added to the reaction mixture which was allowed to warm to rt. The reaction mixture was stirred for 96 h. Following this, H_2O (10 mL) and CH_2Cl_2 (50 mL) were added to the reaction mixture. The product was then extracted into CH_2Cl_2 (2 x 50 mL). The organic fractions were combined and washed with 1 M HCl (1 × 100 mL), sat. aqueous $NaHCO_3$ sol. (1 × 100 mL) and brine (1 × 100 mL). The organic layer was dried over $MgSO_4$, filtered and concentrated *via* reduced pressure. The crude residue was purified by column chromatography (6 g SiO_2: 0 to 2 % MeOH in CH_2Cl_2) with the title compound **C1^{DMB}** isolated (75 mg, 0.11 mmol, 28 %) as an orange powder.

^{1}H NMR ($CDCl_3$, 400 MHz, 298K): δ_H 8.74 (dd, J = 7.2, 2.1 Hz, 4H^{13+14}), 7.15–7.18+6.97–7.00 (2 x m, 1H^{6}), 6.39–6.44 (m, 2H^{7+9}), 6.02–6.08 (m, 1H^{17}), 4.50–4.57 (m, 2H^{12}), 4.50–4.57+4.38–4.45 (2 x m, 2H^{5}), 4.38–4.45 (m, 2H^{15}), 3.79–3.80 (m, 3H^{8}), 3.77–3.79 (m, 3H^{10}), 3.68–3.72 (m, 2H^{16}), 3.33–3.39 (m, 2H^{4}), 3.19–3.23 (m, 2H^{20}), 2.89–2.92+2.84–2.88 (2 x m, 2H^{11}), 2.15–2.19 (m, 4H^{2+18}), 1.89+1.94 (2 x t, J = 2.6 Hz, 1H^{1}), 1.74–1.80 (m, 2H^{19}), 1.74–1.80+1.69–1.74 (2 x m, 2H^{3}). **^{13}C NMR** ($CDCl_3$, 176 MHz, 298K): δ_C 172.4, 172.4, 170.8, 170.2, 163.6, 163.5, 162.8, 160.8, 160.3, 158.59, 158.4, 131.3, 131.1, 131.1, 131.0, 128.7, 127.0, 126.9, 126.9, 126.9, 126.5, 126.4, 118.1, 116.9, 104.4, 104.0, 98.8, 98.4, 83.9, 83.1, 77.3, 77.2, 77.0, 69.4, 68.8, 55.5, 55.5, 55.4, 55.4, 50.8, 47.0, 46.2, 44.8, 42.4, 40.4, 40.4, 39.0, 39.0, 37.7, 37.7, 33.1, 31.2, 27.2, 26.3, 24.7, 16.4, 16.1. **ESI-HRMS** (MeCN, *ve*$^+$): calcd for $C_{37}H_{37}N_7O_8$ = 708.2782 *m*/z; found: $[M+H]^+$ = 708.2786.

^{1}H NMR (DMSO-d_6, 400 MHz, 298 K): δ_H 8.65–8.71 (m, 4H^{13+14}), 7.99–8.04 (m, 1H^{17}), 6.99 (t, J = 8.4 Hz, 1H^{6}), 6.52–6.56 (m, 1H^{9}), 6.44–6.51 (m, 1H^{7}), 4.38 (d, J = 12.7 Hz, 2H^{5}), 4.25–4.33 (m, 2H^{12}), 4.13–4.19 (m, 2H^{15}), 3.72–3.80 (m, 6H^{8+10}) 3.38–3.46 (m, 2H^{16}), 3.18–3.24 (m, 4H^{4+20}), 2.79–2.86 (m, 2H^{11}), 2.72–2.75+2.76–2.78 (2 x m, 1H^{1}), 2.08–2.15 (m, 2H^{2}), 2.00 (t, J = 7.3 Hz, 2H^{18}), 1.52–1.69 (m, 4H^{3+19}).

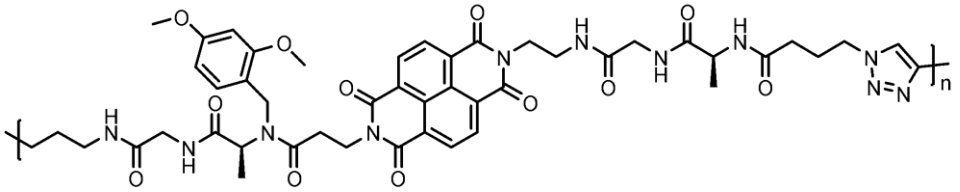

P1^{DMB}: **M1^{DMB}** (5 mg, 5.3 µmol, 1.0 equiv.) and TBTA (0.04 mg, 25 µmol, 1.0 equiv.) were added to anhydrous DMF (10 µL) and the reaction mixture was degassed by three cycles of freeze-pump-thaw. CuOAc (0.3 mg, 0.5 µmol, 0.1 equiv.) was added to the vial and the reaction mixture and a further three cycles of degassing by freeze-pump-thaw were employed. The reaction was stirred at 80 °C for 16 h. MeOH (0.5 mL) was added to the reaction mixture and the crude product was subject to 5 cycles of centrifugation, with the MeOH (0.5 mL) decanted each time. The product **P1^{DMB}** was isolated as a white solid (3 mg, 60%) that was used in analyses without further purification.

^{1}H NMR ($CDCl_3$, 400 MHz, 298K): δ_H 8.53 (s, 4H), 7.77 (s, 1H), 7.61 (s, 1H), 7.50 (s, 1H), 6.82–7.04 (m, 1H), 6.31 (s, 2H), 2.76–3.10 (m, 4H), 1.57–2.13 (m, 4H), 0.94–1.31 (m, 6H). **MALDI–TOF** (ve^+): m/z $[M+Na]^+$ calcd for $C_{390}H_{312}N_{60}O_{72}$ = 6773.8, found: = 6767.7.

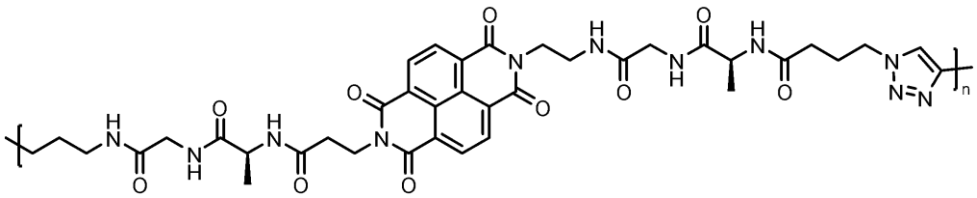

P1: Polymer **P1^{DMB}** (3 mg) was added to a 5 mL round-bottomed flask equipped with a magnetic stirrer. A solution of TFA/TIPS/H_2O (95:2.5:2.5, 0.7 mL) was added to the reaction mixture and it was stirred at room temperature for 1 hour. MeOH (3 mL) was then added to the reaction mixture and the resulting precipitate was collected and purified by centrifugation with MeOH (3 x 1 mL). The successful deprotection was confirmed by TLC analysis (0–12% EtOH in CH_2Cl_2) and the target **P1** isolated as a solid (2 mg, 66%) that was used without further purification.

5.5 Appendix and Supplementary Information

5.5.1 Structural Assignment by Two-Dimensional (2D) NMR

In order to fully assign the ^{1}H and ^{13}C signals of the NDI amino acid **5**, we employed 2D NMR spectroscopy. We determined peak assignments through analysis of COSY (Figure 5.18), HSQC (Figure 5.19) and HMBC (Figure 5.20) correlations. Process of elimination allowed us to attribute any remaining ^{13}C signals to the naphthalene core.

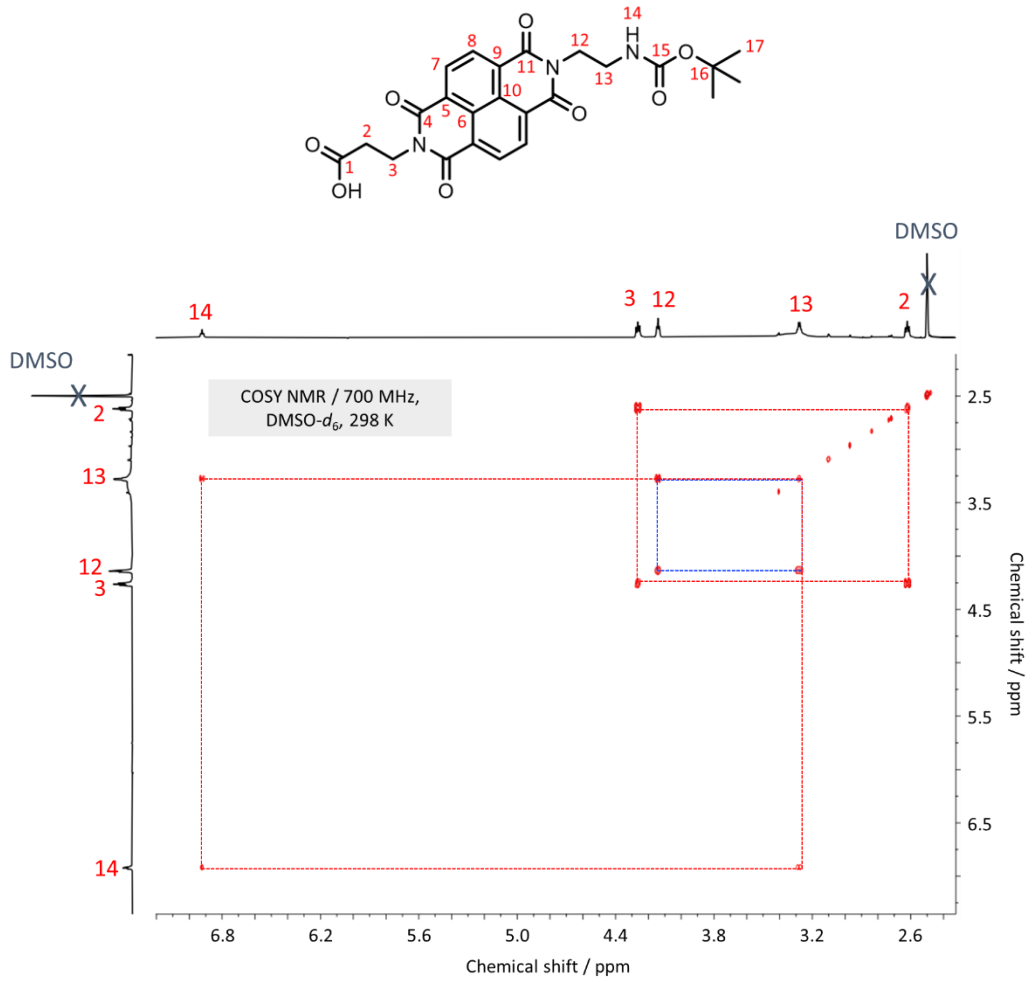

Figure 5.18. Partial ^{1}H–^{1}H COSY NMR spectrum (700 MHz, DMSO-d_6, 298 K) of **5**.

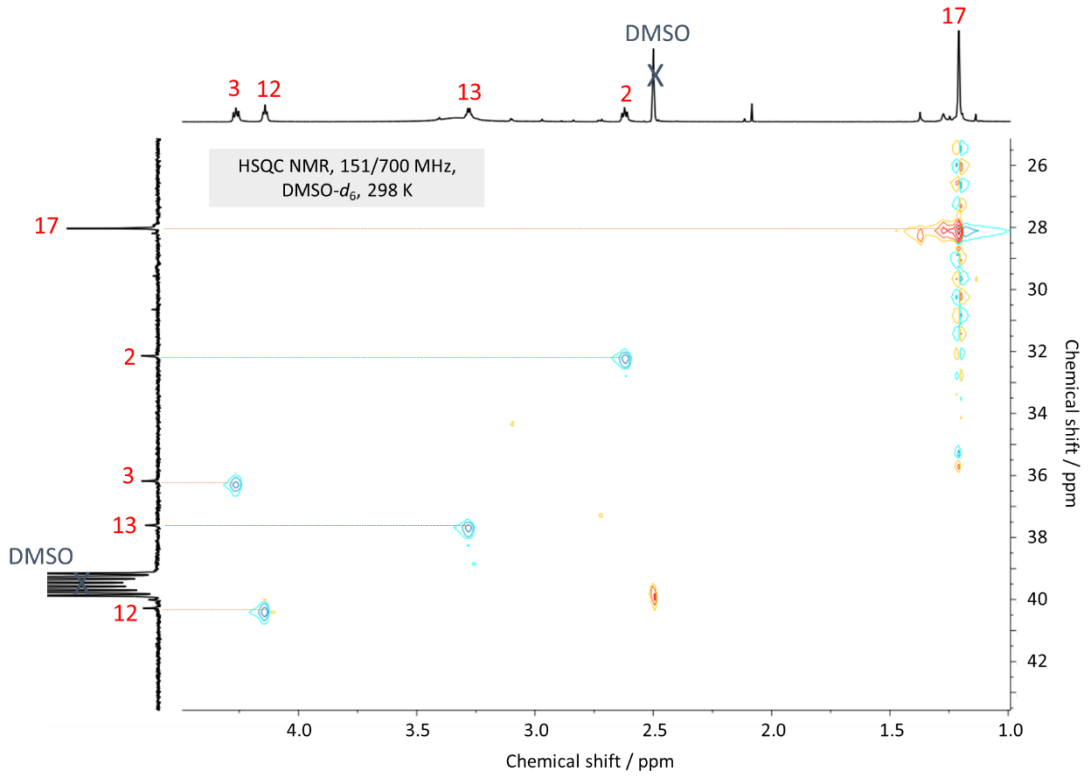

Figure 5.19. Partial ^{1}H–^{13}C HSQC NMR spectrum (151/700 MHz, DMSO-d_6, 298 K) of **5**.

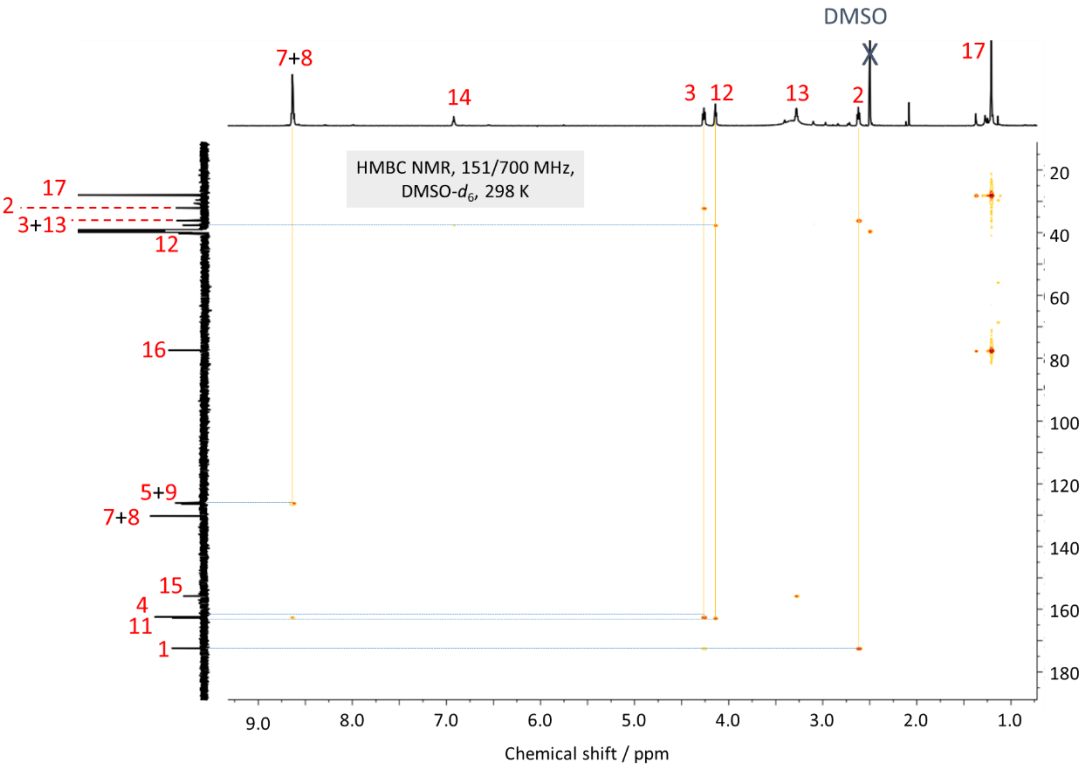

Figure 5.20. Partial ^{1}H–^{13}C HMBC NMR spectrum (151/700 MHz, DMSO-d_6, 298 K) of **5**.

In order to fully assign the ^{1}H and ^{13}C signals of the *C*-activated **AzideAG^{Tfp}** (**18**), we employed 2D NMR spectroscopy. We determined peak assignments through analysis of COSY (Figure 5.21), HSQC (Figure 5.22) and HMBC (Figure 5.23) correlations.

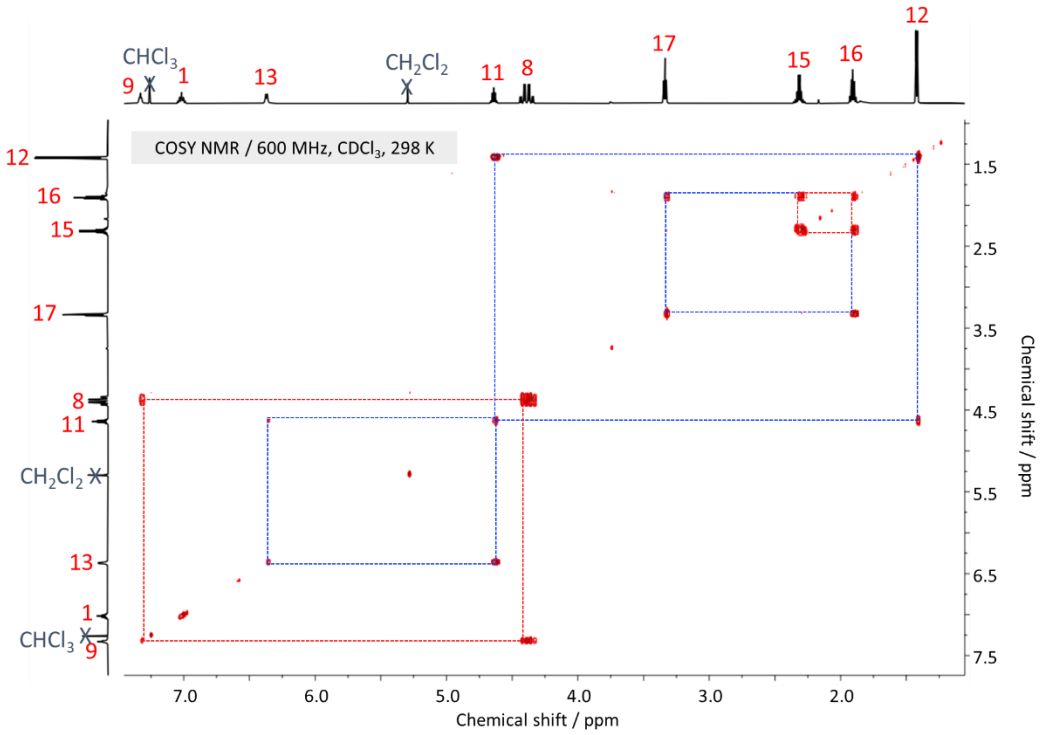

Figure 5.21. Partial ^{1}H–^{1}H COSY NMR spectrum (600 MHz, $CDCl_3$, 298 K) of **18**.

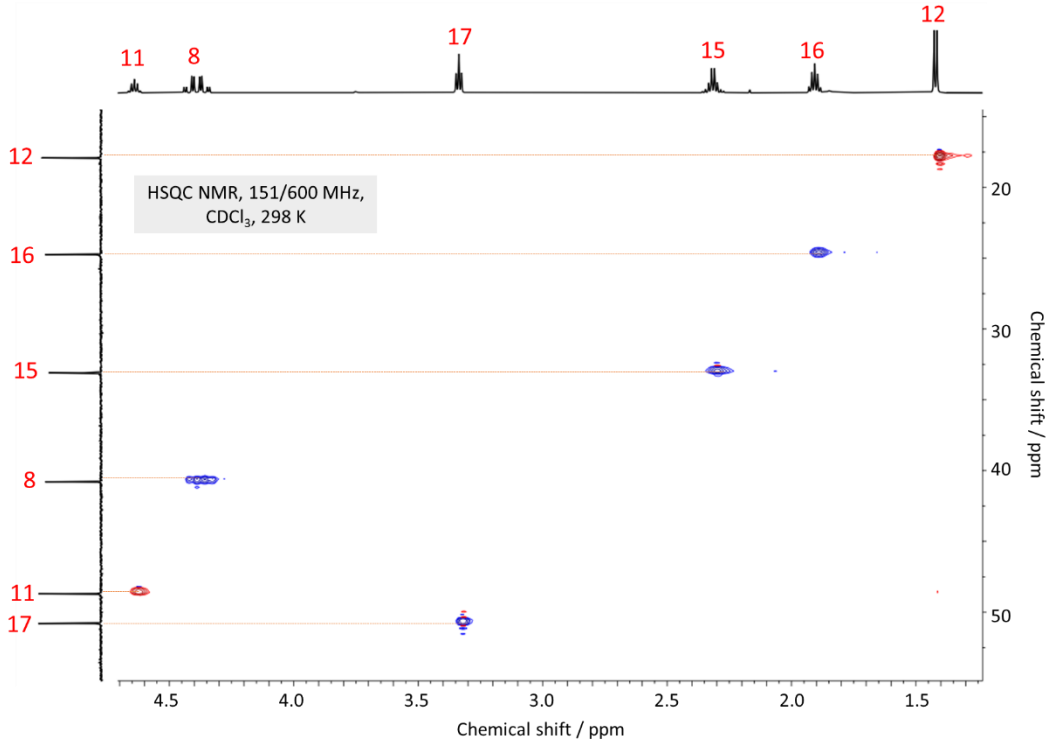

Figure 5.22. Partial $^{1}H–^{13}C$ HSQC NMR spectrum (151/600 MHz, $CDCl_3$, 298 K) of **18**.

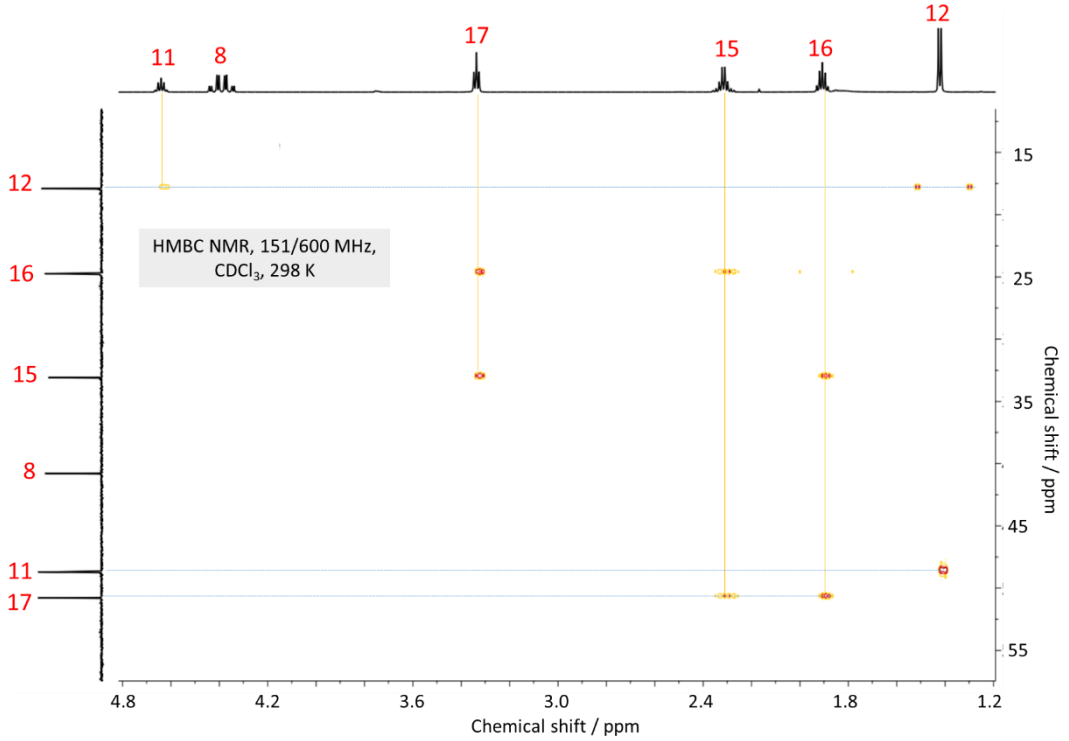

Figure 5.23. Partial $^{1}H–^{13}C$ HMBC NMR spectrum (151/600 MHz, $CDCl_3$, 298 K) of **18**.

With increasing structural order, i.e., intramolecular folding, it became increasingly difficult to fully assign the ^{13}C signal. In order to fully assign the ^{1}H signals of tripeptide **20** as well as **M1**^{DMB}, we employed 2D NMR spectroscopy. We determined peak assignments through analysis of COSY correlations (Figure 5.24/25), in conjunction with signal comparisons with the synthetic pre-cursors.

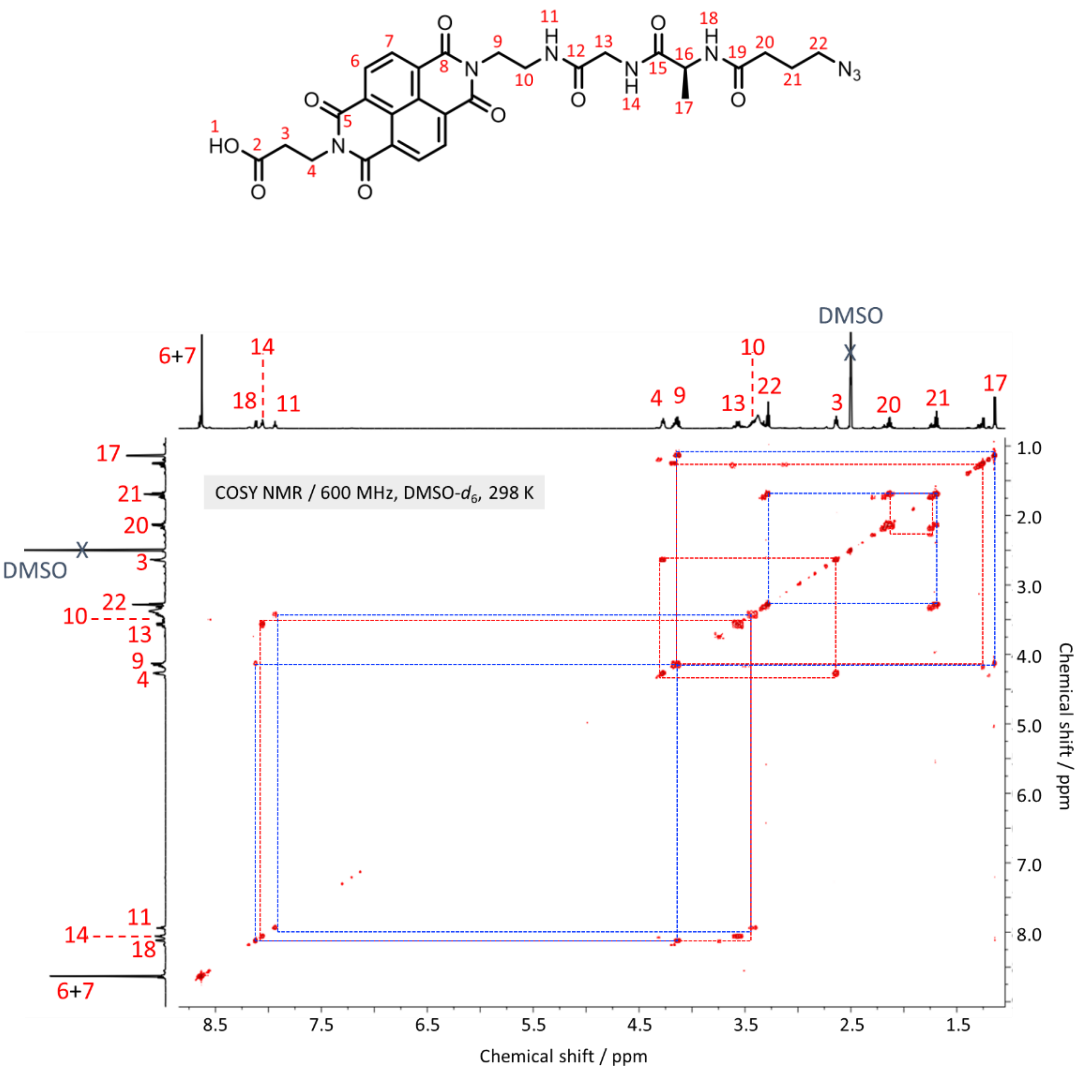

Figure 5.24. Partial ^{1}H–^{1}H COSY NMR spectrum (600 MHz, DMSO-d_6, 298 K) of **20**.

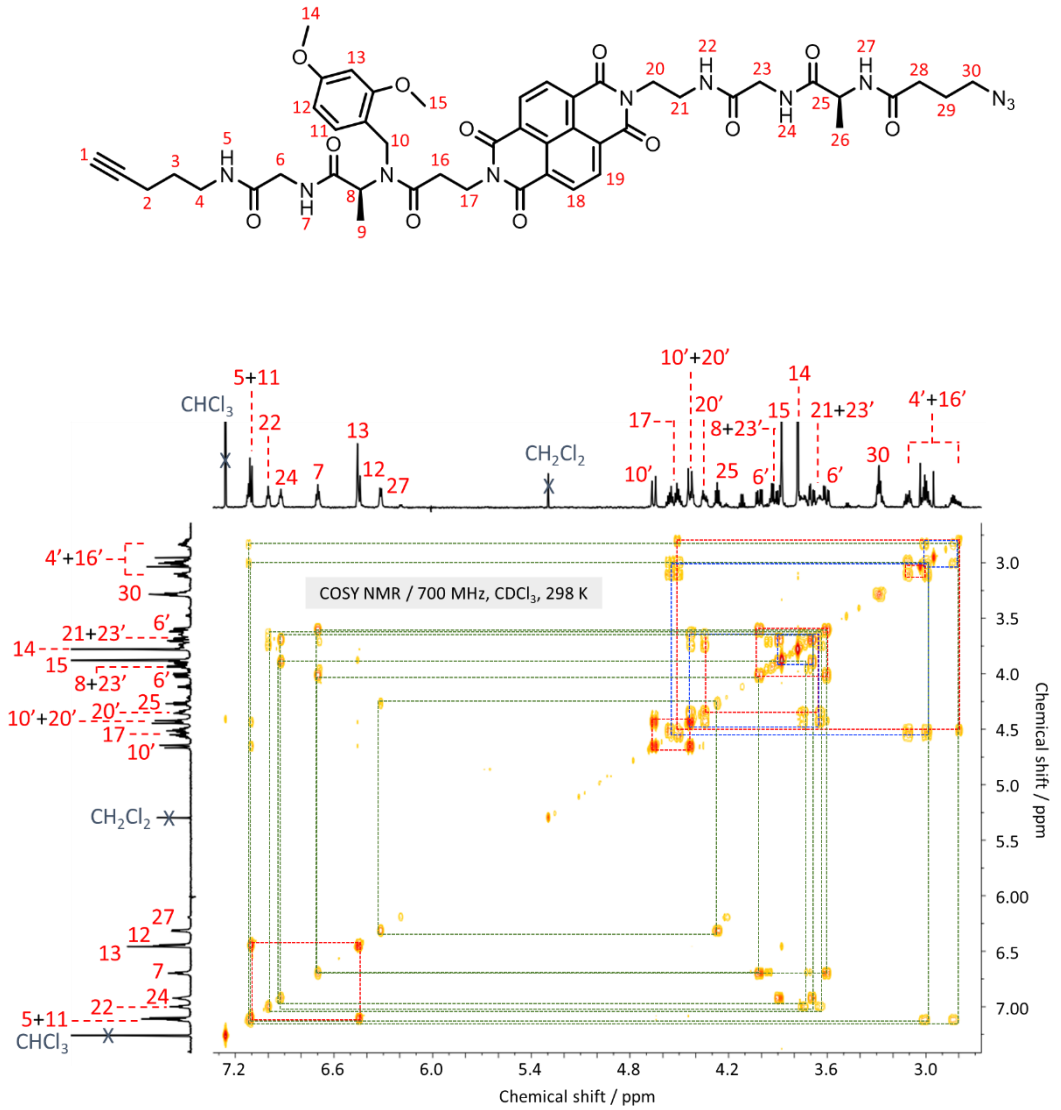

Figure 5.25. Partial ^{1}H–^{1}H COSY NMR spectrum (600 MHz, $CDCl_3$, 298 K) of **M1^{DMB}**. Amide couplings are shown in green for clarity.

In order to fully assign the ^{1}H signals of the control macromonomer **C1^{DMB}**, we employed 2D NMR spectroscopy. However, ^{13}C signals could not be assigned owing to the complexity for **C1^{DMB}**. We first determined peak assignments for the synthetic precursors, **21** (Figures 5.26–28) and **22** (Figures 5.29–31), through analysis of COSY, HSQC, HMBC and NOESY correlations, which enabled us to confidently assign by comparison the analogous peaks present in **C1^{DMB}** (COSY, Figure 5.32).

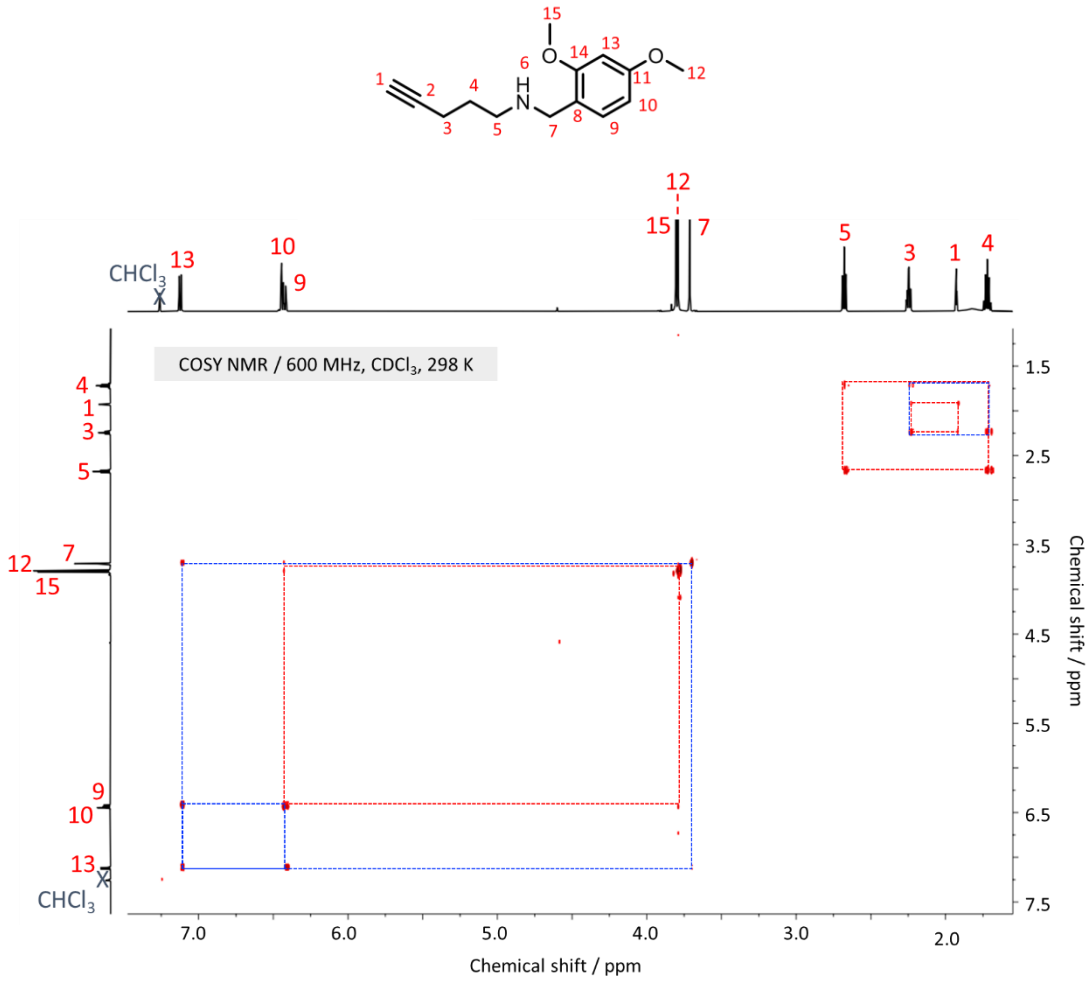

Figure 5.26. Partial ^{1}H–^{1}H COSY NMR spectrum (600 MHz, $CDCl_3$, 298 K) of **22**.

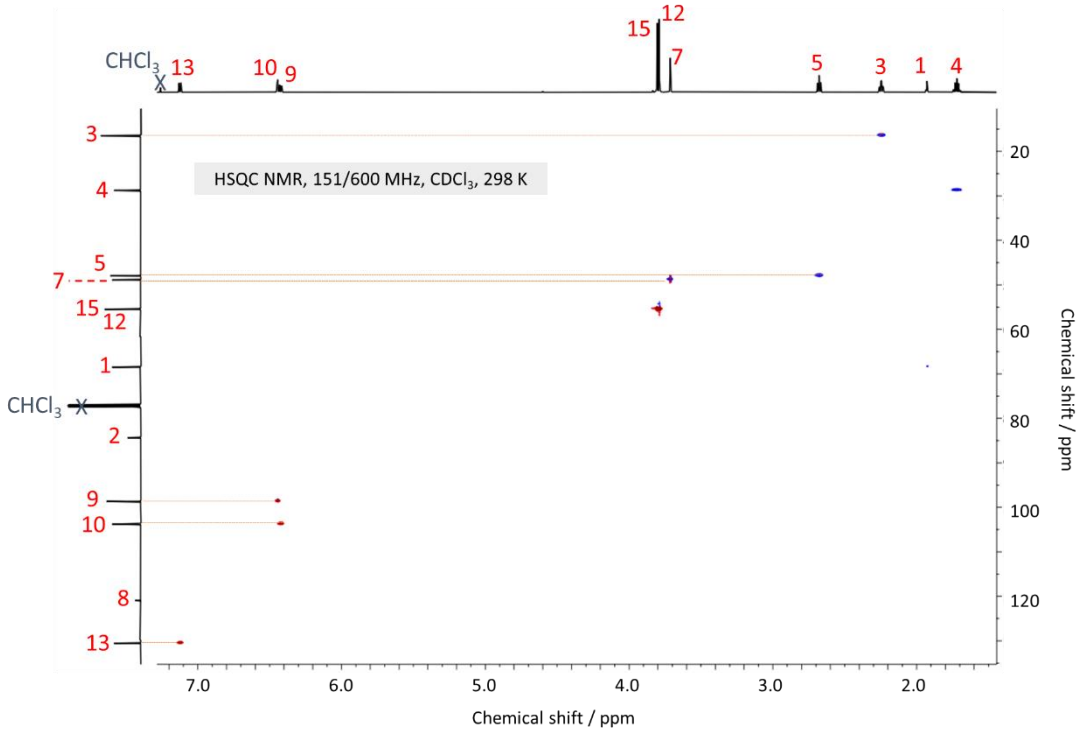

Figure 5.27. Partial ^{1}H–^{13}C HSQC NMR spectrum (151/600 MHz, $CDCl_3$, 298 K) of **22**.

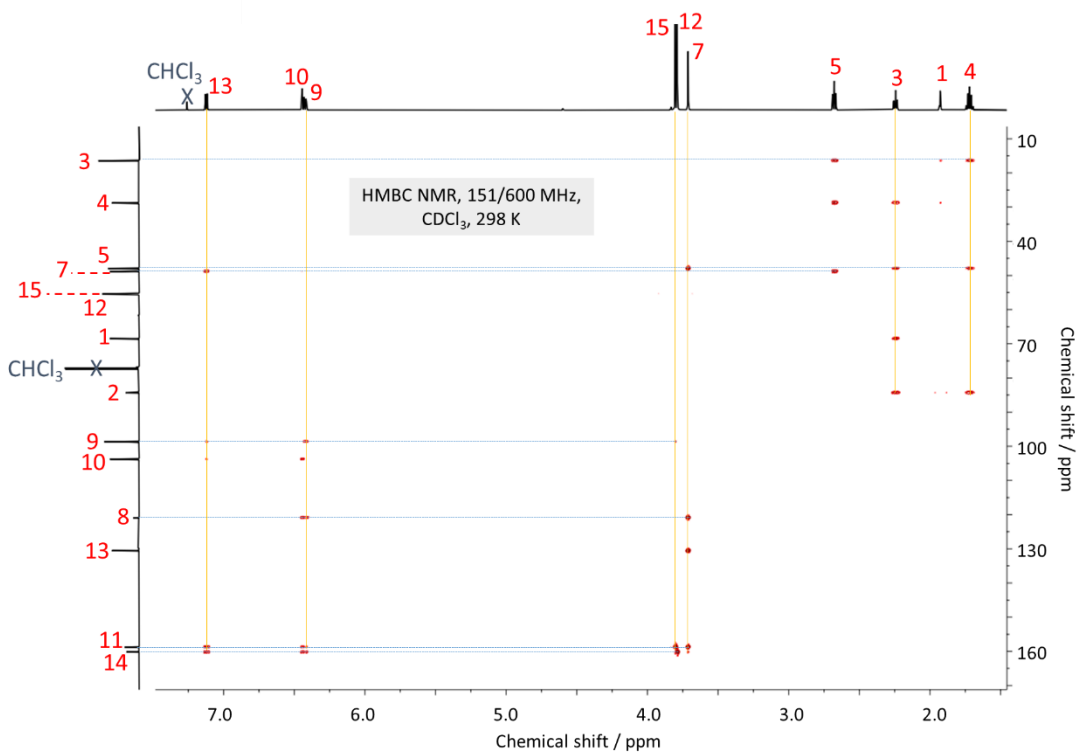

Figure 5.28. Partial ^{1}H–^{13}C HMBC NMR spectrum (151/600 MHz, $CDCl_3$, 298 K) of **22**.

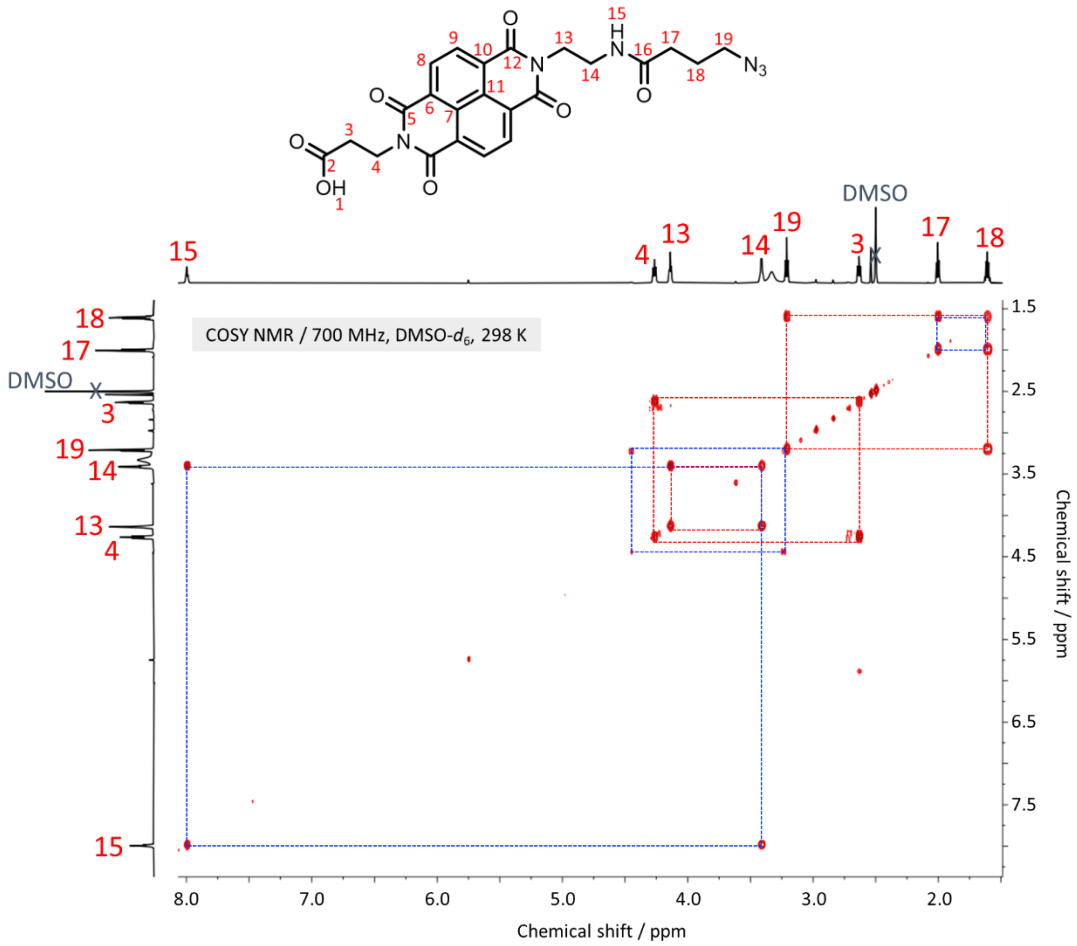

Figure 5.29. Partial ^{1}H–^{1}H COSY NMR spectrum (700 MHz, DMSO-d_6, 298 K) of **21**.

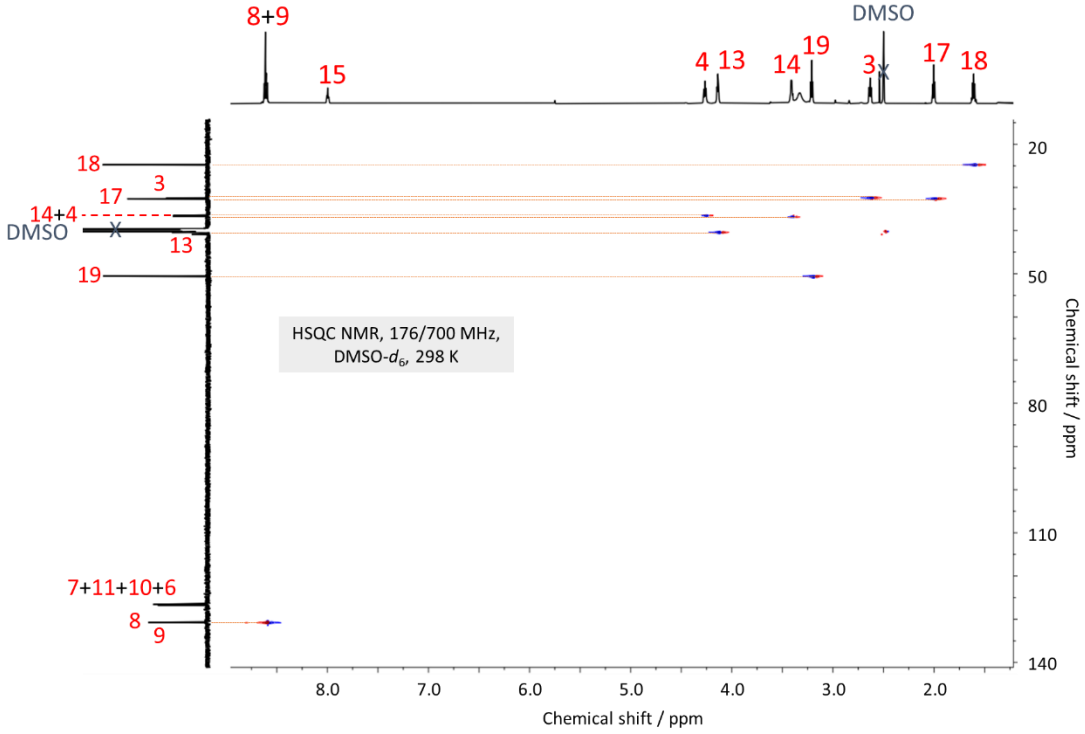

Figure 5.30. Partial ^{1}H–^{13}C HSQC NMR spectrum (176/700 MHz, DMSO-d_6, 298 K) of **21**.

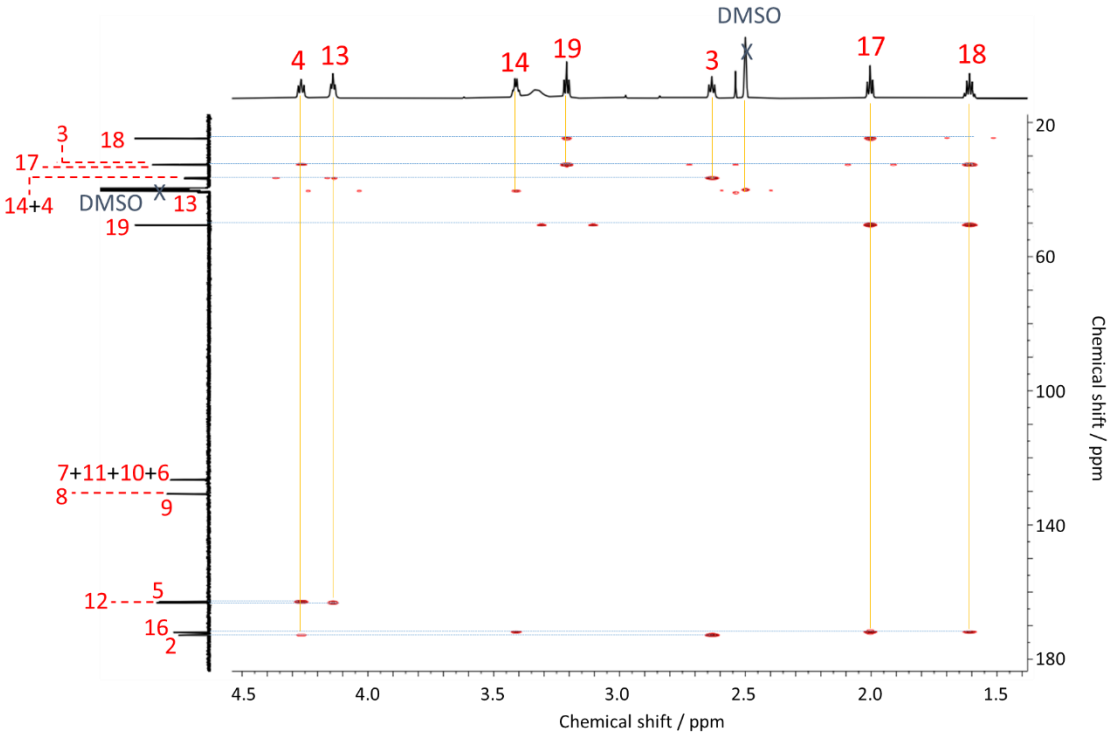

Figure 5.31. Partial ^{1}H–^{13}C HMBC NMR spectrum (176/700 MHz, DMSO-d_6, 298 K) of **21**.

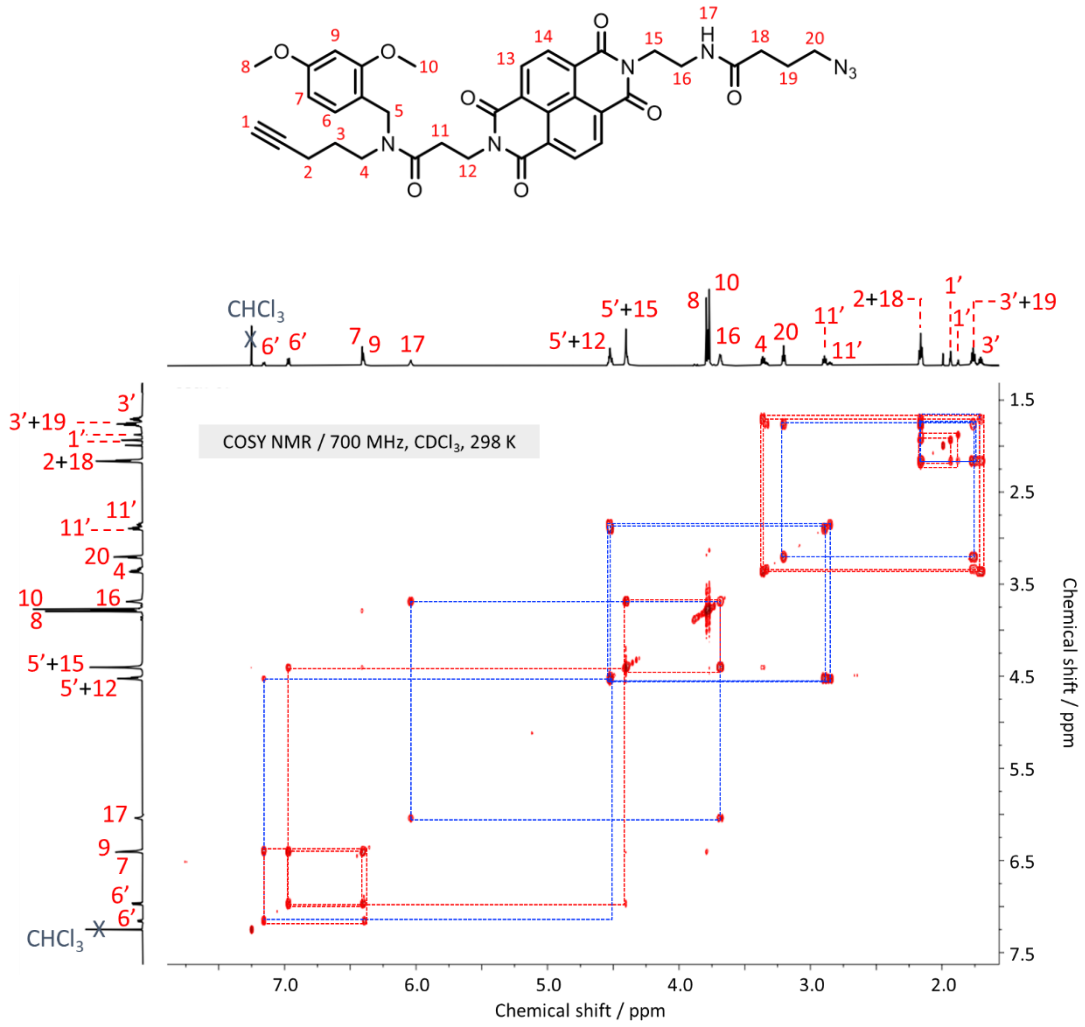

Figure 5.32. Partial ^{1}H–^{1}H COSY NMR spectrum (700 MHz, $CDCl_3$, 298 K) of **C1^{DMB}**.

5.5.2 NMR Spectroscopy

Control macromonomer **C1^{DMB}** exists as two conformations (i.e., rotamers) in $CDCl_3$ (Figure 5.34), with a ratio of ca. 7:3, in favour of what is believed to be as intramolecular aromatic charge transfer interaction between the electron rich dimethoxybenzyl group and the electron poor NDI unit. However, this behaviour is not observed in DMSO-d_6 (Figure 5.33) where only one conformer is present. Intramolecular aromatic CT interactions are usually stabilised in polar solvents such as H_2O and DMSO. However, with only one conformer present in DMSO, there are potential hydrogen bonding[46] or n–π* interactions that prevent a mixture of conformers from forming.

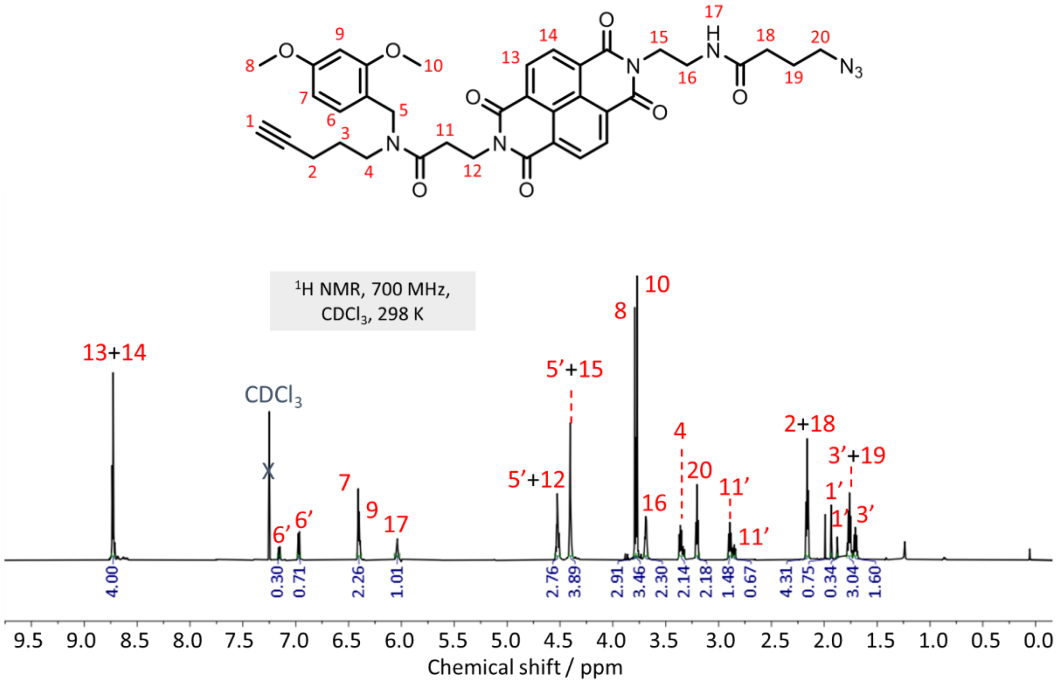

Figure 5.33. ^{1}H NMR spectrum (700 MHz, $CDCl_3$, 298 K) of **C1^{DMB}**.

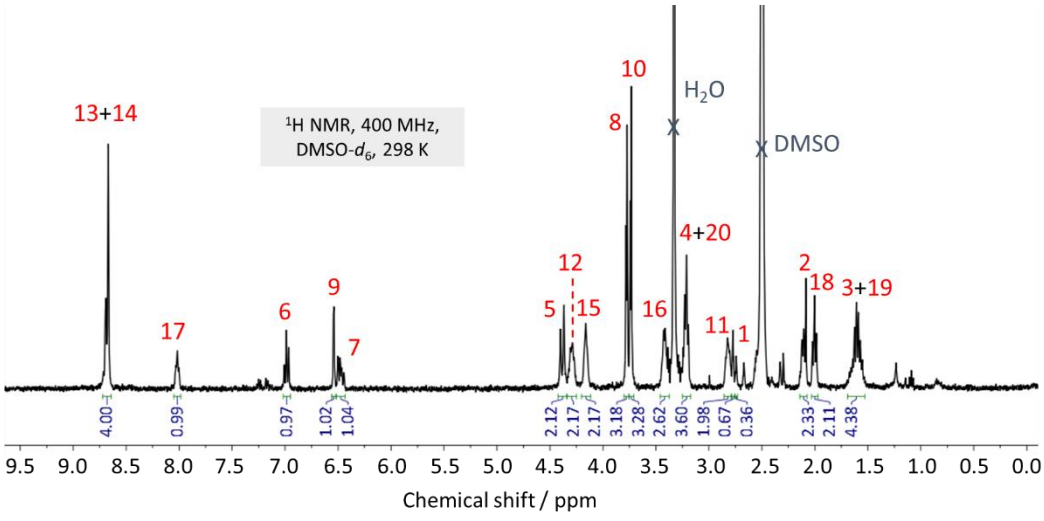

Figure 5.34. ^{1}H NMR spectrum (400 MHz, DMSO-d_6, 298 K) of **C1^{DMB}**.

5.5.3 X-ray Crystallographic Analysis

Analysis of the crystal structure of dipeptide **12** is shown (Figure 5.35) with the crystal system, space group, unit cell parameters reported below. Single crystals of **12** (mono hydrate) were grown from a saturated solution of hot water, confirming the (*S*)-configuration.

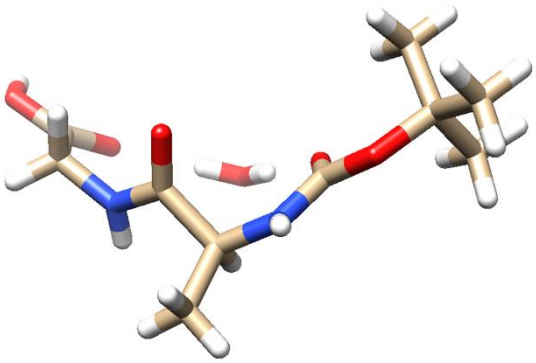

Crystal system: monoclinic

Space group: $P2_1$

Unit Cell Parameters: a = 10.5975(7) Å, b = 6.2531(4) Å, c = 10.9156(7) Å, α = 90°, β = 108.370(3)°, γ = 90°, volume = 686.48(8) $Å^3$, ρ_{cal} g/cm^3 = 1.279, Z = 2, R = 7%.

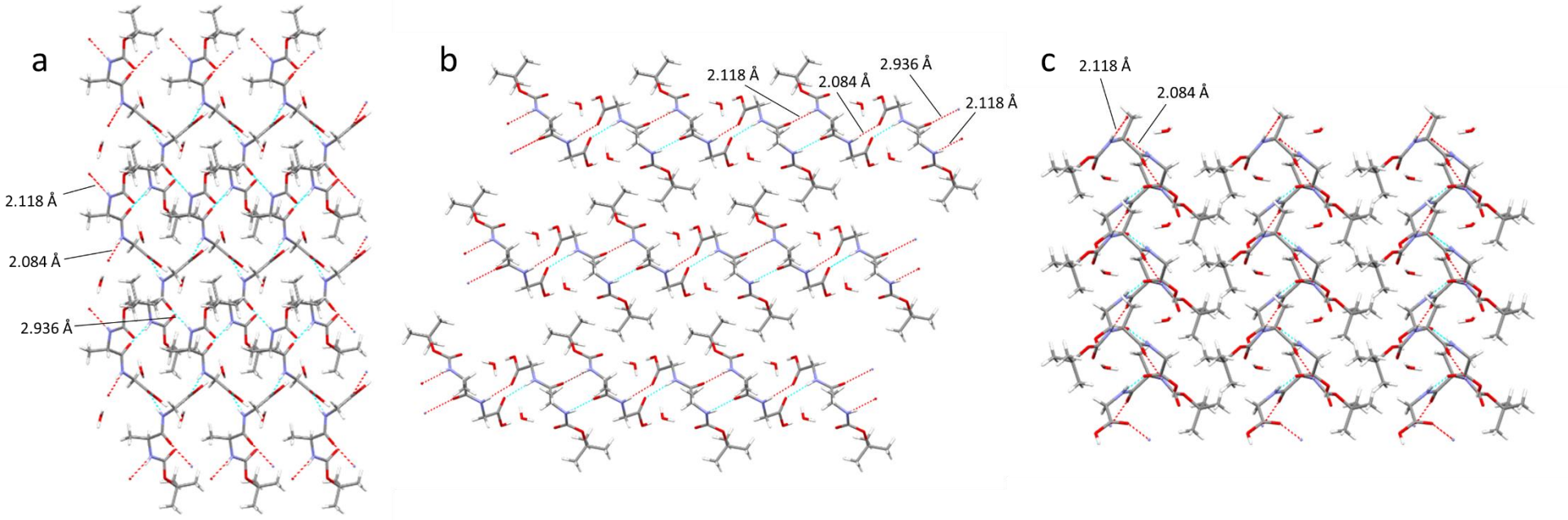

Figure 5.35. Solid-state superstructure of dipeptide **12**. Lattice is made up of 3×3×3 unit cells in order to illustrate the crystal packing that is largely dominated by intrabranch hydrogen bonding, and hydrogen bonding to H_2O molecules. Projections are viewed along the crystallographic a) a-, b) b-, and c) c-axes.

5.5.4 MALDI-TOF

Several matrices (CHCA, DHB, HABA and sinapinic acid) were tested for the deposition of the polymer prior to collecting MALDI-MS spectra. HABA [10 mg/ mL] in THF, spotted with an equal amount of polymer **P1^{DMB}** solution in HFIP gave the best response. Up to seven repeat units were confirmed (Figure 5.36) to have been 'clicked' following the CuAAC polymerisation, all observable as sodiated species.

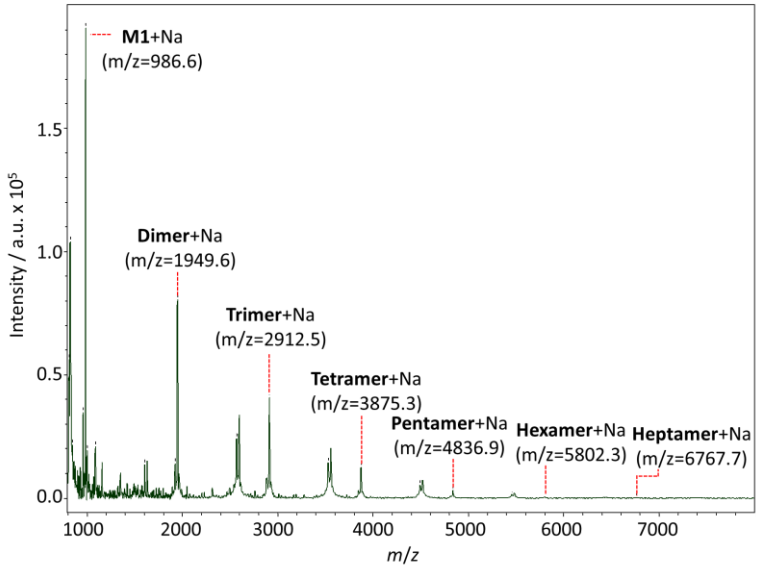

Figure 5.36. MALDI-MS of **P1^{DMB}**, identifying up to the soidated hepatmer (m/z = 6767.7 g/ mol).

5.5.5 GPC

Samples were prepared for SEC analysis by dissolving ca. 2 mg of the polymer in 2 mL DMF for a concentration of ca. 1 mg/ mL. Protected polymer **P1^{DMB}** had a retention volume of 13.55 mL (Figure 5.37) which equates to an M_n of 9,689 gmol^{-1}, as calculated from a calibration of known molecular weight polystyrene

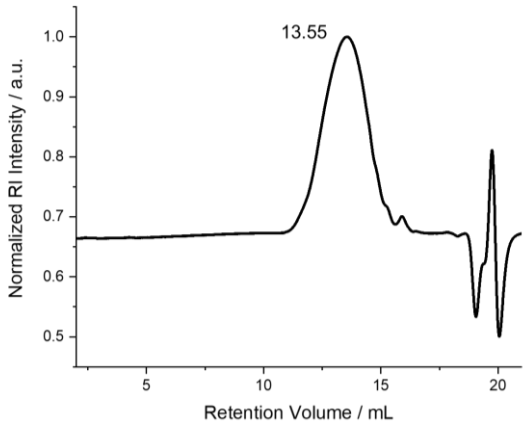

Figure 5.37. GPC trace (RI index) of **P1^{DMB}**, calibrated against polystyrene, M_n of 9,689 gmol^{-1}.

5.6 References

1 K. Liu, A. Levy, C. Liu and J. H. Olivier, *Chem. Mater.*, 2018, **30**, 2143–2150.

2 J. D. Tovar, *Acc. Chem. Res.*, 2013, **46**, 1527–1537.

3 X. Zhao, F. Pan and J. R. Lu, *Prog. Nat. Sci.*, 2008, **18**, 653–660.

4 M. P. Hendricks, K. Sato, L. C. Palmer and S. I. Stupp, *Acc. Chem. Res.*, 2017, **50**, 2440–2448.

5 V. V. Rostovtsev, L. G. Green, V. V. Fokin and K. B. Sharpless, *Angew. Chem. Int. Ed.*, 2002, **41**, 2596–2599.

6 Y. L. Angell and K. Burgess, *Chem. Soc. Rev.*, 2007, **36**, 1674–1689.

7 O. Hakimi, D. P. Knight, F. Vollrath and P. Vadgama, *Compos. Part B Eng.*, 2007, **38**, 324–337.

8 K. Oh and Z. Guan, *Chem. Commun.*, 2006, **0**, 3069–3071.

9 T. Bin Yu, J. Z. Bai and Z. Guan, *Angew. Chem. Int. Ed.*, 2009, **48**, 1097–1101.

10 N. I. Topilina, S. Higashiya, N. Rana, V. V. Ermolenkov, C. Kossow, A. Carlsen, S. C. Ngo, C. C. Wells, E. T. Eisenbraun, K. A. Dunn, I. K. Lednev, R. E. Geer, A. E. Kaloyeros and J. T. Welch, *Biomacromolecules*, 2006, **7**, 1104–1111.

11 W. S. Horne, N. Ashkenasy and M. R. Ghadiri, *Chem. Eur. J.*, 2005, **11**, 1137–1144.

12 C. Hyde, T. Johnson and R. C. Sheppard, *J. Chem. Soc. Chem. Commun.*, 1992, 1573–1575.

13 M. A. McMechen, E. L. Willis, P. C. Gourville and C. Proulx, *Molecules*, 2019, **24**, 1919.

14 V. Armiento, A. Spanopoulou and A. Kapurniotu, *Angew. Chem. Int. Ed.*, 2020, 59, 3372–3384.

15 S. Basak, N. Nandi, K. Bhattacharyya, A. Datta and A. Banerjee, *Phys. Chem. Chem. Phys.*, 2015, **17**, 30398–30403.

16 W.-F. Su, *Principles of Polymer Design and Synthesis*, Springer, Berlin, Heidelberg, 2013, 111–136.

17 J. Yu, D. Qi and J. Li, *Commun. Chem.*, 2020, **3**, 1–14.

18 L. Mao, Y. Hu, Q. Tu, W. L. Jiang, X. L. Zhao, W. Wang, D. Yuan, J. Wen and X. Shi, *Nat. Commun.*, 2020, **11**, 5519.

19 C. Barrère, M. Hubert-Roux, C. M. Lange, M. Rejaibi, N. Kebir, N. Désilles, L. Lecamp, F. Burel and C. Loutelier-Bourhis, *Rapid Commun. Mass Spectrom.*, 2012, **26**, 1347–1354.

20 M. Kumar and S. J. George, *Chem. Eur. J.*, 2011, **17**, 11102–11106.

21 H. Shao, J. Seifert, N. C. Romano, M. Gao, J. J. Helmus, C. P. Jaroniec, D. A. Modarelli and J. R. Parquette, *Angew. Chem. Int. Ed.*, 2010, **49**, 7688–7691.

22 S. Basak, J. Nanda and A. Banerjee, *Chem. Commun.*, 2013, **49**, 6891–6893.

23 M. R. Molla and S. Ghosh, *Chem. Mater.*, 2011, **23**, 95–105.

24 J. Kubelka and T. A. Keiderling, *J. Am. Chem. Soc.*, 2001, **123**, 12048–12058.

25 M. D. Schuh and M. C. Baldwin, *J. Phys. Chem. B*, 2006, **110**, 10903–10909.

26 G. Wei and J. E. Shea, *Biophys. J.*, 2006, **91**, 1638–1647.

27 P. A. Korevaar, C. J. Newcomb, E. W. Meijer and S. I. Stupp, *J. Am. Chem. Soc.*, 2014, **136**, 8540–8543.

28 S. Bayindir, K. S. Lee, N. Saracoglu and J. R. Parquette, *Dalt. Trans.*, 2020, **49**, 13685–13692.

29 C. Aronsson, S. Dånmark, F. Zhou, P. Öberg, K. Enander, H. Su and D. Aili, *Sci. Rep.*, 2015, **5**, 14063.

30 G. Xu, W. Wang, J. T. Groves and M. H. Hecht, *Proc. Natl. Acad. Sci. U. S. A.*, 2001, **98**, 3652–3657.

31 D. Ivnitski, M. Amit, B. Rubinov, R. Cohen-Luria, N. Ashkenasy and G. Ashkenasy, *Chem. Commun.*, 2014, **50**, 6733–6736.

32 P. I. Haris and D. Chapman, *Biopolymers*, 1995, **37**, 251–263.

33 J. De Meutter and E. Goormaghtigh, *Eur. Biophys. J.*, 2021, **50**, 613–628.

34 G. Zandomeneghi, M. R. H. Krebs, M. G. McCammon and M. Fändrich, *Protein Sci.*, 2009, **13**, 3314–3321.

35 T. Miyazawa and E. R. Blout, *J. Am. Chem. Soc.*, 1961, **83**, 712–719.

36 A. J. Avestro, D. M. Gardner, N. A. Vermeulen, E. A. Wilson, S. T. Schneebeli, A. C.

Whalley, M. E. Belowich, R. Carmieli, M. R. Wasielewski and J. F. Stoddart, *Angew. Chem. Int. Ed.*, 2014, **53**, 4442–4449.

37 S. Basak, N. Nandi, S. Paul and A. Banerjee, *ACS Omega*, 2018, **3**, 2174–2182.

38 I. Tabakovic, L. L. Miller, R. G. Duan, D. C. Tully and D. A. Tomalia, *Chem. Mater.* 1997, **9**, 736–745.

39 A. M. Sanders, T. J. Magnanelli, A. E. Bragg and J. D. Tovar, *J. Am. Chem. Soc.*, 2016, **138**, 3362–3370.

40 A. Roldão, M. C. M. Mellado, J. C. Lima, M. J. T. Carrondo, P. M. Alves and R. Oliveira, *PLoS Comput. Biol.*, 2012, **8**, e1002367.

41 Y. Liu, Y. Zhang, Z. Wang, J. Wang, K. Wei, G. Chen and M. Jiang, *J. Am. Chem. Soc.*, 2016, **138**, 12387–12394.

42 M. Foroozandeh, R. W. Adams, N. J. Meharry, D. Jeannerat, M. Nilsson and G. A. Morris, *Angew. Chem. Int. Ed.*, 2014, **53**, 6990–6992.

43 O. V. Dolomanov, L. J. Bourhis, R. J. Gildea, J. A. K. Howard and H. Puschmann, *J. Appl. Crystallogr.*, 2009, **42**, 339–341.

44 G. M. Sheldrick, *Acta Crystallogr. Sect. A.*, 2008, **64**, 112–122.

45 G. Naturale, M. Lamblin, C. Commandeur, F. X. Felpin and J. Dessolin, *Euro. J. Org. Chem.*, 2012, **2012**, 5774–5788.

46 G. M. Prentice, S. I. Pascu, S. V. Filip, K. R. West and G. D. Pantoş, *Chem. Commun.*, 2015, **51**, 8265–8268.

47 B. T. Worrell, J. A. Malik and V. V. Fokin, *Science.*, 2013, **340**, 457–460.

Chapter 6|
Summary and Outlook

This Thesis has highlighted the recent advances in using macromolecular scaffolds to guide aromatic π-assembly, focusing on the emergent optoelectronic properties that may be exploited in future devices—all the work displayed here was achieved in the period of May 2017–August 2021. At the outset of the research discussed in this Thesis a number of different approaches to guiding π-assemblies were acknowledged that have served as a springboard for much of the work discussed herein. The use of three-dimensional (3D) fullerene scaffolds has been explored for mediating π-assembly that allows for access to unique optical and electronic properties. In pursuit of one-dimensional (1D) π-aromatic assembly, supramolecular assemblies based on multicomponent peptide–π-conjugates have been recognised as attractive strategies that can be exploited in macromolecular systems for 1D ordering of functional aromatic units. During the same time frame of this thesis, advances in the synthesis of macromolecular architectures have been reported which in turn can be exploited for guiding aromatic π-interactions in space.

Chapter 2 of this Thesis described the synthesis and π-assembly investigations of a naphthalene diimide (NDI) substituted fullerene hexakis-adduct. The 3D fullerene scaffold pre-organises the pendant NDI units and restricts their movement in space which enforces intramolecular NDI aggregation. The electronic couplings between NDI units are preserved upon reduction with extended mixed-valence NDI stacks evidence by IR bands in the absorption spectra. Furthermore, the tethering of the NDI units by the scaffold helps to observe Coulombically repulsive NDI radical–radical interactions. These NDI radical π-interactions are usually only observable in rigid, covalent systems or under the influence of the hydrophobic effect and therefore this system provides an unexplored avenue to achieving π-assembly of reduced NDI units in a flexible and organic soluble system.

A fullerene hexakis-adduct has also been decorated with electron rich tetrabenzofluorene (TBF) units to investigate the intramolecular π-assembly of the TBF units in 3D space and the energy transfer properties with the fullerene acceptor core. In Chapter 3 a fully decorated TBF fullerene hexakis-adduct and a disubstituted [5:1] fullerene hexakis-adduct have been synthesised and their photophysical properties characterised. The light harvesting properties of the fullerenes were confirmed with energy transfer between the TBF units and fullerene core proceeding *via* a Förster resonance energy transfer (FRET) mechanism. Furthermore, FRET was increased for the fully decorated TBF-substituted fullerene in comparison to the disubstituted analogue which is suggestive of a “multivalent” effect. Despite the first synthesis of TBF in 1960, these studies are some of the first to explore the photodonor properties in pursuit of functional organic materials. A system with an appropriately matched acceptor may allow for electron transfer processes that can be exploited for various applications in organic electronics.

The functionalised fullerenes investigated for their fundamental optoelectronic properties in Chapters 2 and Chapter 3 have been integrated into devices that are described in Chapter 4. Space-charge-limited diodes were fabricated and the electron only mobility quantified for devices containing active layers of the NDI fullerene compound as well structurally related NDI analogues. It was discovered that the fullerene hexakis-adduct molecules had poor charge mobility with the model NDI compounds having higher performance. The poor performance of the NDI fullerene is believed to be as a result incomplete charge transport pathways between the NDI units in 3D space. However, these observations are crucial to rationalising the potential charge transport properties in acceptor fullerene hexakis-adducts based on NDI. A larger aromatic unit, such as perylene diimide, may facilitate greater charge transfer properties when decorated around a fullerene hexakis by completing the charge transfer pathways that eluded the NDI-substituted fullerene. On the other hand, the TBF-decorated fullerene improved the performance of a metal oxide catalyst for dye degradation experiments. As a composite, the TBF-functionalised fullerene increased the rate of dye degradation and decreased the photodegradation properties of ZnO. We currently believe the increased efficacy is as a result of the efficient transport of electrons from the fullerene TBF units to ZnO. This process prevents recombination of holes and electrons and therefore increases the amount of degrading species such as hydroxyl radicals that ultimately break down dye molecules. This study demonstrates the first time a fullerene hexakis-adduct has been used to increase the performance of a metal oxide for photocatalysis—these observations should inspire the implementation of other functionalised fullerene derivatives in such applications. Increasing the local concentration of TBF molecules——or the use of another suitable donor—around the fullerene hexakis could pave the way for devices with increased photocatalytic performance.

In pursuit of 1D assembly of aromatic π-systems, Chapter 5 describes the synthesis and characterisation of a NDI-embedded polypeptide that is designed to fold into β-sheets that have hierarchical ordering. A convergent route is used to synthesise high molecular weight polymers from a macromonomer that is poised of Cu(I)-catalysed azide–alkyne cycloaddition polymerisation. The polymerisation instils an artificial β-turn mimic that induces a partial folding to the polypeptide in an antiparallel arrangement of strands with CD and UV-Vis spectroscopies revealing the macromolecular scaffold facilitates NDI couplings that are not present in the lone macromonomer. The desired folding of the polypeptide into β-sheet assemblies is anticipated following removal of a hydrogen-bond blocking group that is initially used to increase polymer solubility as well as instil the stimuli responsive properties. Currently, there is preliminary evidence to suggest the NDI-embedded polypeptide can fold into β-sheets and this work is underway within the group. It is still uncommon to achieve hierarchical ordering in the macromolecular assembly of optoelectronic materials, however, the strategy

employed here provides a route that can be adapted to various photo- and/or redox-active units that can be 'embedded' in the polymer. Following this proof-of-concept, various homopolymers and hetropolymers, such as donor–acceptor arrays, will allow for properties such as photoinduced energy transfer and conductivity.

The assembly of π-surfaces—whether by intramolecular interactions or intermolecular multicomponent ensembles—can lead to emergent optical, electronic and electrochemical properties that are not present in the lone molecules. Arguably the most popular strategy for assembling aromatic π-surfaces is through supramolecular assemblies that make use of non-covalent interactions in multicomponent systems. However, these assemblies have inherent limitations such as their sensitivity to pH, moisture, temperature, stress, etc., as well the difficulty in controlling nanoscale morphologies. Mediating π-assembly *via* macromolecular scaffolds can help to overcome some of these issues by providing access to, i) more robust materials owing to the macromolecular sizes, ii) more reliable assembly processes, iii) materials that have hierarchical ordering (i.e., multiple levels of assembly) and iv) materials that have advanced functioning. There is still room to broaden the scope of macromolecular π-assembly to study fundamental π-interactions. This strategy to mediate the assembly of functional aromatic units is still in its nascency and we have just scratched the surface in regards to exploring the fundamental properties that are bestowed upon multivalent, redox-active macromolecular materials. We are yet to tap into the full potential of this field, however, this Thesis highlights the strides we have taken towards this goal.

PHILIP A. HOPE

Address 4 Appley Terrace, Sunderland, SR6 0NR, UK
Tel +44 7882611413 **Email** mailto:philip.a.hope@durham.ac.uk

ACADEMIC & INDUSTRIAL CAREER

PhD SOFI CDT
Durham University
Durham, England
Sep 2016 – present

Advisors – Dr Alyssa-Jennifer Avestro & Asst. Prof. Paul R. McGonigal
Controlling π-Interactions Using Three-Dimensional Synthetic and Biomimetic Scaffolds for Optoelectronic Organic Materials.

SGS – Analytical Chemist
SGS United Kingdom Limited
Macklin Avenue, Billingham, England
June 2015 – July 2016

Supervisor – Andrew Nimmo
Quality control for the world's leading inspection, verification, testing and certification company for Oil, Gas and Chemicals.

L'Oréal – Internship
L'Oréal Hair Research Centre
Paris, England
Sept 2013 – June 2014

Supervisor – Yann Waye Keuong
The development of a method involving the use of microwaves to accelerate the hydrolysis of human hair proteins.

Master of Chemistry – 1st Class Honours
The University of Manchester
Manchester, England
Sept 2011 – June 2015

Advisor – Dr Simon Webb
Aggregation Studies of Thioester-Doped-Vesicles; Using Native Chemical Ligation to Make Inter-Membrane Linkages.

A-levels/AS-levels
A-levels in: Biology, Chemistry and Sport
AS-levels in: Philosophy and Ethics & Maths
St. Aidan's Sixth Form, Sunderland, England
Sep 2009 – July 2011

GCSEs
13 A*-A GCSEs gained, including: English Language, English Literature, Mathematics, Physics, Chemistry, Biology & French.
St. Aidan's Secondary School, Sunderland, England
Sep 2004 – Jul 2009

RESEARCH EXPERIENCE

PhD in Chemistry
Durham University,
Stockton Road, County Durham,
DH1 3LE, England

The key aims of my PhD have been to (i) achieve the multi-step chemical syntheses of high molecular weight organic molecules, (ii) investigate their fundamental properties and (iii) where appropriate, validate their function in prototypical devices. I have developed expertise in the synthetic methodology of planar (NDI, perylene, pyrene) and non-planar (C_{60} and TBF) aromatic molecules, in addition to peptide, glovebox and 'click' chemistry techniques; ^{1}H, ^{13}C, 2D NMR, HRMS, MALDI, CHN, GPC. Studying their self-assembly, I have become proficient in collecting data: UV, PL, IR, CD, SEC, CV and SEM for their properties analysis.

L'Oréal – Finished Products and Quality Control Analyst
L'Oréal Hair Research Centre
13 Rue Dora Maar, Saint-Ouen,
93400, France

Routine work for the analytical department was conducted throughout the year. As a large proportion of work involved separating and quantifying the constituent amino acids of hair proteins I became proficient in method development for techniques such as HPLC and UPLC. I was responsible for the upkeep of the machines and their servicing throughout my time there. My main project involved developing a microwave-assisted method for hydrolyzing hair proteins whilst avoiding sample degradation — this was achieved and implemented within my time there.

Master of Chemistry
The University of Manchester
Oxford Road, Manchester
M13 9PL, England

My final year MChem project, based in the Manchester Institute of Biotechnology (MIB), was to (i) synthesize a small library of cysteine-containing linkers, (ii) measure the kinetics (UV) of a native chemical ligation reaction between the cysteine-linkers and a synthetic lipid and (iii) make synthetic vesicles and monitor their aggregation using fluorescence microscopy and UV — rate constants were calculated from the raw UV data.

PUBLICATIONS

3. Arnold, F. H. N.; Hope, P. A.; Yerramsetti, P.; Mothika, V. S. 'Homoconjugation in Aromatic Molecules'. *Manuscript in Preparation.*
2. Munusamy, K.; Hope, P. A.; Ramar, P.; Boopathi, A.A.; Sampath, S.; Avestro, A.-J.; Samanta; D. 'Controlled Decoration of Fullerene by butterfly-shaped Molecule: Self-assembly and Unusual Efficacy in Photocatalytic Dye Degradation'. *Manuscript in Preparation.*
1. Hope, P. A.; Palacios-Gomez, D. A.; Munusamy, K.; Semanta, D.; Groves, C.; Avestro, A.-J. 'A Multi-Electron Redox Acceptor with a Fullerene Core: Evaluating Charge Transfer in Acceptor Hybrids'. *Manuscript in Preparation.*

AWARDS, GRANTS & SCHOLARSHIPS

February 2021	**St Mary's College, Principal's Grant —** Funding of £100 to attend an international chemistry conference (online).
July 2020	**The Soft Matter Showcase 2020 — Poster Prize** | **'**Multivalent Fullerene Adducts for Functional Materials', poster prize (£100) for best overall poster presentation.
Dec 2019	**Royal Society of Chemistry Travel Bursary (Intercontinental)** | Grant of £400 to disseminate research at an international chemistry conference.
Dec 2018	**Royal Society of Chemistry Travel Bursary (Continental)** | Grant of £280 to disseminate research at supramolecular chemistry conference, Supr@Lyon.
Mar 2018	**Chemical Nanoscience Symposium — Poster Prize** | 'Macromolecular Assembly of π-Embedded Synthetic Polypeptides', poster prize winner (£150) for best overall poster presentation.
April 2016	**EPSRC-Funded SOFI CDT Studentship —** Fully funded, 48 month PhD studentship to study at Durham University, Cohort 3. Including £10,000 travel bursary.
Mar 2013	**ERASMUS$^+$ Grant** | University fee waiver (1 year) and living cost bursary (£3000) to undertake a work placement in the EU.

TEACHING & LEADERSHIP EXPERIENCE

Research Supervision & Mentoring | One summer student (F. Arnold, Jun 2016 – Sep 2016 and Jun 2017 – Sep 2017), one MChem student (A. Rebasa-Vallverdu, Jun 2016 – April 2017), one MChem student (I. Fox, Sep 2016 – April 2017), one summer student (A. Carrick, Jun 2018 – Sep 2018 and Jun 2019 – Sep 2019) have been supervised and mentored throughout my time at Durham University as part of the Avestro and McGonigal groups.

Laboratory Demonstrating | Organic chemistry; have completed over 150 hours of demonstrating for the 3rd year organic chemistry laboratories (up to 60 students), marking of pre-lab assessments at Durham University (2018, 2019 & 2020).

Problem Sessions — Outreach | Designing fun science experiments for children (ages 9–11) and leading the demonstrations on school visits to the university.

Workshops | Assisting with workshops to help classes of 1st year undergraduates (up to 60 students) understand the chemistry software ChemDraw (2018).

SYNERGISTIC & EXTRACURRICULAR ACTIVITIES

Member of the Royal Society of Chemistry | Elected full member in 2020.

The University of Manchester Alumni Society | Member since 2016.

SOFI CDT Outreach Representative | Jun 2017 – present.

Chemistry Outreach and Science Communication Participant | Durham University Schools Science Festival, April 2017 & 2018.

Student Ambassador at the University of Manchester | Sept 2012 – June 2013 and Sept 2014 – April 2015.

Sunderland Association Football Club — Supporters member and season ticket holder.

Charity Work — Sponsored walking and running events.

Conferences & Symposia

21. International Symposium on Suprabiomolecular Systems, (online). 2021| **Attended.**
20. RSC Organic Division Online Symposium (UK, online). 2020 | **Oral Presentation.**
19. The Soft Matter Showcase (UK, online). 2020 | **Poster Presentation.**
18. Oxford Synthesis Summer Conference 2020 (UK, online). 2020 | **Attended.**
17. RSC Macrocyclic and Supramolecular Chemistry Meeting, Canterbury (UK). 2019 | **Poster Presentation.**
16. Early Stage Career Researcher Meeting: RSC Macrocyclic and Supramolecular Chemistry Meeting, Lincoln (UK). 2019 | **Poster Presentation.**
15. International Symposium on Suprabiomolecular Systems 2019, Barcelona (Spain). 2019 | **Poster Presentation.**
14. NEPIC Technology Showcase Event 2019 Oral presentation, Middlesbrough (UK). 2019 | **Oral Presentation.**
13. Functional Organic Materials Symposium, Durham (UK). 2019 | **Attended.**
12. Durham University Chemistry Postgraduate Gala, Durham (UK). 2019 | **Oral Presentation.**
11. SUPR@LYON, Lyon (France). 2018 | **Poster Presentation.**
10. ACS ON CAMPUS, Durham (UK). 2018 | **Attended.**
9. Mini MBA with Durham Business School, Durham (UK). 2018 | **Course Attended.**
8. Soft Matter Showcase, Edinburgh (UK). 2018 | **Poster Presentation.**
7. MULTI-APP Marie Curie Network Symposium, Padova (Italy). 2018 | **Poster Presentation.**
6. Chemical Nanoscience Chem, Newcastle (UK). 2018 | **Poster Presentation.**
5. Durham University Chemistry Postgraduate Gala, Durham (UK). 2018 | **Poster Presentation.**
4. Early Stage Career Researcher Meeting: RSC Macrocyclic and Supramolecular Chemistry Meeting. Southampton (UK). 2017 | **Poster Presentation.**
3. Early Stage Researcher Meeting: The Protein and Peptide Science Group, Durham (UK). 2017 | **Oral Presentation.**
2. European Symposium on Organic Reactivity, Durham (UK). 2017 | **Poster Presentation.**
1. International Symposium on Macrocyclic and Supramolecular Chemistry, Cambridge (United Kingdom). 2017 | **Poster Presentation.**

Personal

Born December 7th, 1992, Sunderland, England
Nationality British
Languages English (native speaker), French (intermediate)

References

Dr. Alyssa-Jennifer Avestro
Lecturer (Hon.) in Molecular Materials Chemistry
The University of York
Heslington, York, YO10 5DD, UK
Email alyssa-jennifer.avestro@york.ac.uk
Tel +44 1904 328962

Dr. Simon Webb
Reader in Chemistry
The University of Manchester
Oxford Road, Manchester, M13 9PL, UK
Email S.Webb@manchester.ac.uk
URL http://www.webblab.org

Asst. Prof. Paul R. McGonigal
Assistant Professor in Organic Chemistry
The University of Durham
Stockton Road, County Durham, DH1 3LE, UK
Email paul.mcgonigal@durham.ac.uk
URL http://mcgonigalgroup.com

Andrew Nimmo
Laboratory Supervisor
SGS United Kingdom Limited
Billingham, Co Durham, TS23 4BY, UK
Email Andrew.Nimmo@sgs.com
Tel +44 1642 561612